Advances in Computational Fluid Dynamics
Vol. 3

Lattice Boltzmann Method and its Applications in Engineering

Zhaoli Guo • Chang Shu

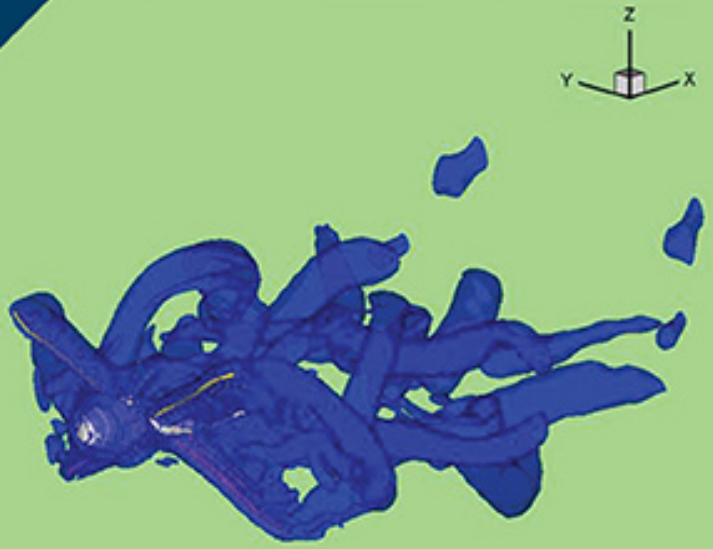

World Scientific

Lattice Boltzmann Method
and its Applications in Engineering

Advances in Computational Fluid Dynamics

Editors-in-Chief: Chi-Wang Shu *(Brown University, USA)* and Chang Shu *(National University of Singapore, Singapore)*

Published

Vol. 2 Adaptive High-Order Methods in Computational Fluid Dynamics
edited by Z. J. Wang (Iowa State University, USA)

Vol. 3 Lattice Boltzmann Method and Its Applications in Engineering
by Zhaoli Guo (Huazhong University of Science and Technology, China) and Chang Shu (National University of Singapore, Singapore)

Forthcoming

Vol. 1 Computational Methods for Two-Phase Flows
by Peter D. M. Spelt (Imperial College London, UK), Stephen J. Shaw (X'ian Jiaotong – University of Liverpool, Suzhou, China) & Hang Ding (University of California, Santa Barbara, USA)

Advances in
Computational Fluid Dynamics
Vol.
3

Lattice Boltzmann Method
and its Applications in Engineering

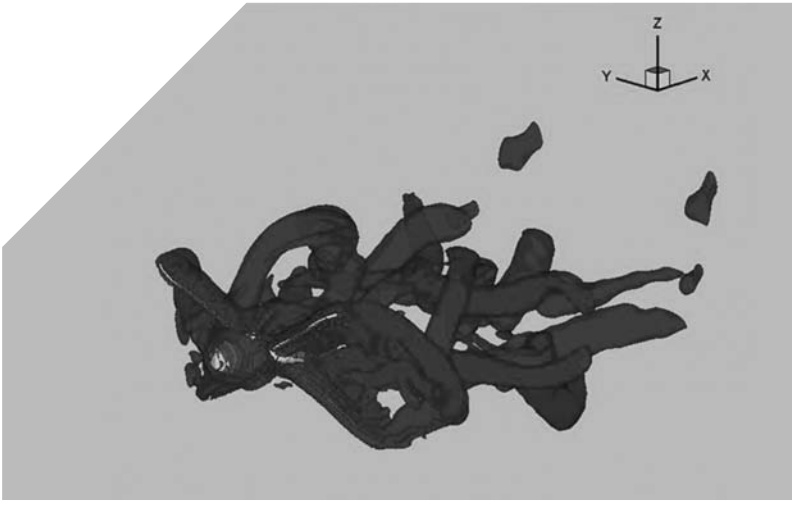

Zhaoli Guo
Huazhong University of Science and Technology, China
Chang Shu
National University of Singapore, Singapore

World Scientific
NEW JERSEY • LONDON • SINGAPORE • BEIJING • SHANGHAI • HONG KONG • TAIPEI • CHENNAI

Published by

World Scientific Publishing Co. Pte. Ltd.

5 Toh Tuck Link, Singapore 596224

USA office: 27 Warren Street, Suite 401-402, Hackensack, NJ 07601

UK office: 57 Shelton Street, Covent Garden, London WC2H 9HE

British Library Cataloguing-in-Publication Data
A catalogue record for this book is available from the British Library.

Advances in Computational Fluid Dynamics — Vol. 3
LATTICE BOLTZMANN METHOD AND ITS APPLICATIONS IN ENGINEERING

ISBN 978-981-4508-29-2

Printed in Singapore.

Dedication

The authors would like to devote this book to their families for their infinite patience and encouragement.

This page intentionally left blank

Preface

The fluid flows can be basically described at three levels: macroscopic, mesoscopic and microscopic. In the macroscopic level, the physical conservation laws of mass, momentum and energy are applied to a control volume to establish a set of partial differential equations (mass, momentum and energy equations) for governing the fluid flow. The conventional computational fluid dynamics (CFD) is to solve these governing equations by using various numerical methods. In contrast, the lattice Boltzmann method (LBM), developed about two decades ago, is an approach at mesoscopic level. LBM studies the microdynamics of fictitious particles by using simplified kinetic models. It provides an alternative way for simulating fluid flows. The kinetic nature brings many distinctive features to LBM such as the clear picture of streaming and collision processes of simulated fluid particles, the simple algorithm structure, the easy implementation of boundary conditions, and the natural parallelism. These appealing features make LBM a powerful numerical tool for simulating fluid systems involving complex physics.

The past two decades have witnessed the rapid development of LBM in fundamental theories, basic models, and wide applications. Indeed, the method has gained much success in modelling and simulating various complicated flows. Several books have been published to address the need of students and researchers in the study, development and applications of LBM. The present book has the following unique features to distinguish it from previous ones. At first, this book is comprehensive in scope. It presents a systemic and self-contained description of LBM, including the basic idea, model construction, algorithm and implementation, and various applications. Secondly, it covers the state-of-the-art development and applications of LBM, and some areas in this

book such as treatments of body force, acceleration techniques, initialization methods, and applications in micro flows and moving boundary flows, have not been addressed in the previous books. Thirdly, through some sample examples, the book provides step by step implementation of algorithms, treatments of boundary conditions and computer codes. It is believed that this part of work is useful to the graduate students and beginners in the area.

The authors of this book, Drs Zhaoli GUO and Chang SHU, have been working on the development and applications of LBM for more than 12 years. They gained much experience from their research in this area. Indeed, many parts of the book are from their research work. For this book, Guo contributed Chapters 1-5, 7, 8 and most parts of Chapter 9, and Shu contributed Chapter 6, the section of Taylor series expansion and least square-based LBM as well as the stencil adaptive LBM in Chapter 3, and the section of immersed boundary-lattice Boltzmann method in Chapter 9.

This book is written for different levels of readers. For students and beginners, the book is easy to understand and follow. The detailed description of algorithms and implementation of initial/boundary conditions as well as sample applications will give a great help to them. The book will also attract experts in the LBM community. The detailed presentation of physical origins, mathematical derivations and theoretical analysis of various LB models provides useful information for researchers in the area. Furthermore, the comprehensive references enable the reader to find more sources if further information is needed.

Finally, the authors would like to thank their research assistants for preparing some of the materials to write this book. Guo also expresses his acknowledgement for the finical supports from the National Natural Science Foundation of China (51125024) and the National Basic Research Programme of China (2011CB707300).

Z. L. Guo and C. Shu

Contents

This page intentionally left blank

Chapter 1

Introduction

1.1 Description of Fluid System at Different Scales

Fluids, such as air and water, are frequently met in our daily life. Physically, all fluids are composed of a large set of atoms or molecules that collide with one another and move randomly. Interactions among molecules in a fluid are usually much weaker than those in a solid, and a fluid can deform continuously under a small applied shear stress. Usually, the microscopic dynamics of the fluid molecules is very complicated and demonstrates strong inhomogeneity and fluctuations. On the other hand, the macroscopic dynamics of the fluid, which is the average result of the motion of molecules, is homogeneous and continuous. Therefore, it is can be expected that mathematical models for fluid dynamics will be strongly dependent on the length and time scales at which the fluid is observed. Generally, the motion of a fluid can be described by three types of mathematical models according to the observed scales, i.e. microscopic models at molecular scale, kinetic theories at mesoscopic scale, and continuum models at macroscopic scale.

1.1.1 *Microscopic description: molecular dynamics*

In microscopic models, the motion of each molecule is tracked so that its position and momentum can be obtained. The collective dynamics of the whole fluid system can then be computed through some statistical methods. Usually, the molecular dynamics of the fluid is described by Newton's second law,

$$m\ddot{\boldsymbol{r}}_i = \boldsymbol{F}_i, \tag{1.1}$$

where m is the mass of the fluid molecule, $\boldsymbol{r}_i$ is the position vector of the molecule i, the dots represent time derivatives, and $\boldsymbol{F}_i$ is the total force experienced by the molecule, which usually includes two parts,

$$\boldsymbol{F}_i = \sum_{j=1, j\neq i}^{N} \boldsymbol{f}_{ij} + \boldsymbol{G}_i, \tag{1.2}$$

where $\boldsymbol{f}_{ij}$ is the force exerted by molecule j, N is the number of molecules in the system, and $\boldsymbol{G}_i$ is the external force such as gravity. The inter-molecular force can be expressed in terms of an interaction potential $\phi(r)$,

$$\boldsymbol{f}_{ij} = -\nabla\phi(|\ \boldsymbol{r}_{ij}\ |), \tag{1.3}$$

where $\boldsymbol{r}_{ij}$ is the displacement between molecules i and j. In microscopic models, the inter-molecular potential plays a vital role. A widely used model is the Lennard-Jones 12-6 potential,

$$\phi(r) = 4\varepsilon\left[\left(\frac{\sigma}{r}\right)^{12} - \left(\frac{\sigma}{r}\right)^{6}\right], \tag{1.4}$$

where ε characterizes the interaction strength and σ represents the interaction range.

By solving Eq. (1.1) we can obtain the position and velocity of each molecule at every time, and then the macroscopic variables of the fluid, such as density, velocity, and temperature, can be measured from the microscopic information: $A = \langle a \rangle$. Here A is a macroscopic quantity and a is the corresponding microscopic quantity; the symbol $\langle \cdot \rangle$ represents the ensemble average of a microscopic variable. The transport coefficients of the fluid (viscosity, thermal conductivity, diffusivity, *etc.*) can also be measured according to the linear response theory, which indicates that each transport coefficient can be obtained through the Einstein expression or the Green-Kubo relation [Rapaport, 2004].

An alternative description of the fluid is to consider the Hamiltonian of the N-body system $\mathcal{H} = \mathcal{H}(\boldsymbol{q}, \boldsymbol{p}, t)$, where $(\boldsymbol{q}, \boldsymbol{p})$ are the generalized coordinates that constitute the phase space of the system, i.e. $\boldsymbol{q} = (\boldsymbol{q}_1, \boldsymbol{q}_2, \ldots, \boldsymbol{q}_N)$ are the $3N$ spatial coordinates of the N molecules, and $\boldsymbol{p} = (\boldsymbol{p}_1, \boldsymbol{p}_2, \ldots, \boldsymbol{p}_N)$ are the $3N$ conjugate momenta. $\mathcal{H}$ is the total energy of the system including the kinetic energy and the potential energy due to molecular

interactions. In terms of the Hamiltonian of the system, the motion of the fluid molecules can be expressed as

$$\dot{\boldsymbol{q}}_i = \frac{\partial \mathcal{H}}{\partial \boldsymbol{p}_i}, \qquad \dot{\boldsymbol{p}}_i = -\frac{\partial \mathcal{H}}{\partial \boldsymbol{q}_i}, \quad i = 1, 2, \ldots, N. \tag{1.5}$$

In either the Newtonian formulation (1.1) or the Hamiltonian formulation (1.5), the numbers of unknowns are very large ($6N$). Even for a small volume of fluid in practice, the number of molecules is so large ($\sim 10^{23}$) that it is impractical to describe the whole system with a molecular model. Actually, even with the most advanced computer resources, molecular dynamics method is still limited to sub-micrometer systems.

1.1.2 *Mesoscopic description: kinetic theory*

A coarser description of the N-body fluid system is to make use of the concept of probability distribution function (pdf) $f_N(\boldsymbol{q}, \boldsymbol{p}, t)$ in the phase space, which determines the probability $f_N d\boldsymbol{q} d\boldsymbol{p}$ that the state of the system falls in the infinitesimal volume $[\boldsymbol{p}, \boldsymbol{p} + d\boldsymbol{p}] \times [\boldsymbol{q}, \boldsymbol{q} + d\boldsymbol{q}]$ in the $6N$ dimensional phase space. From f_N, all of the statistical properties of the molecular dynamics can be extracted. The evolution of f_N follows the Liouville equation [Harris, 1971],

$$\frac{df_N}{dt} = \frac{\partial f_N}{\partial t} + \sum_{j=1}^{N} \left[\frac{\partial f_N}{\partial \boldsymbol{p}_j} \cdot \dot{\boldsymbol{p}}_j + \frac{\partial f_N}{\partial \boldsymbol{q}_j} \cdot \dot{\boldsymbol{q}}_j \right] = 0, \tag{1.6}$$

or

$$\frac{\partial f_N}{\partial t} - \sum_{j=1}^{N} \left[\frac{\partial \mathcal{H}}{\partial \boldsymbol{q}_j} \frac{\partial f_N}{\partial \boldsymbol{p}_j} - \frac{\partial \mathcal{H}}{\partial \boldsymbol{p}_j} \frac{\partial f_N}{\partial \boldsymbol{q}_j} \right] = 0. \tag{1.7}$$

From f_N, we can define some reduced distribution functions,

$$F_s(\boldsymbol{q}_1, \boldsymbol{p}_1, \cdots, \boldsymbol{q}_s, \boldsymbol{p}_s) = \int f_N(\boldsymbol{q}_1, \boldsymbol{p}_1, \cdots, \boldsymbol{q}_N, \boldsymbol{p}_N) d\boldsymbol{q}_{s+1} d\boldsymbol{p}_{s+1} \cdots d\boldsymbol{q}_N d\boldsymbol{p}_N, \tag{1.8}$$

which is termed as the s-particle probability distribution function. We can derive a chain of evolution equations for F_s ($1 \le s \le N$) from the Liouville equation, which is usually called as the BBGKY (Bogoliubov–Born–Green–Kirkwood–Yvon) hierarchy. This hierarchy is identical to

the original Liouville equation completely. In this chain, the first equation for the single-particle pdf contains the two-particle pdf, the second equation for the two-particle pdf contains the three-particle pdf, and generally the s-th equation for the s-particle pdf contains $(s+1)$-th pdf. Therefore, the BBGKY hierarchy is fully coupled, and the difficulties of solving it are the same as solving the Liouville equations. However, under some assumptions, the BBGKY hierarchy can be truncated at certain orders so that a smaller set of equations can be obtained to approximate the original chain. Actually, this approach has served as a common strategy for developing kinetic equations in many applications of kinetic theory. Particularly, the approximation equation truncated at the first order leads to the well known Boltzmann equation for the velocity distribution function f, which is defined as

$$f(\boldsymbol{x}, \boldsymbol{\xi}, t) = mNF_1(\boldsymbol{q}_1, \boldsymbol{p}_1, t)\,, \tag{1.9}$$

where we have changed the notations from phase space to physical space: $\boldsymbol{x} = \boldsymbol{q}_1$ is the position of a particle and $\boldsymbol{\xi} = \boldsymbol{p}_1/m$ is its velocity. The Boltzmann equation, which plays the central role in kinetic theory of gases, describes the transportation of f:

$$\frac{\partial f}{\partial t} + \boldsymbol{\xi} \cdot \nabla f = \Omega(f, f)\,, \tag{1.10}$$

where Ω represents the rate of change in f due to binary molecular collisions. When the velocity distribution function is obtained, the fluid density ρ, velocity $\boldsymbol{u}$, and internal energy e can be determined from its moments:

$$\rho = \int f \, d\boldsymbol{\xi}, \quad \rho\boldsymbol{u} = \int \boldsymbol{\xi} f \, d\boldsymbol{\xi}, \quad \rho e(\boldsymbol{x},t) = \int \tfrac{C^2}{2} f \, d\boldsymbol{\xi}\,, \tag{1.11}$$

where C is the magnitude of the particular velocity $\boldsymbol{C} = \boldsymbol{\xi} - \boldsymbol{u}$ (In this book, the magnitude of a vector $\boldsymbol{a}$ will be always denoted by a). The pressure tensor and heat flux, can also be determined from f:

$$\boldsymbol{P} = \int \boldsymbol{C}\boldsymbol{C} f(\boldsymbol{x}, \boldsymbol{\xi}, t) \, d\boldsymbol{\xi}, \quad \boldsymbol{q} = \int \tfrac{C^2}{2} \boldsymbol{C} f(\boldsymbol{x}, \boldsymbol{\xi}, t) \, d\boldsymbol{\xi}\,. \tag{1.12}$$

The evolution equations for the fluid density, velocity, and energy can be derived from the Boltzmann equation under some assumptions.

The collision operator Ω in the Boltzmann equation (1.10) is a bi-linear integral function of *f*, and conserves mass, momentum, and energy:

$$\int \psi_i(\boldsymbol{\xi}) f(\boldsymbol{x}, \boldsymbol{\xi}, t)\, d\boldsymbol{\xi} = 0\,, \tag{1.13}$$

where $\psi = 1, \boldsymbol{\xi}, C^2 \,/\, 2$ (or ξ^2) are called *summational* or *collisional invariants*. From the Boltzmann equation, it can be shown that the *H*-function, defined by $H(t) = \int f \ln f \; d\boldsymbol{x} d\boldsymbol{\xi}$, will always decrease with time (*H*-theorem), i.e.,

$$\frac{dH}{dt} \leq 0\,. \tag{1.14}$$

The equality holds only and if only the system reaches its equilibrium state, whence the distribution function is a Maxwellian one,

$$f^{(eq)}(\boldsymbol{x}, \boldsymbol{\xi}, t) = \frac{\rho}{(2\pi RT)^{3/2}} \exp\left[-\frac{(\boldsymbol{\xi} - \boldsymbol{u})^2}{2RT} \right], \tag{1.15}$$

where $R = k_B / m$ is the gas constant with k_B the Boltzmann constant and m the molecular mass. At equilibrium, the collision does not take net effects, i.e., $\Omega(f^{(eq)}, f^{(eq)}) = 0$. With this knowledge, the collision operator can be approximated with some simplified models [Harris, 1971], among which the BGK (Bhatnagar-Gross-Krook) model [Bhatnagar *et al.*, 1954] is the most popular one,

$$\Omega_{BGK} = -\frac{1}{\tau_c}\left[f - f^{(eq)} \right], \tag{1.16}$$

where τ_c is the relaxation time. This model reflects the overall effect of intermolecular collisions, i.e., the distribution function relaxes to the equilibrium state with collisions. It can be easily verified that the BGK collision model conserves mass, momentum, and energy, and satisfies the *H*-theorem. However, because only one relaxation time is used to characterize the collision effects, this model also suffers from some limitations. For example, the Prandtl number (Pr), which reflects the difference between momentum exchange and energy exchange during the collision process, is fixed at 1 in the BGK model, while the full Boltzmann collision operator gives $\mathrm{Pr} = 2/3$. Some modified models have been proposed to overcome this problem, such as the

*Ellipsoidal Statistical BGK mode*l [Holway, 1966] and the *Shakhov model* [1968].

1.1.3 *Macroscopic description: hydrodynamic equations*

At macroscopic scale, a fluid is treated as a continuum regardless of its molecular structure and interaction; the fluid is assumed to be continuously distributed throughout the domain of interest, having its own properties such as density, velocity, and temperature. The molecular properties are reflected by the transport coefficients of the fluid such as the viscosity and thermal conductivity. A good criterion to determine if a continuum model is acceptable is to check whether the Knudsen number Kn of the fluid system, which is defined as the ratio of mean-free-path of molecules (λ) to the characteristic length (L) of the flow region, is sufficiently small. The mean free path is the average distance of the fluid molecules between two successive collisions. For an ideal gas composed of hard-sphere molecules, it can be expressed as $\lambda = (\sqrt{2}\pi n d^2)^{-1}$, where n is the number density of the molecules and d is the diameter of the gas molecule. The characteristic length is usually taken as the size of the flow domain or objects in the flow, such as the diameter of an object in the flow. In some cases, it is more suitable to define L based on the scale at which a flow variable changes, e.g. $L = \rho/|\nabla\rho|$.

In continuum theory, the motion of fluid is described by a set of partial differential equations (PDEs), which actually describes the conservation laws of the fluid [Batchelor, 1967]:

$$\frac{\partial \rho}{\partial t} + \nabla \cdot (\rho \boldsymbol{u}) = 0\,, \tag{1.17}$$

$$\frac{\partial (\rho \boldsymbol{u})}{\partial t} + \nabla \cdot (\rho \boldsymbol{u}\boldsymbol{u}) = -\nabla p + \nabla \cdot \boldsymbol{\tau}\,, \tag{1.18}$$

$$\frac{\partial (\rho e)}{\partial t} + \nabla \cdot (\rho \boldsymbol{u} e) = -\nabla \cdot \boldsymbol{q} - p\nabla \cdot \boldsymbol{u} + \boldsymbol{\tau} : \nabla \boldsymbol{u}\,, \tag{1.19}$$

where p is the pressure, $\boldsymbol{\tau}$ is the deviatoric stress tensor, and $\boldsymbol{q}$ is the heat flux. This set of equations are not closed because the variables p, $\boldsymbol{\tau}$, and $\boldsymbol{q}$ are yet unknown. The pressure can be modeled by an equation of state,

i.e. $p = p(e)$, while the deviatoric stress tensor can be modeled by a stress-strain constitution equation,

$$\boldsymbol{\tau} = 2\mu \boldsymbol{S} + \mu'(\nabla \cdot \boldsymbol{u})\boldsymbol{I} = 2\mu \overset{\circ}{\boldsymbol{S}} + \left(\mu' + \frac{2}{3}\mu\right)(\nabla \cdot \boldsymbol{u})\boldsymbol{I}\,, \tag{1.20}$$

where μ and μ' are the first and second dynamic viscosities, $\boldsymbol{I}$ is the second-order unit tensor, and $\boldsymbol{S}$ is the strain-rate tensor defined by $\boldsymbol{S} = [\nabla \boldsymbol{u} + (\nabla \boldsymbol{u})^T] / 2$. Here, a tensor with a notation " $\overset{\circ}{}$ " denotes the traceless part of the original tensor. The coefficient $\eta = \mu' + 2\mu/3$ is also called *bulk viscosity* in some textbooks, which is usually assumed to be zero (Stokes' hypothesis). The heat flux in Eq. (1.19) is usually related to the temperature gradient following Fourier's law,

$$\boldsymbol{q} = -\kappa \nabla \boldsymbol{T}\,, \tag{1.21}$$

where κ is the thermal conductivity. The set of equations (1.17)-(1.19) with the constitution relations (1.20) and (1.21) are the widely used Navier-Stokes-Fourier equations, which are also called *Navier-Stokes equations* sometimes. This set of equations can be simplified in some special cases. If the viscosity and thermal conductivity are neglected, the Navier-Stokes equations then reduce to the Euler equations; If the fluid density does not change with motion, i.e.,

$$\frac{d\rho}{dt} = \frac{\partial \rho}{\partial t} + \boldsymbol{u} \cdot \nabla \rho = 0\,, \tag{1.22}$$

the fluid is said to be *incompressible*, and the continuity equation (1.17) becomes $\nabla \cdot \boldsymbol{u} = 0$, and the stress tensor can be simplified as $\boldsymbol{\tau} = 2\mu \boldsymbol{S}$. The compressibility of a fluid can be characterized by the Mach number of the flow, $M = U/c_s$, where U is the characteristic velocity of the flow and c_s is the sound speed. Usually, the fluid flow can be regarded as incompressible when $M < 0.3$.

Although the conservation equations are developed phenomenologicallly, it is shown that they can also be derived from the Boltzmann equation. Actually, by multiplying the Boltzmann equation (1.10) by the collisional invariants ψ_i and integrating over the molecular velocity space, one can get Eqs. (1.17)~(1.19) after identifying that $\boldsymbol{P} = p\boldsymbol{I} - \boldsymbol{\tau}$.

The stress tensor τ and the heat flux q can be approximated via some asymptotic methods (e.g., Hilbert or Chapman-Enskog expansions).

In most of practical problems, the continuum model works very well. However, with the increasing interests in nano/micro and multi-scale problems, the continuum model becomes inadequate due to the relative large Knudsen number of the system. In viewing that the Navier-Stokes equations can be derived from the Boltzmann equation, some extended hydrodynamic models beyond the Navier-Stokes model have been developed from the Boltzmann equation from different viewpoints, such as the Burnett equations, super-Burnett equations, Grad's 13-moment equations (see a recent comparison of these hydrodynamic models by Lockerby *et al.* [2005]).

1.2 Numerical Methods for Fluid Flows

The mathematical models for fluid flows, either the Newtonian equation for the vast number of molecules, or the Boltzmann equation for the singlet distribution function, or the Navier-Stokes equations for the macroscopic flow variables, are all extremely difficult to solve analytically, if not impossible. Accurate numerical methods, however, have been proven to be able to provide satisfying approximate solutions to these equations. Particularly, with the rapid development of computer hardware and software technology, numerical simulation has become an important methodology for fluid dynamics.

The most successfully and popular fluid simulation method is the *Computational Fluid Dynamics* (CFD) technique, which is mainly designed to solve the hydrodynamic equations based on the continuum assumption. In CFD, the flow domain is decomposed into a set of sub-domains with a computational mesh, and the mathematical equations are discretized using some numerical schemes such as finite-volume, finite-element, or finite-difference methods, which results in an algebraic system of equations for the discrete flow variables associated with the computational mesh. Computation can then be carried out to find the approximate solutions on a computer by solving the algebraic system using some sequential or parallel algorithms. CFD has developed into a

branch of fluid mechanics since 1960s, and many textbooks on different topics in this field are available [e.g., Anderson, 1995; Ferzige and Peric, 2002; Patankar, 1980]. There are also many free and commercial softwares for both fundamental researches and practical engineering applications.

With the increasing interests in micro and nano scale science and technology, molecular dynamic simulation (MDS) techniques have also received much attention in modern fluid mechanics. In MDS, the movements of individual atoms or molecules of the fluid are recorded by solving the Newtonian equations on a computer. The main advantage of MDS is that macroscopic collective behaviors of the fluid can be directly connected with the molecular behaviors, in which the molecular structure and microscopic interactions can be described in a straightforward manner. Therefore, MDS is very helpful for understanding the fundamental microscopic mechanism of macroscopic fluid phenomena. However, due to the vast number of atoms of the fluid, the computational cost of MDS is rather expensive and this disadvantage limits it to systems with a temporal scale of picoseconds and spatial scale of nanometers.

Besides the macroscopic CFD and microscopic MDS methods, another kind of numerical methods for fluid system is developed based on mesoscopic models. Basically, mesoscopic methods can be classed into two types. The first type is to solve the kinetic equations (e.g., the Boltzmann equation) with some numerical schemes. Such methods include the finite difference discretization of the linearized Boltzmann equation [Kanki and Iuchi, 1973], the elementary method [Cercignani, 1988], the discrete velocity or discrete ordinate methods [Aristov, 2001; Sone *et al.*, 1989], the finite difference Monte Carlo method [Cheremisin, 1991], gas kinetic scheme [Xu, 1993], and lattice Boltzmann equation (LBE) method [Benzi *et al.*, 1992]. Another type of mesoscopic method is to construct numerical models to simulate the physical process of some virtual fluid particles directly. The most well-known method of such type is the Direct Simulation Monte Carlo (DSMC) method [Bird, 1994], and other methods of this type include the lattice gas automata (LGA) method [Rothman and Zaleski, 1997] and the dissipative particle dynamics (DPD) method [Hoogerbrugge and Koelman, 1992].

Because the underlying mathematical models have different physical bases, the numerical methods also have their own application ranges. CFD is very successful in continuum flows, and MDS is most suitable for nanoscale flows. With the increasing interests in multiscale flows, the mesoscopic method has received particular attentions in recent years, among which the lattice Boltzmann equation (LBE) method, or lattice Boltzmann method), is perhaps the most active topic in this field due to some distinctive features. In addition to a large amount of journal papers in different research fields, LBE is also a hot topic in many international conferences on fluid dynamics, and some courses on this topic have been set up in some universities. In the rest part of this book, we will give a systemic introduction of this method.

1.3 History of LBE

Historically, the LBE evolved from the LGA method, which is an artificial microscopic model for gases, and later it was shown that LBE could also be derived from the Boltzmann equation following some standard discretization. From the first viewpoint, LBE can be regarded as a fluid model, while the second viewpoint indicates that LBE is just a special numerical scheme for the Boltzmann equation. Despite of this conceptual difference, either approach demonstrates that LBE is a method which is quite different from the traditional CFD algorithms.

1.3.1 *Lattice gas automata*

LGA is the precursor of LBE, which aims to simulate fluid flows with simple fluid models. In LGA, the fluid is treated as a set of simulated particles residing on a regular lattice with certain symmetry properties, where they collide and stream following some prescribed rules that satisfy some necessary physical laws. The philosophy behind LGA is that fluid behaviors at macroscale are nothing but statistical collective results of the micro-dynamics of fluid molecules, and are insensitive to the detailed information of the individual molecules. In other words, fluids with different micro structures and interactions may have the

same macroscopic phenomena. Therefore, it is possible to simulate macroscopic flows with a fictitious micro fluid model which has simple micro-dynamics but satisfies some necessary physical laws. LGA is just one such fluid model, and the key requirement of a LGA model is that the mass, momentum, and energy must be conserved during the particle collision and streaming processes.

The first LGA model was attributed to three French scientists, Hardy, Pomeau, and de Pazzis, which is called the HPP model after the authors [Hardy *et al*., 1973a, 1973b]. This model utilizes a two-dimensional square lattice on which the gas particles at a node can move to any of the four nearest neighboring nodes along the lattice lines (see Fig. 1.1). The collision of the HPP model follows the so called *head-on* rule, namely, when two particles move to one same node with opposite velocities, their velocities will turn around 90° after the collision; In any other cases, no collision occurs and the particle velocities remain unchanged.

Mathematically, the motion of the particles in HPP model can be described by the following discrete kinetic equation,

$$n_i(\boldsymbol{x} + \boldsymbol{c}_i\delta_t, t + \delta_t) = n_i(\boldsymbol{x}, t) + C_i(n(\boldsymbol{x}, t)), \tag{1.23}$$

where $n_i(\boldsymbol{x}, t) = 0$ or 1 representing the number of particles moving with discrete velocity $\boldsymbol{c}_i$ at node $\boldsymbol{x}$ and time t, δ_t is the time step, C_i is the collision operator representing the influence of particle collisions. The

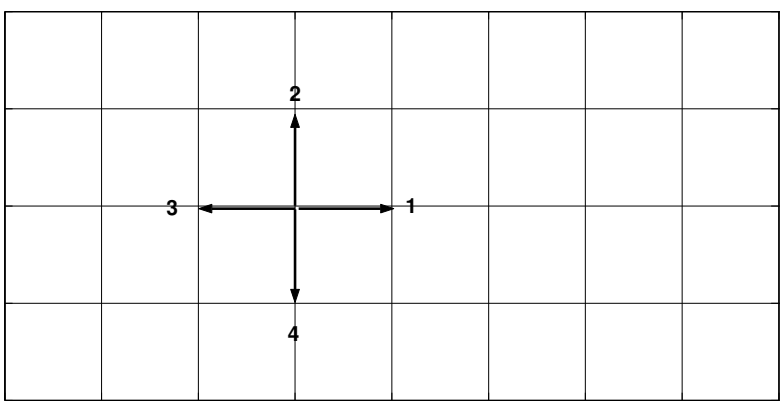

Fig. 1.1. Lattice and discrete velocities of the HPP model.

discrete velocity set of the HPP model is given by $\boldsymbol{c}_i = c\boldsymbol{e}_i$ with $\boldsymbol{e}_1 = (1, 0)$, $\boldsymbol{e}_2 = (0, 1)$, $\boldsymbol{e}_3 = (-1, 0)$, and $\boldsymbol{e}_4 = (0, -1)$, and $c = \delta_x/\delta_t$ is the *lattice speed* where δ_x is the lattice spacing. The collision operator describing the head-on rule can be expressed as

$$C_i = n_{i\oplus1}n_{i\oplus3}(1-n_i)(1-n_{i\oplus2}) - (1-n_{i\oplus1})(1-n_{i\oplus3})n_i n_{i\oplus2}\,, \tag{1.24}$$

where "$\oplus$" represents the modulo 4 addition. It can be verified that C_i conserves mass, momentum, and energy:

$$\sum_i C_i = 0\,,\ \sum_i \boldsymbol{c}_i C_i = 0\,,\ \sum_i \frac{c_i^2}{2} C_i = 0\,. \tag{1.25}$$

The evolution of the fictitious particles can also be decomposed into two sub-processes, i.e,

$$\text{Collision:} \qquad n_i'(\boldsymbol{x},t) = n_i(\boldsymbol{x},t) + C_i(n(\boldsymbol{x},t))\,, \tag{1.26}$$

$$\text{Streaming:} \qquad n_i(\boldsymbol{x} + \boldsymbol{c}_i\delta_t, t+\delta_t) = n_i'(\boldsymbol{x},t)\,. \tag{1.27}$$

The flow variables such as the density, velocity, and temperature can be obtained from the ensemble average (distribution function) of the Boolean number $f_i = \langle n_i \rangle$,

$$\rho = \sum_i m f_i, \quad \rho\boldsymbol{u} = \sum m\boldsymbol{c}_i f_i, \quad \rho e = \rho RT = \sum \frac{m}{2}(\boldsymbol{c}_i - \boldsymbol{u}_i)^2 f_i\,, \tag{1.28}$$

where m is the molecular mass of the gas, and will be assumed to be 1 without loss of generality. It is not straightforward to compute the ensemble average from n_i, and usually it can be replaced by temporal or spatial (or both) average in applications.

Although the microdynamics of the HPP model satisfies the basic conservation laws, the hydrodynamics variables do not satisfy the continuum equations due to the insufficient symmetry of the square lattice. Actually, the HPP model was designed as a micro fluid model rather than a computational method for hydrodynamic flows. Even though, the basic idea behind the HPP model opens a new way for flow computations.

The symmetry requirement on the lattice was first discovered in 1986 when Frisch, Hasslacher, and Pomeau proposed their hexagonal LGA

model [Frisch *et al*., 1986] (and simultaneously by Wolfram [1986]), which is now known as FHP model after the authors. This model uses a triangular lattice, and each node has six nearest neighbours (Fig. 1.2). The discrete velocities can be expressed as $\boldsymbol{c}_i = c(\cos\theta_i, \sin\theta_i)$ with $\theta_i = (i-1)\pi/3$ for $i = 1 \sim 6$. Like in the HPP model, the state of FHP model can be described by six Boolean numbers n_i that represent the number of particles moving with velocity $\boldsymbol{c}_i$. The collision rule of the FHP model includes five different cases, as shown in Fig. 1.2.

It is noted that in some cases, one input state may correspond to two possible output states (cases a and d shown in Fig. 1.2). In such cases, each output state is chosen randomly with equal probability. As such, the mathematical formulation of the collision operator can be written as

$$\begin{aligned} C_i \;=\; & n_{i\oplus1}n_{i\oplus3}n_{i\oplus5}\overline{n}_i\overline{n}_{i\oplus2}\overline{n}_{i\oplus4} - \overline{n}_{i\oplus1}\overline{n}_{i\oplus3}\overline{n}_{i\oplus5}n_i n_{i\oplus2}n_{i\oplus4} \\ & + r n_{i\oplus1}n_{i\oplus4}\overline{n}_i\overline{n}_{i\oplus2}\overline{n}_{i\oplus3}\overline{n}_{i\oplus5} + (1-r)n_{i\oplus2}n_{i\oplus5}\overline{n}_i\overline{n}_{i\oplus1}\overline{n}_{i\oplus3}\overline{n}_{i\oplus4} \\ & - n_i n_{i\oplus3}\overline{n}_{i\oplus1}\overline{n}_{i\oplus2}\overline{n}_{i\oplus4}\overline{n}_{i\oplus5}, \end{aligned} \tag{1.29}$$

where "⊕" represents the modulo 6 addition and r is a random number distributed uniformly in [0,1].

It can be shown that the collision operator of the FHP model leads to a Fermi-Dirac distribution at equilibrium for the distribution function [Frisch *et al*., 1987], i.e.,

$$f_i^{(eq)} = \frac{\rho \,/\, 6}{1 + \exp[A + B\boldsymbol{c}_i \cdot \boldsymbol{u}]}\ , \tag{1.30}$$

where A and B are the Lagrangian multipliers, which can be determined by expanding $f_i^{(eq)}$ into a series of $\boldsymbol{u}$ and imposing the mass and momentum constraints (for isothermal flows) given by Eq. (1.28). The final expression of $f_i^{(eq)}$ for the FHP model can be written as [Frisch *et al.*, 1987],

$$f_i^{(eq)} = \frac{\rho}{6}\left[1 + \frac{\boldsymbol{c}_i \cdot \boldsymbol{u}}{c_s^2} + G(\rho)\frac{\boldsymbol{Q}_i : \boldsymbol{uu}}{2c_s^4}\right], \tag{1.31}$$

where $c_s^2 = c^2/2$ is usually called *sound speed* in LGA (and LBE), $G(\rho)=(6-2\rho)/(6-\rho)$, and $\boldsymbol{Q}_i = \boldsymbol{c}_i\boldsymbol{c}_i - c_s^2\boldsymbol{I}$. With this expanded equilibrium

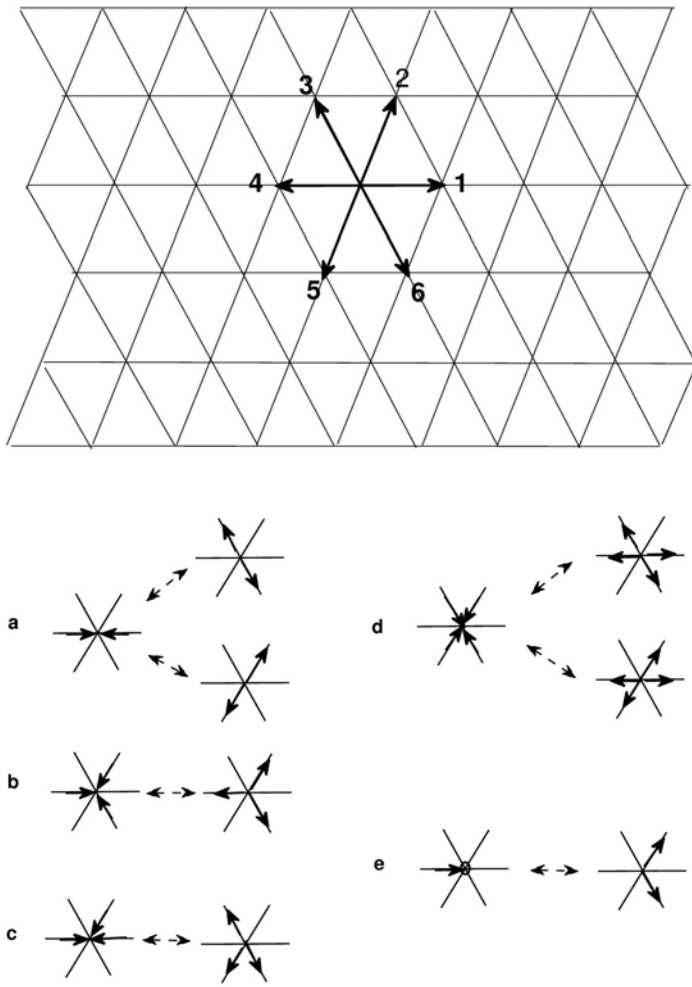

Fig. 1.2. FHP model and the collision rule.

distribution function (EDF), it can be shown that the fluid density and velocity of the FHP model satisfy the following hydrodynamic equations in the incompressible limit ($\rho \rightarrow \rho_0$):

$$\nabla \cdot \boldsymbol{u} = 0\,, \tag{1.32}$$

$$\frac{\partial \boldsymbol{u}}{\partial t} + g(\rho_0)(\boldsymbol{u}\cdot\nabla)\boldsymbol{u} = -\frac{\nabla p}{\rho_0} + \nu^{(0)}\nabla^2\boldsymbol{u}\,, \tag{1.33}$$

where

$$p = c_s^2\rho\left(1 - g\frac{\boldsymbol{u}^2}{c^2}\right), \quad \nu^{(0)} = c_s^2\left[\frac{1}{\rho_0(1-s)^3} - \frac{1}{4}\right]\delta_t\,,$$

with $s=\rho_0/6,\ g=(\rho_0-3)/(\rho_0-6)$. In general $g\neq 1$ and this leads to the breakdown of the Galilean invariance. However, the Galilean invariance can be restored by rescaling the time, i.e., $t\to t/g(\rho_0)$, and the momentum equation becomes

$$\frac{\partial \boldsymbol{u}}{\partial t} + \boldsymbol{u}\cdot\nabla\boldsymbol{u} = -\nabla P + \nu\nabla^2\boldsymbol{u}\,, \tag{1.34}$$

where $P = p/\rho_0 g$ and $\nu=\nu^{(0)}/g$. Equation (1.34) resembles the incompressible Navier-Stokes equation very closely, except that the rescaled pressure P depends on the velocity. This is somewhat unphysical, but as the Mach number is small, the pressure p satisfies an equation of state of ideal gas, $p = c_s^2\rho$.

Both the HPP and FHP models are designed for two-dimensional (2D) flows. It is not an easy task to find a 3D lattice with sufficient symmetries. On the other hand, it was shown that the 4D Face-Centered-Hyper-Cube (FCHC) lattice, which contains 24 discrete velocities with magnitude $2c$, has the desired properties [d'Humières *et al.*, 1986]. By projecting back onto three-dimensional, one can obtain a set of 3D discrete velocities that have the required symmetries. However, the number of possible states of the collision rule in the FCHC model is still very huge (2^{24}!), so it is a tough job to design an efficient collision rule for it, and this was also the target of many subsequent works. The theoretical foundation of the FCHC model was accomplished by Wolfram [1986] and Frisch *et al.* [1987], and after that, many applications have been conducted to complex flows such as multiphase systems and flows in porous media.

The implementation of a LGA model is straightforward, just a following of the collision-streaming paradigm. Particularly, the Boolean representation of the basic variable in LGA means that the computation can be realized with pure Boolean operations without round-off errors,

and the computation will be unconditional stable. Furthermore, because the update of the state at each node is completely local, the algorithm exhibits natural parallelism and thus is very suitable for parallel computations. Despite these advantages, the LGA method also has some disadvantages, such as the statistical noise arising from the Boolean variables, the violation of the Galilean invariance, and the dependence of velocity of the pressure. Historically, it is these unexpected features that motivate the invention of the lattice Boltzmann method.

1.3.2 *From LGA to LBE*

The LBE first appeared in the analysis of the hydrodynamic behaviors of the LGA model [Frisch *et al.*, 1987]. But it was McNamara and Zanetti who first proposed using LBE as a computation method [1988]. In order to reduce the statistical noise in LGA, they replaced the Boolean variable n_i by the real-valued distribution function f_i directly, and the collision rule for f_i is the same form as that for n_i. The evolution equation of this method (MZ model) can be written as

$$f_i(\boldsymbol{x} + \boldsymbol{c}_i\delta_t, t + \delta_t) - f_i(\boldsymbol{x}, t) = \Omega_i(f(\boldsymbol{x}, t)), \tag{1.35}$$

where the term on the right hand is the collision operator, $\Omega_i(f) = \langle C_i(n)\rangle \approx C_i(\langle n\rangle) = C_i(f)$.

Although the MZ model can remove the statistical noise effectively, the collision operator is still rather complicated. Soon after the MZ model, Higuera and Jimenez proposed an improved version (HJ model) [1989]. They showed that the collision operator in the MZ model could be approximated by a linearized one by assuming that f_i is close to its equilibrium,

$$f_i = f_i^{(eq)} + f_i^{(neq)}\ , \tag{1.36}$$

where $f_i^{(eq)}$ is the expansion of the Fermi-Dirac distribution function with a similar formulation as Eq. (1.31), and $f_i^{(neq)}$ is the nonequilibrium part. Expanding Ω_i around $f_i^{(eq)}$ leads to a linearized collision operator,

$$\Omega_i(f) = K_{ij}(f_j - f_j^{(eq)})\ , \tag{1.37}$$

where $K_{ij} = \partial\Omega_i / \partial f_j$ is the collision matrix. Here the fact that $\Omega_i(f_i^{(eq)}) = 0$ has been used. The use of the linearized collision operator significantly simplified the HJ model, although both K_{ij} and $f_i^{(eq)}$ are still dependent on the collision operator of the underlying LGA model.

A LBE model utilizing a collision matrix independent of any LGA models was developed by Higuera *et al*. (HSB model) [1989], but the EDF still comes from the LGA:

$$f_i^{(eq)} = d_0 \left[\frac{\rho}{b d_0} + D \frac{\boldsymbol{c}_i \cdot \boldsymbol{u}}{c_i^2} + G(d_0) \boldsymbol{Q}_i : \boldsymbol{u}\boldsymbol{u} \right], \tag{1.38}$$

where D is the spatial dimensional, b is the number of the discrete velocities, and $bd_0 = \rho_0$ is the mean density, while the function G and the tensor $\boldsymbol{Q}_i$ are given by

$$G(d_0) = \frac{D^2(1 - 2d_0)}{2c_i^4(1 - d_0)}, \quad \boldsymbol{Q}_i = \boldsymbol{c}_i \boldsymbol{c}_i - \frac{c^2}{D} \boldsymbol{I} \ . \tag{1.39}$$

Because the collision matrix K_{ij} in the HSB model can be constructed independently from the LGA models, it is possible to derive the desired hydrodynamic equations when the elements are setup appropriately.

In around 1991, the collision matrix is further simplified by several groups independently [Chen *et al*., 1991; Koelman, 1991; Qian *et al*., 1992], $\boldsymbol{K} = \tau^{-1} \boldsymbol{I}$, where τ is a nondimensional parameter. As such the collision operator can be simply expressed as

$$\Omega_i(f) = -\frac{1}{\tau} \left[f_i - f_i^{(eq)} \right], \tag{1.40}$$

which just has the same formulation as the BGK model in kinetic theory (see Eq. (1.16)). Usually a LBE with such a collision operator is called *lattice BGK* (LBGK) or *single-relaxation-time* (SRT) model. Unlike previous LBE models, the EDF in LBGK model is completely independent of LGA method, and can be constructed with some freedoms such that the corresponding hydrodynamic equations satisfy the desired ones. Therefore, the choice of the equilibrium distribution function is one of the key problems in LBGK method. For isothermal flows, the BGK collision operator should conserve mass and momentum,

i.e.,

$$\rho = \sum_i f_i = \sum_i f_i^{(eq)}, \qquad \rho \boldsymbol{u} = \sum_i \boldsymbol{c}_i f_i = \sum_i \boldsymbol{c}_i f_i^{(eq)} . \tag{1.41}$$

The use of the BGK collision operator enhances greatly the computational efficiency of LBE, and makes the implementation of the collision process much easier than other models. The LBGK model is perhaps the most popular one in the LBE community.

1.3.3 *From continuous Boltzmann equation to LBE*

As shown above, LBE was originated from the LGA method. On the other hand, it can show that LBE can also be derived from the continuous Boltzmann equation. For simplicity and without loss of generality, we take the isothermal LBGK model as an example. The starting point is the Boltzmann equation with the BGK approximation,

$$\frac{\partial f\left(\boldsymbol{x},\boldsymbol{\xi},t\right)}{\partial t} + \boldsymbol{\xi}\cdot\nabla f\left(\boldsymbol{x},\boldsymbol{\xi},t\right) = -\frac{1}{\tau_c}\left[f\left(\boldsymbol{x},\boldsymbol{\xi},t\right) - f^{eq}\left(\boldsymbol{x},\boldsymbol{\xi},t\right)\right], \tag{1.42}$$

where $f^{(eq)}$ is the Maxwellian distribution function. The first step is to discretize the velocity space of $\boldsymbol{\xi}$ into a finite set of velocities $\{\boldsymbol{c}_i\}$ without affecting the conservation laws. To do so, $f^{(eq)}$ is first expanded into a Taylor series in terms of the fluid velocity,

$$f^{(eq)} = \frac{\rho}{(2\pi RT)^{D/2}}\exp\left(-\frac{\boldsymbol{\xi}^2}{2RT}\right)\left[1 + \frac{\boldsymbol{\xi}\cdot\boldsymbol{u}}{RT} + \frac{(\boldsymbol{\xi}\cdot\boldsymbol{u})^2}{2RT} - \frac{u^2}{2RT}\right]. \tag{1.43}$$

It should be born in mind that this expansion can only be used for low Mach number flows, i.e. $|\boldsymbol{u}|/\sqrt{RT} \ll 1$. In order to obtain the correct Navier-Stokes equations in the limit of low Mach number, the discrete velocity set should be chosen so that the following quadratures of the expanded EDF hold exactly

$$\int \boldsymbol{\xi}^k f^{(eq)} d\boldsymbol{\xi} = \sum_i w_i \boldsymbol{c}_i^k f^{(eq)}(\boldsymbol{c}_i), \quad 0 \le k \le 3 \tag{1.44}$$

where w_i and $\boldsymbol{c}_i$ are the weights and points of the numerical quadrature rule. Based on the formulation of the expanded EDF given by Eq. (1.43), it is natural to choose a Gaussian quadrature with at least fifth-order.

Once the quadrature rule is chosen, we can define a *discrete distribution function*, $f_i(\boldsymbol{x},t) = w_i f(\boldsymbol{x},\boldsymbol{c}_i,t)$, which satisfies the following equation

$$\frac{\partial f_i}{\partial t} + \boldsymbol{c}_i \cdot \nabla f_i = -\frac{1}{\tau_c}\Big[f_i - f_i^{(eq)} \Big] , \tag{1.45}$$

where $f_i^{(eq)}(\boldsymbol{x},t) = w_i f_i^{(eq)}(\boldsymbol{x},\boldsymbol{c}_i,t)$. Obviously, the fluid density and velocity can be obtained from the discrete distribution function,

$$\rho = \sum_i f_i, \qquad \rho \boldsymbol{u} = \sum_i \boldsymbol{c}_i f_i \, . \tag{1.46}$$

Integrating equation (1.45) from t to $t + \delta_t$ along the characteristic line and assuming that the collision term is constant during this interval, we can obtain

$$f_i(\boldsymbol{x} + \boldsymbol{c}_i\delta_t, t + \delta_t) - f_i(\boldsymbol{x},t) = -\frac{1}{\tau}\Big[f_i(\boldsymbol{x},t) - f_i^{(eq)}(\boldsymbol{x},t)\Big], \tag{1.47}$$

where $\tau = \tau_c/\delta_t$ is the dimensionless relaxation time. Clearly, this is just the LBGK model.

1.4 Basic Models of LBE

In this section we will list some widely used LBE models for isothermal flows, and then show how to derive macroscopic equations from LBGK models using an asymptotical method. LBE models for thermal flows will be detailed in one specific chapter.

1.4.1 *LBGK models*

The LBGK models are the most popular LBE method and have been widely applied in variety of complex flows. Among the available models, the group of DnQb (n-dimensional b-velocity) models proposed by Qian *et al*. are the most representative ones [1992]. In DnQb, the discrete EDF can be expressed as

$$f_i^{(eq)} = \omega_i \rho \left[1 + \frac{\boldsymbol{c}_i \cdot \boldsymbol{u}}{c_s^2} + \frac{(\boldsymbol{c}_i \cdot \boldsymbol{u})^2}{2c_s^4} - \frac{u^2}{2c_s^2} \right], \tag{1.48}$$

Table 1.1. Parameters of some DnQb models.

Model	Lattice vector $\boldsymbol{c}_i$	Weight w_i	c_s^2
D1Q3	0, ±1	2/3, 1/6	1/3
D1Q5	0, ±1, ±2	6/12, 2/12, 1/12	1
D2Q7	(0,0), $(\pm 1/2, \pm\sqrt{3}/2)$	1/2, 1/12	1/4
D2Q9	(0,0), (±1,0),(0, ±1), (±1, ±1)	4/9, 1/9, 1/36	1/3
D3Q15	(0,0,0), (±1,0,0), (0, ±1,0),(0,0, ±1), (±1, ±1, ±1)	2/9, 1/9, 1/72	1/3
D3Q19	(0,0,0), (±1,0,0), (0, ±1,0),(0,0, ±1), (±1, ±1,0), (±1,0, ±1),(0, ±1, ±1)	1/3, 1/18, 1/36	1/3

where ω_i is the weight associated with the velocity $\boldsymbol{c}_i$, and the sound speed c_s is model dependent. In Tab. 1.1 several popular DnQb models are presented (here the lattice speed c is assumed to be 1).

The lattice velocities of the DnQb models can form certain lattice tensors with different ranks. The n-th rank lattice tensor is defined as

$$L_{\alpha_1\alpha_2\ldots\alpha_n} = \sum_i c_{i\alpha_1} c_{i\alpha_2} \ldots c_{i\alpha_n} . \tag{1.49}$$

Consequently, we have the 1st, 2nd, 3rd and 4th rank lattice tensors as

$$\begin{aligned} &L_\alpha = \sum_i c_{i\alpha}, \quad L_{\alpha\beta} = \sum_i c_{i\alpha} c_{i\beta}, \quad L_{\alpha\beta\gamma} = \sum_i c_{i\alpha} c_{i\beta} c_{i\gamma}, \\ &L_{\alpha\beta\gamma\zeta} = \sum_i c_{i\alpha} c_{i\beta} c_{i\gamma} c_{i\zeta}. \end{aligned} \tag{1.50}$$

A tensor of n-th rank is called *isotropic* if it is invariant with respect to arbitrary orthogonal transformations (rotations and reflections). The most general isotropic tensors up to 4th rank are provided by the following theorem.

- There are no isotropic tensors of rank 1 (vectors).
- An isotropic tensor of rank 2 is proportional to the 2nd Kronecker delta tensor $\delta_{\alpha\beta}$.
- An isotropic tensor of rank 3 is proportional to $\varepsilon_{\alpha\beta\gamma}$ with $\varepsilon_{123} = \varepsilon_{231} = \varepsilon_{312} = 1$, $\varepsilon_{132} = \varepsilon_{213} = \varepsilon_{321} = -1$ and zero others.
- There are three different (linear independent) tensors of rank 4, $\delta_{\alpha\beta}\delta_{\gamma\zeta}$, $\delta_{\alpha\gamma}\delta_{\beta\zeta}$, and $\delta_{\alpha\zeta}\delta_{\beta\gamma}$, which can be combined to give a general form, $L_{\alpha\beta\gamma\zeta} = a\delta_{\alpha\beta}\delta_{\gamma\zeta} + b\delta_{\alpha\gamma}\delta_{\beta\zeta} + c\ \delta_{\alpha\zeta}\delta_{\beta\gamma}$, where α, β, γ and ζ are arbitrary constants.

The lattice tensors can also be generalized to include the weights. A n-th rank generalized lattice tensor is defined as

$$T_{\alpha_1\alpha_2\ldots\alpha_n} = \sum_i \omega_i c_{i\alpha_1} c_{i\alpha_2} \ldots c_{i\alpha_n} , \tag{1.51}$$

where the ω_i's are the weights appearing in the discrete equilibrium function. In the LBE context, the lattice tensors of odd rank are usually zero. With the knowledge about the lattice tensors, it is easy to find the first several velocity moments of the discrete EDF $f_i^{(eq)}$,

$$\begin{aligned} &\sum_i f_i^{(eq)} = \rho\,, \ \sum_i \boldsymbol{c}_i f_i^{(eq)} = \rho\boldsymbol{u}\,, \ \sum_i \boldsymbol{c}_i\boldsymbol{c}_i f_i^{(eq)} = \rho\boldsymbol{u}\boldsymbol{u} + p\boldsymbol{I}\,, \\ &\sum_i c_{i\alpha}c_{i\beta}c_{i\gamma} f_i^{(eq)} = c_s^2\rho\,[\boldsymbol{u}\boldsymbol{\delta}]_{\alpha\beta\gamma} \equiv c_s^2\rho(u_\alpha\delta_{\beta\gamma} + u_\beta\delta_{\alpha\gamma} + u_\gamma\delta_{\alpha\beta}). \end{aligned} \tag{1.52}$$

These relations are helpful in the derivation of the hydrodynamic equations from the DnQb LBGK models.

1.4.2 *From LBE to the Navier-Stokes equations: Chapman-Enskog expansion*

The macroscopic dynamics of a fluid can be seen as the result of the collective behavior of microscopic particles in the system and it is well described by the Navier-Stokes equations. The derivation of the macroscopic Navier-Stokes equations from the LBE runs under the Chapman-Enskog expansion, which is a multi-scale analysis developed by Chapman and Enskog. As an example, in what follows we will perform an analysis of the D2Q9 model. First the following multiscale

expansions are introduced,

$$f_i = f_i^{(0)} + \varepsilon f_i^{(1)} + \varepsilon^2 f_i^{(2)} + \cdots, \quad \partial_t = \varepsilon \partial_{t_0} + \varepsilon^2 \partial_{t_1}, \quad \partial_\alpha = \varepsilon \partial_{0\alpha}, \quad (1.53)$$

where ε is a small number proportional to Kn, and ∂_t and ∂_α are the short notations of $\partial/\partial t$ and $\partial/\partial x_\alpha$, respectively. In this expansion, t_0 is the fast convective scale, and t_1 is the slow diffusive scale. The second order Taylor series expansion of the LBGK equation (1.47) yields

$$D_i f_i + \frac{\delta_t}{2} D_i^2 f_i = -\frac{1}{\tau \delta_t}(f_i - f_i^{eq}) + O(\delta_t^2), \quad (1.54)$$

where $D_i = \partial_t + \boldsymbol{c}_i \cdot \nabla = \partial_t + c_{i\alpha}\partial_\alpha$. Here the Einstein's summation rule is used, i.e., two repeated index means taking the summation over this index. Substituting the expansions (1.53) into Eq. (1.54), and equating the coefficients of each order of ε, one can obtain that

ε^0: $$f_i^{(0)} = f_i^{(eq)}, \quad (1.55)$$

ε^1: $$D_i^{(0)} f_i^{(0)} = -\frac{1}{\tau \delta_t} f_i^{(1)}, \quad (1.56)$$

ε^2: $$\partial_{t_1} f_i^{(0)} + D_i^{(0)} f_i^{(1)} + \frac{\delta_t}{2}[D_i^{(0)}]^2 f_i^{(0)} = -\frac{1}{\tau \delta_t} f_i^{(2)}, \quad (1.57)$$

or

$$\partial_{t_1} f_i^{(0)} + \left(1 - \frac{1}{2\tau}\right) D_i^{(0)} f_i^{(1)} = -\frac{1}{\tau \delta_t} f_i^{(2)}, \quad (1.58)$$

where $D_i^{(0)} = \partial_{t_0} + \boldsymbol{c}_i \cdot \nabla_0$. From Eq. (1.55), together with Eqs. (1.46) and (1.52), we can obtain that

$$\sum_i f_i^{(k)} = 0, \quad \sum_i \boldsymbol{c}_i f_i^{(k)} = \boldsymbol{0} \quad \text{for} \quad k > 0. \quad (1.59)$$

Multiplying Eq. (1.56) by 1 and $\boldsymbol{c}_i$, respectively, and taking summation over i, we can obtain the mass and momentum conservation equations at order of ε,

$$\partial_{t_0} \rho + \nabla_0 \cdot (\rho \boldsymbol{u}) = 0, \quad (1.60)$$

$$\partial_{t_0} (\rho \boldsymbol{u}) + \nabla_0 \cdot \boldsymbol{\pi}^{(0)} = 0, \quad (1.61)$$

where $\pi^{(0)}_{\alpha\beta} = \sum_i c_{i\alpha}c_\beta f_i^{(0)} = \rho u_\alpha u_\beta + p\delta_{\alpha\beta}$ is the zeroth-order momentum flux tensor, with $p = c_s^2\rho$. Here the following properties of the generalized lattice tensors of the D2Q9 model have been used:

$$\sum_i \omega_i c_{i\alpha} = \sum_i \omega_i c_{i\alpha}c_{i\beta}c_{i\gamma} = 0\,,\ \sum_i \omega_i c_{i\alpha}c_{i\beta} = c_s^2\delta_{\alpha\beta}\,,$$
$$\sum_i \omega_i c_{i\alpha}c_{i\beta}c_{i\gamma}c_{i\theta} = c_s^4\Delta_{\alpha\beta\gamma\theta}\,, \tag{1.62}$$

where $\Delta_{\alpha\beta\gamma\zeta} = \delta_{\alpha\beta}\delta_{\gamma\zeta} + \delta_{\alpha\gamma}\delta_{\beta\zeta} + \delta_{\alpha\zeta}\delta_{\beta\gamma}$. Equations (1.60) and (1.61) are the Euler equations, just the same as those from the continuous Boltzmann equation in kinetic theory.

Similarly, the zeroth and first order moments of Eq. (1.58) leads to the conservation equations at order of ε^2,

$$\partial_{t_1}\rho = 0\,, \tag{1.63}$$

$$\partial_{t_1}(\rho\boldsymbol{u}) + \left(1 - \frac{1}{2\tau}\right)\nabla_0\cdot\boldsymbol{\pi}^{(1)} = 0\,, \tag{1.64}$$

where $\pi^{(1)}_{\alpha\beta} = \sum_i c_{i\alpha}c_{i\beta}f_i^{(1)}$. In order to evaluate $\pi^{(1)}_{\alpha\beta}$, we multiply Eq. (1.56) by $c_{i\alpha}c_{i\beta}$ and take summation over i:

$$\begin{aligned}
-\frac{1}{\tau\delta_t}\sum_i c_{i\alpha}c_{i\beta}f_i^{(1)} &= \partial_{t_0}\sum_i c_{i\alpha}c_{i\beta}f_i^{(0)} + \partial_{0\gamma}\sum_i c_{i\alpha}c_{i\beta}c_\gamma f_i^{(0)} \\
&= \partial_{t_0}\left(\rho u_\alpha u_\beta + c_s^2\rho\delta_{\alpha\beta}\right) \\
&\quad + \partial_{0\gamma}\left[c_s^2\rho(u_\alpha\delta_{\beta\gamma} + u_\beta\delta_{\alpha\gamma} + u_\gamma\delta_{\alpha\beta})\right] \\
&= c_s^2\left[\partial_{t_0}\rho + \partial_{0\gamma}(\rho u_\gamma)\right]\delta_{\alpha\beta} + u_\beta\left[\partial_{t_0}(\rho u_\alpha) + \partial_{0\alpha}p\right] \\
&\quad + u_\alpha\left[\rho\partial_{t_0}u_\beta + \partial_{0\beta}p\right] + c_s^2\rho\left[\partial_{0\alpha}u_\beta + \partial_{0\beta}u_\alpha\right] \\
&= c_s^2\rho\left[\partial_{0\alpha}u_\beta + \partial_{0\beta}u_\alpha\right] - \partial_{0\gamma}(\rho u_\alpha u_\beta u_\gamma) \\
&= c_s^2\rho\left[\partial_{0\alpha}u_\beta + \partial_{0\beta}u_\alpha\right] + O(M^3)\ ,
\end{aligned} \tag{1.65}$$

where M is the Mach number. Here the equations on the first order of ε, (1.60) and (1.61) have been used to evaluate the time derivatives. Specifically, the following relations have been applied:

$$\partial_{t_0}\rho = -\partial_{0\beta}(\rho u_\beta)\,, \tag{1.66}$$

$$\partial_{t_0}(\rho u_\alpha) = -\partial_{0\beta}\pi^{(0)}_{\alpha\beta} = -\partial_{0\alpha}p - \partial_{0\beta}(\rho u_\alpha u_\beta)\,, \tag{1.67}$$

$$\rho\partial_{t_0}u_\alpha = -\partial_{0\alpha}p - \rho u_\beta\partial_{0\beta}u_\alpha\,, \tag{1.68}$$

where the last equation is derived from the first two equations. Equation (1.65) gives then that $\pi^{(1)}_{\alpha\beta} = -\tau p \delta t(\partial_{0\alpha} u_\beta + \partial_{0\beta} u_\alpha)$ after neglecting the terms of $O(M^3)$.

Combining the mass and momentum conservation equations on both the ε and ε^2 scales, we can get the hydrodynamic equations corresponding to the D2Q9 model:

$$\partial_t \rho + \nabla \cdot (\rho \boldsymbol{u}) = 0\,, \tag{1.69}$$

$$\frac{\partial(\rho \boldsymbol{u})}{\partial t} + \nabla(\rho \boldsymbol{u}\boldsymbol{u}) = -\nabla p + \nabla \cdot \left[\rho\nu\left(\nabla \boldsymbol{u} + \nabla \boldsymbol{u}^T\right)\right], \tag{1.70}$$

where ν is kinematic viscosity given by

$$\nu = c_s^2\left(\tau - \frac{1}{2}\right)\delta_t\,, \tag{1.71}$$

and $c_s = c/\sqrt{3}$ for the D2Q9 model. In small Mach number limit, the density variation can be negligible. Thus one can further obtain the incompressible Navier-Stokes equations

$$\nabla \cdot \boldsymbol{u} = 0\ , \tag{1.72}$$

$$\frac{\partial \boldsymbol{u}}{\partial t} + \boldsymbol{u} \cdot \nabla \boldsymbol{u} = -\frac{1}{\rho}\nabla p + \nu \nabla^2 \boldsymbol{u}\,. \tag{1.73}$$

It is noted that low Mach number assumption has been employed in both the expansion of the discrete EDF from the Maxwellian distribution function and the derivation given above. As such, the LBGK models are only suitable for low speed flows in principle. On the other hand, it is known that the density variation of a flow is proportional to the square of the Mach number, which means that the LBGK method is actually an artificial compressibility method for the incompressible Navier-Stokes equations. Therefore, besides the temporal and spatial discretization errors, LBGK method also suffers from an additional error from the compressibility when applied to incompressible flows. Several incompressible LBGK models have been developed to overcome the compressibility error from different viewpoints [Zou *et al*., 1995; He and Luo, 1997; Chen and Ohashi, 1997; Guo *et al*., 2000].

Now we discuss the accuracy of the LBGK models. First it is noted that the LBGK equation (1.47) is a first-order finite-difference scheme for the discrete velocity Boltzmann equation (1.45). If we apply the Chapman-Enskog analysis to the Eq. (1.45) directly, we can also derive the isothermal or athermal Navier-stokes equations (1.70), but with a kinematic viscosity $\nu = c_s^2\tau_c = c_s^2\tau\delta_t$ which contains no temporal and spatial discretization errors. In the above analysis, however, the expansion of the LBGK equation (1.47) was truncated up to $O(\delta_t^2)$ and $O(\delta_x^2)$, which means that LBGK method can be viewed as a second-order scheme for the compressible Navier-Stokes equations after absorbing the numerical viscosity $\nu_n = c_s^2\delta_t/2$, which comes from the term $(\delta_t^2/2)D_i^2 f_i$ in Eq. (1.54), into the physical one. This is an appealing feature of the LBGK method for complex flows. Also, because the underlying lattices of the LBGK models posses better rotational symmetry than classical second-order finite-difference/finite-volume schemes, LBGK and other LBE models may yield more accurate results than classical CFD methods with the same temporal and spatial accuracies. Actually, some comparative studies indicate that the results of LBE are even comparable to spectral methods for turbulent flows [Martinez *et al.*, 1994].

1.4.3 *LBE models with multiple relaxation times*

Like the BGK model in kinetic theory, the LBGK model uses a relaxation process with a single relaxation time to characterize the collision effects, which means that all of the modes relax to their equilibria with the same rate. However, physically, these rates should be different during the collision process. In order to overcome this limitation, a collision matrix with different eigenvalues or multiple relaxation times can be used. Actually, such models were proposed by d'Humèriers almost at the same time when the LBGK method was developed [d'Humières, 1992]. Such MRT-LBE models have been attracting more and more attentions recently due to some inherent advantages [Lallemand and Luo, 2000].

The LBE with a MRT collision operator can be expressed as,

$$f_i(\boldsymbol{x} + \boldsymbol{c}_i\delta_t, t + \delta_t) - f_i(\boldsymbol{x}, t) = -\sum_j \Lambda_{ij}\left[f_j - f_j^{(eq)}\right], \quad i = 0 \sim b-1, \quad (1.74)$$

or

$$\boldsymbol{f}(\boldsymbol{x}+\boldsymbol{c}_i\delta t, t+\delta t)-\boldsymbol{f}(\boldsymbol{x},t)=-\boldsymbol{\Lambda}(\boldsymbol{f}-\boldsymbol{f}^{(eq)}), \tag{1.75}$$

where b is the number of discrete velocities, and $\boldsymbol{\Lambda}$ is the collision matrix. Equation (1.74) or (1.75) describes the evolution of the population $\boldsymbol{f}=(f_0, f_1, \cdots, f_{b-1})^T$ in the *velocity space* $\mathbb{V}$. On the other hand, the evolution process can also be described in a *moment space* $\mathbb{M}$. To see how this is realized, we first define b moments based on $\boldsymbol{f}$,

$$m_k=\boldsymbol{f}\cdot\phi_k, \qquad k=0\sim b-1, \tag{1.76}$$

where ϕ_k is a vector with b elements, each of which is a polynomial of the discrete velocities. These b vectors are independent and thus form a basis of the velocity space. The relation between the moments and the distribution functions can also be expressed in a concise form,

$$\boldsymbol{m}=\boldsymbol{M}\boldsymbol{f}=(m_0, m_1, \cdots, m_{b-1})^T, \tag{1.77}$$

where the invertible transformation matrix $\boldsymbol{M}$ is composed of the vectors ϕ_k. The space where the moments take values is just the moment space. From Eq. (1.75), we can obtain the moment evolution equation as,

$$\boldsymbol{m}(\boldsymbol{x}+\boldsymbol{c}_i\delta_t, t+\delta_t)-\boldsymbol{m}(\boldsymbol{x},t)=-\boldsymbol{S}(\boldsymbol{m}-\boldsymbol{m}^{(eq)}), \tag{1.78}$$

where $\boldsymbol{S}=\boldsymbol{M}\boldsymbol{\Lambda}\boldsymbol{M}^{-1}$ is usually a diagonal matrix, i.e. $\boldsymbol{S}=\mathrm{diag}\,(s_0, s_1, \ldots, s_{b-1})$, and $\boldsymbol{m}^{(eq)}=\boldsymbol{M}\boldsymbol{f}^{(eq)}$ is the equilibria in the moment space.

In practical applications, however, the MRT-LBE usually combines the evolutions in the velocity space and moment space. That is, the collision step is executed in the moment space while the streaming step is still performed in the velocity space just like the LBGK method. Therefore, the basic flowchart of a MRT-LBE model can be described as follows,

- Transforming the distribution functions $\boldsymbol{f}$ to moments $\boldsymbol{m}$ according to Eq. (1.77);
- Colliding in moment space: $\boldsymbol{m}'=\boldsymbol{m}-\boldsymbol{S}(\boldsymbol{m}-\boldsymbol{m}^{(eq)})$;
- Transforming the post-collision moments $\boldsymbol{m}'$ back to the post-collision distribution function: $\boldsymbol{f}'=\boldsymbol{M}^{-1}\boldsymbol{m}'$;
- Streaming in velocity space: $f_i(\boldsymbol{x}+\boldsymbol{c}_i\delta_t, t+\delta_t)=f_i'(\boldsymbol{x},t)$.

Therefore, the evolution of the MRT-LBE can be effectively expressed as

$$\boldsymbol{f}(\boldsymbol{x}+\boldsymbol{c}_i\delta_t, t+\delta_t) - \boldsymbol{f}(\boldsymbol{x}, t) = -\boldsymbol{M}^{-1}\boldsymbol{S}(\boldsymbol{m}-\boldsymbol{m}^{(eq)}). \tag{1.79}$$

In MRT-LBE, the relaxation rates s_i, or the relaxation times $\tau_i = 1/s_i$ can be tuned with some freedom. This means that these parameters can be optimized to enhance the performance of the algorithm [Lallemand and Luo, 2000]. It is also noted that as $s_i = 1/\tau$, the MRT-LBE reduces to the LBGK models. Nonetheless, the involvement of the transforms between the velocity and moment spaces will increase some computational costs. However, the increase is not significant because $\boldsymbol{M}$ is usually an orthogonal matrix. Some numerical tests demonstrate that the increase in time is within 20% [d'Humières *et al.*, 2002].

The transformation matrix $\boldsymbol{M}$, or the base vectors ϕ_k, can be constructed from the polynomials $c_{ix}^m c_{iy}^n c_{iz}^l$ $(m,\ n,\ l \geq 0)$ through the Gram-Schmidt orthogonalization [Bouzidi *et al.*, 2001]. Generally, the basis includes the following vectors corresponding to the mass and momentum:

$$\begin{aligned} \boldsymbol{\phi}_0 &= \boldsymbol{1}_b \equiv (\underbrace{1\,,\ 1\,,\ \cdots,\ 1}_{b})^T \\ \boldsymbol{\phi}_\alpha &= (c_{1\alpha}, c_{2\alpha}, \cdots, c_{b\alpha})^T, \quad \alpha = 1\,,\ 2\,,\ \cdots,\ D. \end{aligned} \tag{1.80}$$

Another key point of the MRT-LBE model is the equilibria in moment space. In principle $\boldsymbol{m}^{(eq)}$ can be constructed with some freedoms. But a more convenient way is to compute them from the discrete EDFs $f_i^{(eq)}$ of the DnQb models once the transformation matrix $\boldsymbol{M}$ is determined. Several 2D and 3D MRT-LBE models are listed below. For simplicity, we assume that $c = 1.0$ in all cases, otherwise the base vectors can be normalized by c and the results are similar.

(1) *Standard D2Q9 model*

The lattice is the same as the D2Q9 LBGK model, i.e, a two-dimensional square lattice. The corresponding moments are

$$\boldsymbol{m} = \left(\rho, e, \varepsilon, j_x, q_x, j_y, q_y, p_{xx}, p_{xy}\right)^T,$$

while the equilibria in the moment space are

$$\boldsymbol{m}^{(eq)} = \rho\left(1,-2+3u^2,\alpha+\beta u^2,u_x,-u_x,u_y,-u_y,u_x^2-u_y^2,u_xu_y\right)^T,$$

where α and β are two free parameters, and when $\alpha=1$ and $\beta=-3$, the equilibria are consistent with those of the D2Q9 LBGK model. The transformation matrix is

$$\boldsymbol{M} = \begin{pmatrix} 1 & 1 & 1 & 1 & 1 & 1 & 1 & 1 & 1 \\ -4 & -1 & -1 & -1 & -1 & 2 & 2 & 2 & 2 \\ 4 & -2 & -2 & -2 & -2 & 1 & 1 & 1 & 1 \\ 0 & 1 & 0 & -1 & 0 & 1 & -1 & -1 & 1 \\ 0 & -2 & 0 & 2 & 0 & 1 & -1 & -1 & 1 \\ 0 & 0 & 1 & 0 & -1 & 1 & 1 & -1 & -1 \\ 0 & 0 & -2 & 0 & 2 & 1 & 1 & -1 & -1 \\ 0 & 1 & -1 & 1 & -1 & 0 & 0 & 0 & 0 \\ 0 & 0 & 0 & 0 & 0 & 1 & -1 & 1 & -1 \end{pmatrix}.$$

The relaxation rates corresponding to the moments are

$$\boldsymbol{S} = (0\,,\, s_e\,,\, s_\varepsilon\,,\, 0\,,\, s_q\,,\, 0\,,\, s_q\,,\, s_\nu\,,\, s_\nu),$$

and the kinematic viscosity and bulk viscosity are related to the relaxation rates s_e and s_ν,

$$\nu = c_s^2\left(\frac{1}{s_\nu}-\frac{1}{2}\right)\delta_t, \quad \zeta = c_s^2\left(\frac{1}{s_e}-\frac{1}{2}\right)\delta_t,$$

where $c_s^2 = 1/3$.

(2) *Rectangular D2Q9 model*

An advantage of MRT-LBE is that a nonstandard mesh can be used as the underlying lattice due to the freedoms in choosing the equilibria and the relaxation times. For example, a D2Q9 MRT-LBE model using a rectangular lattice has been developed. The lattice vectors are given by

$$\boldsymbol{c} = \begin{bmatrix} 0 & 1 & 0 & -1 & 0 & 1 & -1 & -1 & 1 \\ 0 & 0 & a & 0 & -a & a & a & -a & -a \end{bmatrix},$$

where $a = \delta_y/\delta_x$ is the ratio of the lattice spacing and here δ_x is set to be unity. The nine moments are

$$\boldsymbol{m} = \left(\rho, e, \varepsilon, j_x, q_x, j_y, q_y, 3p_{xx}, p_{xy}\right)^T,$$

and the corresponding equilibria are given by

$$\begin{aligned}\boldsymbol{m}^{(eq)} = \rho\Big[&1\,,\, 2(3c_s^2 - r_1) + 3u^2,\, \alpha + \beta u^2,\, 1 - 3u^2,\, u_x,\, u_x(\gamma - 4r_4)/2a^2,\\ &u_y,\, \gamma u_y/2,\, r_4(-3r_1c_s^2 - 2a^2)/3a^2 + a^2\left(u_x^2 - u_y^2/a^4\right),\, u_x u_y\Big]^T,\end{aligned}$$

where c_s, α, β, and γ are free parameters. The transformation matrix is

$$\boldsymbol{M} = \begin{pmatrix} 1 & 1 & 1 & 1 & 1 & 1 & 1 & 1 & 1 \\ -2r_1 & r_2 & r_3 & r_2 & r_3 & r_1 & r_1 & r_1 & r_1 \\ 4 & -2 & -2 & -2 & -2 & 1 & 1 & 1 & 1 \\ 0 & 1 & 0 & -1 & 0 & 1 & -1 & -1 & 1 \\ 0 & -2 & 0 & 2 & 0 & 1 & -1 & -1 & 1 \\ 0 & 0 & a & 0 & -a & a & a & -a & -a \\ 0 & 0 & -2a & 0 & 2a & a & a & -a & -a \\ -2r_4 & r_5 & r_6 & r_5 & r_6 & r_4 & r_4 & r_4 & r_4 \\ 0 & 0 & 0 & 0 & 0 & 1 & -1 & 1 & -1 \end{pmatrix},$$

where $r_1 = 1 + a^2$, $r_2 = 1 - 2a^2$, $r_3 = -2 + a^2$, $r_4 = -1 + a^2$, r_5=$2+a^2$, and $r_6 = -1 - 2a^2$. The relaxation rates are similar to those of the standard D2Q9 model,

$$\boldsymbol{S} = (0, s_e, s_\varepsilon, 0, s_q, 0, s_q, s_\nu, s_\nu)\,.$$

The shear and bulk viscosities are

$$\nu = \frac{4 + \gamma}{6}\left(\frac{1}{s_\nu} - \frac{1}{2}\right)\delta_t, \quad \zeta = \frac{7 + 3a^2 + \gamma - 12c_s^2}{12}\left(\frac{1}{s_e} - \frac{1}{2}\right)\delta_t\,.$$

As expected, if $a = 1$, $c_s^2 = 1/3$, and $\gamma = -2$, this rectangular model reduces to the standard D2Q9 model. It should be noted that the corresponding rectangular D2Q9 LBGK model does not exist.

(3) *D3Q13 model*

D3Q13 MRT-LBE model uses the following discrete velocities,

$$\boldsymbol{c}=\begin{bmatrix}0&1&1&1&1&0&0&-1&-1&-1&-1&0&0\\0&1&-1&0&0&1&1&-1&1&0&0&-1&-1\\0&0&0&1&-1&1&-1&0&0&-1&1&-1&1\end{bmatrix}.$$

The corresponding moments are

$$\boldsymbol{m}=\left(\rho,j_x,j_y,j_z,e,3p_{xx},p_{ww},p_{xy},p_{yz},p_{zx},t_x,t_y,t_z\right)^T,$$

with the following equilibrium moments,

$$\boldsymbol{m}^{(eq)}=\rho\Big(1,\,u_x,\,u_y,\,u_z,\,\tfrac{3}{2}(13c_s^2-8)+\tfrac{13}{2}u^2,\,3u_x^2-u^2,\,u_y^2-u_z^2,\\ u_xu_y,\,u_yu_z,\,u_zu_x,\,0,\,0,\,0\Big)^T.$$

The corresponding transformation matrix is

$$\boldsymbol{M}=\begin{pmatrix}1&1&1&1&1&1&1&1&1&1&1&1&1\\0&1&1&1&1&0&0&-1&-1&-1&-1&0&0\\0&1&-1&0&0&1&1&-1&1&0&0&-1&-1\\0&0&0&1&-1&1&-1&0&0&-1&1&-1&1\\-12&1&1&1&1&1&1&1&1&1&1&1&1\\0&1&1&1&1&-2&-2&1&1&1&1&-2&-2\\0&1&1&-1&-1&0&0&1&1&-1&-1&0&0\\0&1&-1&0&0&0&0&1&-1&0&0&0&0\\0&0&0&0&0&1&-1&0&0&0&0&1&-1\\0&0&0&1&-1&0&0&0&0&1&-1&0&0\\0&1&1&-1&-1&0&0&-1&-1&1&1&0&0\\0&-1&1&0&0&1&1&1&-1&0&0&-1&-1\\0&0&0&1&-1&-1&1&0&0&-1&1&1&-1\end{pmatrix},$$

and the relaxation rates are

$$\boldsymbol{S}=(0,\,0,\,0,\,0,\,s_e,\,s_\nu,\,s_\nu,\,s'_\nu,\,s'_\nu,\,s'_\nu,\,s_t,\,s_t,\,s_t),$$

while the shear and bulk viscosities are ($c_s^2=1/3$)

$$\nu=\frac{1}{4}\left(\frac{1}{s_\nu}-\frac{1}{2}\right)\delta_t=\frac{1}{2}\left(\frac{1}{s'_\nu}-\frac{1}{2}\right)\delta_t,\quad \zeta=\frac{2-3c_s^2}{3}\left(\frac{1}{s_e}-\frac{1}{2}\right)\delta_t.$$

(4) *D3Q15 model*

This model shares the same discrete velocities as the D3Q15 LBGK model. The fifteen moments are

$$\boldsymbol{m} = \left(\rho,\, e,\, \varepsilon,\, j_x,\, q_x,\, j_y,\, q_y,\, j_z,\, q_z,\, 3p_{xx},\, p_{ww},\, p_{xy},\, p_{yz},\, p_{zx},\, t_{xyz}\right)^T,$$

with the corresponding equilibria,

$$\begin{aligned}\boldsymbol{m}^{(eq)} = \rho\Bigg(&1,\, u^2-1,\, -1,\, u_x,\, -\frac{7}{3}u_x,\;\; u_y,\, -\frac{7}{3}u_y,\, u_z,\, -\frac{7}{3}u_z,\\ &-3u_x^2-u^2,\, u_y^2-u_z^2,\, u_xu_y,\, u_yu_z,\, u_zu_x,\, 0\Bigg)^T.\end{aligned}$$

The transformation matrix is given as follows,

$$\boldsymbol{M} = \begin{pmatrix}
1 & 1 & 1 & 1 & 1 & 1 & 1 & 1 & 1 & 1 & 1 & 1 & 1 & 1 & 1\\
-2 & -1 & -1 & -1 & -1 & -1 & -1 & 1 & 1 & 1 & 1 & 1 & 1 & 1 & 1\\
16 & -4 & -4 & -4 & -4 & -4 & -4 & 1 & 1 & 1 & 1 & 1 & 1 & 1 & 1\\
0 & 1 & -1 & 0 & 0 & 0 & 0 & 1 & -1 & 1 & -1 & 1 & -1 & 1 & -1\\
0 & -4 & 4 & 0 & 0 & 0 & 0 & 1 & -1 & 1 & -1 & 1 & -1 & 1 & -1\\
0 & 0 & 0 & 1 & -1 & 0 & 0 & 1 & 1 & -1 & -1 & 1 & 1 & -1 & -1\\
0 & 0 & 0 & -4 & 4 & 0 & 0 & 1 & 1 & -1 & -1 & 1 & 1 & -1 & -1\\
0 & 0 & 0 & 0 & 0 & 1 & -1 & 1 & 1 & 1 & 1 & -1 & -1 & -1 & -1\\
0 & 0 & 0 & 0 & 0 & -4 & 4 & 1 & 1 & 1 & 1 & -1 & -1 & -1 & -1\\
0 & 2 & 2 & -1 & -1 & -1 & -1 & 0 & 0 & 0 & 0 & 0 & 0 & 0 & 0\\
0 & 0 & 0 & 1 & 1 & -1 & -1 & 0 & 0 & 0 & 0 & 0 & 0 & 0 & 0\\
0 & 0 & 0 & 0 & 0 & 0 & 0 & 1 & -1 & -1 & 1 & 1 & -1 & -1 & 1\\
0 & 0 & 0 & 0 & 0 & 0 & 0 & 1 & 1 & -1 & -1 & -1 & -1 & 1 & 1\\
0 & 0 & 0 & 0 & 0 & 0 & 0 & 1 & -1 & 1 & -1 & -1 & 1 & -1 & 1\\
0 & 0 & 0 & 0 & 0 & 0 & 0 & 1 & -1 & -1 & 1 & -1 & 1 & 1 & -1
\end{pmatrix}.$$

The relaxation rates are set as follows,

$$\boldsymbol{S} = (0, s_e, s_\varepsilon, 0, s_q, 0, s_q, 0, s_q, s_\nu, s_\nu, s_\nu, s_\nu, s_\nu, s_t)\,,$$

which are related to the viscosities as follows,

$$\nu = \frac{1}{3}\left(\frac{1}{s_\nu}-\frac{1}{2}\right)\delta_t, \quad \zeta = \frac{2}{9}\left(\frac{1}{s_e}-\frac{1}{2}\right)\delta_t\,.$$

(5) *D3Q19 model*

The discrete velocity set of the D3Q19 MRT model is the same as that of the LBGK model. The corresponding moments are

$$\boldsymbol{m} = \left(\rho,\, e,\, \varepsilon,\, j_x,\, q_x,\, j_y,\, q_y,\, j_z,\, q_z,\, 3p_{xx},\, 3\pi_{xx},\, p_{ww},\, \pi_{ww},\, p_{xy},\, p_{yz},\, p_{zx}, t_x,\, t_y,\, t_z\right)^T,$$

while the corresponding equilibrium moments are

$$m^{(eq)} = \rho\Bigg(1, -11 + 19u^2, \alpha + \beta u^2, u_x, -\frac{2}{3}u_x, u_y, -\frac{2}{3}u_y, u_z, -\frac{2}{3}u_z,$$
$$3u_x^2 - u^2, \frac{\gamma p_{xx}^{(eq)}}{\rho}, u_y^2 - u_z^2, \frac{\gamma p_{ww}^{(eq)}}{\rho}, u_x u_y, u_y u_z, u_z u_x, 0, 0, 0\Bigg)^T,$$

where α, β, and γ are free parameters. As $\alpha = 3$, $\beta = -11/2$, and $\gamma = -1/2$, the equilibria reduce to those of the D3Q19 LBGK model. The transformation matrix of this model is

$$\boldsymbol{M} = \begin{pmatrix}
1 & 1 & 1 & 1 & 1 & 1 & 1 & 1 & 1 & 1 & 1 & 1 & 1 & 1 & 1 & 1 & 1 & 1 & 1 & 1 \\
-30 & -11 & -11 & -11 & -11 & -11 & -11 & 8 & 8 & 8 & 8 & 8 & 8 & 8 & 8 & 8 & 8 & 8 & 8 & 8 \\
12 & -4 & -4 & -4 & -4 & -4 & -4 & 1 & 1 & 1 & 1 & 1 & 1 & 1 & 1 & 1 & 1 & 1 & 1 & 1 \\
0 & 1 & -1 & 0 & 0 & 0 & 0 & 1 & -1 & 1 & -1 & 1 & -1 & 1 & -1 & 0 & 0 & 0 & 0 & 0 \\
0 & -4 & 4 & 0 & 0 & 0 & 0 & 1 & -1 & 1 & -1 & 1 & -1 & 1 & -1 & 0 & 0 & 0 & 0 & 0 \\
0 & 0 & 0 & 1 & -1 & 0 & 0 & 1 & 1 & -1 & -1 & 0 & 0 & 0 & 0 & 1 & -1 & 1 & -1 & 0 \\
0 & 0 & 0 & -4 & 4 & 0 & 0 & 1 & 1 & -1 & -1 & 0 & 0 & 0 & 0 & 1 & -1 & 1 & -1 & 0 \\
0 & 0 & 0 & 0 & 0 & 1 & -1 & 0 & 0 & 0 & 0 & 1 & 1 & -1 & -1 & 1 & 1 & -1 & -1 & 0 \\
0 & 0 & 0 & 0 & 0 & -4 & 4 & 0 & 0 & 0 & 0 & 1 & 1 & -1 & -1 & 1 & 1 & -1 & -1 & 0 \\
0 & 2 & 2 & -1 & -1 & -1 & -1 & 1 & 1 & 1 & 1 & 1 & 1 & 1 & 1 & -2 & -2 & -2 & -2 & 0 \\
0 & -4 & -4 & 2 & 2 & 2 & 2 & 1 & 1 & 1 & 1 & 1 & 1 & 1 & 1 & -2 & -2 & -2 & -2 & 0 \\
0 & 0 & 0 & 1 & 1 & -1 & -1 & 1 & 1 & 1 & 1 & -1 & -1 & -1 & -1 & 0 & 0 & 0 & 0 & 0 \\
0 & 0 & 0 & -2 & -2 & 2 & 2 & 1 & 1 & 1 & 1 & -1 & -1 & -1 & -1 & 0 & 0 & 0 & 0 & 0 \\
0 & 0 & 0 & 0 & 0 & 0 & 0 & 1 & -1 & -1 & 1 & 0 & 0 & 0 & 0 & 0 & 0 & 0 & 0 & 0 \\
0 & 0 & 0 & 0 & 0 & 0 & 0 & 0 & 0 & 0 & 0 & 0 & 0 & 0 & 0 & 1 & -1 & -1 & 1 & 0 \\
0 & 0 & 0 & 0 & 0 & 0 & 0 & 0 & 0 & 0 & 0 & 1 & 1 & -1 & -1 & 0 & 0 & 0 & 0 & 0 \\
0 & 0 & 0 & 0 & 0 & 0 & 0 & 1 & -1 & 1 & -1 & -1 & 1 & -1 & 1 & 0 & 0 & 0 & 0 & 0 \\
0 & 0 & 0 & 0 & 0 & 0 & 0 & -1 & -1 & 1 & 1 & 0 & 0 & 0 & 0 & 1 & -1 & 1 & -1 & 0 \\
0 & 0 & 0 & 0 & 0 & 0 & 0 & 0 & 0 & 0 & 0 & 1 & 1 & -1 & -1 & -1 & -1 & 1 & 1 & 0
\end{pmatrix}.$$

The relaxation rates of this model are

$$\boldsymbol{S} = (0,\, s_e,\, s_\varepsilon,\, 0,\, s_q,\, 0,\, s_q,\, 0,\, s_q,\, s_\nu,\, s_\pi,\, s_\nu,\, s_\pi,\, s_\nu,\, s_\nu,\, s_\nu,\, s_t,\, s_t,\, s_t),$$

while the shear and bulk viscosities as

$$\nu = \frac{1}{3}\left(\frac{1}{s_\nu} - \frac{1}{2}\right)\delta_t, \qquad \zeta = \frac{2}{9}\left(\frac{1}{s_e} - \frac{1}{2}\right)\delta_t.$$

It can be shown that with the equilibrium moments described above, the Navier-Stokes equations can be obtained either by the Chapman-Enskog expansion method [d'Humières, 1992; d'Humières *et al*., 2002] or a linear analysis [Lallemand and Luo, 2000].

1.5 Summary

In this chapter we have presented an overview of the LBE method. It can be seen that the LBE is a novel approach for fluid dynamics, quite different from the classical CFD techniques that are based on the solution of Navier-Stokes equations. Firstly, although LBE aims to solve continuum flows at macroscopic scales, it is developed based on microscopic models (LGA) or kinetic theory (Boltzmann equation). This feature suggests that the LBE has the potential to model nonequilibrium flows which cannot be described by the Navier-Stokes equations. Secondly, the kinetic nature of LBE makes it suitable for describing the internal interactions among fluid particles and those between the fluid and external environment, and this brings great advantages in simulating complex flows such as multi-component/phase flows and flows in porous media. Finally, the clear evolution picture of LBE makes it quite easy to code; Particularly, the collision process involves only local computations and the streaming process can be realized by simple index shift operations, which makes LBE well suited for massive parallel computers.

These distinctive features have made LBE an attractive numerical tool for modeling and simulating complicated fluid flows and associated phenomena. Actually, LBE can find its applications in simulation of laminar and turbulent flows, interfacial dynamics of multiphase flows, flows in porous media, particulate and suspension systems, bio-fluid mechanics, electro-kinetic flows, magneto-hydrodynamics, quantum and relativistic flows, nano/micro fluidics, and multiscale flows. The developments of LBE at different stages have been summarized in several excellent review papers [Benzi *et al*., 1992; Chen and Doolen, 1998; Yu *et al*., 2003; Aidun and Clausen, 2010], and a number of books on both general LBE methods [Wolf-Gladrow, 2000; Succi, 2001] and specific topics [Sukop and Thorne, 2006; Zhou, 2004] are also available.

The past two decades have witnessed the rapid development and great success of LBE in fundamental theory and applications in a variety of related areas, and nowadays the research in this field is still very active and exciting. The LBE has been becoming a topic of great interest in many international conferences, and even two specific conferences on this subject, DSFD (*International Conference on the Discrete Simulation of Fluid Dynamics*) and ICMMES (*International Conference for Mesoscopic Methods in Engineering and Science*), have been established.

Chapter 2

Initial and Boundary Conditions for Lattice Boltzmann Method

Initial and boundary conditions play an important role in fluid dynamics since they are essential in the determination of the solution of the flow. Generally, these conditions are specified in terms of the fluid variables such as velocity, pressure, and temperature. However, the primitive variable in LBE is the discrete distribution function. The fluid density and velocity (and temperature in thermal flows) can be determined uniquely by the distribution function, but not vice versa. Therefore, it is critical for LBE to find a way to transform the initial and boundary conditions from the fluid variables to those for the distribution functions. Some studies have revealed that these conditions do have significant influences on the accuracy, stability, and convergence of LBE. So, the treatments of initial and boundary conditions are a fundamental topic in the study and applications of LBE. In this chapter, we will present some useful rules for realizing these conditions in LBE. We will focus on isothermal cases unless mentioned otherwise.

2.1 Initial Conditions

2.1.1 *Equilibrium scheme*

The equilibrium scheme is a widely used method for imposing initial conditions in LBE. In this scheme, the distribution functions are initialized as the equilibria directly,

$$f_i(t_0) = f_i^{(eq)}(\rho_0, \boldsymbol{u}_0), \quad i = 0 \sim b-1, \tag{2.1}$$

where ρ_0 and $\boldsymbol{u}_0$ are the initial values of density and velocity at time t_0. In many problems, only the velocity is initialized and the density (or pressure) is unknown. In such case, the density must be determined first from the velocity field in a compatible manner. For instance, the initial pressure p_0 can be obtained by solving a Poisson equation for incompressible flows, and then the density can be initialized as

$$\rho_0 = \overline{\rho} + \frac{p - \overline{p}}{c_s^2}, \tag{2.2}$$

where $\overline{\rho}$ and $\overline{p}$ are the average density and pressure, respectively.

For steady or quasi-steady flows, the final results are independent of initial conditions, and the equilibrium scheme will work well. But for unsteady or strong nonlinear flows which are very sensitive to initial conditions, this scheme may lead to large errors due to the initial layers in the discrete distribution functions. In such cases, more accurate initial schemes should be adopted.

2.1.2 *Non-equilibrium scheme*

In order to increase the approximation accuracy to $f_i(t_0)$, we can introduce some corrections from the non-equilibrium part of the distribution function, $f_i^{(neq)} = f_i - f_i^{(eq)}$. This technique was first proposed by Skordos [1993]. The key point of such schemes is how to obtain the non-equilibrium part from initial conditions.

We first consider the LBGK models. The LBGK equation gives that

$$f_i^{(neq)}(\boldsymbol{x}, t) = -\tau\Big[f_i(\boldsymbol{x} + \boldsymbol{c}_i\delta_t, t + \delta_t) - f_i(\boldsymbol{x}, t)\Big]. \tag{2.3}$$

The Taylor expansion of the right hand side gives that

$$f_i^{(neq)} = -\tau\delta_t D_i f_i + O(\delta_t^2), \tag{2.4}$$

where $D_i = \partial_t + \boldsymbol{c}_i \cdot \nabla$. On the other hand, the distribution function can be expanded into a series following the Chapman-Enskog method,

$$f_i = f_i^{(eq)} + \varepsilon f_i^{(1)} + \varepsilon^2 f_i^{(2)} + \cdots, \tag{2.5}$$

where the expansion parameter ε is proportional to the Knudsen number which is very small for continuum flows. Therefore, the non-equilibrium distribution function can be approximated as

$$f_i^{(neq)} \approx -\tau\delta_t D_i f_i^{(eq)} = -\tau\delta_t \left[\frac{\partial f_i^{(eq)}}{\partial \rho} D_i \rho + \frac{\partial f_i^{(eq)}}{\partial \boldsymbol{j}} \cdot D_i \boldsymbol{j} \right], \tag{2.6}$$

where $\boldsymbol{j}=\rho\boldsymbol{u}$. In the above equation $\partial f_i^{(eq)}/\partial\rho$ and $\partial f_i^{(eq)}/\partial\boldsymbol{j}$ can be evaluated exactly from the expressions of $f_i^{(eq)}$. For example, the EDF of the D*n*Q*b* models gives that

$$\frac{\partial f_i^{(eq)}}{\partial \rho} = \omega_i \left[1 - \frac{(\boldsymbol{c}_i \cdot \boldsymbol{u})^2}{2c_s^4} + \frac{\boldsymbol{u}^2}{2c_s^2} \right], \tag{2.7}$$

$$\frac{\partial f_i^{(eq)}}{\partial \boldsymbol{j}} = \omega_i \left[\frac{\boldsymbol{c}_i - \boldsymbol{u}}{c_s^2} + \frac{(\boldsymbol{c}_i \cdot \boldsymbol{u})\boldsymbol{c}_i}{c_s^4} \right]. \tag{2.8}$$

The temporal and spatial derivatives in Eq. (2.6) should be evaluated numerically, and the two temporal derivatives can be converted into spatial gradients first following the conservation equations. If the hydrodynamic equations at the t_0 scale in the Chapman-Enskog expansion (i.e. the Euler equations) are used, we can obtain that

$$D_i\rho = (\boldsymbol{c}_i - \boldsymbol{u}) \cdot \nabla\rho - \rho\nabla \cdot \boldsymbol{u}\,, \quad D_i\boldsymbol{j} = -\nabla p + (\boldsymbol{c}_i - \boldsymbol{u}) \cdot \nabla\boldsymbol{j} - \boldsymbol{j}\nabla \cdot \boldsymbol{u}\,. \tag{2.9}$$

Alternatively, we can use the Navier-Stokes equations to evaluate the temporal derivatives, which give that

$$\begin{aligned} D_i\rho &= (\boldsymbol{c}_i - \boldsymbol{u}) \cdot \nabla\rho + \rho\nabla \cdot \boldsymbol{u}, \\ D_i\boldsymbol{j} &= -\nabla p + \nabla \cdot \boldsymbol{\tau} + (\boldsymbol{c}_i - \boldsymbol{u}) \cdot \nabla\boldsymbol{j} - \boldsymbol{j}\nabla \cdot \boldsymbol{u}, \end{aligned} \tag{2.10}$$

where $\boldsymbol{\tau}$ is the stress tensor.

Substituting the above results into Eq. (2.6), one can obtain an explicit approximation to the non-equilibrium distribution function, which is quite complicated. In order to simplify the expressions, one can ignore terms of second and high-order of M (Mach number). For example, the final formulation of Eq. (2.6) can be expressed as

$$f_i^{(neq)} = -\tau\delta_t\omega_i\rho \left[\frac{1}{c_s^2} \boldsymbol{c}_i\boldsymbol{c}_i : \nabla\boldsymbol{u} - \nabla \cdot \boldsymbol{u} \right]. \tag{2.11}$$

Guo *et al.* [2003] made a further simplification by noticing that $\rho = \overline{\rho}(1+\delta\rho) = \overline{\rho} + O(M^2)$ for nearly incompressible flows,

$$f_i^{(neq)} = -\tau\delta_t\omega_i \frac{\overline{\rho}}{c_s^2} \boldsymbol{c}_i\boldsymbol{c}_i : \nabla\boldsymbol{u} \,. \tag{2.12}$$

This result is consistent with the mass and momentum conservation constraints for incompressible flows,

$$\sum_i f_i^{(neq)} = -\tau\delta_t\overline{\rho}\ \nabla\cdot\boldsymbol{u} = 0, \quad \sum_i \boldsymbol{c}_i f_i^{(neq)} = 0 \,. \tag{2.13}$$

The above non-equilibrium schemes are designed for LBGK models, and they can also be extended to MRT-LBE models. For instance, Lallemand and Luo [2000] suggested correcting the initial moments using the non-equilibria ones in moment space first, and then transform back to the velocity to obtain the initial distribution functions:

$$\boldsymbol{m}^{(neq)} = -\delta_t\boldsymbol{S}^{-1}\boldsymbol{M}\boldsymbol{C}_\alpha\partial_\alpha\boldsymbol{f}^{(eq)} = -\delta_t\boldsymbol{S}^{-1}\hat{\boldsymbol{C}}_\alpha\partial_\alpha\boldsymbol{m}^{(eq)}, \ \boldsymbol{f}^{(neq)} = \boldsymbol{M}^{-1}\boldsymbol{m}^{(neq)}, \tag{2.14}$$

where $\boldsymbol{C}_\alpha = diag\left(c_{0\alpha}, c_{0\alpha}, \cdots, c_{b-1,\alpha}\right)$ and $\hat{\boldsymbol{C}}_\alpha = \boldsymbol{M}\boldsymbol{C}_\alpha\boldsymbol{M}^{-1}$.

2.1.3 *Iterative method*

In order to obtain consistent initial distribution functions from a given velocity field, some researchers suggested solving a Poisson equation using a LBE, which can provide both the desired pressure (or density) and the distribution functions [Caiazzo, 2005; Mei *et al.*, 2006]. For the LBGK equation,

$$f_i(\boldsymbol{x}+\boldsymbol{c}_i\delta_t, t+\delta_t) - f_i(\boldsymbol{x},t) - \frac{1}{\tau}\Big[f_i(\boldsymbol{x},t) - f_i^{(eq)}\left(\rho(\boldsymbol{x},t), \boldsymbol{u}(\boldsymbol{x},t)\right)\Big], \tag{2.15}$$

the procedure of iterative initialization method is as follows,

(a) Collision:

$$\tilde{f}_i'(\boldsymbol{x},\tilde{t}) = \tilde{f}_i(\boldsymbol{x},\tilde{t}) - \frac{1}{\tau}\Big[\tilde{f}_i(\boldsymbol{x},\tilde{t}) - f_i^{(eq)}\left(\tilde{\rho}(\boldsymbol{x},\tilde{t}), \boldsymbol{u}_0\right)\Big].$$

(b) Streaming:

$$\tilde{f}_i(\boldsymbol{x}+\boldsymbol{c}_i\delta_t, \tilde{t}+\delta_t) = \tilde{f}_i'(\boldsymbol{x},\tilde{t}) \,.$$

(c) Calculating the predicted initial density:

$$\tilde{\rho}(\boldsymbol{x}, \tilde{t} + \delta_t) = \sum_i \tilde{f}_i(\boldsymbol{x}, \tilde{t} + \delta_t)\,.$$

(d) If $\tilde{\rho}$ converges to its steady state ρ_0, the iteration will end, and the initial distribution functions as well as the density are set to be $f_i(\boldsymbol{x}, t_0) = \tilde{f}_i(\boldsymbol{x}, \tilde{t} + \delta_t)$ and $\rho(\boldsymbol{x}, t_0) = \rho_0 \equiv \tilde{\rho}(\boldsymbol{x}, \tilde{t} + \delta_t)$, respectively; otherwise, go to (a) for next iteration.

Note that in the above iterative procedure we have used the notation with a tilde to distinguish the variables from the physical ones. Meanwhile, in the EDF $\tilde{f}_i^{(eq)}$, the velocity always takes the initial value during the pseudo time evolution, and only the density $\tilde{\rho}$ acts as a conservative variable. Actually, the iterative procedure corresponds to the following modified LBGK equation,

$$\tilde{f}_i(\boldsymbol{x} + \boldsymbol{c}_i\delta_t, \tilde{t} + \delta_t) - \tilde{f}_i(\boldsymbol{x}, \tilde{t}) = \frac{1}{\tau}\Big[\tilde{f}_i(\boldsymbol{x}, \tilde{t}) - f_i^{(eq)}\Big(\tilde{\rho}(\boldsymbol{x}, \tilde{t}), \boldsymbol{u}_0\Big)\Big], \tag{2.16}$$

with the constraint that

$$\tilde{\rho} = \sum_i \tilde{f}_i = \sum_i f_i^{(eq)}\Big(\tilde{\rho}, \boldsymbol{u}_0\Big)\,. \tag{2.17}$$

One can show that the hydrodynamic equation derived from this LBGK equation via the Chapman-Enskog method is

$$\frac{\partial\tilde{\rho}}{\partial\tilde{t}} + \nabla\cdot(\tilde{\rho}\boldsymbol{u}_0) = \frac{\nu}{c_s^2}\Big[c_s^2\nabla^2\tilde{\rho} + \nabla\nabla : (\tilde{\rho}\boldsymbol{u}_0\boldsymbol{u}_0)\Big]. \tag{2.18}$$

If the initial velocity field is incompressible, i.e., $\nabla\cdot\boldsymbol{u}_0 = 0$, at steady state the leading order of the above equation is

$$\nabla^2 P = -\nabla\cdot(\boldsymbol{u}_0\cdot\nabla\boldsymbol{u}_0)\,, \tag{2.19}$$

where $P = c_s^2\delta\rho$ is the dynamic pressure. This means that the above iterative procedure leads to a consistent initialized pressure field and the distribution functions as well.

The iterative procedure can also be applied to MRT-LBE models with some slight modifications [Mei *et al.*, 2006]. The procedure is the same

as that for the LBGK model except that the collision is carried out in the moment space, i.e., the collision step (a) is replaced by the following one:

(a') Collision:

$$\tilde{\boldsymbol{m}}_k'(\boldsymbol{x}, \tilde{t}) = \tilde{\boldsymbol{m}}_k(\boldsymbol{x}, \tilde{t}) - s_k \left[\tilde{\boldsymbol{m}}_k(\boldsymbol{x}, \tilde{t}) - \tilde{\boldsymbol{m}}_k^{(eq)} \left(\tilde{\rho}(\boldsymbol{x}, \tilde{t}), \boldsymbol{u}_0 \right) \right],$$

$$\boldsymbol{f}'(\boldsymbol{x}, \tilde{t}) = \boldsymbol{M}^{-1} \tilde{\boldsymbol{m}}'(\boldsymbol{x}, \tilde{t}) .$$

Note that the momentum $\boldsymbol{j}$ is not a conservative variable and the corresponding relaxation rate s_j is nonzero. The corresponding hydrodynamic equation is the same as Eq. (2.18) except that the kinematic viscosity appearing on the right hand side is now replaced by a diffusivity $D = c_s^2(\tau_j - 0.5)\delta_t$ where $\tau_j = 1/s_j$. Because the relaxation time τ_j can be adjusted independently from that for the kinematic viscosity, the iteration can achieve a faster convergence than that for the LBGK models. This feature is particularly useful for high Reynolds number flows where the viscosity is small.

2.2 Boundary Conditions for Flat Walls

Similar to initial conditions, the distribution functions at a boundary should also be constructed to reflect specified boundary conditions for fluid variables (pressure, velocity, and temperature). A variety of boundary schemes have been introduced for LBE. According to methodology employed, boundary conditions in LBE can be classified into heuristic schemes, hydrodynamic schemes, and interpolation/ extrapolation schemes. We first present some boundary schemes for flat boundaries.

2.2.1 *Heuristic schemes*

Heuristic or phenomenological schemes are designed based on the dynamics of fluid particles as they encounter a wall. Several such schemes are sketched in Fig. 2.1 for a flat wall. The *bounce-back scheme* is the most widely used rule for stationary no-slip walls. This scheme assumes that a particle just reverses its velocity after colliding with the

wall, which means that the post-collision distribution function at a boundary node $\boldsymbol{x}_b$ is

$$f_{\bar{i}}'(\boldsymbol{x}_b, t) = f_i'(\boldsymbol{x}_f, t)\,, \tag{2.20}$$

where $\boldsymbol{c}_{\bar{i}} = -\boldsymbol{c}_i$ with $\boldsymbol{c}_i$ pointing to the fluid, $\boldsymbol{x}_b$ is a node located on the wall, and $\boldsymbol{x}_f = \boldsymbol{x}_b - \boldsymbol{c}_i\delta_t$ is the neighboring fluid node. Based on the collision-streaming process, the bounce-back scheme can also be expressed in alternative formulations,

$$f_{\bar{i}}(\boldsymbol{x}_f, t+\delta_t) = f_i'(\boldsymbol{x}_f, t)\,, \tag{2.21}$$

or

$$f_{\bar{i}}(\boldsymbol{x}_f, t+\delta_t) = f_i(\boldsymbol{x}_b, t+\delta t)\,. \tag{2.22}$$

Particularly, the formulation given by Eq. (2.21) has nothing to do with boundary nodes and the computation is completely local, and therefore is

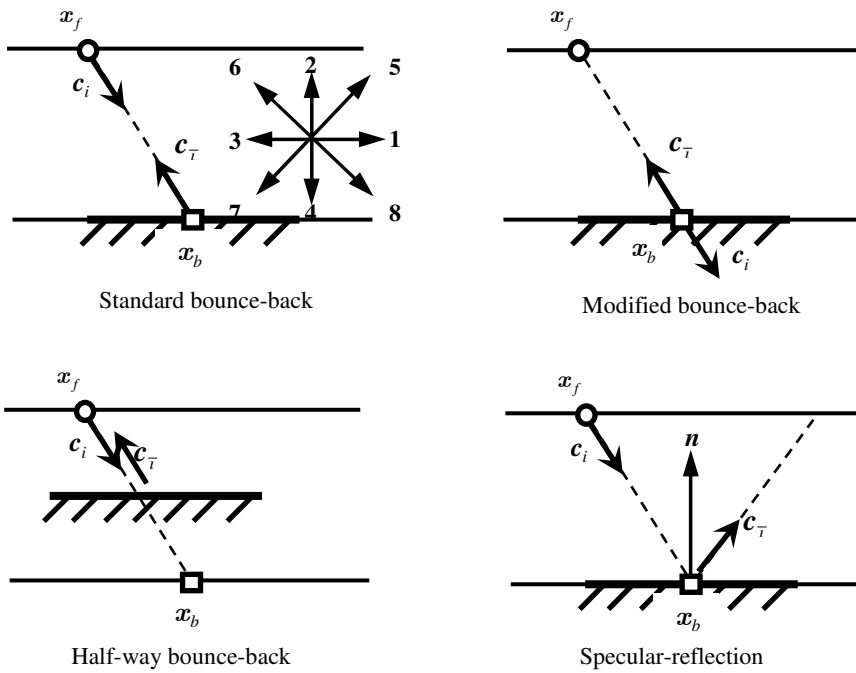

Fig. 2.1. Sketch of several heuristic schemes.

widely used in practical applications. For example, for the D2Q9 model the unknown distribution functions in the directions 2, 5, and 6 can be easily obtained as (see Fig. 2.1)

$$f_2(\boldsymbol{x}_f, t+\delta_t) = f_4'(\boldsymbol{x}_f, t),\ f_5(\boldsymbol{x}_f, t+\delta_t) = f_7'(\boldsymbol{x}_f, t)\,,$$
$$f_6(\boldsymbol{x}_f, t+\delta_t) = f_8'(\boldsymbol{x}_f, t)\,. \tag{2.23}$$

It is noted that in the standard bounce-back scheme the collision process is not carried out on the boundary nodes. If the collision is also imposed on the boundary, the method is called *modified bounce-back scheme*, which specifies the unknown pre-collision distributions at the boundary nodes as follows,

$$f_{\bar{i}}(\boldsymbol{x}_b, t) = f_i(\boldsymbol{x}_b, t)\,. \tag{2.24}$$

Then the fluid density and velocity at the boundary nodes can be calculated from the distribution functions, and the collision step can be executed. The modified bounce-back scheme for the D2Q9 model can be expressed as

$$f_2(\boldsymbol{x}_b, t) = f_4(\boldsymbol{x}_b, t)\,,\ f_5(\boldsymbol{x}_b, t) = f_7(\boldsymbol{x}_b, t)\,,\ f_6(\boldsymbol{x}_b, t) = f_8(\boldsymbol{x}_b, t)\,. \tag{2.25}$$

Another modification of the standard bounce-back scheme is the *half-way bounce-back scheme*, whose formulation is totally identical to the standard one except that the wall is placed at the middle of the link, $(\boldsymbol{x}_b + \boldsymbol{x}_f)/2$. The physical picture of this scheme is clear: The post-collision particles with velocity $\boldsymbol{c}_i$ at node $\boldsymbol{x}_f$ will arrive at the wall after time $\delta_t/2$, and are then reflected back to $\boldsymbol{x}_f$ with a reversed velocity $\boldsymbol{c}_{\bar{i}}$ after another $\delta_t/2$, and so $f_{\bar{i}}(\boldsymbol{x}_f, t+\delta_t) = f_i'(\boldsymbol{x}_f, t)$, which is the same as the standard bounce-back scheme. This also implies that the standard bounce-back scheme does not exhibit such a physical picture. Actually, some studies have shown that the half-way bounce-back scheme is of second-order accuracy, while the standard one is only of first order [He *et al.*, 1997]. Similar to the half-way bounce-back scheme, the modified bounce-back scheme is also of second-order accuracy.

It is clear that in the bounce-back schemes, the momentum of a particle is just reversed before and after it hits the wall, which means that the macroscopic velocity at the wall is zero. Therefore, these bounce-back

schemes work for stationary walls. As the wall moves with a velocity $\boldsymbol{u}_w$, the schemes should be modified to include the contribution of the wall motion. For example, Ladd has suggested a revised half-way bounce-scheme,

$$f_{\bar{i}}(\boldsymbol{x}_f, t+\delta_t) = f_i'(\boldsymbol{x}_f, t) - 2\omega_i \rho(\boldsymbol{x}_f)\frac{\boldsymbol{c}_i \cdot \boldsymbol{u}_w}{c_s^2}, \tag{2.26}$$

where ω_i is the weight appearing in the EDF of the DnQb model.

The bounce-back schemes given above can also be extended to complicated geometrics straightforwardly. The main advantage of such schemes is its simplicity and easy implementation. Particularly, the locality makes it very efficient for flows with complex geometries such as porous flows, which are difficult to solve for the classical CFD methods.

Similar to the standard bounce-back scheme, another heuristic boundary condition is the *specular reflection scheme*, which assumes that the particle hitting the wall will be reflected to the fluid specularly,

$$f_{\bar{i}}'(\boldsymbol{x}_b, t) = f_i'(\boldsymbol{x}_f, t), \tag{2.27}$$

where $\boldsymbol{c}_{\bar{i}} = \boldsymbol{c}_i - 2(\boldsymbol{c}_i \cdot \boldsymbol{n})\boldsymbol{n}$ is the mirror-symmetric velocity of $\boldsymbol{c}_i$ with respect to $\boldsymbol{n}$, the outward unit vector normal to the wall. Like the standard bounce-back scheme, the collision is not performed on boundary nodes in this scheme, and we can construct a *modified specular-reflection scheme* where collisions also occur on the boundary, $f_{\bar{i}}(\boldsymbol{x}_b, t) = f_i(\boldsymbol{x}_b, t)$, or a *half-way specular-reflection scheme*. It is clear that the tangential velocity of the particle does not change during the collision, while the normal momentum velocity is just reversed in the specular-reflection schemes. Therefore, these schemes can be used to realize the free-slip boundary condition on a smooth surface.

2.2.2 *Hydrodynamic schemes*

The simple heuristic schemes given in the above subsection can be used to realize no-slip and free-slip boundary conditions in a straightforward way. However, these schemes will also introduce some errors inevitably

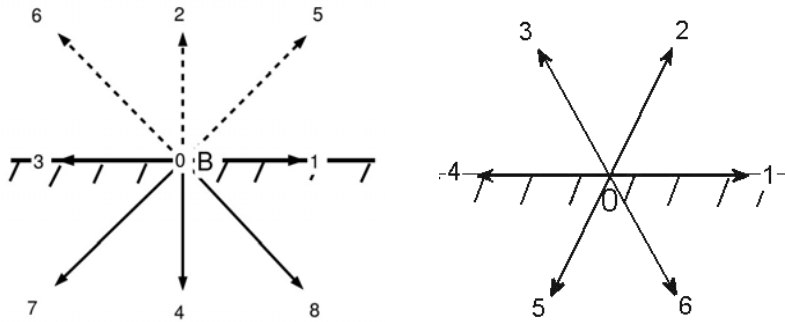

Fig. 2.2. Sketch of the hydrodynamic scheme for the D2Q9 and D2Q7 model.

[He *et al*., 1997]. To overcome such limitations, some more elaborated approaches, i.e. *hydrodynamic schemes,* have been developed to realize the exact boundary conditions based on the relations between the macroscopic fluid variables and the distribution functions. For isothermal LBE models, the constraints in constructing a hydrodynamic scheme are

$$\sum_i f_i = \rho_w, \quad \sum_i \boldsymbol{c}_i f_i = \rho_w \boldsymbol{u}_w , \tag{2.28}$$

where ρ_w is the density at the wall which is not necessarily a known variable. Generally these two constraints are not sufficient to determine the unknown distribution functions on the wall nodes. For instance, for the D2Q9 model sketched in Fig. 2.2, after streaming, the distribution functions f_0, f_1, f_3, f_4, f_7, f_8 are known, the unknowns are f_2, f_5, f_6, and ρ_w, which cannot be determined from the three equations given in (2.28).

The first hydrodynamic scheme for velocity boundary condition was developed by Noble *et al.* [1995] for the D2Q7 model. In this case the unknown variables are f_2, f_5, and ρ_w, which can be determined exactly from the following equations:

$$\begin{aligned} f_2 + f_3 - \rho_w &= -A \equiv -(f_0 + f_1 + f_4 + f_5 + f_6), \\ f_2 - f_3 - \frac{2u_x}{c}\rho_w &= -B \equiv -(2f_1 - 2f_4 - f_5 + f_6), \\ f_2 + f_3 - \frac{2u_y}{\sqrt{3}c}\rho_w &= f_5 + f_6, \end{aligned} \tag{2.29}$$

where u_x and u_y are the two components of $\boldsymbol{u}_w$. From these three equations we can obtain that,

$$\begin{aligned}
&\rho_w = \frac{f_0 + f_1 + f_4 + 2(f_5 + f_6)}{1 - 2u_y/\sqrt{3}c}, \quad f_2 = \frac{1}{2}\left[-A - B + \left(1 + \frac{2u_x}{c}\right)\rho_w\right], \\
&f_3 = \frac{1}{2}\left[-A + B + \left(1 - \frac{2u_x}{c}\right)\rho_w\right] .
\end{aligned} \tag{2.30}$$

For more general cases, Noble *et al.* suggested using the energy condition as a complementary condition [Noble *et al.*, 1995],

$$\sum_i (\boldsymbol{c}_i - \boldsymbol{u})^2 f_i = \rho_w D R T_w , \tag{2.31}$$

where D is the spatial dimension, R is the gas constant, and T_w is the wall temperature which is a constant and related to the lattice speed c for isothermal LBE models (e.g., $RT_w = c_s^2$ for the D*n*Q*b* models). With this condition, the unknown distribution functions in D2Q9 can be solved analytically.

Inamuro *et al.* [1995] proposed another hydrodynamic scheme (*counter-slip scheme*), which assumes that the unknown distribution functions on a boundary node take the same formulation as the discrete EDF but with an undetermined density and velocity:

$$f_i = f_i^{(eq)}(\rho', \boldsymbol{u}_w + \boldsymbol{u}') \quad (\boldsymbol{c}_i \cdot \boldsymbol{n} > 0), \tag{2.32}$$

where ρ' is a fictitious density and $\boldsymbol{u}' = (u', 0)$ is a counter-slip velocity, both of which are determined so that the fluid velocity at the wall is equal to the wall velocity. With this condition and Eq. (2.28), one can obtain the following results for the D2Q9 model [Inamuro *et al.*, 1995],

$$\begin{aligned}
\rho_w &= \frac{1}{1 - u_y/c}\left[f_0 + f_1 + f_3 + 2(f_4 + f_7 + f_8)\right], \\
\rho' &= 6\frac{\rho_w u_y/c + (f_4 + f_7 + f_8)}{1 + 3u_y/c + 3(u_y/c)^2}, \\
u' &= \frac{1}{1 + 3u_y/c}\left[6\frac{\rho_w u_x/c - (f_1 - f_3 - f_7 + f_8)}{\rho'} - \frac{u_x}{c} - 3\frac{u_x u_y}{c^2}\right] .
\end{aligned} \tag{2.33}$$

With these results, the unknown distributions can then be calculated according to Eq. (2.32).

Zou and He [1997] proposed an alternative supplementary condition, i.e., bounce-back of the non-equilibrium distribution functions. For the D2Q9 model as sketched in Fig. 2.2, this scheme assumes that

$$f_2(\boldsymbol{x}_b) - f_2^{(eq)}(\boldsymbol{x}_b) = f_4(\boldsymbol{x}_b) - f_4^{(eq)}(\boldsymbol{x}_b)\,, \tag{2.34}$$

or

$$f_2(\boldsymbol{x}_b) - f_4(\boldsymbol{x}_b) = f_2^{(eq)}(\boldsymbol{x}_b) - f_4^{(eq)}(\boldsymbol{x}_b) = \frac{2\rho_w u_y}{3c}\,. \tag{2.35}$$

With this condition and Eq. (2.28), the unknown distributions at the wall nodes can be determined,

$$\begin{aligned} f_2 &= f_4 + \frac{2}{3}\frac{\rho_w u_y}{c}, \quad f_5 = f_7 - \frac{f_1 - f_3}{2} + \frac{1}{2}\frac{\rho_w u_x}{c} + \frac{1}{6}\frac{\rho_w u_y}{c}, \\ f_5 &= f_8 + \frac{f_1 - f_3}{2} - \frac{1}{2}\frac{\rho_w u_x}{c} + \frac{1}{6}\frac{\rho_w u_y}{c}, \end{aligned} \tag{2.36}$$

where the wall density is given by

$$\rho_w = \frac{1}{1 - u_y/c}\left[f_0 + f_1 + f_3 + 2(f_4 + f_7 + f_8)\right], \tag{2.37}$$

which is the same as that in Inamuro's counter-slip scheme.

The main advantage of the hydrodynamic schemes is that they can realize the specified velocity boundary conditions exactly. As discussed above, however, these schemes depend severely on the LBE models, and special treatments are required for corner nodes. Therefore, most of the applications of the hydrodynamic schemes are focused on flows with simple flat boundaries.

2.2.3 *Extrapolation schemes*

The heuristic and hydrodynamic schemes given above are mainly used for velocity boundary conditions. In many practical problems, however, the boundary conditions may also involve gradients of fluid variables

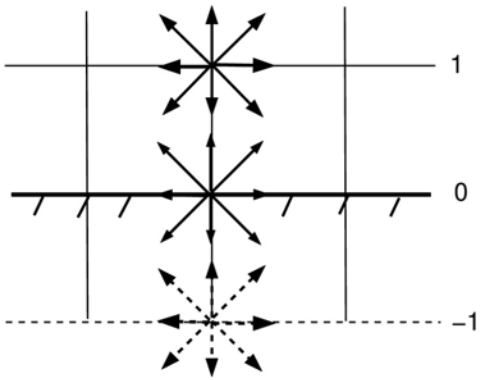

Fig. 2.3. Sketch of the extrapolation scheme.

(e.g. the Neumann boundary conditions). For such boundary conditions, the previous schemes are not applicable. By borrowing ideas from the finite-difference methods for partial differential equations, some researchers were able to develop more general boundary schemes for such problems, and a good example is the *extrapolation schemes.*

The first extrapolation scheme was due to Chen *et al.* [1996]. As sketched in Fig. 2.3, a ghost layer is put outside the wall and the physical wall is just treated as an inner part of the flow domain where the standard collision and streaming processes are carried out. The distribution functions at the ghost nodes are obtained by a second-order extrapolation from those at inner nodes:

$$f_i(\boldsymbol{x}_{-1}, t) = 2f_i(\boldsymbol{x}_0, t) - f_i(\boldsymbol{x}_1, t)\,, \tag{2.38}$$

where −1, 0, and 1 are the labels of the ghost layer, the wall, and the first fluid layer, respectively. After this extrapolation, collisions are conducted at all inner nodes, including the wall nodes. But it is noted that the specified density or velocity given by the boundary conditions is used in the calculation of the EDFs for wall nodes.

It can be shown that the above extrapolation scheme is of second-order accuracy, which is consistent with the accuracy of LBE. Unlike the hydrodynamic schemes, this scheme is easy for implementation, and can be extended straightforwardly to other types of boundary conditions.

However, some studies showed that the extrapolation scheme may suffer from numerical instabilities [Zou and He, 1997; Guo *et al.*, 2002a].

Guo *et al.* [2002a] proposed an alternative extrapolation scheme based on non-equilibrium distribution functions. The basic idea of this *non-equilibrium extrapolation scheme* is to decompose the distribution functions at a wall node into its equilibrium and non-equilibrium parts, where the equilibrium one is constructed based on the specified macroscopic boundary conditions, while the non-equilibrium part is approximated with a first-order extrapolation. Because for continuum flows the non-equilibrium part is a small quantity in comparison with the equilibrium one (cf. the Chapman-Enskog expansion), the overall accuracy will be of second-order, and the use of the lower order extrapolation can ensure a good numerical stability.

We take the D2Q9 model as an example to illustrate the basic structure of this scheme. As shown in Fig. 2.2, at time t the unknown distributions at the boundary node $\boldsymbol{x}_b$ after the streaming step are f_2, f_5, and f_6, while these at the neighboring nodes $\boldsymbol{x}_f = \boldsymbol{x}_b + \boldsymbol{c}_i \delta t$ $(i = 2, 5, 6)$, together with the fluid density and velocity, are all known. To determine the unknown distribution functions at $\boldsymbol{x}_b$, they are first decomposed as

$$f_i(\boldsymbol{x}_b, t) = f_i^{(eq)}(\boldsymbol{x}_b, t) + f_i^{(neq)}(\boldsymbol{x}_b, t), \quad i = 2, 5, 6\,. \tag{2.39}$$

For velocity boundary conditions where $\boldsymbol{u}_w$ is known while ρ_w is unknown, the EDF is approximated by

$$\overline{f}_i^{(eq)}(\boldsymbol{x}_b, t) = f_i^{(eq)}[\rho(\boldsymbol{x}_f, t), \boldsymbol{u}_w], \quad i = 2,5,6\,, \tag{2.40}$$

in which the density at the wall is approximated by that at the neighboring fluid nodes. Similarly, the non-equilibrium part in Eq. (2.39) is also approximated by that at $\boldsymbol{x}_f$,

$$f_i^{(neq)}(\boldsymbol{x}_b, t) = f_i^{(neq)}(\boldsymbol{x}_f, t) = f_i(\boldsymbol{x}_f, t) - f_i^{(eq)}(\boldsymbol{x}_f, t), \quad i = 2, 5, 6\,. \tag{2.41}$$

Therefore, the non-equilibrium extrapolation scheme can be expressed as

$$f_i(\boldsymbol{x}_b, t) = f_i^{(eq)}\left[\rho(\boldsymbol{x}_f, t), \boldsymbol{u}_w\right] + \left[f_i(\boldsymbol{x}_f, t) - f_i^{(eq)}(\boldsymbol{x}_f, t)\right], \tag{2.42}$$

for $i = 2, 5, 6$.

The accuracy of the non-equilibrium extrapolation scheme can be estimated by analyzing the approximations of the equilibrium and non-equilibrium parts. It is well understood that the density variation in nearly incompressible flows is in the order of M^2. Therefore,

$$\rho(\boldsymbol{x}_f, t) - \rho(\boldsymbol{x}_b, t) \approx (\boldsymbol{c}_i \cdot \nabla\rho)\delta_t = O(\varepsilon M^2)\,, \tag{2.43}$$

where $\varepsilon = \delta_x/L$ with L representing the characteristic length. On the other hand, it is known that

$$M = \frac{U}{c_s^2} \sim \left(\tau - \frac{1}{2}\right)\frac{\delta_x}{L}\mathrm{Re} \sim \varepsilon\,, \tag{2.44}$$

where U is the velocity and $\mathrm{Re} = LU/\nu$ is the Reynolds number. With this result we can see that

$$\overline{f}_i^{(eq)}(\boldsymbol{x}_b, t) - f_i^{(eq)}(\boldsymbol{x}_b, t) \sim \delta_x^3\,. \tag{2.45}$$

Now we come to the non-equilibrium part. As implied in the Chapman-Enskog analysis, the nonequilibrium is of $\mathrm{O}(\varepsilon)$, i.e,

$$f_i^{(neq)} \approx -\tau\delta_t D_i f_i^{(eq)} \sim \delta_x f_i^{(1)}\,, \tag{2.46}$$

where $f_i^{(1)}$ is at the same order as $f_i^{(eq)}$ (here we have assumed that $\delta_t \sim \delta_x$). On the other hand,

$$f_i^{(1)}(\boldsymbol{x}_f, t) = f_i^{(1)}(\boldsymbol{x}_b, t) + O(\delta_x)\,, \tag{2.47}$$

which means that

$$f_i^{(neq)}(\boldsymbol{x}_b) - f_i^{(neq)}(\boldsymbol{x}_f) \sim \delta_x\left[f_i^{(1)}(\boldsymbol{x}_b) - f_i^{(1)}(\boldsymbol{x}_f)\right] \sim \delta_x^2\,. \tag{2.48}$$

With Eqs. (2.45) and (2.48), we can conclude that the non-equilibrium extrapolation scheme (2.42) is of second-order accuracy in both time and space.

2.3 Boundary Conditions for Curved Walls

In the previous section we have discussed boundary conditions for flat walls. We now turn our attention to curved walls where lattice nodes generally do not fall at the physical boundaries. Fig. 2.4 illustrates a

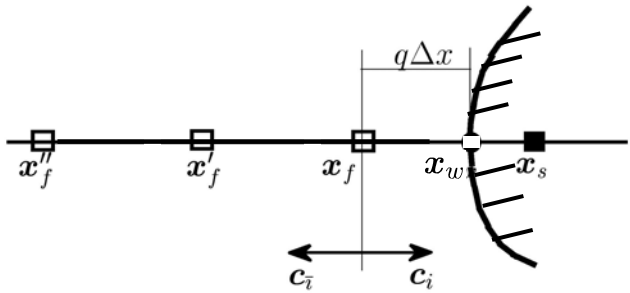

Fig. 2.4. Sketch of a curved wall and the lattice nodes near the wall.

curved wall together with the neighboring lattice nodes along the direction $\boldsymbol{c}_i$. The link between the fluid node $\boldsymbol{x}_f$ (nodes in the fluid region) and the solid node $\boldsymbol{x}_s$ (nodes in the solid wall) is cut by the wall at the point $\boldsymbol{x}_w$, and the fraction of the intersected link in the fluid region is

$$q = \frac{|\boldsymbol{x}_f - \boldsymbol{x}_w|}{|\boldsymbol{x}_f - \boldsymbol{x}_s|} = \frac{|\boldsymbol{x}_f - \boldsymbol{x}_w|}{\Delta x}, \tag{2.49}$$

where the spacing Δx depends on $\boldsymbol{c}_i$ and may be different from the lattice spacing δ_x. It is clear that $0 < q \leq 1$, and generally the boundary schemes for flat walls are not suitable for such type of problems. In order to treat such boundary conditions, we must revise the above mentioned schemes or develop new methods.

2.3.1 *Bounce-back schemes*

The bounce-back schemes given in Sec. 2.2.1 can be applied to no-slip boundary conditions of a curved wall after making some necessary approximations. According to the location where the bouncing occurs, the bounce-back schemes can be classified into two types. The first kind is *nodal bounce-back scheme*, in which the bouncing occurs at the node nearest to the physical wall, or in other words, the wall boundary is approximated by the lattice nodes according to the value of q:

$$\boldsymbol{x}_w = \begin{cases} \boldsymbol{x}_f, & q \leq 1/2 \\ \boldsymbol{x}_s, & \text{otherwise} \end{cases}. \tag{2.50}$$

Another type is the so-called *link bounce-back scheme*, which is similar to the half-way bounce-back scheme. In this scheme the wall node is taken as the mid-point of the link between $\boldsymbol{x}_f$ and $\boldsymbol{x}_s$ regardless of the values of q, i.e., $\boldsymbol{x}_w = (\boldsymbol{x}_f + \boldsymbol{x}_s)/2$.

It is obvious that in either of the bounce-back schemes, the physical wall is approximated by a staggered stair step. This will degenerate the accuracy of the schemes and subsequently the overall accuracy of LBE. However, the simplicity of the bounce-back schemes is still very appealing, particularly for flows with highly complicated geometries such as porous media.

2.3.2 *Fictitious equilibrium schemes*

The first boundary condition which considers the accurate shape of a curved wall was proposed by Filippova and Hänel [1998]. In order to calculate the unknown post-streaming distribution function at the fluid node $\boldsymbol{x}_f$, i.e. $f_{\bar{i}}(\boldsymbol{x}_f, t+\delta_t)$ shown in Fig. 2.4, this scheme (referred to FH) defines a post-collision distribution function at the solid node $\boldsymbol{x}_s$ formally, which is a combination of the bounce-backed distribution and a fictitious EDF,

$$f'_{\bar{i}}(\boldsymbol{x}_s, t) = (1-\chi) f'_i(\boldsymbol{x}_f, t) + \chi f^*_i(\boldsymbol{x}_s, t) - 2\omega_i \rho(\boldsymbol{x}_f, t) \frac{\boldsymbol{c}_i \cdot \boldsymbol{u}_w}{c_s^2}, \qquad (2.51)$$

where χ is the combination coefficient and f_i^* is the fictitious EDF defined by

$$f_i^*(\boldsymbol{x}_s, t) = \omega_i \rho(\boldsymbol{x}_f, t) \left[1 + \frac{\boldsymbol{c}_i \cdot \boldsymbol{u}^*}{c_s^2} + \frac{(\boldsymbol{c}_i \cdot \boldsymbol{u}_f)^2}{2c_s^4} - \frac{\boldsymbol{u}_f^2}{2c_s^2} \right], \qquad (2.52)$$

where $\boldsymbol{u}^*$ is a fictitious velocity to be determined, and $\boldsymbol{u}_f = \boldsymbol{u}(\boldsymbol{x}_f, t)$. The parameter χ depends on the choice of the temporary velocity $\boldsymbol{u}^*$. The FH scheme uses the following choices,

$$q < 1/2: \qquad \boldsymbol{u}^* = \boldsymbol{u}_f, \quad \chi = \frac{2q-1}{\tau - 1}, \qquad (2.53)$$

$$q \geq 1/2: \qquad \boldsymbol{u}^* = \frac{q-1}{q} \boldsymbol{u}_f + \frac{1}{q} \boldsymbol{u}_w, \quad \chi = \frac{2q-1}{\tau}. \qquad (2.54)$$

The parameter χ depends on the relaxation time τ in the FH scheme, particularly as τ is close to 1, χ will become very large as $q < 1/2$, and the FH scheme will suffer from severe numerical instability. Later, Mei *et al*. [1999] proposed an improved fictitious equilibrium scheme (denoted as MLS after the authors), which still uses Eq. (2.54) if $q \geq 1/2$, and uses

$$\boldsymbol{u}^* = \boldsymbol{u}_f', \quad \chi = \frac{2q-1}{\tau-2}, \tag{2.55}$$

if $q < 1/2$. It is obvious that by employing the information at the next neighboring fluid node $\boldsymbol{x}_f'$, the MLS scheme can release the constraint of the FH scheme to some extent. With the help of the Chapman-Enskog analysis, it can be shown that both the FH and MLS are of second-order accuracy [Filippova and Hänel, 1998; Mei *et al*., 1999].

2.3.3 *Interpolation schemes*

The FH and MLS schemes can be viewed as a correction to the bounce-backed scheme. Later Bouzidi *et al.* [2001] proposed an interpolation scheme (referred to BFL) based on bounce-back scheme from an alternative viewpoint. First we consider a stationary wall ($\boldsymbol{u}_w = 0$). As shown in Fig. 2.5, if the wall node $\boldsymbol{x}_w$ is closer to the solid node $\boldsymbol{x}_s$ than to the fluid node $\boldsymbol{x}_f$ (i.e. $q \geq 1/2$), the post-collision particles at $\boldsymbol{x}_f$ with velocity $\boldsymbol{c}_i$ will arrive at and collide with the wall after a time duration $q\delta_t$, and the particle velocity changes to $\boldsymbol{c}_{\bar{i}}$. After another time duration $(1-q)\delta_t$, the particles will arrive at the location $\boldsymbol{x}_t$ between $\boldsymbol{x}_f$ and $\boldsymbol{x}_w$:

$$\boldsymbol{x}_t = \boldsymbol{x}_w + \boldsymbol{c}_{\bar{i}}(1-q)\delta_t = \boldsymbol{x}_f + (2q-1)\Delta x \boldsymbol{e}_i, \tag{2.56}$$

where $\boldsymbol{e}_i = \boldsymbol{c}_i / c$. Therefore, the distribution function at this location is known at time $t + \delta_t$:

$$f_{\bar{i}}(\boldsymbol{x}_t, t+\delta_t) = f_i'(\boldsymbol{x}_f, t). \tag{2.57}$$

At the same time, the distribution function $f_i(\boldsymbol{x}_f', t+\delta_t)$ is also known after streaming, and therefore the unknown distribution function $f_{\bar{i}}(\boldsymbol{x}_f, t+\delta_t)$ can be approximated by a linear interpolation:

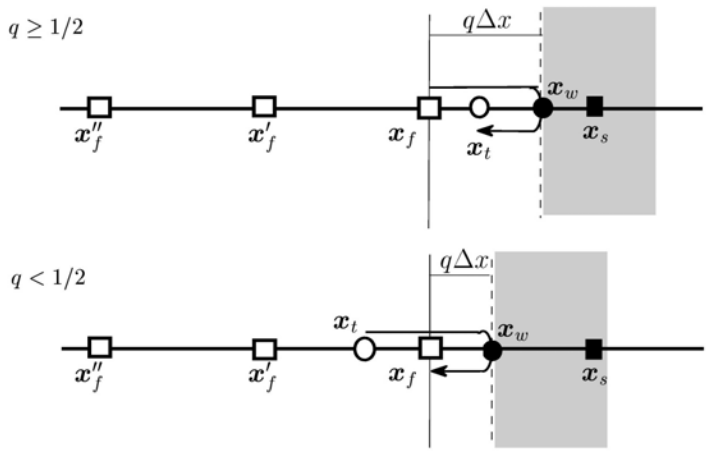

Fig. 2.5. Diagram of the BFL scheme. The open circle ($\boldsymbol{x}_f$) is the interpolation point.

$$f_{\bar{i}}(\boldsymbol{x}_f, t+\delta_t) = \frac{1}{2q} f_{\bar{i}}(\boldsymbol{x}_t, t+\delta_t) + \frac{2q-1}{2q} f_{\bar{i}}(\boldsymbol{x}'_f, t+\delta_t)$$
$$= \frac{1}{2q} f'_i(\boldsymbol{x}_f, t) + \frac{2q-1}{2q} f_{\bar{i}}(\boldsymbol{x}'_f, t+\delta_t). \tag{2.58}$$

As $q < 1/2$, the location $\boldsymbol{x}_t$ given by Eq. (2.56) is between $\boldsymbol{x}_f$ and $\boldsymbol{x}'_f$, and Eq. (2.58) becomes an extrapolation which may induce numerical instability. In order to avoid this possibility, the BFL scheme suggests constructing the post-collision distribution function at location

$$\boldsymbol{x}_t = \boldsymbol{x}_w + (\Delta x - q)\boldsymbol{e}_{\bar{i}} = \boldsymbol{x}_f + (\Delta x - 2q)\boldsymbol{e}_{\bar{i}}\,. \tag{2.59}$$

Since $0 < q < 1/2$, this point locates between $\boldsymbol{x}_f$ and $\boldsymbol{x}'_f$, and so we can obtain the post- collision distribution function by a linear interpolation,

$$f'_i(\boldsymbol{x}_t, t) = 2q f'_i(\boldsymbol{x}_f, t) + (1-2q) f'_i(\boldsymbol{x}'_f, t)\,. \tag{2.60}$$

After a time duration $(1-q)\delta_t$ the particle will arrive at the wall, then leave the wall with an inversed velocity and arrive at $\boldsymbol{x}_f$ at time $t+\delta_t$. So the unknown distribution is

$$f_{\bar{i}}(\boldsymbol{x}_f, t+\delta_t) = f'_i(\boldsymbol{x}_t, t) = 2q f'_i(\boldsymbol{x}_f, t) + (1-2q) f'_i(\boldsymbol{x}'_f, t)\,. \tag{2.61}$$

The above scheme works for a stationary wall. For a moving wall, the contribution from the wall should also be considered. After making a similar analysis, the BFL scheme can be expressed as

$$f_{\bar{i}}'(\boldsymbol{x}_f, t+\delta_t) = f_{\bar{i}}'(\boldsymbol{x}_s, t) = \begin{cases} 2qf_i'(\boldsymbol{x}_f, t) + (1-2q)f_i'(\boldsymbol{x}_f', t) + 2\omega_i\rho_f \dfrac{\boldsymbol{c}_{\bar{i}} \cdot \boldsymbol{u}_w}{c_s^2}, & q < 1/2, \\ \dfrac{1}{2q} f_i'(\boldsymbol{x}_f, t) + \dfrac{2q-1}{2q} f_{\bar{i}}'(\boldsymbol{x}_f, t) + \dfrac{\omega_i\rho_f}{q} \dfrac{\boldsymbol{c}_{\bar{i}} \cdot \boldsymbol{u}_w}{c_s^2}, & q \geq 1/2. \end{cases} \tag{2.62}$$

It is also obvious that as $q = 1/2$ the BFL scheme reduces to the Link-Bounce-Back scheme. Furthermore, we can also use a second-order interpolation in the BFL scheme, which gives

$$f_{\bar{i}}'(\boldsymbol{x}_s, t) = \begin{cases} q(1+2q)f_i'(\boldsymbol{x}_f, t) + (1-4q^2)f_i'(\boldsymbol{x}_f', t) \\ -q(1-2q)f_i'(\boldsymbol{x}_f'', t) + 2\omega_i\rho_f \dfrac{\boldsymbol{c}_{\bar{i}} \cdot \boldsymbol{u}_w}{c_s^2}, & q < 1/2, \\ \dfrac{1}{q(2q+1)} \Bigg[f_i'(\boldsymbol{x}_f, t) + (4q^2-1)f_{\bar{i}}'(\boldsymbol{x}_f, t) \\ -q(2q-1)f_{\bar{i}}'(\boldsymbol{x}_f', t) + \dfrac{2\omega_i\rho_f}{q(2q+1)} \dfrac{\boldsymbol{c}_{\bar{i}} \cdot \boldsymbol{u}_w}{c_s^2} \Bigg], & q \geq 1/2. \end{cases} \tag{2.63}$$

The BFL schemes use different interpolations for $q < 1/2$ and $q \geq 1/2$, which may induce some undesirable oscillations near the wall. Yu *et al.* [2003] developed a unified interpolation scheme (refereed to YMS hereafter). As illustrated in Fig. 2.5, the YMS scheme assumes that the post-collision distribution functions $f_i'(\boldsymbol{x}_f, t)$ can arrive at the solid node $\boldsymbol{x}_s$ across the wall so that $f_i'(\boldsymbol{x}_s, t+\delta_t) = f_i'(\boldsymbol{x}_f, t)$. The distribution function at $\boldsymbol{x}_w$ can then be approximated using a linear interpolation,

$$f_i(\boldsymbol{x}_w, t+\delta_t) = (1-q)f_i(\boldsymbol{x}_f, t+\delta_t) + qf_i(\boldsymbol{x}_s, t+\delta_t). \tag{2.64}$$

Then the bounce-back is employed at the wall node to ensure a no-slip boundary condition,

$$f_{\bar{i}}(\boldsymbol{x}_w, t+\delta_t) = f_i(\boldsymbol{x}_w, t+\delta_t) - 2\omega_i\rho_f \frac{\boldsymbol{c}_i \cdot \boldsymbol{u}_w}{c_s^2}. \tag{2.65}$$

Using the linear interpolation again, we can obtain that

$$f_{\bar{i}}(\boldsymbol{x}_f, t+\delta_t) = \frac{q}{1+q} f_{\bar{i}}(\boldsymbol{x}'_f, t+\delta_t) + \frac{1}{1+q} f_{\bar{i}}(\boldsymbol{x}_w, t+\delta_t), \quad (2.66)$$

and the final expression of the YMS scheme can be written as

$$f'_{\bar{i}}(\boldsymbol{x}_s, t) = \frac{1}{1+q}\left[q f'_{\bar{i}}(\boldsymbol{x}_f, t) + q f'_i(\boldsymbol{x}_f, t) + (1-q) f'_i(\boldsymbol{x}'_f, t) - 2\omega_i \rho_f \frac{\boldsymbol{c}_i \cdot \boldsymbol{u}_w}{c_s^2}\right]. \quad (2.67)$$

It is noted that as $q = 1/2$, the YMS scheme does not reduce to the half-way bounce-back scheme. One can prove that the YMS scheme is also of second order accuracy, and high-order interpolations can also be employed to obtain better accuracy.

2.3.4 *Non-equilibrium extrapolation scheme*

The non-equilibrium extrapolation scheme for flat walls given in Sec. 2.2.3 can also be extended to boundary conditions for curved walls [Guo *et al.*, 2002b]. Unlike the fictitious and interpolation schemes, the extrapolation scheme performs the collision step at the solid node $\boldsymbol{x}_s$. To do so, $f_{\bar{i}}(\boldsymbol{x}_s, t)$ is first decomposed into its equilibrium and non-equilibrium parts,

$$f_{\bar{i}}(\boldsymbol{x}_s, t) = f_{\bar{i}}^{(eq)}(\boldsymbol{x}_s, t) + f_{\bar{i}}^{(neq)}(\boldsymbol{x}_s, t). \quad (2.68)$$

The equilibrium is approximated as,

$$f_{\bar{i}}^{(eq)}(\boldsymbol{x}_s, t) \approx f_{\bar{i}}^{*}(\boldsymbol{x}_s, t) \equiv \omega_{\bar{i}} \rho(\boldsymbol{x}_f, t)\left[1 + \frac{\boldsymbol{c}_{\bar{i}} \cdot \boldsymbol{u}_s}{c_s^2} + \frac{(\boldsymbol{c}_{\bar{i}} \cdot \boldsymbol{u}_s)^2}{2c_s^4} - \frac{\boldsymbol{u}_s^2}{2c_s^2}\right], \quad (2.69)$$

where $\boldsymbol{u}_s$ is determined from $\boldsymbol{u}(\boldsymbol{x}_w, t)$, $\boldsymbol{u}(\boldsymbol{x}_f, t)$, and $\boldsymbol{u}(\boldsymbol{x}'_f, t)$,

$$\boldsymbol{u}_s = \begin{cases} \boldsymbol{u}_{s1} , & q \geq 3/4 \\ q\boldsymbol{u}_{s1} + (1-q)\boldsymbol{u}_{s2} , & q < 3/4 \end{cases} \quad (2.70)$$

where

$$\boldsymbol{u}_{s1} = \frac{1}{q}\boldsymbol{u}_w + \frac{q-1}{q}\boldsymbol{u}(\boldsymbol{x}_f), \qquad \boldsymbol{u}_{s2} = \frac{2}{q+1}\boldsymbol{u}_w + \frac{q-1}{q+1}\boldsymbol{u}(\boldsymbol{x}'_f). \quad (2.71)$$

The non-equilibrium part is approximated as

$$f_{\bar{i}}^{(neq)}(\boldsymbol{x}_s,t)=\begin{cases} f_{\bar{i}}^{(neq)}(\boldsymbol{x}_f,t), & q\geq 3/4 \\ qf_{\bar{i}}^{(neq)}(\boldsymbol{x}_f,t)+(1-q)f_{\bar{i}}^{(neq)}(\boldsymbol{x}_f',t) & q<3/4 \end{cases}. \tag{2.72}$$

With these approximations, the post-collision distribution function at node $\boldsymbol{x}_s$ can be obtained,

$$f_{\bar{i}}'(\boldsymbol{x}_s,t)=f_{\bar{i}}(\boldsymbol{x}_s,t)-\frac{1}{\tau}f_{\bar{i}}^{(neq)}(\boldsymbol{x}_s,t)=f_{\bar{i}}^{*}(\boldsymbol{x}_s,t)+\frac{\tau-1}{\tau}f_{\bar{i}}^{(neq)}(\boldsymbol{x}_s,t). \tag{2.73}$$

Guo *et al.* [2002b] have shown that the non-equilibrium extrapolation has good numerical stability and is of second-order accuracy.

2.4 Pressure Boundary Conditions

Besides velocity boundary conditions, pressure boundary conditions are also frequently encountered in many problems such as pipe or porous flows. Some schemes were also developed to implement such boundary conditions in LBE from different viewpoints.

2.4.1 *Periodic boundary conditions*

For problems where the pressure gradient is a constant, such as flow in a long channel driven by a pressure drop, we can replace the pressure gradient by a body force and apply *periodic boundary conditions* to the stream-wise boundaries, which means that a particle leaving a boundary will re-enter the fluid domain from the opposite side. For instance, if we apply the D2Q9 model to the flow in a channel of length L, the periodic boundary conditions at the inlet and outlet can be expressed as (see Fig. 2.6)

Inlet: $$f_i(x_0,y,t+\delta_t)=f_i'(x_L,y-c_{iy}\delta_t,t), \qquad i=1,5,8. \tag{2.74}$$

Outlet: $$f_i(x_L,y,t+\delta_t)=f_i'(x_0,y-c_{iy}\delta_t,t), \qquad i=3,6,7. \tag{2.75}$$

where x_0 and x_L denote the nodes at the inlet and outlet, respectively.

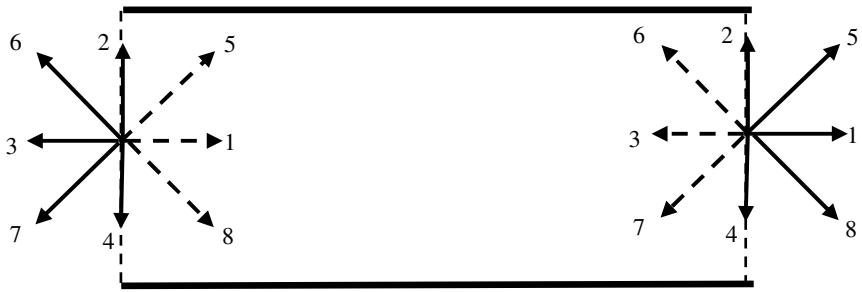

Fig. 2.6. Sketch of pressure boundary conditions.

Periodic boundary conditions are usually applied to flows with spatial periodicities, and the above treatment is only an approximation. Furthermore, the rule given by Eqs. (2.74) and (2.75) indicates that the pressure values at x_0 and x_L are identical. Recently, Zhang and Kwok [2006] extended the above rule to incorporate pressure difference for fully developed periodic flows where the pressure gradient may be not a constant. Assuming that

$$\boldsymbol{u}(x_0, y, t) = \boldsymbol{u}(x_L, y, t)\,,\ p(x_0, y, t) = p(x_L, y, t) + \beta L\,, \tag{2.76}$$

the modified periodic boundary conditions can then be implemented as follows,

Inlet:

$$f_i(x_0, y, t + \delta_t) = f_i'(x_L, y - c_{iy}\delta_t, t)\frac{\rho_0 + \beta/c_s^2}{\rho_{out}}, \qquad i = 1, 5, 8\,, \tag{2.77}$$

Outlet:

$$f_i(x_L, y, t + \delta_t) = f_i'(x_0, y - c_{iy}\delta_t, t)\frac{\rho_0 - \beta/c_s^2}{\rho_{in}}, \qquad i = 3, 6, 7\,, \tag{2.78}$$

where ρ_0 is a reference density, and ρ_{in} and ρ_{out} are the average densities at the inlet and outlet, respectively. With this periodic boundary conditions, Zhang and Kwok [2006] simulated several fully developed flows driven by a pressure drop and reported satisfactory results.

2.4.2 *Hydrodynamic schemes*

With the idea of bounce-back of non-equilibrium distribution functions, Zou and He [1997] developed a hydrodynamic scheme for pressure boundary conditions. As shown in Fig. 2.6, for the D2Q9 model the unknown distribution functions f_1, f_5, and f_8 at the inlet are determined from the following conditions,

$$f_1 + f_5 + f_8 = \rho_{in} - (f_0 + f_2 + f_3 + f_4 + f_6 + f_7)\,, \tag{2.79}$$

$$f_1 + f_5 + f_8 - \rho_{in} u_{in} / c = f_3 + f_6 + f_7\,, \tag{2.80}$$

$$f_5 - f_8 = -f_2 + f_4 - f_6 + f_7\,, \tag{2.81}$$

$$f_1 - f_1^{(eq)} = f_3 - f_3^{(eq)}\,, \tag{2.82}$$

where the velocity at the inlet is $\boldsymbol{u}_{in} = (u_{in}, 0)$ and it is unknown, while the density at the inlet, ρ_{in}, can be obtained from the specified pressure. By solving this set of equations, one can get the unknown distributions at the inlet, and those at the outlet can be determined similarly.

2.4.3 *Extrapolation schemes*

Based on the extrapolation technique, Chen *et al.* [1996] devised a simple extrapolation scheme for pressure boundary conditions similar to that for velocity boundary conditions. Again consider the inlet shown in Fig. 2.6, a ghost layer is appended to the layer at the inlet, and the distribution functions at the ghost layer are approximated by

$$f_i(-1) = 2f_i(0) - f_i(1)\,, \tag{2.83}$$

where -1, 0, and 1 are the labels for the ghost layer, the inlet, and the first fluid layer, respectively. Then the collision process can be carried out on all nodes including the ghost ones, but it should be noted that the specified pressure/density is used in calculating the EDFs at the inlet. Maier *et al.* [1996] also presented a similar method.

The non-equilibrium technique can also be used to treat pressure boundary conditions. In this case the unknown distribution functions at the inlet are again decomposed into two parts, where the equilibrium part

is approximated by

$$\hat{f}_i^{(eq)}(\boldsymbol{x}_b, t) = f_i^{(eq)}(\rho_{in}, \boldsymbol{u}_{in}), \quad i = 1, 5, 8\,, \tag{2.84}$$

where $\boldsymbol{u}_{in}(\boldsymbol{x}_0) = \boldsymbol{u}(\boldsymbol{x}_f = \boldsymbol{x}_0 + \boldsymbol{c}_i\delta_t)$ is the velocity at the nearest neighboring fluid node along the particle velocity. The non-equilibrium part is approximated by that at the same fluid node, too. The final expressions of the unknown distribution functions then read,

$$f_i(\boldsymbol{x}_b, t) = f_i^{(eq)}[\rho_{in}, \boldsymbol{u}(\boldsymbol{x}_f, t)] + [f_i(\boldsymbol{x}_f, t) - f_i^{(eq)}(\boldsymbol{x}_f, t)], \quad i = 1, 5, 8\,. \tag{2.85}$$

Similar to the analysis for the non-equilibrium extrapolation schemes for velocity boundary conditions, it can be shown that this scheme is also of second-order accuracy. Also, because only first order extrapolations are involved, this scheme has good numerical stability as well [Guo *et al.*, 2002a].

2.5 Summary

In this chapter we have discussed the initial and boundary conditions in LBE, which are fundamental topics in this field. For initial conditions, two main approaches are presented, i.e. the earlier non-equilibrium correction method and the recent iterative method. Some schemes for velocity and pressure boundary conditions, which are widely used in the applications of LBE, are also described.

It is noted that the simple equilibrium schemes are not discussed in the above sections, since it is quite straightforward to implement such boundary conditions. For example, when the pressure is given, with an extrapolated velocity, the EDFs can be approximately used in the required unknown directions. Some theoretical studies of boundary conditions for LBE, were not detailed in this chapter, either. For instance, He *et al.* [1997] found the analytical solutions of the LBE under different boundary conditions, based on which the accuracies of the schemes were analyzed. Junk and Yang [2005a] made an asymptotic analysis of the bounce-back, BFL, FH, and MLS schemes. Kao and Yan [2008] compared the FH, BFL, and YMS schemes, and developed a scheme

without interpolation. On the other hand, Suh *et al*. [2008] performed theoretical and numerical comparisons of the YMS, BFL, and non-equilibrium extrapolation schemes for curved walls. Some new boundary schemes are also developed from different pictures [Junk and Yang, 2005b; Chun and Ladd, 2007]. In summary, developing accurate, effective, and simple schemes for initial and boundary conditions is still a very active branch in LBE.

Chapter 3

Improved Lattice Boltzmann Models

In Chapter 1, we have described the general LBE models for isothermal flows. These models (particularly the DnQb LBGK models), together with the initial and boundary conditions introduced in Chapter 2, have been successfully applied to many simple and complicated flow problems. However, there is still much space to improve the performance of these models, and in this chapter we will give a few examples.

3.1 Incompressible Models

As shown in Chapter 1, the hydrodynamic equations derived from the LBE equation are actually the compressible Navier-Stokes equations. Meanwhile, the intrinsic low Mach number requirement of LBE indicates that it is limited to nearly incompressible flows. Therefore, the LBE can be viewed as a special artificial compressibility method for incompressible flows [He *et al.*, 2002; Ohwada *et al.*, 2011]. As such, a numerical error related to the artificial compressibility will arise in addition to those from the spatial and temporal discretization. The compressible effect may lead to significant errors in some cases. For instance, in a comparative study of a two-dimensional turbulent flow [Zou *et al*., 1995], Martinez *et al.* found that the LBE results deviated greatly from the spectral data at the late stage, and they attributed this deviation to the compressible effects of the LBE.

In order to reduce the compressible effects in LBE, some modifications to the standard models have been developed from different viewpoints, and we will call such models as *incompressible LBE models* although they may still contain some compressibility errors. In 1995, Zou and his coworkers made the first attempt to construct an incompressible

D2Q9 model for steady flows. In this model, the evolution equation is the same as the standard LBGK model, but the discrete EDF is re-defined as

$$f_i^{(eq)} = \omega_i \left[\rho + \frac{\boldsymbol{c}_i \cdot \boldsymbol{u}}{c_s^2} + \frac{(\boldsymbol{c}_i \cdot \boldsymbol{u})^2}{2c_s^4} - \frac{\boldsymbol{u}^2}{2c_s^2} \right]. \tag{3.1}$$

It can be seen that this EDF is very similar to that of the standard D2Q9 model except that the density is decoupled from the momentum. The fluid density and velocity in Zou's model are calculated as

$$\rho = \sum_i f_i, \qquad \boldsymbol{u} = \sum_i \boldsymbol{c}_i f_i \,. \tag{3.2}$$

The hydrodynamic equations derived from Zou's model via the Chapman-Enskog expansion read,

$$\partial_t \rho + \nabla \cdot \boldsymbol{u} = 0 \,, \tag{3.3}$$

$$\frac{\partial \boldsymbol{u}}{\partial t} + \nabla \cdot (\boldsymbol{u}\boldsymbol{u}) = -\nabla p + \nabla \cdot \left[\rho \nu \left(\nabla \boldsymbol{u} + \nabla \boldsymbol{u}^T \right) \right], \tag{3.4}$$

where the pressure p and the kinematic viscosity are both the same as the standard D2Q9 model. It is clear that Eqs. (3.3) and (3.4) reduce to the standard incompressible Navier-Stokes equations at steady state, namely, the compressible effects are removed totally.

It is noted that in Zou's incompressible model, the pressure is still related to the fluid density. Sometime later, Lin *et al*. [1996] proposed a similar incompressible model which used a density-independent pressure.

Numerical results show that Zou's model works well for steady flows. But for unsteady flows, this model still contains compressibility error. Chen and Ohashi [1997] extended Zou's model for general flows by introducing a correction to the velocity defined by Eq. (3.2). That is, the flow velocity is

$$\boldsymbol{w} = \boldsymbol{u} + \tau \nabla \phi \,, \tag{3.5}$$

where ϕ is a scalar to be determined. In order to enforce $\boldsymbol{w}$ to be divergent free, ϕ should satisfy the following Poisson equation,

$$\nabla^2 \phi = -\frac{1}{\tau} \nabla \cdot \boldsymbol{u} \,. \tag{3.6}$$

After solving the above equation, one can obtain the fluid velocity $\boldsymbol{w}$ according to Eq. (3.5).

It is noted that in the Chen-Ohashi model, the fluid velocity appearing in the discrete EDF is $\boldsymbol{w}$ instead of $\boldsymbol{u}$. The Chapman-Enskog expansion of this model leads to the exact incompressible Navier-Stokes equations for $\boldsymbol{w}$, and the pressure is given by $p = c_s^2\rho - \phi$. The basic idea of the velocity correction method employed in the Chen-Ohashi model is similar to the pressure-correction method for incompressible Navier-Stokes equations in traditional CFD method. Because the Laplacian operator in the Poisson equation (3.6) is non-local, the computational costs of the Chen-Ohashi model will be greater than Zou's model.

Almost at the same time when Chen-Ohashi model was proposed, He and Luo [1997] developed another general incompressible LBGK model. The basic idea is to remove terms of high-order Mach number due to density variations in the EDF. In this model, the independent variables are the pressure and velocity rather than the density and momentum.

As known, the density variation of the density, $\delta\rho/\rho_0$, in nearly incompressible flows is of order M^2, where ρ_0 is a averaged density. Therefore, the standard EDF of the D*n*Q*b* models can be approximated as

$$f_i^{(eq)} = \omega_i\rho + \rho_0\left(1 + \frac{\delta\rho}{\rho_0}\right)s_i(\boldsymbol{u}) = \omega_i\rho + \rho_0 s_i(\boldsymbol{u}) + O(M^3), \qquad (3.7)$$

where s_i is the collective of the velocity terms in the EDF,

$$s_i(\boldsymbol{u}) = \omega_i\left[\frac{\boldsymbol{c}_i\cdot\boldsymbol{u}}{c_s^2} + \frac{(\boldsymbol{c}_i\cdot\boldsymbol{u})^2}{2c_s^4} - \frac{\boldsymbol{u}^2}{2c_s^2}\right]. \qquad (3.8)$$

Therefore, after neglecting the $O(M^3)$ terms, and let $p_i^{(eq)} = c_s^2 f_i^{(eq)}$, one can obtain a pressure EDF,

$$p_i^{(eq)} = \omega_i\left[p + p_0\left(\frac{\boldsymbol{c}_i\cdot\boldsymbol{u}}{c_s^2} + \frac{(\boldsymbol{c}_i\cdot\boldsymbol{u})^2}{2c_s^4} - \frac{\boldsymbol{u}^2}{2c_s^2}\right)\right], \qquad (3.9)$$

where $p = c_s^2\rho$ and $p_0 = c_s^2\rho_0$, and the evolution equation of the He-Luo model is,

$$p_i(\boldsymbol{x} + \boldsymbol{c}_i\delta_t, t + \delta_t) - p_i(\boldsymbol{x}, t) = -\frac{1}{\tau}\big[p_i(\boldsymbol{x}, t) - p_i^{(eq)}(\boldsymbol{x}, t)\big], \qquad (3.10)$$

while the pressure and velocity are defined by

$$p = \sum_i p_i, \qquad p_0 \boldsymbol{u} = \sum_i \boldsymbol{c}_i p_i \,. \tag{3.11}$$

The hydrodynamic equations derived from the He-Luo model are

$$\frac{1}{c_s^2}\partial_t P + \nabla \cdot \boldsymbol{u} = 0\,, \tag{3.12}$$

$$\frac{\partial \boldsymbol{u}}{\partial t} + \boldsymbol{u} \cdot \nabla \boldsymbol{u} = -\nabla P + \nu \nabla^2 \boldsymbol{u}\,, \tag{3.13}$$

where $P = p/\rho_0$. It is clear that Eqs. (3.12) and (3.13) are just the artificial compressible version of the incompressible Navier-Stokes equations. The solution of the above equations can be a good approximation to that of the incompressible Navier-Stokes equations provided that the first term in Eq. (3.12) can be neglected. In order to see how this can be achieved, we rewrite Eq. (3.12) in dimensionless form,

$$\frac{L}{c_s t_0}\frac{\partial P'}{\partial t'} + \nabla' \cdot \boldsymbol{u}' = 0\,, \tag{3.14}$$

where the nondimensional variables with a prime are defined by,

$$\boldsymbol{u}' = \frac{\boldsymbol{u}}{c_s}\,,\; P' = \frac{P}{c_s^2}\,,\; t' = \frac{t}{t_0}\,,\; \boldsymbol{x}' = \frac{\boldsymbol{x}}{L}\,, \tag{3.15}$$

with t_0 and L being the characteristic time and length, respectively. Therefore, in order to neglect the transient term in Eq. (3.14), it is required that $t_0 \gg L/c_s$.

The He-Luo model has the same structure as the standard LBGK method and shares all of its advantages. Particularly, in this model the pressure behaves as an independent variable and can even take negative values. Actually, in some works the pressure in the EDF (3.9) is defined from the density variation directly, i.e. $p = c_s^2 \delta\rho$. In this regard, p acts as a dynamic pressure rather than a thermodynamic one.

Guo *et al*. [2000] developed another pressure-based incompressible LBGK model later. Unlike the previous incompressible models which

are based on the original density-based models, Guo's model is designed with intent to solve the incompressible Navier-Stokes equations directly. The EDF in Guo's D2Q9 model reads,

$$g_i^{(eq)} = \begin{cases} -4\sigma \dfrac{P}{c^2} + s_0(\boldsymbol{u}), & i = 0 \\ \lambda \dfrac{P}{c^2} + s_i(\boldsymbol{u}), & i = 1, 2, 3, 4 \\ \gamma \dfrac{P}{c^2} + s_i(\boldsymbol{u}), & i = 5, 6, 7, 8 \end{cases} \tag{3.16}$$

where s_i is defined by Eq. (3.8), and the parameters σ, λ, and γ satisfy the following relation

$$\lambda + \gamma = \sigma, \qquad 2\lambda + 4\gamma = 1\,. \tag{3.17}$$

With this EDF, the evolution equation of Guo's model is expressed as

$$g_i(\boldsymbol{x} + \boldsymbol{c}_i\delta_t, t + \delta_t) - g_i(\boldsymbol{x}, t) = -\frac{1}{\tau}\Big[g_i(\boldsymbol{x}, t) - g_i^{(eq)}(\boldsymbol{x}, t)\Big], \tag{3.18}$$

and the pressure and velocity are defined by

$$\boldsymbol{u} = \sum_i \boldsymbol{c}_i g_i, \quad P = \frac{c^2}{4\sigma}\left[\sum_i g_i + s_0(\boldsymbol{u})\right]. \tag{3.19}$$

The Chapman-Enskog expansion of this model leads to the exact incompressible Navier-Stokes equations,

$$\nabla \cdot \boldsymbol{u} = 0\,, \tag{3.20}$$

$$\frac{\partial \boldsymbol{u}}{\partial t} + \boldsymbol{u} \cdot \nabla \boldsymbol{u} = -\nabla P + \nu \nabla^2 \boldsymbol{u}\,, \tag{3.21}$$

where the shear viscosity is the same as the standard D2Q9 model.

The above incompressible LBGK models can be easily extended to MRT models. For example, the MRT version of the He-Luo model has been proposed in [d'Humières *et al*., 2002], while the MRT version of Guo's model was reported in [Du *et al*., 2006].

3.2 Forcing Schemes with Reduced Discrete Lattice Effects

Fluid flows are usually exposed to external or internal forces, such as gravity or intermolecular interactions. In the continuous Boltzmann equation, the contribution of a body force $\boldsymbol{F} = \rho \boldsymbol{a}$, where $\boldsymbol{a}$ is the force acceleration, to the change of the distribution function f is described by a forcing term $\boldsymbol{a} \cdot \nabla_{\xi} f(\boldsymbol{x}, \boldsymbol{\xi}, t)$. In LBE, however, this forcing term cannot be employed straightforwardly because the particle velocity is discretized. Therefore, it is a fundamental topic to include such forces into the LBE, and a variety of discrete forcing schemes have been developed from different physical pictures. For convenience, we will express the EDF as a function of the fluid density and velocity,

$$f_i^{(eq)}(\boldsymbol{x}, t) = E_i(\rho, \boldsymbol{u}) \equiv \omega_i \rho \left[1 + \frac{\boldsymbol{c}_i \cdot \boldsymbol{u}}{c_s^2} + \frac{(\boldsymbol{c}_i \cdot \boldsymbol{u})^2}{2c_s^4} - \frac{\boldsymbol{u}^2}{2c_s^2} \right]. \tag{3.22}$$

3.2.1 *Scheme with modified equilibrium distribution function*

If the force is induced by a potential and the density variation is small, i.e. $\boldsymbol{F} = -\rho \nabla \phi \approx -\nabla(\rho \phi)$, it can be included into the LBE by modifying the EDF [Buick and Greated, 2000],

$$\begin{aligned} \overline{f}_0^{(eq)} &= \rho \left[1 - (1 - \omega_0) \frac{p(\phi)}{c_s^2 \rho} - \omega_0 \frac{u^2}{2c_s^2} \right], \\ \overline{f}_i^{(eq)} &= \omega_i \rho \left[\frac{p(\phi)}{c_s^2 \rho} + \frac{\boldsymbol{c}_i \cdot \boldsymbol{u}}{c_s^2} + \frac{(\boldsymbol{c}_i \cdot \boldsymbol{u})^2}{2c_s^4} - \frac{u^2}{2c_s^2} \right], \quad i \neq 0 \end{aligned} \tag{3.23}$$

where $p = (c_s^2 + \phi)\rho$, and $\boldsymbol{u}$ is defined by

$$\rho \boldsymbol{u} = \sum_i \boldsymbol{c}_i f_i \,. \tag{3.24}$$

It is easy to verify that the zeroth, first, and third order moments of $\overline{f}_i^{(eq)}$ are the same as those of the standard D*n*Q*b* models (c.f. Eq. (1.52)), but the second-order moment involves the potential,

$$\sum_i c_{i\alpha} c_{i\beta} \overline{f}_i^{(eq)} = p(\phi) \delta_{\alpha\beta} + \rho u_\alpha u_\beta \,. \tag{3.25}$$

With this change, we can show that the momentum flux at the order of ε in the Chapman-Enskog expansion is (neglecting the terms of $O(M^2)$),

$$\pi_{\alpha\beta}^{(1)} = -\tau\delta_t\Big[c_s^2\rho\Big(\partial_{0\alpha}u_\beta + \partial_{0\beta}u_\alpha\Big) + \partial_{t_0}\partial_{0\alpha}(\rho\phi) - \partial_\beta\Big(u_\alpha\partial_{0\beta}(\rho\phi) + u_\beta\partial_{0\alpha}(\rho\phi)\Big)\Big]. \tag{3.26}$$

Therefore, the momentum equation will be

$$\frac{\partial(\rho\boldsymbol{u})}{\partial t} + \nabla\cdot(\rho\boldsymbol{u}\boldsymbol{u}) = -\nabla(c_s^2\rho) + \nabla\cdot\Big[\rho\nu\Big(\nabla\boldsymbol{u} + \nabla\boldsymbol{u}^T\Big)\Big] + \boldsymbol{F} + R\,, \tag{3.27}$$

where the residual term R is given by

$$R = \tau\delta_t\Big[-\partial_t F_\alpha + \partial_\beta\Big(u_\alpha F_\beta + u_\beta F_\alpha\Big)\Big]. \tag{3.28}$$

Clearly, R does not vanish in general, and so the above method will bring some additional errors due to the force field.

The force can also be included in LBE by modifying the fluid velocity appearing in the EDF [Shan and Chen, 1993], namely, the *equilibrium velocity* is now given by,

$$\boldsymbol{u}^{(eq)} = \boldsymbol{u} + \boldsymbol{a}\tau\delta_t\,. \tag{3.29}$$

In the original method developed by Shan and Chen (referred to SC) [1993], the fluid velocity $\boldsymbol{u}$ is still defined by Eq. (3.24). In a later work, it was argued that the fluid velocity (denoted by $\boldsymbol{v}$ for clarity) should be defined as the average of pre- and post-collision velocities (referred to SD scheme) [Shan and Doolen, 1995],

$$\rho\boldsymbol{v} = \frac{1}{2}\sum_i \boldsymbol{c}_i(f_i + f_i') = \rho\boldsymbol{u} + \frac{\delta_t}{2}\boldsymbol{F}\,. \tag{3.30}$$

3.2.2 *Schemes with a forcing term*

The most straightforward way to account for the body force is to add a forcing term to the LBE, like that in the Boltzmann equation,

$$f_i(\boldsymbol{x} + \boldsymbol{c}_i\delta_t, t + \delta_t) - f_i(\boldsymbol{x}, t) = -\frac{1}{\tau}\Big[f_i(\boldsymbol{x}, t) - f_i^{(eq)}(\boldsymbol{x}, t)\Big] + \delta_t F_i\,, \tag{3.31}$$

where the forcing term $\boldsymbol{F}_i$ depends on the body force $\boldsymbol{F}$. A variety of expressions for $\boldsymbol{F}_i$ have been proposed with different interpretations of the fluid velocity.

Scheme based on LGA

The early widely used forcing scheme originates from the LGA method [Frisch *et al*., 1987; Luo, 1997], which can be written as,

$$F_i = \omega_i \frac{\boldsymbol{c}_i \cdot \boldsymbol{F}}{c_s^2}. \tag{3.32}$$

This forcing scheme is constructed to enforce mass and momentum conservations [Frisch *et al*., 1987; Luo, 1997],

$$\sum_i F_i = 0, \qquad \sum_i \boldsymbol{c}_i F_i = \boldsymbol{F}. \tag{3.33}$$

In this forcing scheme, the EDF and the fluid velocity are both the same as the standard D*n*Q*b* models, i.e. $f_i^{(eq)} = E_i(\rho, \boldsymbol{u})$ and the fluid velocity is still defined by Eq. (3.24). It was also suggested by some researchers that the fluid velocity takes $\boldsymbol{v}$ instead of $\boldsymbol{u}$ [Ginzbourg and Adler, 1994], and we will call this scheme as *modified LGA scheme* and denoted by mLGA.

Buick-Greated scheme

In this scheme the forcing term is defined by [Buick and Greated, 2000],

$$F_i = \omega_i \left(1 - \frac{1}{2\tau}\right) \frac{\boldsymbol{c}_i \cdot \boldsymbol{F}}{c_s^2}, \tag{3.34}$$

while the fluid velocity is defined again as the average of the pre- and post-collision velocities,

$$\rho \boldsymbol{v} = \sum_i \boldsymbol{c}_i f_i + \frac{\boldsymbol{F}\delta_t}{2}, \tag{3.35}$$

which is also used in the EDF, i.e. $f_i^{(eq)} = E_i(\rho, \boldsymbol{v})$.

He-Shan-Doolen scheme

This model (denoted by HSD) was developed based on the continuous Boltzmann equation [He *et al*., 1998]. The forcing term in the continuous

velocity space is first approximated as,

$$\boldsymbol{a}\cdot\nabla_{\xi}f(\boldsymbol{x},\boldsymbol{\xi},t)\approx\boldsymbol{a}\cdot\nabla_{\xi}f^{(eq)}(\boldsymbol{x},\boldsymbol{\xi},t)=-\frac{(\boldsymbol{\xi}-\boldsymbol{v})\cdot\boldsymbol{a}}{c_s^2}f^{(eq)}(\boldsymbol{x},\boldsymbol{\xi},t)\,, \tag{3.36}$$

where $f^{(eq)}(\boldsymbol{x},\boldsymbol{\xi},t)=f^{(eq)}\left(\boldsymbol{\xi};\rho(\boldsymbol{x},t),\boldsymbol{v}(\boldsymbol{x},t)\right)$ is the equilibrium distribution function given by

$$f^{(eq)}=\frac{\rho}{(2\pi RT)^{D/2}}\exp\left[-\frac{(\boldsymbol{\xi}-\boldsymbol{v})^2}{2RT}\right], \tag{3.37}$$

and here D is the spatial dimension. Following the standard discretization procedure as given in Chapter 1, one can obtain a discrete velocity model with a forcing term,

$$\frac{\partial\overline{f}_i}{\partial t}+\boldsymbol{c}_i\cdot\nabla\overline{f}_i=-\frac{1}{\tau_c}\left[\overline{f}_i-\overline{f}_i^{(eq)}\right]+F_i, \tag{3.38}$$

where the forcing term is given by

$$F_i=\frac{(\boldsymbol{c}_i-\boldsymbol{v})\cdot\boldsymbol{a}}{c_s^2}\overline{f}_i^{(eq)}\,, \tag{3.39}$$

with $c_s^2=RT$ being the sound speed, and $\overline{f}_i^{(eq)}=E_i(\rho,\boldsymbol{v})$. The density and velocity of the fluid are given by

$$\rho=\sum_i\overline{f}_i\,,\qquad\rho\boldsymbol{v}=\sum_i\boldsymbol{c}_i\overline{f}_i\,. \tag{3.40}$$

Integrating Eq. (3.38) along the characteristic line leads to

$$\overline{f}_i(\boldsymbol{x}+\boldsymbol{c}_i\delta_t,t+\delta_t)-\overline{f}_i(\boldsymbol{x},t)=\int_0^{\delta_t}\Lambda_i(\boldsymbol{x}+\boldsymbol{c}_it',t+t')dt'\,, \tag{3.41}$$

where

$$\Lambda_i=-\frac{1}{\tau_c}\left[\overline{f}_i-\overline{f}_i^{(eq)}\right]+F_i\,. \tag{3.42}$$

Evaluating the integral on the right hand side of Eq. (3.41) using the trapezoidal rule one can obtain that

$$\overline{f}_i(\boldsymbol{x}+\boldsymbol{c}_i\delta_t,t+\delta_t)-\overline{f}_i(\boldsymbol{x},t)=\frac{\delta_t}{2}\left[\Lambda_i(\boldsymbol{x}+\boldsymbol{c}_i\delta_t,t+\delta_t)+\Lambda_i(\boldsymbol{x},t)\right]. \tag{3.43}$$

The above scheme is implicit. However, the implicitness can be eliminated by introducing the following distribution function,

$$f_i = \overline{f}_i(\boldsymbol{x},t) - \frac{\delta_t}{2}\Lambda_i(\boldsymbol{x},t)\,. \tag{3.44}$$

Equation (3.43) can then be rewritten as Eq. (3.31) with $\tau = \tau_c/\delta_t + 1/2$, and

$$f_i^{(eq)} = \left[1 - \frac{(\boldsymbol{c}_i - \boldsymbol{v})\cdot\boldsymbol{a}}{2c_s^2}\right]E_i(\rho,\boldsymbol{v})\,. \tag{3.45}$$

From Eq. (3.44) we can see that the density and velocity of the fluid can be computed from the new distribution function directly,

$$\rho = \sum_\iota \overline{f}_i = \sum_\iota f_i\,, \quad \rho\boldsymbol{v} = \sum_\iota \boldsymbol{c}_i\overline{f}_i = \sum_\iota \boldsymbol{c}_i f_i + \frac{\delta_t}{2}\boldsymbol{F}\,. \tag{3.46}$$

It is also noted that the term associated with the force in the EDF given by Eq. (3.45) can be regrouped into the forcing term so that the He-Shan-Doolen forcing scheme becomes

$$f_i^{(eq)} = E_i(\rho,\boldsymbol{v}), \quad F_i = \left(1 - \frac{1}{2\tau}\right)\frac{(\boldsymbol{c}_i - \boldsymbol{v})\cdot\boldsymbol{a}}{c_s^2}f_i^{(eq)}\,. \tag{3.47}$$

Moment-expansion scheme

Luo noted that although the forcing term $\boldsymbol{a}\cdot\nabla_\xi f(\boldsymbol{x},\boldsymbol{\xi},t)$ in the Boltzmann equation cannot be discretized in the discrete velocity space, the first three moments of this term can be written out explicitly [Luo, 1998],

$$\begin{aligned}
&\int \boldsymbol{a}\cdot\nabla_\xi f\,d\boldsymbol{\xi} = 0,\\
&\int \boldsymbol{\xi}\boldsymbol{a}\cdot\nabla_\xi f\,d\boldsymbol{\xi} = -\rho\boldsymbol{a},\\
&\int \boldsymbol{\xi}\boldsymbol{\xi}\boldsymbol{a}\cdot\nabla_\xi f\,d\boldsymbol{\xi} = -\rho(\boldsymbol{a}\boldsymbol{u} + \boldsymbol{u}\boldsymbol{a})\,.
\end{aligned} \tag{3.48}$$

Therefore, the forcing term can be expanded as a series of $\boldsymbol{\xi}$,

$$\boldsymbol{a}\cdot\nabla_\xi f = \rho\omega(\boldsymbol{\xi})\left[c^{(0)} + \boldsymbol{c}^{(1)}\cdot\boldsymbol{\xi} + \boldsymbol{c}^{(2)} : \boldsymbol{\xi}\boldsymbol{\xi} + \cdots\right], \tag{3.49}$$

where

$$\omega(\boldsymbol{\xi}) = \frac{1}{(2\pi c_s^2)^{D/2}}\exp\left(\frac{-\boldsymbol{\xi}^2}{2c_s^2}\right), \tag{3.50}$$

and the expansion coefficients are

$$c^{(0)} = -\frac{\boldsymbol{a}\cdot\boldsymbol{u}}{c_s^2},\quad \boldsymbol{c}^{(1)} = -\frac{\boldsymbol{a}}{c_s^2},\quad \boldsymbol{c}^{(2)} = -\frac{1}{2c_s^4}\big(\boldsymbol{au}+\boldsymbol{ua}\big). \tag{3.51}$$

Substituting these results into Eq. (3.49) we can express the forcing term explicitly, which further leads to the following discrete forcing scheme,

$$F_i = \omega_i\rho\left[\frac{\boldsymbol{c}_i-\boldsymbol{u}}{c_s^2}+\frac{(\boldsymbol{c}_i\cdot\boldsymbol{u})\boldsymbol{c}_i}{c_s^4}\right]\cdot\boldsymbol{a}\,. \tag{3.52}$$

It is noted that in the moment-expansion scheme, the fluid velocity $\boldsymbol{v}$ is the same as $\boldsymbol{u}$.

The moment-expansion scheme was also obtained independently by Martys *et al*. [1998] based on Hermite expression of the distribution function, and Shan *et al*. [2006] made a further extension by including higher-order moments. It is also noted that if only the zeroth moment is considered in the expansion, the moment-expansion scheme reduces to the scheme based on the LGA method.

Modified moment-expansion schemes

Ladd and Verberg [2001] proposed another two moment-expansion schemes (denoted by LV-I and LV-II, respectively), which can be expressed as,

$$F_i = \omega_i\left[\frac{\boldsymbol{B}\cdot\boldsymbol{c}_i}{c_s^2}+\frac{\boldsymbol{C}:\big(\boldsymbol{c}_i\boldsymbol{c}_i-c_s^2\boldsymbol{I}\big)}{2c_s^4}\right]. \tag{3.53}$$

The coefficients and the EDF are

$$\begin{aligned}
&\text{LV-1:}\quad \boldsymbol{B}=\boldsymbol{F},\quad \boldsymbol{C}=\left(1-\frac{1}{2\tau}\right)(\boldsymbol{uF}+\boldsymbol{Fu}),\quad \rho\boldsymbol{v}=\rho\boldsymbol{u}=\sum_i\boldsymbol{c}_i f_i,\\
&\qquad f_i^{(eq)} = E_i(\rho,\boldsymbol{u});\\
&\text{LV-2:}\quad \boldsymbol{B}=\boldsymbol{F},\quad \boldsymbol{C}=\boldsymbol{uF}+\boldsymbol{Fu},\quad \rho\boldsymbol{u}=\sum_i\boldsymbol{c}_i f_i,\quad \boldsymbol{v}=\boldsymbol{u}+\frac{\delta_t}{2}\boldsymbol{a},\\
&\qquad f_i^{(eq)} = E_i(\rho,\boldsymbol{u}).
\end{aligned} \tag{3.54}$$

Later, Guo *et al*. [2002c] proposed another moment-expansion scheme (denoted by GZS) which has the same formulation as Eq. (3.53) and the

coefficients are given by

$$\boldsymbol{B} = \left(1 - \frac{1}{2\tau}\right)\boldsymbol{F}, \quad \boldsymbol{C} = \left(1 - \frac{1}{2\tau}\right)(\boldsymbol{vF} + \boldsymbol{Fv}),$$

$$\rho\boldsymbol{v} = \sum_i \boldsymbol{c}_i f_i + \frac{\delta_t}{2}\boldsymbol{F}, \quad f_i^{(eq)} = E_i(\rho, \boldsymbol{v}). \tag{3.55}$$

3.2.3 *Analysis of the forcing schemes*

We now make an analysis of the LBE with a forcing scheme through the Chapman-Enskog expansion method. The derived hydrodynamic equations will contain some additional terms due to the forcing term in comparison with the standard Navier-Stokes equations, through which we can evaluate the accuracy of the forcing schemes.

First, we express the forcing schemes (except for the HSD scheme) given in previous sections in a general formulation,

$$\begin{aligned} F_i &= \omega_i \left[\frac{B\boldsymbol{F}\cdot\boldsymbol{c}_i}{c_s^2} + \frac{C\left(\boldsymbol{u}^*\boldsymbol{F} + \boldsymbol{F}\boldsymbol{u}^*\right) : \left(\boldsymbol{c}_i\boldsymbol{c}_i - c_s^2\boldsymbol{I}\right)}{2c_s^4} \right] \\ &= \omega_i \left[\frac{B\boldsymbol{F}\cdot\boldsymbol{c}_i}{c_s^2} + \frac{C\boldsymbol{u}^*\boldsymbol{F} : \left(\boldsymbol{c}_i\boldsymbol{c}_i - c_s^2\boldsymbol{I}\right)}{c_s^4} \right], \end{aligned} \tag{3.56}$$

together with the following EDF, equilibrium velocity $\boldsymbol{u}^*$, and fluid velocity $\boldsymbol{v}$,

$$f_i^{(eq)} = E_i(\rho, \boldsymbol{u}^*), \quad \rho\boldsymbol{u}^* = \sum_i \boldsymbol{c}_i f_i + m\boldsymbol{F}\delta_t, \qquad \rho\boldsymbol{v} = \sum_i \boldsymbol{c}_i f_i + l\delta_t\boldsymbol{F}\,, \tag{3.57}$$

where B, C, m, and l are scalar parameters. It can be easily shown that

$$\sum_i F_i = 0, \quad \sum_i \boldsymbol{c}_i F_i = B\boldsymbol{F}, \quad \sum_i \boldsymbol{c}_i\boldsymbol{c}_i F_i = C(\boldsymbol{u}^*\boldsymbol{F} + \boldsymbol{F}\boldsymbol{u}^*). \tag{3.58}$$

In Tab. 3.1 the parameters of different forcing schemes are listed. It is noted the HSD scheme can also be expressed as Eq. (3.56) together with some terms of $O(\boldsymbol{u}^2)$, and the zeroth- and first-order moments are also the same as those given in Eq. (3.58), but the second-order moment is

$$\sum_i \boldsymbol{c}_i\boldsymbol{c}_i F_i = \left(1 - \frac{1}{2\tau}\right)\left[\boldsymbol{u}^*\boldsymbol{F} + \boldsymbol{F}\boldsymbol{u}^* - \frac{(\boldsymbol{F}\cdot\boldsymbol{u}^*)}{c_s^2}\boldsymbol{u}^*\boldsymbol{u}^*\right]. \tag{3.59}$$

Table 3.1. Parameters of the forcing schemes.

Scheme	m	l	B	C
LGA	0	0	1	0
mLGA	0	1/2	1	0
SC	τ	0	0	0
SD	τ	1/2	0	0
BG	1/2	1/2	$(2\tau-1)/2\tau$	0
Luo	0	0	1	1
LV-I	0	0	1	$(2\tau-1)/2\tau$
LV-II	0	1/2	1	1
GZS	1/2	1/2	$(2\tau-1)/2\tau$	$(2\tau-1)/2\tau$
HSD*	1/2	1/2	$(2\tau-1)/2\tau$	$(2\tau-1)/2\tau$

*The second-order moment of the HSD scheme is $C(\boldsymbol{u}^*\boldsymbol{F}+\boldsymbol{F}\boldsymbol{u}^*-\boldsymbol{F}\cdot\boldsymbol{u}^*\boldsymbol{u}^*\boldsymbol{u}^*/c_s^2)$.

After neglecting the term of order $O(\boldsymbol{u}^3)$, it can be seen that the parameters of the HSD and GZS schemes are just the same, although their expressions are different.

With the general formulation, the LBE with a forcing term can be expressed as

$$f_i(\boldsymbol{x}+\boldsymbol{c}_i\delta_t, t+\delta_t)-f_i(\boldsymbol{x},t)=-\frac{1}{\tau}\left[f_i(\boldsymbol{x},t)-E_i(\rho,\boldsymbol{u}^*)\right]+\delta_t F_i(\boldsymbol{x},t)\,. \quad (3.60)$$

The hydrodynamics equations can be derived from Eq. (3.60) following the standard Chapman-Enskog expansion method. With the expansions given by Eq. (1.53), the equations of the Taylor series expansion of Eq. (3.60) can be expressed at each time scale as,

$$\varepsilon^0: \qquad f_i^{(0)}=E_i(\rho,\boldsymbol{u}^*)\,, \quad (3.61)$$

$$\varepsilon^1: \qquad D_{0i}f_i^{(0)}=-\frac{1}{\tau_c}f_i^{(1)}+F_i^{(0)}\,, \quad (3.62)$$

$$\varepsilon^2: \qquad \partial_{t_1}f_i^{(0)}+D_{0i}f_i^{(1)}+\frac{\delta_t}{2}D_{0i}^2f_i^{(0)}=-\frac{1}{\tau_c}f_i^{(2)}\,, \quad (3.63)$$

where $\tau_c = \tau\delta_t$ and $D_{0i} = \partial_{t_0} + c_{i\alpha}\partial_{0\alpha}$. Here we have assumed that $\boldsymbol{F} = \varepsilon\boldsymbol{F}^{(0)}$ and $F_i = \varepsilon\boldsymbol{F}_i^{(0)}$. Equation (3.63) can also be rewritten as

$$\partial_{t_1} f_i^{(0)} + \left(1 - \frac{1}{2\tau}\right) D_{0i} f_i^{(1)} + \frac{\delta_t}{2} D_{0i} F_i^{(0)} = -\frac{1}{\tau_c} f_i^{(2)}. \tag{3.64}$$

From the definitions of ρ and $\boldsymbol{u}^*$ we can see that

$$\sum_i f_i^{(k)} = 0 \ \ (k > 0), \ \ \sum_i \boldsymbol{c}_i f_i^{(1)} = -m\delta_t \boldsymbol{F}^{(0)}, \ \ \sum_i \boldsymbol{c}_i f_i^{(k)} = 0 \ \ (k > 1). \tag{3.65}$$

With these results, we can obtain the hydrodynamics equations at t_0 scale,

$$\partial_{t_0}\rho + \partial_{0\alpha}(\rho u_\alpha^*) = 0, \tag{3.66}$$

$$\partial_{t_0}(\rho u_\alpha^*) + \partial_{0\beta}\pi_{\alpha\beta}^{(0)} = \left(B + \frac{m}{\tau}\right) F_\alpha^{(0)}, \tag{3.67}$$

where $\pi_{\alpha\beta}^{(0)} = \rho u_\alpha^* u_\beta^* + p\delta_{\alpha\beta}$. It is apparent that all of the forcing schemes listed in Tab. 3.1 satisfy the condition that $B + m/\tau = 1$, which means that Eqs. (3.66) and (3.67) are the Euler equations for the velocity $\boldsymbol{u}^*$ and pressure $p = c_s^2\rho$ with a body force.

The equations at t_1 scale are obtained from Eq. (3.64), which can be expressed as

$$\partial_{t_1}\rho - \delta_t\left(m - \frac{1}{2}\right)\partial_{0\alpha}F_\alpha^{(0)} = 0, \tag{3.68}$$

$$\partial_{t_1}(\rho u_\alpha^*) - \partial_{0\alpha}\sigma_{\alpha\beta}^{(1)} - \delta_t\left(m - \frac{1}{2}\right)\partial_{t_0}F_\alpha^{(0)} = 0, \tag{3.69}$$

where

$$\sigma_{\alpha\beta}^{(1)} = -\left(1 - \frac{1}{2\tau}\right)\pi_{\alpha\beta}^{(1)} - \frac{C\delta_t}{2}\left[u_\alpha^* F_\beta^{(0)} + u_\beta^* F_\alpha^{(0)}\right], \ \ \pi_{\alpha\beta}^{(1)} = \sum_i c_{i\alpha}c_{i\beta}f_i^{(1)}. \tag{3.70}$$

The first order momentum flux can be evaluated from the equations at t_0 scale. After some algebra, we can obtain that

$$\pi_{\alpha\beta}^{(1)} = -\tau\delta_t\left[(1 - C)(u_\alpha^* F_\beta^{(0)} + u_\beta^* F_\alpha^{(0)}) + c_s^2\rho(\partial_{0\alpha}u_\beta^* + \partial_{0\beta}u_\alpha^*)\right], \tag{3.71}$$

where the terms of order $O(\boldsymbol{u}^3)$ have been neglected.

Combining the equations at t_0 and t_1 time scales we can obtain the following hydrodynamic equations

$$\frac{\partial \rho}{\partial t} + \nabla \cdot (\rho \boldsymbol{u}^*) = \delta_t \left(m - \frac{1}{2} \right) \nabla \cdot \boldsymbol{F} , \tag{3.72}$$

$$\frac{\partial (\rho \boldsymbol{u}^*)}{\partial t} + \nabla \cdot (\rho \boldsymbol{u}^* \boldsymbol{u}^*) = -\nabla p + \nabla \cdot (2\rho \upsilon \boldsymbol{S}^*) + \boldsymbol{F} + \delta_t \left(m - \frac{1}{2} \right) \frac{\partial \boldsymbol{F}}{\partial t} + \delta_t \nabla \cdot \left[\left(\tau - \frac{1}{2} - \tau C \right) (\boldsymbol{u}^* \boldsymbol{F} + \boldsymbol{F} \boldsymbol{u}^*) \right], \tag{3.73}$$

where $S^*_{\alpha\beta} = (\partial_\alpha u^*_\beta + \partial_\beta u^*_\alpha) / 2$, and we have assumed that $\varepsilon \partial \boldsymbol{F} / \partial t_0 \approx \partial \boldsymbol{F} / \partial t$ or $\varepsilon^2 \partial \boldsymbol{F} / \partial t_1 = 0$. The above equations can also be written in terms of the fluid velocity $\boldsymbol{v}$ by noticing that $\boldsymbol{v} = \boldsymbol{u}^* + (l - m) \delta_t \boldsymbol{a}$,

$$\frac{\partial \rho}{\partial t} + \nabla \cdot (\rho \boldsymbol{v}) = R_\rho , \tag{3.74}$$

$$\frac{\partial (\rho \boldsymbol{v})}{\partial t} + \nabla \cdot (\rho \boldsymbol{v} \boldsymbol{v}) = -\nabla p + \nabla \cdot (2\rho \nu \boldsymbol{S}) + \boldsymbol{F} + R_v , \tag{3.75}$$

where R_ρ and R_v are the residual terms that reflect the derivations of the derived hydrodynamic equations from the desired mass and momentum conservation equations. These terms can be written out explicitly as,

$$R_\rho = \delta_t \left(l - \frac{1}{2} \right) \nabla \cdot \boldsymbol{F} , \tag{3.76}$$

$$\boldsymbol{R}_v = \delta_t \left(l - \frac{1}{2} \right) \frac{\partial \boldsymbol{F}}{\partial t} - \nabla \cdot \left[\rho (\boldsymbol{v} \boldsymbol{u}' + \boldsymbol{u}' \boldsymbol{v} + \boldsymbol{u}' \boldsymbol{u}') \right] + \nabla \cdot (2\rho \nu \boldsymbol{S}') + \delta_t \nabla \cdot \left\{ \left(\tau - \frac{1}{2} - \tau C \right) \left[(\boldsymbol{v} \boldsymbol{F} + \boldsymbol{F} \boldsymbol{v}) + (\boldsymbol{u}' \boldsymbol{F} + \boldsymbol{F} \boldsymbol{u}') \right] \right\}, \tag{3.77}$$

where $\boldsymbol{u}' = (m - l) \boldsymbol{a} \delta_t$ and $S'_{\alpha\beta} = (\partial_\alpha u'_\beta + \partial_\beta u'_\alpha) / 2$. It is clear that different forcing schemes will give different residuals. In Tab. 3.2 R_ρ and R_v are listed for some forcing schemes.

It is clear that most of the forcing schemes give nonvanishing residuals in the mass and momentum conservation equations. Specifically, only those using $\boldsymbol{v} = \sum_i \boldsymbol{c}_i f_i + \boldsymbol{F} \delta_t / 2$ (i.e. $l = 1/2$) as the fluid velocity satisfy the mass conservation equation in general, and the spurious velocity $\boldsymbol{u}'$ due to the body force vanishes only when the equilibrium velocity $\boldsymbol{u}^*$ is taken as the fluid velocity $\boldsymbol{v}$ (i.e $m = l$);

Table 3.2. Residual terms of the hydrodynamics equations for some forcing schemes.

Scheme	R_ρ	R_v
LGA	$-\frac{\delta_t}{2}\nabla\cdot\boldsymbol{F}$	$-\frac{\delta_t}{2}\partial_t\boldsymbol{F}+\delta_t\left(\tau-\frac{1}{2}\right)\nabla\cdot\left(\boldsymbol{vF}+\boldsymbol{Fv}\right)$
mLGA	0	$-\delta_t\nabla\cdot\left[\frac{\mu}{2}\left(\nabla\boldsymbol{a}+\nabla\boldsymbol{a}^T\right)-\tau\left(\boldsymbol{vF}+\boldsymbol{Fv}\right)+\delta_t\left(\tau-\frac{1}{4}\right)\rho\boldsymbol{aa}\right]$
SC	$-\frac{\delta_t}{2}\nabla\cdot\boldsymbol{F}$	$-\frac{\delta_t}{2}\partial_t\boldsymbol{F}+\delta_t\nabla\cdot\begin{bmatrix}\tau\mu\left(\nabla\boldsymbol{a}+\nabla\boldsymbol{a}^T\right)-\frac{\delta_t}{2}\left(\boldsymbol{vF}+\boldsymbol{Fv}\right)\\+\delta_t\tau(\tau-1)\rho\boldsymbol{aa}\end{bmatrix}$
SD	0	$\delta_t\left(\tau-\frac{1}{2}\right)\nabla\cdot\left[\mu\left(\nabla\boldsymbol{a}+\nabla\boldsymbol{a}^T\right)+\delta_t\left(\tau-\frac{1}{2}\right)\rho\boldsymbol{aa}\right]$
BG	0	$\delta_t\left(\tau-\frac{1}{2}\right)\nabla\cdot\left(\boldsymbol{vF}+\boldsymbol{Fv}\right)$
Luo	$-\frac{\delta_t}{2}\nabla\cdot\boldsymbol{F}$	$-\frac{\delta_t}{2}\partial_t\boldsymbol{F}-\frac{\delta_t}{2}\nabla\cdot\left(\boldsymbol{vF}+\boldsymbol{Fv}\right)$
LV-I	$-\frac{\delta_t}{2}\nabla\cdot\boldsymbol{F}$	$-\frac{\delta_t}{2}\partial_t\boldsymbol{F}$
LV-II	0	$-\frac{\delta_t}{2}\nabla\cdot\left[\mu\left(\nabla\boldsymbol{a}+\nabla\boldsymbol{a}^T\right)+\frac{\delta_t}{2}\rho\boldsymbol{aa}\right]$
GZS	0	0
HSD	0	0

Furthermore, it is found that the force contribution to the momentum flux does not appear only when $C=1-1/2\tau$. It is apparent that only the GZS and HSD schemes satisfy these constraints and yield the correct hydrodynamics equations. It is also noted that when the acceleration $\boldsymbol{a}$ is a constant and the density changes slowly in both time and space, the continuity equation holds for all of the forcing schemes, and the terms of temporal/spatial derivatives of the force in the momentum equation can be neglected, which means that the SD, LV-I, and LV-II schemes also give the desired hydrodynamic equations. On the other hand, the residual term R_v in the momentum equation of the other five schemes does not disappear even in such case due to the coupling terms $\boldsymbol{vF}$ and $\boldsymbol{Fv}$.

3.2.4 *Forcing scheme for MRT-LBE*

The forcing schemes for the LBGK models can be easily extended to MRT-LBE models. For example, Guo and Zheng [2007] have extended

the GZS scheme to MRT-LBE recently, and the evolution equation with a forcing term is written as

$$\boldsymbol{f}(\boldsymbol{x}+\boldsymbol{c}_i\delta_t, t+\delta_t) - \boldsymbol{f}(\boldsymbol{x},t) = -\boldsymbol{M}^{-1}\boldsymbol{S}\boldsymbol{M}[\boldsymbol{f}-\boldsymbol{f}^{(eq)}] + \delta_t\boldsymbol{M}^{-1}\hat{\boldsymbol{F}}\,, \tag{3.78}$$

for $i=0,\,1,\,\ldots,\,b-1$, where $\boldsymbol{M}$ is the transform matrix, $\boldsymbol{S}=\mathrm{diag}(s_0,\,s_1,\,\ldots,\,s_{b\text{-}1})$ is the relaxation matrix, and $\hat{\boldsymbol{F}}$ is the moments of the forcing term in the moment space which can be expressed as

$$\hat{\boldsymbol{F}} = \left(\boldsymbol{I}-\frac{1}{2}\boldsymbol{S}\right)\boldsymbol{M}\bar{\boldsymbol{F}}\,, \tag{3.79}$$

where $\bar{\boldsymbol{F}} = \left(\bar{F}_0,\,\bar{F}_1,\,\cdots,\,\bar{F}_{b-1}\right)^T$ is related to the body force $\boldsymbol{F}$,

$$\bar{F}_i = \omega_i\left[\frac{\boldsymbol{c}_i\cdot\boldsymbol{F}}{c_s^2} + \frac{\boldsymbol{v}\boldsymbol{F}:(\boldsymbol{c}_i\boldsymbol{c}_i - c_s^2\boldsymbol{I})}{c_s^4}\right], \tag{3.80}$$

and here the fluid velocity $\boldsymbol{v}$ is defined by Eq. (3.55). Obviously, when $s_i = 1/\tau$ the forcing scheme reduces to that for the LBGK model. The forcing moments can be computed explicitly. For example, for the D2Q9 MRT model the nine moments are

$$\hat{F}_0 = 0\,,\ \hat{F}_1 = 6\left(1-\frac{s_e}{2}\right)\boldsymbol{v}\cdot\boldsymbol{F}\,,\ \hat{F}_2 = -6\left(1-\frac{s_\varepsilon}{2}\right)\boldsymbol{v}\cdot\boldsymbol{F}\,,\hat{F}_3 = F_x\,,$$

$$\hat{F}_4 = -\left(1-\frac{s_q}{2}\right)F_x\,,\ \hat{F}_5 = F_y\,,\ \hat{F}_6 = -\left(1-\frac{s_q}{2}\right)F_y\,,$$

$$\hat{F}_7 = 2\left(1-\frac{s_\nu}{2}\right)(v_xF_x - v_yF_y)\,,\ \hat{F}_8 = \left(1-\frac{s_\nu}{2}\right)(v_xF_y + v_yF_x)\,.$$

With the forcing moments, the collision process of a MRT-LBE can be implemented in moment space as

$$m_k'(\boldsymbol{x},t) = m_k(\boldsymbol{x},t) - s_k\left[m_k(\boldsymbol{x},t) - m_k^{(eq)}\right] + \delta_t\hat{F}_i\,. \tag{3.81}$$

Then the post-collision moments are transformed back to the velocity space where the standard streaming process is carried out.

The Chapman-Enskog expansion of Eq. (3.78) together with the forcing term given by Eq. (3.79) leads to the correct hydrodynamics equations, where the shear and bulk viscosities are the same as those

given in Chapter 1. It is noted that the above forcing scheme is closely related to that for the LBGK model. But due to the freedom of MRT models, the forcing scheme can also be constructed directly in moment space.

3.3 LBE with Nonuniform Grids

The standard LBE models utilize certain regular lattices associated with the discrete velocities as the computational meshes. The flexibility of such meshes is rather limited, particularly for flows with irregular geometries. The choice of the computational meshes as the underlying lattice is not essential, however. Such choice is mainly due to historic reasons that LBE is a descendant of the LGA method which utilizes a regular lattice. Once the fact that LBE is a special finite-difference scheme of the continuous Boltzmann equation is recognized, we can decouple the computation mesh from the underlying lattice.

A number of LBE methods using irregular meshes have been developed in the past years. The method can be classified into six types: (1) Grid-refinement and multi-block methods, (2) interpolation methods, (3) finite-difference based methods (FD-LBE), (4) finite-volume based methods (FV-LBE), (5) finite-element based methods (FE-LBE), (6) Taylor series expansion and least square-based methods (TLLBE). In this section we will present some examples of these non-standard LBE methods.

3.3.1 *Grid-refinement and multi-block methods*

Grid-refinement technique is widely used in CFD methods to treat the regions where flow variables change rapidly. The main advantage of the grid refinement method is that the boundary information can be spread to the flow domain quickly on the coarser grid and the overall flow pattern can be captured with low computational costs. The detailed information in the regions where large gradients exist can be captured more accurately on the refined grid. This technique was introduced into LBE first by Filippova and Hänel (referred to as FH) [1998]. In their method a

coarse mesh $\mathcal{L}_c$ is first used to cover the flow domain, and then one or several patches $\mathcal{L}_f$ with refined resolutions will be inserted into some regions on $\mathcal{L}_c$ where the flow may change significantly. Different patches can be used in different regions, and nest refinements can be employed if necessary. As an example, in what follows we will consider a mesh composed of a coarse lattice with spacing δ_x^c and a fine one with spacing δ_x^f, and assume that $n = \delta_x^c/\delta_x^f$ is an integer.

The evolutions on the coarse and fine grids can be written as

$$f_i^k(\boldsymbol{x}^k + \boldsymbol{c}_i\delta_t^k, t+\delta_t^k) - f_i^k(\boldsymbol{x}^k, t) = -\frac{1}{\tau^k}\Big[f_i^k(\boldsymbol{x}^k, t) - f_i^{(eq)}(\boldsymbol{x}^k, t)\Big], \quad (3.82)$$

where the variables with a superscript $k = c$ or f represent quantities on the coarse or fine grid. Note that the EDF is identical on both coarse and fine grid since it depends only on the grid-independent variables (sound speed, fluid density, and velocity). Furthermore, since the sound speed and viscosity of the fluid should be independent of the meshes, the following relations must hold,

$$\delta_t^f = \frac{1}{n}\delta_t^c, \quad \tau^f = \frac{1}{2} + n\left(\tau^c - \frac{1}{2}\right). \quad (3.83)$$

On the other hand, from the Chapman-Enskog analysis we can see that the nonequilibrium parts of the distribution functions on the nodes shared by both grids satisfy the following condition,

$$-D_i^{(0)} f_i^{(eq)}(\rho, \boldsymbol{u}) = \frac{f_i^{c,(neq)}}{\tau^c\delta_t^c} = \frac{f_i^{f,(neq)}}{\tau^f\delta_t^f}, \quad (3.84)$$

or in other words,

$$\frac{1}{(\tau^c - 1)\delta_t^c}\Big[f_i'^{\,c} - f_i^{(eq)}\Big] = \frac{1}{(\tau^f - 1)\delta_t^f}\Big[f_i'^{\,f} - f_i^{(eq)}\Big], \quad (3.85)$$

where the prime denotes the post-collision state. Therefore, the post-collision distribution functions on the node shared by the two grids have the following relations,

$$f_i'^{\,c} = f_i^{(eq)} + \frac{n(\tau^c - 1)}{(\tau^f - 1)}\Big[f_i'^{\,f} - f_i^{(eq)}\Big], \quad f_i'^{\,f} = \tilde{f}_i^{\,(eq)} + \frac{\tau^f - 1}{n(\tau^c - 1)}\Big[\tilde{f}_i'^{\,c} - \tilde{f}_i^{\,(eq)}\Big], \quad (3.86)$$

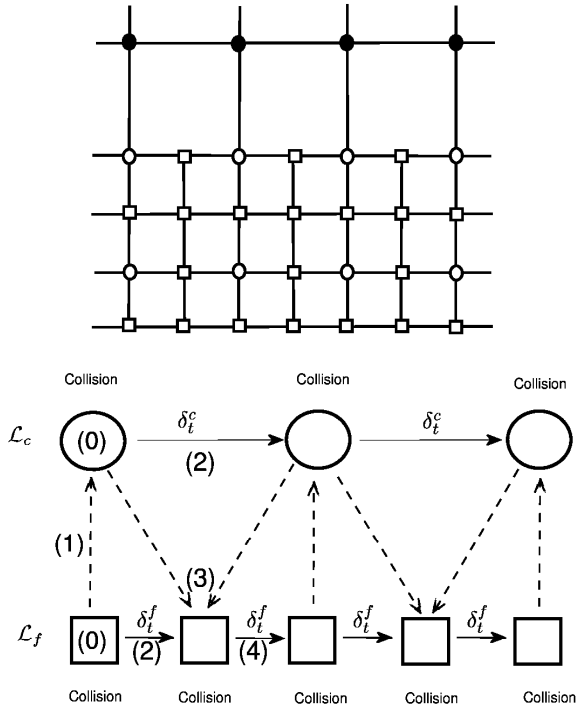

Fig. 3.1. Schematic of the FH grid-refinement method. Top: Coarse and fine grids for $n = 2$. Solid circle: node of coarse grid; open square: node of fine grid; open circle: common node. Bottom: Evolution process on two grids. (0)-(4): computation order; dashed arrow: information exchange between grids; solid arrow: streaming.

where the variables with a tilde represent the counterparts on the fine grid interpolated from the coarse one. As such, the relationship between the two grids is well established.

The grid-refinement method developed by Filippova and Hänel is sketched in Fig. 3.1, and the process can be described as follows:

(1) Initializing the distribution functions on both coarse and fine grids;

(2) Calculating the post distribution functions $f_i'^{\,c}(\boldsymbol{x}^c, t_0)$ and $f_i'^{\,c}(\boldsymbol{x}^c, t_0)$ at all nodes;

(3) Evolution on the coarse grid at time *t*:

   (a) Re-calculating $f_i'^{\,c}(\boldsymbol{x}^c, t)$ at the common nodes according to Eq. (3.86);

(b) Streaming: $f_i^c(\boldsymbol{x}^c + \boldsymbol{c}_i\delta_t^c, t+\delta_t^c) = f_i'^c(\boldsymbol{x}^c, t)$;

(c) Collision: $f_i'^c(\boldsymbol{x}^c, t+\delta_t^c) = f_i^c(\boldsymbol{x}^c, t) - [f_i^c(\boldsymbol{x}, t) - f_i^{(eq)}(\boldsymbol{x}^c, t)] / \tau^c$.

(4) Evolution on the fine grid at time steps $t_k = t + k\delta_t^f (k = 0, 1, n\text{–}1)$:

(a) calculating $\tilde{f}_i'^c(\boldsymbol{x}_b^f, t_k)$ by interpolation from those on the coarse grid;

(b) Streaming: $f_i^f(\boldsymbol{x}^f + \boldsymbol{c}_i\delta_t^f, t_{k+1}) = f_i'^f(\boldsymbol{x}^f, t_k)$;

(c) Collision: $f_i'^f(\boldsymbol{x}^f, t_{k+1}) = f_i^f(\boldsymbol{x}^f, t) - [f_i^f(\boldsymbol{x}, t) - f_i^{(eq)}(\boldsymbol{x}^f, t)] / \tau^f$.

(5) Go to (3) until certain stop criterion is satisfied.

It is noted that the FH scheme may encounter numerical instability if $\tau_c \approx 1$ or $\tau_f \approx 1$. Dupuis and Chopard [2003] suggested another grid refinement method (referred to as DC). Like the FH method, the information exchange in the DC method is also based on Eq. (3.84), but this is achieved through the distribution functions rather than the post-collision ones,

$$f_i^c = f_i^{(eq)} + \frac{n\tau_c}{\tau_f}\left[f_i^f - f_i^{(eq)}\right], \quad f_i^f = \tilde{f}_i^{(eq)} + \frac{\tau_f}{n\tau_c}\left[\tilde{f}_i^f - \tilde{f}_i^{(eq)}\right]. \tag{3.87}$$

These distributions are then used in the collision processes on both grids. Based on this grid refinement method, Dupuis and Chopard further proposed an acceleration technique: a coarse grid is used first to obtain a solution, from which an initial state on a finer grid can be constructed based on Eq. (3.87). Repeating this process can lead to a more accurate solution on a finer grid. It was shown that this technique could improve the computational efficiency greatly [Dupuis and Chopard, 2003].

In the grid-refinement methods, a coarse grid is first generated to cover the flow region, and some finer patches are then put at certain regions. The refined regions are covered by both the coarse and fine grids, and information exchanges on all common nodes. As shown previously, the information exchange needs special treatments and may lead to some undesired artifacts. An alternative technique that employs grids with different resolutions is the *multi-block* method, as developed by Yu *et al*. [2002]. In this method, the flow domain is first decomposed into several blocks, and the flow in each block is solved by a LBE using

a grid with an independent resolution. Information between different blocks exchanges only on nodes at block interfaces. In Yu's method, the strategy used in the FH method was suggested for this purpose.

Guo *et al*. [2003] proposed a more flexible multi-block method, i.e. *domain decomposition* method. In this approach, the flow domain is decomposed into several sub-domains that may overlap or not. On each sub-domain, an independent LBE with an independent lattice runs. An extreme example is that the D2Q9 LBE is used on a sub-domain while the D2Q7 LBE is used on another one. The ghost boundaries of the sub-domains are treated by the non-equilibrium extrapolation method as described in Chapter 2, and the information exchange is realized through the equilibrium parts where the fluid density and velocity are interpolated from the sub-domains involved.

Recent development in grid-refinement method in LBE is the use of adaptive grids. The first attempt towards this direction was attributed to Crouse *et al.* [2003]. In their method, a sensor variable ϕ , which is based on heuristic expressions for primary or derived quantities of the flow field, is used to detect the location of new refinement zones. An example of the sensor is $\left|\nabla \cdot \boldsymbol{u}\right| \delta_x^{3/2}$ that measures the errors with respect to mass conservation. The adaptive refinement starts with an initial grid. After a preliminary solution is achieved, the sensor is evaluated in each cell surrounded by some neighboring nodes. If the value of the sensor in a cell exceeds a critical value, the cell will be marked for refinement. The unknown distribution functions on the new refined grid nodes can be constructed from the parent cells using certain interpolation schemes as used in the FH method, and simulation process continues then on the improved grid. Crouse's method was developed based on LBGK models, and recently it was generalized for MRT-LBE models [Tölke *et al.*, 2006]. A similar approach was also proposed based on the volumetric formulation of LBE [Yu and Fan, 2009].

More recently, Wu and Shu [2011] presented a stencil adaptive LBE for two-dimensional problems. It incorporates the stencil adaptive algorithm developed by Ding and Shu [2006] for the solution of Navier–Stokes equations into the LBE calculation. Based on the uniform mesh, the stencil adaptive algorithm refines the mesh by two types of

5-points symmetric stencils, which are used in an alternating sequence for increased refinement levels. The two types of symmetric stencils can be easily combined to form a 9-points symmetric structure. Using the one-dimensional second-order interpolation along the straight line and the D2Q9 model, the adaptive LBE calculation can be effectively carried out. Unlike other works, where the FH scheme is usually used, and the relaxation parameters and time step sizes are used differently on different grid levels, in the work of Wu and Shu [2011], the same relaxation parameter and time step size are used at every mesh point. The stencil adaptive LBE has been effectively applied to simulate the lid-driven cavity flow and the flow around a circular cylinder [Wu and Shu, 2011].

3.3.2 *Interpolation methods*

He *et al*. [1996] pointed out that the computational mesh of LBE can be separated from underlying lattice associated with the discrete velocity set. Based on this understanding, they proposed an *interpolation supplemented LBE* method (ISLBE) that uses an arbitrary computational mesh. The procedure of ISLBE is similar to the standard LBE except for an additional interpolation step, and can be described as follows.

(1) Initializing the distribution functions $f_i(\boldsymbol{X})$ on each node $\boldsymbol{X}$ of the computational mesh (denoted by $\mathcal{M}$);
(2) Collision: $f_i'(\boldsymbol{X},t) = f_i(\boldsymbol{X},t) - \tau^{-1}[f_i(\boldsymbol{X},t) - f_i^{(eq)}(\boldsymbol{X},t)]$;
(3) Streaming: $f(\boldsymbol{X}_i', t+\delta_t) = f_i'(\boldsymbol{X},t)$, where $\boldsymbol{X}_i' = \boldsymbol{X} + \boldsymbol{c}_i\delta_t$, which does not locate at the mesh $\mathcal{M}$ in general. Actually, all of these points constitute a new mesh $\mathcal{M}_i'$ which is a translation of the original mesh $\mathcal{M}$ along $\boldsymbol{c}_i$, i.e. $\mathcal{M}_i' = \mathcal{M} + \mathbf{c}_i\delta_t$.
(4) Interpolation: construct the distribution functions at nodes of $\mathcal{M}$ from those at $\mathcal{M}_i'$ using some interpolation schemes, $f_i(\boldsymbol{X}, t+\delta_t) = \boldsymbol{P}f_i(\boldsymbol{X}', t+\delta_t)$ where $\boldsymbol{P}$ is an interpolation operator.
(5) Calculating the fluid density and velocity at $\mathcal{M}$: $\rho(\boldsymbol{X}, t+\delta_t) = \sum_i f_i(\boldsymbol{X}, t+\delta_t)$, $\rho\boldsymbol{u}(\boldsymbol{X}, t+\delta_t) = \sum_i \boldsymbol{c}_i f_i(\boldsymbol{X}, t+\delta_t)$.
(6) Repeat (2)-(5) until some stop criterion is satisfied.

It should be noted that the time step in ISLBE should satisfy the Courant-Friedrichs-Lewy (CFL) condition, which means that the lattice spacing $\delta_x = c\delta_t$ should be smaller than the minimum of the mesh spacing of $\mathcal{M}$ (denoted by $\Delta_X^{\min}$), so that the particles can only move to neighboring cells. Furthermore, interpolation schemes with at least second order accuracy should be used in the interpolation step in order to reduce the numerical dissipation. In practical applications, second order upwind schemes are usually adopted. It can be shown that interpolations with second order accuracy do not influence the viscosity of the ISLBE. However, linear analysis indicates that such interpolations will influence the hyper-viscosities in the spectral space, and may influence the Galilean invariant property [Lallemand and Luo, 2000].

Another advantage of ISLBE in addition to the use of non-uniform meshes is that the simulated Reynolds number can be increased. For the standard D*n*Q*b* LBGK models, the Reynolds number can be expressed as

$$\mathrm{Re} = \frac{LU}{\nu} \approx \frac{LM}{\delta_x(\tau - 1/2)}, \tag{3.88}$$

where L and U are the characteristic length and velocity of the flow. This indicates that a larger Re can be achieved by increasing the Mach number M or decreasing τ or δ_x. However, numerical instability will appear if M is large or τ is close to 0.5, while a small δ_x means high computational costs. On the other hand, the lattice spacing δ_x is independent of the computational mesh, which means that a coarse mesh can be used with a finer underlying lattice in ISLBE. Actually, the local Reynolds number of ISLBE is $\mathrm{Re}_\Delta^* = r\,\mathrm{Re}_\Delta$, where $r = \Delta_X^{\min}/\delta_x$, and $\mathrm{Re}_\Delta = c_s\delta_x/\nu$ is the grid Reynolds number of the standard LBE. So, the ISLBE can increase the simulated Reynolds number by r times under the same conditions as the standard LBE [He *et al*., 1997].

3.3.3 *Finite-difference based LBE methods*

As shown in Chapter 1, the LBE can be viewed as a special numerical scheme of the continuous Boltzmann equation. Specifically, LBE is an upwind finite-difference scheme of the following discrete velocity model

(DVM) obtained from the Boltzmann-BGK equation,

$$\frac{\partial f_i}{\partial t} + \boldsymbol{c}_i \cdot \nabla f_i = \Omega_i(f) = -\frac{1}{\tau_c}\left[f_i - f_i^{eq} \right]. \tag{3.89}$$

The discrete velocity set $\{\boldsymbol{c}_i : i = 0, 1, \cdots, b-1\}$ is determined by the requirements of velocity moments of the distribution function $f(\boldsymbol{x}, \boldsymbol{\xi}, t)$ [Shan *et al*., 2006]. Particularly, the following quadratures should be evaluated exactly,

$$\int \boldsymbol{\xi}^k \overline{f}^{(eq)}(\boldsymbol{x}, \boldsymbol{\xi}, t) = \sum_i w_i \overline{f}^{(eq)}(\boldsymbol{x}, \boldsymbol{c}_i, t), \; 0 \le k \le K, \tag{3.90}$$

where the w_i's are the weights and K is an integer, and $\overline{f}^{(eq)}$ is an expansion of the Maxwellian-Boltzmann distribution,

$$\overline{f}^{(eq)}(\boldsymbol{x}, \boldsymbol{\xi}, t) = \sum_{n=0}^{N} \boldsymbol{a}_n \cdot \boldsymbol{u}^n, \tag{3.91}$$

where the coefficient $\boldsymbol{a}_n$ is a rank-n tensor and the dot product represents full contraction. The expansion can be a Taylor or Hermite expansion. In terms of the Chapman-Enskog analysis, the above quadratures determine the accuracy of the DVM as an approximation to the original Boltzmann equation. For example, in order to make the DVM (3.89) match the Boltzmann equation at the Navier-Stokes order (i.e. the t_1 time scale) for isothermal flows in the low Mach limit, it is necessary to choose $N \ge 2$ in the expansion (3.91) and $K \ge 3$ in Eq. (3.90), which means that a quadrature formula of at least 5 degree of precision should be used. For the full thermal Navier-Stokes equations, the expansion must be up to $N \ge 3$ and the moments with $K \ge 4$ should be evaluated using a quadrature formula of degree of greater than 6.

The discrete velocity set together with the discrete EDF $f_i^{(eq)}(\boldsymbol{x}, t) = w_i \overline{f}^{(eq)}(\boldsymbol{x}, \boldsymbol{c}_i, t)$ are determined in such a way that the hydrodynamic equations are ensured to have the desired rotational invariance, and this feature is called *physical symmetry* by Cao *et al*. [1997]. A concept related to the physical symmetry is the *lattice symmetry*, which means that the number of links at a node is the same as the discrete velocities. In LGA, these two symmetries are identical because the particles resident on the lattice. But in the LBE framework,

they are not required to be coupled. Once this fact is recognized, the discretization of the spatial space x can be done independently from the discrete velocities. Actually, the ISLBE has made use of this knowledge. More general numerical methods for partial differential equations, such as finite-difference, finite-volume, and finite-element schemes, can also be applied to the DVM (3.89), which lead to different non-standard LBE methods.

The first attempt to discretize Eq. (3.89) using certain finite-difference schemes was attributed to Cao *et al*. [1997]. In their method, the spatial gradient is first discretized,

$$\nabla f_i = \nabla^h f_i, \tag{3.92}$$

where ∇^h is a discrete gradient operator depending on the coordinate system and computational mesh. For example, the central difference scheme on a uniform mesh in the Cartesian coordinate system can be expressed as

$$\partial_\alpha^h f_i = \frac{f_i(x_\alpha + \Delta x_\alpha) - f_i(x_\alpha - \Delta x_\alpha)}{2\Delta x_\alpha}, \tag{3.93}$$

where Δx_α is the mesh spacing in the direction of x_α. For general coordinate systems, the gradient can be discretized on a regular computational mesh which is constructed from the physical mesh using some transformations. For example, in the polar coordinate system (r, θ) the spatial gradient is expressed as

$$\boldsymbol{c}_i \cdot \nabla f_i = (\boldsymbol{c}_i \cdot \boldsymbol{e}_r)\ \frac{\partial f_i}{\partial r} + \frac{(\boldsymbol{c}_i \cdot \boldsymbol{e}_\theta)}{r}\frac{\partial f_i}{\partial \theta}, \tag{3.94}$$

where $\boldsymbol{e}_r$ and $\boldsymbol{e}_\theta$ are the unit vectors for the polar coordinates. Then the derivatives with respect to r and θ can be discretized using some standard finite-difference schemes.

For the temporal derivative in the DVM (3.89), Cao *et al*. suggested the second-order Runge-Kutta method so that the evolution of the distribution functions f_i follows the following procedure,

$$f_i(\boldsymbol{x}, t + \Delta t\ /\ 2) = f_i(\boldsymbol{x}, t) - \frac{\Delta t}{2} R_i(\boldsymbol{x}, t), \tag{3.95}$$

$$f_i(\boldsymbol{x}, t + \Delta t) = f_i(\boldsymbol{x}, t) - \Delta t R_i(\boldsymbol{x}, t + \Delta t \,/\, 2)\,, \tag{3.96}$$

where $R_i = -c_{i\alpha}\partial^h_\alpha f_i + \Omega_i(f)$, and Δt is the time step that obeys the CFL condition $\max_i \mid \boldsymbol{c}_i \Delta t \mid \leq \Delta x_{min}$. The above method was used to discretize a thermal DVM which was then successfully applied to the heat conduction between two plates with a large temperature difference [Cao *et al*., 1997].

Instead of using the Runge-Kutta method, Cao *et al*. [1997] also suggested an semi-implicit scheme to solve the DVM (3.89), where the convection term is discretized by an explicit downwind scheme while the collision term is treated implicitly,

$$\begin{aligned} f_i(\boldsymbol{x}, t + \Delta t) = f_i(\boldsymbol{x}, t) &- \frac{\Delta t}{\Delta x}\big[f_i(\boldsymbol{x}, t) - f_i(\boldsymbol{x} - \boldsymbol{c}_i \Delta t, t)\big] \\ &- \frac{\Delta t}{\tau_c}\big[f_i(\boldsymbol{x}, t + \Delta t) - f_i^{(eq)}(\boldsymbol{x}, t + \Delta t)\big]. \end{aligned} \tag{3.97}$$

Mei and Shyy [1998] further generalized the semi-implicit scheme to curved coordinate systems later. In a general coordinate system $\boldsymbol{\zeta} = (\zeta_1, \zeta_2, \zeta_3)$ the DVM (3.89) can be expressed as

$$\frac{\partial f_i}{\partial t} + \frac{1}{\sqrt{g}} \boldsymbol{c}_i \cdot \sum_{m=1}^{3} (a_j \times a_k) \frac{\partial f_i}{\partial \zeta_m} = -\frac{1}{\tau_c}\big(f_i - f_i^{(eq)} \big), \tag{3.98}$$

where

$$\boldsymbol{a}_j = \frac{\partial \boldsymbol{x}}{\partial \zeta_j}, \quad \sqrt{g} = \det|g_{jk}| = \boldsymbol{a}_1 \cdot (\boldsymbol{a}_2 \times \boldsymbol{a}_3)\,.$$

For example, in the polar coordinate system, Eq. (3.98) can be written out explicitly as

$$\frac{\partial f_i}{\partial t} + \frac{c_{i\theta}}{r}\frac{\partial f_i}{\partial \theta} + c_{ir}\frac{\partial f_i}{\partial r} = -\frac{1}{\tau_c}\big(f_i - f_i^{(eq)} \big)\,. \tag{3.99}$$

One can further assume that $r = r(\eta)$ and Eq. (3.99) becomes

$$\frac{\partial f_i}{\partial t} + \frac{c_{i\theta}}{r}\frac{\partial f_i}{\partial \theta} + \frac{c_{ir}}{h_r}\frac{\partial f_i}{\partial \eta} = -\frac{1}{\tau_c}\big(f_i - f_i^{(eq)} \big), \tag{3.100}$$

where $h_r = dr/d\eta$. Another special case supposes the two dimensional Cartesian coordinates x and y are functions of two independent variables ξ and η, respectively, viz. $x = x(\zeta),\ y = y(\eta)$, then Eq. (3.98) reduces to

$$\frac{\partial f_i}{\partial t} + \frac{c_{ix}}{h_x}\frac{\partial f_i}{\partial \zeta} + \frac{c_{ir}}{h_y}\frac{\partial f_i}{\partial \eta} = -\frac{1}{\tau_c}\left(f_i - f_i^{(eq)}\right), \tag{3.101}$$

where $h_x = dx/d\zeta$ and $h_y = dy/d\eta$. It is apparent that the DVM in a general coordinate system is much simpler in comparison with those of the Navier-Stokes equations due to the absence of second order derivatives.

The generalized DVM (3.98) can be easily discretized using standard finite-difference schemes. For instance, Mei and Shyy (1998) suggested to discretize the convection term in Eq. (3.100) using a second-order upwind scheme,

$$\partial_\theta^h f_i = \begin{cases} \dfrac{1}{2\Delta\theta}\left(3f_i(\theta_j, r_k) - 4f_i(\theta_{j-1}, r_k) + f_i(\theta_{j-2}, r_k)\right), & c_{i\theta} \geq 0 \\ \dfrac{-1}{2\Delta\theta}\left(3f_i(\theta_j, r_k) - 4f_i(\theta_{j+1}, r_k) + f_i(\theta_{j+2}, r_k)\right), & c_{i\theta} < 0 \end{cases} \tag{3.102}$$

where $\Delta\theta$ is the increment in θ. The upwind scheme for $\partial f_i/\partial\eta$ is similar. The collision term was treated implicitly in the original Mei-Shyy method, i.e. it is discretized as

$$\Omega_i = -\frac{1}{\tau_c}\left[f_i^{n+1} - f_i^{(eq),n+1}\right], \tag{3.103}$$

where the superscript n denotes the time step. Because the unknowns ρ^{n+1} and $\boldsymbol{u}^{n+1}$ are involved in $f_i^{(eq),n+1}$, the following approximation was suggested [Mei and Shyy, 1998],

$$f_i^{(eq),n+1} = 2f_i^{(eq),n} - f_i^{(eq),n-1}. \tag{3.104}$$

Therefore, the final FD-LBE for the DVM (3.100) developed by Mei and Shyy [1998] can be written as

$$f_i^{n+1} = \frac{f_i^n}{1+\tau} + \frac{\tau}{1+\tau}\left(2f_i^{(eq),n} - f_i^{(eq),n-1}\right) - \frac{c_{i\theta}\Delta t}{r(1+\tau)}\partial_\theta^h f_i^n - \frac{c_{ir}\Delta t}{h_r}\partial_\eta^h f_i^n, \tag{3.105}$$

where $\tau = \tau_c/\Delta t$. Similar methods can also be derived for the DVM in other coordinate systems.

The implicit treatment of the collision term in the Mei-Shyy method is advantageous to the numerical stability. On the other hand, the extrapolation used in the EDF may have a negative effect on the stability. Furthermore, the Mei-Shyy method is a three-time-level scheme, which requires more computational memory. Guo and Zhao [2003a] later proposed an alternative semi-implicit FD-LBE, which is free of such disadvantages. First, integrating Eq. (3.89) in the time interval $[t_n,\ t_{n+1}]$ leads to,

$$f_i^{n+1} - f_i^n + \Delta t \boldsymbol{c}_i \cdot \nabla f_i^n = \Delta t \Big[q\Omega_i^{n+1} + (1-q)\Omega_i^n \Big], \tag{3.106}$$

where $0 \le q \le 1$. Apparently the scheme is fully explicit as $q = 0$ and fully implicit as $q = 1$. However, only as $q = 1/2$ the discretization of the collision term is of second-order accuracy.

In order to remove the implicitness, Guo and Zhao [2003a] introduced a new type of distribution functions,

$$g_i = f_i - \Delta t q \Omega_i = f_i + \omega q \Big[f_i - f_i^{(eq)} \Big], \tag{3.107}$$

where $\omega = \Delta t / \tau_c$. In terms of the new distribution functions, Eq. (3.106) can be rewritten as

$$\begin{aligned} g_i^{n+1} = & -\frac{\Delta t}{1+\omega q} \boldsymbol{c}_i \cdot \nabla \Big[g_i^n + \omega q f_i^{(eq),n} \Big] \\ & + \frac{1-\omega(1-q)}{1+\omega q} \Big[g_i^n + \omega q f_i^{(eq),n} \Big] + \omega(1-q) f_i^{(eq),n}, \end{aligned} \tag{3.108}$$

or

$$g_i^{n+1} = -\Delta t \boldsymbol{c}_i \cdot \nabla f_i^n + (1 - \omega + \omega q) f_i^{(n)} + \omega(1-q) f_i^{(eq),n}, \tag{3.109}$$

where

$$f_i^n = \frac{1}{1+\omega q} \Big[g_i^n + \omega q f_i^{(eq),n} \Big]. \tag{3.110}$$

Once the spatial gradient is discretized, the values of g_i at t_{n+1} can be obtained, and the fluid density and velocity can be calculated by

$$\rho = \sum_i g_i, \quad \rho \boldsymbol{u} = \sum_i \boldsymbol{c}_i g_i \ . \tag{3.111}$$

The explicit scheme (3.108) is identical to the implicit one (3.106), and both share the same accuracy and numerical stability. But it is obvious that the former is more efficient than the latter. Actually, the trick that transforms an implicit scheme to an explicit one by introducing a new type of distribution functions can serve as a common strategy for designing efficient LBE methods. With this FD-LBE, Guo and Zhao [2003a] have successfully simulated the cavity flow and the flow around a cylinder at different Reynolds numbers with non-uniform meshes.

3.3.4 *Finite-volume based LBE methods*

The first finite-volume based LBE was developed by Nannelli and Succi [1992] when they introduced coarse-grained distribution functions over a control volume Ω

$$F_i(\boldsymbol{C},t)=\frac{1}{V_c}\int_{\Omega_c} f_i(\boldsymbol{x},t)d\boldsymbol{x}\,, \tag{3.112}$$

where $\boldsymbol{C}$ is the center of the cell and V_c is its volume. Applying this coarse-graining projection operator to the DVM (3.89) and discretizing the time derivative with the explicit Euler rule lead to

$$\begin{aligned} &F_i(\boldsymbol{C},t+\Delta t)-F_i(\boldsymbol{C},t)+\frac{\Delta t}{V_c}\int_{\partial\Omega_c}\boldsymbol{c}_i\cdot\boldsymbol{n}f_i(\boldsymbol{x},t)dS \\ &\quad=\Delta t\Big[F_i(\boldsymbol{C},t)-F_i^{(eq)}(\boldsymbol{C},t)\Big], \end{aligned} \tag{3.113}$$

where $\boldsymbol{n}$ is the outward unit normal vector of the cell, and $F_i^{(eq)}$ is the coarse-grained EDF. The original distribution function f_i in the numerical flux should be reconstructed from the coarse-grained distribution functions, which can be achieved by using certain interpolation schemes.

Later some alternative FV-LBE methods were developed based on more advanced finite-volume techniques. An example is the series of cell-vertex models developed by Peng *et al*. [1998,1999] and Xi *et al*. [1999a, 1999b]. In these models the computational domain is covered by some irregular polygonal or polyhedral meshes, on which the cell-vertex control volumes are defined. In Fig. 3.2 a two-dimensional control volume (the dashed polygon $CED\ldots$) around a node P on a triangular

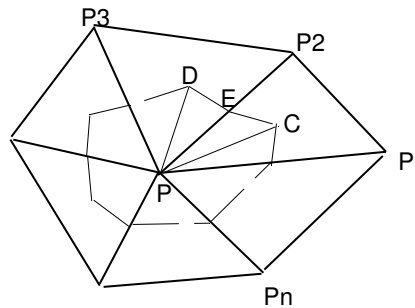

Fig. 3.2. Diagram of finite volumes sharing a common node *P*. The dashed polygon around *P* is its control volume.

mesh is sketched. Here C and D are the centers of the triangles PP_1P_2 and PP_2P_3 respectively, and E is the midpoint of the edge PP_2. It is clear that the control cell can be decomposed into some sub-triangles like PCE, PED, *etc.*, and the integration of Eq. (3.89) over the cell is just the sum of those over these sub-triangles. In what follows we will focus on the triangle PCE.

The integration of the temporal term of Eq. (3.89) over PCE can be approximated as

$$\int_{PCE} \frac{\partial f_i}{\partial t} d\boldsymbol{x} = \frac{\partial f_i(P)}{\partial t} A_{PCE}\,, \tag{3.114}$$

where A_{PCE} is the area of the triangle PCE, and $f_i(P)$ is the value of f_i on node P. Here it is assumed that f_i is constant over PCE.

The fluxes across the edges PC, CE, and EP can be obtained by integrating the convection term on PCE,

$$\int_{PCE} \boldsymbol{c}_i \cdot \nabla f_i d\boldsymbol{x} = \boldsymbol{c}_i \cdot \boldsymbol{n}_{CE} l_{CE} f_i(CE) + I_s\,, \tag{3.115}$$

where $\boldsymbol{n}_{CE}$ is the outward unit normal vector of the edge CE, and l_{CE} is the length of CE, while I_s is the total fluxes through the internal edges PC and PD, which will cancel out over the whole control volume. $f_i(CE)$ is the average value of f_i on CE, and Peng *et al*. suggested a linear interpolation,

$$f_i(CE) = \frac{f_i(C) + f_i(E)}{2}\,. \tag{3.116}$$

In the collision term, if f_i and $f_i^{(eq)}$ are both assumed to be linear functions, the integration of this term can be approximated as

$$-\int_{PCE}\Omega_i d\boldsymbol{x} = -\frac{A_{PCE}}{3\tau_c}\Big[f_i(P)+f_i(C)+f_i(E)-f_i^{(eq)}(P) - f_i^{(eq)}(C)-f_i^{(eq)}(E)\Big], \tag{3.117}$$

where $f_i(C)$ and $f_i(E)$ are approximated as

$$f_i(C)=\frac{f_i(P)+f_i(P_1)+f_i(P_2)}{3},\quad f_i(E)=\frac{f_i(P)+f_i(P_2)}{2}. \tag{3.118}$$

The EDFs $f_i^{(eq)}(C)$ and $f_i^{(eq)}(E)$ can be approximated similarly.

Integrations over other sub-triangles can be obtained similarly. Therefore, the update of $f_i(P)$ can be obtained by summing up these integrations over the control volume and discretizing the temporal derivative using the Euler forward method,

$$f_i(P,t+1)=f_i(P,t)+\Delta t R[f_i(P,t)], \tag{3.119}$$

where

$$R[f_i(P,t)]=\sum_{k=1}^{n}S_{ik}f_i(P_k)-\frac{1}{\tau_c}\sum_{k=1}^{n}C_{ik}\Big[f_i(P_k)-f_i^{(eq)}(P_k)\Big]. \tag{3.120}$$

Here S_{ik} and C_{ik} represent the contributions from the streaming and collision, respectively. It can be verified that these two matrices satisfy the following properties,

$$\sum_k S_{ik}=0,\quad \sum_k C_{ik}=1,\quad \forall i\,. \tag{3.121}$$

It should be noted that the FV-LBE (3.119) is of first-order accuracy in time, although the spatial accuracy is second-order. In order to improve the time accuracy, Uberttini and Succi [2005] proposed a fourth-order Runge-Kutta FV-LBE,

$$f_i(P,t+\Delta t)=f_i(P,t)+\frac{1}{6}(k_1+2k_2+2k_3+k4), \tag{3.122}$$

where

$$k_1=\Delta t R[f_i(P,t)],\ k_2=\Delta t R[f_i(P,t)+k_1/2],$$

$$k_3=\Delta t R[f_i(P,t)+k_2/2],\ k_4=\Delta t R[f_i(P,t)+k_3].$$

On the other hand, Stiebler *et al*. [2006] proposed a least-square-linear-reconstruction (LSLR) method in evaluating the numerical flux after noticing that the approximations in Eqs. (3.116) and (3.118) may lead to some numerical instability. They assume that the distribution function is linear in the cell around node P,

$$f_i(\boldsymbol{x}) = f_i(P) + (\boldsymbol{x} - \boldsymbol{x}_P) \cdot \boldsymbol{G}\,, \tag{3.123}$$

where $\boldsymbol{G}(P) = \nabla f_i(P)$, which is obtained by solving the following minimization problem,

$$\min_{\boldsymbol{G}(P)} \sum_{k=1}^{n} w_k \left[f_i(P_k) - f_i(P) - (\boldsymbol{x}_{P_k} - \boldsymbol{x}_P) \cdot \boldsymbol{G} \right]^2, \tag{3.124}$$

where $w_k = \| \boldsymbol{x}_{P_k} - \boldsymbol{x}_P \|^{-2}$. After obtaining the solution by solving a linear algebra system, the average value of f_i on the edge CE can be approximated by

$$f_i(CE) = \begin{cases} f_i(P) + \boldsymbol{G}(P) \cdot \left[\dfrac{\boldsymbol{x}_C + x_E}{2} - \boldsymbol{x}_P \right], & \boldsymbol{c}_i \cdot \boldsymbol{n}_{CE} > 0\,, \\ f_i(P) + \boldsymbol{G}(P_1) \cdot \left[\dfrac{\boldsymbol{x}_C + x_E}{2} - \boldsymbol{x}_{P_1} \right], & \text{otherwise}. \end{cases}$$

Recently, Patila and Lakshmisha [2009] further introduced the total variation diminishing (TVD) approach in evaluating the numerical flux, and Rossi *et al*. [2005] and Succi and Ubertini and Succi [2006] have made some theoretical discussions about several fundamental issues of FV-LBE, such as temporal and spatial accuracy and boundary conditions.

3.3.5 *Finite-element based LBE methods*

The finite-element method has also been used to solve the DVM (3.89). Lee and Lin [2001] made the first contribution toward this direction when they proposed their characteristic Galerkin (CG) FE-LBE. First, integrating Eq. (3.89) along the characteristic line leads to

$$f_i(\tilde{\boldsymbol{x}}(t_{n+1}), t_{n+1}) - f_i(\tilde{\boldsymbol{x}}(t_n), t_n) = (1-q)\Delta t \Omega_i(\tilde{\boldsymbol{x}}(t_{n+1}), t_{n+1}) + q\Delta t \Omega_i(\tilde{\boldsymbol{x}}(t_n), t_n)\,, \tag{3.125}$$

where $\tilde{\boldsymbol{x}}(t)$ is the trajectory of the particle moving with velocity $\boldsymbol{c}_i$, $0 \le q \le 1$ is a free parameter. The terms on the right hand-side are the

approximation of the collision term, which is similar to that in the semi-explicit FD-LBE given by Eq. (3.106). The distribution function on the trajectory, $f_i(\tilde{\boldsymbol{x}}(t_n), t_n)$, is approximated as

$$f_i\left(\tilde{\boldsymbol{x}}(t_n), t_n\right) = f_i(\boldsymbol{x}_0, t_n) - \Delta t \boldsymbol{c}_i \cdot \nabla f_i(\boldsymbol{x}_0, t_n) + \frac{\Delta t^2}{2}(\boldsymbol{c}_i \cdot \nabla)^2 f_i(\boldsymbol{x}_0, t_n) + O(\Delta t^3), \tag{3.126}$$

and the EDF is approximated similarly. Substituting these results into Eq. (3.126) and setting $q = 1/2$ lead to

$$f_i^{n+1} = f_i^n - \Delta t\left[\boldsymbol{c}_i \cdot \nabla f_i^n + \frac{1}{\tau_c}\left(f_i^{n+1/2} - f_i^{(eq),n+1/2}\right)\right] + \frac{\Delta t^2}{2}\boldsymbol{c}_i \cdot \nabla\left[\boldsymbol{c}_i \cdot \nabla f_i^n + \frac{1}{\tau_c}\left(f_i^n - f_i^{(eq),n}\right)\right]. \tag{3.127}$$

The distribution function at $t_{n+1/2}$ can be approximated with the Crank-Nicolson scheme, i.e., $f_i^{n+1/2} = (f_i^{n+1} + f_i^n)\,/\,2$; but such treatment will involve the unknown fluid density and velocity at t_{n+1}, which will bring some difficulties. One can use the extrapolation method as used in the FD-LBE proposed by Mei and Shyy [1998], or using the transformation approach to construct an explicit one as done in the FD-LBE by Guo and Zhao [2003a]. In the CG FE-LBE of Lee and Lin, this was achieved by using a second-order prediction-correction method,

$$\hat{f}_i = f_i^n - \Delta t\left[\boldsymbol{c}_i \cdot \nabla f_i^n + \frac{1}{\tau_c}\left(\hat{f}_i - f_i^{(eq),n}\right)\right] + \frac{\Delta t^2}{2}\boldsymbol{c}_i \cdot \nabla\left[\boldsymbol{c}_i \cdot \nabla f_i^n + \frac{1}{\tau_c}\left(f_i^n - f_i^{(eq),n}\right)\right], \tag{3.128}$$

$$f_i^{n+1} = \hat{f}_i^n - \omega\left[f_i^{(eq),n} - \hat{f}_i^{(eq)}\right], \tag{3.129}$$

where $\hat{f}_i^{(eq)} = f_i^{(eq)}(\hat{\rho}, \hat{\boldsymbol{u}})$ with

$$\hat{\rho} = \sum_i \hat{f}_i\,, \quad \hat{\rho}\hat{\boldsymbol{u}} = \sum_i \boldsymbol{c}_i \hat{f}_i\,.$$

In finite-element method, the flow domain is decomposed into a set of non-overlapping elements, i.e., $\Omega = \cup_k \Omega_k$, where the number of vertex nodes of element Ω_k is N_k. The Galerkin method assumes that the distribution function f_i can be projected onto a set of localized basis

functions which are generally piecewise polynomials associated with the elements,

$$f_i^h(\boldsymbol{x},t)=\sum_{l=1}^{N_k} f_{il}(t)\phi_{kl}(\boldsymbol{x}) \equiv \boldsymbol{f}_i\cdot\boldsymbol{\phi_k},\quad \boldsymbol{x}\in\Omega_k\,, \tag{3.130}$$

where ϕ_{kl} $(l=1,\ 2,\ \ldots,\ N_k)$ are the basis functions on Ω_k and f_{i1} is the distribution function at the l-th node of Ω_k. Substituting f_i^h into Eqs. (3.128) and (3.129), and multiplying the equations by ϕ_{kl} as a test function, and then integrating over the element Ω_k, we can obtain the CG FE-LBE,

$$\begin{aligned}\boldsymbol{M}\left(\hat{\boldsymbol{f}}_i-\boldsymbol{f}_i^n\right)=-\Delta t\left[\boldsymbol{C}_i\boldsymbol{f}_i^n+\frac{\boldsymbol{M}}{\tau_c}\left(\hat{\boldsymbol{f}}_i^n-\boldsymbol{f}_i^{(eq),n}\right)\right]\\ +\Delta t^2\left[\boldsymbol{D}_i\boldsymbol{f}_i^n+\boldsymbol{Q}_i\left(\boldsymbol{f}_i^n-\boldsymbol{f}_i^{(eq),n}\right)\right],\end{aligned} \tag{3.131}$$

$$\boldsymbol{f}_i^{n+1}=\hat{\boldsymbol{f}}_i^n+\omega\left[\hat{\boldsymbol{f}}_i^{(eq),n}-\boldsymbol{f}_i^{(eq),n}\right], \tag{3.132}$$

where $\boldsymbol{M}$, $\boldsymbol{C}_i$, $\boldsymbol{D}_i$, and $\boldsymbol{Q}_i$ are $N_k\times N_k$ matrices,

$$M_{mn}=\left\langle\phi_{km},\phi_{kn}\right\rangle,\ C_{imn}=\left\langle\phi_{km},\boldsymbol{c}_i\cdot\phi_{kn}\right\rangle,\ D_{imn}=-\frac{1}{2}\left\langle\phi_{km},(\boldsymbol{c}_i\cdot\nabla)^2\phi_{kn}\right\rangle,$$
$$Q_{imn}=-\frac{1}{\tau_c}\left\langle\phi_{km},(\boldsymbol{c}_i\cdot\nabla)\phi_{kn}\right\rangle.$$

Here the inner product is defined by $\langle f,g\rangle=\int fgd\boldsymbol{x}$. Equations (3.131) and (3.132) constitute the basic process of the CG FE-LBE by Lee and Lin [2001]. Based on the similar strategy, Min and Lee [2011] developed a spectral-element discontinuous Galerkin (SEDG) method for solving the DVM (3.89). Several other FE-LBE methods based on SEDG were also proposed by independent groups [Shi *et al*., 2003; Düster *et al*., 2006].

Another kind of FE-LBE was developed by Li *et al*. [2004] based on the least-squares finite-element (LSFE) method, in which the time evolution of DVM (3.89) is first discretized as

$$\frac{f_i^{n+1}-f_i^n}{\Delta t}+\boldsymbol{c}_i\cdot\nabla\left[qf_i^{n+1}+(1-q)f_i^n\right]=q\Omega_i^{n+1}+(1-q)\Omega_i^n\,, \tag{3.133}$$

where q is again a parameter like that used in the FD-LBE and FV-LBE. Obviously, Equation (3.133) reduces to the Crank-Nicolson scheme as

$q = 0.5$, which can be expressed as

$$Lf_i^{n+1} \equiv \boldsymbol{c}_i \cdot \nabla f_i^{n+1} + \frac{2\tau_c + \Delta t}{\tau_c \Delta t} f_i^{n+1} = p_i , \tag{3.134}$$

where

$$p_i = \frac{2\tau_c - \Delta t}{\tau_c \Delta t} f_i^n + \frac{1}{\tau_c}\left[f_i^{(eq),n+1} + f_i^{(eq),n} \right] - \boldsymbol{c}_i \cdot \nabla f_i^n . \tag{3.135}$$

The spatial gradients in Eq. (3.134) can then be discretized by the finite-element method. As before, the flow domain is also decomposed into some elements, and the distribution functions are approximated by f_i^h defined by Eq. (3.130). Generally, the populations f_i^h do not satisfy Eq. (3.134), and the residual is

$$E = Lf_i^{h,n+1} - p^h . \tag{3.136}$$

The LSFE aims to minimize the squares of the residual,

$$\min\left[\psi(f_i^{n+1}) \right] \equiv \min \int_{\Omega_k} E^2 d\boldsymbol{x} \ , \tag{3.137}$$

which is equivalent to the following set of linear algebra equations,

$$\frac{\partial \psi(f^{n+1})}{\partial f_{il}^{n+1}} = \int_{\Omega_k} L\phi_{kl} E d\boldsymbol{x} = 0 , \ l = 1, \ 2, \ \cdots, \ N_k , \tag{3.138}$$

or

$$\boldsymbol{M} \boldsymbol{f}_i^{n+1} = \boldsymbol{P}_k , \tag{3.139}$$

where the elemental matrix $\boldsymbol{M}$ and vector $\boldsymbol{P}_k$ are defined by

$$\boldsymbol{M} = \int_{\Omega_k} \boldsymbol{Q} \cdot \boldsymbol{Q} \, d\boldsymbol{x} , \quad \boldsymbol{P}_k = \int_{\Omega_k} \boldsymbol{Q} \cdot \boldsymbol{p}_k^h \, d\boldsymbol{x} , \tag{3.140}$$

with

$$\boldsymbol{Q} = \boldsymbol{c}_i \cdot \nabla \boldsymbol{\phi}_k + \frac{2\tau_c + \Delta t}{\tau_c \Delta t} \boldsymbol{\phi}_k \ .$$

It is noted that in Eq. (3.135) the computation of $f_i^{(eq),n+1}$ requires the unknown density and velocity. In LS-FELBE, this was achieved by extrapolation as done in the Mei-Shyy FD-LBE method. Then the nodal distribution functions can be obtained by solving Eq. (3.139).

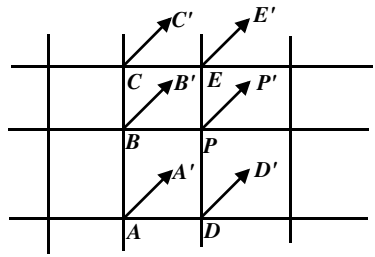

Fig. 3.3. Configuration of particle movement along $\boldsymbol{c}_i$.

3.3.6 *Taylor series expansion and least square based methods*

In this part, we will introduce a new version of LBE (refereed to as TLLBE) with nonuniform meshes, which was developed by Shu and his coworkers [Chew *et al*., 2002; Niu *et al*., 2003; Shu *et al*., 2001; Shu *et al*., 2002]. This method is based on the conventional LBE, the well-known Taylor series expansion, the idea of developing Runge-Kutta method, and the least squares approach. The final form of the method is an algebraic formulation, in which the coefficients only depend on the coordinates of mesh points and lattice velocity and can be computed in advance. Furthermore, the method is also free of lattice models.

Taylor series expansion-based method

Without loss of generality, we consider a two-dimensional (2D) case. As shown in Fig. 3.3, point A represents the grid point $(x_A,\ y_A)$ at time t, and A' represents the position $(x_A + c_{ix}\delta_t,\quad y_A + c_{iy}\delta_t)$ at time $t + \delta_t$, and P represents the position $(x_P,\ y_P)$ with $x_p = x_A + \delta_x$ and $y_p = y_A + \delta_y$. The LBE gives that

$$f_i(A', t + \delta_t) = f_i(A, t) - \frac{1}{\tau}\left[f_i(A, t) - f_i^{(eq)}(A, t)\right]. \tag{3.141}$$

For general cases, A' may not coincide with the mesh point *P*. We first consider the Taylor series expansion with truncation to the first order derivative terms. Then, $f_i(A', t + \delta_t)$ can be approximated by the corresponding function and its derivatives at the mesh point *P* as

$$f_i(A',t+\delta_t) = f_i(P,t+\delta_t) + \Delta x_A \frac{\partial f_i(P,t+\delta_t)}{\partial x} + \Delta y_A \frac{\partial f_i(P,t+\delta_t)}{\partial y} + O\left[(\Delta x_A)^2,(\Delta y_A)^2\right], \quad (3.142)$$

where $\Delta x_A = x_A + c_{ix}\delta_t - x_P$, $\Delta y_A = y_A + c_{iy}\delta_t - y_P$. Note that the above approximation has a truncation error of second order. Substituting equation (3.142) into equation (3.141) gives

$$f_i(P,t+\delta_t) + \Delta x_A \frac{\partial f_i(P,t+\delta_t)}{\partial x} + \Delta y_A \frac{\partial f_i(P,t+\delta_t)}{\partial y} = f_i(A,t) + \frac{f_i^{(eq)}(A,t) - f_i(A,t)}{\tau}. \quad (3.143)$$

It is indicated that equation (3.143) is a first order differential equation, which only involves two mesh points A and P. When a uniform grid is used, $\Delta x = \Delta y = 0$, then Eq. (3.143) reduces to the standard LBE. Solving equation (3.143) can provide the density distribution functions at all of the mesh points. An explicit formulation to update the distribution function was developed by Shu *et al.*, which is inspired by the Runge-Kutta method. As we know, the Runge-Kutta method is developed to improve the Taylor series method in the solution of ordinary differential equations (ODEs). Usually the Taylor series method involves evaluation of different orders of derivatives to update the functional value at the next time level. For a given ODE with a complicated expression, this application is very difficult. To improve the Taylor series method, the Runge-Kutta method evaluates the functional values at some intermediate points and then combines them (through the Taylor series expansion) to form a scheme with the same order of accuracy.

With this idea in mind, we now look at Eq. (3.143). Notice that the distribution function and its derivatives at the mesh point P are all unknowns at the time level $t+\delta_t$. So Eq. (3.143) has three unknowns in total. To solve for the three unknowns, three equations are required. However, Eq. (3.143) provides only one equation, and two additional equations should be provided to close the system. As shown in Fig. 3.3, the particles with velocity $\boldsymbol{c}_i$ at two mesh points P and B at time t will stream to the new positions P' and B' at $t+\delta_t$. The distribution functions

at these new positions can be computed through the standard LBE, which are given below,

$$f_i(P',t+\delta_t) = f_i(P,t) - \frac{1}{\tau}\Big[f_i(P,t) - f_i^{(eq)}(P,t)\Big], \tag{3.144}$$

$$f_i(B',t+\delta_t) = f_i(B,t) - \frac{1}{\tau}\Big[f_i(B,t) - f_i^{(eq)}(B,t)\Big]. \tag{3.145}$$

Using Taylor series expansion with truncation to the first order derivative terms, $f_i(P',t+\delta_t)$ and $f_i(B',t+\delta_t)$ in the above equations can be approximated by the function and its derivatives at the mesh point P. As a result, Eqs. (3.144) and (3.145) reduce to

$$\begin{aligned} &f_i(P,t+\delta_t) + \Delta x_P \frac{\partial f_i(P,t+\delta_t)}{\partial x} + \Delta y_P \frac{\partial f_i(P,t+\delta_t)}{\partial y} \\ &\quad = f_i(P,t) + \frac{f_i^{(eq)}(P,t) - f_i(P,t)}{\tau}, \end{aligned} \tag{3.146}$$

$$\begin{aligned} &f_i(P,t+\delta_t) + \Delta x_B \frac{\partial f_i(P,t+\delta_t)}{\partial x} + \Delta y_B \frac{\partial f_i(P,t+\delta_t)}{\partial y} \\ &\quad = f_i(B,t) + \frac{f_i^{(eq)}(B,t) - f_i(B,t)}{\tau}, \end{aligned} \tag{3.147}$$

where $\Delta x_P = c_{ix}\delta_t$, $\Delta y_P = c_{iy}\delta_t$, $\Delta x_B = x_B + c_{ix}\delta_t - x_P$, and $\Delta y_B = y_B + c_{iy}\delta_t - y_P$.

Equations (3.143), (3.146), and (3.147) form a system to solve for the three unknowns. The solution of this system gives

$$f_i(P,t+\delta_t) = \Delta_P/\Delta, \tag{3.148}$$

where

$$\Delta = \Delta x_A \Delta y_B - \Delta x_B \Delta y_A + \Delta x_B \Delta y_P - \Delta x_P \Delta y_B + \Delta x_P \Delta y_A - \Delta x_A \Delta y_P,$$

$$\begin{aligned} \Delta_P = &(\Delta x_A \Delta y_B - \Delta x_B \Delta y_A) g_{i,P} + (\Delta x_B \Delta y_P - \Delta x_P \Delta y_B) g_{i,A} \\ &+ (\Delta x_P \Delta y_A - \Delta x_A \Delta y_P) g_{i,B}, \end{aligned}$$

$$g_{i,J} = f_i(J,t) + \tau^{-1}\Big[f_i^{(eq)}(J,t) - f_i(J,t)\Big],\ J = P,\ A,\ B.$$

It should be noted that $g_{i,P}$, $g_{i,A}$, and $g_{i,B}$ are actually the post-collision state of the distribution functions f_i at time t and the mesh point P, A, and B, respectively. Equation (3.148) has the second order of

truncation error, which may introduce a large numerical diffusion. To improve the accuracy of numerical computation, the Taylor series expansion can be truncated to the second order derivative terms. For the two-dimensional case, this expansion involves six unknowns, that is, one distribution function at the time level $t+\delta_t$, two first order derivatives, and three second order derivatives. To solve for these unknowns, six equations are required to close the system. This can be done by applying the second order Taylor series expansion at 6 points. As shown in Fig. 3.3, the particles at six mesh points P, A, B, C, D, E at t will stream to positions P', A', B', C', D', E' at $t+\delta_t$.. The distribution functions at these new positions can be computed through the standard LBE. Then by using the second order Taylor series expansion at these new positions in terms of the distribution function and its derivatives at the mesh point P, we can obtain the following equation system

$$g_{i:k} = \{s_{i:k}\}^T \{V_i\} = \sum_{j=1}^{6} s_{i:k,j} V_{i:j}\,, \quad i = P, A, B, C, D, E\,, \tag{3.149}$$

where

$$g_{i:k} = f_{i(x_k, y_k, t)} + \frac{1}{\tau}\Big(f_i^{(eq)}{}_{(x_k, y_k, t)} - f_{i(x_k, y_k, t)} \Big),$$

$$\{s_{i:k}\}^T = \left\{1, \Delta x_k, \Delta y_k, \frac{(\Delta x_k)^2}{2}, \frac{(\Delta y_k)^2}{2}, \Delta x_k \Delta y_k\right\},$$

$$\{V_i\} = \left\{f_i, \frac{\partial f_i}{\partial x}, \frac{\partial f_i}{\partial y}, \frac{\partial^2 f_i}{\partial x^2}, \frac{\partial^2 f_i}{\partial y^2}, \frac{\partial^2 f_i}{\partial x \partial y}\right\}^T.$$

Here $g_{i:k}$ is the post-collision state of the distribution function f_i at the k-th point and the time t, $\{s_{i:k}\}^T$ is a vector with six elements formed by the coordinates of mesh points, $\{V_i\}$ is the vector of unknowns at the mesh point P and time $t+\delta_t$, which also has six elements, $s_{i:k,j}$ is the j-th element of the vector $\{s_{i:k}\}^T$ and $V_{i:j}$ is the j-th element of the vector $\{V_i\}$. Our target is to find its first element $V_{i:1} = f_i(P, t+\delta_t)$. Equation system (3.149) can be put into the following matrix form

$$[S_i]\{V_i\} = \{g_i\}, \tag{3.150}$$

where

$$\{g_i\} = \{g_{i,P}, g_{i,A}, g_{i,B}, g_{i,C}, g_{i,D}, g_{i,E}\}^T ,$$

$$[S_\alpha] = [s_{\alpha:i,j}]$$

$$= \begin{bmatrix} \{s_{\alpha:P}\}^T \\ \{s_{\alpha:A}\}^T \\ \{s_{i:B}\}^T \\ \{s_{i:C}\}^T \\ \{s_{i:D}\}^T \\ \{s_{i:E}\}^T \end{bmatrix} = \begin{bmatrix} 1 & \Delta x_P & \Delta y_P & (\Delta x_P)^2/2 & (\Delta y_P)^2/2 & \Delta x_P \Delta y_P \\ 1 & \Delta x_A & \Delta y_A & (\Delta x_A)^2/2 & (\Delta y_A)^2/2 & \Delta x_A \Delta y_A \\ 1 & \Delta x_B & \Delta y_B & (\Delta x_B)^2/2 & (\Delta y_B)^2/2 & \Delta x_B \Delta y_B \\ 1 & \Delta x_C & \Delta y_C & (\Delta x_C)^2/2 & (\Delta y_C)^2/2 & \Delta x_C \Delta y_C \\ 1 & \Delta x_D & \Delta y_D & (\Delta x_D)^2/2 & (\Delta y_D)^2/2 & \Delta x_D \Delta y_D \\ 1 & \Delta x_E & \Delta y_E & (\Delta x_E)^2/2 & (\Delta y_E)^2/2 & \Delta x_E \Delta y_E \end{bmatrix},$$

$$\Delta x_C = x_C + c_{ix}\delta_t - x_P , \; \Delta y_C = y_C + c_{iy}\delta_t - y_P ,$$

$$\Delta x_D = x_D + c_{ix}\delta_t - x_P , \; \Delta y_D = y_D + c_{iy}\delta_t - y_P ,$$

$$\Delta x_E = x_E + c_{ix}\delta_t - x_P , \; \Delta y_E = y_E + c_{iy}\delta_t - y_P .$$

The expressions of Δx_P , Δy_P , Δx_A , Δy_A , Δx_B and Δy_B have been given previously. Since $[S_\alpha]$ is a 6×6 matrix, it is very difficult to obtain an analytical expression for the solution of equation system (3.150), and a numerical algorithm can be used to obtain an approximated solution. Note that the matrix $[S_\alpha]$ only depends on the coordinates of the mesh points, which can be computed once and stored for the application of Eq. (3.150) at all time steps.

Improvement by least square method

In practical applications, it was found that the matrix $[S_\alpha]$ might be singular or ill-conditioned. To overcome this difficulty and ensure that the method is more general, Shu *et al.* [2002] suggested making use of the least squares approach to optimize the approximation by Eq. (3.149). This equation has 6 unknowns (elements of the vector $\{V_\alpha\}$). If Eq. (3.149) is applied at more than 6 mesh points, the system will be over-determined. For this case, the unknown vector can be decided from the least squares method. For simplicity, let the mesh point P be represented by the index $i = 0$, and its adjacent points be represented by index $i = 1, 2, \ldots, N$, where N is the number of neighboring points around P and it should be larger than 5. At each point, an error in terms

of Eq. (3.149) can be defined,

$$err_{i:k} = g_{i:k} - \sum_{j=1}^{6} s_{i:k,j} V_{i:j} , \quad i = 0, 1, 2 , \ldots , N . \tag{3.151}$$

The square sum of all the errors is

$$E_i = \sum_{k=0}^{N} err_{i:k}^2 = \sum_{k=0}^{N} \left(g_{i:k} - \sum_{j=1}^{6} s_{i:k,j} V_{i:j} \right)^2 . \tag{3.152}$$

To minimize the error E_i, we need to set $\partial E_i / \partial V_{i:j} = 0$, which leads to

$$[S_i]^T [S_i] \{V_i\} = [S_i]^T \{g_i\} , \tag{3.153}$$

where $[S_i]$ is a $(N+1) \times 6$ dimensional matrix, which is given as

$$[S_i] = \begin{bmatrix} 1 & \Delta x_0 & \Delta y_0 & (\Delta x_0)^2/2 & (\Delta y_0)^2/2 & \Delta x_0 \Delta y_0 \\ 1 & \Delta x_1 & \Delta y_1 & (\Delta x_1)^2/2 & (\Delta y_1)^2/2 & \Delta x_1 \Delta y_1 \\ - & - & - & - & - & - \\ - & - & - & - & - & - \\ - & - & - & - & - & - \\ 1 & \Delta x_N & \Delta y_N & (\Delta x_N)^2/2 & (\Delta y_N)^2/2 & \Delta x_N \Delta y_N \end{bmatrix} ,$$

and $\{g_i\} = \{g_{i:0} , g_{i:1} , \ldots , g_{i:N}\}^T$; The Δx_k and Δy_k values in the matrix $[S_i]$ are given by

$$\Delta x_0 = c_{ix} \delta_t , \; \Delta y_0 = c_{iy} \delta_t , \; \Delta x_k = x_k + c_{ix} \delta_t - x_0 , \; \Delta y_k = y_k + c_{iy} \delta_t - y_0 ,$$

for $k = 1, 2, \ldots, N$. Clearly, when the coordinates of mesh points are given, and the particle velocity and time step size are specified, the matrix $[S_\alpha]$ is determined. Then from Eq. (3.153) we can obtain

$$\{V_i\} = \left([S_i]^T [S_i] \right)^{-1} [S_i]^T \{g_i\} = [A_i] \{g_i\} . \tag{3.154}$$

Note that $[A_i]$ is a 6×(N+1) dimensional matrix. So Eq. (3.154) suggests that

$$f_i(x_0, y_0, t + \delta_t) = V_{i:1} = \sum_{j=1}^{N+1} a_{i:1,j} g_{i:j-1} , \tag{3.155}$$

where $a_{i:1,j}$ are the elements of the first row of the matrix $[A_i]$, which are pre-computed before the LBE is applied. Therefore, little computational

effort is introduced as compared with the standard LBE. Note that the function g is evaluated at the time level t. So Eq. (3.155) is actually an explicit form to update the distribution function at the time level $t + \delta_t$. In the above process, there is no requirement for the selection of neighboring points, or in other words, Eq. (3.155) is independent from the mesh structure, and we only need to know the coordinates of the mesh points. Therefore Eq. (3.155) is basically a meshless form.

Theoretical analysis has shown that the above least square-based LBE can recover the Navier-Stokes equations with second order of accuracy, no matter whether the mesh is uniform or non-uniform. The TLLBE has been successfully applied to a variety of flows with nonuniform meshes. An example for the flow around a circular cylinder is shown in Fig. 3.4.

3.4 Accelerated LBE Methods for Steady Flows

Steady flows appear in many physical and engineering situations. As a time-marching method, however, the LBE may encounter some convergence difficulties when applied to steady flows. The slow convergence rate is an inherent disadvantage of the standard LBE. As shown previously, the LBE is an explicit time-marching method for

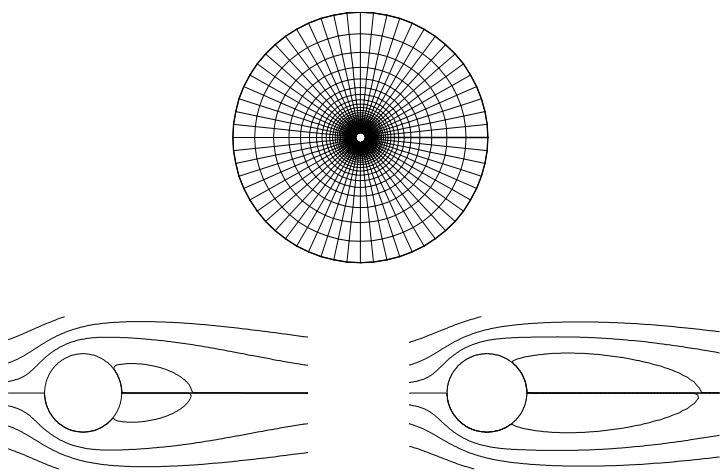

Fig. 3.4. Flow around a circular cylinder. Top: Computational mesh; Bottom: Streamline with Re=20(left) and 40 (right).

compressible fluid flows with low Mach numbers, and can be viewed as an explicit artificial compressibility scheme for incompressible Navier-Stokes equations. In addition to the error due to numerical discretization, the finite Mach number effect also introduces a grid independent compressibility error. To reduce this error, the Mach number must be kept sufficiently small. As the Mach number becomes smaller, however, it would become increasingly computational expensive to solve the compressible Navier-Stokes equations using the standard LBE [Lai *et al*., 2001].

Some efforts have been made to accelerate the convergence rate of the LBE from different viewpoints. In general, the existing accelerated LBE models fall into two categories, i.e., time dependent methods and time-independent methods. In the former, the LBE still evolves as a time-marching process, but the evolution equation is altered. On the other hand, in the time independent approach, a linear or nonlinear algebra system derived from the time independent form of the steady LBE or DVM is solved directly.

3.4.1 *Spectrum analysis of the hydrodynamic equations of the standard LBE*

The convergence difficulty of LBE roots in the large disparity between the acoustic wave speed and the fluid speed in low Mach number flows, as in the classical CFD methods [Turkel, 1999]. Usually, for any explicit scheme, the CFL condition should be fulfilled for the sake of numerical stability. Therefore, the time step should be chosen such that it is inversely proportional to the sound speed of the acoustic wave, during which the waves driven by the fluid change slightly. As a result, a large number of time steps are needed to reach the steady state of the flow. As an explicit scheme, the LBE also suffers from this problem.

To see this more clearly, we now make a spectral analysis of the hydrodynamic equations derived from standard LBGK models (see Eqs. (1.69) and (1.70)). For two-dimensional flows, these equations can be written in a vector form,

$$\frac{\partial \boldsymbol{Q}}{\partial t}+\frac{\partial \boldsymbol{E}}{\partial x}+\frac{\partial \boldsymbol{F}}{\partial y}=\boldsymbol{R}\{\boldsymbol{Q}_v\}, \tag{3.156}$$

where $\boldsymbol{R}$ represents the vector associated with the viscous terms, and $\boldsymbol{Q} = (\rho,\ \rho u,\ \rho v)^T$, $\boldsymbol{E} = (\rho u,\ \rho u^2 + c_s^2\rho,\ \rho uv)^T$, $\boldsymbol{F} = (\rho v,\ \rho uv,\ \rho v^2 + c_s^2\rho)^T$, where u and v are the x- and y- components of the fluid velocity $\boldsymbol{u}$, respectively. Equation (3.156) can be further written as

$$\frac{\partial \boldsymbol{Q}}{\partial t} + \boldsymbol{A}\frac{\partial \boldsymbol{Q}}{\partial x} + \boldsymbol{B}\frac{\partial \boldsymbol{Q}}{\partial y} = \boldsymbol{R}\{\boldsymbol{Q}_v\}, \tag{3.157}$$

where

$$\boldsymbol{A} = \frac{\partial \boldsymbol{E}}{\partial \boldsymbol{Q}} = \begin{bmatrix} 0 & 1 & 0 \\ c_s^2 - u^2 & 2u & 0 \\ -uv & v & u \end{bmatrix},\ \boldsymbol{B} = \frac{\partial \boldsymbol{F}}{\partial \boldsymbol{Q}} = \begin{bmatrix} 0 & 0 & 1 \\ -uv & v & u \\ c_s^2 - v^2 & 0 & 2v \end{bmatrix}. \tag{3.158}$$

It can be easily shown that the eigenvalues of the matrices $\boldsymbol{A}$ and $\boldsymbol{B}$ are respectively

$$\lambda(\boldsymbol{A}) = \left\{u,\ u \pm c_s\right\},\quad \lambda(\boldsymbol{B}) = \left\{v,\ v \pm c_s\right\}. \tag{3.159}$$

Therefore, the condition number of $\boldsymbol{A}$ is

$$\kappa(\boldsymbol{A}) = \max_{i,j}\left\{\frac{\lambda_i(\boldsymbol{A})}{\lambda_j(\boldsymbol{A})}\right\} \sim 1 + \frac{1}{M}, \tag{3.160}$$

where M is the Mach number. The condition number of matrix B is similar. Therefore, $\kappa(A)$ and $\kappa(B)$ will be very large as the Mach number of the flow is small, which means that the waves in the fluid transfer with quite different speeds, and this will make the LBE converge very slowly. It is noted the viscous terms also have complex influences on the wave speeds, depending on the Reynolds number and the ratio of the Reynolds number to the Mach number, and the convergence difficulty can be further exacerbated by the magnitude of the diffusion terms [Lee, 1996].

3.4.2 *Time-independent methods*

At steady state, the standard LBGK equation with a body force $\boldsymbol{F}$ can be written as

$$f_i(\boldsymbol{x} + \boldsymbol{c}_i\delta_t) - f_i(\boldsymbol{x}) = -\frac{1}{\tau}\left[f_i(\boldsymbol{x}) - f_i^{(eq)}(\boldsymbol{x})\right] + \delta_t F_i,\ i = 0 \sim b-1\,. \tag{3.161}$$

This equation can also be rewritten in matrix formulation,

$$\boldsymbol{S}\cdot\boldsymbol{f}(\boldsymbol{x})+\boldsymbol{K}\cdot\boldsymbol{f}(\boldsymbol{x})=\delta_t\boldsymbol{F}', \tag{3.162}$$

where $\boldsymbol{S}$ and $\boldsymbol{K}$ are the local streaming and collision matrices, respectively, which are defined by [Bernaschi *et al*., 2002; Bernaschi and Succi, 2003],

$$\boldsymbol{S}\cdot\boldsymbol{f}(\boldsymbol{x})=\left[f_0(\boldsymbol{x}+\boldsymbol{c}_0\delta_t),f_1(\boldsymbol{x}+\boldsymbol{c}_0\delta_t),\cdots,f_{b-1}(\boldsymbol{x}+\boldsymbol{c}_0\delta_t)\right]^T,$$

$$K_{ij}=\frac{1}{\tau}\delta_{ij}-\frac{\omega_i}{\tau}\left[1+\frac{c_{i\alpha}c_{j\alpha}}{c_s^2}+\frac{(c_{i\alpha}c_{i\beta}-c_s^2\delta_{a\beta})c_{j\alpha}u_\beta}{2c_s^4}\right],$$

while $\boldsymbol{F}'$ is a vector consisting of the forcing terms, $\boldsymbol{F}'=[F_0,F_1,\cdots,F_{b-1}]^T$. For a lattice with N nodes, Eq. (3.162) represents a nonlinear algebraic system of the form

$$[A][f]=[F], \tag{3.163}$$

where $[A]$ is a $bN\times bN$ block matrix consisting of $\boldsymbol{S}$ and $\boldsymbol{K}$, [*f*] and [*F*] are two vectors with bN elements. This nonlinear system can be solved iteratively. For example, Bernaschi *et al*. [2002, 2003] suggested a Newton-Raphson procedure to linearize Eq. (3.163), which is then solved by a *generalized method of residuals* (GMRES). However, it was found that the convergence of this method may be rather slow for high-Reynolds number flows. In order to release this difficulty, a *viscosity annealing* technique was introduced into the iterative process [Bernaschi and Succi, 2003]. This is achieved by letting the relaxation time change with the iteration, i.e.,

$$\frac{1}{\tau_{k+1}}=\frac{1}{\tau_k}+\alpha_k,\quad k=0,1,\ldots,$$

where α_k is the annealing increments at the k-th iteration. This annealing technique makes the iteration process start with a low Reynolds number and attain the desired one at the final state.

For Stokes flows with a low Reynolds number, the matrix formulation of the steady LBE (3.162) can be simplified. In this case, the nonlinear terms in the fluid velocity in the EDF can be neglected, i.e.,

$$f_i^{(eq)} = \omega_i \rho \left[1 + \frac{\boldsymbol{c}_i \cdot \boldsymbol{u}}{c_s^2} \right]. \tag{3.164}$$

If the relaxation time is set to be 1.0, the steady LBE becomes,

$$f_i(\boldsymbol{x} + \boldsymbol{c}_i \delta_t) = f_i^{(eq)}(\boldsymbol{x}) + \delta_t F_i = \sum_j \omega_i \left[1 + \frac{\boldsymbol{c}_i \cdot \boldsymbol{c}_j}{c_s^2} \right] f_j + \delta_t F_i. \tag{3.165}$$

With the relation between the conserved quantities $\boldsymbol{m} = (\rho,\ \rho \boldsymbol{u})$, the above formulation can be further written as a linear system of these variables [Verberg and Ladd, 1999],

$$[A][m] = [B], \tag{3.166}$$

where $[A] = \boldsymbol{I} - \boldsymbol{PTE}$ and $[B] = \boldsymbol{PTF}$, with $\boldsymbol{P}$ being a $(D + 1)N \times bN$ block-diagonal matrix, $\boldsymbol{P} = \mathrm{diag}(\boldsymbol{p},\ \boldsymbol{p},\ \ldots,\ \boldsymbol{p})$, $\boldsymbol{p}_i = (1,\ \boldsymbol{c}_i)^T$, $\boldsymbol{T}$ is a $bN \times bN$ transition matrix, and $\boldsymbol{E} = \mathrm{diag}(\boldsymbol{e},\ \boldsymbol{e},\ \ldots,\ \boldsymbol{e})$, with $\boldsymbol{e}_i = (\omega_i,\ \omega_i \boldsymbol{c}_i / c_s^2)^T$. A biconjugate gradient algorithm was proposed to solve the above algebra system [Verberg and Ladd, 1999].

It was found that with the matrix formulation, the accelerated LBE methods could be 1~2 orders of magnitude faster than the standard one [Bernaschi *et al*., 2002; Bernaschi and Succi, 2003; Verberg and Ladd, 1999; Noble and Holdych, 2007]. Some methods were also developed to solve the steady discrete velocity model (3.89) directly using certain finite-difference schemes. For instance, Tölke *et al*. [2002] proposed an implicit second-order finite difference scheme, and introduced a nonlinear multigrid method to solve the nonlinear algebra system.

3.4.3 *Time-dependent methods*

Some time-independent acceleration techniques have also been introduced to improve the convergence of LBE for steady flows. The most straightforward way is employing certain implicit schemes to discretize the time-dependent equation (3.89) so that a larger time step can be used [Lee and Lin, 2003; Seta and Takahashi, 2002; Tölke *et al*., 1998]. On the other hand, Mavriplis [2006] developed a multigrid technique which makes use of the non-linear LBE time-stepping scheme on each grid level. Although all these schemes can improve the

convergence rates, their formulation and implementation are much more complicated than the standard LBE.

Motivated by the precondition method for solving the compressible Navier-Stokes equations, Guo *et al.* [2004] developed a time-independent preconditioned LBE (PLBE) with the same structure as the standard one. The evolution equation of PLBE without considering the influence of body forces is

$$f_i(\boldsymbol{x}+\boldsymbol{c}_i\delta_t, t+\delta_t) - f_i(\boldsymbol{x},t) = -\frac{1}{\tau_p}\Big[f_i(\boldsymbol{x},t) - f_i^{(eq)}(\rho,\boldsymbol{u};\gamma)\Big], \quad (3.167)$$

where τ_p is a relaxation time to be determined, and the modified EDF contains an adjustable parameter γ,

$$f_i^{(eq)} = \omega_i\rho\left[1+\frac{\boldsymbol{c}_i\cdot\boldsymbol{u}}{c_s^2}+\frac{\boldsymbol{uu}:\left(\boldsymbol{c}_i\boldsymbol{c}_i-c_s^2\boldsymbol{I}\right)}{2\gamma c_s^4}\right]. \quad (3.168)$$

The fluid density and velocity in the PLBE are defined as those in the standard LBE. Through the Chapman-Enskog procedure, we can derive the macroscopic equations from the LBE (3.167) as

$$\frac{\partial\rho}{\partial t}+\nabla\cdot(\rho\boldsymbol{u}) = 0\,, \quad (3.169)$$

$$\frac{\partial(\rho\boldsymbol{u})}{\partial t}+\frac{1}{\gamma}\nabla\cdot\left(\rho\boldsymbol{uu}\right) = -\frac{1}{\gamma}\nabla p^* + \frac{1}{\gamma}\nabla\cdot(\rho\upsilon\boldsymbol{S})\,, \quad (3.170)$$

where $p^* = \gamma c_s^2\rho$, and $\nu = \gamma c_s^2(\tau_p - 0.5)\delta_t$. It is clear that for steady flows, Eqs. (3.169) and (3.170) are identical to those derived from the standard LBE except for a different equation of state. It is clear that the effective sound speed $c_s^* = \sqrt{\partial p^*/\partial\rho} = \sqrt{\gamma}c_s$ is decreased as $\gamma < 1$.

In the presence of a body force $\boldsymbol{F}$, the PLBE (3.167) should be modified by adding a forcing term $\delta_t F_i$ on its the right hand side. The forcing term can be taken as those described in Sec. 3.2, but with a body force scaled by γ. For instance, the scaled LGA forcing scheme can be expressed as $F_i = \omega_i\boldsymbol{c}_i\cdot\boldsymbol{F}/\gamma c_s^2$. With this forcing term, the resultant momentum equation takes the same form as Eq. (3.170) but with a scaled body force $\boldsymbol{F}/\gamma$.

The macroscopic equations (3.169) and (3.170) can be interpreted as preconditioned Navier-Stokes equations. In fact, the vector form of this system is

$$\frac{\partial \boldsymbol{Q}}{\partial t} + \boldsymbol{PA}\frac{\partial \boldsymbol{Q}}{\partial x} + \boldsymbol{PB}\frac{\partial \boldsymbol{Q}}{\partial y} = \boldsymbol{PR}\{\boldsymbol{Q}_v\}\,, \tag{3.171}$$

where $\boldsymbol{Q}$, $\boldsymbol{A}$, $\boldsymbol{B}$, and $\boldsymbol{R}$ are the same as defined earlier except that c_s is replaced by the effective sound speed c_s^*. The matrix $\boldsymbol{P} = \mathrm{diag}(1, \gamma^{-1}, \gamma^{-1})$ is a preconditioner. It can be shown that the eigenvalues of the preconditioned convection matrix $\boldsymbol{PA}$ are now,

$$\lambda(\boldsymbol{PA}) = \frac{1}{\gamma}(u, u \pm \overline{c}_s)\,, \tag{3.172}$$

where

$$\overline{c}_s = \sqrt{(1-\gamma)u^2 + (\gamma c_s)^2} \tag{3.173}$$

is an effective sound speed. It is clear that $\overline{c}_s$ reduces to the original sound speed c_s as $\gamma = 1$. Conversely, as γ approaches to zero, $\overline{c}_s$ approaches to the fluid speed *u*. Therefore, one can decrease the disparity between the speeds of the acoustic wave and the waves propagating with the fluid velocity by adjusting this parameter, and thus accelerate the convergence rate of the LBE. It is also noted that for low Mach number flows as $u \to 0$, we have $\overline{c}_s = c_s^* = \sqrt{\gamma} c_s$.

According to the effective sound speed c_s^*, one can define an effective Mach number M^* as $M^* = U_0 \,/\, c_s^*$. It is clear that $M^* = \sqrt{\gamma} M \le M$ as $0 < \gamma \le 1$. In practical applications, the parameter γ can be chosen such that M^* is low enough for a given flow condition. This can be done by first specifying the value of M^* according to the flow condition and then setting $\gamma = (M/M^*)^2$.

The parameter γ will influence on the numerical stability of the PLBE. In fact, from the relationship between the viscosity and the relaxation time, one can obtain that

$$\tau_p - 0.5 = \frac{\sqrt{3} NM}{\gamma \mathrm{Re}}\,, \tag{3.174}$$

which indicates that the value of $\tau_p - 0.5$ increases with decreasing γ for a given M and Re on a fixed lattice. Therefore, it is expected that the

PLBE (3.167) has a better numerical stability range than the standard one for small Mach number or high Reynolds number flows. It is also noted that γ can also influence the EDF $f_i^{(eq)}$. The decrease in γ means an increase in the last term in the brackets of the EDF given by Eq. (3.168), which may make the EDF become negative, and thus cause numerical instability. These arguments indicate that the parameter γ have complicated influences on the numerical stability of the PLBE.

The stability of the PLBE can be analyzed using the von Neumann linear analysis method. To do so, the distribution function $f_i(\boldsymbol{x},t)$ is first expanded around a constant global EDF $\overline{f}_i^{(0)}$,

$$f_i(\boldsymbol{x},t) = \overline{f}_i^{(0)}(\rho_0,\boldsymbol{u}_0) + f_i'(\boldsymbol{x},t), \tag{3.175}$$

where ρ_0 and $\boldsymbol{u}_0$ are the constant density and velocity, respectively, and $f_i'(\boldsymbol{x},t)$ is the fluctuation of f_i around $\overline{f}_i^{(0)}$. With this expansion, the linearized PLBE reads

$$f_i'(\boldsymbol{x}+\boldsymbol{c}_i\delta_t, t+\delta_t) - f_i'(\boldsymbol{x},t) = -\frac{1}{\tau_p}\left[f_i'(\boldsymbol{x},t) - G_{ij}f_j'(\boldsymbol{x},t)\right], \tag{3.176}$$

where

$$G_{ij} = \frac{\partial f_i^{(eq)}(\rho_0,\boldsymbol{u}_0)}{\partial f_j}$$

is the Jacobian matrix evaluated at the uniform mean density and velocity. It is noted that $\boldsymbol{G}$ does not vary in space or time. Equation (3.176) can be rewritten in a compact form as

$$f_i'(\boldsymbol{x}+\boldsymbol{c}_i\delta_t, t+\delta_t) = M_{ij}f_j'(\boldsymbol{x},t), \tag{3.177}$$

where the matrix $\boldsymbol{M}$ is defined by

$$M_{ij} = \left(1-\frac{1}{\tau_p}\right)\delta_{ij} + \frac{1}{\tau_p}G_{ij}.$$

The Fourier transform of Eq. (3.177) gives that

$$F_i(\boldsymbol{k}, t+\delta_t) = \exp[-\mathrm{i}\boldsymbol{k}\cdot\boldsymbol{e}_i]M_{ij}F_j(\boldsymbol{k},t), \tag{3.178}$$

where $\mathrm{i} = \sqrt{-1}$, $F_j(\boldsymbol{k},t)$ is the Fourier transform of $f_i'(\boldsymbol{x},t)$, $\boldsymbol{k}$ is the wave number in units of $1/\delta_x$, and $\boldsymbol{e}_i = \boldsymbol{c}_i/c$ is the dimensionless discrete

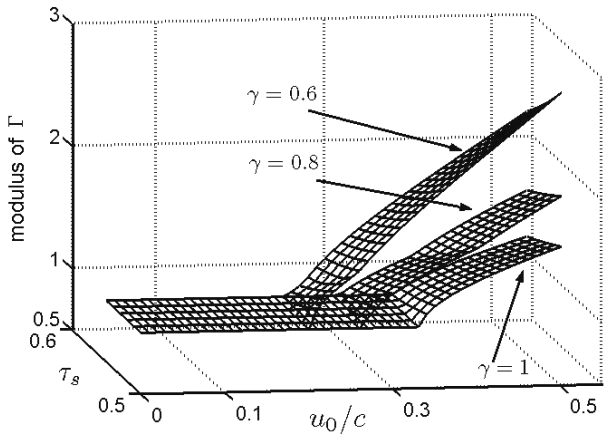

Fig. 3.5. The modulus of $\mathbf{\Gamma}$ vs τ_s and $\boldsymbol{u}_0'$ for different γ (Guo *et al.*, Phys. Rev. E 70, 066706, 2004).

velocity. The spatial dependence of the stability of the PLBE is determined by the eigenvalues of the matrix $\mathbf{\Gamma}$,

$$\Gamma_{ij}(\boldsymbol{k}) = \exp[-\mathrm{i}\boldsymbol{k}\cdot\boldsymbol{e}_i]M_{ij}\,.$$

For the D2Q9 model, the explicit expression of the Jacobian matrix $\boldsymbol{G}$ can be written as

$$G_{ij} = \omega_i\left\{1 + 3(\boldsymbol{e}_i\cdot\boldsymbol{e}_j) - \frac{3}{2\gamma}\left[2(\boldsymbol{e}_j\cdot\boldsymbol{u}_0') - \boldsymbol{u}_0'^2\right]\right.$$
$$\left. + \frac{9}{2\gamma}\left[2(\boldsymbol{e}_i\cdot\boldsymbol{u}_0')(\boldsymbol{e}_i\cdot\boldsymbol{e}_j) - (\boldsymbol{e}_i\cdot\boldsymbol{u}_0')^2\right]\right\}, \qquad (3.179)$$

where $\boldsymbol{u}_0' = \boldsymbol{u}_0/c$. It can be shown that the eigenvalues of $\boldsymbol{G}$ are 1 and 0 with multiplicities 3 and 6, respectively, which are independent of γ and $\boldsymbol{u}_0'$. Accordingly, the eigenvalues of the matrix $\boldsymbol{M}$ are 1 and $1-1/\tau_p$.

It is clear that $\mathbf{\Gamma} = \boldsymbol{M}$ as $\boldsymbol{k} = \mathbf{0}$, therefore the PLBE (3.167) is asymptotically stable if $|1 - 1/\tau_p| < 1$, i.e. $\tau_p > 0.5$, which is the same as the standard LBE. As $\boldsymbol{k} \neq \mathbf{0}$, the eigenvalues of $\mathbf{\Gamma}$ has a complex dependence on the parameters γ, $\boldsymbol{u}_0'$, $\boldsymbol{k}$, and τ_p, and hence it is rather difficult to give a complete mapping of all the stability boundaries. Guo *et al.* have made an analysis in a special case, i.e. both the wave number $\boldsymbol{\kappa}$ and the uniform velocity $\boldsymbol{u}_0$ are aligned with $\boldsymbol{e}_1$. In Fig. 3.5 the

modulus of the matrix $\mathbf{\Gamma}$, i.e., the maximum magnitude of the eigenvalues, are shown as a function of $\boldsymbol{u}_0'$ and the relaxation time τ_s, which corresponds to the standard LBE and is related to τ_p by $\tau_s = 0.5 + \gamma(\tau_p - 0.5)$.

It is observed that for each value of γ, there exists a critical value of the velocity, $\boldsymbol{u}_c$, above which the modulus of $\mathbf{\Gamma}$ increases dramatically, meaning that the PLBE would become unstable. This critical value clearly depends on the parameter γ : the smaller the γ, the lower the $\boldsymbol{u}_c$. It indicates that the stable range of PLBE is reduced as compared to the standard LBE. Fortunately, for small Mach number flows when LBE works, the fluid velocity is usually much lower than $\boldsymbol{u}_c$, and under such a circumstance the PLBE is expected to have a stability similar to the standard LBE.

The PLBE has been shown to be able to accelerate the convergence rate significantly by adjusting the control parameter γ. In Fig. 3.6, the convergence processes of the PLBE and the standard LBE for the lid-driven flow in a square cavity are presented at $\mathrm{Re} = 400$ and 1000 (based on the driven velocity and cavity height), respectively. It is clearly seen

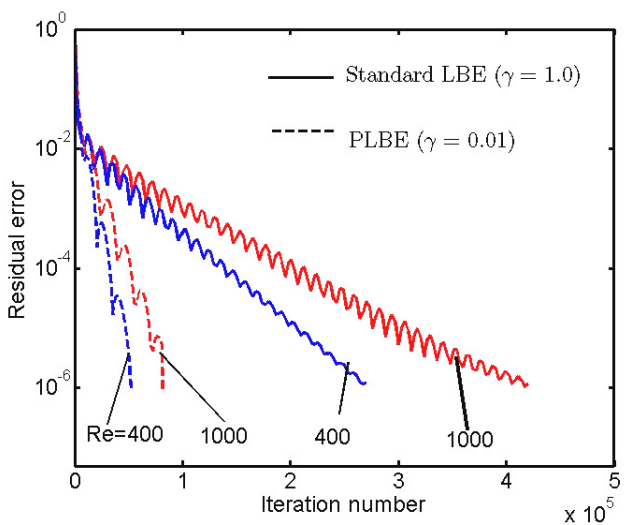

Fig. 3.6. Time histories of PLBE and standard LBE for the cavity flow. M^*=0.058. Lattice size: 257×257 (Guo *et al.*, Phys. Rev. E 70, 066706, 2004).

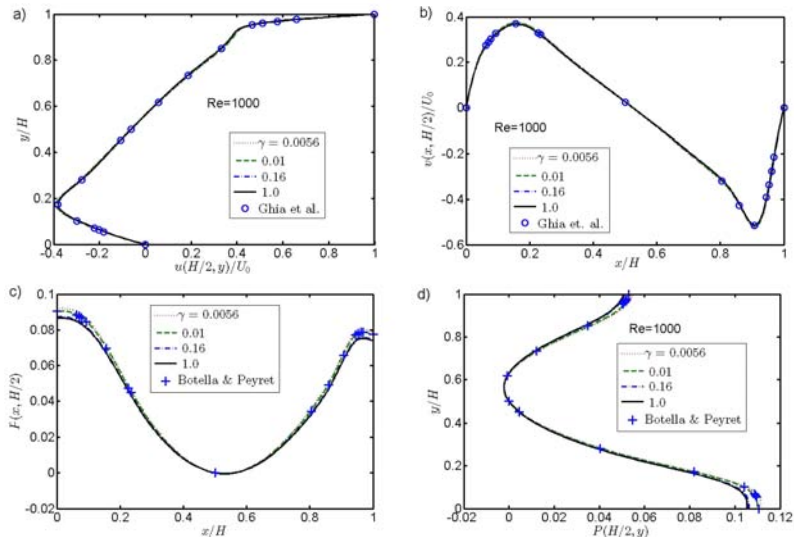

Fig. 3.7. Velocity [(a) and (b)] and pressure [(c) and (d)] profiles through the cavity center at $\mathrm{Re} = 1000$ (Guo *et al.*, Phys. Rev. E 70, 066706, 2004).

that the PLBE enhanced the convergence rate greatly for both cases compared with the standard LBE.

It should be emphasized that the acceleration of PLBE is achieved without sacrificing the accuracy of the solution. In Fig. 3.7, the velocity and pressure distributions along the vertical and horizontal lines through the cavity center are presented for $\mathrm{Re} = 1000$, together with the benchmark results [Ghia *et al.*, 1982; Botella and Peyret, 1998]. It is seen that in all cases the velocity distributions predicted by the PLBE agree well with the benchmark solutions, and the difference between these results with different γ is nearly indistinguishable. However, some prominent differences are observed among the pressure distributions for different values of γ. The differences are small in the central region, but become larger near the walls. Also, the differences increase as Re becomes larger. The comparison shows that the pressure distributions predicted by the PLBE with $\gamma < 1$ agree better with the benchmark solutions [Botella and Peyret, 1998] than that by the standard LBE ($\gamma = 1$), which demonstrates the desirable properties of PLBE.

It is noted that some oscillations occur during the convergence process. This is due to the reflection of acoustic waves on the walls. Such oscillations can be damped out by enhancing the bulk viscosity, which does not alter the solutions for incompressible flow or compressible flow with low Mach number. The suppression of such oscillations can further accelerate the convergence process. This technique can be achieved straightforwardly in MRT-LBE, and several such methods have been developed recently by Izquierdo and Fueyo [2008, 2009].

3.5 Summary

This chapter has presented some improved LBE methods from different viewpoints. Particularly, we have focused on the following five special topics:

(i) LBE models with reduced compressibility errors. Because the standard LBE simulates the compressible Navier-Stokes equations, errors due to the compressibility will arise when applied to incompressible flows. In order to reduce such errors, some *incompressible* LBE models have been developed. For steady incompressible flows, the models developed in [Zou *et al.*, 1995; Lin *et al.*, 1996] can be employed, while for unsteady flows several other more elaborated models [Chen and Ohashi, 1997; He and Luo, 1997; Guo *et al.*, 2000] should be used.

(ii) LBE models with reduced compressibility errors. Because the standard LBE simulates the compressible Navier-Stokes equations, errors due to the compressibility will arise when applied to incompressible flows. In order to reduce such errors, some *incompressible* LBE models have been developed. For steady incompressible flows, the models developed in [Zou *et al.*, 1995; Lin *et al.*, 1996] can be employed, while for unsteady flows several other more elaborated models [Chen and Ohashi, 1997; He and Luo, 1997; Guo *et al.*, 2000] should be used.

(iii) Treatment of body force in LBE with reduced discrete effects. As the fluid is exposed to a body force field, it is important to incorporate its effect into LBE. Although a variety of methods have

been proposed, the analysis indicates that care must be taken when implementing these methods because of the discrete lattice effects. In this regard, the forcing schemes developed in [He *et al*., 1998] and [Guo *et al*., 2002] are the most accurate methods, satisfying certain necessary constraints required for reproducing the desired body force in the hydrodynamic equations.

(iv) LBE methods with nonuniform grids. The use of a regular lattice as the computational mesh limits the applications of the standard LBE for flows with irregular geometries. One straightforward extension of the standard LBE in this respect is to make use of grid-refinement or multi-block techniques [Filippova and Hänel, 1998; Dupuis and Chopard, 2003; Yu *et al*., 2002; Guo *et al*., 2003; Crouse *et al*., 2003; Tölke *et al*., 2006; Yu and Fan, 2009]. Meanwhile, the interpolation supplemented method [He *et al.*, 1996] utilizes the fact that the computational mesh can be decoupled from the underlying discrete velocity set. It is noted that both of the above methods still depend on the standard LBE. On the other hand, after recognizing that the LBE can be viewed as a special finite-difference scheme of the Boltzmann equation, some LBE methods using nonuniform grids have been developed by discretizing the DVM using the finite-difference, finite-volume, or finite-element methods. The Taylor series expansion- and least square-based LBE method developed by Shu *et al*. [2001] provides a meshless- like version.

(v) Accelerated LBE methods for steady flows. Because of the low Mach number limitation, the standard LBE usually suffers from a slow convergence rate for steady flows. In order to improve the convergence, two types of techniques, i.e., time-independent and time-dependent approaches, have been introduced into LBE. In general, the time-independent methods involve a large scale linear or nonlinear algebraic system which can be solved by iterative algorithms. The solution procedure of such methods is quite different from the standard LBE. On the other hand, the time-dependent accelerated LBE is more resemble the standard LBE. Particularly, the preconditioned LBE proposed by Guo *et al.* [2004] has the same structure as and shares all of the advantages of the standard one.

It should be pointed out that the improved methods listed in this chapter can be combined with each other to improve the performance of LBE further. For example, a nonuniform grid can be used in the PLBE, and the convergence rate of LBE can also be accelerated by adding a fictitious body force [Kandhai *et al*., 1999].

Chapter 4

Sample Applications of LBE for Isothermal Flows

In the previous three chapters we have presented some standard and improved LBE models for isothermal flows, and some methods to realize certain prescribed initial and boundary conditions were also discussed. With these basic ingredients, now we are ready to simulate some simple isothermal flows. In this chapter we will first discuss the structure of an LBE algorithm, and then present several sample applications to demonstrate the implementation details and numerical results.

4.1 Algorithm Structure of LBE

The picture of the collision and streaming processes of LBE, in either LBGK or MRT-LBE models, is rather clear, and it is straightforward to implement both processes. Generally, an LBE algorithm can be designed following two kinds of structures, i.e., *collision-streaming* fashion where at each time step the collision is first executed and then the post-collision distributions are shifted to their neighbors, and *streaming-collision* fashion which exchanges the above procedure. It can be shown these two algorithm structures are identical, and we will follow the former one in this book. A typical flowchart of such LBE algorithm is shown in Fig. 4.1, but it should be noted that the sequence of the subroutines can be adjusted in some cases. In what follows the main subroutines of the algorithm will be described. For clarity and simplicity, we will take the D2Q9 model as an example, and the code will be written in ANSI-C language. The global variables are defined in a header file `D2Q9.h`:

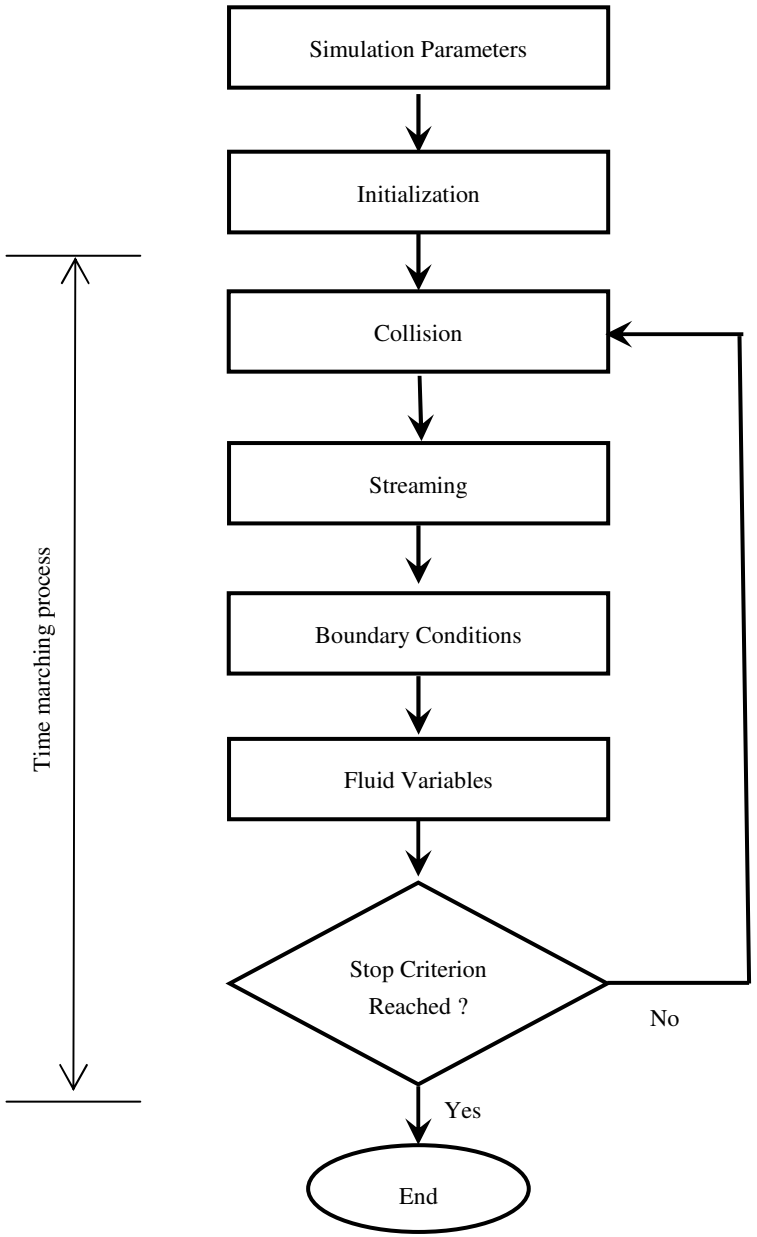

Fig. 4.1. Flowchart of LBE algorithm.

```
//-----------------------------------------------
//   ----- Header file of the D2Q9 model --
//-----------------------------------------------
//File name: D2Q9.h
#include <stdio.h>
#include <stdlib.h>
#include <math.h>
#define  Nx 100 // number of cells in x-direction
#define  Ny 100 // number of cells in y-direction
#define Nx1 (Nx+1)
#define Ny1 (Ny+1)
#define  Q 9     // number of discrete velocities
#define rho0 1.0   // initial density
#define ux0  0.0
#define uy0  0.0   // (ux0, uy0) is the initial velocity
int cx[Q]={0, 1, 0, -1, 0, 1, -1, -1, 1};
int cy[Q]={0, 0, 1, 0, -1, 1, 1, -1, -1};
double f[Ny1][Nx1][Q]; //array of the distribution functions
double f_post[Ny1][Nx1][Q]; // array of the post-collision
                            // distribution functions
double rho[Ny1][Nx1], ux[Ny1][Nx1], uy[Ny1][Nx1];
                            // arrays of  fluid density and velocity
double tau;   // relaxation time for BGK model
double s[Q]; // relaxation rates for MRT model
double D[Q]={9, 36, 36, 6, 12, 6, 12, 4, 4}; // D = M*M^T
double  w[Q]={4.0/9,  1.0/9,  1.0/9,  1.0/9,  1.0/9,  1.0/36,
              1.0/36, 1.0/36, 1.0/36}; // weights in  EDF
int rc[Q]={0,3,4,1,2,7,8,5,6};
// index of the reversed velocity used in bounce-back scheme
//---------- end of header file------------------
```

Initialization

As described in Chapter 3, the distribution functions can be initialized by either the equilibrium or non-equilibrium methods, or the more elaborated iterative method. The following subroutine gives the equilibrium initialization method.

```
//-----------------------------------------------------------
//Subroutine: initialization with the equilibrium method
//-----------------------------------------------------------
void Init_Eq()
{
  int j, i, k;
  for (j=0;j<=Ny;j++) for(i=0;i<=Nx;i++)
  {
   rho[j][i]=rho0;
   ux[j][i]=ux0;
   uy[j][i]=uy0;
   for(k=0;k<Q;k++)
   f[j][i][k]=feq(rho[j][i],ux[j][i],uy[j][i],k);
  }
}
//-------------- end of initialization ----------
```

The calculation of the EDF is realized by the function `feq()`:

```
//-----------------------------------------------
// Subroutine: calculation the equilibrium distribution
//-----------------------------------------------
double feq(double RHO, double U, double V, int k)
{
  double cu, U2;
  cu=cx[k]*U+cy[k]*V; // c_k*u
  U2=U*U+V*V;         // u*u;
  return w[k]*RHO*(1+3*cu+4.5*cu*cu-1.5*U2);
}
//----------- end of equilibrium ---------------
```

The equilibrium method works well for steady flows. But it may introduce some initial errors for unsteady flows. The nonequilibrium or the iteration method [Mei *et al.*, 2006] can give more accurate initial values. Particularly, the latter can provide the compatible pressure as

well as the distribution functions. The codes for these methods can be composed with similar structure, and will not be included in this book.

Collision

The subroutine for the BGK collision model is given below.

```
//-----------------------------------------------
// Subroutine: BGK collision
//-----------------------------------------------
void Coll_BGK()
{
  int j, i, k;
   double FEQ;
   for(j=0;j<=Ny;j++) for(i=0;i<=Nx;i++)
   for(k=0;k<Q;k++)
   {
     // the value of the EDF:
     FEQ=feq(rho[j][i],ux[j][i],uy[j][i],k);
     // the post-collision distribution function:
     f_post[j][i][k]=f[j][i][k]-(f[j][i][k]-FEQ)/tau;
   }
}
//---------------- end of BGK collision ---------
```

The collision process of MRT model contains three phases: (1) transforming the distribution functions from velocity space to moment space; (2) performing relaxation in moment space; (3) transforming the moments back to the velocity space. With the transformation matrix given in Chapter 1, the subroutine for the MRT collision model is described as follows.

```
//-----------------------------------------------
// Subroutine: MRT collision
//-----------------------------------------------
void Coll_MRT()
{
  int j, i, k;
```

```
double MEQ;
double m[Q];   // moments defined by m=M*f
for (j=0;j<=Ny;j++) for(i=0;i<=Nx;i++)
{
 // Transformation from velocity space to moment space:
  m[0] = f[j][i][0]+f[j][i][1]+f[j][i][2]+f[j][i][3]
         +f[j][i][4]+f[j][i][5]+f[j][i][6]+f[j][i][7]
         +f[j][i][8];
  m[1] = -4*f[j][i][0]-f[j][i][1]-f[j][i][2]-f[j][i][3]
         -f[j][i][4]+2*(f[j][i][5]+f[j][i][6]+f[j][i][7]
         +f[j][i][8]);
  m[2] = 4*f[j][i][0]-2*(f[j][i][1]+f[j][i][2]+f[j][i][3]
         +f[j][i][4])+f[j][i][5]+f[j][i][6]+f[j][i][7]
         +f[j][i][8];
  m[3] = f[j][i][1]-f[j][i][3]+f[j][i][5]-f[j][i][6]
         -f[j][i][7]+f[j][i][8];
  m[4]  =  -2*(f[j][i][1]-f[j][i][3])+f[j][i][5]-f[j][i][6]
         -f[j][i][7]+f[j][i][8];
  m[5] = f[j][i][2]-f[j][i][4]+f[j][i][5]+f[j][i][6]
         -f[j][i][7]-f[j][i][8];
  m[6] = -2*(f[j][i][2]-f[j][i][4])+f[j][i][5]+f[j][i][6]
         -f[j][i][7]-f[j][i][8];
  m[7] = f[j][i][1]-f[j][i][2]+f[j][i][3]-f[j][i][4];
  m[8] = f[j][i][5]-f[j][i][6]+f[j][i][7]-f[j][i][8];
 // Relaxation:
  for(k=0;k<Q;k++)
  {
   // the equilibrium moment:
    MEQ = meq(rho[j][i],ux[j][i],uy[j][i],k);
    m[k] = m[k]-s[k]*(m[k]-MEQ);   // relaxation
    m[k] /= D[k];                 // rescaling
  }
// Transforming back to the velocity space:
  f_post[j][i][0] = m[0]-4*(m[1]-m[2]);
  f_post[j][i][1] = m[0]-m[1]-2*(m[2]+m[4])+m[3]+m[7];
```

```
    f_post[j][i][2] = m[0]-m[1]-2*(m[2]+m[6])+m[5]-m[7];
    f_post[j][i][3] = m[0]-m[1]-2*(m[2]-m[4])-m[3]+m[7];
    f_post[j][i][4] = m[0]-m[1]-2*(m[2]-m[6])-m[5]-m[7];
    f_post[j][i][5] = m[0]+m[1]+m[1]+m[2]+m[3]+m[4]+m[5]
                      +m[6]+m[8];
    f_post[j][i][6] = m[0]+m[1]+m[1]+m[2]-m[3]-m[4]+m[5]
                      +m[6]-m[8];
    f_post[j][i][7] = m[0]+m[1]+m[1]+m[2]-m[3]-m[4]-m[5]
                      -m[6]+m[8];
    f_post[j][i][8] = m[0]+m[1]+m[1]+m[2]+m[3]+m[4]-m[5]
                      -m[6]-m[8];
  }
}
//------------- end of MRT collision-------------
```

In the subroutine `m[Q]` is the moment array, and `s[Q]` is the corresponding relaxation rates. $\boldsymbol{D}$ is a diagonal matrix relating to the transformation matrix $\boldsymbol{M}$, i.e. $\boldsymbol{D}=\boldsymbol{M}\boldsymbol{M}^T$. So, the inverse of $\boldsymbol{M}$ can be simply expressed as $\boldsymbol{M}^{-1} = \boldsymbol{M}^T\boldsymbol{D}^{-1}$. `meq()` is the function of calculating the equilibrium moments:

```
//-----------------------------------------------
// Subroutine: calculation the equilibrium moment
//-----------------------------------------------
double meq(double RHO, double U, double V, int k)
{
  double x;
  switch(k)
  {
   case 0: {x=RHO; break;}
   case 1: {x=RHO*(-2+3*(U*U+V*V)); break;}
   case 2: {x=RHO*(1-3*(U*U+V*V)); break;}
   case 3: {x=RHO*U; break;}
   case 4: {x=-RHO*U; break;}
   case 5: {x=RHO*V; break;}
   case 6: {x=-RHO*V; break;}
```

```
   case 7: {x=RHO*(U*U-V*V); break;}
   case 8: {x=RHO*U*V; break;}
   default: x=0;
  }
  return x;
}
//----------- end of equilibrium moments --------
```

Streaming

The streaming process can be implemented straightforwardly. Furthermore, certain boundary conditions such as the bounce-back scheme can also be incorporated into this process. The subroutine reads,

```
//-----------------------------------------------
// Subroutine: Streaming
//-----------------------------------------------
void Streaming()
{
  int j, i, jd, id, k;
  for (j=0;j<=Ny;j++) for(i=0;i<=Nx;i++)
   for(k=0;k<Q;k++)
   {
       jd=j-cy[k]; id=i-cx[k]; // upwind node
      if(!boundary[jd][id])    // fluid node
        f[j][i][k]=f_post[jd][id][k]; // streaming
      else                          // boundary node
     // bounce-back on the boundary node:
          f[j][i][k]=f_post[jd][id][rc[k]]+6*w[k]*rho[j][i]*
                     (cx[k]*uwx[jd][id]+cy[k]*uwy[jd][id]);
   }
}
//-----------------------------------------------
```

Here `boundary[Ny1][Nx1]` is a Boolean array that characterizes the boundary nodes, and `uw=(uwx, uwy)` is the velocity of the

boundary node. Incorporating the bounce-back scheme into the streaming process is efficient for flows with irregular boundaries such as porous media. If only simple boundaries, such as flat walls, are involved, the code can be improved by separating the boundary condition treatments from the streaming process, and the flag `boundary [Ny1][Nx1]` can be deleted in such case.

Boundary conditions

Assuming that the boundary is a flat wall located at $y = 0$, then for the standard bounce-back scheme, the first layer of fluid nodes on the lattice ($j = 0$) locates at $y = \delta_x$; For the half-way bounce-back scheme, the location is at $y = \delta_x/2$. For the modified bounce-back scheme, the non-equilibrium extrapolation, and the hydrodynamic boundary conditions, the location falls on the wall. As an example, in the following we will give several subroutines to realize the boundary conditions of the Couette flow confined between two parallel plates. The top plate moves with a constant velocity $\boldsymbol{u}_0 = (u_w, 0)$, and the bottom plate is kept stationary. Periodic boundary conditions are applied to the inlet and outlet.

The subroutine of the bounce-back rule is given as follows:

```
//-----------------------------------------------
// Subroutine: Bounce-back scheme
//-----------------------------------------------
void Bounce_back()
{
  int i;
 // j=0: bottom plate
  for(i=0;i<=Nx;i++)
  {
    // bounce-back for particles hitting on the wall:
    f[0][i][2]=f_post[0][i][4];
    f[0][i][5]=f_post[0][i][7];
    f[0][i][6]=f_post[0][i][8];
  }
 // j=Ny: top plate
  for(i=0;i<=Nx;i++)
```

```
  {
    f[Ny][i][4]=f_post[Ny][i][4];
    f[Ny][i][7]=f_post[Ny][i][5]+6*rho[Ny][i]*w[7]*cx[7]*uw;
    f[Ny][i][8]=f_post[Ny][i][6]+6*rho[Ny][i]*w[8]*cx[8]*uw;
  }
}
//-----------------------------------------------
```

The above bounce-back subroutine is executed after the collision process. On the other hand, the modified bounce-back scheme should be executed after the streaming process, and the collision is also performed on the wall nodes. The subroutine reads as below:

```
//-----------------------------------------------
// Subroutine: Modified bounce-back scheme
//-----------------------------------------------
void M_bounce_back()
{
  int i;
 // j=0: bottom plate
  for(i=0;i<=Nx;i++)
  {
 // bounce-back for particles hitting on the wall:
    f[0][i][2]=f[0][i][4];
    f[0][i][5]=f[0][i][7];
    f[0][i][6]=f[0][i][8];
  }
 // j=Ny: top plate
  for(i=0;i<=Nx;i++)
  {
    f[Ny][i][4]=f[Ny][i][2];
    f[Ny][i][7]=f[Ny][i][5]+6*rho[Ny][i]*w[7]*cx[7]*uw;
    f[Ny][i][8]=f[Ny][i][6]+6*rho[Ny][i]*w[8]*cx[8]*uw;
  }
}
//-----------------------------------------------
```

Similarly, the non-equilibrium extrapolation scheme [Guo *et al*., 2002a] is also executed after the streaming process. The subroutine of this scheme is described below:

```
//-----------------------------------------------
// Subroutine: Non-equilibrium extrapolation
//-----------------------------------------------
void Noneq_BC()
{
  int i, jd, id;
  double FMf, FMb;
 // j=0: bottom plate
  for(i=0;i<=Nx;i++)
  {
    jd=1; id=i; // nearest neighboring fluid node
   FMb=feq(rho[jd][id],0,0,2);    // equilibrium at the boundary node
   FMf=feq(rho[jd][id],ux[jd][id],uy[jd][id],2);  // equilibrium
                                                  // at the fluid node
/*****
    the extrapolation can also be taken from the  nearest neighboring node along the
    discrete velocity, i.e, jd=(Nx1+cy[2])%N1; id = (Nx1+i+cx[2])%Nx1;
*****/
   // non-equilibrium extrapolation
    f[0][i][2]=FMb+(f[jd][id][2]-FMf);
    FMb=feq(rho[jd][id],0,0,5);
    FMf=feq(rho[jd][id],ux[jd][id],uy[jd][id],5);
    f[0][i][5]=FMb+(f[jd][id][5]-FMf);

    FMb=feq(rho[jd][id],0,0,6);
    FMf=feq(rho[jd][id],ux[jd][id],uy[jd][id],6);
    f[0][i][6]=FMb+(f[jd][id][6]-FMf);
  }
 // j=Ny: top plate
  for(i=0;i<=Nx;i++)
  {
    jd=Ny-1; id=i;
    FMb=feq(rho[jd][id],u0,0,4);
```

```
    FMf=feq(rho[jd][id],ux[jd][id],uy[jd][id],4);
    f[Ny][i][4]=FMb+(f[jd][id][4]-FMf);

    FMb=feq(rho[jd][id],u0,0,7);
    FMf=feq(rho[jd][id],ux[jd][id],uy[jd][id],7);
    f[Ny][i][7]=FMb+(f[jd][id][7]-FMf);

    FMb=feq(rho[jd][id],u0,0,8);
    FMf=feq(rho[jd][id],ux[jd][id],uy[jd][id],8);
    f[Ny][i][8]=FMb+(f[jd][id][8]-FMf);
  }
}
//-----------------------------------------------
```

Both the bounce-back schemes and the non-equilibrium extrapolation method will introduce some approximation errors in the velocity boundary conditions. On the other hand, the hydrodynamic scheme is able to give the prescribed velocity exactly. The following subroutine realizes the method developed by Zou *et al.* [1997]. Other hydrodynamic schemes can be realized similarly.

```
//-----------------------------------------------
// Subroutine: Hydrodynamic scheme by Zou and He
//-----------------------------------------------
void Hydro_BC()
{
  Int i;
  double rhow;
 // j=0: bottom plate
  for(i=0;i<=Nx;i++)
  {
  // the density at wall node:
    rhow = f[0][i][0]+f[0][i][1]+f[0][i][3]+2*(f[0][i][4]
           +f[0][i][7]+f[0][i][8]);
    f[0][i][2]=f[0][i][4];
    f[0][i][5]=f[0][i][7]-0.5*(f[0][i][1]-f[0][i][3]);
    f[0][i][6]=f[0][i][8]+0.5*(f[0][i][1]-f[0][i][3]);
```

```
  }
 // j=Ny: top plate
  for(i=0;i<=Nx;i++)
  {
  // the density at wall node:
    rhow = f[Ny][i][0]+f[Ny][i][1]+f[Ny][i][3]+2*(f[Ny][i][4]
           +f[Ny][i][7]+f[Ny][i][8]);
    f[Ny][i][4] = f[Ny][i][2];
    f[Ny][i][7] = f[Ny][i][5]+0.5*(f[Ny][i][1]-f[Ny][i][3])
                  -0.5*rhow*u0;
    f[Ny][i][8] = f[Ny][i][6]-0.5*(f[Ny][i][1]-f[Ny][i][3])
                  +0.5*rhow*u0;
  }
}
//-----------------------------------------------
```

Fluid variables

The fluid variables, i.e., density and velocity, can be calculated from the distribution functions directly. This is achieved by the subroutine `Den_Vel()` given below.

```
//-----------------------------------------------
// Subroutine: Fluid density and velocity
//-----------------------------------------------
void Den_Vel()
{
  int j, i;
  for(j=0;j<=Ny;j++) for(i=0;i<=Nx;i++)
  {
   // density:
    rho[j][i] = f[j][i][0]+f[j][i][1]+f[j][i][2]+f[j][i][3]
                +f[j][i][4]+f[j][i][5]+f[j][i][6]+f[j][i][7]
                +f[j][i][8];
    ux[j][i] = (f[j][i][1]+f[j][i][5]+f[j][i][8]-f[j][i][3]
                -f[j][i][6]-f[j][i][7])/rho[j][i];
```

```
    uy[j][i] = (f[j][i][5]+f[j][i][6]+f[j][i][2]-f[j][i][7]
                -f[j][i][8]-f[j][i][4])/rho[j][i];
  }
}
//-----------------------------------------------
```

The above subroutines constitute the basic package for a typical LBE algorithm. Of course, in practical applications these subroutines may be modified to account for the particular situations. With a `main()` function that controls the overall order of computations and operations, one can design his own program for specific problems. Furthermore, the codes listed above only provide a direct realization of the LBE method without optimizations, and one can design more efficient algorithms and codes. In the following sections we will demonstrate some sample applications of LBE for incompressible flows.

4.2 Lid-Driven Cavity Flow

In this section we will simulate a two-dimensional steady flow in a square cavity via the D2Q9 LBGK model. This problem is industrially important and usually taken as one of the standard benchmark cases to test computational schemes. The LBE was also applied to this problem by many researchers. For example, Hou and Zou have performed some detailed simulations [Hou and Zou, 1995]. The configuration of this problem is shown in Fig. 4.2. The flow in the cavity is driven by the top lid moving from left to right with a constant velocity u_0. The flow is characterized by the Reynolds number, $\mathrm{Re} = Lu_0/\nu$, where L is the length of the cavity and ν is the shear viscosity of the fluid. In the simulation, a lattice with size of $(N+1)\times(N+1)$ is used, so that the lattice spacing is $\delta_x = L/N$ for the standard bounce-back, modified bounce-back, and the non-equilibrium boundary conditions, while $\delta_x = L/(N+1)$ for the half-way bounce- back scheme.

For convenience, we will take the lattice spacing δ_x, time increment δ_t, and lattice speed $c = \delta_x/\delta_t$, as the units of length, time, and velocity, and assuming that the average density ρ_0 is the density unit. As such, the

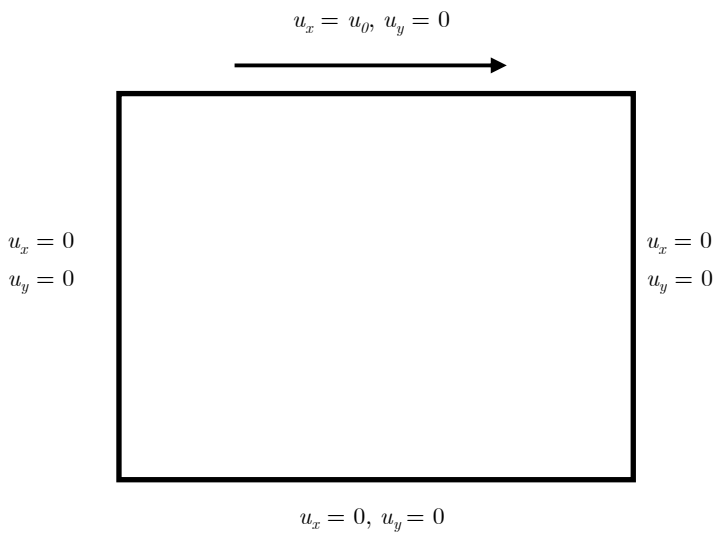

Fig. 4.2. Sketch of Lid-driven cavity flow.

viscosity of the Navier-Stokes equations derived from the LBE model is

$$\nu = c_s^2\left(\tau - \frac{1}{2}\right), \tag{4.1}$$

with $c_s = 1/\sqrt{3}$. In the literature, the simulated fluid with the above viscosity is termed as *lattice Boltzmann fluid* (LBF) sometimes. The Reynolds number of such fluid flows is then

$$\mathrm{Re} = \frac{Lu_0}{c_s^2(\tau - 0.5)} = \frac{\sqrt{3}LM}{\tau - 0.5}, \tag{4.2}$$

where $M = u_0/c_s$ is the Mach number. It should be born in mind that the LBE is an artificial compressibility method for incompressible fluid flows that has a vanishing Mach number. Provided the Mach number in LBE is low enough (e.g. $M < 0.3$), the LBE results can serve as a good approximation to the solutions of the incompressible Navier-Stokes equations. Therefore, the Reynolds number is the only similitude parameter between the LBE system and other fluid systems, while the Mach number is not.

According to the principle of similitude, one can obtain the relationships between the variables of simulated physical system and those of the LBE fluids:

$$\frac{\overline{\boldsymbol{x}}}{\overline{L}} = \frac{\boldsymbol{x}}{L}, \ \frac{\overline{t}}{\overline{t}_0} = \frac{t}{t_0}, \ \frac{\overline{p}}{\overline{p}_0} = \frac{p}{p_0}, \ \frac{\overline{\boldsymbol{u}}}{\overline{u}_0} = \frac{\boldsymbol{u}}{u_0}, \tag{4.3}$$

with

$$p_0 = \rho_0 u_0^2, \ \overline{p}_0 = \overline{\rho}_0 \overline{u}_0^2, \ \frac{\overline{L}_0 \overline{u}_0}{\overline{\nu}} = \frac{L_0 u_0}{\nu} = \mathrm{Re}, \tag{4.4}$$

where the variables with a bar represent the dimensional quantities of the real system, while those without a bar are quantities in LBE. The variables with a subscript "0" are characteristic quantities of the real and LBE systems, respectively. With these relationships, one can calculate the dimensional quantities of the real system from the LBE solutions.

In the simulations, the lattice size is taken to be 257×257, and the driven velocity u_0 is set to be 0.1. The relaxation time τ is determined from the Reynolds number according to Eq. (4.2). The half way bounce-back scheme is applied to the stationary and moving walls. An advantage of this scheme is that no special treatment is required for the four corners. It is noted that the top left and right corners are two singularities due to the velocity difference of the side and top walls. We treat the corner

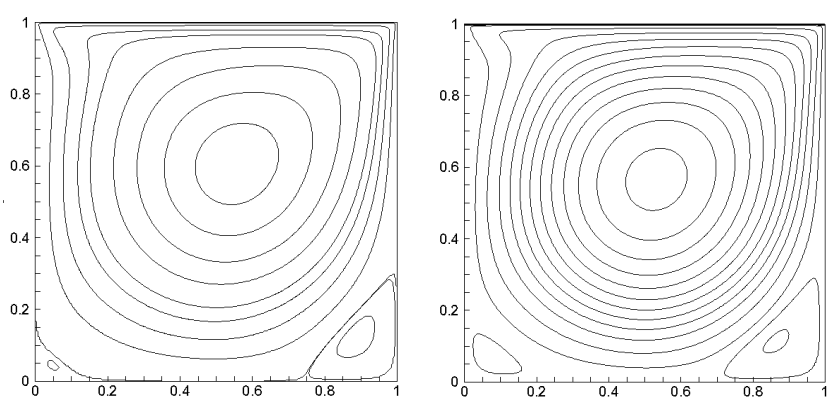

Fig. 4.3. Streamline of the cavity flow at Re=400 (left) and 1000 (right).

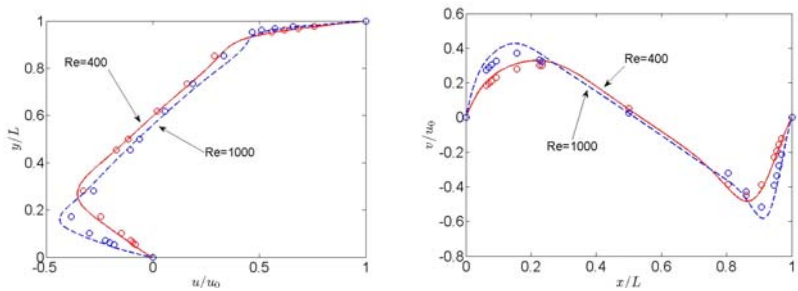

Fig. 4.4. Velocity profiles across the cavity center. Solid: LBGK results; Open circle: data by Ghia *et al.* [1982].

points as parts of the stationary walls in our simulations. The convergence criterion is set to be

$$e = \frac{\sum_{x,y} \left| \boldsymbol{u}(x,y,t+1000) - \boldsymbol{u}(x,y,t) \right|}{\sum_{x,y} \left| \boldsymbol{u}(x,y,t+1000) \right|} < 10^{-6} . \tag{4.5}$$

Figure 4.3 shows the streamlines of the cavity flow at $\mathrm{Re} = 400$ and 1000. It is seen that the fundamental characteristic of this flow is the appearance of a large primary vortex in the center and two secondary vortices near the two lower corners. These plots show clearly the effect of the Reynolds number on the flow pattern. The velocity components, u_x and u_y, along the vertical and horizontal center lines for different Re are shown in Fig. 4.4, together with the results by Ghia *et al*. [1982]. It is seen that the LBGK results agree well with the benchmark data. Recently, a more careful comparative study on the computational performance of several LBE models has been made [Luo *et al*., 2011].

The complete program for this test can be found in Appendix A.

4.3 Flow around a Fixed Circular Cylinder

Although the flow in the square cavity is complex, the geometry is nevertheless simple since only flat boundaries are involved. In order to demonstrate the performance of LBE for more general flows, we now apply the LBE to the flow past a fixed circular cylinder. This flow has been extensively studied both experimentally and numerically, and some

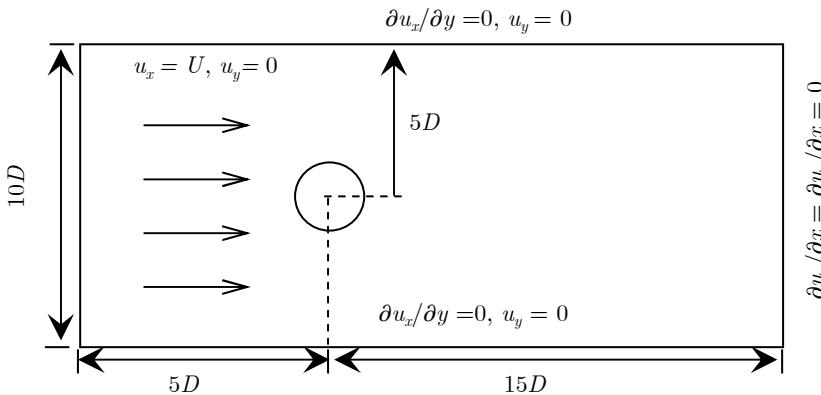

Fig. 4.5. Sketch of the flow around a circular cylinder.

applications of LBE based on uniform meshes [Guo *et al.*, 2000; Higuera and Succi, 1989; Wagner, 1994; Wagner and Hayot, 1995] or nonuniform meshes [Filippova and Hänel, 1998; He and Doolen, 1997; Mei and Shyy, 1998] have also been reported.

The D2Q9 LBGK model is again adopted in the simulations. The flow domain and boundary conditions are sketched in Fig. 4.5. The cylinder with a diameter D is put at $5D$ downstream from the entrance, and the free-stream velocity U is set to be 0.1. Outflow condition is imposed at the outlet, and free-slip boundary conditions are applied at the two side boundaries. At the surface of the cylinder, no-slip boundary condition is used. The Reynolds number of the flow is defined based on the free-stream velocity and the cylinder diameter, $\mathrm{Re} = DU/\nu$.

In the simulations, a lattice with size of $N_x \times N_y = 401 \times 201$ is used. The non-equilibrium extrapolation scheme for curved walls is used to treat the no-slip boundary condition at the cylinder surface, and that for flat walls is used to treat the inlet, outlet, and two side boundaries. The velocity gradients in the boundary conditions are first discretized to obtain the values of velocity at boundary nodes before implementing the non-equilibrium extrapolation scheme.

Another important problem is the calculation of the force exerted by the fluid on the cylinder. In classical CFD methods, this is usually done by integrating the overall hydrodynamic forces along the surface,

$$\boldsymbol{F} = \int_{\partial\Omega} \left[-p\boldsymbol{I} + \tau \right] \cdot \boldsymbol{n} dA \,, \tag{4.6}$$

where $\boldsymbol{n}$ is the outward unit normal vector to the cylinder surface $\partial\Omega$, and $\tau = \rho\nu(\nabla \boldsymbol{u} + \nabla \boldsymbol{u}^T)$ is the deviatoric stress tensor. Usually, the velocity gradients in the above equation can be discretized as usual with certain numerical schemes, as done by He and Luo [1997]. However, because the stress is related to the second-order moments of the non-equilibrium distribution functions, the calculation of the stress can be simplified in LBE [Filippova and Hänel, 1998],

$$\tau_{ij} = \left(1 - \frac{1}{2\tau}\right) \sum_i f_i^{(neq)} \left(c_{i\alpha} c_{i\beta} - D^{-1} \boldsymbol{c}_i^2 \delta_{ij} \right), \tag{4.7}$$

where D is the spatial dimension. The stress and the pressure on the cylinder surface can then be calculated using suitable extrapolation schemes based on those at the neighboring fluid nodes, which are then used to evaluate the integration of Eq. (4.6) to obtain the hydrodynamic force on the cylinder.

An alternative and more efficient approach for calculating the force exerting on the solid body is the so-called *momentum-exchange* method [Ladd, 1994a; Ladd, 1994b]. As shown in Fig. 2.4, after collision the momentum carried by the particle moving with $\boldsymbol{c}_i$ is $\boldsymbol{c}_i \cdot f_i'(\boldsymbol{x}_f, t)$, and after interacting with the solid wall, the momentum of the particle leaving the surface is $\boldsymbol{c}_{\bar{i}} \cdot f_{\bar{i}} (\boldsymbol{x}_f, t + \delta_t) = \boldsymbol{c}_{\bar{i}} \cdot f_{\bar{i}}' (\boldsymbol{x}_s, t)$. Therefore, the momentum loss of the particle is $\boldsymbol{c}_i \cdot f_{\bar{i}}' (\boldsymbol{x}_s, t) + f_i'(\boldsymbol{x}_f, t)]$. As a result, the total force on the cylinder exerted by all of the particles with velocity $\boldsymbol{c}_i$ in the cell around $\boldsymbol{x}_f$ can be calculated as

$$\boldsymbol{F}(\boldsymbol{x}_w) = \frac{\delta_x^D}{\delta_t} \boldsymbol{c}_i [f_{\bar{i}}'(\boldsymbol{x}_s, t) + f_i'(\boldsymbol{x}_f, t)], \tag{4.8}$$

and the total force on the solid body are the sum of all the forces on the wall nodes,

$$\boldsymbol{F} = \frac{\delta_x^D}{\delta_t} \sum_{\boldsymbol{x}_w} \boldsymbol{c}_i [f_{\bar{i}}'(\boldsymbol{x}_s, t) + f_i'(\boldsymbol{x}_f, t)]. \tag{4.9}$$

This momentum-exchange method is independent of the schemes for the boundary conditions, and can be implemented at the same time with the collision process. Mei *et al.* have compared the above two force

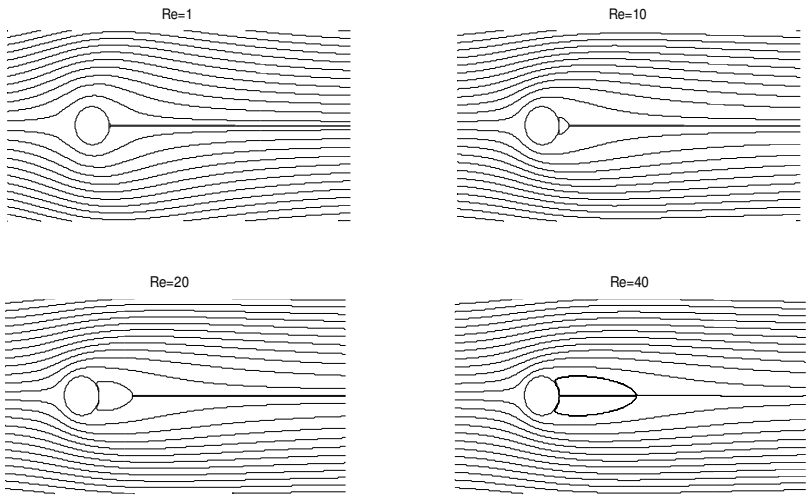

Fig. 4.6. Streamlines of the steady flows around a circular cylinder.

evaluation methods, and recommended the momentum-exchange method due to its simplicity, accuracy, and robustness [Mei *et al*., 2002]. This method is also employed in the following simulations.

First, steady flows with $\mathrm{Re} = 1,\ 10,\ 20$, and 40 are simulated. The streamlines at steady states are shown in Fig. 4.6. As $\mathrm{Re} = 1.0$, the upstream and downstream flow patterns are almost symmetric, and no boundary layer appears around the cylinder surface; As Re increases to

Table 4.1. Flow parameters of the steady flows around a circular cylinder.

	Re=10			Re=20			Re=40		
	$2L_c/D$	θ_s	C_D	$2L_c/D$	θ_s	C_D	$2L_c/D$	θ_s	C_D
A	0.474	26.89	3.170	1.842	42.9	2.152	4.490	52.84	1.499
B	0.434	27.96	2.828	1.786	43.37	2.053	4.357	53.34	1.550
C	0.68	32.5	—	1.86	44.8	—	4.26	53.5	—
D	0.542	27.3	2.942	1.895	44.8	2.155	4.43	53.13	1.604

A: He & Doolen [1997]; *B*: Nieuwstadt & Keller [1973]; *C*: Coutanceau & Bouard [1977]; *D*: Present results

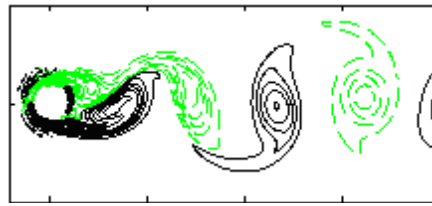

Fig. 4.7. Vorticity of the flow past a circular cylinder at Re=200. Solid line: positive value; dashed line: negative value.

10, a boundary layer is formed and the flow becomes detached from the surface of the object. A wake containing a pair of vortices appears behind the cylinder, and the wake length L_c becomes larger with increasing Re. The separation angle θ_s, at which the oncoming flow detaches first from the surface (zero shear stress), also increases with Re. In Tab. 4.1 both of the flow geometric parameters are presented and compared with available data from references. Also, the drag and lift coefficients, C_D and C_L, which are defined by

$$C_D = \frac{2F_x}{\rho U^2 D}, \quad C_L = \frac{2F_y}{\rho U^2 D}, \tag{4.10}$$

are listed in the table.

As Re is above a critical value (around 46), the wake becomes longer and longer and starts to oscillate, and finally the two vortices in the wake are shed alternatively from the cylinder to form the well-known *von Karman vortex street*. The flow is characterized by the Strouhal number

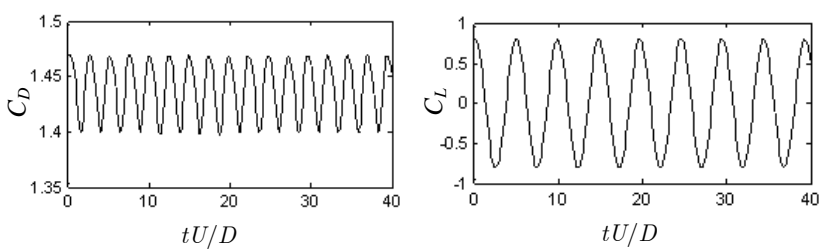

Fig. 4.8. Time histories of the drag (left) and lift (right) coefficients of the flow past a circular cylinder at Re=200.

Table 4.2. Strouhal number of the flow past a circular cylinder.

Re	140	150	160	185	200
A	——	0.185	——	—	—
B	0.179 ~ 0.182	—	0.185 ~ 0.188	—	—
C	——	—	——	0.195	—
D	——	—	——	—	0.202
E	0.184	0.186	0.188	0.196	0.204

A: Williamson & Roshko [1988]; B: Williamson [1996]; C: Lu & Dalton [1996]; D: Zheng & Zhang [2008]; *E*: Present results

defined as

$$St = \frac{D}{U \cdot T}, \tag{4.11}$$

where T is the period of vortex shedding. Figure 4.7 shows the vorticity of the flow at $\mathrm{Re}=200$. The time histories of the drag and lift coefficients are shown in Fig. 4.8. The periodic behavior of the flow is clearly shown from these figures, and the Strouhal number can be measured from the periodicity of C_D. Table 4.2 presents the values of St at several Reynolds numbers, which are in good agreement with reported values.

4.4 Flow around an Oscillating Circular Cylinder with a Fixed Downstream One

Flows around multiple structures are frequently seen in many practical engineering problems. Similar to the flow around a circular cylinder, such flow will become unsteady and vortices will shed alternately from the two sides of a structure as the Reynolds number exceeds a critical value. Furthermore, the alternate vortex shedding may induce a structural oscillation, which may affect the wake formation and impact upon fluid dynamics around downstream structures. It is of both fundamental and practical importance to study the possible influences of the structural oscillation on the downstream flow. The simplest model of such flow is a two-cylinder system, where the two cylinders are either in tandem, side-by-side or staggered arrangements.

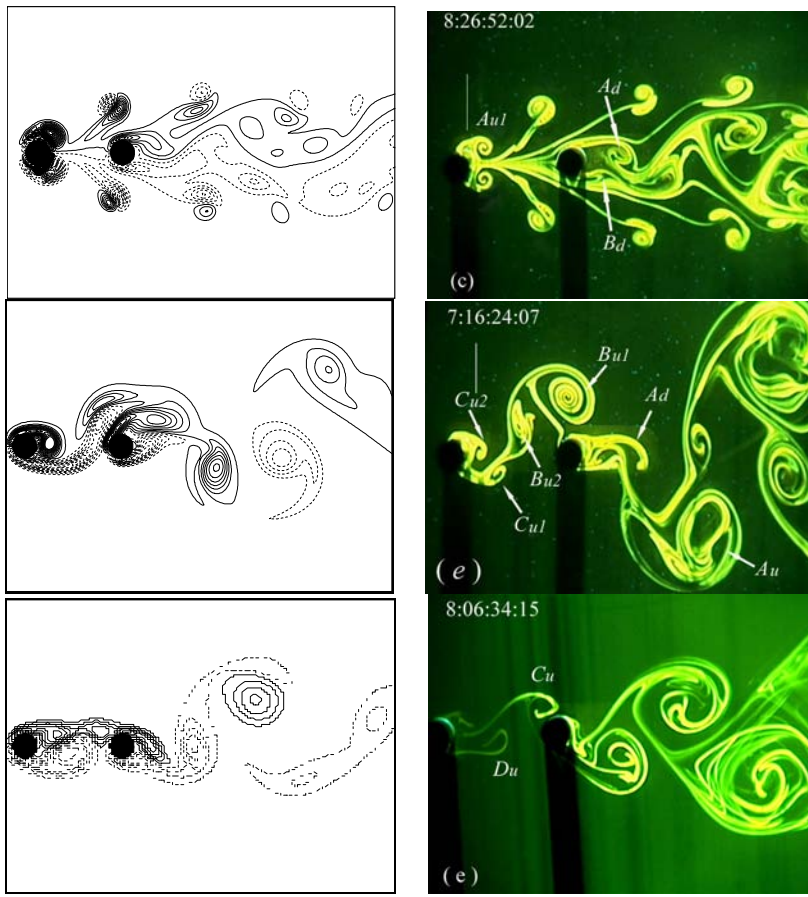

Fig. 4.9. Left: vorticity contours from numerical simulation (Re=150); Right: flow visualizations in a water tunnel using the LIF technique (Courtesy of Y. Zhou). $A/D = 0.5$, $L/D = 3.5$; $f_e/f_s = 1.8$, 1.08, and 0.5 from top to bottom.

Xu & Zhou [2002] have attempted to examine a two-cylinder system in tandem experimentally. It is reported that three flow regimes can be identified as the cylinder-oscillating amplitude was fixed at 0.5 cylinder diameter while the frequency ratio, f_e/f_s, varied between 0 and 2, where f_e is the oscillating frequency of the upstream cylinder and f_s is the natural vortex shedding frequency of an isolated stationary cylinder. A symmetric binary vortex street was observed in the range of $1.6 \leq f_e/f_s \leq 2$, and

alternative vortex shedding from both cylinders was seen in the cases of $0.8 \leq f_e/f_s < 1.6$ and $0 < f_e/f_s < 0.8$, although the flow structure corresponding to $f_e/f_s = 0.8 \sim 1.6$ is totally different from that at $f_e/f_s = 0 \sim 0.8$. Due to the limitation of experiments, many aspects of the physics for this flow remain to be clarified. For example, there was insufficient information on how the oscillating amplitude of the upstream cylinder and the spacing between the cylinders would affect the flow structure, the information about the pressure field was not clear, too. Furthermore, the dependence on the flow regimes of the drag and lift forces on the cylinders was not easy to measure.

Guo and Zhou [2004] conducted a numerical investigation on this flow using the D2Q9 LBGK model. The simulations are carried out in a two-dimensional space at the same conditions as [Xu and Zhou, 2002]. Two circular cylinders with an identical diameter D are placed in a cross flow in tandem, and the center-to-center spacing of them is set to be $3.5D$. The upstream cylinder oscillates harmonically in the streamwise direction at a fixed amplitude of $A/D = 0.5$. The Reynolds number based on D and the free-stream velocity U is $150 \sim 300$ (the flow is essentially

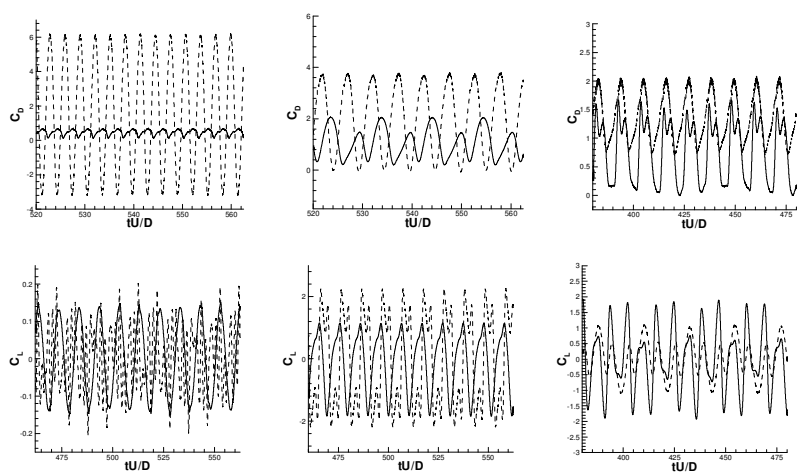

Fig. 4.10. Time histories of the drag and lift coefficients of the upstream and downstream cylinders with $A/D = 0.5$, $L/D = 3.5$. (a) $f_e/f_s = 1.8$, (b) $f_e/f_s = 1.08$, (c) $f_e/f_s = 0.5$. Dashed line: upstream cylinder; Solid line: downstream cylinder.

laminar) and f_e/f_s ranges between 0.5 and 1.8. The computational domain is a $40D \times 20D$ rectangular area.

Figure 4.9 compares the calculated flow structure with the experimental data [Xu and Zhou, 2002]. The three flow regimes based on the distinctive flow patterns identified by Xu & Zhou [2002] are reproduced numerically. The excellent agreement in the flow structure between the numerical and experimental data provides a validation for the present numerical scheme. In all cases, vortex shedding from the upstream cylinder is locked on with the cylinder oscillation.

At $f_e/f_s = 1.8$, vortices shed from the upstream cylinder are symmetrically arranged; each structure embraces a pair of counter-rotating vortices (binary vortices). The flow behind the downstream cylinder is characterized by a binary street, consisting of two inner rows of alternately arranged vortices and two outer rows of symmetrically arranged binary vortices. The spatial arrangement of vortices about the centerline results in a lift coefficient, C_L, of no more than 0.2 on either cylinder (Fig. 4.10a). The drag coefficient, C_D, on the downstream cylinder is small but very large on the upstream cylinder (Fig. 4.10b). Correspondingly, the time-averaged lift coefficient, $\overline{C}_L$, and root mean square value, C_L', are small on both cylinders. On the other hand, the time-averaged drag coefficient, $\overline{C}_D$, and root mean square value, C_D', are both very large on the upstream cylinder. Although $\overline{C}_D$ on the downstream cylinder is 0.46, smaller than that (about 1) on an isolated circular cylinder, the corresponding C_D' reaches 0.48, one order of magnitude larger than its counterpart of a single cylinder.

As f_e/f_s reduces to 1.08, alternative vortex shedding occurs from both cylinders. The flow structure behind the downstream cylinder is characterized by two rows of vortices: one consisting of single vortices, and the other consisting of counter-rotating vortex pairs. The maximum C_L and C_D (Fig. 4.10b) on the downstream cylinder increase significantly, compared with $f_e/f_s = 1.8$. While the corresponding $\overline{C}_L$ is small, and C_L' increases greatly, exceeding that (0.45~0.75 for $\mathrm{Re} = 200 \sim 700$, Chen 1978) on a single cylinder, as a result from alternating vortex shedding associated with both cylinders. Interestingly, $\overline{C}_D$ as well as C_D' climbs considerably.

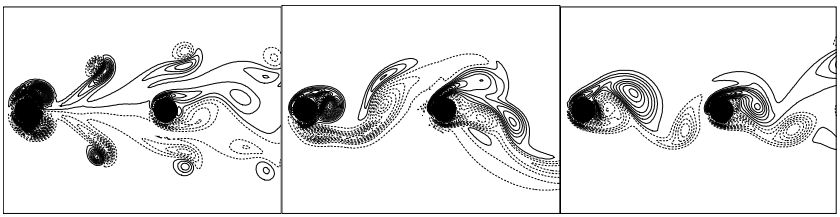

(a) (b) (c)

Fig. 4.11. Vorticity contours at $L/D = 6$ ($A/D = 0.5$, Re=150). (a) $f_e/f_s = 1.8$; (b) $f_e/f_s = 1.08$; (c) $f_e/f_s = 0.5$.

For $f_e/f_s = 0.5$, alternative vortex shedding occurs for both cylinders. The successive vortices shed from the upstream cylinders will hit the downstream cylinder alternatively, forming a single staggered street downstream. While the maximum C_D on the downstream cylinder is smaller than that at f_e/f_s =1.08, the maximum C_L increases marginally. Accordingly, $\overline{C}_D$ and C'_D reduce appreciably, and C'_L increases slightly.

Zdravkovich [1987] classified flows around two tandem stationary cylinders into three flow regimes based on the behaviors of the free shear layers separated from the upstream cylinder. The free shear layers do not reattach on the downstream cylinder and roll up behind it to form the vortex street for $1 < L/D < 1.2 \sim 1.8$, where the upper limit is dependent on Re; they reattach on the upstream side of the downstream cylinder for $1.2 \sim 1.8 < L/D < 3.4 \sim 3.8$. When L/D exceeds $3.4 \sim 3.8$, the shear layers roll up alternately, forming vortices between the cylinders, both cylinders generating vortices. Evidently, the flow structures at $L/D = 3.5$, shown in Fig. 4.9, fall into the third regime, that is, vortices are generated between the cylinders and behind the downstream cylinder, irrespective of the f_e/f_s value.

Simulations are also performed to investigate the effects of center-to-center spacing. At $L/D = 6.0$, the shear layers separated from the upstream cylinder are expected to have sufficient space to form vortices before reaching the downstream cylinder. Therefore, given the same A/D, the flow structures are likely to resemble those at $L/D = 3.5$. The flow structures (Fig. 4.11) are indeed qualitatively the same as those in Fig. 4.9 for the same f_e/f_s. Nevertheless, there is a slight increase in the

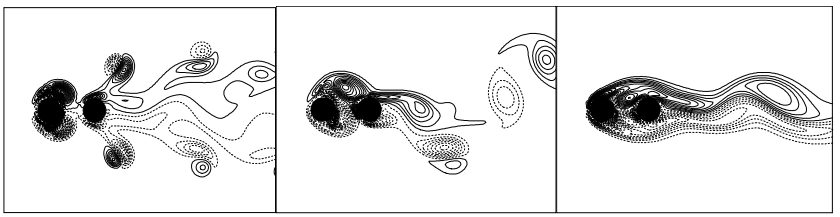

(a) (b) (c)

Fig. 4.12. Vorticity contours at $L/D = 2$ (A/D $= 0.5$, Re=150): (a) $f_e/f_s = 1.8$; (b) $f_e/f_s = 1.08$; (c) $f_e/f_s = 0.5$.

maximum spanwise vorticity due to a larger L/D. For example, the normalized maximum vorticity $\omega_z D/U$ increases from 1.09 at $L/D = 3.5$ to 1.15 at $L/D = 6$ for $f_e/f_s = 1.8$, from 0.35 at $L/D = 3.5$ to 0.63 at $L/D = 6$ for $f_e/f_s = 1.08$, and from 0.25 at $L/D = 3.5$ to 0.5 at $L/D = 6$.

As $L/D = 2.0$, it is found that at $f_e/f_s = 1.8$ the shear layers separated from the upstream cylinder manage to form two binary structures, symmetrically arranged about the centerline, before reaching the downstream cylinder. As a result, the flow structure (Fig. 4.12) at $L/D = 2.0$ is qualitatively the same as that (Fig. 4.9) at $L/D = 3.5$. As f_e/f_s reduces to 1.08, the rolling-up shear layers separated from the upstream cylinder reattach on the upstream side of the downstream cylinder before completely forming vortices (Fig. 4.11b). The flow structure between the cylinders is thus not quite the same as that at $L/D = 3.5$. Nonetheless, the flow structure behind the downstream cylinder is qualitatively the same (c.f. Fig. 4.9).

A further reduction in f_e/f_s to 0.5 results in a completely different flow structure. The two free shear layers separated from the upstream cylinder (Fig. 4.11c) now roll up symmetrically about the centerline and, before the complete formation of vortices, reattach on the upstream side of the downstream cylinder. As a matter of fact, the free shear layers also tend to separate, symmetrically with respect to the centerline, from the downstream cylinder. Consequently, the flow structure behind the downstream cylinder is rather different from that at $L/D = 3.5$.

4.5 Summary

The simplicity in programming has been recognized as an advantage of LBE method in simulating fluid flows. In this chapter the algorithm structure and basic subroutines of LBE are presented. Several examples, including the lid-driven cavity flow, the flow around a fixed circular cylinder, and the flow around an oscillating cylinder with a downstream cylinder of identical diameter, are presented. The results of LBE are compared with other numerical and/or experimental data reported in the literature. These results demonstrate that LBE is a viable method for incompressible fluid flow simulation.

It should be noted that the algorithm presented in this chapter is an elementary implementation and is not optimized. Some methods to improve the performance of LBE have been developed from different viewpoints. For example, Pohl *et al*. [2003] employed a grid compression technique to raise cache hit rate. Mattila *et al.* [2007] introduced a swap algorithm to reduce memory consumption. Some parallel algorithms were also developed for LBE on different computer architectures [e.g., Desplat *et al*., 2001; Kandhai *et al.*, 1998; Wellein *et al*., 2005]. The most recent trend in this direction is the use of graphics processing unit (GPU) architectures, which are ideally suited for LBE [Bernaschi *et al*., 2009; Li *et al.*, 2004; Tölke, 2009; Zhao, 2008].

Chapter 5

LBE for Low Speed Flows with Heat Transfer

The LBE method has achieved great successes for isothermal or athermal flows where temperature variations are ignored. In many scientific and engineering problems, however, heat transfer is important or may be dominant. Many efforts have been devoted to extend LBE to such flows. In general, the existing LBE models for thermal flows can be classified into three categories, i.e., multi-speed (MS) models, double-distribution-function (DDF) models, and hybrid models.

In MS-LBE models, the fluid density, velocity, and temperature are obtained from zeroth through second velocity moments of the distribution function f_i. Usually, in order to obtain the macroscopic evolution equation of the temperature, a MS-LBE uses a larger set of discrete velocities than that used in the corresponding isothermal model, and the lattice can be decomposed into a set of basic sub-lattices (such as square, hexagon, or cube), with identical link length in each sub-lattice. In addition, the equilibrium distribution function (EDF) of the MS-LBE model includes higher order velocity terms which are absent in that of an isothermal model. A major shortage of the early MS-LBE models which employ certain BGK collision operators is that the Prandtl number is fixed. Some later models have overcome this problem, but the viscosity appearing in the viscous dissipation in the energy equation may be incorrect. Another shortcoming of the MS-LBE models is that the numerical stability is not satisfied, which severely limits their applications.

In contrast, the DDF-LBE and hybrid models can effectively overcome the aforementioned two limitations of the MS-LBE models. In the DDF-LBE model, two types of distribution functions are used to

describe the evolutions of the velocity and temperature, respectively. The LBE for the velocity is usually the same as the isothermal model, and that for the temperature solves an advection-diffusion equation with the same lattice or a simpler one. It has been demonstrated that the DDF-LBE has a better numerical stability and can achieve a wider temperature range than the MS-LBE. A major deficiency of DDF-LBE model is that the equation of state is independent of temperature so that such models are intrinsically only suitable for Boussinesq flows. Similar to DDF-LBE, hybrid LBE models also treat the energy equation separately, and solve it by some standard numerical schemes such as finite-difference method. An advantage of this approach is that the pressure can be coupled with the temperature explicitly.

As can be seen, all of the available thermal LBE models have their own advantages and disadvantages, so that further developments and refinements are still in need. In this chapter, we will present some basic thermal LBE models.

5.1 Multi-speed Models

Earlier MS-LBE models usually adopt a lattice based on those of isothermal models by including some new discrete velocities so that the particles can move to farther neighboring grid points. In these models, the discrete velocities are coupled with the associated lattices, and so such models are also termed as *space-filling* models. According to the terms of velocity expansion in the EDF, MS-LBE models can be classified into low-order models and high-order ones. In the former type the EDF contains some terms up to $O(\boldsymbol{u}^3)$, while the latter type contains terms up to $O(\boldsymbol{u}^4)$, where $\boldsymbol{u}$ is the fluid velocity. It can be shown that the corresponding macroscopic equations of the low-order models may contain some undesirable artifacts, while those of the high-order MS-LBE models have no such problem.

5.1.1 *Low-order models*

The first MS-LBE model was proposed by Alexander *et al*. [1993]. This is a two-dimensional model (referred to as ACS model) containing 13

discrete velocities associated with two hexagons with links of length c and $2c$, respectively:

$$\boldsymbol{c}_0 = (0,0)\,,\ \boldsymbol{c}_{\sigma i} = \sigma\Big(\cos\theta_i,\ \sin\theta_i\Big)c\,,\ \theta_i = i\pi/3\,,\ i = 1\sim 6\,,\ \sigma = 1,2\,, \tag{5.1}$$

where $c = \delta_x/\delta_t$ is the lattice speed and we will assume $c = 1$ in the following sections without statement otherwise. The BGK collision operator is adopted in the ACS model, i.e.,

$$f_{\sigma i}(\boldsymbol{x} + \boldsymbol{c}_{\sigma i}\delta_t, t+\delta_t) - f_{\sigma i}(\boldsymbol{x},t) = -\frac{1}{\tau}\Big[f_{\sigma i}(\boldsymbol{x},t) - f_{\sigma i}^{(eq)}(\boldsymbol{x},t)\Big], \tag{5.2}$$

where the equilibrium distribution function is defined by

$$f_{\sigma i}^{(eq)} = A_\sigma + B_\sigma \boldsymbol{c}_{\sigma i}\cdot\boldsymbol{u} + C_\sigma(\boldsymbol{c}_{\sigma i}\cdot\boldsymbol{u})^2 + D_\sigma u^2 + E_\sigma(\boldsymbol{c}_{\sigma i}\cdot\boldsymbol{u})^3 + F_\sigma(\boldsymbol{c}_{\sigma i}\cdot\boldsymbol{u})u^2\,. \tag{5.3}$$

Here the fluid velocity is still defined by $\rho\boldsymbol{u} = \sum_{\sigma i}\boldsymbol{c}_{\sigma i}f_{\sigma i}$, and the coefficients $A_\sigma \sim F_\sigma$ are functions of the local density $\rho = \sum_{\sigma i} f_{\sigma i}$ and the internal energy $\rho e = \frac{1}{2}\sum_{\sigma i}|\boldsymbol{c}_{\sigma i} - \boldsymbol{u}|^2 f_{\sigma i}$. These coefficients should be chosen so that the following constraints are satisfied:

$$\begin{aligned}
&\sum_{\sigma i} f_{\sigma i}^{(eq)} = \rho\,,\ \sum_{\sigma i}\boldsymbol{c}_{\sigma i}f_{\sigma i}^{(eq)} = \rho\boldsymbol{u}\,,\ \frac{1}{2}\sum_{\sigma i}|\boldsymbol{c}_{\sigma i} - \boldsymbol{u}|^2 f_{\sigma i}^{(eq)} = \rho e\,,\\
&\sum_{\sigma i}\boldsymbol{c}_{\sigma i}\boldsymbol{c}_{\sigma i}f_{\sigma i}^{(eq)} = \rho\boldsymbol{u}\boldsymbol{u} + \rho e\,,\ \sum_{\sigma i}|\boldsymbol{c}_{\sigma i} - \boldsymbol{u}|^2(\boldsymbol{c}_{\sigma i} - \boldsymbol{u})f_{\sigma i}^{(eq)} = 0\,.
\end{aligned} \tag{5.4}$$

One possible solution is [Alexander *et al*., 1993]:

$$A_0 = \frac{\rho}{2}\big(2 - 5e + 4e^2\big),\quad A_1 = \frac{4\rho}{9}\big(e - e^2\big),\quad A_2 = \frac{\rho}{36}\big(-e + 4e^2\big),$$

$$B_1 = \frac{4\rho}{9}\big(1 - e\big),\quad B_2 = \frac{\rho}{36}\big(-1 + 4e\big),$$

$$C_1 = \frac{4\rho}{9}\big(2 - 3e\big),\quad C_2 = \frac{\rho}{72}\big(-1 + 6e\big),$$

$$D_0 = \frac{\rho}{4}\big(-5 + 8e\big),\quad D_1 = \frac{2\rho}{9}\big(-1 + e\big),\quad D_2 = \frac{\rho}{72}\big(1 - 4e\big),$$

$$E_1 = -\frac{4\rho}{27},\quad E_2 = \frac{\rho}{108},\quad F_1 = F_2 = 0.$$

With the above parameters, it can be shown that the macroscopic equations of the ACS model are

$$\frac{\partial \rho}{\partial t} + \nabla \cdot (\rho \boldsymbol{u}) = 0\,, \tag{5.5}$$

$$\frac{\partial (\rho \boldsymbol{u})}{\partial t} + \nabla \cdot (\rho \boldsymbol{u}\boldsymbol{u}) = -\nabla p + \nabla \cdot \boldsymbol{\tau}\,, \tag{5.6}$$

$$\frac{\partial (\rho e)}{\partial t} + \nabla \cdot (\rho \boldsymbol{u} e) = -p \nabla \cdot \boldsymbol{u} + \nabla \cdot q + \boldsymbol{\tau} : \nabla \boldsymbol{u}\,, \tag{5.7}$$

where $p = \rho e$, and the viscous stress $\boldsymbol{\tau}$ and the heat flux $\boldsymbol{q}$ are given by

$$\boldsymbol{\tau} = 2\mu \boldsymbol{S} + \mu'(\nabla \cdot \mu)\boldsymbol{I}\,, \quad \boldsymbol{q} = \kappa \nabla T\,, \tag{5.8}$$

in which the first and second dynamic viscosities and the thermal conductivity are given by

$$\mu = \rho\left(\tau - \frac{1}{2}\right)e\,,\ \mu' = -\mu\,,\ \kappa = 2\mu\,. \tag{5.9}$$

It is easy to check that the specific heat capacities of the ACS model are $c_p = (D+2)R/2$ and $c_v = DR/2$, respectively, which means that the Prandtl number is $\mathrm{Pr} = \mu c_p/\kappa = 1$. This limitation is due to the use of the single relaxation BGK model for the collision, and other MS-LBGK models also suffer from this problem.

Soon after the emergence of the ACS model, Qian [1993] developed a series of MS-LBE models based on the D*n*Q*b*-LBGK isothermal models. The lattice employed in such a model is usually composed of a group of sub-lattices L_σ, each of which having b_σ links with length $\sqrt{\sigma} = c_\sigma$. For example, the lattice used in the D2Q13 model is composed of 4 sub-lattices with $\sigma = 0,\ 1,\ 2$ and 4, respectively (Fig. 5.1). Generally, the EDF of Qian's MS-LBE models can be expressed as

$$f_{\sigma_i}^{(eq)} = \rho\left[A_\sigma + B_\sigma(\boldsymbol{c}_{\sigma i} \cdot \boldsymbol{u}) + \omega_\sigma \frac{(\boldsymbol{c}_i \cdot \boldsymbol{u})^2 - c_s^2 u^2}{2c_s^4} + D_\sigma(\boldsymbol{c}_{\sigma i} \cdot \boldsymbol{u})u^2\right], \tag{5.10}$$

where ω_σ is the same as that used in the isothermal *DnQb*-LBGK model. The undetermined coefficients A_σ, B_σ, and D_σ satisfy the following

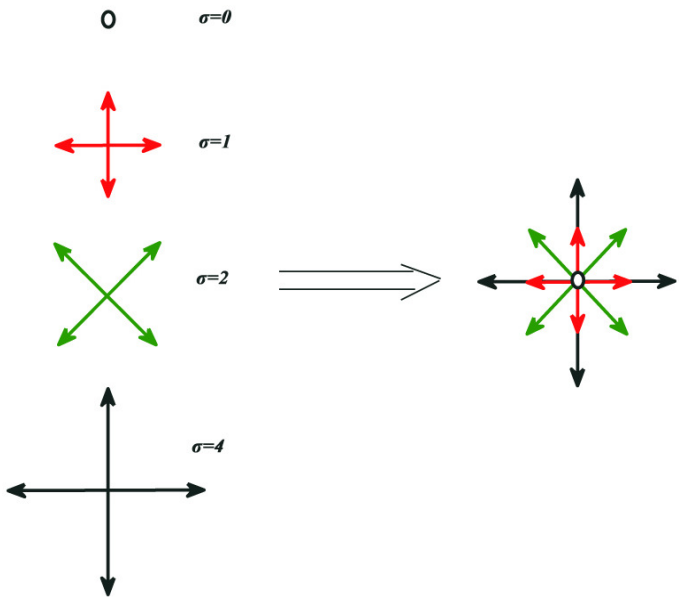

Fig. 5.1. D2Q13 lattice form structure.

conservation constraints,

$$\sum_{\sigma} b_{\sigma} A_{\sigma} = 1\,,\ \frac{1}{2}\sum_{\sigma} \sigma^2 b_{\sigma} A_{\sigma} = e\,,\ \sum_{\sigma} \sigma^2 b_{\sigma} B_{\sigma} = D\,,\ \frac{1}{2}\sum_{\sigma} \sigma^2 b_{\sigma} D_{\sigma} = 0\,, \quad (5.11)$$

where D is the spatial dimensions. The number of links of the sub-lattice (or sub-discrete velocities in L_{σ}) b_{σ} depends on the model and the spatial dimension. For example, for the D2Q13 model shown in Fig. 5.1, $b_0 = 1$ and $b_1 = b_2 = b_4 = 4$. Furthermore, the following additional constraints must be satisfied in order to obtain correct transport coefficients,

$$\sum_{\sigma} \sigma^4 b_{\sigma} A_{\sigma} = 2(D+2)se^2\,,\ \sum_{\sigma} \sigma^4 b_{\sigma} B_{\sigma} = D(D+2)se\,, \quad (5.12)$$

where s is an adjustable parameter. Based on these arguments, Qian proposed a set of D*n*Q*b* MS-LBGK models, which are listed as follows.

(1) D1Q5 model

The discrete velocities are given by $c = [0, \pm 1, \pm 2]$, and the parameters in

the EDF are

$$\omega_0 = \frac{1}{2}, \quad \omega_1 = \frac{1}{6}, \quad \omega_4 = \frac{1}{12}, \quad c_s^2 = 1,$$
$$A_0 = 1 - \frac{5e}{2} + 3e^2, \quad A_1 = \frac{4e}{3} - 2e^2, \quad A_4 = -\frac{e}{12} + \frac{e^2}{2},$$
$$B_1 = \frac{2}{3} - \frac{se}{2}, \quad B_4 = -\frac{1}{24} + \frac{se}{24}, \quad D_1 = -\frac{1}{6}, \quad D_4 = \frac{1}{24} \ .$$

(2) D2Q13 model

The discrete velocities include those of the isothermal D2Q9 model and 4 additional velocities along the x and y directions with modulus 2 (i.e. the sub-lattice with $\sigma = 4$ in Fig. 5.1),

$$\boldsymbol{c}_{4i} = \begin{bmatrix} 2 & -2 & 0 & 0 \\ 0 & 0 & 2 & -2 \end{bmatrix}.$$

The parameters of the EDF are given by

$$\omega_0 = \frac{4}{9}, \quad \omega_1 = \frac{1}{9}, \quad \omega_2 = \frac{1}{36}, \quad c_s^2 = \frac{1}{3},$$
$$A_0 = 1 - \frac{5e}{2} + \frac{9e^2}{4}, \quad A_1 = \frac{2e}{3} - \frac{5e^2}{6}, \quad A_2 = \frac{e^2}{8}, \quad A_4 = -\frac{e}{24} + \frac{7e^2}{48},$$
$$B_1 = \frac{2}{3} - se, \quad B_2 = \frac{se}{4}, \quad B_4 = -\frac{1}{24} + \frac{se}{8},$$
$$D_1 = -\frac{1}{18}, \quad D_2 = -\frac{1}{12}, \quad D_4 = \frac{1}{18} \ .$$

(3) D3Q21 model

The discrete velocities include those of the D3Q15 model and 6 additional velocities along the x, y, and z axes with modulus 2,

$$\boldsymbol{c}_{4i} = \begin{bmatrix} 2 & -2 & 0 & 0 & 0 & 0 \\ 0 & 0 & 2 & -2 & 0 & 0 \\ 0 & 0 & 0 & 0 & 2 & -2 \end{bmatrix},$$

and the parameters of the EDF are given by

$$\omega_0 = \frac{2}{9}, \quad \omega_1 = \frac{1}{9}, \quad \omega_3 = \frac{1}{72}, \quad c_s^2 = \frac{1}{3},$$
$$A_0 = 1 - \frac{5e}{2} + \frac{11e^2}{4}, \quad A_1 = \frac{4e}{9} - \frac{23e^2}{36}, \quad A_3 = \frac{e^2}{16},$$
$$A_4 = -\frac{e}{36} + \frac{7e^2}{72} \quad B_1 = \frac{2}{3} - se, \quad B_3 = \frac{se}{8}, \quad B_4 = -\frac{1}{24} + \frac{se}{8},$$
$$D_1 = -\frac{1}{36}, \quad D_3 = -\frac{5}{36}, \quad D_4 = \frac{1}{18} \ .$$

(4) D3Q25 model

The discrete velocities include those of the D3Q19 model with 6 additional ones of modulus 2 along the x, y, and z axis. The weight coefficients and parameters of the EDF are:

$$\omega_0 = \frac{1}{3}, \quad \omega_1 = \frac{1}{18}, \quad \omega_2 = \frac{1}{36}, \quad c_s^2 = \frac{1}{3},$$
$$A_0 = 1 - \frac{5e}{2} + 3e^2, \quad A_1 = \frac{4e}{9} - \frac{7e^2}{9}, \quad A_2 = \frac{e^2}{12}, \quad A_4 = -\frac{e}{36} + \frac{e^2}{9},$$
$$B_1 = \frac{2}{3} - \frac{3se}{2}, \quad B_2 = \frac{se}{4}, \quad B_4 = -\frac{1}{24} + \frac{se}{8},$$
$$D_1 = 0, \quad D_2 = -\frac{1}{16}, \quad D_4 = \frac{1}{16} \ .$$

In the above EDF, the parameter s can be adjusted with some freedom. In the original models by Qian [1993], s is set to be 1 in all of the models except for the D1Q5 one which takes $s = 2$. With these parameters, the thermohydrodynamic equations derived from Qian's MS-LBGK models through the Chapman-Enskog expansion have the following form,

$$\partial_t \rho + \partial_\beta(\rho u_\beta) = 0 \,, \tag{5.13}$$

$$\partial_t(\rho u_\alpha) + \partial_\beta(\rho u_\alpha u_\beta) = -\partial_\alpha p + \partial_\beta\big[\nu\partial_\beta(\rho u_\alpha) + \zeta\partial_\alpha(\rho u_\beta)\big], \tag{5.14}$$

$$\partial_t(\rho e) + \partial_\beta(\rho u_\beta e) = -p\partial_\beta u_\beta + \partial_\beta(\kappa\partial_\beta e) + \partial_\alpha\Big\{u_\beta\big[\nu\partial_\beta(\rho u_\alpha) + \zeta\partial_\alpha(\rho u_\beta)\big]\Big\}, \tag{5.15}$$

where $p = (2/D)\rho e = c_s^2\rho$ is the pressure, and the transport coefficients are given by

$$\nu = \left(\tau - \frac{1}{2}\right)se,\ \ \zeta = 2\left(s - \frac{2+D}{D^2}\right)\left(\tau - \frac{1}{2}\right)e,\ \ \kappa = \frac{D+2}{D}\left(\tau - \frac{1}{2}\right)\rho e. \tag{5.16}$$

5.1.2 *High-order models*

In the low-order MS LBE models given above, the EDFs only involve terms up to $O(\boldsymbol{u}^3)$. Chen *et al.* [1994] found that, however, the EDF should contain terms of in order to obtain the correct momentum flux and heat flux for deriving macroscopic equations, i.e.,

$$\begin{aligned} f_{\sigma_i}^{(eq)} = A_\sigma &+ B_\sigma(\boldsymbol{c}_{\sigma i}\cdot\boldsymbol{u}) + C_\sigma u^2 + D_\sigma(\boldsymbol{c}_{\sigma i}\cdot\boldsymbol{u})^2 + E_\sigma(\boldsymbol{c}_{\sigma i}\cdot\boldsymbol{u})u^2 \\ &+ F_\sigma(\boldsymbol{c}_{\sigma i}\cdot\boldsymbol{u})^3 + G_\sigma(\boldsymbol{c}_{\sigma i}\cdot\boldsymbol{u})^2u^2 + H_\sigma u^4, \end{aligned} \tag{5.17}$$

where the undetermined coefficients $A_\sigma \sim H_\sigma$ are quadratic polynomials of the internal energy that can be expressed as,

$$X_\sigma = \rho(x_{\sigma 0} + x_{\sigma 1}e + x_{\sigma 2}e^2)\,. \tag{5.18}$$

Furthermore, the following constraints are required [Chen *et al.*, 1994],

$$\sum_{\sigma i} f_{\sigma i}^{(eq)} = \rho, \quad \sum_{\sigma i}\boldsymbol{c}_{\sigma i}f_{\sigma i}^{(eq)} = \rho\boldsymbol{u}, \quad \sum_{\sigma i}\boldsymbol{c}_{\sigma i}\boldsymbol{c}_{\sigma i}f_{\sigma i}^{(eq)} = \rho\boldsymbol{u}\boldsymbol{u} + p\boldsymbol{I}, \tag{5.19}$$

$$\sum_{\sigma i}\boldsymbol{c}_{\sigma i}\boldsymbol{c}_{\sigma i}\boldsymbol{c}_{\sigma i}f_{\sigma i}^{(eq)} = \rho\boldsymbol{u}\boldsymbol{u}\boldsymbol{u} + p[\boldsymbol{u}\boldsymbol{\delta}], \tag{5.20}$$

$$\sum_{\sigma i}\boldsymbol{c}_{\sigma i}\boldsymbol{c}_{\sigma i}c_{\sigma i}^2 f_{\sigma i}^{(eq)} = \rho\boldsymbol{u}\boldsymbol{u}u^2 + p(D+4)\boldsymbol{u}\boldsymbol{u} + pu^2\boldsymbol{I} + \frac{2(D+2)}{D}pe, \tag{5.21}$$

where $p = (2/D)\rho e$ and $[\boldsymbol{u}\boldsymbol{\delta}]_{\alpha\beta\gamma} = u_\alpha\delta_{\beta\gamma} + u_\beta\delta_{\alpha\gamma} + u_\gamma\delta_{\beta\alpha}$. In order to meet the above conditions, Chen *et al.* pointed out that the discrete velocity set should have enough symmetry. More specifically, the velocity tensors

$$T_\sigma^n \equiv \sum_i \overbrace{\boldsymbol{c}_{\sigma i}\ \boldsymbol{c}_{\sigma i}\cdots\ \boldsymbol{c}_{\sigma i}}^{n},\ ,\ \ n = 0,\ 1,\ .....,\ 6, \tag{5.22}$$

must be all isotropic (note that the low order models can only give the $0\sim4$-th order isotropic tensors). To achieve this purpose, Chen *et al.* chose a composite lattice based on a D-dimensional unit cube to define

the discrete velocity set,

$$\boldsymbol{c}_{\sigma i} = \boldsymbol{c}'_{pki} \in \mathrm{Perm}\{k(\underbrace{\pm 1, \pm 1, \cdots, \pm 1}_{p}, \overbrace{0, \cdots, 0, 0}^{D-p})\}, \tag{5.23}$$

where the operator "Prem(·)" represents a set composed of all the possible permutations of (·), k is a scaling coefficient of the basic lattice, and it is clear that $\sigma = c_{\sigma i}^2 = k^2 p$. For example, for the D2Q13 lattice shown in Fig. 5.1, the velocities of the sub-lattices (from top to bottom) are $\boldsymbol{c}_0 = \boldsymbol{c}'_0$, $\boldsymbol{c}_{1i} = \boldsymbol{c}'_{11i}$, $\boldsymbol{c}_{2i} = \boldsymbol{c}'_{21i}$, and $\boldsymbol{c}_{4i} = \boldsymbol{c}'_{12i}$, respectively.

Based on such lattices and EDF, Chen *et al*. [1994] developed a series of 1~3 dimensional D*n*Q*b* MS-LBGK models, which are listed below.

(1) D1Q5 model

Discrete velocities: $c = [0, \pm 1, \pm 2]$.

Parameters in the EDF:

$$A_0 = 1 - \frac{5e}{2} + 3e^2, \quad A_1 = \frac{4e}{3} - 2e^2, \quad A_4 = -\frac{e}{12} + \frac{e^2}{2},$$

$$B_1 = \frac{2}{3} - e, \quad B_4 = -\frac{1}{24} + \frac{e}{4},$$

$$C_0 = -\frac{5}{4} + 3e, \quad C_1 = -\frac{1}{3} + \frac{e}{2}, \quad C_4 = \frac{1}{48} - \frac{e}{8},$$

$$D_1 = 1 - \frac{5e}{2}, \quad D_4 = -\frac{1}{64} + \frac{5e}{32}, \quad E_1 = -\frac{17}{12}, \quad E_4 = \frac{1}{24},$$

$$F_1 = \frac{5}{4}, \quad G_1 = -\frac{1}{4}, \quad G_4 = \frac{1}{64}, \quad H_0 = \frac{1}{4}, \quad H_1 = \frac{1}{12}, \quad H_4 = -\frac{1}{48}.$$

(2) D2Q16 model

Discrete velocities:

$$\boldsymbol{c}_{1i} = \boldsymbol{c}'_{11i} \in \mathrm{Prem}\{(\pm 1, 0)\}, \boldsymbol{c}_{2i} = \boldsymbol{c}'_{21i} \in \mathrm{Prem}\{(\pm 1, \pm 1)\},$$

$$\boldsymbol{c}_{4i} = \boldsymbol{c}'_{12i} \in \mathrm{Prem}\{2(\pm 1, 0)\}, \boldsymbol{c}_{8i} = \boldsymbol{c}'_{22i} \in \mathrm{Prem}\{2(\pm 1, \pm 1)\}.$$

Parameters in the EDF:

$$C_1 = -\frac{2}{3} + \frac{5e}{6}, \quad C_2 = \frac{1}{6} - \frac{7e}{24}, \quad C_4 = \frac{1}{24} - \frac{e}{12}, \quad C_8 = -\frac{1-e}{96},$$

$$D_1 = \frac{2}{3} - e, \quad D_2 = \frac{1}{6} - \frac{e}{8}, \quad D_4 = -\frac{1}{96} + \frac{e}{16}, \quad D_8 = -\frac{1}{384} + \frac{e}{128},$$
$$E_1 = -\frac{1}{2}, \quad E_2 = -\frac{1}{8}, \quad E_4 = E_8 = 0,$$
$$F_1 = \frac{1}{3}, \quad F_2 = \frac{1}{8}, \quad F_4 = \frac{1}{96}, \quad F_8 = 0,$$
$$G_1 = -\frac{1}{6}, \quad G_2 = -\frac{1}{48}, \quad G_4 = -\frac{1}{96}, \quad G_8 = -\frac{1}{768},$$
$$H_1 = \frac{1}{8}, \quad H_2 = -\frac{1}{32}, \quad H_4 = -\frac{1}{64}, \quad H_8 = 0.$$

(3) D3Q40 model

Discrete velocities:

$$\boldsymbol{c}_{1i} = \boldsymbol{c}'_{11i} \in \mathrm{Prem}\{(\pm 1, 0, 0)\}, \quad \boldsymbol{c}_{2i} = \boldsymbol{c}'_{21i} \in \mathrm{Prem}\{(\pm 1, \pm 1, 0)\},$$
$$\boldsymbol{c}_{3i} = \boldsymbol{c}'_{31i} \in \mathrm{Prem}\{(\pm 1, \pm 1, \pm 1)\}, \quad \boldsymbol{c}_{4i} = \boldsymbol{c}'_{12i} \in \mathrm{Prem}\{2(\pm 1, 0, 0)\},$$
$$\boldsymbol{c}_{12i} = \boldsymbol{c}'_{32i} \in \mathrm{Prem}\{2(\pm 1, \pm 1, \pm 1)\}.$$

Parameters in the EDF:

$$A_1 = \frac{4}{15} - \frac{29e}{36} + \frac{8e^2}{135}, \quad A_2 = \frac{5e}{8}, \quad A_3 = -\frac{1}{15} - \frac{15e}{16} - \frac{19e^2}{270},$$
$$A_4 = -\frac{1}{60} - \frac{e}{36} + \frac{13e^2}{540}, \quad A_{12} = \frac{1}{240} + \frac{17e^2}{2160},$$
$$B_1 = \frac{2}{3} - e, \quad B_2 = \frac{e}{6}, \quad B_3 = 0, \quad B_4 = -\frac{1}{24} + \frac{e}{12}, \quad B_8 = 0,$$
$$C_1 = -\frac{1}{3} - \frac{7e}{32}, \quad C_2 = \frac{53e}{192}, \quad C_3 = -\frac{23e}{128}, \quad C_4 = \frac{1-2e}{48}, \quad C_{12} = 0,$$
$$D_1 = \frac{2}{3} - \frac{e}{4}, \quad D_2 = \frac{e}{24}, \quad D_3 = \frac{1}{12} - \frac{e}{32}, \quad D_4 = -\frac{1-e}{96},$$
$$D_{12} = -\frac{1}{768} + \frac{e}{1536},$$
$$E_1 = \frac{1}{2}, \quad E_2 = -\frac{1}{8}, \quad E_3 = 0, \quad E_4 = -\frac{3}{64}, \quad E_{12} = 0,$$
$$F_1 = \frac{1}{24}, \quad F_2 = \frac{1}{48}, \quad F_3 = \frac{1}{192}, \quad F_4 = \frac{1}{384}, \quad F_{12} = 0,$$
$$G_1 = -\frac{3}{56}, \quad G_2 = \frac{1}{112}, \quad G_3 = -\frac{3}{448}, \quad G_4 = \frac{3}{448}, \quad G_{12} = -\frac{1}{7168},$$

$$H_1 = -\frac{177}{2240}, \quad H_2 = \frac{401}{4480}, \quad H_3 = -\frac{513}{8960}, \quad H_4 = -\frac{1}{80}, \quad H_{12} = 0.$$

Chen *et al*. [1994] have shown that with the above discrete velocity sets and EDFs, the MS-LBGK models could give the standard compressible Navier-Stokes equations with the following transport coefficients

$$\mu = \frac{2}{D}\left(\tau - \frac{1}{2}\right)\rho e\,,\ \mu' = -\frac{2}{D}\mu\,,\ \kappa = \frac{D+2}{D}\left(\tau - \frac{1}{2}\right)\rho e\,. \qquad (5.24)$$

It is apparent that these high-order MS-LBGK models give a zero bulk viscosity and a unit Prandtl number.

Chen *et al*. [1995] have simulated the thermal Couette flow with both the high-order MS-LBGK models and Qian's low-order models. It is shown that the difference between the results of the two types of models is significant for high Mach number flows, and usually the high-order models could give better predictions. This fact indicates that the terms of $O(\boldsymbol{u}^4)$ in the EDF are critical for high speed flows.

5.2 MS-LBE Models Based on Boltzmann Equation

The MS-LBE models described above are designed in a top-down fashion, i.e. the discrete velocities and the EDFs are determined by enforcing the corresponding macroscopic equations to match the thermohydrodynamic equations with certain accuracy. The parameters determined in this way are somewhat empirical, and it is not an easy task to find these parameters by solving the constraint equations. On the other hand, it is known that the isothermal LBGK models can be obtained from the continuous Boltzmann equation following certain systematic discretization techniques. Similar approach can also be used to establish MS-LBE models [Philippi *et al*., 2006; Shan *et al*., 2006].

5.2.1 *Hermite expansion of distribution function*

From kinetic theory, it is known that the distribution function f for a Maxwell gas can be expanded into a series of Hermite tensor

polynomials, which is defined by

$$H_{\boldsymbol{i}}^{(n)}(\zeta) = (-1)^n \exp\left[\frac{\zeta^2}{2}\right]\left(\frac{\partial}{\partial\zeta_{i_1}}\cdots\frac{\partial}{\partial\zeta_{i_n}}\right)\exp\left[-\frac{\zeta^2}{2}\right] = \frac{(-1)^n}{\omega(\zeta)}\nabla^{(n)}\omega(\zeta), \tag{5.25}$$

where $\boldsymbol{i} = i_1 i_2 \cdots i_n$ and $\omega(\zeta)=(2\pi)^{-D/2}\exp(-\zeta^2/2)$. The first few generalized Hermite polynomials can be easily computed from Eq. (5.25), e.g.,

$$H^{(0)} = 1,\ H_i^{(1)} = \zeta_i,\ H_{ij}^{(2)} = \zeta_i\zeta_j - \delta_{ij},\ H_{ijk}^{(3)} = \zeta_i\zeta_j\zeta_k - [\boldsymbol{\zeta\delta}]_{ijk}, \tag{5.26}$$

where $[\boldsymbol{\zeta\delta}]_{ijk} \equiv \zeta_i\delta_{jk} + \zeta_j\delta_{ik} + \zeta_k\delta_{ij}$. The tensor Hermite polynomials are orthonormal with respect to the weight $\omega(\boldsymbol{\zeta})$, i.e.,

$$\int \omega(\boldsymbol{\zeta}) H_{\boldsymbol{i}}^{(m)}(\boldsymbol{\zeta}) H_{\boldsymbol{j}}^{(n)}(\boldsymbol{\zeta}) d\boldsymbol{\zeta} = \delta_{mn}\delta_{\boldsymbol{ij}}^{(n)}, \tag{5.27}$$

where $\delta_{\boldsymbol{ij}}^{(n)}$ is zero unless $\boldsymbol{i} = (i_1\ i_2 \cdots\ i_m)$ is a permutation of $\boldsymbol{j} = (j_1\ j_2 \cdots j_n)$.

The Maxwellian distribution function $f^{(eq)}(\boldsymbol{x},\boldsymbol{\xi},t)$ can be expanded in terms of Hermite polynomials as [Harris, 1971],

$$f^{(eq)}(\boldsymbol{x},\boldsymbol{\xi},t) = f^M(\boldsymbol{\vartheta},\boldsymbol{\eta})\sum_{n=0}^{\infty}\frac{1}{n!}\boldsymbol{a}_{\boldsymbol{i}}^{(n)}(\boldsymbol{x},t)H_{\boldsymbol{i}}^{(n)}(\boldsymbol{\eta}), \tag{5.28}$$

where the expansion coefficients are functions of time and space,

$$\boldsymbol{a}_{\boldsymbol{i}}^{(n)} = \rho^{-1}\int f^{(eq)}(\boldsymbol{\xi}) H_{\boldsymbol{i}}^{(n)}(\boldsymbol{\eta}) d\boldsymbol{\xi}. \tag{5.29}$$

In Eq. (5.28), f^M is the local Maxwellian distribution function in the form of

$$f^M(\vartheta,\boldsymbol{\eta}) = \frac{\rho}{(2\pi\vartheta)^{D/2}}\exp\left(-\frac{\eta^2}{2}\right), \tag{5.30}$$

where the parameters ϑ and $\boldsymbol{\eta}$ can have different choices. Three types of ϑ and $\boldsymbol{\eta}$ were suggested by Philippi *et al*. [2006],

- A: $\vartheta = \theta = RT$ and $\boldsymbol{\eta} = (\boldsymbol{\xi} - \boldsymbol{u})/\sqrt{\theta}$.
- B: $\vartheta = \theta$ and $\boldsymbol{\eta} = \boldsymbol{\xi}/\sqrt{\theta}$.
- C: $\vartheta = \theta_0$ and $\boldsymbol{\eta} = \boldsymbol{\xi}/\sqrt{\theta_0}$, where $\theta_0 = RT_0$ and T_0 is a reference temperature.

In order to determine the discrete velocities and the discrete EDF for constructing thermal LBE, first the above expansion needs to be

truncated at certain orders, i.e.,

$$f^{(eq)}(\boldsymbol{x},\boldsymbol{\xi},t) \approx f_N^{(eq)}(\boldsymbol{x},\boldsymbol{\xi},t) \equiv f^M(\vartheta,\boldsymbol{\eta})\sum_{i=0}^{N}\frac{1}{n!}\boldsymbol{a}_i^{(n)}(\boldsymbol{x},t)H_i^{(n)}(\boldsymbol{\eta})\,, \quad (5.31)$$

where N is an integer. Then a numerical quadrature is chosen so that the velocity moments of the truncated expansion hold up to a certain order,

$$\int \boldsymbol{\xi}^k f_N^{(eq)}(\boldsymbol{x},\boldsymbol{\xi},t)d\boldsymbol{\xi} = \sum_{i=1}^{b} W_i\boldsymbol{\xi}_i^k f_N^{(eq)}(\boldsymbol{x},\boldsymbol{c}_i,t)\,,\ \ k=0,\,1,\,\ldots,\,K \quad (5.32)$$

where K is an integer, W_i and $\boldsymbol{c}_i$ are the weights and abscissas of the quadrature, respectively. The discrete velocities are then chosen to be the abscissas $\boldsymbol{c}_i$. Therefore, the choice of quadrature plays a critical role in determining the discrete velocities and the corresponding LBE model.

Equation (5.28) indicates that $f_N^{(eq)}$ can be expressed as

$$f_N^{(eq)}(\boldsymbol{\xi}) = f^M(\,\vartheta,\boldsymbol{\eta})h_N(\boldsymbol{\eta})\,, \quad (5.33)$$

where h_N is a polynomial of degree N. Therefore a natural choice of the numerical quadrature in Eq. (5.32) is the Gauss-Hermite formulation of degree $N+K$ with the weight function $\omega(\boldsymbol{\eta})$, i.e.,

$$\int \omega(\boldsymbol{\eta})\phi(\boldsymbol{\eta})d\boldsymbol{\eta} = \sum_{i=1}^{b} w_i\phi(\boldsymbol{\eta}_i)\,, \quad (5.34)$$

where ϕ is a polynomial of degree $N+K$, w_i and $\boldsymbol{\eta}_i$ are the weights and integration nodes, respectively. From Eqs. (5.32) and (5.34) we can identify that $W_i = w_i\rho/f^M(\vartheta,\boldsymbol{\eta}_i)$, and $\boldsymbol{c}_i$ can be obtained from $\boldsymbol{\eta}_i$. The discrete EDF is obtained by setting $f_i^{(eq)} = W_i f_N^{(eq)}(\boldsymbol{x},\boldsymbol{c}_i,t)$.

The continuous distribution function $f(\boldsymbol{x},\boldsymbol{\xi},t)$ can also be expanded in the tensor Hermite polynomials [Shan *et al.*, 2006], from which we can define the discrete distribution functions $f_i = W_i\,f(\boldsymbol{x},\boldsymbol{c}_i,t)$. The evolution equation of f_i, which is usually called as *discrete velocity Boltzmann equation* (DVBE), can be deduced from the Boltzmann equation,

$$\frac{\partial f_i}{\partial t} + \boldsymbol{c}_i\cdot\nabla f_i = -\frac{1}{\tau_c}\left[f_i - f_i^{(eq)}\right]. \quad (5.35)$$

Further discretizations in time and space will lead to MS-LBE models.

The order of the truncated expansion of $f^{(eq)}$, N, and the highest order of the velocity moments required in Eq. (5.32), K, determine the consistency between the DVBE (and the resultant LBE) and the continuous Boltzmann equation. In what follows we will discuss the resultant DVBE models corresponding to the three different choices of f_M given by Eq. (5.30).

5.2.2 *Temperature/flow-dependent discrete velocities*

In the first choice, the local Maxwellian distribution function uses $\vartheta = \theta$ and $\boldsymbol{\eta} = (\boldsymbol{\xi} - \boldsymbol{u})/\sqrt{\theta}$, which means that $f^{(eq)}(\boldsymbol{\xi}) = f^M(\theta, \boldsymbol{\eta})$. Therefore the coefficients of its Hermite expansion are $a_0 = 1$ and $\boldsymbol{a}_i^{(n)} = 0\,(n > 0)$, i.e., $h_N = 1$. Consequently, for a given K one can just choose the Gaussian quadrature of degree K, and the discrete EDF is simply as

$$f_i^{(eq)} = W_i f^M(\theta, \boldsymbol{\eta}_i) = w_i \rho\,. \tag{5.36}$$

It is obvious that $f_i^{(eq)}$ is independent of the fluid velocity. However, in this case the discrete velocities are functions of both the fluid velocity and temperature,

$$\boldsymbol{c}_i = \boldsymbol{u} + \boldsymbol{\eta}_i \sqrt{\theta}\,. \tag{5.37}$$

This means that the particle velocity changes locally with the temperature and fluid velocity, which may bring many difficulties in practical applications. Sun [1998] has proposed one LBE model based on this idea, but the implementation is rather difficult.

5.2.3 *Temperature-dependent discrete velocities*

The second kind of Hermite expansion sets $\vartheta = \theta$ and $\boldsymbol{\eta} = \boldsymbol{\xi}/\sqrt{\theta}$ in the local Maxwellian distribution function, and so $f^{(eq)}(\boldsymbol{x}, \boldsymbol{\xi}, t) = f^M(\theta, \boldsymbol{\eta} - \hat{\boldsymbol{u}})$ with $\hat{\boldsymbol{u}} = \boldsymbol{u}/\sqrt{\theta}$. The expansion coefficients are then

$$\boldsymbol{a}_i^{(n)} = \frac{1}{\rho}\int f^M(\theta, \boldsymbol{\eta} - \hat{\boldsymbol{u}}) H_i^{(n)}(\boldsymbol{\eta}) d\boldsymbol{\eta} = \int \omega(\boldsymbol{\eta}) H_i^{(n)}(\boldsymbol{\eta} + \hat{\boldsymbol{u}}) d\boldsymbol{\eta}\,, \tag{5.38}$$

and the first few coefficients can be expressed as

$$a^{(0)} = 1\,,\ a_i^{(1)} = \hat{u}_i\,,\ a_{ij}^{(2)} = \hat{u}_i\hat{u}_j\,,\ a_{ijk}^{(3)} = \hat{u}_i\hat{u}_j\hat{u}_k\,,\ a_{ijkl}^{(4)} = \hat{u}_i\hat{u}_j\hat{u}_k\hat{u}_l\,. \quad (5.39)$$

On the other hand, in order to make Eq. (5.34) hold exactly, we should choose a Gaussian quadrature of degree $N+K$ at least. Then the discrete velocities are set to be $\boldsymbol{c}_i = \sqrt{\theta}\boldsymbol{\eta}_i$, and so the discrete equilibrium distribution function can be expressed as

$$\begin{aligned} f_i^{(eq)} &= W_i f_N^{(eq)}(\boldsymbol{x}, \boldsymbol{c}_i, t) = w_i\rho\left[1 + \hat{u}_i\eta_i + \hat{u}_i\hat{u}_j(\eta_i\eta_j - \delta_{ij}) + \cdots\right] \\ &= w_i\rho\left[1 + \frac{\boldsymbol{c}_i\cdot\boldsymbol{u}}{\theta} + \frac{\boldsymbol{uu}:(\boldsymbol{c}_i\boldsymbol{c}_i - \theta\boldsymbol{I})}{2\theta^2} + \cdots\right]. \end{aligned} \quad (5.40)$$

It should be noted that although the quadrature nodes $\boldsymbol{\eta}_i$ are some constants, the discrete velocities $\boldsymbol{c}_i$ can change in both time and space through the local temperature. Consequently, the particles may not arrive at lattice nodes during the propagation, which means that interpolations or other techniques should be adopted in the computation [Pavlo *et al.*, 2002]. However, this numerical difficulty is not the main problem of such DVBE (and LBE) models. A more serious problem is the coupling between $\boldsymbol{c}_i$ and $\boldsymbol{x}$ and t, which should be independent as that in the continuous Boltzmann equation. As a result, in the DVBE (5.35) $\boldsymbol{c}_i$ is non-commutative with the temporal and spatial derivatives, i.e.,

$$\boldsymbol{c}_i^k\partial_t f_i \neq \partial_t(\boldsymbol{c}_i^k f_i)\,,\quad \boldsymbol{c}_i^k\partial f_i \neq \partial(\boldsymbol{c}_i^k f_i)\,. \quad (5.41)$$

Consequently, even though the discrete velocity moments can match the continuous ones up to the required order, the macroscopic hydrodynamic equations from the DVBE (5.35) may still be incorrect. For example, although the discrete velocities can ensure that $\sum_i \boldsymbol{c}_i f_i^{(eq)} = \sum_i \boldsymbol{c}_i f = \rho\boldsymbol{u}$, the continuity equation on the t_0 time scale in the Chapman-Enskog expansion is

$$\partial_{t0}\rho + \sqrt{\theta}\nabla_0\cdot\left(\frac{\rho\boldsymbol{u}}{\sqrt{\theta}}\right) = 0\,, \quad (5.42)$$

or

$$\partial_{t_0}\rho + \nabla_0\cdot(\rho\boldsymbol{u}) = \frac{1}{2}\rho\boldsymbol{u}\cdot\nabla_0\ln\theta \neq 0\,, \quad (5.43)$$

which indicates that the DVBE (5.35) is inconsistent with the continuous Boltzmann equation even at the Euler level.

5.2.4 *Constant discrete velocities*

The third Hermite expansion method uses $\vartheta = \theta_0$ and $\boldsymbol{\eta} = \boldsymbol{\xi} / \sqrt{\theta_0}$ in the Maxwellian distribution function f^M. In this case, ϑ and $\boldsymbol{\eta}$ are independent of time and space, and f^M is a global equilibrium distribution function. The equilibrium distribution function can then be expressed as

$$f^{(eq)}(\boldsymbol{x},\boldsymbol{\xi},t) = \frac{\rho}{(2\pi\theta)^{D/2}}\exp\left[-\frac{(\eta-\hat{u})^2}{2}\frac{\theta_0}{\theta}\right] = \rho\theta^{-D/2}\omega\left(\frac{\boldsymbol{\eta}-\widehat{\boldsymbol{u}}}{\sqrt{\hat{\theta}}}\right), \tag{5.44}$$

where $\hat{\theta} = \theta/\theta_0$. The expansion coefficients of $f^{(eq)}$ are

$$\boldsymbol{a}_i^{(n)} = \int \hat{\theta}^{-D/2}\omega\left(\frac{\boldsymbol{\eta}-\hat{\boldsymbol{u}}}{\sqrt{\hat{\theta}}}\right)H_i^{(n)}(\boldsymbol{\eta})d\boldsymbol{\xi} = \int \omega(\boldsymbol{\eta})H_i^{(n)}(\sqrt{\hat{\theta}}\boldsymbol{\eta}+\hat{\boldsymbol{u}})d\boldsymbol{\eta}, \tag{5.45}$$

and the first four coefficients can be evaluated as

$$a^{(0)} = 1, \tag{5.46}$$

$$a_i^{(1)} = \int \omega(\boldsymbol{\eta})\left[\sqrt{\hat{\theta}}\eta_i + \hat{u}_i\right]d\boldsymbol{\eta} = \hat{u}_i, \tag{5.47}$$

$$a_{ij}^{(2)} = \int \omega(\boldsymbol{\eta})\left[(\sqrt{\hat{\theta}}\eta_i + \hat{u}_i)(\sqrt{\hat{\theta}}\eta_j + \hat{u}_j) - \delta_{ij}\right]d\boldsymbol{\eta} = \hat{u}_i\hat{u}_j + (\hat{\theta}-1)\delta_{ij}, \tag{5.48}$$

$$a_{ijk}^{(3)} = \hat{u}_i\hat{u}_j\hat{u}_k + (\hat{\theta}-1)[\boldsymbol{u}\boldsymbol{\delta}]_{ijk}, \tag{5.49}$$

$$a_{ijkl}^{(4)} = \hat{u}_i\hat{u}_j\hat{u}_k\hat{u}_l + (\hat{\theta}-1)[\boldsymbol{u}\boldsymbol{u}\boldsymbol{\delta}]_{ijkl} + (\hat{\theta}-1)^2[\boldsymbol{\delta}\boldsymbol{\delta}]_{ijkl}, \tag{5.50}$$

where

$$[\boldsymbol{\delta}\boldsymbol{\delta}]_{ijkl} = \delta_{ij}\delta_{jk} + \delta_{ik}\delta_{jl} + \delta_{il}\delta_{jk},$$

$$[\boldsymbol{u}\boldsymbol{u}\delta]_{ijkl} = u_iu_j\delta_{jk} + u_iu_k\delta_{jl} + u_iu_l\delta_{jk} + u_ju_k\delta_{il} + u_ju_l\delta_{ik} + u_ku_l\delta_{ij}. \tag{5.51}$$

In this kind of expansion, the discrete velocities obtained from the quadrature (5.34) are independent of time and space. Actually, the discrete velocities $\boldsymbol{c}_i = \sqrt{\theta_0}\boldsymbol{\eta}_i$ are some constant vectors depending on the selected quadrature. The discrete EDF corresponding to the above

Hermite expansion can be written as

$$f_i^{(eq)} = w_i\rho\Big[a^{(0)} + \boldsymbol{a}^{(1)}\cdot\boldsymbol{H}^{(1)}(\boldsymbol{\eta}_i) + \boldsymbol{a}^{(2)}:\boldsymbol{H}^{(2)}(\boldsymbol{\eta}_i) + \cdots\Big]$$
$$= w_i\rho\left[1 + \frac{\boldsymbol{c}_i\cdot\boldsymbol{u}}{\theta_0} + \mathcal{T}_2 + \mathcal{T}_3 + \cdots\right], \tag{5.52}$$

where

$$\mathcal{T}_2 = \frac{1}{2}\boldsymbol{a}^{(2)}\cdot\boldsymbol{H}^{(2)} = \frac{1}{2}\left[\frac{(\boldsymbol{c}_i\cdot\boldsymbol{u})^2}{\theta_0^2} - \frac{u^2}{\theta_0} + (\hat{\theta}-1)\left(\frac{c_i^2}{\theta_0} - D\right)\right],$$

$$\mathcal{T}_3 = \frac{1}{3!}\boldsymbol{a}^{(3)}\cdot\boldsymbol{H}^{(3)} = \frac{\boldsymbol{c}_i\cdot\boldsymbol{u}}{6}\left[\frac{(\boldsymbol{c}_i\cdot\boldsymbol{u})^2}{\theta_0^2} - 3\frac{u^2}{\theta_0} + 3(\hat{\theta}-1)\left(\frac{c_i^2}{\theta_0} - D - 2\right)\right]. \tag{5.53}$$

Although the $0\sim K$-th order velocity moments of the EDF (5.52) are just the same as those of the EDF given by Eq. (5.40), the discrete velocity set obtained by this way has the advantage that it is independent on time and space so that the DVBE is in consistent with the continuous Boltzmann equations more closely than that derived in Subsec. 5.2.3 in terms of the Chapman-Enskog analysis.

Now we discuss how to construct thermohydrodynamic MS-LBE models based on the above expansion method. The Chapman-Enskog analysis of the continuous Boltzmann equation shows that the hydrodynamic equations on the Navier-Stokes level depend on the following velocity moments,

$$\int f^{(eq)}d\boldsymbol{\xi} = \rho\,,\ \int \boldsymbol{\xi} f^{(eq)}d\boldsymbol{\xi} = \rho\boldsymbol{u}\,,\ \frac{1}{2}\int C^2 f^{(eq)}d\boldsymbol{\xi} = \rho e\,,$$

$$\int \boldsymbol{C}\boldsymbol{C} f^{(eq)}d\boldsymbol{\xi} = \boldsymbol{P}^{(0)} = \rho\theta\boldsymbol{I}\,,\ \frac{1}{2}\int \boldsymbol{C}C^2\boldsymbol{\xi} f^{(eq)}d\boldsymbol{\xi} = \boldsymbol{q}^{(0)} = 0\,,$$

$$\int \boldsymbol{C}\boldsymbol{C} f^{(1)}d\boldsymbol{\xi} = \boldsymbol{P}^{(1)}\,,\ \frac{1}{2}\int \boldsymbol{C}C^2 f^{(1)}d\boldsymbol{\xi} = \boldsymbol{q}^{(1)}\,, \tag{5.54}$$

where $\boldsymbol{C} = \boldsymbol{\xi} - \boldsymbol{u}$ is the peculiar velocity, and $f^{(1)}$ is the first-order distribution function, which can be expressed as,

$$f^{(1)} = -\tau_c\left[\partial_{t_0} f^{(eq)} + \boldsymbol{\xi}\cdot\nabla_0 f^{(eq)}\right]. \tag{5.55}$$

Therefore, the constraints given by Eq. (5.54) indicate that the zeroth through 4th order velocity moments of $f^{(eq)}$ are all critical for recovering

the thermohydrodynamic equations at the Navier-Stokes level. On the other hand, since the $0 \sim N$-th order velocity moments of $f_N^{(eq)}$ are identical to those of $f^{(eq)}$, the Hermite expansion of $f^{(eq)}$ should contain the term of $\boldsymbol{H}_i^{(4)}$, namely, $f_N^{(eq)}$ with $N \geq 4$ should be used as the truncated approximation of $f^{(eq)}$.

If $f_4^{(eq)}$ is used as the approximation of the EDF, the degree of the quadrature used in evaluating the moments given by Eq. (5.54) should be at least 8. In general, in order to ensure that the $0 \sim N$-th-order velocity moments of $f^{(eq)}$ can be accurately evaluated, $f_N^{(eq)}$ should be used and a quadrature of degree at least $2N$ should be adopted [Shan *et al*., 2006].

The above analysis shows that the discrete EDF $f_i^{(eq)}$ must include terms of order $O(\boldsymbol{u}^4)$ for thermal flows, which is consistent with Chen's arguments about the high-order MS-LBE models. An advantage of the Hermite expansion method is that the discrete velocity set and the associated EDFs can be deduced systematically.

5.2.5 *MS-LBGK models based on DVBE with constant discrete velocities*

The most efficient quadrature in Eq. (5.32) is the Gauss-Hermite type with unknown weights and nodes. The discrete velocities $\boldsymbol{c}_i$ obtained this way do not coincide with a regular lattice in general, i.e., the velocity set is *off-lattice* or *non-space-filling* [Shan *et al*., 2006]. An alternative method is to define some lattice vectors $\boldsymbol{e}_i$ associated with a regular lattice first, and then determine the weights ω_i and discrete velocities $\boldsymbol{\eta}_i = r\boldsymbol{e}_i$ (i.e $\boldsymbol{c}_i = r\sqrt{\theta_0}\boldsymbol{e}_i$) according to some Gaussian quadrature rules so that the velocity moments are accurately evaluated. Several two-dimensional models of this kind have been developed [Philippi *et al*., 2006; Siebert *et al*., 2007], in which the EDFs given by Eq. (5.52) are used. Three MS-LBE models of this type are listed below (discrete velocities are expressed as $\boldsymbol{c}_i = r\sqrt{\theta_0}\boldsymbol{e}_i$).

(1) D2Q25a model

The discrete velocities are generated from the lattice vectors $\boldsymbol{e}_0 = (0,0)$, Prem$\{k(\pm 1, 0)\}$, and Prem$\{k(\pm 1, \pm 1)\}$ ($k = 1, 2, 3$) (see Fig. 5.2), and

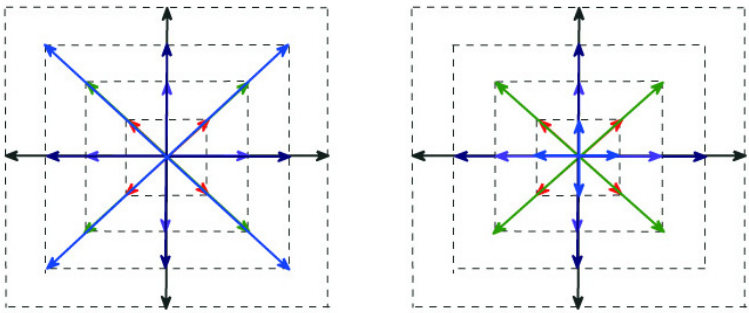

Fig. 5.2. Lattice vector of D2Q25a(left) and D2Q25b(right).

the parameter $r = 0.834659$, while the weights in the EDF are given by

$$w_i = \begin{cases} 0.235184, & |\boldsymbol{e}_i| = 0, \\ 0.101817, & |\boldsymbol{e}_i| = \sqrt{2}, \\ 5.92134 \times 10^{-2}, & |\boldsymbol{e}_i| = 2, \\ 2.00409 \times 10^{-2}, & |\boldsymbol{e}_i| = 2\sqrt{2}, \end{cases} \quad \text{and} \quad w_i = \begin{cases} 6.79523 \times 10^{-3}, & |\boldsymbol{e}_i| = 3, \\ 1.14376 \times 10^{-3}, & |\boldsymbol{e}_i| = 3\sqrt{2}, \\ 2.19788 \times 10^{-3}, & |\boldsymbol{e}_i| = 4. \end{cases}$$

(2) D2Q25b model

The discrete velocities are generated from the lattice vectors $\boldsymbol{e}_0 = (0, 0)$, Prem$\{k(\pm 1, 0)\}$ $(k = 1, 2, 3, 4)$, and Prem$\{k(\pm 1, \pm 1)\}$ $(k = 1, 2)$ (Fig. 5.2.), the parameter r = 1.075607, and the weights in the EDF are given by

$$w_i = \begin{cases} 0.239059, & |\boldsymbol{e}_i| = 0, \\ 0.063158, & |\boldsymbol{e}_i| = 1, \\ 8.75957 \times 10^{-2}, & |\boldsymbol{e}_i| = \sqrt{2}, \\ 3.11800 \times 10^{-2}, & |\boldsymbol{e}_i| = 2, \end{cases} \quad \text{and} \quad w_i = \begin{cases} 6.19896 \times 10^{-3}, & |\boldsymbol{e}_i| = 2\sqrt{2}, \\ 2.02013 \times 10^{-3}, & |\boldsymbol{e}_i| = 3, \\ 8.38224 \times 10^{-5}, & |\boldsymbol{e}_i| = 4. \end{cases}$$

(3) D2Q37

The discrete velocities are generated from the lattice vectors $\boldsymbol{e}_0 = (0, 0)$, Prem$\{k(\pm 1, 0)\}$ $(k = 1, 2, 3)$, Prem$\{k(\pm 1, \pm 1)\}$ $(k = 1, 2)$, and Prem$\{(\pm 1, \pm 2)\}$ (Fig. 5.3.), the parameter r = 1.196980, and the weights in EDF are

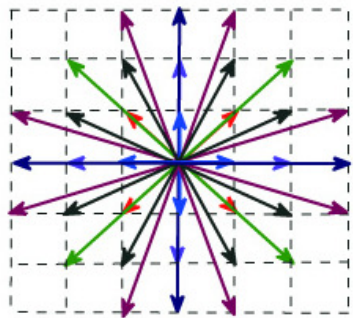

Fig. 5.3. Lattice vector of D2Q37.

given by

$$w_i=\begin{cases}0.846393, & |\boldsymbol{e}_i|=0,\\ 0.107306, & |\boldsymbol{e}_i|=1,\\ 5.76679\times10^{-2}, & |\boldsymbol{e}_i|=\sqrt{2},\\ 1.42082\times10^{-2}, & |\boldsymbol{e}_i|=2,\end{cases}\quad\text{and}\quad w_i=\begin{cases}5.35305\times10^{-3}, & |\boldsymbol{e}_i|=\sqrt{5},\\ 1.01194\times10^{-3}, & |\boldsymbol{e}_i|=2\sqrt{2},\\ 2.45301\times10^{-4}, & |\boldsymbol{e}_i|=3,\\ 2.83414\times10^{-4}, & |\boldsymbol{e}_i|=\sqrt{10}.\end{cases}$$

It is noteworthy that for low Mach number thermal flows, the terms of $O(\boldsymbol{u}^4)$ can be neglected in both the expansion of $f^{(eq)}$ and the velocity moments. Consequently, $f^{(eq)}$ can be approximated by $f_3^{(eq)}$, and a quadrature of degree 7 can be used to determine the discrete velocity set and the EDFs [Philippi *et al*., 2006; Shan *et al*., 2006; Siebert *et al*., 2007]. Two examples are given below.

(1) D2Q17 model

The discrete velocity set is $\boldsymbol{c}_i = r\boldsymbol{e}_i$ with $r = 1.64343$, and the lattice vectors include $\boldsymbol{e}_0=(0, 0)$, Prem$\{k(\pm1, 0)\}$ $(k = 1, 3)$, and Prem$\{k(\pm1, \pm1)$ $(k = 1, 2)$. The corresponding weights in EDF are given by

$$w_i=\begin{cases}0.402005, & |\boldsymbol{e}_i|=0,\\ 0.116155, & |\boldsymbol{e}_i|=1,\\ 3.30064\times10^{-2}, & |\boldsymbol{e}_i|=2,\end{cases}\quad\text{and}\quad w_i=\begin{cases}7.90786\times10^{-5}, & |\boldsymbol{e}_i|=2\sqrt{2},\\ 2.584145\times10^{-4}, & |\boldsymbol{e}_i|=3.\end{cases}$$

(2) D3Q37 model

The discrete velocity set is $\boldsymbol{c}_i = \sqrt{3/2}\boldsymbol{e}_i$, and the lattice vectors include $\boldsymbol{e}_0=(0, 0)$, Prem$\{(\pm1, \pm1, \pm1)\}$, Prem$\{2(\pm1, \pm1, 0)\}$, and Prem$\{k(\pm1, 0, 0)\}$

$(k=1,\ 2,\ 3)$. The weights in EDF are

$$w_i = \begin{cases} 1/12, & |\boldsymbol{e}_i| = 0, \\ 1/12, & |\boldsymbol{e}_i| = 1, \\ 1/27, & |\boldsymbol{e}_i| = \sqrt{3}, \end{cases} \quad \text{and} \quad w_i = \begin{cases} 2/135, & |\boldsymbol{e}_i| = 2, \\ 1/432, & |\boldsymbol{e}_i| = 2\sqrt{2}, \\ 1/1620, & |\boldsymbol{e}_i| = 3. \end{cases}$$

5.3 Off-Lattice LBE Models

Due to the coupling between the discrete velocities and the underlying lattices, the MS-LBE models described so far usually involve a large discrete velocity set in order to satisfy the necessary moment constraints. On the other hand, off-lattice LBE models can release this problem by decoupling the discrete velocity set and the lattice. But due to this decoupling, the particles do not evolve on the lattice any more in such LBE models, and some special treatments such as interpolation must be employed.

The first off-lattice LBE may be attributed to Pavlo *et al*. [1998], who developed a D2Q17 model based on a lattice consisting of two composite octagons, where the discrete velocities are given by

$$\boldsymbol{c}_0 = (0, 0)\,,\ \boldsymbol{c}_i = \boldsymbol{c}'_{pi} = p\Big[\cos(i\pi/4), \sin(i\pi/4)\Big],\ i = 0 \sim 7\,,\ p = 1, 2\,. \tag{5.56}$$

In order to make the computational mesh match these discrete velocities as much as possible, Pavlo *et al*. employed the square lattice used in the standard D2Q17 for spatial discretization (see Fig. 5.4). As such, in the streaming step, only those particles with velocities $\boldsymbol{c}_0$, $\boldsymbol{c}'_{p0}$, $\boldsymbol{c}'_{p2}$, ..., $\boldsymbol{c}'_{p6}$ can reach the lattice nodes, while the others will fail. Pavlo *et al*. [1998] suggested using a second-order interpolation scheme as a supplementation. It was shown that such interpolation method did not cause serious numerical diffusion, and the stability analysis indicated that this model has a better numerical stability than the aforementioned D2Q13 models based on hexagon and square lattice as well as the standard D2Q17 model based on the composite square lattice. A three-dimensional D3Q53 model was also constructed following a similar approach.

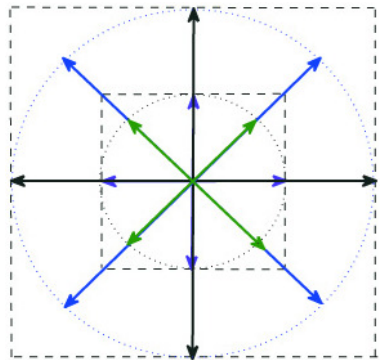

Fig. 5.4. Discrete velocities and computation mesh of the D2Q17 based on octagons.

Watari and Tsutahara [2003] proposed a similar MS-LBE model (WT model), which uses a composite lattice with four octagons. The discrete velocities are given by

$$\boldsymbol{c}_0 = (0,0)\,,\ \boldsymbol{c}_{pi} = c_p\Big[\cos(i\pi/4), \sin(i\pi/4)\Big],\ i = 0 \sim 7\,,\ p = 1 \sim 4\,, \quad (5.57)$$

where the c_p's are undetermined parameters. The EDF of the WT model is given as,

$$f_{pi}^{(eq)} = \omega_p \rho\left[\left(1 - \frac{u^2}{2e} + \frac{u^4}{8e^2}\right) + \left(1 - \frac{u^2}{2e}\right)\frac{\boldsymbol{c}_{pi}\cdot\boldsymbol{u}}{e} + \left(1 - \frac{u^2}{2e}\right)\frac{(\boldsymbol{c}_{pi}\cdot\boldsymbol{u})^2}{2e^2} + \frac{(\boldsymbol{c}_{pi}\cdot\boldsymbol{u})^3}{6e^3} + \frac{(\boldsymbol{c}_{pi}\cdot\boldsymbol{u})^4}{24e^3}\right], \quad (5.58)$$

where the weights ω_p depend on the magnitude of the discrete velocities. With the consideration of numerical stability, Watari and Tsutahara [2003] suggested setting $(c_1,\ c_2,\ c_3,\ c_4)$ = (1, 1.92, 2.99, 4.49), and the corresponding ω_i can be determined accordingly. To discretize the DVBE (5.35) with these discrete velocities, an explicit scheme was suggested [Watari and Tsutahara, 2003],

$$f_{pi}(\boldsymbol{x}, t+\Delta t) = f_{pi}(\boldsymbol{x}, t) - \Delta t\left(c_{pix}\frac{\partial f_{pi}}{\partial x} + c_{piy}\frac{\partial f_{pi}}{\partial \mathrm{y}}\right) - \frac{\Delta t}{\tau_c}\Big[f_{pi}(\boldsymbol{x}, t) - f_{pi}^{(eq)}\Big], \quad (5.59)$$

where the spatial derivatives were discretized by upwind schemes.

Recently Gan *et al*. [2008] developed another finite difference scheme based on the WT model. Instead of solving DVBE (5.35) directly, they suggested solving the following modified DVBE with an additional dispersion term and an artificial viscosity term,

$$\frac{\partial f_{pi}}{\partial t} + \boldsymbol{c}_{pi} \cdot \nabla f_{pi} = -\frac{1}{\tau_c}\left[f_{pi} - f_{pi}^{(eq)} \right] + A_{pi\alpha}\partial_\alpha^3 f_{pi} + B_{pi}\nabla^2 f_{pi}, \quad (5.60)$$

where $A_{pi\alpha}$ and $B_{pi\alpha}$ are functions depending on the discrete velocity $\boldsymbol{c}_{pi}$. Gan *et al.* [2008] used the Lax-Wendroff (LW) scheme to discretize the left hand side of the equation and the central difference scheme is used to the right hand side. Numerical results showed that this LW-LBE has good numerical accuracy and stability.

Shan *et al*. [2006] also developed some off-lattice models based on the Gauss-Hermite quadrature. A few examples for low Mach number flows, in which $f_3^{(eq)}$ and the 7th-degree Gaussian quadrature are used, are given below (discrete velocities are given by $\boldsymbol{c}_i = \sqrt{\theta_0}\boldsymbol{e}_i$ and the $\boldsymbol{e}_i$'s are the corresponding lattice vectors).

(1) D1Q4 model

The lattice vectors are $\boldsymbol{e}_i = \sqrt{3 \pm \sqrt{6}}$, and the corresponding weight coefficients are given by $w_i = (3 \pm \sqrt{6}) / 12$.

(2) D2Q12 model

The lattice vectors are defined by Prem$\{(\pm r, 0)\}$, Prem$\{(\pm s, \pm s)\}$, and Prem$\{(\pm t, \pm t)\}$, with $r = \sqrt{6}$, $s = \sqrt{9 - \sqrt{5}}$, and $t = \sqrt{9 + \sqrt{5}}$. The weight coefficients are

$$w_i = \begin{cases} 1/36, & |\boldsymbol{e}_i| = r, \\ (5 + 2\sqrt{5})/45, & |\boldsymbol{e}_i| = \sqrt{2}s, \\ (5 - 2\sqrt{5})/45, & |\boldsymbol{e}_i| = \sqrt{2}t. \end{cases}$$

(3) D2Q16 model

The lattice vectors consist of Prem$\{(\pm r, 0)\}$, Prem$\{(\pm s, 0)\}$, and Prem$\{(\pm r, \pm s)\}$, with $r = \sqrt{3 + \sqrt{6}}$ and $s = \sqrt{3 - \sqrt{6}}$. The weight coefficients are

$$w_i = \begin{cases} (5-2\sqrt{6})/48, & |\boldsymbol{e}_i| = r, \\ (5+2\sqrt{6})/48, & |\boldsymbol{e}_i| = s, \\ 1/48, & |\boldsymbol{e}_i| = \sqrt{6}. \end{cases}$$

(4) D3Q27 model

Lattice vectors consists of $\boldsymbol{e}_0$=(0, 0), Prem{$(\pm r, 0, 0)$}, Prem{$(\pm s, \pm s, 0)$}, and Prem{$(\pm t, \pm t, \pm t)$}, with $r = \sqrt{15+\sqrt{15}/2}$, $s = \sqrt{6-\sqrt{15}}$, and $t = \sqrt{9+\sqrt{15}}$. The weight coefficients are

$$w_i = \begin{cases} (720+8\sqrt{15})/2205, & |\boldsymbol{e}_i| = 0, \\ (270-46\sqrt{15})/15435, & |\boldsymbol{e}_i| = r, \\ (162+41\sqrt{15})/6174, & |\boldsymbol{e}_i| = \sqrt{2}s, \\ (783-202\sqrt{15})/24696, & |\boldsymbol{e}_i| = \sqrt{3}t. \end{cases}$$

Based on the above discrete velocities and the corresponding EDFs, one can solve the corresponding DVBE (5.35) using certain numerical schemes, which will lead to non-standard MS-LBE models for thermo-hydrodynamic problems.

5.4 MS-LBE Models with Adjustable Prandtl Number

The low-order, high-order, and kinetic-theory-based MS-LBE models presented above all give a fixed Prandtl number, which severely limits their applications. This difficulty can be resolved by introducing some additional parameters. For example, Chen *et al*. [1997] developed a two-relaxation-time model,

$$f_i(\boldsymbol{x}+\boldsymbol{c}_i\delta_t, t+\delta_t) - f_i(\boldsymbol{x},t) = \Omega_i + \Omega_{\bar{i}}, \tag{5.61}$$

where

$$\Omega_i = -\frac{1}{\tau_1}\left(f_i - f_i^{(eq)}\right), \quad \Omega_{\bar{i}} = -\frac{1}{\tau_2}\left(f_{\bar{i}} - f_{\bar{i}}^{(eq)}\right), \tag{5.62}$$

where $\boldsymbol{c}_{\bar{i}} = -\boldsymbol{c}_i$. It is easy to verify that the collision process satisfies conservation laws due to the symmetry of the lattice.

The Chapman-Enskog analysis shows that the recovered macroscopic equations of LBE (5.61) are

$$\frac{\partial \rho}{\partial t} + \nabla \cdot (\rho \boldsymbol{u}) = 0\,, \tag{5.63}$$

$$\frac{\partial (\rho \boldsymbol{u})}{\partial t} + \nabla \cdot (\rho \boldsymbol{u}\boldsymbol{u}) = -\nabla p + \nabla \cdot \boldsymbol{\tau}_{\nu}\,, \tag{5.64}$$

$$\frac{\partial (\rho e)}{\partial t} + \nabla \cdot (\rho \boldsymbol{u} e) = p \nabla \cdot \boldsymbol{u} + \nabla \cdot (\kappa \nabla T) + \boldsymbol{\tau}_{\kappa} : \nabla \boldsymbol{u}\,, \tag{5.65}$$

where

$$\boldsymbol{\tau}_{\nu} = 2\mu_{v}\boldsymbol{S} + \lambda_{v}(\nabla \cdot \boldsymbol{u})\boldsymbol{I}\,, \quad \boldsymbol{\tau}_{\kappa} = 2\mu_{k}\boldsymbol{S} + \lambda_{k}(\nabla \cdot \boldsymbol{u})\boldsymbol{I}\,, \tag{5.66}$$

and the transport coefficients are given by

$$\mu_{v} = \frac{2}{D}\rho e\left(\tau_{v} - \frac{1}{2}\right), \quad \lambda_{v} = -\frac{4}{D^{2}}\rho e\left(\tau_{v} - \frac{1}{2}\right), \tag{5.67}$$

$$\mu_{k} = \frac{2}{D}\rho e\left(\tau_{k} - \frac{1}{2}\right), \quad \lambda_{k} = -\frac{4}{D^{2}}\rho e\left(\tau_{k} - \frac{1}{2}\right), \tag{5.68}$$

$$\kappa = \frac{D+2}{D}\rho e\left(\tau_{k} - \frac{1}{2}\right), \tag{5.69}$$

where

$$\frac{1}{\tau_{v}} = \frac{1}{\tau_{1}} + \frac{1}{\tau_{2}}, \quad \frac{1}{\tau_{k}} = \frac{1}{\tau_{1}} - \frac{1}{\tau_{2}}\,. \tag{5.70}$$

Accordingly, the Prandtl number is

$$\mathrm{Pr} = \frac{\mu_{v} c_{p}}{\kappa} = \frac{2\tau_{v} - 1}{2\tau_{k} - 1}\,, \tag{5.71}$$

which means that the Prandtl number can be adjusted by changing the values of the two relaxation times τ_1 and τ_2. However, it is noted that the viscous stress in the dissipation term in the energy equation is $\boldsymbol{\tau}_{k}$, which is inconsistent with that appeared in the momentum equation (i.e. $\boldsymbol{\tau}_{v}$).

Recently Prasianakis and Boulouchos [2007] proposed a similar two-relaxation-time model, which starts from the following DVBE,

$$\frac{\partial f_{i}}{\partial t} + \boldsymbol{c}_{i} \cdot \nabla f_{i} = -\frac{1}{\tau_{1}}\left[f_{i} - f_{i}^{*}\right] - \frac{1}{\tau_{2}}\left[f_{i}^{*} - f_{i}^{(eq)}\right], \tag{5.72}$$

where f_i^* is an intermediate state. The physical meaning of this collision model is that the non-equilibrium state first relaxes to the intermediate state f_i^* with a time scale τ_1, and then to the local equilibrium state $f_i^{(eq)}$ with another time scale τ_2. It is clear that the model reduces to the standard BGK model as $\tau_1 = \tau_2$. In the above model, the intermediate state plays a key role. In general it can be assumed that

$$f_i^* = f_i^{(eq)} + \delta f_i^* , \tag{5.73}$$

where the correction δf_i^* can be determined by projecting the DVBE onto the moment space and then transforming back to the velocity space. For example, the correction terms of D2Q9 model can be expressed as

$$\begin{aligned}\delta f_i^* = \frac{1}{4}\big[& 0, -2\delta\psi_x^*, -2\delta\psi_y^*, 2\delta\psi_x^*, 2\delta\psi_y^*, \delta\psi_x^* + \delta\psi_y^*, \delta\psi_y^* - \delta\psi_x^*, \\ & -\delta\psi_x^* - \delta\psi_y^*, \delta\psi_x^* - \delta\psi_y^* \big],\end{aligned} \tag{5.74}$$

where

$$\delta\psi_\alpha^* = \psi_\alpha - \psi_\alpha^{(eq)} - 2u_\gamma (P_{\alpha\gamma} - P_{\alpha\gamma}^{(eq)}) , \psi_\alpha = \sum_i c_{i\alpha} c_i^2 f_i , \quad P_\alpha = \sum_i c_{i\alpha} c_{i\beta} f_i ,$$

$$\psi_\alpha^{(eq)} = \sum_i c_{i\alpha} c_i^2 f_i^{(eq)} , \quad P_\alpha^{(eq)} = \sum_i c_{i\alpha} c_{i\beta} f_i^{(eq)} . \tag{5.75}$$

The corresponding macroscopic equations of the DVBE (5.72) can be obtained by the Chapman-Enskog analysis, in which the viscosity coefficients and thermal conductivity are

$$\mu = \tau_1 \rho \theta_0 , \quad \kappa = \frac{1}{2} \tau_2 \rho \theta_0 . \tag{5.76}$$

Therefore the Prandtl number of this model is $\mathrm{Pr} = 4\tau_1/\tau_2$, which can be adjusted by changing τ_1 and τ_2. The LBE model can be obtained by discretizing the DVBE (5.72) with certain numerical schemes. But unfortunately the consistency of the viscous stress in the momentum and energy equations was not discussed by Prasianakis and Boulouchos [2007].

Some more general two-relaxation-time LBE models were also developed [Chen *et al.*, 1997; Teixeira *et al.*, 2000]. For instance, with discrete velocities based on composite lattices, the collision operators can be written as,

$$\Omega_{pi} = -\frac{1}{\tau_1}\Big(f_{pi} - f_{pi}^{(eq)} \Big) - \left(\frac{1}{\tau_2} - \frac{1}{\tau_1} \right) \frac{D}{b_p c_{pi}^2} \sum_j (\boldsymbol{c}_{pi} \cdot \boldsymbol{c}_{pj}) \Big(f_{pj} - f_{pj}^{(eq)} \Big) , \tag{5.77}$$

where b_p is the number of links of the sub-lattice p. The hydrodynamic equations recovered from this LBE are again those given by Eqs. (5.63) ~(5.65), with the following viscosity and thermal conductivity,

$$\mu_v = \frac{2}{D}\rho e\left(\tau_1 - \frac{1}{2}\right), \quad \kappa = \frac{D+2}{D}\rho e\left(\tau_2 - \frac{1}{2}\right). \tag{5.78}$$

Similar to the two-parameter model of Chen *et al*. [1997], the Prandtl number of the above LBE can be adjusted by changing the values of τ_1 and τ_2, but the viscous stress in the momentum equation is still incompatible with that in the energy equation. It is argued by some researchers that for any collision operators such inconsistency will appear, given that the moments corresponding to the viscous tensor and the heat flux relax with different rates [McNamara *et al.*, 1995; Shan *et al.*, 2006; Teixeira *et al*., 2000]. This also indicates the inherent deficiency of MS-LBE models.

To overcome this disadvantage, McNamara *et al*. [1997] constructed a MS-LBE model (referred to as MGA model) in which the collision process is carried out in moment space. Clearly, this feature is similar to that of the multi-relaxation-time model developed by d′Humères [1992]. But with a larger discrete velocity set, the MGA model is able to produce the correct thermohydrodynamic equations. An example is a D3Q27 model which uses 27 discrete velocities, whose collision process can be expressed as

$$f_i'(\boldsymbol{x},t) = f_i(\boldsymbol{x},t) + \sum_j \Omega_{ij}\left(f_j - f_j^{eq)}\right). \tag{5.79}$$

This process is achieved by relaxing different velocity moments in the moment space. Specifically, the five low-order velocity moments, ρ, $\boldsymbol{j} = \rho\boldsymbol{u}$, and ρe, are conserved variables and do not change in the collision processes. The high-order velocity moments associated with viscous stress and heat flux are relaxed as follows,

$$\sum_i (c_{i\alpha}c_{i\beta} - \tfrac{1}{3}c_i^2\delta_{\alpha\beta})f_i'^{(ne)} = (\lambda_v + 1)\sum_i (c_{i\alpha}c_{i\beta} - \tfrac{1}{3}c_i^2\delta_{\alpha\beta})f_i^{(ne)}, \tag{5.80}$$

$$\sum_i C_i^2\boldsymbol{C}_i f_i'^{(ne)} = (\lambda_\kappa + 1)\sum_i C_i^2\boldsymbol{C}_i f_i^{(ne)}, \tag{5.81}$$

where λ_v and λ_κ are the eigenvalues of the collision operator Ω. It can be shown that the transport coefficients corresponding to this collision

operator are

$$\mu = -\frac{2}{3}\left(\lambda_v + \frac{1}{2}\right)\rho e\delta_t\,,\quad \kappa = -\frac{2}{3}\left(\lambda_k + \frac{1}{2}\right)\rho e\delta_t\,. \tag{5.82}$$

Because the third-order velocity moments are relaxed in the frame moving with the fluid rather than a fixed one, the viscous stress in the momentum equation is now compatible with that in the energy equation. However, practical simulations indicate that the MGA model suffers from serious numerical instability [McNamara *et al.*, 1997], and the recent linear analysis also shows that the momentum and energy modes in MS-LBE models have an unphysical coupling, which seriously affects the numerical stability [Lallemand and Luo, 2000].

5.5 DDF-LBE Models without Viscous Dissipation and Compression Work

The multi-speed LBE models are a straightforward extension of isothermal models. As mentioned above, the MS-LBE models usually involve a large discrete velocity set which requires high storage and computational costs. Furthermore, the numerical stability of such models is also not satisfactory.

In many problems, the compression work and viscous dissipation can be neglected. In such cases, the temperature can be regarded as a scalar which is governed by a convection-diffusion equation. Consequently, the velocity and temperature fields can be solved separately, which means that we can simulate the velocity field with an isothermal LBE and the temperature field with another one for convection-diffusion equation. This idea was first adopted in a model by Bartoloni *et al*. [1993], where the temperature was treated as a pure passive scalar that has no effects on the velocity field. Since then, a variety of LBE models with double distribution functions (DDF-LBE) have been developed from different ways.

5.5.1 *DDF-LBE based on multi-component models*

Based on a multi-component LBE model, Shan constructed a DDF-LBE model which treats the temperature as a component of fluid mixture

[Shan, 1997]. The effect of temperature on the velocity field is modeled following an approach similar to that in LBE for binary mixtures. Specifically, this model uses the following multi-component LBE model:

$$f_i^\sigma(\boldsymbol{x} + \boldsymbol{c}_i\delta_t, t + \delta_t) = f_i^\sigma(\boldsymbol{x}, t) - \frac{1}{\tau_\sigma}\left[f_i^\sigma(\boldsymbol{x}, t) - f_i^{\sigma,(eq)}(\boldsymbol{x}, t)\right], \tag{5.83}$$

for $\sigma = 1, 2, \ldots, S$, where S is the number of components in the mixture, f_i^σ is the distribution function of the component σ, and $f_i^{\sigma,(eq)}$ is the corresponding EDF,

$$f_i^{\sigma,(eq)} = \omega_i\rho_\sigma\left[1 + \frac{\boldsymbol{c}_i \cdot \boldsymbol{u}_\sigma^{(eq)}}{c_s^2} + \frac{(\boldsymbol{c}_i \cdot \boldsymbol{u}_\sigma^{(eq)})^2}{2c_s^4} - \frac{(u_\sigma^{(eq)})^2}{2c_s^2}\right], \tag{5.84}$$

in which $\rho_\sigma = \sum_i f_i^\sigma$ and $\boldsymbol{u}_\sigma = (\sum_i f_i^\sigma \boldsymbol{c}_i)/\rho_\sigma$ are the density and velocity components of σ, respectively, and $\boldsymbol{u}_\sigma^{(eq)}$ is the equilibrium velocity that is not necessarily equal to $\boldsymbol{u}_\sigma$; In the absence of internal interactions and external forces, it is assumed that the equilibrium velocities of all components share a common one,

$$\boldsymbol{u}_\sigma^{(eq)} = \boldsymbol{u}^{eq} \equiv \sum_{j=1}^{S}\frac{\rho_j\boldsymbol{u}_j}{\tau_j}\Bigg/\sum_{j=1}^{S}\frac{\rho_j}{\tau_j}. \tag{5.85}$$

On the other hand, if the component σ is subject to a body force F_σ, the equilibrium velocity is given by

$$\boldsymbol{u}_\sigma^{(eq)} = \boldsymbol{u}^{(eq)} + \frac{\tau_\sigma\delta_t\boldsymbol{F}_\sigma}{\rho_\sigma}. \tag{5.86}$$

Shan suggested using the above LBE model for binary mixtures ($S = 2$) to model thermal flows: the fluid motion is simulated by component A, while the temperature is simulated by component B, under the assumption that the two components share a common velocity. If only the gravity is considered, $\boldsymbol{u}_A + \tau_A\delta_t\boldsymbol{g}$ will be used in the EDF, and the density, velocity, and temperature of the fluid are defined as,

$$\rho = \sum_i f_i^A\,,\ \rho\boldsymbol{u} = \sum_i \boldsymbol{c}_i f_i^A + \frac{\delta_t}{2}\rho\boldsymbol{g}\,,\ T = \sum_i f_i^B\,. \tag{5.87}$$

The corresponding macroscopic equations can be obtained via the Chapman-Enskog expansion,

$$\frac{\partial \rho}{\partial t} + \nabla \cdot \left(\rho \boldsymbol{u}\right) = 0 \,, \tag{5.88}$$

$$\frac{\partial \left(\rho \boldsymbol{u}\right)}{\partial t} + \nabla \cdot (\rho \boldsymbol{u}\boldsymbol{u}) = -\nabla p + \nabla \cdot \left(2\rho\nu \boldsymbol{S}\right) + \rho \boldsymbol{g} \,, \tag{5.89}$$

$$\frac{\partial T}{\partial t} + \boldsymbol{u} \cdot \nabla T = \nabla \cdot \left(\alpha \nabla T\right), \tag{5.90}$$

where $p = c_s^2 \rho$, ν and α are the kinematic viscosity and thermal diffusivity, respectively,

$$\nu = c_s^2 \left(\tau_A - \frac{1}{2}\right)\delta_t \,, \; \alpha = c_s^2 \left(\tau_B - \frac{1}{2}\right)\delta_t \,. \tag{5.91}$$

Therefore, the corresponding Prandtl number of this model is $\mathrm{Pr} = \nu/\alpha = (2\tau_A - 1) / (2\tau_B - 1)$, which can be adjusted by changing τ_A and τ_B.

5.5.2 *DDF-LBE for non-ideal gases*

Palmer and Rector [2000a, 2000b] proposed another DDF-LBE model which can be used to simulate thermal flows of non-ideal gases. The model adopts a velocity distribution function f_i and an internal energy distribution function g_i to simulate the velocity and temperature fields respectively,

$$f_i(\boldsymbol{x} + \boldsymbol{c}_i \delta_t, t + \delta_t) = f_i(\boldsymbol{x}, t) - \frac{1}{\tau_1}\left[f_i(\boldsymbol{x}, t) - f_i^{(eq)}(\boldsymbol{x}, t)\right], \tag{5.92}$$

$$g_i(\boldsymbol{x} + \boldsymbol{c}_i \delta_t, t + \delta_t) = g_i(\boldsymbol{x}, t) - \frac{1}{\tau_2}\left[g_i(\boldsymbol{x}, t) - g_i^{(eq)}(\boldsymbol{x}, t)\right], \tag{5.93}$$

where the two EDFs are defined by

$$f_i^{(eq)} = \begin{cases} \omega_i \rho \left[\chi_0 - \dfrac{u^2}{2c_s^2}\right], & i = 0, \\ \omega_i \rho \left[\chi + \dfrac{\boldsymbol{c}_i \cdot \boldsymbol{u}}{c_s^2} + \dfrac{(\boldsymbol{c}_i \cdot \boldsymbol{u})^2}{2c_s^4} - \dfrac{u^2}{2c_s^2}\right], & i \neq 0, \end{cases} \tag{5.94}$$

$$g_i^{(eq)} = e f_i^{(eq)} \,. \tag{5.95}$$

Here the parameters χ_0 and χ are related by $\chi_0\omega_0 + \chi\sum_i \omega_i = 1$, or $\chi_0 = (1 - \chi + \chi\omega_0)/\omega_0$. The fluid density, velocity, and temperature are defined as

$$\rho = \sum_i f_i\,,\ \rho\boldsymbol{u} = \sum_i \boldsymbol{c}_i f_i\,,\ \rho T = \sum_i g_i\,. \tag{5.96}$$

It is obvious that $f_i^{(eq)}$ is the EDF of the standard isothermal LBE as $\chi = 1$. The Chapman-Enskog analysis shows that the recovered macroscopic equations of this LBE are just as those given by Eqs. (5.88) to (5.90) (without the body force) with the same viscosity and thermal diffusivity. As $\chi \neq 1$, however, some errors exist in the momentum equations, which can be ignored if the time step is sufficiently small. Meanwhile, the equation of state of the LBE is also related to χ, $p = c_s^2\rho\chi$, which means that an equation of state for non-ideal gases can be obtained by selecting an appropriate formulation of χ.

5.5.3 *DDF-LBE for incompressible flows*

DDF-LBE models, which treat the velocity and temperature fields separately, make use of an intrinsic assumption that the temperature variations have little effects on the fluid motion. This assumption is valid only for small Mach number flows, in which the fluid can be regarded as incompressible and the fluid density can be considered to be constant except in the buoyancy term (Boussinesq assumption). Under such circumstances, the governing equations for the velocity and temperature are

$$\nabla\cdot\boldsymbol{u}=0\,, \tag{5.97}$$

$$\frac{\partial\boldsymbol{u}}{\partial t} + \boldsymbol{u}\cdot\nabla\boldsymbol{u} = -\nabla P + \nu\nabla^2\boldsymbol{u} + \boldsymbol{g}\beta(T - T_0)\,, \tag{5.98}$$

$$\frac{\partial T}{\partial t} + \boldsymbol{u}\cdot\nabla T = \alpha\nabla^2 T\,, \tag{5.99}$$

where $P = p/\rho_0$ is the reduced dynamic pressure, β is the thermal expansion coefficient, and T_0 is a referenced temperature.

In order to solve the above equations, Guo *et al.* [2002] constructed a type of DDF-LBE models based on incompressible LBE models. For example, the D2Q9 model of this type can be written as,

$$f_i(\boldsymbol{x} + \boldsymbol{c}_i\delta_t, t + \delta_t) = f_i(\boldsymbol{x}, t) - \frac{1}{\tau_1}\Big[f_i(\boldsymbol{x}, t) - f_i^{(eq)}(\boldsymbol{x}, t)\Big] + \delta_t F_i, \tag{5.100}$$

for $i = 0 \sim 8$, and

$$g_i(\boldsymbol{x} + \boldsymbol{c}_i\delta_t, t + \delta_t) = g_i(\boldsymbol{x}, t) - \frac{1}{\tau_2}\Big[g_i(\boldsymbol{x}, t) - g_i^{(eq)}(\boldsymbol{x}, t)\Big], \quad (5.101)$$

for $i = 1 \sim 4$. Here $f_i^{(eq)}$ are given by Eq. (3.16), and the EDF for the temperature distribution function is defined by

$$T_i^{(eq)} = \frac{T}{4}\left[1 + 2\frac{\boldsymbol{c}_i \cdot \boldsymbol{u}}{c^2}\right], \quad i = 1 \sim 4\,. \quad (5.102)$$

The velocity, pressure, and temperature, are defined as

$$\boldsymbol{u} = \sum_{i=1}^{8} \boldsymbol{c}_i f_i\,,\ P = \frac{c^2}{4\sigma}\left[\sum_{i=1}^{8} f_i + s_0(\boldsymbol{u})\right],\ T = \sum_{i=1}^{4} g_i\,, \quad (5.103)$$

where σ is the parameter in $f_i^{(eq)}$ (see Eq. (3.16) in Chap. 3).

In the original model, the forcing term F_i is suggested to take the following form,

$$F_i = \begin{cases} \dfrac{\boldsymbol{c}_i \cdot \boldsymbol{g}}{2c^2}\beta(T - T_0), & i = 2, 4, \\ 0, & \text{other.} \end{cases} \quad (5.104)$$

It can be verified easily that $\sum_i F_i = 0\,, \sum_i \boldsymbol{c}_i F_i = \boldsymbol{F} \equiv \boldsymbol{g}\beta(T - T_0)$, and $\sum_i \boldsymbol{c}_i\boldsymbol{c}_i F_i = 0$. Therefore, the zeroth through second velocity moments of F_i defined in this way are the same as those of $F_i' = \omega_i \boldsymbol{c}_i \cdot \boldsymbol{F}/c_s^2$. As discussed in Chapter 3, the forcing term defined this way will produce some artifacts. However, if the Mach number and temperature variations are small, the error due to this forcing term is not significant. In such cases it can be shown that Eqs. (5.97)-(5.99) can be recovered from the above DDF-LBE, with the following transport coefficients,

$$\nu = \frac{c^2}{3}\left(\tau_1 - \frac{1}{2}\right)\delta_t\,,\ \ \alpha = \frac{c^2}{2}\left(\tau_2 - \frac{1}{2}\right)\delta_t\,. \quad (5.105)$$

The corresponding Prandtl number is therefore $\mathrm{Pr} = \frac{2}{3}(\tau_1 - 0.5)/(\tau_2 - 0.5)$.

The above incompressible DDF-LBE model can also be extended to three-dimensional flows. A small advantage of such models is that the LBE for the energy equations uses only $2D$ discrete velocities, which

needs less computational memory than the aforementioned DDF-LBE models. Furthermore, compressibility errors in such models can be reduced, as their isothermal counterparts.

5.6 DDF-LBE with Viscous Dissipation and Compression Work – Internal Energy Formulation

The DDF-LBE models presented in the above sections all neglect the viscous dissipation and the compression work, which may be important in some cases. The first DDF-LBE with the consideration of these two factors is due to He *et al*. (HCD model) [1998], which introduces an internal energy distribution function based on the continuous Boltzmann equation.

5.6.1 *Internal energy distribution function*

The HCD model starts from the continuous Boltzmann equation,

$$\frac{\partial f}{\partial t} + \boldsymbol{\xi} \cdot \nabla f = \Omega(f)\,, \tag{5.106}$$

where $f = f(\boldsymbol{x}, \boldsymbol{\xi}, t)$ is the velocity distribution function. For monatomic gases, the density ρ, velocity $\boldsymbol{u}$, and internal energy e, are determined as

$$\rho = \int f d\boldsymbol{\xi}\,, \quad \rho \boldsymbol{u} = \int \boldsymbol{\xi} f d\boldsymbol{\xi}\,, \quad \rho e = \frac{DRT}{2} = \frac{1}{2}\int (\xi - u)^2 f d\boldsymbol{\xi}\,. \tag{5.107}$$

If we introduce an internal energy distribution function,

$$g(\boldsymbol{x}, \boldsymbol{\xi}, t) = \frac{(\xi - u)^2 f}{2}, \tag{5.108}$$

the internal energy can then be defined as,

$$\rho e = \int g d\boldsymbol{\xi}\,. \tag{5.109}$$

According to the Boltzmann equation (5.106), the evolution equation for the international energy distribution function g can be deduced,

$$\frac{\partial g}{\partial t} + \boldsymbol{\xi} \cdot \nabla g = \frac{(\xi - u)^2}{2}\Omega(f) - fq \equiv \Omega(g) - fq\,, \tag{5.110}$$

where

$$q = (\boldsymbol{\xi} - \boldsymbol{u}) \cdot \left[\frac{\partial \boldsymbol{u}}{\partial t} + \boldsymbol{\xi} \cdot \nabla \boldsymbol{u} \right]. \tag{5.111}$$

He *et al*. suggested using the BGK models with different relaxation times to approximate the collision operators $\Omega(f)$ and $\Omega(g)$,

$$\frac{\partial f}{\partial t} + \boldsymbol{\xi} \cdot \nabla f = -\frac{1}{\tau_u}\left(f - f^{(eq)} \right), \tag{5.112}$$

$$\frac{\partial g}{\partial t} + \boldsymbol{\xi} \cdot \nabla g = -\frac{1}{\tau_e}\left(g - g^{(eq)} \right) - fq, \tag{5.113}$$

where $f^{(eq)}$ is the Maxwell distribution, and $g^{(eq)}$ is defined by

$$g^{(eq)} = \frac{(\xi - u)^2}{2} f^{(eq)} = \frac{\rho(\xi - u)^2}{2(2\pi RT)^{D/2}} \exp\left[-\frac{(\xi - u)^2}{2RT} \right]. \tag{5.114}$$

Using the Chapman-Enskog expansion we can obtain the following thermohydrodynamic equations from Eqs. (5.112) and (5.113),

$$\frac{\partial \rho}{\partial t} + \nabla \cdot (\rho \boldsymbol{u}) = 0, \tag{5.115}$$

$$\frac{\partial (\rho \boldsymbol{u})}{\partial t} + \nabla \cdot (\rho \boldsymbol{u}\boldsymbol{u}) = -\nabla p + \nabla \cdot \boldsymbol{\tau}, \tag{5.116}$$

$$\frac{\partial (\rho e)}{\partial t} + \nabla \cdot (\rho \boldsymbol{u} e) = \nabla \cdot (\rho \alpha \nabla e) + \boldsymbol{\tau} : \nabla \boldsymbol{u} - p \nabla \cdot \boldsymbol{u}, \tag{5.117}$$

where $p = \rho RT$ is the pressure, $\boldsymbol{\tau} = 2\rho\nu \boldsymbol{S}$ is the viscous stress with $\nu = \tau_u RT$, and $\alpha = (D+2)\tau_e RT/D$ is the thermal diffusivity. These equations are similar to those corresponding to the continuous Boltzmann-BGK equation, but the Prandtl number now can be tuned to be consistent with that of the Boltzmann equation by adjusting τ_e. Furthermore, the viscous dissipation in the energy equation is also consistent with that in the momentum equation.

In the above discussions no body forces are considered. In the presence of a body force $\boldsymbol{F}$, a forcing term F should be included in

Eq. (5.112),

$$\frac{\partial f}{\partial t} + \boldsymbol{c} \cdot \nabla f = -\frac{1}{\tau_u}\left(f - f^{(eq)}\right) + F, \tag{5.118}$$

where

$$F = \boldsymbol{F} \cdot \nabla_{\xi} f \approx \frac{\boldsymbol{F} \cdot (\boldsymbol{\xi} - \boldsymbol{u})}{RT} f^{(eq)}. \tag{5.119}$$

5.6.2 *Lattice Boltzmann equations*

The HCD model is obtained by discretizing the kinetic equations (5.112) and (5.113). In order to discretize the velocity space, the two EDFs are first expanded into their Taylor series up to $O(\boldsymbol{u}^2)$,

$$f^{(eq)} = \frac{\rho}{(2\pi RT)^{D/2}} \exp\left(-\frac{\xi^2}{2RT}\right)\left[1 + \frac{\boldsymbol{\xi} \cdot \boldsymbol{u}}{RT} + \frac{(\boldsymbol{\xi} \cdot \boldsymbol{u})^2}{2(RT)^2} - \frac{u^2}{2RT}\right], \tag{5.120}$$

$$\begin{aligned} g^{(eq)} &= \frac{e(\xi - u)^2}{DRT} f^{(eq)} \\ &= \frac{\rho e}{(2\pi RT)^{D/2}} \exp\left(-\frac{\xi^2}{2RT}\right)\left[\frac{\xi^2}{DRT} + \left(\frac{\xi^2}{DRT} - \frac{2}{D}\right)\frac{\boldsymbol{\xi} \cdot \boldsymbol{u}}{RT}\right. \\ &\quad \left. + \left(\frac{\xi^2}{DRT} - \frac{4}{D}\right)\frac{(\boldsymbol{\xi} \cdot \boldsymbol{u})^2}{2\left(RT\right)^2} - \left(\frac{\xi^2}{DRT} - \frac{2}{D}\right)\frac{u^2}{2RT}\right]. \end{aligned} \tag{5.121}$$

Because $g^{(eq)}$ contains terms of $\boldsymbol{\xi}^3$, a Gaussian quadrature of degree greater than 2 should be used in order to obtain the desired thermohydrodynamic equations, as discussed in Sec. 5.2. However, He *et al*. found that this can be simplified by regrouping $g^{(eq)}$, in which some terms do not affect the final macroscopic equations and can be omitted. The final simplified $g^{(eq)}$ can be written as

$$\begin{aligned} g^{(eq)} = \frac{\rho e}{(2\pi RT)^{D/2}} \exp\left(-\frac{\xi^2}{2RT}\right)\left[\frac{\xi^2}{DRT} + \left(\frac{\xi^2}{DRT} - \frac{2}{D}\right)\frac{\boldsymbol{\xi} \cdot \boldsymbol{u}}{RT}\right. \\ \left. + \frac{(\boldsymbol{\xi} \cdot \boldsymbol{u})^2}{2(RT)^2} - \frac{u^2}{2RT}\right]. \end{aligned} \tag{5.122}$$

Now $f^{(eq)}$ and $g^{(eq)}$ only contain terms of $O(\boldsymbol{\xi}^2)$, and so the Gaussian quadrature of degree 3 can be employed to obtain the discrete velocities

satisfying the necessary conditions. The velocities determined in this way depend on the local temperature, i.e, $\boldsymbol{c}_i = \boldsymbol{c}_i(T)$. With this discrete velocity set, the HCD LBE can be obtained by discretizing the discrete velocity kinetic equations corresponding to Eqs. (5.118) and (5.113),

$$f_i(\boldsymbol{x} + \boldsymbol{c}_i\delta_t, t + \delta_t) = f_i(\boldsymbol{x}, t) - \omega_u\left(f_i - f_i^{(eq)}\right) + \tau_u\omega_u F_i\,, \quad (5.123)$$

$$g_i(\boldsymbol{x} + \boldsymbol{c}_i\delta_t, t + \delta_t) = g_i(\boldsymbol{x}, t) - \omega_e\left(g_i - g_i^{(eq)}\right) - \tau_e\omega_e\overline{f}_i(\boldsymbol{x}, t)q_i(\boldsymbol{x}, t)\,, \quad (5.124)$$

where $\omega_u = \delta_t/(\tau_u + 0.5\delta_t)$ and $\omega_e = \delta_t/(\tau_e + 0.5\delta_t)$, and the discrete EDFs are given by

$$f_i^{(eq)} = \omega_i\rho\left[1 + \frac{\boldsymbol{c}_i\cdot\boldsymbol{u}}{RT} + \frac{(\boldsymbol{c}_i\cdot\boldsymbol{u})^2}{2(RT)^2} - \frac{u^2}{2RT}\right], \quad (5.125)$$

$$g_i^{(eq)} = \omega_i\rho e\left[\frac{c_i^2}{DRT} + \left(\frac{c_i^2}{DRT} - \frac{2}{D}\right)\frac{\boldsymbol{c}_i\cdot\boldsymbol{u}}{RT} + \frac{(\boldsymbol{c}_i\cdot\boldsymbol{u})^2}{2(RT)^2} - \frac{u^2}{2RT}\right]. \quad (5.126)$$

The discrete forcing term in Eq. (5.123) is defined as

$$F_i = \frac{\boldsymbol{G}\cdot(\boldsymbol{c}_i - \boldsymbol{u})}{RT}f_i^{(eq)}, \quad (5.127)$$

and $\overline{f}_i$ and q_i in the last term on the right hand of Eq. (5.124) are given by

$$\overline{f}_i = \omega_u\left(\frac{\tau_u}{\delta_t}f + 0.5f_i^{(eq)} + \tau_u F_i\right), \quad (5.128)$$

$$q_i = (\boldsymbol{c}_i - \boldsymbol{u})\cdot\left[\frac{1}{\rho}\left(-\nabla p + \nabla\cdot\boldsymbol{\tau}\right) + (\boldsymbol{c}_i - \boldsymbol{u})\cdot\nabla\boldsymbol{u}\right], \quad (5.129)$$

where q_i is obtained from Eq. (5.111) and the momentum equation.

The fluid density, velocity, and internal energy in the HCD LBE model are defined by,

$$\rho = \sum_i f_i, \quad \rho\boldsymbol{u} = \sum_i \boldsymbol{c}_i f_i + \frac{\rho\boldsymbol{G}\delta_t}{2}, \quad \rho e = \sum_i g_i - \frac{\delta_t}{2}\sum\overline{f}_i q_i\,. \quad (5.130)$$

Although the DDF-LBE described by Eqs. (5.123) and (5.124) are discrete versions of the discrete velocity equations (5.112) and (5.113), the corresponding hydrodynamic equations of the LBE are different from

those given by Eqs. (5.115)-(5.117). As mentioned previously, if the discrete velocities change locally with temperature T, the discrete velocity model will not lead to valid thermohydrodynamic equations. Furthermore, the variation of $\boldsymbol{c}_i$ in both time and space also leads to difficulties in implementation. In order to avoid these problems, He *et al.* suggested replacing the local temperature T in the discrete velocities and the EDFs with the averaged temperature T_0. As shown later, however, this replacement will lead to a different equation of state, transport coefficients, and Prandtl number.

5.6.3 *Some simplified models*

The original HCD model involves a source term q_i which includes the calculations of the gradients of velocity and viscous stress, the calculation of these terms may introduce additional errors and may lead to some numerical instabilities. In order to improve the original HCD model, some simplified versions have been developed by different groups.

As the fluid is incompressible (so the compression work is absent) and the viscous dissipation is negligible, He *et al.* [1998] proposed an incompressible DDF-LBE model based on the full HCD LBE, where the LBE for the internal energy distribution function is the same as that in the original HCD model, while the LBE for the velocity field is changed to be the incompressible one [He and Luo, 1997], in which the EDF is

$$f_i^{(eq)} = \omega_i \rho_0 \left[\frac{3p}{\rho_0 c^2} + \frac{\boldsymbol{c}_i \cdot \boldsymbol{u}}{RT_0} + \frac{(\boldsymbol{c}_i \cdot \boldsymbol{u})^2}{2(RT_0)^2} - \frac{u^2}{2RT_0} \right], \tag{5.131}$$

where ρ_0 is the constant density, while the pressure p and velocity u are defined as

$$p = RT_0 \sum_i f_i , \quad \rho_0 \boldsymbol{u} = \sum_i \boldsymbol{c}_i f_i . \tag{5.132}$$

The term q_i can also be simplified since the fluid is incompressible and the viscous dissipation is ignored, i.e.,

$$q_i = (\boldsymbol{c}_i - \boldsymbol{u}) \cdot \left[\frac{1}{\rho_0} (-\nabla p + \nabla \cdot \boldsymbol{\tau}) \right]. \tag{5.133}$$

It is seen that even as the compression work and viscous heat dissipation are neglected, the simplified version of the HCD model still involves the term q_i that contains pressure and velocity gradients, which is more complicated than the incompressible DDF LBE developed by Guo *et al*. [2002].

On the other hand, Peng *et al*. [2003] proposed to abandon the source term q_i in the LBE for the internal energy distribution function as the compression work and viscous dissipation are neglected. The evolution equation of g_i then reduces to

$$g_i(\boldsymbol{x}+\boldsymbol{c}_i\delta_t, t+\delta_t) = g_i(\boldsymbol{x},t) - \omega_e\left(g_i - g_i^{(eq)}\right), \tag{5.134}$$

which leads to the following energy equation

$$\frac{\partial(\rho e)}{\partial t} + \nabla\cdot(\rho \boldsymbol{u} e) = \nabla\cdot(\rho D\nabla e). \tag{5.135}$$

It is clear that this model is very close to that developed by Palmer and Rector [2000a, 2000b].

For low Mach number flows, although the compression work can be ignored, the viscous dissipation may be important in some cases. For such flows, Shi *et al*. [2004] developed another simplified model (SZG model) based on the original HCD one. The SZG model adopts two strategies in the simplifications. First, the term fq is decomposed into three parts, $fq = R_1 + R_2 + R_3$, where

$$\begin{aligned} &R_1 = f\boldsymbol{C}\cdot\left[\partial_t\boldsymbol{u} + \boldsymbol{u}\cdot\nabla\boldsymbol{u}\right],\ \ R_2 = f^{(eq)}\boldsymbol{C}\boldsymbol{C}:\nabla\boldsymbol{u},\\ &R_3 = (f - f^{(eq)})\boldsymbol{C}\boldsymbol{C}:\nabla\boldsymbol{u}. \end{aligned} \tag{5.136}$$

It is easy to verify that R_1 and R_2 do not change the energy equation for low Mach number flows and thus can be ignored, and so the evolution equation for the internal energy distribution function can be simplified as

$$\frac{\partial g}{\partial t} + \boldsymbol{\xi}\cdot\nabla g = \frac{(\xi-u)^2}{2}\Omega(f) - R_3. \tag{5.137}$$

The second simplification strategy adopted in the SZG model is about $g_i^{(eq)}$. Regrouping the Taylor expansion of $g_i^{(eq)}$, Eq. (5.121), and omitting the terms which have no effects on the final energy equation, one can

obtain the following simplified EDF,

$$g^{(eq)} = \frac{\rho e}{(2\pi RT)^{D/2}} \exp\left(-\frac{\xi^2}{2RT}\right)\left[1 + \frac{\boldsymbol{\xi}\cdot\boldsymbol{u}}{RT} + \frac{(\boldsymbol{\xi}\cdot\boldsymbol{u})^2}{2(RT)^2} - \frac{u^2}{2RT}\right]. \quad (5.138)$$

The SGZ model is then constructed based on Eqs. (5.137) and (5.138), in which the LBE for the energy equation is,

$$g_i(\boldsymbol{x} + \boldsymbol{c}_i\delta_t, t + \delta_t) = g_i(\boldsymbol{x}, t) - \omega_e\left(g_i - g_i^{(eq)}\right) - \delta_t R_3, \quad (5.139)$$

where $g_i^{(eq)} = ef_i^{(eq)}$, and $f_i^{(eq)}$ used in SGZ model is the same as that in the HCD model.

5.7 DDF-LBE with Viscous Dissipation and Compression Work – Total Energy Formulation

The HCD model is able to include the effects of compression work and viscous dissipation, and the Prandtl number can be adjusted by tuning the two relaxation times. However, the model involves some terms of gradients of pressure, velocity, and stress, which need additional discretizations. Furthermore, the model is limited to monatomic gases with a fixed specific capacity ratio, and cannot be applied to polyatomic gases with internal freedoms. To overcome these difficulties, Guo *et al*. [2007] proposed a DDF-LBE based on the concept of total energy distribution function.

5.7.1 *Total energy distribution function*

The total energy E is defined as,

$$\rho E = \rho\left(e + \frac{u^2}{2}\right) = \rho c_v T + \frac{1}{2}\rho u^2 = \int \frac{\xi^2}{2} f d\boldsymbol{\xi}\,, \quad (5.140)$$

where c_v is the specific heat capacity at constant volume. Therefore, we can introduce a total energy distribution function,

$$h(\boldsymbol{x}, \boldsymbol{\xi}, t) = \frac{\xi^2}{2} f(\boldsymbol{x}, \boldsymbol{\xi}, t)\,. \quad (5.141)$$

Then the total energy can be defined by

$$\rho E = \int h(\boldsymbol{x}, \boldsymbol{\xi}, t) d\boldsymbol{\xi} \,. \tag{5.142}$$

From the continuous Boltzmann equation with a body force $\boldsymbol{F} = \rho \boldsymbol{a}$,

$$\frac{\partial f}{\partial t} + \boldsymbol{\xi} \cdot \nabla f + \boldsymbol{a} \cdot \nabla_{\xi} f = \Omega_f \,, \tag{5.143}$$

we can derive the evolution equation for h,

$$\frac{\partial h}{\partial t} + \boldsymbol{\xi} \cdot \nabla f + \boldsymbol{a} \cdot \nabla_{\xi} h - \boldsymbol{\xi} f = \Omega_h \,, \tag{5.144}$$

where $\Omega_h = \xi^2 \Omega_f / 2$.

In order to establish a simple kinetic model for the total energy distribution function h, we first examine the properties of the collision operator Ω_h. Physically, this operator reflects the energy change due to particle collisions, and the contribution includes two parts, i.e.,

$$\Omega_h = \Omega_i + \Omega_m \,, \tag{5.145}$$

where the first and second terms on the right side represent the changes of internal energy and mechanical energy, respectively,

$$\Omega_i = \frac{(\xi - u)^2}{2} \Omega_f \,, \; \Omega_m = \frac{1}{2} \left[\xi^2 - (\xi - u)^2 \right] \Omega_f \equiv Z \Omega_f \,, \tag{5.146}$$

where $Z = \boldsymbol{\xi} \cdot \boldsymbol{u} - u^2/2$. If Ω_f is modeled by a BGK operator,

$$\Omega_f = -\frac{1}{\tau_f} \left(f - f^{(eq)} \right) , \tag{5.147}$$

Ω_m can then be approximated by

$$\Omega_m = -\frac{Z}{\tau_f} \left(f - f^{(eq)} \right) . \tag{5.148}$$

Now we consider the internal energy part. According to the theory of Woods [1993], the relaxation times of momentum and internal energy changes during the collision are different, so we can model Ω_i as a relaxation process of the internal energy distribution function

$g = h - Zf$ with a different relaxation time, i.e.,

$$\Omega_i = -\frac{1}{\tau_h}\big[g - g^{(eq)}\big] = -\frac{1}{\tau_h}\big[h - h^{(eq)} - Z(f - f^{(eq)})\big], \quad (5.149)$$

where $h^{(eq)} = \xi^2 f^{(eq)} / 2$, and τ_h is the relaxation time for internal energy. Therefore, the collision operator of the total energy can be expressed as

$$\Omega_h = -\frac{1}{\tau_h}\big[h - h^{(eq)}\big] + \frac{Z}{\tau_{hf}}\big[f - f^{(eq)}\big], \quad (5.150)$$

where

$$\frac{1}{\tau_{hf}} = \frac{1}{\tau_h} - \frac{1}{\tau_f}. \quad (5.151)$$

Obviously the second term of Ω_h is 0 as $\tau_h = \tau_f$, and the above collision model reduces to the standard BGK model. Otherwise, the second term should be considered as a correction to the BGK model. Actually, without this term the viscous stress in the derived momentum equation will be inconsistent with that in the energy equation, although the Prandtl number can be tuned.

In summary, by introducing the total energy distribution function one can obtain the following two-relaxation-time kinetic model that is consistent with the Boltzmann equation,

$$\frac{\partial f}{\partial t} + \boldsymbol{\xi}\cdot\nabla f + \boldsymbol{a}\cdot\nabla_{\xi} f = -\frac{1}{\tau_f}\big(f - f^{(eq)}\big), \quad (5.152)$$

$$\frac{\partial h}{\partial t} + \boldsymbol{\xi}\cdot\nabla h + \boldsymbol{a}\cdot\nabla_{\xi} h = -\frac{1}{\tau_h}\big(h - h^{(eq)}\big) + \frac{Z}{\tau_{hf}}\big(f - f^{(eq)}\big) + f\boldsymbol{\xi}\cdot\boldsymbol{a}. \quad (5.153)$$

The Chapman-Enskog analysis shows that the thermohydrodynamic equations corresponding to the kinetic model are

$$\frac{\partial \rho}{\partial t} + \nabla\cdot(\rho\boldsymbol{u}) = 0, \quad (5.154)$$

$$\frac{\partial(\rho\boldsymbol{u})}{\partial t} + \nabla\cdot(\rho\boldsymbol{u}\boldsymbol{u}) = -\nabla p + \nabla\cdot\boldsymbol{\tau} + \rho\boldsymbol{a}, \quad (5.155)$$

$$\frac{\partial(\rho E)}{\partial t} + \nabla\cdot\big[(p + \rho E)\boldsymbol{u}\big] = \nabla\cdot(\kappa\nabla T) + \nabla\cdot\big(\boldsymbol{\tau}\cdot\boldsymbol{u}\big) - \rho\boldsymbol{u}\cdot\boldsymbol{a}, \quad (5.156)$$

where $p=\rho RT$ and $\boldsymbol{\tau}=2\mu[\boldsymbol{S}-D^{-1}(\nabla\cdot\boldsymbol{u})\boldsymbol{I}]$, and the viscosity and thermal conductivity are given by

$$\mu=\tau_f p\,,\ \kappa=\frac{(D+2)R}{2}\tau_h p=c_p\tau_h p\,. \tag{5.157}$$

Therefore, the Prandtl number of the above kinetic model is $\mathrm{Pr}=\mu c_p/\kappa=\tau_f/\tau_h$. It can be found that the above thermohydrodynamic equations are the same as those of the continuous Boltzmann equation with the full collision operator or Woods' model [1993].

The above kinetic model can also be extended to polyatomic gases which exhibit internal degrees of freedom such as rotation or vibration. The distribution function f can take account of the internal motions as well through a vector variable $\boldsymbol{\eta}=(\eta_1,\eta_2,\cdots,\eta_K)$, namely, $f=f(\boldsymbol{x},\boldsymbol{\xi},\boldsymbol{\eta},t)$, where K is the number of internal degree of freedoms. The evolution equation of f can also be described by the Boltzmann-BGK equation as

$$\frac{\partial f}{\partial t}+\boldsymbol{\xi}\cdot\nabla f+\boldsymbol{a}\cdot\nabla_{\boldsymbol{\xi}}f=-\frac{1}{\tau_f}[f-f^{(eq)}], \tag{5.158}$$

where

$$f^{(eq)}=\frac{\rho}{(2\pi RT)^{(D+K)/2}}\exp\left[-\frac{(\xi-u)^2+\eta^2}{2RT}\right]. \tag{5.159}$$

The fluid variables for polyatomic gases are defined as

$$\begin{aligned}&\rho=\int f d\boldsymbol{\xi}d\boldsymbol{\eta},\qquad \rho\boldsymbol{u}=\int\boldsymbol{\xi}f d\boldsymbol{\xi}d\boldsymbol{\eta},\\&\frac{(D+K)\rho RT}{2}=\int\frac{(\xi-u)^2+\eta^2}{2}f d\boldsymbol{\xi}d\boldsymbol{\eta}.\end{aligned} \tag{5.160}$$

In order to eliminate the explicit dependence of the internal variable $\boldsymbol{\eta}$, we can introduce two reduced distribution functions,

$$\bar{f}=\int f d\boldsymbol{\eta}\,,\ \bar{h}=\int\frac{\xi^2+\eta^2}{2}f d\boldsymbol{\eta}\,, \tag{5.161}$$

whose evolution equations can be obtained from the generalized Boltzmann-BGK equation (5.158),

$$\frac{\partial \overline{f}}{\partial t} + \boldsymbol{\xi} \cdot \nabla \overline{f} + \boldsymbol{a} \cdot \nabla_{\xi} \overline{f} = -\frac{1}{\tau_f}\left[\overline{f} - \overline{f}^{(eq)}\right], \tag{5.162}$$

$$\frac{\partial \overline{h}}{\partial t} + \boldsymbol{\xi} \cdot \nabla \overline{h} + \boldsymbol{a} \cdot \nabla_{\xi} \overline{h} = -\frac{1}{\tau_h}\left[\overline{h} - \overline{h}^{(eq)}\right] + \frac{Z}{\tau_{hf}}\left[\overline{f} - \overline{f}^{(eq)}\right] + \overline{f}\boldsymbol{\xi} \cdot \boldsymbol{a}, \tag{5.163}$$

where

$$\overline{f}^{(eq)} = \int f^{(eq)} d\boldsymbol{\eta} = \frac{\rho}{(2\pi RT)^{D/2}} \exp\left[-\frac{(\xi - u)^2}{2RT}\right], \tag{5.164}$$

$$\overline{h}^{(eq)} = \int \frac{\xi^2 + \eta^2}{2} f^{(eq)} d\boldsymbol{\eta} = \frac{\rho(\xi^2 + KRT)}{2(2\pi RT)^{D/2}} \exp\left[-\frac{(\xi - u)^2}{2RT}\right]. \tag{5.165}$$

The fluid variables can be calculated from these two reduced distribution functions,

$$\rho = \int \overline{f}\, d\boldsymbol{\xi}, \ \rho \boldsymbol{u} = \int \boldsymbol{\xi} \overline{f}\, d\boldsymbol{\xi}, \ \rho E = \int \overline{h}\, d\boldsymbol{\xi}. \tag{5.166}$$

Obviously, the kinetic equations (5.162) and (5.163) for polyatomic gases have similar structures as those for monatomic gases given by Eqs. (5.152) and (5.153). Furthermore, the Chapman-Enskog analysis shows that the hydrodynamic equations derived from this kinetic model are the same as Eqs. (5.154) ~ (5.156), except that now the two specific heat capacities depend on the degree of freedom K, i.e., $c_v = (D + K)R/2$ and $c_p = (D + K + 2)R/2$. In what follows we will only consider the case of polyatomic gases and will omit the overbar symbols on the variables.

5.7.2 *Discrete velocity model*

(1) Hermite expansions of the EDFs

In the HCD model, the EDF in polynomial form is obtained by making use of the Taylor expansion of the continuous Maxwellian distribution function. Alternatively, we can also employ the Hermite expansion. For isothermal flows, the final formulations of these two expansions are

identical up to second-order, but the expressions for non-isothermal flow will be different. Here we will adopt the latter method since the first few moments of the expanded EDFs could be the same as the continuous ones with suitable truncations.

The EDFs defined by Eqs. (5.164) and (5.165) can be expanded into the Hermite polynomials,

$$f^{(eq)} = \omega(\boldsymbol{\xi},T)\sum_i \frac{A^{(n)}_{\boldsymbol{\alpha}}(\boldsymbol{x},t)}{n!} H^{(n)}_{\boldsymbol{\alpha}}(\hat{\boldsymbol{\xi}})\,. \tag{5.167}$$

$$h^{(eq)} = \omega(\boldsymbol{\xi},T)\sum_i \frac{B^{(n)}_{\boldsymbol{\alpha}}(\boldsymbol{x},t)}{n!} H^{(n)}_{\boldsymbol{\alpha}}(\hat{\boldsymbol{\xi}})\,, \tag{5.168}$$

where

$$\omega(\boldsymbol{\xi},T) = \frac{1}{(2\pi RT)^{D/2}}\exp\left(-\frac{\boldsymbol{\xi}^2}{2RT}\right),\ \hat{\boldsymbol{\xi}} = \boldsymbol{\xi}/\sqrt{RT}\,. \tag{5.169}$$

The expansion coefficients are given by

$$A^{(n)}_{\boldsymbol{\alpha}} = \int f^{(eq)} H^{(n)}_{\boldsymbol{\alpha}}(\hat{\boldsymbol{\xi}})d\boldsymbol{\xi}\,,\ B^{(n)}_{\boldsymbol{\alpha}} = \int h^{(eq)} H^{(n)}_{\boldsymbol{\alpha}}(\hat{\boldsymbol{\xi}})d\boldsymbol{\xi}\,. \tag{5.170}$$

In the Chapman-Enskog expansion, in order to obtain the desired hydrodynamic equations at the second-order (i.e. Navier-Stokes) level, the third-order term should be retained in the expansion of $f^{(eq)}$, as well as the second-order term in the expansion of $h^{(eq)}$. For low Mach number flows, it is enough to truncate the expansion of $f^{(eq)}$ up to the second order. The first few expansion coefficients can be easily evaluated,

$$A^{(0)} = \rho\,,\ \boldsymbol{A}^{(1)} = \rho\boldsymbol{u}\,,\ \ \boldsymbol{A}^{(2)} = \rho\boldsymbol{u}\boldsymbol{u}\,, \tag{5.171}$$

$$B^{(0)} = \rho E\,, \boldsymbol{B}^{(1)} = (p+\rho E)\boldsymbol{u}\,,\ \boldsymbol{B}^{(2)} = pRT\boldsymbol{I} + (2p+\rho E)\boldsymbol{u}\boldsymbol{u}\,. \tag{5.172}$$

As such, the second-order Hermite expansions of $f^{(eq)}$ and $h^{(eq)}$ can be explicitly written as

$$f^{(eq)} = \omega\rho\left\{1 + \frac{\boldsymbol{\xi}\cdot\boldsymbol{u}}{RT} + \frac{1}{2}\left(\frac{\boldsymbol{\xi}\cdot\boldsymbol{u}}{RT}\right)^2 - \frac{\boldsymbol{u}^2}{2RT} + \frac{\boldsymbol{\xi}\cdot\boldsymbol{u}}{6RT}\left[\left(\frac{\boldsymbol{\xi}\cdot\boldsymbol{u}}{RT}\right)^2 - \frac{3\boldsymbol{u}^2}{RT}\right]\right\}, \tag{5.173}$$

$$h^{(eq)} = \omega\left\{\rho E + (p+\rho E)\frac{\boldsymbol{\xi}\cdot\boldsymbol{u}}{RT} + \frac{p}{2}\left(\frac{\boldsymbol{\xi}^2}{RT} - D\right) + \left(p+\frac{\rho E}{2}\right)\left[\left(\frac{\boldsymbol{\xi}\cdot\boldsymbol{u}}{RT}\right)^2 - \frac{\boldsymbol{u}^2}{RT}\right]\right\}$$
$$= \omega p\left[\frac{\boldsymbol{\xi}\cdot\boldsymbol{u}}{RT} + \left(\frac{\boldsymbol{\xi}\cdot\boldsymbol{u}}{RT}\right)^2 - \frac{\boldsymbol{u}^2}{RT} + \frac{1}{2}\left(\frac{\boldsymbol{\xi}^2}{RT} - D\right)\right] + Ef^{(eq)}. \tag{5.174}$$

Accordingly, the terms associated with the body force, $\boldsymbol{a}\cdot\nabla_{\xi}f$ and $\boldsymbol{a}\cdot\nabla_{\xi}h$, can also be expanded into Hermite polynomials, which should retain the terms up to second and first orders, respectively,

$$\boldsymbol{a}\cdot\nabla_{\xi}f = -\omega(\boldsymbol{\xi},T)\rho\left[\frac{\boldsymbol{\xi}\cdot\boldsymbol{a}}{RT} + \frac{(\boldsymbol{\xi}\cdot\boldsymbol{a})(\boldsymbol{\xi}\cdot\boldsymbol{u})}{(RT)^2} - \frac{\boldsymbol{a}\cdot\boldsymbol{u}}{RT}\right], \tag{5.175}$$

$$\boldsymbol{a}\cdot\nabla_{\xi}h = -\omega(\boldsymbol{\xi},T)\rho E\frac{\boldsymbol{\xi}\cdot\boldsymbol{a}}{RT}. \tag{5.176}$$

It is easy to verify that the thermohydrodynamic equations with the above expanded EDFs and forcing terms are the same as those with the original ones after neglecting the terms of $O(M^3)$ (M is the Mach number).

(2) Discretization of the velocity space

The expanded EDFs given by (5.173) and (5.174) depend on the local temperature T, which will lead to temperature-dependent discrete velocities and some unphysical problems as mentioned previously. In order to avoid this difficulty, Guo *et al*. suggested replacing T with a reference temperature T_0,

$$f^{(eq)}(T_0) = \omega(\boldsymbol{\xi};T_0)\rho\left[1 + \frac{\boldsymbol{\xi}\cdot\boldsymbol{u}}{RT_0} + \frac{1}{2}\left(\frac{\boldsymbol{\xi}\cdot\boldsymbol{u}}{RT_0}\right)^2 - \frac{\boldsymbol{u}^2}{2RT_0}\right], \tag{5.177}$$

$$h^{(eq)}(T_0) = \omega(\boldsymbol{\xi},T_0)p_0\left[\frac{\boldsymbol{\xi}\cdot\boldsymbol{u}}{RT_0} + \left(\frac{\boldsymbol{\xi}\cdot\boldsymbol{u}}{RT_0}\right)^2 - \frac{\boldsymbol{u}^2}{RT_0} + \frac{1}{2}\left(\frac{\boldsymbol{\xi}^2}{RT_0} - D\right)\right], + Ef^{(eq)}(T_0), \tag{5.178}$$

where $\omega(\boldsymbol{\xi}, T_0) = (2\pi R T_0)^{-D/2} \exp(-\xi^2/2RT_0)$ and $p_0 = \rho R T_0$. But it should be noted that the temperature in the total energy E is still the local one, i.e., $E = c_v T + u^2/2$. In the two forcing terms the local temperature T is also replaced by the reference one T_0.

From the expressions of the expanded EDFs we can show that

$$\int f^{(eq)}(T_0) d\boldsymbol{\xi} = \rho = \int f^{(eq)}(T) d\boldsymbol{\xi}\,, \tag{5.179}$$

$$\int \boldsymbol{\xi} f^{(eq)}(T_0) d\boldsymbol{\xi} = \rho \boldsymbol{u} = \int \boldsymbol{\xi} f^{(eq)}(T) d\boldsymbol{\xi}\,, \tag{5.180}$$

$$\int h^{(eq)}(T_0) d\boldsymbol{\xi} = \rho E = \int h^{(eq)}(T) d\boldsymbol{\xi}\,. \tag{5.181}$$

But the high-order moments of $f^{(eq)}(T_0)$ and $h^{(eq)}(T_0)$ are different from their counterparts of $f^{(eq)}(T)$ and $h^{(eq)}(T)$,

$$\int \xi_\alpha \xi_\beta f^{(eq)}(T_0) d\boldsymbol{\xi} = \rho u_\alpha u_\beta + p_0 \delta_{\alpha\beta}\,, \tag{5.182}$$

$$\int \xi_\alpha \xi_\beta \xi_\gamma f^{(eq)}(T_0) d\boldsymbol{\xi} = p_0 (u_\alpha \delta_{\beta\gamma} + u_\beta \delta_{\alpha\gamma} + u_\gamma \delta_{\alpha\beta})\,, \tag{5.183}$$

$$\int \xi_\alpha h^{(eq)}(T_0) d\boldsymbol{\xi} = (p_0 + \rho E) u_\alpha\,, \tag{5.184}$$

$$\int \xi_\alpha \xi_\beta h^{(eq)}(T_0) d\boldsymbol{\xi} = p_0 (RT_0 + E)\delta_{\alpha\beta} + (2p_0 + \rho E) u_\alpha u_\beta\,. \tag{5.185}$$

These differences will lead to some differences in the hydrodynamic equations, which will be discussed in more detail later.

Based on the velocity moments of $f^{(eq)}(T_0)$ and $h^{(eq)}(T_0)$, we can choose the Gaussian quadrature of degree 5 to obtain the discrete velocities $\boldsymbol{c}_i$ and weight coefficients w_i, with which the following discrete distribution functions can be defined,

$$f_i(\boldsymbol{x}, t) = \frac{w_i f(\boldsymbol{x}, \boldsymbol{c}_i, t)}{\omega(\boldsymbol{c}_i, T_0)}\,, \quad h_i(\boldsymbol{x}, t) = \frac{w_i h(\boldsymbol{x}, \boldsymbol{c}_i, t)}{\omega(\boldsymbol{c}_i, T_0)}\,. \tag{5.186}$$

The fluid variables can then be calculated as

$$\rho = \sum_i f_i\,,\ \rho \boldsymbol{u} = \sum_i \boldsymbol{c}_i f_i\,,\ \rho E = \sum_i h_i\,. \tag{5.187}$$

The following discrete velocity model (DVM) can be obtained from the kinetic equations (5.162) and (5.163),

$$\frac{\partial f_i}{\partial t} + \boldsymbol{c}_i \cdot \nabla f_i = -\frac{1}{\tau_f}\left[f_i - f_i^{(eq)} \right] + F_i \,, \tag{5.188}$$

$$\frac{\partial h_i}{\partial t} + \boldsymbol{c}_i \cdot \nabla h_i = -\frac{1}{\tau_h}\left[h_i - h_i^{(eq)} \right] + \frac{Z_i}{\tau_{hf}}\left[f_i - f_i^{(eq)} \right] + q_i \,, \tag{5.189}$$

where $Z_i = \boldsymbol{c}_i \cdot \boldsymbol{u} - u^2/2$, and

$$f_i^{(eq)} = w_i \rho \left[1 + \frac{\boldsymbol{c}_i \cdot \boldsymbol{u}}{RT_0} + \frac{1}{2}\left(\frac{\boldsymbol{c}_i \cdot \boldsymbol{u}}{RT_0} \right)^2 - \frac{\boldsymbol{u}^2}{2RT_0} \right], \tag{5.190}$$

$$h_i^{(eq)} = w_i p_0 \left[\frac{\boldsymbol{c}_i \cdot \boldsymbol{u}}{RT_0} + \left(\frac{\boldsymbol{c}_i \cdot \boldsymbol{u}}{RT_0} \right)^2 - \frac{\boldsymbol{u}^2}{RT_0} + \frac{1}{2}\left(\frac{\boldsymbol{c}_i^2}{RT_0} - D \right) \right] + E f_i^{(eq)} . \tag{5.191}$$

F_i and q_i are the two forcing terms,

$$\begin{aligned} F_i &= w_i \rho \left[\frac{\boldsymbol{c}_i \cdot \boldsymbol{a}}{RT_0} + \frac{(\boldsymbol{c}_i \cdot \boldsymbol{a})(\boldsymbol{c}_i \cdot \boldsymbol{u})}{(RT_0)^2} - \frac{\boldsymbol{a} \cdot \boldsymbol{u}}{RT_0} \right], \\ q_i &= w_i \rho E \frac{\boldsymbol{c}_i \cdot \boldsymbol{a}}{RT_0} + f_i \boldsymbol{c}_i \cdot \boldsymbol{a}. \end{aligned} \tag{5.192}$$

With these expressions, the thermohydrodynamic equations corresponding to the DVM (5.188) and (5.189) can be derived through the Chapman-Enskog analysis,

$$\frac{\partial \rho}{\partial t} + \nabla \cdot (\rho \boldsymbol{u}) = 0 \,, \tag{5.193}$$

$$\frac{\partial (\rho \boldsymbol{u})}{\partial t} + \nabla \cdot (\rho \boldsymbol{u}\boldsymbol{u}) = -\nabla p_0 + \nabla \cdot \boldsymbol{\tau} + \rho \boldsymbol{a} \,, \tag{5.194}$$

$$\frac{\partial (\rho E)}{\partial t} + \nabla \cdot \left[(p_0 + \rho E)\boldsymbol{u} \right] = \nabla \cdot (\kappa \nabla T) + \nabla \cdot \left(\boldsymbol{\tau} \cdot \boldsymbol{u} \right) + \rho \boldsymbol{u} \cdot \boldsymbol{a} \,, \tag{5.195}$$

where $\boldsymbol{\tau} = 2\mu \boldsymbol{S}$ with $\mu = \tau_f p_0$, and the thermal conductivity is $\kappa = c_v \tau_h \, p_0$.

Although the macroscopic equations (5.193)~(5.195) are similar to those given by Eqs. (5.154)~(5.156), which are derived from the original kinetic model, some differences should be noted.

- The equation of state and transport coefficients in Eqs. (5.154)~(5.156) are functions of the local temperature T, while those in Eqs. (5.193)~(5.195) are independent of T, and p_0 behaves as a dynamic pressure rather than a thermodynamic one. Therefore, the temperature field does not affect the velocity field through the equation of state and the viscosity coefficient, which means that the energy equation is decoupled from the momentum equation. In this regard, the DVM described by Eqs. (5.188) and (5.189) is a decoupling model.
- The Prandtl numbers in the two systems are different. In Eqs. (5.193)~(5.195), the thermal conductivity is $\kappa = c_v \tau_h p_0$ and the Prandtl number is $\mathrm{Pr} = \mu c_p / \kappa = \gamma \tau_f / \tau_h$, where $\gamma = c_p / c_v$ is the specific heat ratio. On the other hand, in Eqs. (5.154)-(5.156) $\kappa = c_p \tau_h p$ and $\mathrm{Pr} = \tau_f / \tau_h$.

5.7.3 *Lattice Boltzmann equations*

Integrating Eqs. (5.188) and (5.189) along the characteristic line and applying the trapezoidal rule to the collision terms lead to following kinetic equations

$$f_i(\boldsymbol{x} + \boldsymbol{c}_i\delta_t, t + \delta_t) - f_i(\boldsymbol{x}, t) = \frac{\delta_t}{2}\left[\Omega_f(\boldsymbol{x}, t) + F_i(\boldsymbol{x}, t)\right] + \frac{\delta_t}{2}\left[\Omega_f(\boldsymbol{x} + \boldsymbol{c}_i\delta_t, t + \delta_t) + F_i(\boldsymbol{x} + \boldsymbol{c}_i\delta_t, t + \delta_t)\right], \quad (5.196)$$

$$h_i(\boldsymbol{x} + \boldsymbol{c}_i\delta_t, t + \delta_t) - h_i(\boldsymbol{x}, t) = \frac{\delta_t}{2}\left[\Omega_h(\boldsymbol{x}, t) + S_i(\boldsymbol{x}, t)\right] + \frac{\delta_t}{2}\left[\Omega_h(\boldsymbol{x} + \boldsymbol{c}_i\delta_t, t + \delta_t) + S_i(\boldsymbol{x} + \boldsymbol{c}_i\delta_t, t + \delta_t)\right], \quad (5.197)$$

where $\Omega_f = [f_i^{(eq)} - f_i]/\tau_f$ and $S_i = Z_i\Omega_f/\tau_{hf} + q_i$. In order to avoid the implicit computation of the terms on the right hand sides, two new distribution functions are introduced,

$$\overline{f_i} = f_i - \frac{\delta_t}{2}\left[\Omega_f + F_i\right], \quad \overline{h_i} = h_i - \frac{\delta_t}{2}\left[\Omega_h + S_i\right]. \quad (5.198)$$

Then Eqs. (5.196) and (5.197) can be rewritten as

$$\overline{f}_i(\boldsymbol{x}+\boldsymbol{c}_i\delta_t,t+\delta_t)=\overline{f}_i(\boldsymbol{x},t)-\omega_f[\overline{f}_i(\boldsymbol{x},t)-\overline{f}_i^{(eq)}(\boldsymbol{x},t)]+\frac{2-\omega_f}{2}\delta_t F_i\,, \quad (5.199)$$

$$\overline{h}_i(\boldsymbol{x}+\boldsymbol{c}_i\delta_t,t+\delta_t)=\overline{h}_i(\boldsymbol{x},t)-\omega_h[\overline{h}_i(\boldsymbol{x},t)-h_i^{eq}(\boldsymbol{x},t)] + \frac{2-\omega_h}{2}\delta_t q_i+(\omega_h-\omega_f)Z_i\Phi_i, \quad (5.200)$$

where $\omega_f=2\delta_t/(2\tau_f+\delta_t)$, $\omega_h=2\delta_t/(2\tau_h+\delta_t)$, $\Phi_i=\overline{f}_i-f_i^{(eq)}+F_i\delta_t/2$, and q_i is rewritten in terms of the new distribution function as

$$q_i=\left[\omega_i\frac{\rho E}{RT_0}+f_i^{(eq)}+\left(1-\frac{\omega_f}{2}\right)\Phi_i\right]\boldsymbol{c}_i\cdot\boldsymbol{a}\,. \quad (5.201)$$

With Eq. (5.198) and the conservative properties of the collision operator, it is easy to show that

$$\rho=\sum_i\overline{f}_i\,,\ \rho\boldsymbol{u}=\sum_i\boldsymbol{c}_i\overline{f}_i+\frac{\delta_t}{2}\rho\boldsymbol{a}\,,\ \rho E=\sum_i\overline{h}_i+\frac{\delta_t}{2}\rho\boldsymbol{u}\cdot\boldsymbol{a}\,. \quad (5.202)$$

Equations (5.199) and (5.200) then constitute the DDF-LBE model with total energy distribution function. The Chapman-Enskog analysis shows that the thermohydrodynamic equations of this model are just Eqs. (5.193)-(5.195). Compared with the DDF-LBE model with internal energy distribution function, this model does not involve gradient discretizations, which simplifies the computation greatly. Furthermore, the specific heat coefficient c_v in this model is an adjustable parameter, which is useful for thermal flows with a variable specific heat ratio.

The DDF-LBE model with total energy distribution function was validated by simulating several typical thermal flow problems [Guo *et al.*, 2007]. For example, Fig. 5.5 shows the temperature distribution in a thermal Poiseuille flow between two flat plates at different Prandtl numbers and different Eckert numbers, $Ec=u_0^2/c_p\Delta T$, where $u_0=ah^2/8\nu$ is the maximum velocity along the channel centerline, a is the driven force, h is the distance between the two plates, and ΔT is temperature difference between the top (T_h) and bottom (T_c) walls. The numerical results are found to be in good agreement with the analytical

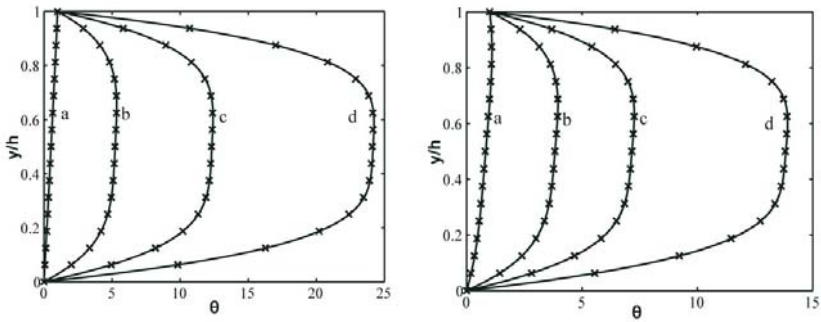

Fig. 5.5. Temperature distribution of thermal Poiseuille flow ($\mathrm{Re} = u_0 h/\nu = 20$). Left: $\mathrm{Pr} = 0.71$, (a) ~ (d): Ec = 0.1, 20, 50, 100. Right: Ec = 10, (a) - (d): Pr = 0.1,1.0, 2.0, 4.0. The solid lines are the analytical solutions, the symbols are numerical results (Guo *et al.*, Phys. Rev. E 75, 036704, 2007).

solution,

$$\theta = \frac{T(y) - T_c}{T_h - T_c} = \frac{y}{h} + \frac{\mathrm{PrEc}}{3}\left[1 - \left(1 - 2\frac{y}{h}\right)^4\right]. \tag{5.203}$$

5.8 Hybrid LBE Models

It was shown that there are some unphysical mode-couplings in the MS-LBE models, which may lead to serious numerical instability [Lallemand and Luo, 2000]. The DDF-LBE models can improve the numerical stability by treating the energy equation and velocity equation separately. On the other hand, some hybrid LBE models that combine an isothermal LBE for velocity field and a finite-difference scheme for the energy equation, have also been developed [Filippova and Hänel, 2000; Mezrhab *et al.*, 2004; Verhaeghe *et al.*, 2007]. But unlike the conventional CFD methods, the solver for the energy equation in hybrid LBE models usually employs some special finite-difference schemes on the regular lattice of the isothermal LBE model for the velocity field.

The velocity field can be solved by either a LBGK model or a MRT-LBE. Without loss of generality, here the hybrid MRT-LBE model developed in [Lallemand and Luo, 2000]. will be presented. Assuming

that the compression work and viscous heat dissipation are negligible, the temperature equation can be expressed as

$$\frac{\partial T}{\partial t} + \boldsymbol{u} \cdot \nabla T = D\nabla^2 T \,. \tag{5.204}$$

In the hybrid MRT-LBE, this equation is discretized using the following scheme,

$$T(\boldsymbol{x}, t + \delta_t) - T(\boldsymbol{x}, t) = -\boldsymbol{u} \cdot \nabla_h T(\boldsymbol{x}, t) + D\nabla_h^2 T(\boldsymbol{x}, t)\,, \tag{5.205}$$

where ∇_h and ∇_h^2 are the discrete gradient and Laplace operators depending on the lattice of the isothermal LBE for the velocity field. For example, if the D2Q9 MRT model is employed, these operators are defined by

$$\nabla_{h,x} T = T_{i+1,j} - T_{i-1,j} + \frac{1}{4}\big[T_{i+1,j+1} - T_{i-1,j+1} + T_{i+1,j-1} - T_{i-1,j-1}\big], \tag{5.206}$$

$$\nabla_{h,y} T = T_{i,j+1} - T_{i,j-1} + \frac{1}{4}\big[T_{i+1,j+1} - T_{i+1,j-1} + T_{i-1,j+1} - T_{i-1,j-1}\big], \tag{5.207}$$

$$\begin{aligned} \nabla_h^2 T = {} & 2\big[T_{i+1,j} + T_{i-1,j} + T_{i,j+1} + T_{i,j-1}\big] - \frac{1}{2}\big[T_{i+1,j+1} + T_{i-1,j+1} \\ & + T_{i-1,j-1} + T_{i+1,j-1}\big] - 6T_{ij}, \end{aligned} \tag{5.208}$$

where $T_{ij} \equiv T(x_i, y_j)$ and $\nabla_h \equiv (\nabla_{h,x}, \nabla_{h,y})$.

The local temperature T is coupled with the velocity field by modifying the equilibrium distribution function of the MRT-LBE. For instance, the moment associated with the energy, $e^{(eq)}$, is changed to be

$$e^{(eq),new} = e^{(eq)} + \hbar T\,, \tag{5.209}$$

where $\hbar$ is a coupling parameter. With an appropriate choice of $\hbar$, the correct momentum equation can be derived from the hybrid LBE [Lallemand and Luo, 2000].

A variety of applications of hybrid LBE models can be found in the literature, such as the natural convection in a square cavity, Rayleigh-Bénard convection, convection between concentric cylinders, double-diffusive convections, and combustion [Filippova and Hänel, 2000; Mezrhab *et al.*, 2004; Verhaeghe *et al.*, 2007].

5.9 Summary

Thermal flows with heat transfer are frequently seen in scientific and engineering problems. This chapter presents several types of LBE models for such flows, including multi-speed models, double-distribution-function models, and hybrid models. These models all have some advantages and disadvantages. In multi-speed models the energy and velocity fields are coupled naturally, which is necessary for high-speed flows. Unfortunately, this type of LBE model usually involves a large set of discrete velocities, and may suffer from serious numerical instability. On the other hand, DDF-LBE models, as well as the hybrid LBE models, solve the momentum equation and the energy equation via different schemes. This decoupling is helpful to improve the numerical stability, and the algorithm structure is also simple. However, although such decoupling methods work well for low-speed flows, it is still difficult to simulate high-speed flows with these models.

In summary, fully thermohydrodynamic LBE schemes represent a challenge to LBE research. Despite several brilliant attempts, a consistent thermodynamic LBE scheme working over a wide range of temperatures remains to be developed, and this is still one of the most challenging issues left with LBE research.

Chapter 6

LBE for Compressible Flows

In the previous chapters, it has been shown that LBE has a wide application in simulation of various incompressible flows. In contrast, its application to simulate compressible flows is quite limited. The major cause is due to the equilibrium distribution functions used in LBE. As required by the Chapman-Enskog expansion to recover the Navier-Stokes equations, the equilibrium distribution functions in LBE should be in the polynomial form of particle velocity. Thus, the Maxwellian distribution function of Boltzmann equation, which is in the exponential form of particle velocity, cannot be directly applied in LBE. In fact, the equilibrium distribution function in LBE is derived by applying the truncated Taylor series expansion to Maxwell function in terms of Mach number. This process inevitably limits the range of applied Mach number. Nevertheless, there are some attempts to apply LBE for simulation of compressible flows.

In the attempt to apply LBE to simulate compressible flows, the equilibrium distribution functions from truncated Maxwell function have to be changed. There are several ways in the literature to construct new equilibrium distribution functions and form compressible lattice Boltzmann models. These models will be described in this chapter. The compressible models are usually complicated, and may encounter numerical instability when the streaming-collision process is performed. To get a stable solution, they often need to solve the discrete velocity Boltzmann equation (DVBE). This may degrade the efficiency of LBE computation. To overcome this difficulty, the lattice Boltzmann flux solver is proposed, in which the one-dimensional compressible LBE model is applied to the local Riemann problem to find its exact solution

so that the flux at the interface can be simply evaluated. This kind of work will also be presented in this chapter.

6.1 Limitation of Conventional LBE Models for Compressible Flows

As shown in the previous chapters, the lattice Boltzmann equation

$$f_i(\boldsymbol{x}+\boldsymbol{c}_i\delta_t, t+\delta_t) - f_i(\boldsymbol{x},t) = -\frac{1}{\tau}\left[f_i(\boldsymbol{x},t) - f_i^{(eq)}(\boldsymbol{x},t)\right], \tag{6.1}$$

can be derived from integration of the following DVBE with the BGK collision model

$$\frac{\partial f_i}{\partial t} + \boldsymbol{c}_i \cdot \nabla f_i = \frac{f_i^{(eq)} - f_i}{\tau_c}, \tag{6.2}$$

where f_i is the distribution function, $f_i^{(eq)}$ is its corresponding function at equilibrium state, N is the number of particles in a lattice Boltzmann model. $\boldsymbol{c}_i$ and $\tau = \tau_c/\delta_t$ are the particle velocity and the non-dimensional relaxation time respectively. The equilibrium distribution function $f_i^{(eq)}$ used in LBE can be derived from the Maxwellian distribution function

$$f^{(eq)}(\boldsymbol{x},\boldsymbol{\xi},t) = \rho\left(2\pi RT\right)^{-D/2}\exp\left[-\frac{\left\|\boldsymbol{\xi}-\boldsymbol{u}\right\|^2}{2RT}\right], \tag{6.3}$$

where D is the dimension of space. At a lattice velocity of $\boldsymbol{c}_i$, using Taylor series expansion, the Maxwellian distribution function can be expanded in the small Mach number limit as

$$f_i^{(eq)}(\boldsymbol{x},t) = w(\boldsymbol{c}_i)\rho\left(1 + \frac{\boldsymbol{c}_i\cdot\boldsymbol{u}}{RT} + \frac{(\boldsymbol{c}_i\cdot\boldsymbol{u})^2}{2(RT)^2} - \frac{u^2}{2RT}\right) + O(\boldsymbol{u}^3). \tag{6.4}$$

All the conventional LBE models with the BGK collision take the form of Eq. (6.4). Thus, they are only applicable for incompressible or weak compressible flows. For compressible flows where the Mach number is usually not small, the form of Eq. (6.4) cannot be directly employed. One has to revise this form or use other appropriate forms. This will be discussed in the following sections. Another limitation of conventional

lattice Boltzmann models for compressible flows is the fixed value of specific heat ratio, γ. For an incompressible flow, only continuity equation and momentum equations are solved, and we are only interested in the macroscopic variables ρ (density), $\boldsymbol{u}$ (velocity) and p (pressure). They are given from mass conservation, momentum conservation, and equation of state, respectively,

$$\rho = \sum_i f_i \ = \sum_i f_i^{(eq)}\,,\ \rho \boldsymbol{u} = \sum_i \boldsymbol{c}_i f_i \ = \sum_i \boldsymbol{c}_i f_i^{(eq)}\,,\ p = \rho c_s^2\,. \quad (6.5)$$

However, for a compressible flow, we also need to solve energy equation. In other words, the macroscopic variable of energy density, ρE, should also be calculated from the density distribution function. According to the definition, ρE is computed by

$$\rho E = \sum_i \frac{1}{2}\boldsymbol{c}_i^2 f_i^{(eq)} = \sum_i \frac{1}{2} c_{i\alpha} c_{i\alpha} f_i^{(eq)} = \frac{1}{2}\left(\rho u^2 + Dp\right), \quad (6.6)$$

where E is the total energy of the mean flow. For a perfect gas, the energy density can also be written as

$$\rho E = \rho\left(\frac{u^2}{2} + \frac{RT}{\gamma - 1}\right) = \frac{1}{2}\rho u^2 + \frac{p}{\gamma - 1}\,, \quad (6.7)$$

where R is the specific gas constant, and T is the temperature of the mean flow. By comparing Eq. (6.6) and Eq. (6.7), we can get the expression of the specific heat ratio as

$$\gamma = \frac{D+2}{D}\,. \quad (6.8)$$

Obviously, γ is fixed for a designated dimension. In Eq. (6.8), it can be found that the specific heat ratio with a clear and definite physical meaning is only for monotonic gases in three-dimensions ($D = 3$).

The major reason of fixed specific heat ratio is due to the definition of energy density in Eq. (6.6), which only contains the contribution of kinetic energy from translational velocity. For the real compressible flow, the rotational velocity also plays an important role. The contribution of rotational velocity to the energy density is served as the potential energy. Thus, the compressible lattice Boltzmann model should also include the potential energy in the calculation of energy density and energy flux.

6.2 Conventional Equilibrium Function-based LBE Models for Compressible Flows

The initial work of extending the application of LBE for compressible flows is based on the existing work for incompressible flows. The form of equilibrium distribution functions derived from the Maxwell function is still used, but the coefficients are adjusted to consider the energy conservation. Besides, the basic configuration of lattice velocity model for isothermal flows is also adopted.

The early attempts for simulating compressible and thermodynamic flows were made by Qian [1993], Alexander *et al*. [1993] and other researchers, as discussed in Chapter 5. However, these works are only limited for weak compressible flows and the specific heat ratio is fixed. To derive a compressible lattice Boltzmann model with flexible specific heat ratio, Hu *et al*. [1997] and Yan *et al*. [1999] developed two two-dimensional models by introducing the energy level into the definition of energy density. One model has 13 lattice velocities (the so-called 13-bit model), and the other has 17 lattice velocities (the so-called 17-bit model). Take the 17-bit model as an example. As shown in Fig. 6.1, this model also uses a square lattice (D2Q9 model) as the basic configuration for lattice velocity distribution. Different from the conventional D2Q9

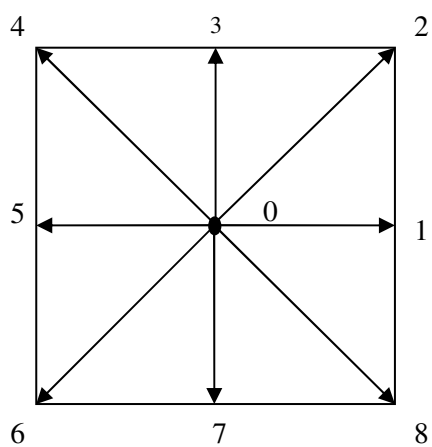

Fig. 6.1. A square lattice with 9 lattice velocities.

model, this model introduces 3 energy levels. One energy level is for the static particle, while the other two energy levels are for the 8 moving particles. So, in total there are 17 lattice particles at a physical position. For simplicity, let ε_A, ε_B, ε_D be the particle energy for energy levels A, B and D respectively. ε_A and ε_B, are for the moving particles while ε_D is for the static particle. f_{iA} and f_{iB} $(i = 1,2,...,8)$ are respectively the density distribution functions at energy level ε_A and ε_B. According to the conservation law, the macroscopic density, velocity and energy can be computed by

$$\rho = \sum_{i,X=A,B,D} f_{iX} = \sum_{i,X=A,B,D} f_{iX}^{(eq)} , \tag{6.9}$$

$$\rho \boldsymbol{u} = \sum_{i,X=A,B,D} f_{iX} \boldsymbol{c}_i = \sum_{i,X=A,B,D} f_{iX}^{(eq)} \boldsymbol{c}_i , \tag{6.10}$$

$$\rho E = \sum_{i,X=A,B,D} f_{iX} \varepsilon_X = \sum_{i,X=A,B,D} f_{iX}^{(eq)} \varepsilon_X . \tag{6.11}$$

Note that Eq. (6.11) is different from Eq. (6.6) in the calculation of macroscopic energy. In order to recover the Euler equations from LBE, the equilibrium distribution function $f_{iX}^{(eq)}$ should also satisfy the flux conditions of momentum and energy, that is,

$$\rho \boldsymbol{u}\boldsymbol{u} + p\boldsymbol{I} = \sum_{i,X=A,B,D} f_{iX}^{(eq)} \boldsymbol{c}_i \boldsymbol{c}_i , \tag{6.12}$$

$$\left(\rho E + p\right)\boldsymbol{u} = \sum_{i,X=A,B,D} f_{iX}^{(eq)} \varepsilon_X \boldsymbol{c}_i . \tag{6.13}$$

As indicated in Sec. 6.1, the form of equilibrium distribution functions is critical for the simulation of compressible flows. In the work of Yan *et al*. [1999], the form of equilibrium distribution functions for the standard D2Q9 model (used for incompressible flows) is adopted, but the coefficients for different energy levels are taken differently. The polynomial form of $f_{iX}^{(eq)}$ can be written as

$$f_{0D}^{(eq)} = \rho\left[D_0 + D_3 u^2 \right], \tag{6.14a}$$

$$f_{iX}^{(eq)} = \rho\left[X_{01} + X_{11}\left(\boldsymbol{c}_i \cdot \boldsymbol{u}\right) + X_{21}\left(\boldsymbol{c}_i \cdot \boldsymbol{u}\right)^2 + X_{31} u^2 \right], \tag{6.14b}$$

for $i = 1, 3, 5, 7$ and

$$f_{iX}^{(eq)} = \rho\Big[X_{02} + X_{12}\big(\boldsymbol{c}_i \cdot \boldsymbol{u}\big) + X_{22}\big(\boldsymbol{c}_i \cdot \boldsymbol{u}\big)^2 + X_{32}u^2 \Big], \qquad (6.14c)$$

for $i = 2, 4, 6, 8$, where $X = A$ and B.

There are 18 coefficients in Eq. (6.14). In principle, these coefficients could be determined from the relationships given by Eqs. (6.9)~(6.13). However, the number of unknown coefficients is still larger than that of given equations. To close the system, some assumptions or introduction of free parameters are needed. The process is quite tedious. This greatly limits the application of this model. Another drawback of this model is the specification of particle energy for the 3 energy levels. Although Sod and Lax shock tube problems are successfully simulated by this model with the streaming-collision process, there is no clear way to specify the particle energy for a given physical problem.

To overcome the drawback of above model, Shi *et al*. [2001] and Kataoka and Tsutahara [2004a, 2004b] proposed some new models, in which the particle energy is defined as the sum of kinetic energy and particle potential energy. These models are equivalent to subjoin the internal degrees of freedom to achieve the goal of adjusting the specific heat ratio. In the following, the details of the model proposed by Kataoka and Tsutahara [2004a, 2004b] will be presented.

The conservation forms of moments utilized in the work of Kataoka and Tsutahara [2004a, 2004b] are given by

$$\rho = \sum_i f_i^{(eq)}\,, \qquad (6.15)$$

$$\rho u_\alpha = \sum_i f_i^{(eq)} c_{i\alpha}\,, \qquad (6.16)$$

$$p\delta_{\alpha\beta} + \rho u_\alpha u_\beta = \sum_i f_i^{(eq)} c_{i\alpha} c_{i\beta}\,, \qquad (6.17)$$

$$\rho\big(bRT + u_\alpha u_\alpha\big) = \sum_i f_i^{(eq)}\big(c_{i\alpha}c_{i\alpha} + \eta_i^2\big), \qquad (6.18)$$

$$\rho\big[\big(b+2\big)RT + u_\beta u_\beta\big]u_\alpha = \sum_i f_i^{(eq)}\big(c_{i\beta}c_{i\beta} + \eta_i^2\big)c_{i\alpha}\,, \qquad (6.19)$$

$$\rho\big[RT\big(u_\alpha\delta_{\beta\chi} + u_\beta\delta_{\chi\alpha} + u_\chi\delta_{\alpha\beta}\big) + u_\alpha u_\beta u_\chi\big] = \sum_i f_i^{(eq)} c_{i\alpha}c_{i\beta}c_{i\chi}\,, \qquad (6.20)$$

$$\rho\left\{\left(b+2\right)R^2T^2\delta_{\alpha\beta}+\left[\left(b+4\right)u_\alpha u_\beta+u_\chi u_\chi\delta_{\alpha\beta}\right]RT+u_\chi u_\chi u_\alpha u_\beta\right\}$$
$$=\sum_i f_i^{(eq)}\left(c_{i\chi}c_{i\chi}+\eta_i^2\right)c_{i\alpha}c_{i\beta}, \tag{6.21}$$

where $\eta_i^2/2$ is the particle potential energy which is introduced to adjust the specific heat ratio, b is a constant related to the specific heat ratio. Note that the tensor notations have been used in Eqs. (6.15)~(6.21) for the subscripts α, β, and χ, i.e., two repeated subscripts mean summation. Equations (6.15), (6.16), and (6.18) are used to define the density, momentum and total energy of the mean flow. Equations (6.17) and (6.19) are respectively used to recover the convective flux in the momentum and energy equations, while equations (6.20) and (6.21) are to recover the viscous flux in the momentum equation and diffusive flux in the energy equation. When the inviscid flow is considered or the Euler equations are solved, we only need to use Eqs. (6.15)~(6.19).

By means of the Chapman-Enskog analysis, one can get

$$\gamma=\frac{b+2}{b}, \tag{6.22}$$

$$\mu=\rho RT\tau, \tag{6.23}$$

$$\mu_B=2\left(\frac{1}{3}-\frac{1}{b}\right)\rho RT\tau, \tag{6.24}$$

$$k=\frac{b+2}{2}\rho R^2T\tau, \tag{6.25}$$

where, μ, μ_B, and k are the dynamic viscosity, bulk viscosity, and thermal conductivity of the Navier-Stokes equations, respectively. b is actually the total number of degrees of freedom which includes degrees of translation, rotation, vibration, *etc*. In other words, b is equal to the summation of space dimension and internal degrees of freedom. For example, $b=3$ is for monatomic gases, and $b=5$ is for diatomic gases. It can be seen from Eq. (6.24) that, in the model of Kataoka and Tsutahara [2004a, 2004b], the bulk viscosity is zero only for monatomic gases. In addition, the Prandtl number of this model is fixed as

$$\mathrm{Pr}=\frac{\gamma\mu R}{\left(\gamma-1\right)k}=1. \tag{6.26}$$

This is a drawback of Kataoka and Tsutahara's model.

Like other compressible LBE models, the form of equilibrium distribution functions is also the key in the model of Kataoka and Tsutahara [2004a, 2004b]. Basically, it also takes the form of existing LBE models for incompressible flows, but the expressions of coefficients are quite different. Even within the framework of Kataoka and Tsutahara [2004a, 2004b], the expressions of the coefficients are also quite different for the Navier-Stokes equations and the Euler equations. In the following, we only list some formulations for the Euler equations.

D1Q5 model

This model has 5 lattice velocities. Its lattice velocities and particle potential energy are defined as

$$c_i = \begin{cases} 0, & \text{for } i = 1, \\ v_1 \cos\left(\pi i\right), & \text{for } i = 2,3, \\ v_2 \cos\left(\pi i\right), & \text{for } i = 4,5. \end{cases} \tag{6.27}$$

$$\eta_i = \begin{cases} \eta_0, & \text{for } i = 1, \\ 0, & \text{for } i = 2,3,4,5. \end{cases} \tag{6.28}$$

Its equilibrium distribution function takes the following form,

$$f_i^{(eq)} = \rho(A_i + B_i u c_i) \ , \ i = 1,\ 2,\ 3,\ 4,\ 5. \tag{6.29}$$

Substituting Eqs. (6.27)~(6.29) into Eqs. (6.15)~(6.19), the coefficients in Eq. (6.29) can be determined as

$$A_i = \begin{cases} \dfrac{b-1}{\eta_0^2}T, & i = 1, \\ \dfrac{1}{2\left(v_1^2 - v_2^2\right)}\left[-v_2^2 + \left(\left(b-1\right)\dfrac{v_2^2}{\eta_0^2} + 1\right)T + u^2\right], & i = 2,3, \\ \dfrac{1}{2\left(v_2^2 - v_1^2\right)}\left[-v_1^2 + \left(\left(b-1\right)\dfrac{v_1^2}{\eta_0^2} + 1\right)T + u^2\right], & i = 4,5. \end{cases} \tag{6.30}$$

$$B_i = \begin{cases} \left[-v_2^2 + \left(b+2\right)T + u^2\right]/2v_1^2\left(v_1^2 - v_2^2\right), & \text{for } i = 2,3, \\ \left[-v_1^2 + \left(b+2\right)T + u^2\right]/2v_2^2\left(v_2^2 - v_1^2\right), & \text{for } i = 4,5. \end{cases} \tag{6.31}$$

D2Q9 model

This model has 9 lattice velocities. Its lattice velocities and particle potential energy are defined as

$$(c_{i1}, c_{i2}) = \begin{cases} \big(0,0\big), & i = 1, \\ v_1\left[\cos\dfrac{\pi i}{2}, \sin\dfrac{\pi i}{2}\right], & i = 2,3,4,5, \\ v_2\left[\cos\pi\left(\dfrac{i}{2}+\dfrac{1}{4}\right), \sin\pi\left(\dfrac{i}{2}+\dfrac{1}{4}\right)\right], & i = 6,7,8,9 \end{cases} \tag{6.32}$$

$$\eta_i = \begin{cases} \eta_0, & \text{for } i = 1, \\ 0, & \text{for } i = 2,3,...,9. \end{cases} \tag{6.33}$$

The equilibrium distribution function of this model takes the following form,

$$f_i^{(eq)} = \rho\big(A_i + B_i u_\alpha c_{i\alpha} + D_i u_\alpha c_{i\alpha} u_\beta c_{i\beta}\big). \tag{6.34}$$

The coefficients in Eq. (6.34) are given by

$$A_i = \begin{cases} \dfrac{b-2}{\eta_0^2}T, & i = 1 \\ \dfrac{1}{4\big(v_1^2 - v_2^2\big)}\left[-v_2^2 + \left(\big(b-2\big)\dfrac{v_2^2}{\eta_0^2} + 2\right)T + \dfrac{v_2^2}{v_1^2}u_\alpha u_\alpha\right], & i = 2,3,4,5, \\ \dfrac{1}{4\big(v_2^2 - v_1^2\big)}\left[-v_1^2 + \left(\big(b-2\big)\dfrac{v_1^2}{\eta_0^2} + 2\right)T + \dfrac{v_1^2}{v_2^2}u_\alpha u_\alpha\right], & i = 5,6,7,8. \end{cases} \tag{6.35}$$

$$B_i = \begin{cases} \dfrac{-v_2^2 + \big(b+2\big)T + u_\beta u_\beta}{2v_1^2\big(v_1^2 - v_2^2\big)}, & i = 2,3,4,5, \\ \dfrac{-v_1^2 + \big(b+2\big)T + u_\beta u_\beta}{2v_2^2\big(v_2^2 - v_1^2\big)}, & i = 6,7,8,9. \end{cases} \tag{6.36}$$

$$D_i = \begin{cases} 1/2v_1^4, & \text{for } i = 2,3,4,5, \\ 1/2v_2^4, & \text{for } i = 6,7,8,9. \end{cases} \tag{6.37}$$

D3Q15 model

This model has 15 lattice velocities. Its lattice velocities and particle potential energy are defined as

$$(c_{i1},c_{i2},c_{i3})=\begin{cases}(0,0,0), & i=1,\\ v_1\left(\pm1,0,0\right),v_1\left(0,\pm1,0\right),v_1\left(0,0,\pm1\right), & i=2,3,...,7,\\ \dfrac{v_2}{\sqrt{3}}\left(\pm1,\pm1,\pm1\right), & i=8,9,...,15.\end{cases} \tag{6.38}$$

$$\eta_i=\begin{cases}\eta_0, & \text{for } i=1,\\ 0, & \text{for } i=2,3,...,15.\end{cases} \tag{6.39}$$

The equilibrium distribution function of this model takes the same form as for the two-dimensional case, that is,

$$f_i^{(eq)}=\rho\left(A_i+B_iu_\alpha c_{i\alpha}+D_iu_\alpha c_{i\alpha}u_\beta c_{i\beta}\right), \qquad \text{for } i=1,2,...,15. \tag{6.40}$$

The coefficients in Eq. (6.40) are given by

$$A_i=\begin{cases}\dfrac{b-3}{\eta_0^2}T, & i=1,\\ \dfrac{1}{6(v_1^2-v_2^2)}\left[-v_2^2+\left((b-3)\dfrac{v_2^2}{\eta_0^2}+3\right)T+\dfrac{v_2^2}{v_1^2}u_\alpha u_\alpha\right], & i=2,3,...,7,\\ \dfrac{1}{8(v_2^2-v_1^2)}\left[-v_1^2+\left((b-3)\dfrac{v_1^2}{\eta_0^2}+3\right)T+\dfrac{3v_1^2-v_2^2}{2v_2^2}u_\alpha u_\alpha\right], & i=8,9,...,15.\end{cases} \tag{6.41}$$

$$B_i=\begin{cases}\dfrac{-v_2^2+\left(b+2\right)T+u_\beta u_\beta}{2v_1^2\left(v_1^2-v_2^2\right)}, & \text{for } i=2,3,...,7,\\ \dfrac{3\left[-v_1^2+\left(b+2\right)T+u_\beta u_\beta\right]}{8v_2^2\left(v_2^2-v_1^2\right)}, & \text{for } i=8,9,...,15.\end{cases} \tag{6.42}$$

$$D_i=\begin{cases}1/2v_1^4, & \text{for } i=2,3,...,7,\\ 1/16v_2^4, & \text{for } i=8,9,...,15.\end{cases} \tag{6.43}$$

Note that for all the above 3 models, v_1, v_2 ($\neq v_1$), and η_0 are nonzero constants. When two-dimensional viscous flows are considered, one can use the D2Q16 model, and the details can be found in Kataoka and Tsutahara [2004a].

When the conventional streaming-collision process is applied, the model of Kataoka and Tsutahara [2004a, 2004b] often encounters

numerical instability. To overcome this difficulty, one has to solve the DVBE (6.2). The solution of DVBE will be discussed in Section 6.6.

Another drawback of the model of Kataoka and Tsutahara [2004a, 2004b] is that the Prandtl number is fixed as 1. To develop a compressible lattice Boltzmann model with variable Prandtl number, Li *et al*. [2007] proposed a coupled double-distribution-function lattice Boltzmann model for the Navier-Stokes equations, in which the specific heat ratio and Prandtl number can be chosen freely. In this model, a density distribution function based on a multi-speed lattice is used to recover the compressible continuity and momentum equations, while the compressible energy equation is recovered by an energy distribution function. The energy distribution function is then coupled with the density distribution function via the thermal equation of state. Some test cases with a range of specific heat ratio and Prandtl number were successfully simulated by this model [2007].

Moreover, to develop a compressible lattice Boltzmann model with better stability than single-relaxation-time model, the multiple-relaxation-time lattice Boltzmann models for simulation of compressible flows also received attention in recent years. In the work of Chen *et al*. [2010, 2011], a multiple-relaxation-time lattice Boltzmann model with flexible specific heat ratio and Prandtl number is proposed for solving the Navier-Stokes equations. Numerical experiments showed that compressible flows with strong shocks can be well simulated by this model.

There are some other works in this category. The common feature of these models is that they use the same form of equilibrium distribution functions as for the incompressible flows, but the coefficients are determined by conservation of mass, momentum, energy, and flux conditions of momentum and energy. The resultant coefficients are not constants. They are the functions of particle velocity and macroscopic variables.

6.3 Circular Function-based LBE Models for Compressible Flows

As shown in the above sections, the equilibrium density distribution functions in LBE are derived from the Maxwell function, which is in an

exponential form. In order to use isotropic properties of the lattice tensors in the application of Chapman-Enskog expansion, one has to do Taylor series expansion to the Maxwell function in terms of Mach number. This process limits the application of LBE to flows with a low Mach number. To release this limitation, one may take other functions as the basic form of equilibrium distribution functions for LBE. One of such attempts was made by Qu *et al*. [2007a, 2007b], who developed several compressible LBE models by means of a circular function. The basic process of this development is shown below. At first, the Maxwellian distribution function is replaced by a circular function and the integral in the infinite domain of velocity space is reduced to the line integral along the circle. After that, the continuous circular function is distributed to discrete points in the velocity space in such a way that the conservation of moments is kept when the line integral is replaced by the weighted sum of functional values at discrete points. The functional value at the discrete velocity point is in fact the equilibrium distribution function. The details of circular function-based lattice Boltzmann model will be shown as follows.

6.3.1 *Definition of circular equilibrium function*

It is well known that the Maxwellian distribution function satisfies the following 7 conservation forms of moments,

$$\int f^{(eq)} d\boldsymbol{\xi} = \rho\,, \tag{6.44}$$

$$\int f^{(eq)} \xi_\alpha d\boldsymbol{\xi} = \rho u_\alpha\,, \tag{6.45}$$

$$\int f^{(eq)} \left(\xi_\alpha \xi_\alpha + 2e_p\right) d\boldsymbol{\xi} = \rho\left(u_\alpha u_\alpha + bRT\right), \tag{6.46}$$

$$\int f^{(eq)} \xi_\alpha \xi_\beta d\boldsymbol{\xi} = \rho u_\alpha u_\beta + p\delta_{\alpha\beta}\,, \tag{6.47}$$

$$\int f^{(eq)} \left(\xi_\alpha \xi_\alpha + 2e_p\right) \xi_\beta d\boldsymbol{\xi} = \rho\left[u_\alpha u_\alpha + \left(b+2\right)RT\right] u_\beta\,, \tag{6.48}$$

$$\int f^{(eq)} \xi_\alpha \xi_\beta \xi_\chi d\boldsymbol{\xi} = p\left(u_\alpha \delta_{\beta\chi} + u_\beta \delta_{\chi\alpha} + u_\chi \delta_{\alpha\beta}\right) + \rho u_\alpha u_\beta u_\chi\,, \tag{6.49}$$

$$\int f^{(eq)}\left(\xi_\chi\xi_\chi + 2e_p\right)\xi_\alpha\xi_\beta d\boldsymbol{\xi}$$
$$= \rho\left\{\left(b+2\right)R^2T^2\delta_{\alpha\beta} + \left[\left(b+4\right)u_\alpha u_\beta + u_\chi u_\chi\delta_{\alpha\beta}\right]RT + u_\chi u_\chi u_\alpha u_\beta\right\}, \quad (6.50)$$

where ξ_α, ξ_β, and ξ_χ are the components of the lattice velocity in the α, β, and χ directions, respectively. Similar to Eqs. (6.15)~(6.21), Eqs. (6.44)~(6.46) are used to define the macroscopic density, momentum, and total energy, and Eqs. (6.47) and (6.48) are applied to recover the convective flux in the momentum and energy equations, while Eqs. (6.49) and (6.50) are used to represent the viscous flux in the momentum equation and the diffusive flux in the energy equation respectively. The integral domain in Eqs. (6.44)~(6.50) is from $-\infty$ to ∞. When the above 7 equations are applied, the Navier-Stokes equations can be recovered. However, when the Euler equations are concerned, we just need to solve Eqs. (6.44)~(6.48). Note that different from Eqs. (6.15)~(6.21), the particle potential energy e_p in Eqs. (6.44)~(6.50) is independent of the direction of the lattice velocity.

For two-dimensional cases, the circular function is defined as

$$f^{(eq)} = \begin{cases} \dfrac{\rho}{2\pi c}, & \left\|\boldsymbol{\xi} - \boldsymbol{u}\right\| = c = \sqrt{D\left(\gamma-1\right)e} \text{ and } e_p = \left[1 - \dfrac{D\left(\gamma-1\right)}{2}\right]e, \\ 0, & \text{otherwise}, \end{cases} \quad (6.51)$$

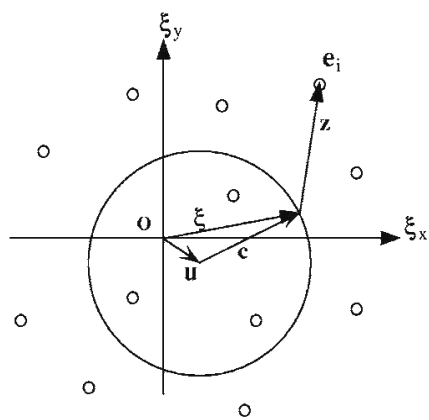

Fig. 6.2. Configuration of the circle and lattice points in the velocity space.

where e is the potential energy of the mean flow, which is defined as $e = p/(\gamma-1)\rho$. The physical meaning of Eq. (6.51) is that all the mass, momentum, and energy are concentrated on a circle as shown in Fig. 6.2. The particle velocity on the circle can be written as

$$\boldsymbol{\xi} = \boldsymbol{u} + \boldsymbol{c}\,. \tag{6.52}$$

Thus, the integral over the infinite domain of velocity space in Eqs. (6.44)~(6.50) reduces to the line integral along the circle, i.e.,

$$d\boldsymbol{\xi} = ds = cd\theta\,. \tag{6.53}$$

Substituting Eqs. (6.51)~(6.53) into Eqs. (6.44)~(6.50), one can get

$$\int f^{(eq)} d\boldsymbol{\xi} = \int_0^{2\pi} \frac{\rho}{2\pi c} cd\theta = \rho\,, \tag{6.54}$$

$$\int f^{(eq)} \xi_\alpha d\boldsymbol{\xi} = \int_0^{2\pi} \frac{\rho}{2\pi c} \big(\boldsymbol{u}+\boldsymbol{c}\big)_\alpha cd\theta = \rho u_\alpha\,, \tag{6.55}$$

$$\begin{aligned}\int f^{(eq)} \big(\xi_\alpha\xi_\alpha + 2e_p\big) d\boldsymbol{\xi} &= \int_0^{2\pi} \frac{\rho}{2\pi c} \big(\boldsymbol{u}+\boldsymbol{c}\big)\cdot\big(\boldsymbol{u}+\boldsymbol{c}\big) cd\theta + 2\rho e_p \\ &= \rho\big(u_\alpha u_\alpha + bRT\big)\,,\end{aligned} \tag{6.56}$$

$$\int f^{(eq)} \xi_\alpha\xi_\beta d\boldsymbol{\xi} = \int_0^{2\pi} \frac{\rho}{2\pi c} \big(\boldsymbol{u}+\boldsymbol{c}\big)_\alpha \big(\boldsymbol{u}+\boldsymbol{c}\big)_\beta cd\theta = \rho u_\alpha u_\beta + p\delta_{\alpha\beta}\,, \tag{6.57}$$

$$\begin{aligned}&\int f^{(eq)} (\xi_\alpha\xi_\alpha + 2e_p)\xi_\beta d\boldsymbol{\xi} \\ &\quad= \int_0^{2\pi} \frac{\rho}{2\pi c} \big[(\boldsymbol{u}+\boldsymbol{c})\cdot(\boldsymbol{u}+\boldsymbol{c})\big](\boldsymbol{u}+\boldsymbol{c})_\beta cd\theta + 2\rho e_p u_\beta\,, \\ &\quad= \rho\big[u_\alpha u_\alpha + (b+2)RT\big]u_\beta\,,\end{aligned} \tag{6.58}$$

$$\begin{aligned}\int f^{(eq)} \xi_\alpha\xi_\beta\xi_\chi d\boldsymbol{\xi} &= \int_0^{2\pi} \frac{\rho}{2\pi c} \big(\boldsymbol{u}+\boldsymbol{c}\big)_\alpha \big(\boldsymbol{u}+\boldsymbol{c}\big)_\beta \big(\boldsymbol{u}+\boldsymbol{c}\big)_\chi cd\theta \\ &= p\big(u_\alpha\delta_{\beta\chi} + u_\beta\delta_{\chi\alpha} + u_\chi\delta_{\alpha\beta}\big) + \rho u_\alpha u_\beta u_\chi\,,\end{aligned} \tag{6.59}$$

$$\begin{aligned}&\int f^{(eq)} (\xi_\chi\xi_\chi + 2e_p)\xi_\alpha\xi_\beta d\boldsymbol{\xi} \\ &= \int_0^{2\pi} \frac{\rho}{2\pi c} \big[(\boldsymbol{u}+\boldsymbol{c})\cdot(\boldsymbol{u}+\boldsymbol{c})\big](\boldsymbol{u}+\boldsymbol{c})_\alpha(\boldsymbol{u}+\boldsymbol{c})_\beta cd\theta + 2\rho e_p(u_\alpha u_\beta + RT\delta_{\alpha\beta}) \\ &= \rho\big\{bR^2T^2\delta_{\alpha\beta} + \big[\big(b+4\big)u_\alpha u_\beta + u_\chi u_\chi \delta_{\alpha\beta}\big]RT + u_\chi u_\chi u_\alpha u_\beta\big\}\,.\end{aligned} \tag{6.60}$$

By comparing Eqs. (6.54)~(6.60) with Eqs. (6.44)~(6.50), it can be found that only Eq. (6.60) has a little difference from Eq. (6.50) for the coefficient of the first term on the right-hand side, which only affects the heat conductivity.

6.3.2 *Distribution of circular function to lattice points in velocity space*

It has been shown above that the circular function can satisfy the constraints to recover the compressible Navier-Stokes equations. However, the circular function cannot be directly applied in the LBE. Although the circular function is greatly simplified as compared to the Maxwellian distribution function, it is still a continuous function and the integral in the velocity space is performed along the circle. In the context of LBE, the discrete lattice velocity is specified, and the integral in the relevant constraints is replaced by a summation over all lattice velocity directions. It is expected that the equilibrium distribution function in a lattice model can be obtained by distributing the circular function into lattice points in the velocity space in such a way that the conservation forms of moments (6.54)~(6.60) can be satisfied in the context of LBE when the integral is replaced by summation.

Suppose that in the ξ_x–ξ_y space, there are N lattice points, $\boldsymbol{e}_i$. As shown in Fig. 6.2, the discrete velocity $\boldsymbol{e}_i$ and the original velocity $\boldsymbol{\xi}$ have the following relationship

$$\boldsymbol{e}_i = \boldsymbol{\xi} + \boldsymbol{z}_i \,. \tag{6.61}$$

The continuous circular function is needed to be distributed to all discrete points $\boldsymbol{e}_i$. For any $d\rho$ on the circle, it has a contribution $\phi_i(\boldsymbol{\xi})d\rho$ at the discrete point $\boldsymbol{e}_i$, where $\phi_i(\boldsymbol{\xi})$ is the assigning function. Thus, the contribution of the whole circle to $\boldsymbol{e}_i$ can be written as

$$f_i^{(eq)} = \oint \phi_i(\boldsymbol{\xi})d\rho = \oint \rho(2\pi c)^{-1}\phi_i(\boldsymbol{\xi})ds \,, \tag{6.62}$$

where $f_i^{(eq)}$ is the equilibrium distribution function in the $\boldsymbol{e}_i$ direction. At a physical position, the macroscopic density is the summation of all $f_i^{(eq)}$, $i = 1, 2, \ldots, N$, that is

$$\rho = \sum_{i=1}^{N} f_i^{(eq)} = \sum_{i=1}^{N} \oint \rho(2\pi c)^{-1}\phi_i(\boldsymbol{\xi})ds = \oint \rho(2\pi c)^{-1}\sum_{i=1}^{N}\phi_i(\boldsymbol{\xi})ds \,. \tag{6.63}$$

Equation (6.63) requires

$$\sum_{i=1}^{N} \phi_i \left(\boldsymbol{\xi} \right) = 1 \,. \tag{6.64}$$

In a similar way, we can get the relationships

$$\sum_{i=1}^{N} \phi_i \left(\boldsymbol{\xi} \right) z_{i\alpha} = 0 \,, \tag{6.65}$$

$$\sum_{i=1}^{N} \phi_i \left(\boldsymbol{\xi} \right) z_{i\alpha} z_{i\beta} = 0 \,, \tag{6.66}$$

$$\sum_{i=1}^{N} \phi_i \left(\boldsymbol{\xi} \right) z_{i\alpha} z_{i\beta} z_{i\chi} = 0 \,. \tag{6.67}$$

Equations (6.64)~(6.67) are actually the constrains for the assigning function $\phi_i(\boldsymbol{\xi})$. It was found that when the third-order Lagrange interpolated polynomial is taken as the assigning function $\phi_i(\boldsymbol{\xi})$, the constraints (6.64)~(6.67) can be satisfied. It is shown in [Qu *et al.*, 2007a] that, when 13 lattice points as shown in Fig. 6.3 are taken in the ξ_x–ξ_y plane, the assigning function $\phi_i(\boldsymbol{\xi})$ can take the following form,

$$\phi_1(x,y) = 1 - 5x^2/4 - 5y^2/4 + x^4/4 + x^2y^2 + y^4/4 \,, \tag{6.68a}$$

$$\phi_2(x,y) = 2x/3 + 2x^2/3 - x^3/6 - xy^2/2 - x^4/6 - x^2y^2/2 \,, \tag{6.68b}$$

$$\phi_3(x,y) = 2y/3 + 2y^2/3 - x^2y/2 - y^3/6 - x^2y^2/2 - y^4/6 \,, \tag{6.68c}$$

$$\phi_4(x,y) = -2x/3 + 2x^2/3 + x^3/6 + xy^2/2 - x^4/6 - x^2y^2/2 \,, \tag{6.68d}$$

$$\phi_5(x,y) = -2y/3 + 2y^2/3 + x^2y/2 + y^3/6 - x^2y^2/2 - y^4/6 \,, \tag{6.68e}$$

$$\phi_6(x,y) = yx/4 + x^2y/4 + xy^2/4 + x^2y^2/4 \,, \tag{6.68f}$$

$$\phi_7(x,y) = -yx/4 + x^2y/4 - xy^2/4 + x^2y^2/4 \,, \tag{6.68g}$$

$$\phi_8(x,y) = yx/4 - x^2y/4 - xy^2/4 + x^2y^2/4 \,, \tag{6.68h}$$

$$\phi_9(x,y) = -yx/4 - x^2y/4 + xy^2/4 + x^2y^2/4 \,, \tag{6.68i}$$

$$\phi_{10}(x,y) = -x/12 - x^2/24 + x^3/12 + x^4/24 \ , \tag{6.68j}$$

$$\phi_{11}(x,y) = -y/12 - y^2/24 + y^3/12 + y^4/24 \ , \tag{6.68k}$$

$$\phi_{12}(x,y) = x/12 - x^2/24 - x^3/12 + x^4/24 \, , \tag{6.68l}$$

$$\phi_{13}(x,y) = y/12 - y^2/24 - y^3/12 + y^4/24 \ , \tag{6.68m}$$

where x and y are lattice velocity components in the ξ_x and ξ_y directions respectively. Once the assigning function is obtained, the equilibrium distribution function at the i-th lattice point can be evaluated as

$$f_i^{(eq)} = \oint \rho(2\pi c)^{-1} \phi_i(\boldsymbol{\xi}) ds, \qquad i = 1, 2, \ldots, 13 \, . \tag{6.69}$$

Substituting Eq. (6.68) into Eq. (6.69) gives

$$\begin{aligned} f_1^{(eq)} = \frac{\rho}{16}\Big(& 4\,u^4 + 5\,c^4 - 20\,c^2 + 16 + 16\,u^2v^2 + 4\,v^4 \\ & -20\,v^2 + 20\,c^2v^2 + 20\,c^2u^2 - 20\,u^2 \Big), \end{aligned} \tag{6.70a}$$

$$\begin{aligned} f_2^{(eq)} = -\frac{\rho}{24}\Big(& -16\,u^2 + 3\,c^4 + 4\,u^4 - 8\,c^2 + 6\,c^2v^2 + 12\,uv^2 \\ & +18\,c^2u^2 + 12\,c^2u + 12\,u^2v^2 - 16\,u + 4\,u^3 \Big), \end{aligned} \tag{6.70b}$$

$$\begin{aligned} f_3^{(eq)} = -\frac{\rho}{24}\Big(& 12\,u^2v^2 + 6\,c^2u^2 + 18\,c^2v^2 + 12\,c^2v + 12\,u^2v \\ & +3\,c^4 - 8\,c^2 + 4\,v^4 - 16\,v^2 + 4\,v^3 - 16\,v \Big), \end{aligned} \tag{6.70c}$$

$$\begin{aligned} f_4^{(eq)} = -\frac{\rho}{24}\Big(& -16\,u^2 + 3\,c^4 + 4\,u^4 - 8\,c^2 + 6\,c^2v^2 - 12\,uv^2 \\ & +18\,c^2u^2 - 12\,c^2u + 12\,u^2v^2 + 16\,u - 4\,u^3 \Big), \end{aligned} \tag{6.70d}$$

$$\begin{aligned} f_5^{(eq)} = -\frac{\rho}{24}\Big(& -4\,v^3 - 12\,c^2v - 12\,u^2v + 3\,c^4 - 8\,c^2 + 4\,v^4 \\ & -16\,v^2 + 16\,v + 12\,u^2v^2 + 18\,c^2v^2 + 6\,c^2u^2 \Big), \end{aligned} \tag{6.70e}$$

$$\begin{aligned} f_6^{(eq)} = \frac{\rho}{32}\Big(& 8\,uv^2 + 8\,vu + 4\,c^2u + 4\,c^2v + 8\,u^2v \\ & + c^4 + 8\,u^2v^2 + 4\,c^2v^2 + 4\,c^2u^2 \Big), \end{aligned} \tag{6.70f}$$

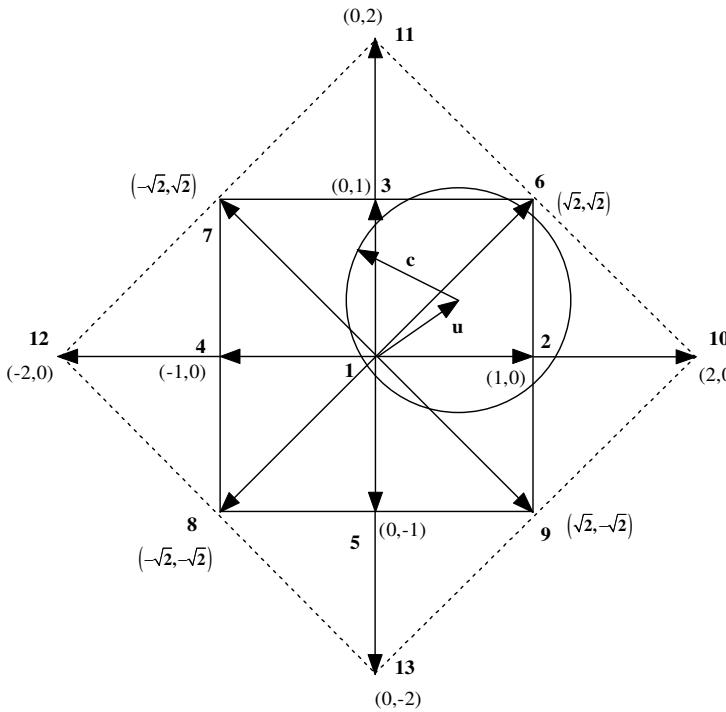

Fig. 6.3. Configuration of 13 lattice points in the ξ_x-ξ_y plane.

$$f_7^{(eq)} = \frac{\rho}{32}\Big(c^4 + 4\,c^2 v - 8\,uv^2 - 8\,vu + 4\,c^2u^2 - 4\,c^2u + 4\,c^2v^2 + 8\,u^2v^2 + 8\,u^2v\Big), \tag{6.70g}$$

$$f_8^{(eq)} = \frac{\rho}{32}\Big(c^4 - 4\,c^2 v - 8\,uv^2 + 8\,vu + 4\,c^2u^2 - 4\,c^2u + 4\,c^2v^2 + 8\,u^2v^2 - 8\,u^2v\Big), \tag{6.70h}$$

$$f_9^{(eq)} = \frac{\rho}{32}\Big(c^4 - 4\,c^2 v + 8\,uv^2 - 8\,vu + 4\,c^2u^2 + 4\,c^2u + 4\,c^2v^2 + 8\,u^2v^2 - 8\,u^2v\Big), \tag{6.70i}$$

$$f_{10}^{(eq)} = \frac{\rho}{192}\Big(8\,u^4 + 16\,u^3 - 8\,u^2 - 16\,u + 24\,c^2u^2 + 24\,c^2u - 4\,c^2 + 3\,c^4\Big), \tag{6.70j}$$

$$f_{11}^{(eq)} = \frac{\rho}{192}\Big(-16\,v + 24\,c^2 v - 8\,v^2 + 8\,v^4 - 4\,c^2 + 24\,c^2 v^2 + 16\,v^3 + 3\,c^4\Big), \tag{6.70k}$$

$$f_{12}^{(eq)} = \frac{\rho}{192}\Big(8\,u^4 - 16\,u^3 - 8\,u^2 + 16\,u + 24\,c^2 u^2 - 24\,c^2 u - 4\,c^2 + 3\,c^4\Big), \tag{6.70l}$$

$$f_{13}^{(eq)} = \frac{\rho}{192}\Big(16\,v - 24\,c^2 v - 8\,v^2 + 8\,v^4 - 4\,c^2 + 24\,c^2 v^2 - 16\,v^3 + 3\,c^4\Big), \tag{6.70m}$$

where u and v are the velocity components of $\boldsymbol{u}$.

Note that Eq. (6.70) is formed in the ξ_x–ξ_y plane. No particle potential energy has been considered. Next, we will use the same distribution process to assign the potential energy to each lattice point. As e_p is linearly appeared in Eqs. (6.54)~(6.60), it means that only two energy levels are needed. As shown in Fig. 6.4, two energy levels, $\lambda_1 = 0$ and $\lambda_2 > e_p$, are assigned. At each energy level, there are 13 lattice points (the configuration of these lattice points is shown in Fig. 6.3). So, there are 26 lattice points in total, and this lattice model is termed as D2Q13L2 model.

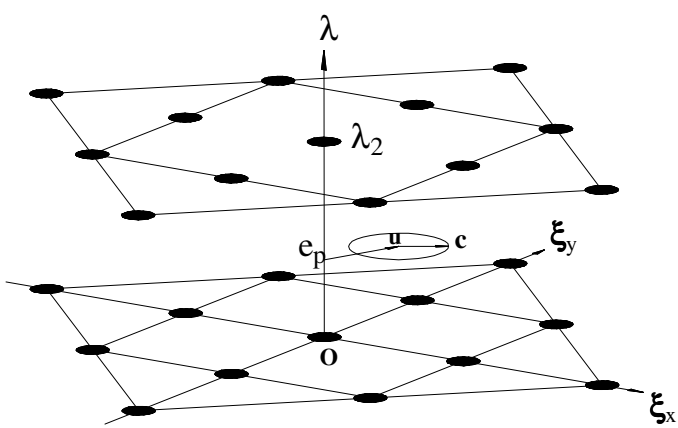

Fig. 6.4. Configuration of lattice points on two energy levels.

With the particle potential energy $\lambda_1 = 0$ and λ_2 at two energy levels, the summation form of Eq. (6.56) can be written as

$$\rho\left(u_\alpha u_\alpha + bRT\right) = \sum_{i=1}^{N} f_i^{(eq)}\left(e_{i\alpha}e_{i\alpha} + 2e_p\right) = \sum_{i=1}^{N}\sum_{v=1}^{2} f_{iv}^{(eq)}\left(e_{i\alpha}e_{i\alpha} + 2\lambda_v\right) \quad (6.71)$$

where $f_{i1}^{(eq)}$ and $f_{i2}^{(eq)}$ are the equilibrium distribution functions associated with energy levels of λ_1 and λ_2. By unwrapping Eq. (6.71), one can get

$$\begin{cases} f_i^{(eq)} e_p = f_{i1}^{(eq)}\lambda_1 + f_{i2}^{(eq)}\lambda_2, \\ f_i^{(eq)} = f_{i1}^{(eq)} + f_{i2}^{(eq)}. \end{cases} \quad (6.72)$$

Thus, the final expression of the equilibrium distribution function $f_{iv}^{(eq)}$ can be written as

$$\begin{cases} f_{i1}^{(eq)} = f_i^{(eq)}\dfrac{\lambda_2 - e_p}{\lambda_2 - \lambda_1}, \\ f_{i2}^{(eq)} = f_i^{(eq)}\dfrac{e_p - \lambda_1}{\lambda_2 - \lambda_1}. \end{cases} \quad (6.73)$$

As $\lambda_1 = 0$ and λ_2 can be taken as 1 from normalization, Eq. (6.73) can be finally simplified to

$$\begin{cases} f_{i1}^{(eq)} = f_i^{(eq)}(1 - e_p), \\ f_{i2}^{(eq)} = f_i^{(eq)} e_p. \end{cases} \quad (6.74)$$

Note that the above D2Q13L2 model is only applicable for simulation of inviscid flows. It also encounters numerical instability when the streaming-collision process is applied. Thus, it should be combined with the solution of DVBE, which will be discussed in Section 6.6. For simulation of one-dimensional inviscid flows such as shock tube problems or application of LBE to evaluate inviscid flux at the cell interface in the solution of Euler equations, Qu *et al.* [2007a] also presented a one-dimensional model, D1Q5L2, which is shown below. For the one-dimensional case, the circular function is reduced to the following form

$$f^{(eq)} = \begin{cases} \dfrac{\rho}{2}, & |\boldsymbol{\xi} - \boldsymbol{u}| = \boldsymbol{c} = \sqrt{(\gamma - 1)e} \text{ and } e_p = \left[1 - \dfrac{1}{2}(\gamma - 1)\right]e. \\ 0, & \text{otherwise.} \end{cases} \quad (6.75)$$

The equilibrium distribution functions at 5 lattice points, $\boldsymbol{e}_i=\{0,\ d_1,\ -d_1,\ d_2,\ -d_2\}$, are given by

$$f_1^{(eq)} = \frac{\rho\left(d_1^2d_2^2 - d_1^2u^2 - d_1^2c^2 - d_2^2u^2 - d_2^2c^2 + u^4 + 6\,u^2c^2 + c^4\right)}{d_1^2d_2^2}, \quad (6.76a)$$

$$f_2^{(eq)} = \frac{\rho\left(3\,d_1uc^2 - d_1d_2^2u - d_2^2u^2 - d_2^2c^2 + 6\,u^2c^2 + c^4 + u^4 + d_1u^3\right)}{2d_1^2\left(d_1^2 - d_2^2\right)}, \quad (6.76b)$$

$$f_3^{(eq)} = \frac{\rho\left(d_1d_2^2u - 3\,d_1uc^2 - d_2^2u^2 - d_2^2c^2 + 6\,u^2c^2 + c^4 + u^4 - d_1u^3\right)}{2d_1^2\left(d_1^2 - d_2^2\right)}, \quad (6.76c)$$

$$f_4^{(eq)} = \frac{\rho\left(d_2d_1^2u - 3\,d_2uc^2 + d_1^2u^2 + d_1^2c^2 - 6\,u^2c^2 - c^4 - u^4 - d_2u^3\right)}{2d_2^2\left(d_1^2 - d_2^2\right)}, \quad (6.76d)$$

$$f_5^{(eq)} = \frac{\rho\left(3\,d_2uc^2 - d_2{d_1}^2u + {d_1}^2u^2 + {d_1}^2c^2 - 6\,u^2c^2 - c^4 - u^4 + d_2u^3\right)}{2{d_2}^2\left({d_1}^2 - {d_2}^2\right)}, \quad (6.76e)$$

where d_1 and d_2 can be taken as $d_1 = 1$ and $d_2 = 2$. Finally, we can use Eq. (6.74) to calculate the equilibrium distribution functions at the lattice points of each energy level.

Qu *et al*. [2007a, 2007b] successfully applied the above models to the one-dimensional shock tube problems, the two-dimensional shock reflection on the wall, and the double Mach reflection as well as shock wave propagation in an enclosure. After initial work of Qu *et al*. [2007a, 2007b], Li *et al*. [2009] further improved the model, where a three-dimensional circular function (spherical function) is used to construct a D3Q25 model for simulation of inviscid compressible flows.

6.4 Delta Function-based LBE Models for Compressible Flows

Also aiming at the simulation of compressible flows, Sun [1998, 2000a, 2000b] and Sun and Hsu [2003, 2004] developed an adaptive lattice Boltzmann model. Unlike the compressible lattice Boltzmann models shown above, the adaptive lattice Boltzmann model is based on a simple

delta function. The pattern of the lattice velocities of this model varies with mean flow velocity and internal energy. The adaptive lattice Boltzmann model contains several discrete velocity vectors which are symmetrically located around the mean velocity in the velocity space. And density is equally distributed on all the discrete velocity vectors.

Let $\boldsymbol{x}$ be an arbitrary node of a lattice, $f(\boldsymbol{x},\boldsymbol{r},m,\boldsymbol{\xi},\zeta,t)$ be the density distribution function for the particle with the migrating velocity $\boldsymbol{r}$, moving to $\boldsymbol{x}+\boldsymbol{r}\Delta t$ during Δt, and transporting the mass m, velocity $\boldsymbol{\xi}$, and energy ζ. Let $D=\{\boldsymbol{\xi}\}\times\{\zeta\}$ be a set of the phase velocity $\boldsymbol{\xi}$, and phase energy ζ, $S=\{\boldsymbol{r}\}$ be a set of migrating velocity. Then the macroscopic conservative variables can be defined as

$$\rho \equiv \sum_{\boldsymbol{r}\in S}\int_D mf\left(\boldsymbol{x},\boldsymbol{r},m,\boldsymbol{\xi},\zeta,t\right)dmd\boldsymbol{\xi}d\zeta\,, \tag{6.77}$$

$$\rho\boldsymbol{v} \equiv \sum_{\boldsymbol{r}\in S}\int_D \boldsymbol{\xi}f\left(\boldsymbol{x},\boldsymbol{r},m,\boldsymbol{\xi},\zeta,t\right)dmd\boldsymbol{\xi}d\zeta\,, \tag{6.78}$$

$$\rho E \equiv \sum_{\boldsymbol{r}\in S}\int_D \zeta f\left(\boldsymbol{x},\boldsymbol{r},m,\boldsymbol{\xi},\zeta,t\right)dmd\boldsymbol{\xi}d\zeta\,. \tag{6.79}$$

If we define

$$\boldsymbol{\eta} \equiv \left[m,\boldsymbol{\xi},\zeta\right], \tag{6.80}$$

$$f(\mathrm{x},\mathrm{r},\boldsymbol{\eta},t) \equiv f(\mathrm{x},\mathrm{r},m,\boldsymbol{\xi},\zeta,t)\,, \tag{6.81}$$

$$\mathrm{Y} \equiv \left[\rho,\rho\boldsymbol{v},\rho E\right], \tag{6.82}$$

Eqs. (6.77)~(6.79) can be written in a compact form as

$$\mathrm{Y} \equiv \sum_{\boldsymbol{r}\in S}\int_D \boldsymbol{\eta}f\left(\boldsymbol{x},\boldsymbol{r},\boldsymbol{\eta},t\right)d\boldsymbol{\eta}\,. \tag{6.83}$$

As shown in Fig. 6.5, suppose that we consider a hexagonal lattice with lattice velocity set as

$$\{\mathrm{c}'_{jv};j=1,2,...,b_v=6,v=1,2\}\,. \tag{6.84}$$

In the adaptive LBE model, the total mass, momentum and energy are all transported by the particle velocity, $\boldsymbol{c}_{jvk}$, which is defined as,

$$\boldsymbol{c}_{jvk} = \boldsymbol{v}_k + \boldsymbol{c}'_{jv}\,, \tag{6.85}$$

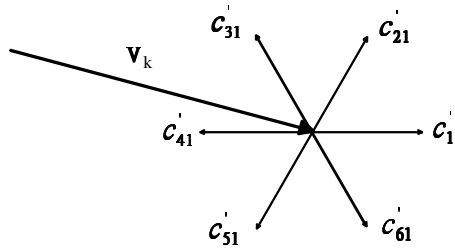

Fig. 6.5. Configuration of fluid velocity and a symmetric set of velocities.

where v_k is the approximated fluid velocity at a mesh point. Consider an arbitrary node x, where its fluid velocity is v. As shown in Fig. 6.6, the node x should fall into one of triangles. We note this triangle as ΔABC. The approximated fluid velocity at nodes *A, B* and *C* are noted as v_1, v_2 and v_3. The particle velocity at x and the approximated fluid velocity v_k are defined as

$$\overline{c}_{jv} = v + c'_{jv}\,, \tag{6.86}$$

$$v_k = v + v'_k\,. \tag{6.87}$$

In the adaptive LBE model, all the particles are concentrated at $r = c_{jvk}$, $m = m_{jvk}$, $\xi = \xi_{jvk}$, $\zeta = \zeta_{jvk}$, and the equilibrium distribution function can be written as

$$f^{(eq)}_{jvk}\left(x,\eta,t\right) \equiv \begin{cases} d_{vk}\delta\left(m - m_{jvk}\right)\delta\left(\xi - \xi_{jvk}\right)\delta\left(\zeta - \zeta_{jvk}\right), & r = c_{jvk}, \\ 0, & \text{other } r \in S, \end{cases} \tag{6.88}$$

where δ is the delta function, $\delta(\xi) = 0$ for $\xi \neq 0$; $\int f^{(eq)}(\xi)\delta(\xi)d\xi = f^{(eq)}(0)$. d_{vk} is a function of macroscopic variables. With Eq. (6.88), the macroscopic variables can be determined as

$$Y = \sum_{j,v,k} d_{vk}\eta_{jvk}\,, \tag{6.89}$$

where $\eta_{jvk} \equiv [m_{jvk}, \xi_{jvk}, \zeta_{jvk}]$. Sun [2000a] proposed two models to compute the particle mass, velocity, and energy. Model I gives

$$m^I_{jvk} = 1\,, \tag{6.90}$$

$$\xi^I_{jvk} = \overline{c}_{jv}\,, \tag{6.91}$$

$$\zeta^I_{jvk} = \frac{1}{2}(v^2 + 2\boldsymbol{c}'_{jv} \cdot \boldsymbol{v} + \overline{c}'^2_v) + \Phi\,, \tag{6.92}$$

$$\boldsymbol{\eta}^I_{jvk} \equiv \left[m^I_{jvk}, \boldsymbol{\xi}^I_{jvk}, \zeta^I_{jvk} \right]^T, \tag{6.93}$$

where Φ is the particle potential energy,

$$\Phi = \left[1 - \frac{D}{2}(\gamma - 1)\right] e\,. \tag{6.94}$$

Model II introduces corrections to Model I, and it is given as

$$m^{II}_{jvk} = m^I_{jvk} - \chi_{jvk}\,, \tag{6.95}$$

$$\boldsymbol{\xi}^{II}_{jvk} = \boldsymbol{\xi}^I_{jvk} - \chi_{jvk}\boldsymbol{v}\,, \tag{6.96}$$

$$\zeta^{II}_{jvk} = \zeta^I_{jvk} - \chi_{jvk}\left[\frac{1}{2}(v^2 + \overline{c}'^2) + \Phi\right], \tag{6.97}$$

$$\boldsymbol{\eta}^{II}_{jvk} \equiv \left[m^{II}_{jvk}, \boldsymbol{\xi}^{II}_{jvk}, \zeta^{II}_{jvk} \right]^T, \tag{6.98}$$

where $\chi_{jvk} = D(2c'^2_v)^{-1}(\boldsymbol{c}'_{jv} \cdot \boldsymbol{v}'_k)$. With the introduction of density portion, $\alpha_k = \rho_k/\rho$, d_{vk} can be taken as

$$d_{vk} = \alpha_k d_v\,. \tag{6.99}$$

As shown in Fig. 6.6, with the given location $\boldsymbol{x}$, it is not difficult to calculate the density portion. For the hexagonal lattice, there are two levels of $\boldsymbol{c}'_v$. Then d_1 and d_2 in Eq. (6.99) can be determined by

$$d_1 = \rho\frac{c'^2_2 - D(\gamma - 1)e}{b_1(c'^2_2 - c'^2_1)}, \tag{6.100}$$

$$d_2 = \rho\frac{D(\gamma - 1)e - c'^2_1}{b_2(c'^2_2 - c'^2_1)}\,. \tag{6.101}$$

In order to ensure the positivity of d_1 and d_2, c'_1 and c'_2 are required to satisfy $c'^2_1 < D(\gamma - 1)e < c'^2_2$. In practice, c'_1 is set to be the integer part of $\sqrt{D(\gamma - 1)e}$, and $c'_2 = c'_1 + 1$. When $c'_1 = 0$, the correction parameter in Eqs. (6.95)~(6.97) should be modified to

$$\chi_{j1k} = 0, \quad \chi_{j2k} = \frac{d_1 + d_2}{d_2}\frac{D}{2c'^2_2}(\boldsymbol{c}'_{j2} \cdot \boldsymbol{v}'_k)\,. \tag{6.102}$$

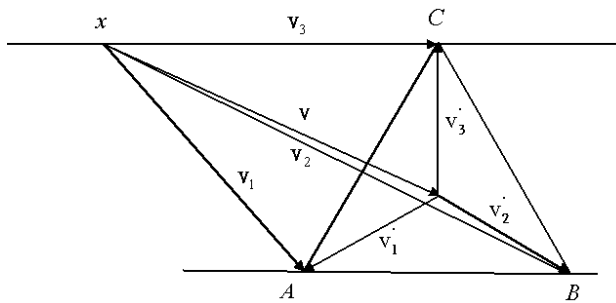

Fig. 6.6. Illustration of fluid velocity at $\boldsymbol{x}$ and its approximated velocity at apexes of a triangle.

The pressure in the adaptive LBE can be computed by

$$p = \sum_v b_v d_v \frac{1}{D} c_v'^2 . \tag{6.103}$$

In the application of adaptive LBE, the relaxation parameter τ is usually set as one due to huge requirement of computer memory and computational effort for other cases. When $\tau = 1$, the lattice Boltzmann equation is reduced to

$$f(\boldsymbol{x} + \boldsymbol{r}\Delta t, \boldsymbol{r}, \boldsymbol{\eta}, t + \Delta t) = f^{(eq)}(\boldsymbol{x}, \boldsymbol{r}, \boldsymbol{\eta}, t) . \tag{6.104}$$

Some compressible flows with weak or strong shock waves were simulated successfully by the adaptive LBE. Note that since the viscosity cannot be adjusted by changing τ, the model can only be used to simulate inviscid flows if the viscosity terms are regarded as numerical dissipation.

6.5 Direct Derivation of Equilibrium Distribution Functions from Conservation of Moments

All of the LBE models described above are based on a given form of equilibrium distribution functions. On the other hand, it was found that the equilibrium distribution functions can also be derived from the

conservation forms of moments. The initial work was made by McNamara *et al*. [1995] and Dellar [2008]. In the work of McNamare *et al*. [1995], a system of 21 moment conservation equations is used to determine the distribution functions of thermal lattice Boltzmann model. Later, Dellar [2008] derived two one-dimensional models, unsplit 7 velocity model and split 4+3 velocity model, by solving a linear system of 7 moment conservation equations. In the following, the unsplit 7 velocity model is briefly described.

This model chooses 7 lattice velocities as $\xi_i = i$, $i = 0, \pm1, \pm2, \pm3$. With the introduction of a particle potential energy $\varepsilon_i/2$, the 7 conservation forms of moments can be written as

$$\sum_{i=-3}^{3} f_i^{(eq)} = \rho\,, \tag{6.105}$$

$$\sum_{i=-3}^{3} \xi_i f_i^{(eq)} = \rho u\,, \tag{6.106}$$

$$\sum_{i=-3}^{3} \xi_i^2 f_i^{(eq)} = \rho\theta + \rho u^2\,, \tag{6.107}$$

$$\sum_{i=-3}^{3} \xi_i^3 f_i^{(eq)} = \rho u^3 + 3\rho u\theta\,, \tag{6.108}$$

$$\frac{1}{2}\sum_{i=-3}^{3}\left(\xi_i^2 + \varepsilon_i\right) f_i^{(eq)} = \frac{1}{2}\rho u^2 + \frac{\rho\theta}{\gamma - 1}\,, \tag{6.109}$$

$$\frac{1}{2}\sum_{i=-3}^{3}\left(\xi_i^2 + \varepsilon_i\right)\xi_i f_i^{(eq)} = \frac{1}{2}\rho u^3 + \frac{\gamma}{\gamma - 1}\rho u\theta\,, \tag{6.110}$$

$$\frac{1}{2}\sum_{i=-3}^{3}\left(\xi_i^2 + \varepsilon_i\right)\xi_i^2 f_i^{(eq)} = \frac{1}{2}\rho u^4 + \left(\frac{5}{2} + \frac{1}{\gamma - 1}\right)\rho u^2\theta + \frac{\gamma}{\gamma - 1}\rho\theta^2\,, \tag{6.111}$$

where θ is proportional to the temperature T, and $\theta = RT$. Note that although different notations are used, Eqs. (6.105)~(6.111) are actually the one-dimensional forms of Eqs. (6.15)~(6.21). By taking $\varepsilon_i = (0, 0, 1, 4, 1, 0, 0)$, equations. (6.105)~(6.111) can be put in the following matrix

form,

$$\begin{pmatrix} 1 & 1 & 1 & 1 & 1 & 1 & 1 \\ -3 & -2 & -1 & 0 & 1 & 2 & 3 \\ 9 & 4 & 1 & 0 & 1 & 4 & 9 \\ -27 & -8 & -1 & 0 & 1 & 8 & 27 \\ 9 & 4 & 2 & 4 & 2 & 4 & 9 \\ -27 & -8 & -2 & 0 & 2 & 8 & 27 \\ 81 & 16 & 2 & 0 & 2 & 16 & 81 \end{pmatrix} \begin{pmatrix} f_{-3}^{(eq)} \\ f_{-2}^{(eq)} \\ f_{-1}^{(eq)} \\ f_{0}^{(eq)} \\ f_{1}^{(eq)} \\ f_{2}^{(eq)} \\ f_{3}^{(eq)} \end{pmatrix} = \rho \begin{pmatrix} 1 \\ u \\ u^2 + \theta \\ u^3 + 3\theta u \\ u^2 + 2\theta/(\gamma - 1) \\ u^3 + 2\theta u\gamma/(\gamma - 1) \\ \left\{ u^4 + 2\theta^2\gamma/(\gamma - 1) \right. \\ \left. +\theta u^2(5\gamma - 3) \right\} \end{pmatrix}. \quad (6.112)$$

The solution of equation system (6.112) can be obtained analytically. For example, the equilibrium distribution function of static particle is

$$f_0^{(eq)} = \frac{\rho}{64}\left(-36 + 13u^2 - u^4 - \frac{12\gamma - 62}{\gamma - 1}\theta - \frac{5\gamma - 3}{\gamma - 1}\theta u^2 - \frac{2\gamma}{\gamma - 1}\theta^2 \right). \quad (6.113)$$

Recently, Yang *et al*. [2012] did a systematic study on derivation of one-dimensional lattice Boltzmann models from conservation forms of moments in order to simulate compressible inviscid flows. As discussed in the previous sections, for the inviscid flow, only 5 conservation forms of moments are needed. Their one-dimensional forms can be written as

$$\rho = \sum_i f_i^{(eq)} , \quad (6.114)$$

$$\rho u = \sum_i f_i^{(eq)} \xi_i , \quad (6.115)$$

$$\rho u^2 + p = \sum_i f_i^{(eq)} \xi_i \xi_i , \quad (6.116)$$

$$\rho\left(u^2 + bRT \right) = \sum_i f_i^{(eq)} \xi_i \xi_i + 2\lambda \sum_i f_i^{eq} , \quad (6.117)$$

$$\rho\left[u^2 + \left(b + 2 \right) RT \right] u = \sum_i f_i^{(eq)} \xi_i \xi_i \xi_i + 2\lambda \sum_i f_i^{(eq)} \xi_i , \quad (6.118)$$

where b is defined by Eq. (6.22), and λ is the particle potential energy. Note that different from other LBE models [Kataoka, T. and Tsutahara, 2004a, 2004b; Dellar, 2008], the particle potential energy in Eqs. (6.117) and (6.118) is independent of the lattice velocity direction i. This is reasonable as the particle potential energy reflects the contribution of

kinetic energy in the rotational velocity space, which is independent of translational velocity space. Unlike the previous work [Kataoka, T. and Tsutahara, 2004a, 2004b; Dellar, 2008], the particle potential energy λ in Eqs. (6.114)~(6.118) cannot be arbitrarily specified. In fact, it can be determined from the equation system. By substituting Eqs. (6.114) and (6.116) into Eq. (6.117), one can get the expression of λ as

$$\lambda = \frac{\left(b-1\right)}{2} RT = \left[1 - \frac{D}{2}\left(\gamma - 1\right)\right] e \,. \tag{6.119}$$

Due to the use of Eq. (6.119), only 4 equations of (6.114)~(6.118) are independent, which can be written as

$$\rho = \sum_i f_i^{(eq)} \,, \tag{6.120}$$

$$\rho u = \sum_i f_i^{(eq)} \xi_i \,, \tag{6.121}$$

$$\rho u^2 + \rho c^2 = \sum_i f_i^{(eq)} \xi_i \xi_i \,, \tag{6.122}$$

$$\rho u^3 + 3\rho u c^2 = \sum_i f_i^{(eq)} \xi_i \xi_i \xi_i \,, \tag{6.123}$$

where c is the peculiar velocity of particles defined as $c = \sqrt{D(\gamma-1)e}$. When the lattice velocities are taken as $\xi_i = \{0, \pm d_1, \pm d_2\}$, where d_1 and d_2 are constants, there are 5 unknowns, $f_i^{(eq)},\ i = 1, 2, ..., 5$. As equation system (6.120)~(6.123) only has 4 equations, we have to regard one of $f_i^{(eq)}$ as given in order to obtain a well-posed equation system. If we set $f_1^{(eq)}$ as known, we can get the solution of equation system (6.120) ~ (6.123) as

$$f_1^{(eq)} = f_1^{(eq)}\left(\rho, u, c\right), \tag{6.124}$$

$$f_2^{(eq)} = \frac{-\left(\rho - f_1^{(eq)}\right) d_1 d_2^{\,2} - \rho d_2^{\,2} u + \rho d_1 u^2 + \rho d_1 c^2 + \rho u^3 + 3\,\rho u c^2}{2 d_1 \left(d_1^{\,2} - d_2^{\,2}\right)}, \tag{6.125}$$

$$f_3^{(eq)} = \frac{-\left(\rho - f_1^{(eq)}\right) d_1 d_2^{\,2} + \rho d_2^{\,2} u + \rho d_1 u^2 + \rho d_1 c^2 - \rho u^3 - 3\,\rho u c^2}{2 d_1 \left(d_1^{\,2} - d_2^{\,2}\right)}, \tag{6.126}$$

$$f_4^{(eq)} = \frac{\left(\rho - f_1^{(eq)}\right) d_1^{\,2} d_2 + \rho d_1^{\,2} u - \rho d_2 u^2 - \rho d_2 c^2 - \rho u^3 - 3\,\rho u c^2}{2 d_2 \left(d_1^{\,2} - d_2^{\,2}\right)}, \tag{6.127}$$

$$f_5^{(eq)} = \frac{\left(\rho - f_1^{(eq)}\right) d_1^2 d_2 - \rho d_1^2 u - \rho d_2 u^2 - \rho d_2 c^2 + \rho u^3 + 3\rho u c^2}{2d_2\left(d_1^2 - d_2^2\right)}. \quad (6.128)$$

In fact, if we take $f_1^{(eq)}$ as the following form,

$$f_1^{(eq)} = \frac{\rho\left(d_1^2 d_2^2 - d_1^2 u^2 - d_1^2 c^2 - d_2^2 u^2 - d_2^2 c^2 + u^4 + 6u^2 c^2 + c^4\right)}{d_1^2 d_2^2}, \quad (6.129)$$

we can get exactly the same results as D1Q5L2 model of Qu *et al*. [2007] given by Eq. (6.76). Furthermore, when 4 lattice velocities are taken, that is, $\xi_i = \{\pm d_1, \pm d_2\}$, the equation system (6.120)~(6.123) gives the 4 equilibrium distribution functions as

$$f_1^{(eq)} = \frac{\rho\left(-d_1 d_2^2 - d_2^2 u + d_1 u^2 + d_1 c^2 + u^3 + 3uc^2\right)}{2d_1\left(d_1^2 - d_2^2\right)}, \quad (6.130)$$

$$f_2^{(eq)} = \frac{\rho\left(-d_1 d_2^2 + d_2^2 u + d_1 u^2 + d_1 c^2 - u^3 - 3uc^2\right)}{2d_1\left(d_1^2 - d_2^2\right)}, \quad (6.131)$$

$$f_3^{(eq)} = \frac{\rho\left(d_1^2 d_2 + d_1^2 u - d_2 u^2 - d_2 c^2 - u^3 - 3uc^2\right)}{2d_2\left(d_1^2 - d_2^2\right)}, \quad (6.132)$$

$$f_4^{(eq)} = \frac{\rho\left(d_1^2 d_2 - d_1^2 u - d_2 u^2 - d_2 c^2 + u^3 + 3uc^2\right)}{2d_2\left(d_1^2 - d_2^2\right)}. \quad (6.133)$$

The equation system (6.120)~(6.123) is a useful platform to derive various one-dimensional LBE models for compressible inviscid flows.

6.6 Solution of Discrete Velocity Boltzmann Equation

The application of lattice Boltzmann models for simulation of compressible flows often encounters numerical instability. To obtain a stable solution, very few of existing models such as those of Yan *et al*. [1999] and Yu and Zhao [2000] can be applied with normal streaming-collision process. Most of existing models have to be applied with the solution of DVBE (6.2). In fact, in the literature, there are many works [Chew *et al*., 2002; Gan *et al*., 2008; Li *et al*., 2007; Li *et al*., 2009; Mei and Shyy,

1998; Mezrhab *et al.*, 2004; Peng *et al.*, 1999; Watari, M. and Tsutahara, 2003] available to address the solution of DVBE for problems with complex geometry, thermal flows, and compressible flows. Some techniques for solving the DVBE for compressible flows are described in this section.

To apply their compressible LBE models, Kataoka and Tsutahara [2004] solved the DVBE by the following Crank-Nicolson scheme,

$$f_i\Big|_{t+\Delta t} = f_i\Big|_t - \frac{c_{i\alpha}\Delta t}{2}\left(\frac{\partial f_i}{\partial x_\alpha}\bigg|_t + \frac{\partial f_i}{\partial x_\alpha}\bigg|_{t+\Delta t}\right) + \frac{f_i^{(eq)} - f_i}{\tau}\bigg|_t \Delta t\,, \qquad (6.134)$$

where Δt is the time step. The spatial derivatives $\partial f_i \big/ \partial x_\alpha$ can be approximated by the following second-order upwind scheme,

$$\frac{\partial f_i}{\partial x_\alpha} = \begin{cases} \left[3f_i(x_\alpha) - 4f_i(x_\alpha - \Delta x) + f_i(x_\alpha - 2\Delta x)\right]\big/(2\Delta x), & c_{i\alpha} \geq 0, \\ \left[-3f_i(x_\alpha) + 4f_i(x_\alpha + \Delta x) - f_i(x_\alpha + 2\Delta x)\right]\big/(2\Delta x), & c_{i\alpha} < 0. \end{cases} \qquad (6.135)$$

Kataoka and Tsutahara [2004] found that the application of Eqs. (6.134)~(6.135) with $\Delta t \sim \tau$ and $\Delta x \sim \tau\sqrt{RT}$ can obtain stable solutions with the second-order of accuracy. The DVBE can also be solved by some powerful flux solvers such as MUSCL which are often used to solve the Euler equations. For a two-dimensional case, Qu *et al.* [2007] wrote Eq. (6.2) into the following conservative form

$$\frac{\partial f_\alpha}{\partial t} + \frac{\partial F_\alpha}{\partial x} + \frac{\partial G_\alpha}{\partial y} = \Omega_\alpha\,, \qquad (6.136)$$

where

$$F_\alpha = f_\alpha c_{\alpha x}, G_\alpha = f_\alpha c_{\alpha y}, \Omega_\alpha = -\frac{f_\alpha - f_\alpha^{eq}}{\tau}. \qquad (6.137)$$

As *i* will be used as the index to indicate x-coordinate, we have used α in Eqs. (6.136) and (6.137) to replace i in Eq. (6.2). Using the explicit Euler scheme for temporal discretization and finite volume method for spatial discretization, Eq. (6.136) can be discretized as

$$\frac{f_\alpha^{n+1} - f_\alpha^n}{\Delta t} = -\frac{1}{\Delta x}\left[F^n_{\alpha,i+\frac{1}{2},j} - F^n_{\alpha,i-\frac{1}{2},j}\right] - \frac{1}{\Delta y}\left[G^n_{\alpha,i,j+\frac{1}{2}} - G^n_{\alpha,i,j-\frac{1}{2}}\right] + \Omega^n_{\alpha,i,j}\,, \qquad (6.138)$$

where $F^n_{\alpha,i\pm1/2,j}$ and $G^n_{\alpha,i,j\pm1/2}$ are the numerical fluxes at the interfaces of a cell $(i,\ j)$. In order to compute the numerical fluxes, the 3-rd order MUSCL (Monotone Upstream-centered Scheme for Conservation Laws) scheme [van Leer, 1982] with van Albada limiter [1982] is applied to evaluate the functional value on two sides of an interface

$$\begin{cases} \left(f_L\right)_{i+\frac{1}{2}} = f_i + \left\{\dfrac{s}{4}\left[\left(1-\kappa s\right)\Delta_- + \left(1+\kappa s\right)\Delta_+\right]\right\}_i, \\ \left(f_R\right)_{i+\frac{1}{2}} = f_{i+1} - \left\{\dfrac{s}{4}\left[\left(1-\kappa s\right)\Delta_+ + \left(1+\kappa s\right)\Delta_-\right]\right\}_{i+1}, \end{cases} \tag{6.139}$$

where $\kappa = 1/3$, and s is the van Albada limiter given by

$$s = \frac{2\Delta_+\Delta_- + \varepsilon}{\Delta_+^2 + \Delta_-^2 + \varepsilon}. \tag{6.140}$$

Here ε is a small number (usually set as $\varepsilon = 10^{-6}$) preventing division by zero in region of null gradient and

$$\left(\Delta_+\right)_i = f_{i+1} - f_i, \quad \left(\Delta_-\right)_i = f_i - f_{i-1}. \tag{6.141}$$

With $(f_L)_{i+1/2}$ and $(f_R)_{i+1/2}$, the numerical flux at the interface $i+1/2$ can be computed with a Riemann solver. For Eq. (6.136), the exact Riemann solution can be found since it is a linear hyperbolic system. The solution is

$$F_{i+1/2} = \begin{cases} \left(f_L\right)_{i+1/2} c_x, & \text{if } c_x > 0, \\ \left(f_R\right)_{i+1/2} c_x, & \text{if } c_x < 0. \end{cases} \tag{6.142}$$

$G^n_{\alpha,i,j\pm1/2}$ can be evaluated in the same way.

Note that when the DVBE is solved by the upwind schemes, the artificial dissipation comes from two parts. One is the model dissipation which is from the collision term. This part is usually very small. The other is the numerical dissipation resulted from spatial discretization. Numerical results have shown that the solution of the DVBE by upwind schemes with associated compressible LBE models can well capture both the shock waves and contact discontinuities without oscillation.

6.7 Lattice Boltzmann Flux Solver for Solution of Euler Equations

As shown in previous sections, the developed lattice Boltzmann models for compressible flows are usually very complicated, especially for two- and three-dimensional cases. And the compressible LBE models are often associated with the solution of DVBE, which may encounter numerical instability. To overcome these drawbacks, some efforts [Ji *et al*., 2009; Joshi *et al.*, 2010; Yang *et al*., 2012] have been made to combine one-dimensional compressible LBE models with the solution of the Euler equations by the finite volume method (FVM). In other words, the one-dimensional models are used to the local Riemann problem at the cell interface to evaluate the inviscid flux. The work is actually an inviscid flux solver by the lattice Boltzmann method. In this section, we will briefly describe how to apply the one-dimensional LBE model to evaluate the inviscid flux at a cell interface for one-dimensional and two-dimensional problems.

For simplicity, we first consider the one-dimensional case, for which the Euler equations can be written as

$$\frac{\partial \boldsymbol{W}}{\partial t} + \frac{\partial \boldsymbol{F}}{\partial x} = 0\,, \tag{6.143}$$

where

$$\boldsymbol{W} = \begin{bmatrix} \rho \\ \rho u \\ \dfrac{\rho}{2}[u^2 + bRT] \end{bmatrix}, \qquad \boldsymbol{F} = \begin{bmatrix} \rho u \\ \rho u^2 + p \\ \dfrac{\rho}{2}[u^2 + (b+2)RT]u \end{bmatrix}. \tag{6.144}$$

Using FVM, Eq. (6.143) can be discretized as

$$\frac{d\boldsymbol{W}_i}{dt} = -\frac{1}{\Delta x_i}(\boldsymbol{F}_{i+1/2} - \boldsymbol{F}_{i-1/2})\,. \tag{6.145}$$

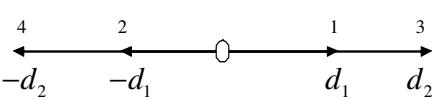

Fig. 6.7. Configuration of a D1Q4 lattice Boltzmann model.

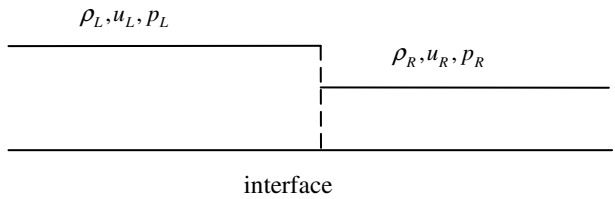

Fig. 6.8. Sketch of a local Riemann problem.

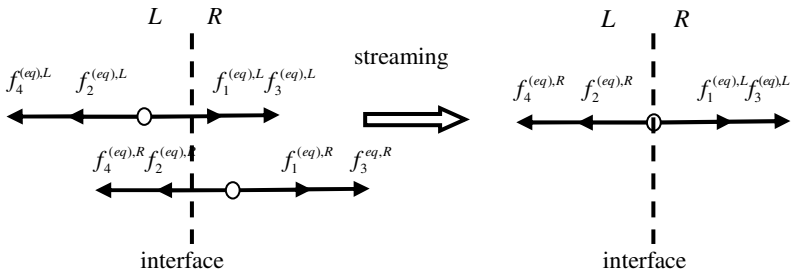

Fig. 6.9. Streaming process of D1Q4 model near the interface.

Here $\boldsymbol{F}_{i+1/2}$ is the inviscid flux at the cell interface $i+1/2$. Conventionally, $\boldsymbol{F}_{i+1/2}$ can be evaluated by certain upwind schemes such as the Roe scheme [Roe, 1981]. In the following, we will show that $\boldsymbol{F}_{i+1/2}$ can also be evaluated by the compressible LBE model.

For illustration, we consider a D1Q4 lattice Boltzmann model as shown in Fig. 6.7. This model will be applied to a local Riemann problem at the interface, which is shown in Fig. 6.8, where the flow variables are constants at the left and right sides.

Now, at the interface, suppose that there are two neighbouring points L and R located respectively at the left and right sides of the interface. We apply the D1Q4 model to the points L and R at the time t. Since macroscopic variables at points L and R are known, we initialize the computation by using their equilibrium distribution functions. After a time step Δt, the particles 1 and 3 from point L and particles 2 and 4 from point R will stream to the interface. The streaming process is demonstrated in Fig. 6.9.

From the streaming process, we have the density distribution functions at the interface as follows,

$$f_1 = f_1^{(eq),L}, \quad f_2 = f_2^{(eq),R}, \quad f_3 = f_3^{(eq),L}, \quad f_4 = f_4^{(eq),R}. \tag{6.146}$$

With Eqs. (6.146), (6.115)~(6.118), the inviscid flux $\boldsymbol{F}$ at the interface can be calculated by

$$\boldsymbol{F} = \begin{bmatrix} F_1 \\ F_2 \\ F_3 \end{bmatrix} = \begin{bmatrix} \rho u \\ \rho u^2 + p \\ \dfrac{\rho}{2}[u^2 + (b+2)RT]u \end{bmatrix} = \begin{bmatrix} \sum\limits_{i=1}^{N} f_i \, d_i \\ \sum\limits_{i=1}^{N} f_i \, d_i d_i \\ \sum\limits_{i=1}^{N} f_i \, d_i \left(\dfrac{1}{2} d_i d_i + \lambda \right) \end{bmatrix}, \tag{6.147}$$

where N is taken as 4 in Eq. (6.147) for the D1Q4 model. When multi-dimensional problems are considered, the above 1D model needs to be applied along the normal direction of interface. For example, for the 2D case, as shown in Fig. 6.10, we can use the normal velocity U_n to replace u in the 1D model (6.147). Suppose that the unit normal vector at the interface is $(n_x, \ n_y)$ for the 2D case, we will have the following relationships,

$$U_n = n_x u + n_y v, \qquad U_\tau = n_x v - n_y u, \tag{6.148}$$

$$u = n_x U_n - n_y U_\tau, \quad v = n_x U_\tau + n_y U_n, \tag{6.149}$$

where U_n and U_τ are the normal and tangential velocity components at the interface, and u and v are the velocity components in the x and y directions, respectively. The two-dimensional Euler equations can be

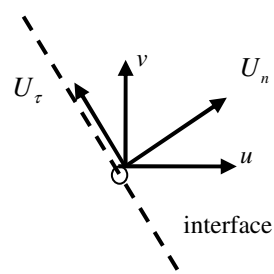

Fig. 6.10. Illustration of normal and tangential velocities at an interface.

written as

$$\frac{\partial \boldsymbol{W}}{\partial t} + \frac{\partial \boldsymbol{F}_x}{\partial x} + \frac{\partial \boldsymbol{F}_y}{\partial y} = 0\,, \tag{6.150}$$

where

$$\boldsymbol{W} = \begin{bmatrix} \rho \\ \rho u \\ \rho v \\ \dfrac{\rho}{2}[u^2 + v^2 \\ +bRT] \end{bmatrix},\ \boldsymbol{F}_x = \begin{bmatrix} \rho u \\ \rho u^2 + p \\ \rho uv \\ \dfrac{\rho}{2}[u^2 + v^2 \\ +(b+2)RT]u \end{bmatrix},\ \boldsymbol{F}_y = \begin{bmatrix} \rho v \\ \rho uv \\ \rho v^2 + p \\ \dfrac{\rho}{2}[u^2 + v^2 \\ +(b+2)RT]v \end{bmatrix}. \tag{6.151}$$

Integrating Eq. (6.150) over a control volume *I* gives

$$\frac{d\boldsymbol{W}_I}{dt} = -\frac{1}{V_I}\sum_{i=1}^{N_f} \boldsymbol{F}_{ni} S_i\,, \tag{6.152}$$

where $\boldsymbol{W}_I$ is the vector of conservative variables for the control cell I, V_I, and N_f are the volume and the number of faces of the cell, respectively, and S_i is the area of the i-th face of the control cell. The flux vector at the interface is given by

$$\boldsymbol{F}_n = n_x \boldsymbol{F}_x + n_y \boldsymbol{F}_y = \begin{bmatrix} \rho U_n \\ \rho U_n u + p n_x \\ \rho U_n v + p n_y \\ \dfrac{\rho}{2} U_n [u^2 + v^2 + (b+2)RT] \end{bmatrix}. \tag{6.153}$$

Using Eq. (6.149), equation (6.153) can also be written as

$$\boldsymbol{F}_n = \begin{bmatrix} \rho U_n \\ \big(\rho U_n U_n + p\big) n_x \\ \big(\rho U_n U_n + p\big) n_y \\ \dfrac{\rho}{2} U_n \big[{U_n}^2 + (b+2)RT\big] \end{bmatrix} + \begin{bmatrix} 0 \\ -\rho U_n U_\tau n_y \\ \rho U_n U_\tau n_x \\ \dfrac{\rho}{2} U_n {U_\tau}^2 \end{bmatrix}. \tag{6.154}$$

Note that in the last component of the flux vector in Eq. (6.154), we have used the relationship of $u^2 + v^2 = U_n^2 + U_\tau^2$ (velocity magnitude does not

change). If we define $F_1 = \rho U_n = \sum_{i=1}^{N} f_i d_i$, and apply the one-dimensional results of Eq. (6.147) to the normal direction, the flux vector at the interface (Eq. (6.154)) can be finally written as

$$\boldsymbol{F}_n = \begin{bmatrix} F_1 \\ F_2 \\ F_3 \\ F_4 \end{bmatrix} = \begin{bmatrix} \sum_{i=1}^{N} f_i d_i \\ \sum_{i=1}^{N} f_i d_i d_i \cdot n_x + F_1 \cdot U_\tau \cdot (-n_y) \\ \sum_{i=1}^{N} f_i d_i d_i \cdot n_y + F_1 \cdot U_\tau \cdot (n_x) \\ \sum_{i=1}^{N} f_i d_i \left(\frac{1}{2} d_i d_i + \lambda \right) + \frac{1}{2} F_1 \cdot {U_\tau}^2 \end{bmatrix}. \tag{6.155}$$

In the above equations, the tangential velocity U_τ is still unknown. One feasible way to calculate the terms of $F_1 \cdot \boldsymbol{U}_\tau$ and $F_1 \cdot U_\tau^2$ is given by

$$F_1 \cdot U_\tau = F_1^L \cdot U_\tau^L + F_1^R \cdot U_\tau^R, \tag{6.156}$$

$$F_1 \cdot U_\tau^2 = F_1^L \cdot \left(U_\tau^L \right)^2 + F_1^R \cdot \left(U_\tau^R \right)^2, \tag{6.157}$$

where U_τ^L and U_τ^R are the tangential velocities at the two sides of the interface. F_1^L and F_1^R denote the mass fluxes calculated by the equilibrium distribution functions (only consider the components pointing to the interface) at the two sides of the interface. When the D1Q4 model is applied, we have $F_1^L = f_1^{(eq),L} d_1 + f_3^{(eq),L} d_2$ and $F_1^R = -f_2^{(eq),R} d_1 - f_4^{(eq),R} d_2$. Once the flux vector at the interface is obtained from Eq. (6.155), we can simply solve Eq. (6.152) by multi-stage Runge-Kutta methods. The above process can also be easily extended to the three-dimensional case.

6.8 Some Sample Applications

In the previous sections, a number of LBE models have been described for compressible flows. In this section, we will show some sample applications of these models.

One-dimensional case

Almost all the compressible LBE models introduced in the previous sections can be used to simulate the one-dimensional shock tube

problems. Here, we only show some results of Qu *et al.* [2007] by using their developed D1Q5L2 model. The initial condition of the Sod shock tube problem is

$$\begin{aligned} \left(\rho_L, u_L, e_L\right) &= \left(1, 0, 2.5\right), && -0.5 < x < 0, \\ \left(\rho_R, u_R, e_R\right) &= \left(0.125, 0, 2\right), && 0 < x < 0.5. \end{aligned} \tag{6.158}$$

For the simulation, Qu *et al*. [2007] set $d_1 = 1,\ d_2 = 2,\ \hat{\tau} = \varepsilon = 10^{-4}$. The reference density and length are taken as $\rho_0 = 1,\ L_0 = 1$, and the reference internal energy is chosen as $e_0 = 4 > \max(e) = 2.5$. Here, e is the internal energy. The mesh size is taken as $\Delta x = 1/200$ and the time step size is chosen as $\Delta t = \varepsilon/4$. Before the waves propagate to the two boundary points, the distribution functions at the boundary are set as the equilibrium distribution functions computed from the initial value of macroscopic variables. The computed density, velocity, pressure, and internal energy profiles (symbols) at $t = 0.22$ together with the exact solutions (solid lines) are displayed in Fig. 6.11. Clearly, the numerical

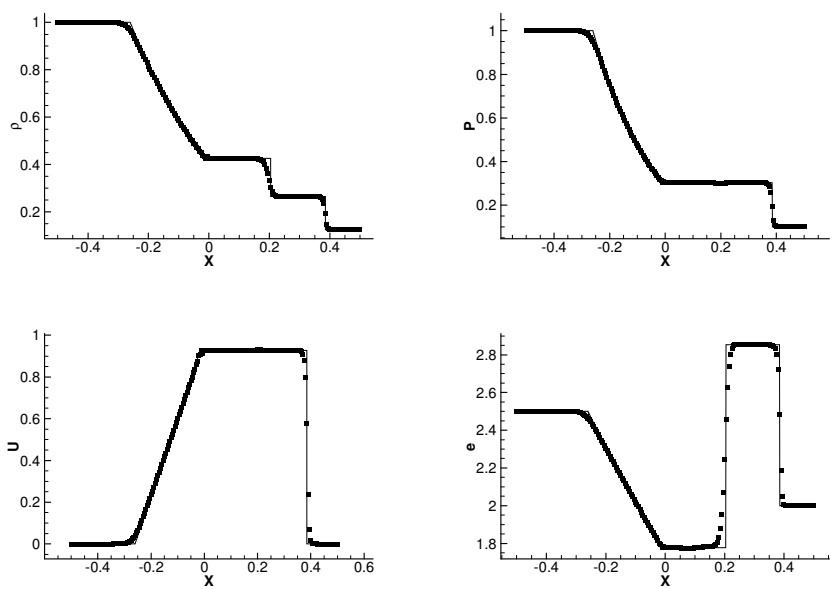

Fig. 6.11. Density (left up), pressure (right up), velocity (left bottom) and internal energy (right bottom) profiles of Sod shock tube problem.

results obtained by the compressible LBE model agree well with the exact solution.

Two-dimensional case

In the literature, the compressible LBE models shown in the previous sections can be well employed to simulate two-dimensional shock reflection on the wall and double Mach reflection problem. The computational domain of these problems is rectangular. For application of compressible LBE models on irregular domains, the process is quite tedious. However, the lattice Boltzmann flux solver shown in Section 6.7 offers a promising way to simulate compressible flows around a curved boundary. The compressible flow around airfoils is a good example. Consider a flow around the RAE2822 airfoil with free stream Mach number of 0.75 and angle of attack of 3^0. In the simulation, a 225×65 *C*-type grid is used. The D1Q5L2 model of Qu *et al*. [2007] is applied to evaluate the inviscid flux at the cell interface in the solution of the Euler equations by FVM. The pressure coefficient distribution along the airfoil surface [Qu, 2009] is presented in Fig. 6.12, in which the results computed from the Euler solver of Jameson's scheme [Jameson *et al*., 1991] are shown as symbols. Clearly, the two results agree very well.

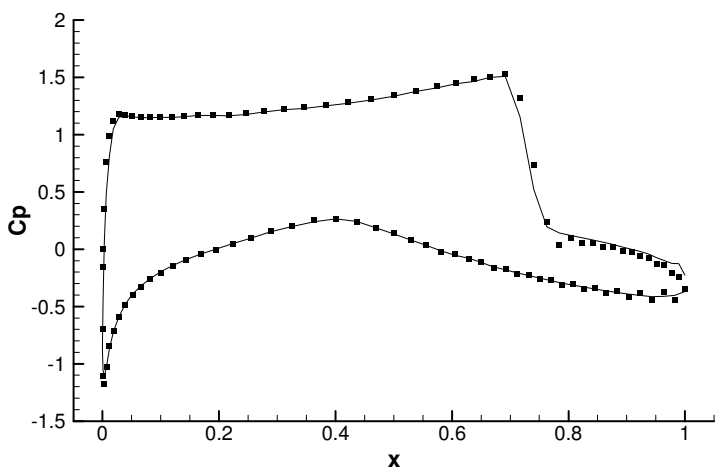

Fig. 6.12. Pressure coefficient distribution of flow around the RAE2822 airfoil (M_∞= 0.75 and $\alpha = 3^\circ$).

Three-dimensional case

Due to the complexity, very few work is available in the literature for the simulation of three-dimensional compressible flows by using LBE models. Qu [2009] managed to incorporate the lattice Boltzmann flux solver developed in Section 6.7 into an existing FVM Euler/NS solver in order to simulate the transonic flow around an aircraft. Figure 6.13 compares the pressure coefficient contours computed by the central difference scheme with artificial dissipation [Jameson *et al*., 1981], the flux vector splitting (FVS) scheme [van Leer, 1982], and the lattice Boltzmann flux solver. In the simulation, the free stream Mach number of 0.8 and angle of attack of 2° are selected, and a 3D multi-block structured grid with about 310,000 mesh points is used.

We can see clearly from Fig. 6.13 that the three results agree very well, especially between the results of the FVS and present lattice Boltzmann flux solver. Indeed, the present results are closer to those of the FVS. The lift coefficients computed by the central difference scheme [Jameson *et al*., 1981], the FVS scheme [van Leer, 1982], and the lattice Boltzmann flux solver, are respectively 0.2303, 0.2384, and 0.2375. This example shows that the lattice Boltzmann flux solver could become an effective way for simulating compressible flows around complex geometries.

6.9 Summary

This chapter presents several LBE models for compressible flows. As compared to the incompressible LBE models, the compressible models have two major differences. One is about the equilibrium distribution functions. Although some compressible models still adopt the same form of incompressible models, the coefficients are determined differently. Generally they are not constants in the compressible models, which are determined from conservation of moments and are functions of particle velocity and macroscopic flow variables. This chapter also shows that the equilibrium distribution functions can be directly derived from the model of Yan *et al*. [1999], where the particle energy is introduced to calculate

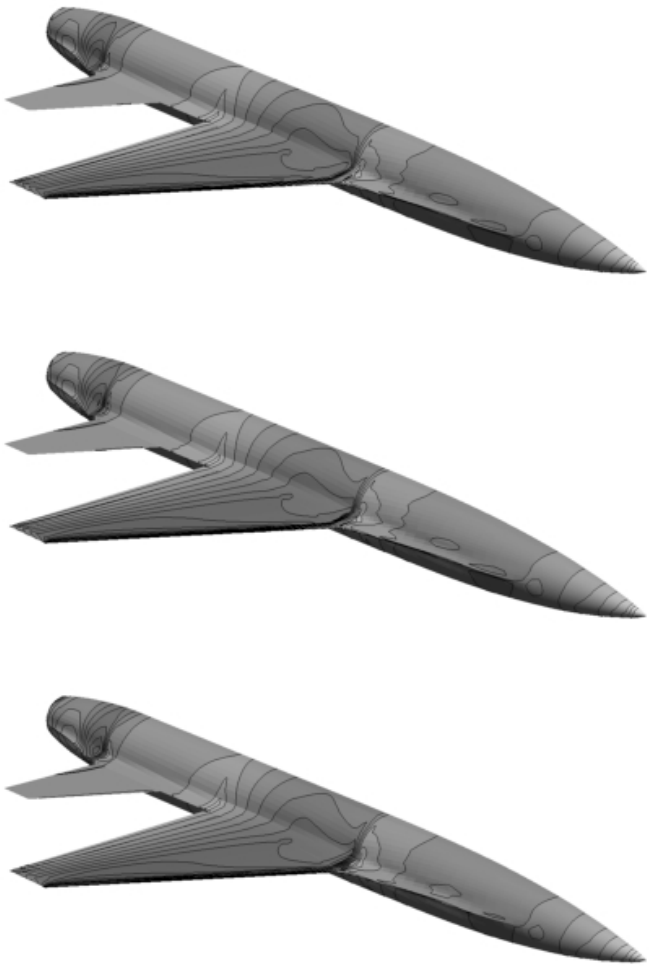

Fig. 6.13. Surface pressure coefficient contours computed with FV-LBE (top), Van Leer FVS (middle) and Jameson's central scheme (bottom). Contour levels are from –0.6 to 0.5 with increment of 0.05.

the total energy and the energy flux. Its difficulty lies in the specification of the particle energy for different problems. This difficulty can be overcome by the model of Kataoka and Tsutahara [2004a, 2004b], where the particle energy is considered as the sum of particle kinetic energy and potential energy. Although different values of potential energy are

assigned to different lattice directions, the model in fact only assigns the potential energy to the static particle. In contrast, the model of Qu *et al*. [2007a, 2007b], which is based on the circular function, takes the same particle potential energy for different lattice directions. This is reasonable as the potential energy reflects the contribution of kinetic energy from the rotational velocity, which is independent of the translational velocity. The particle potential energy of Qu *et al*. [2007a, 2007b] cannot be chosen arbitrarily. It is calculated from the internal energy of the mean flow. The adaptive model of Sun [2000b] is different from other compressible models in the way that the particle mass, momentum and energy are all transported along a streaming velocity, which is the sum of the mean flow velocity and the lattice velocity. In general, the position after the streaming is not on the mesh point. Thus, interpolation is necessary. Another drawback of the adaptive model is that the relaxation parameter τ is usually fixed as 1.

The compressible LBE models often encounter numerical instability when the normal streaming-collision process is applied. To get a stable solution, they are usually applied with the solution of discrete velocity Boltzmann equation (DVBE). As upwind schemes are needed to solve DVBE, the numerical stability of compressible models with solution of DVBE is actually enhanced by artificial dissipation.

As compared to the incompressible models, the form of equilibrium distribution functions is much more complicated for the compressible models, especially for two- and three-dimensional cases. To overcome this difficulty, this chapter presents a lattice Boltzmann flux solver, which applies a one-dimensional LBE model to the local Riemann problem at the cell interface. The flux evaluated by LBE at the cell interface can be used in the solution of Euler equations by the finite volume method. Numerical experiments showed that this solver can be effectively applied to complicated two- and three-dimensional compressible flows, indicating that this solver has a great potential for real application.

In summary, the work for compressible flows is far behind that for incompressible flows. More research efforts are needed to tackle the challenging issues occurred in the application of LBE for compressible flows.

This page intentionally left blank

Chapter 7

LBE for Multiphase and Multi-component Flows

In the natural world and industrial processes, fluids usually contain impurities more or less, and so most flows, strictly speaking, are multiphase and/or multi-component ones. A multi-component system is a mixture comprised of different fluid species, while a multiphase fluid system involves obvious phase interfaces (e.g. gas-liquid mixture). Furthermore, a multi-component fluid can be either miscible (e.g., air) or immiscible (e.g., air-water), and a multiphase system can contain one or more components.

The macroscopic dynamics of a multiphase or multi-component flow is usually very complicated due to large scale disparities and the coupling between mass transfer, phase segregations/separations, and even chemical reactions. Traditional fluid dynamical models and numerical methods may encounter difficulties for these systems. For example, an equation of state is required in order to model two-phase flows, which is usually difficult to obtain in the interfacial region. On the other hand, it is well understood that the macroscopic behaviors of multiphase and multi-component flows are the natural consequences of microscopic interactions among fluid molecules. Therefore, in principle, multiphase flows can be simulated by numerical methods based on realistic microscopic physics such as molecular dynamics (MD). However, such methods are usually very computational expensive and consequently become impractical for simulating macroscopic flows. In recent years, there is a trend to construct numerical methods for such flows based on mesoscopic theories that connect the microscopic and macroscopic descriptions of the dynamics, among which the LBE has received particular attentions. Thanks to the kinetic nature of the LBE,

inter-molecular interactions can be incorporated into a LBE model in a straightforward way so that it can be used to simulate a multiphase or multi-component system effectively. This feature is also recognized as one of the main advantages of LBE that distinguishes it from other numerical methods.

A variety of LBE models for multiphase and multi-component flows have been established from different viewpoints, and in this chapter several typical kinds of such models will be presented.

7.1 Color Models

7.1.1 *LBE model for immiscible fluids*

The first LBE model for multiphase flows is put forward by Gunstensen *et al.* [1991], which is an improved version of the multiphase LGA model of Rothman and Keller [1988]. In this model, phases are denoted by different colors, and inter-particle interactions, which are responsible for phase separations and segregations, are modeled by local color gradients associated with density differences between two phases.

Taking a two-phase system as an example, the color-gradient model uses two types of distribution functions, f_{ri} and f_{bi}, to represent the red and blue fluids, respectively. The total distribution function for the mixture, $f_i = f_{ri} + f_{bi}$, evolves as [Alexander *et al.*, 1993; Gunstensen *et al.*, 1991]

$$f_i(\boldsymbol{x} + \boldsymbol{c}_i\delta_t, t + \delta_t) - f_i(\boldsymbol{x}, t) = \Omega_i^c + \Omega_i^p\,, \tag{7.1}$$

where Ω_i^c denotes the collision effects and Ω_i^p means the perturbation aroused by interfacial tensions. The densities and velocities for each fluid and the mixture are defined as

$$\begin{aligned} &\rho_k = \sum_i f_{ki}, \quad \rho_k \boldsymbol{u}_k = \sum_i \boldsymbol{c}_i f_{ki}, \quad k = r, b, \\ &\rho = \rho_r + \rho_b, \quad \rho\boldsymbol{u} = \rho_r \boldsymbol{u}_r + \rho_b \boldsymbol{u}_b. \end{aligned} \tag{7.2}$$

In the model of Gunstensen *et al.*, the collision term is constructed from the MZ collision model [McNamara and Zanetti 1988], which originates from LGA collision rules. As mentioned in Chapter 1, such a

model may encounter some numerical instabilities and the computational efficiency is not satisfactory, either. Later Alexander *et al.* [1993] proposed a BGK model for Ω_i^c. In order to determine Ω_i^p, an order parameter is introduced first to describe the phase difference,

$$\psi(\boldsymbol{x},t) = \rho_r(\boldsymbol{x},t) - \rho_b(\boldsymbol{x},t)\,. \tag{7.3}$$

A local color gradient is then defined as

$$\boldsymbol{G}(\boldsymbol{x},t) = \sum_i \boldsymbol{c}_i \psi(\boldsymbol{x} + \boldsymbol{c}_i\delta_t, t)\,, \tag{7.4}$$

from which Ω_i^p is defined,

$$\Omega_i^p = A|\boldsymbol{G}|\cos(2\theta_i)\,, \tag{7.5}$$

where θ_i is the angle between $\boldsymbol{c}_i$ and $\boldsymbol{G}$, A is a parameter that controls the surface tension σ, i.e., $\sigma \sim A\rho\lambda$, where λ is the eigenvalue of the collision operator Ω_i^c related to the viscosity. Obviously, the color gradient is 0 in bulk regions, and so is Ω_i^p. In other words, surface tension only takes effects in the interfacial region, which is physically sound.

After obtaining Ω_i^p and Ω_i^c, the total distribution function can be calculated according to Eq. (7.1), and the red and blue distribution functions are then obtained by a *re-coloring* step, which solves the following maximum value problem

$$W(f_{ri}'', f_{bi}'') = \max_{f_{ri}'', f_{bi}''}\left[\sum_i (f_{ri}'' - f_{bi}'')\boldsymbol{c}_i\right], \tag{7.6}$$

subjected to the following constraints,

$$\rho_r'' = \sum_i f_{ri}'' = \rho_r, \quad f_{ri}'' + f_{bi}'' = f_i\,, \tag{7.7}$$

where f_{ki}'' is the distribution function after the re-coloring, ρ_r and f_i are the density and distribution function before the collision step. The essence of this re-coloring step is to enforce the direction of the color flux $\boldsymbol{H} \equiv \rho_r\boldsymbol{u}_r - \rho_b\boldsymbol{u}_b$ to match that of the color gradient $\boldsymbol{G}$. During this process, the fluid is driven to the bulk region with the same color, and phase separation is then induced.

In summary, the color-gradient model of Gunstensen *et al.* can be realized by the following four steps:

- Collision: $f_i' = f_i + \Omega_i^c$;
- Perturbation: $f_i'' = f_i' + \Omega_i^p$;
- Re-coloring: Compute f_{ri}'' and f_{bi}'' from Eq. (7.6);
- Streaming: $f_{ri}(\boldsymbol{x} + \boldsymbol{c}_i\delta_t, t + \delta_t) = f_{ri}''(\boldsymbol{x}, t)$, $f_{bi}(\boldsymbol{x} + \boldsymbol{c}_i\delta_t, t + \delta_t) = f_{bi}''(\boldsymbol{x}, t)$.

In the original model, the collision process is made for the total distribution function of the mixture. Grunau *et al*. [1993] presented a slightly modified color-gradient model in which collisions are also carried out for the distribution functions of different fluids,

$$f_{ri}(\boldsymbol{x} + \boldsymbol{c}_i\delta_t, t + \delta_t) - f_{ri}(\boldsymbol{x}, t) = \Omega_{ri} + \Omega_{ri}^p, \tag{7.8}$$

$$f_{bi}(\boldsymbol{x} + \boldsymbol{c}_i\delta_t, t + \delta_t) - f_{bi}(\boldsymbol{x}, t) = \Omega_{bi} + \Omega_{bi}^p, \tag{7.9}$$

where Ω_{ri} and Ω_{bi} are the collision operators for the red and blue fluids, respectively,

$$\Omega_{ki} = -\frac{1}{\tau_k}\left[f_{ki} - f_{ki}^{(eq)}\right], \quad k = r,\ b\,. \tag{7.10}$$

Here the equilibrium distribution function depends on the density ρ_k and the mixture velocity $\boldsymbol{u}$. As an example, the equilibrium distribution function of the D2Q7 model is defined by

$$f_{ki}^{(eq)} = \begin{cases} \rho_k\left[\dfrac{m_k}{6 + m_k} - u^2\right], & i = 0, \\ \rho_k\left[\dfrac{1}{6 + m_k} + \dfrac{1}{3}\boldsymbol{c}_i \cdot \boldsymbol{u} + \dfrac{2}{3}(\boldsymbol{c}_i \cdot \boldsymbol{u})^2 - \dfrac{u^2}{3}\right], & i \neq 0, \end{cases} \tag{7.11}$$

where $k = r,\ b$ and m_k denotes the ensemble average value of the static particles of phase k. When the velocity is zero, in order to obtain a stable phase interface, it requires

$$\frac{\rho_r}{6 + m_r} = \frac{\rho_b}{6 + m_b} = d\,. \tag{7.12}$$

The additional terms Ω_{ki}^p in Eqs. (7.8) and (7.9) represent the perturbations caused by the surface tension,

$$\Omega_{ki}^p = \frac{A_k}{2} \mid \boldsymbol{G} \mid \left[\frac{\boldsymbol{c}_i \cdot \boldsymbol{G}}{G^2} - \theta_0\right], \tag{7.13}$$

with A_k being a parameter related to surface tension and θ_0 a model-dependent constant. For example, $\theta_0 = 1/2$ for the D2Q7-FHP model.

The model of Grunau *et al*. also needs the re-coloring processes. Specifically, the direction of the momentum of the red fluid is enforced to match that of the color gradient by maximizing the function $-(\rho_r \boldsymbol{u}_r \cdot \boldsymbol{G})$, which can give the new value of f_{ri}; then the distribution function of the blue fluid is calculated as $f_{bi} = f_i - f_{ri}$. Theoretical analysis shows that the surface tension in the color model of Grunau is related to A_r and A_b. Particularly, when $A_r = A_b = A$, the coefficient of surface tension in the D2Q7 model is

$$\sigma = 9A\tau d(12 + m_r + m_b), \tag{7.14}$$

where $\tau = 2\tau_r\tau_b/(\tau_r + \tau_b)$ is the average relaxation time at the phase interface.

In the above color-gradient models, the solution of the maximum value problem in the re-coloring process is usually computational expensive. Some simplified versions have been developed later. For example, d'Ortona *et al.* [1995] proposed an alternative re-coloring method based on Gunstensen's model,

$$f_{ri}'' = \frac{\rho_r}{\rho} f_i'' + \beta \frac{\rho_r \rho_b}{\rho^2} \cos\theta_i, \quad f_{bi}'' = \frac{\rho_b}{\rho} f_i'' - \beta \frac{\rho_r \rho_b}{\rho^2} \cos\theta_i, \tag{7.15}$$

where the parameter $0 \le \beta \le 1$ is related to the interface width: a larger value of β will give a thinner interface. Specifically, the above color model can be applied to miscible fluids as $A = \beta = 0$. Further improvements in color models can also be found in [Tölke *et al*., 2002].

7.1.2 *LBE model for miscible fluids*

Although the color-gradient models can be used to simulate miscible fluids by adjusting the model parameters, the main aim of these models is to capture the interfacial dynamics in multiphase systems. Flekkøy [1993] established an alternative kind of color model for miscible fluids directly. Instead of describing the distribution function of each fluid, this model adopts the sum and difference of the distribution functions as the

new basic variables,

$$f_i = f_{ri} + f_{bi}, \quad g_i = f_{ri} - f_{bi}\,. \tag{7.16}$$

The corresponding evolution equations are

$$f_i(\boldsymbol{x} + \boldsymbol{c}_i\delta_t, t + \delta_t) - f_i(\boldsymbol{x}, t) = -\frac{1}{\tau_\nu}\left[f_i - f_i^{(eq)}\right], \tag{7.17}$$

$$g_i(\boldsymbol{x} + \boldsymbol{c}_i\delta_t, t + \delta_t) - g_i(\boldsymbol{x}, t) = -\frac{1}{\tau_d}\left[g_i - g_i^{(eq)}\right], \tag{7.18}$$

where τ_v and τ_d are the corresponding dimensionless relaxation times, and $f_i^{(eq)}$ has the same form as that of the standard D*n*Q*b*-LBGK model, while

$$g_i^{(eq)} = \omega_i\varphi\left[1 + \frac{\boldsymbol{c}_i \cdot \boldsymbol{u}}{c_s^2}\right], \tag{7.19}$$

where $\varphi = \rho_r - \rho_b = \sum_i g_i$ is the density difference, and $\rho = \sum_i f_i$ and $\rho\boldsymbol{u} = \sum_i \boldsymbol{c}_i f_i$ are the density and momentum of the mixture.

The evolution equation of f_i is the same as that in single component LBE models. As a result, the corresponding hydrodynamic equations of the mixture are also the Navier-Stokes equations. On the other hand, the Chapman-Enskog analysis of Eq. (7.18) gives the following convection-diffusion equation,

$$\frac{\partial\varphi}{\partial t} + \boldsymbol{u}\cdot\nabla\varphi = D\nabla^2\varphi - \frac{D}{c_s^2}(\boldsymbol{u}\cdot\nabla)^2\varphi\,, \tag{7.20}$$

where the diffusion coefficient D is

$$D = c_s^2\left(\tau_d - \frac{1}{2}\right)\delta_t\,. \tag{7.21}$$

Dimensional analysis shows that the ratio of the second term over the first one on the right hand side of Eq. (7.20) is in the order of

$$\frac{u_0^2/c_s^2L^2}{1/L^2} = M^2\,, \tag{7.22}$$

where u_0 and L_0 are the characteristic velocity and length, respectively. This result indicates that for flows with a small Mach number, the second term can be neglected and thus Eq. (7.20) becomes a standard convection-diffusion equation. As a result, this LBE model can capture the hydrodynamics and diffusion process of a miscible fluid.

Remark: *The color models are the earlier LBE methods for multiphase/multi-component systems. These models have been successfully applied to complex interfacial flows such as multiphase flows in porous media [Tölke et al., 2002] and the spinodal decomposition [Alexander et al., 1993]. However, LBE models of this type also suffer from several limitations, such as the anisotropy of surface tension, the spurious currents in the vicinity of interfaces, and the difficulty to include thermodynamics.*

7.2 Pseudo-Potential Models

7.2.1 *Shan-Chen model*

The key point of the color models is to redistribute the fluid particles based on the color gradient. Actually, the interaction force in such models comes from the difference between the averaged molecular forces on the two sides of the interface. Shan and Chen [1993] presented a LBE model (referred to SC model) which could depict the interaction between fluid particles more accurately and straightforwardly by introducing a pseudo potential.

For a fluid composed of S components, the SC LBE model can be written as

$$f_{ki}(\boldsymbol{x}+\boldsymbol{c}_i\delta_t, t+\delta_t) - f_{ki}(\boldsymbol{x},t) = -\frac{1}{\tau_k}\left[f_{ki} - f_{ki}^{(eq)}\right],\ k=1\sim S\,, \qquad (7.23)$$

where $f_{ki}^{(eq)} = E_i(\rho_k,\ \boldsymbol{u}_k^{(eq)})$ is the equilibrium distribution function of the k-th component, $\rho_k = \sum_i f_{ki}$ is the density of the k-th component, and $\boldsymbol{u}_k^{(eq)}$ is the equilibrium velocity to be determined. The formulation of E_i depends on the choice of the lattice model. For the FHP or FCHC lattice,

$$E_i\left(\rho_k, \boldsymbol{u}_k^{(eq)}\right) = \rho_k\left[d_k - \left(u^{(eq)}\right)^2\right], \qquad i=0,$$

$$E_i\left(\rho_k, \boldsymbol{u}_k^{(eq)}\right) = \frac{1-d_k}{b}\rho_k + \frac{D\rho_k(\boldsymbol{c}_i \cdot \boldsymbol{u}_k^{(eq)})}{b} + \frac{D(D+2)\left(\boldsymbol{c}_i \cdot \boldsymbol{u}_k^{(eq)}\right)^2}{2b}\rho_k - \frac{D\rho_k}{2b}\left(u^{(eq)}\right)^2, \quad i \neq 0, \tag{7.24}$$

where $d_k < 1$ is a constant. The SC model employs a non-local interaction which comes from a potential,

$$V_{k\bar{k}}(\boldsymbol{x}, \boldsymbol{x}') = G_{k\bar{k}}(\mid \boldsymbol{x} - \boldsymbol{x}' \mid)\psi_k(\boldsymbol{x})\psi_{\bar{k}}(\boldsymbol{x}'), \tag{7.25}$$

where $G_{k\bar{k}}$ is a Green function which controls the interaction intensity between component k and $\bar{k}$; ψ_k denotes an effective density of the component k and is usually a function of ρ_k. Generally, the SC model considers only the nearest neighbour interactions, and the function $G_{k\bar{k}}$ can be modelled as

$$G_{k\bar{k}}(\mid \boldsymbol{x} - \boldsymbol{x}' \mid) = \begin{cases} 0, & \mid \boldsymbol{x} - \boldsymbol{x}' \mid > \delta_x, \\ \mathcal{G}_{k\bar{k}}, & \mid \boldsymbol{x} - \boldsymbol{x}' \mid = \delta_x. \end{cases} \tag{7.26}$$

In the above model, the modulus of $\mathcal{G}_{k\bar{k}}$ decides the interaction intensity between component k and $\bar{k}$. The sign of $\mathcal{G}_{k\bar{k}}$ determines whether the interaction force is attractive (negative) or repulsive (positive). The $\mathcal{G}_{k\bar{k}}$ forms a symmetric $S \times S$ interaction matrix G. According to this pseudo potential, the total force acting on the k-th fluid can be expressed as

$$\boldsymbol{F}_k(\boldsymbol{x}) = -\psi_k(\boldsymbol{x})\sum_{\bar{k}} \mathcal{G}_{k\bar{k}} \sum_i \psi_{\bar{k}}(\boldsymbol{x} + \boldsymbol{c}_i\delta_t)\boldsymbol{c}_i \,. \tag{7.27}$$

Obviously, when $\delta_x \to 0$, $\boldsymbol{F}_k = -\nabla_{\boldsymbol{x}'}\sum_{\bar{k}} V_{k\bar{k}}(\boldsymbol{x}, \boldsymbol{x}')$. As mentioned in Chapter 3, there are several approaches to include the interaction force into LBE. In the original SC model, this is achieved through the equilibrium velocity $\boldsymbol{u}_i^{(eq)}$,

$$\boldsymbol{u}_k^{(eq)}(\boldsymbol{x}) = \boldsymbol{u}(\boldsymbol{x}) + \tau_k\delta_t\frac{\boldsymbol{F}_k}{\rho_k}, \tag{7.28}$$

where $\boldsymbol{u}$ is the velocity of the mixture defined by

$$\rho\boldsymbol{u} = \sum_k \rho_k\boldsymbol{u}_k = \sum_k\sum_i \boldsymbol{c}_i f_{ki}\,, \tag{7.29}$$

where $\rho = \sum_k \rho_k$ is the density of the mixture. This approach will introduce some discrete lattice errors as described in Chapter 3. After neglecting such errors, the macroscopic equations derived from the SC model for a single component system (i.e. $S = 1$) can be expressed as

$$\frac{\partial \rho}{\partial t} + \nabla \cdot \left(\rho \boldsymbol{u} \right) = 0 \,, \tag{7.30}$$

$$\frac{\partial \left(\rho \boldsymbol{u} \right)}{\partial t} + \nabla \cdot \left(\rho \boldsymbol{u} \boldsymbol{u} \right) = -\nabla p + \nabla \cdot \boldsymbol{\tau} \,, \tag{7.31}$$

where $\boldsymbol{\tau}$ is the viscous stress, the same as the standard LBGK models; the pressure p now depends on the interaction force,

$$p = \frac{(1 - d_0)}{D} \rho + \frac{b}{2D} \mathcal{G} \psi^2(\rho) \,, \tag{7.32}$$

where $\mathcal{G} = \mathcal{G}_{11}$ is the internal interaction among the fluid. Obviously the equation of state is one for non-ideal gases. When the potential V is properly chosen so that p is a non-monotonic increasing function of the density ρ, phase separation can appear. For the potential with the form (7.25), phase separation can be initiated by choosing a strong $\mathcal{G}$ with a nonlinear potential function ψ. Shan and Chen suggested using the following effective density function,

$$\psi_k = \rho_{k0} \left[1 - e^{-\rho_k / \rho_{k0}} \right] \,, \tag{7.33}$$

where ρ_{k0} is a reference density of the k-th component. On the other hand, Qian *et al.* [1995] proposed a fractional form for the density function.

7.2.2 *Shan-Doolen model*

Soon after the Shan-Chen model, Shan and Doolen [1995] developed an improved version (denoted by SD model) to reduce some of the artifacts. First, the definition of the equilibrium velocity $\boldsymbol{u}_k^{(eq)}$ is changed to

$$\boldsymbol{u}_k^{(eq)} = \boldsymbol{u}' + \tau_k \delta_t \frac{\boldsymbol{F}}{\rho_k} \,, \tag{7.34}$$

where $\boldsymbol{u}'$ is required to satisfy momentum conservation in the case of no forces, i.e.,

$$\sum_k \sum_i \frac{\boldsymbol{c}_i}{\tau_k}\left[f_{ki} - f_{ki}^{(eq)}(\rho_k, \boldsymbol{u}')\right] = 0\,, \tag{7.35}$$

which gives that

$$\boldsymbol{u}' = \sum_k \frac{\rho_k \boldsymbol{u}_k}{\tau_k} \Big/ \sum_k \frac{\rho_k}{\tau_k}\,. \tag{7.36}$$

In the presence of the interaction force, particle collisions do not conserve the momentum locally. But the overall momentum of the system is conserved as the interaction matrix G is symmetric. In the SD model, the velocity of the fluid is redefined by the average of pre- and post-collision momenta, $\rho\boldsymbol{u} = \sum_k \rho_k \boldsymbol{u}_k + \delta_t \sum_k \boldsymbol{F}_k/2$, which can reduce the discrete errors significantly.

The Chapman-Enskog analysis shows that the SD model leads to the following continuity equation for each species,

$$\frac{\partial \rho_k}{\partial t} + \nabla \cdot (\rho_k \boldsymbol{u}) = -\nabla \cdot \boldsymbol{j}_k\,, \tag{7.37}$$

where $\boldsymbol{j}_k = \rho_k(\boldsymbol{u}_k - \boldsymbol{u})$ is the diffusive mass flux of the k-th component, which is related to the pressure, interaction force, and species concentrations. For the FHP and FCHC models, it can be shown that

$$\begin{aligned}\frac{\boldsymbol{j}_k}{\delta_t} = &-\tau_k \boldsymbol{F}_k + \left(\tau_k - \frac{1}{2}\right)\left[\frac{(1-d_k)}{D}\nabla\rho_k - x_k \nabla p\right] \\ &+ x_k\left[\sum_k (\tau_k + 1/2)\boldsymbol{F}_k + \nabla p \sum_k \tau_k x_k - \frac{1}{D}\sum_k \tau_k (1-d_k)\nabla\rho_k\right],\end{aligned} \tag{7.38}$$

where $x_k = \rho_k/\rho$ is the mass fraction of the k-th species. The pressure is similar to that of the SC model,

$$p = \frac{1}{D}\left[\sum_k (1-d_k)\rho_k + \frac{b}{2}\sum_{k,\bar{k}} \mathcal{G}_{k\bar{k}}\psi_k\psi_{\bar{k}}\right]. \tag{7.39}$$

It is noteworthy that when $\mathcal{G}_{k\bar{k}} = 0$, the pressure should obey an equation of state of ideal gases, i.e. $p = \sum_k p_k$. This leads to $1 - d_k = Dc_s^2/m_k$, where c_s is the sound speed in the fluid mixture, and $\boldsymbol{m}_k$ is the molecular mass of the k-th component.

The mass diffusive flux $\boldsymbol{j}_k$ can be decomposed into two parts, $\boldsymbol{j}_k = \boldsymbol{j}_k^{(x)} + \boldsymbol{j}_k^{(p)}$, where

$$\boldsymbol{j}_k^{(x)} = \frac{b\rho}{D}\sum_{m=1}^{S}\left\{\left[\sum_{n=1}^{S}(\alpha_{km}A_n - \alpha_{kn}A_m)x_n \Big/ \sum_{n=1}^{S}A_n x_n\right]\nabla x_m\right\}, \tag{7.40}$$

$$\boldsymbol{j}_k^{(p)} = \left[\sum_{m=1}^{S}\alpha_{km}x_m \Big/ \sum_{m=1}^{S}A_m x_m\right]\nabla p\,, \tag{7.41}$$

where the coefficients are given by

$$\begin{aligned}\alpha_{km} = {} & \frac{1-d_m}{b}\left[(\tau_m - 0.5)(x_k - \delta_{km}) + x_k\left(\tau_k - \sum_{n=1}^{S}\tau_n x_n\right)\right]\delta_t + \\ & \sum_{n=1}^{S}\left[\tau_n(x_k - \delta_{kn}) + x_k\left(\tau_k - \sum_{n=1}^{S}\tau_n x_n\right)\right]\zeta_{nm}\psi_n\frac{\partial\psi_m}{\partial\rho_m}\delta_t,\end{aligned} \tag{7.42}$$

$$A_m = \frac{1-d_m}{b} + \frac{\partial\psi_m}{\partial\rho_m}\sum_{n=1}^{S}\zeta_{mn}\psi_m\,. \tag{7.43}$$

The coefficient before the concentration gradient in Eq. (7.40) is just the mutual diffusivity.

It can be proved that $\sum_k \boldsymbol{j}_k = 0$. Then the mass conservation equation of the mixture can be obtained by summing up Eq. (7.37) over k,

$$\frac{\partial\rho}{\partial t} + \nabla\cdot(\rho\boldsymbol{u}) = 0\,. \tag{7.44}$$

The momentum equation can also be derived based on the Chapman-Enskog expansion, which is similar to that of the SC model except with a viscosity defined by

$$\nu = \frac{1}{D+2}\left(\sum_k x_k\tau_k - \frac{1}{2}\right)\,. \tag{7.45}$$

7.2.3 *Numerical schemes for interaction force*

In either the SC model or the SD model, spurious velocities often appear in the vicinity of a phase interface [Hou *et al*., 1997]. Recently, Shan [2006] found that the isotropy of the force discretization schemes has significant influences on the spurious velocities, and the use of

high-order isotropic schemes can reduce the magnitudes of spurious velocity greatly.

Consider a single component fluid with long distance interactions. In this system the force on a particle located at $\boldsymbol{x}$ exerted by a particle located at $\boldsymbol{x}'$ can be written as

$$\boldsymbol{F}(\boldsymbol{x},\boldsymbol{x}') = -G(|\ \boldsymbol{x}'-\boldsymbol{x}\ |)\psi(\boldsymbol{x})\psi(\boldsymbol{x}')(\boldsymbol{x}'-\boldsymbol{x})\ . \tag{7.46}$$

Then the total force experienced by the fluid particle can be expressed as

$$\boldsymbol{F}(\boldsymbol{x}) = -\psi(\boldsymbol{x})\int G(|\ \boldsymbol{x}'-\boldsymbol{x}\ |)\psi(\boldsymbol{x}')(\boldsymbol{x}'-\boldsymbol{x})\,d\boldsymbol{x}'\,. \tag{7.47}$$

Assuming that $G(|\boldsymbol{x}'-\boldsymbol{x}\,|\,)$ is isotropic, the above integral can be evaluated by the discrete values at the neighboring nodes,

$$\boldsymbol{F}(\boldsymbol{x}) = -\mathcal{G}\psi(\boldsymbol{x})\sum_{i=1}^{N} w(c_i^2)\psi(\boldsymbol{x}+\boldsymbol{c}_i)\boldsymbol{c}_i\ , \tag{7.48}$$

where $\{\boldsymbol{x}+\boldsymbol{c}_i : i = 1,2,\cdots,N\}$ are N nodes surrounding $\boldsymbol{x}$, $w(c_i^2)$ is the weight coefficient of the integral. Take Taylor expansion of $\psi(\boldsymbol{x}+\boldsymbol{c}_i)$, $\boldsymbol{F}(\boldsymbol{x})$ can be approximated as

$$\boldsymbol{F}(\boldsymbol{x}) = -\zeta\psi(\boldsymbol{x})\sum_{n=0}^{\infty}\frac{1}{n!}[\nabla^{(n)}\psi(\boldsymbol{x})] : \boldsymbol{E}^{(n+1)}\ , \tag{7.49}$$

where

$$\boldsymbol{E}^{(n)} = \sum_{i=1}^{N} w(c_i^2)\underbrace{\boldsymbol{c}_i\boldsymbol{c}_i\cdots\boldsymbol{c}_i}_{n}\ . \tag{7.50}$$

The symmetric properties of the lattice lead to

$$\boldsymbol{E}^{(n)} = \begin{cases} 0, & n = 1, 3, 5,\cdots \\ e_n\delta_x^n\Delta^{(n)}, & n = 0, 2, 4,\cdots \end{cases} \tag{7.51}$$

where e_n is a constant and $\Delta^{(n)}$ is an n-th order symmetric tensor.

Since the interaction force $\boldsymbol{F}(\boldsymbol{x})$ is isotropic, Eq. (7.49) holds only when all the $\boldsymbol{E}^{(n)}$ are so. But due to the finiteness of the discrete velocity set, this condition cannot be fulfilled. However, $\boldsymbol{E}^{(n)}$ can achieve high-order isotropy by properly choosing the weight coefficients $w(c_i^2)$. Table 7.1 gives several isotropic tensors $\boldsymbol{E}^{(n)}$ and the corresponding weights for two- and three-dimensional lattices. Numerical results of a

Table 7.1. Weight coefficients and isotropic $E^{(n)}$ (Shan, Phys. Rev. E 73, 047701 2006).

	$E^{(n)}$		e_i^2/δ_x^2						
	n		1	2	3	4	5	6	8
2D	4	w	1/3	1/12					
	6		4/15	1/10		1/120			
	8		4/21	4/45		1/60	2/315	1/5040	
3D	4	w	1/6	1/12					
	6		2/15	1/15	1/60	1/120			
	8		4/45	1/21	2/105	5/504	1/315	1/630	1/5040

static droplet show that high-order isotropic schemes can decrease the spurious velocity greatly [Shan, 2006].

Remark: *In pseudo-potential LBE models, the microscopic interactions, which reflect the physical nature of the multiphase/multi-component flows, are modelled directly. Due to this clear picture and the simplicity, such models are widely used in many fields. However, theoretical analysis shows that the pseudo-potential models are consistent with thermodynamic theories only when the effective density function takes a special exponent form [Shan and Chen, 1994].*

7.3 Free Energy Models

The color and pseudo-potential LBE models are both phenomenological models. Swift *et al.* [1995, 1996] developed an alternative type of LBE models for multiphase/multi-component systems based on free energy theory. The basic idea is to devise a suitable equilibrium distribution function based on some free energy functions, in which the thermodynamic pressure tensor is incorporated.

7.3.1 *Models for single component non-ideal fluid flows*

For a one-component non-ideal fluid, the van der Waals theory shows that the free energy of the system can be expressed as

$$\Psi = \int \left[\psi(\rho(\boldsymbol{x}), T(\boldsymbol{x})) + W(\nabla\rho(\boldsymbol{x})) \right] d\boldsymbol{x}\,, \tag{7.52}$$

where $\psi(\rho)$ is the free energy density in the bulk phase, and $W(\nabla\rho)$ is the free energy related to surface tension. One common free energy formulation is

$$W = \frac{\kappa}{2}|\nabla\rho|^2\,, \tag{7.53}$$

where the parameter κ is related to the surface tension. For example, for a flat interface located at $z = 0$, the surface tension is defined as

$$\sigma = \kappa\int\left(\frac{\partial\rho}{\partial z}\right)^2 dz\,. \tag{7.54}$$

According to the free energy Ψ, a non-local pressure can be defined as

$$p(\boldsymbol{x}) = \rho\frac{\delta\Psi}{\delta\rho} - \Psi = p_0 - \kappa\rho\nabla^2\rho - \frac{\kappa}{2}\mid\nabla\rho\mid^2\,, \tag{7.55}$$

where $p_0 = \rho\psi'(\rho) - \psi(\rho)$ is the equation of state. Then the thermodynamic pressure tensor, which considers the contribution of the interface, can be written as

$$P'_{\alpha\beta} = p\delta_{\alpha\beta} + \kappa\frac{\partial\rho}{\partial x_\alpha}\frac{\partial\rho}{\partial x_\beta}\,. \tag{7.56}$$

Note that $\boldsymbol{P'}$ is different from the pressure tensor $\boldsymbol{P} \equiv \int \boldsymbol{CC}f = \boldsymbol{P'} + \boldsymbol{\tau}$ in kinetic theory.

In order to obtain a LBE model which is consistent with the above thermodynamical theory, Swift *et al.* suggested using an equilibrium distribution function with the density gradient in the LBGK model,

$$f_i(\boldsymbol{x} + \boldsymbol{c}_i\delta_t, t + \delta_t) - f_i(\boldsymbol{x}, t) = -\frac{1}{\tau}\Big[f_i - f_i^{(eq)}\left(\rho, \boldsymbol{u}, \nabla\rho\right)\Big], \tag{7.57}$$

where $f_i^{(eq)}$ are constructed to enforce the following constraints,

$$\sum_i f_i^{(eq)} = \rho, \quad \sum_i \boldsymbol{c}_i f_i^{(eq)} = \rho\boldsymbol{u}, \quad \sum_i \boldsymbol{c}_i\boldsymbol{c}_i f_i^{(eq)} = \boldsymbol{P'} + \rho\boldsymbol{uu}\,. \tag{7.58}$$

Similar to the standard LBGK model, the equilibrium distribution function $f_i^{(eq)}$ is also a polynomial of the fluid velocity $\boldsymbol{u}$. For example, in the FHP model $f_i^{(eq)}$ can be expressed as

$$f_i^{(eq)} = A + B(\boldsymbol{c}_i \cdot \boldsymbol{u}) + Cu^2 + D(\boldsymbol{c}_i \cdot \boldsymbol{u})^2 + G : \boldsymbol{c}_i\boldsymbol{c}_i, \quad i \neq 0\,, \tag{7.59}$$

$$f_0^{(eq)} = A_0 + C_0 u^2\,. \tag{7.60}$$

According to the conditions given by Eq. (7.58), the coefficients in $f_i^{(eq)}$ can be obtained as

$$A_0 = \rho - 6A, \quad C_0 = -\rho\,, \tag{7.61}$$

$$A = \frac{1}{3}(p_0 - \kappa\rho\nabla^2\rho), \quad B = \frac{\rho}{3}, \quad C = -\frac{\rho}{6}, \quad D = \frac{2\rho}{3}, \tag{7.62}$$

$$G_{xx} = -G_{yy} = \frac{\kappa}{3}\left[\left(\frac{\partial\rho}{\partial x}\right)^2 - \left(\frac{\partial\rho}{\partial y}\right)^2\right], \quad G_{xy} = \frac{2\kappa}{3}\frac{\partial\rho}{\partial x}\frac{\partial\rho}{\partial y}. \tag{7.63}$$

Equation (7.58) also indicates that the collision operator of the free-energy model conserves both mass and momentum locally.

With the above equilibrium distribution function, together with the definition of fluid velocity as $\rho\boldsymbol{u} = \sum_i \boldsymbol{c}_i f_i$, the hydrodynamic equations recovered from the free-energy model are

$$\frac{\partial\rho}{\partial t} + \nabla\cdot(\rho\boldsymbol{u}) = 0\,, \tag{7.64}$$

$$\begin{aligned}\frac{\partial(\rho\boldsymbol{u})}{\partial t} + \nabla\cdot(\rho\boldsymbol{u}\boldsymbol{u}) = {} & -\nabla p_0 + \nu\nabla^2(\rho\boldsymbol{u}) + \nabla[\lambda\nabla\cdot(\rho\boldsymbol{u})] \\ & - \left(\tau - \frac{1}{2}\right)\frac{\partial p_0}{\partial\rho}\,\delta_t\nabla\cdot[\boldsymbol{u}\nabla\rho + (\nabla\rho)\boldsymbol{u}],\end{aligned} \tag{7.65}$$

where

$$\nu = \frac{1}{4}\left(\tau - \frac{1}{2}\right)\delta_t, \quad \lambda = \left(\tau - \frac{1}{2}\right)\left(\frac{1}{2} - \frac{\partial p_0}{\partial\rho}\right)\delta_t\,. \tag{7.66}$$

The last term on the right hand side of the momentum equation is zero in the bulk phase, where the equations reduce to the standard Navier-Stokes equations. But in the vicinity of phase interface where density gradient is large, this term should be considered.

7.3.2 *Model for binary fluid flows*

Free-energy LBE model for non-ideal fluid flows with two components was also developed [Swift *et al.*, 1996]. This model uses two distribution functions to simulate the overall system, which is similar to the miscible model presented by Flekkøy [1993] as described in subsection 7.1.2. The difference between these two models lies in the equilibrium distribution functions $f_i^{(eq)}$ and $g_i^{(eq)}$: the free-energy model considers the in-homogeneity of the fluid. Specifically, $f_i^{(eq)}$ still satisfies the constraints given by Eq. (7.58), except that the density ρ and velocity $\boldsymbol{u}$ are for the mixture; on the other hand, $g_i^{(eq)}$ now are enforced to satisfy the following constraints,

$$\sum_i g_i^{(eq)} = \varphi, \quad \sum_i \boldsymbol{c}_i g_i^{(eq)} = \varphi \boldsymbol{u}, \quad \sum_i \boldsymbol{c}_i \boldsymbol{c}_i g_i^{(eq)} = \Gamma \Delta\mu \boldsymbol{I} + \varphi \boldsymbol{u}\boldsymbol{u}\,, \tag{7.67}$$

where $\Delta\mu$ is the chemical potential difference between the two components, and Γ is the mobility. Here the thermodynamic pressure tensor $\boldsymbol{P}'$ and the chemical potential difference $\Delta\mu$ can be obtained according to certain free energy models for two-phase systems. Swift *et al.* [1996] considered the following free energy,

$$\Psi = \int \left[\psi(\rho, T, \varphi) + \tfrac{\kappa}{2} |\nabla\rho|^2 + \tfrac{\kappa}{2} |\nabla\varphi|^2 \right] d\boldsymbol{x}\,, \tag{7.68}$$

where the bulk free-energy density is given by

$$\begin{aligned} \psi = {} & \frac{G}{4}\rho\left(1 - \frac{\varphi^2}{\rho^2}\right) - \rho RT + \frac{RT}{2}(\rho + \varphi)\ln\left(\frac{\rho + \varphi}{2}\right) \\ & + \frac{RT}{2}(\rho - \varphi)\ln\left(\frac{\rho - \varphi}{2}\right), \end{aligned} \tag{7.69}$$

where G denotes the interaction strength. As $RT < G/2$, phase separation will occur. Furthermore, from this free-energy, one can derive the chemical potential difference and the thermodynamic pressure tensor,

$$\Delta\mu = -\frac{G}{2}\frac{\varphi}{\rho} + \frac{RT}{2}\ln\left(\frac{1 + \varphi/\rho}{1 - \varphi/\rho}\right) - \kappa\nabla^2\varphi\,, \tag{7.70}$$

$$P'_{\alpha\beta} = p\delta_{\alpha\beta} + \kappa\frac{\partial\rho}{\partial x_\alpha}\frac{\partial\rho}{\partial x_\beta} + \kappa\frac{\partial\varphi}{\partial x_\alpha}\frac{\partial\varphi}{\partial x_\beta}\,, \tag{7.71}$$

where

$$p = \rho RT - \kappa(\rho\nabla^2\rho + \varphi\nabla^2\varphi) - \frac{\kappa}{2}\big(|\nabla\rho|^2 + |\nabla\varphi|^2\big). \tag{7.72}$$

With these expressions, the coefficients in $f_i^{(eq)}$ can be written as

$$A_0 = \rho - 6A, \quad C_0 = -\rho\,, \tag{7.73}$$

$$A = \frac{1}{3}(p_0 - \kappa\rho\nabla^2\rho - \kappa\varphi\nabla^2\varphi), \quad B = \frac{\rho}{3}, \quad C = -\frac{\rho}{6}, \quad D = \frac{2\rho}{3}, \tag{7.74}$$

$$G_{xx} = -G_{yy} = \frac{\kappa}{3}\left[\left(\frac{\partial\rho}{\partial x}\right)^2 - \left(\frac{\partial\rho}{\partial y}\right)^2 + \left(\frac{\partial\varphi}{\partial x}\right)^2 - \left(\frac{\partial\varphi}{\partial y}\right)^2\right], \tag{7.75}$$

$$G_{xy} = \frac{2\kappa}{3}\left[\frac{\partial\rho}{\partial x}\frac{\partial\rho}{\partial y} + \frac{\partial\varphi}{\partial x}\frac{\partial\varphi}{\partial y}\right]. \tag{7.76}$$

Similarly, $g_i^{(eq)}$ reads

$$g_i^{(eq)} = H + K(\boldsymbol{c}_i\cdot\boldsymbol{u}) + Ju^2 + Q(\boldsymbol{c}_i\cdot\boldsymbol{u})^2, \ i \neq 0\,, \tag{7.77}$$

$$g_0^{(eq)} = H_0 + J_0u^2\,, \tag{7.78}$$

where

$$H_0 = \varphi - 6H, \quad J_0 = -\varphi\,, \tag{7.79}$$

$$H = \frac{1}{3}\Gamma\Delta\mu, \quad K = \frac{\varphi}{3}, \quad J = -\frac{\varphi}{6}, \quad Q = \frac{2\varphi}{3}\,. \tag{7.80}$$

With the above expressions, the recovered hydrodynamic equations of the FHP free-energy model read

$$\frac{\partial\rho}{\partial t} + \nabla\cdot(\rho\boldsymbol{u}) = 0\,, \tag{7.81}$$

$$\frac{\partial\varphi}{\partial t} + \nabla\cdot(\varphi\boldsymbol{u}) = \Gamma\theta\nabla^2\varphi - \theta\nabla\cdot\left[\frac{\varphi}{\rho}\nabla\cdot\boldsymbol{P}'\right], \tag{7.82}$$

$$\frac{\partial(\rho\boldsymbol{u})}{\partial t} + \nabla\cdot(\rho\boldsymbol{u}\boldsymbol{u}) = -\nabla p_0 + \nu\nabla^2(\rho\boldsymbol{u}) + \nabla[\lambda\nabla\cdot(\rho\boldsymbol{u})]\,, \tag{7.83}$$

where ν and λ is given by Eq. (7.66). The transport coefficient in Eq. (7.82) is

$$\theta = \left(\tau_d - \frac{1}{2}\right)\delta_t, \tag{7.84}$$

where τ_d is the relaxation time in the evolution equation of g_i.

7.3.3 *Galilean invariance of the free-energy LBE models*

Although the free-energy LBE model is constructed from thermodynamic theories, it still has some undesirable features, one of which is the violation of the Galilean invariance. In the recovered momentum equation, the density in the viscous stress appears in the first order derivative, i.e.

$$\boldsymbol{\tau} = \nu\nabla^2(\rho\boldsymbol{u}) + \nabla[\lambda\nabla\cdot(\rho\boldsymbol{u})]. \tag{7.85}$$

In bulk region the density is nearly constant and Eq. (7.85) is Galilean invariant approximately. However, in the vicinity of an interface where the density gradient is large, the Galilean invariance of Eq. (7.85) will be broken and nonphysical phenomenon will appear. Actually, it has been reported that a droplet with an initial sphere shape will become an elliptic one in a uniform flow field [Inamuro *et al*., 2000; Kalarakis *et al*., 2002].

The lack of Galilean invariance of the free-energy model was first found by Swift *et al.* [1996]. They proposed a method to remedy this problem, which enforces the second-order moment of the equilibrium distribution function to satisfy the following condition,

$$\sum_i c_{i\alpha}c_{i\beta}f_i^{(eq)} = \rho u_\alpha u_\beta + P'_{\alpha\beta} + \omega_1(u_\alpha\partial_\beta\rho + u_\beta\partial_\alpha\rho) + \omega_2 u_\gamma\partial_\gamma\rho, \tag{7.86}$$

where ω_1 and ω_2 are two parameters that can be adjusted to recover the Galilean invariance partially. For the aforementioned FHP model, the Chapman-Enskog analysis shows that the viscous stress is now,

$$\begin{aligned}\tau_{\alpha\beta} = {} & \nu\partial_\alpha\left(\rho\partial_\alpha u_\beta\right) + \partial_\beta\left(\lambda\rho\partial_\alpha u_\alpha\right) + \partial_\alpha\left[(\lambda-\nu-\omega_1)u_\beta\partial_\alpha\rho\right] \\ & + \partial_\beta\left[(\lambda-\omega_2)u_\alpha\partial_\alpha\rho\right] - \partial_\alpha\left[(2\nu-\lambda+\omega_1)u_\alpha\partial_\beta\rho\right].\end{aligned} \tag{7.87}$$

In order to recover the Galilean invariance, the last three terms in Eq. (7.87) should vanish. However, since the viscosity ν is always positive, these three non-Galilean invariant terms cannot be completely

removed by choosing ω_1 and ω_2. On the other hand, by choosing $\omega_1 = \lambda - 2\nu$ and $\omega_1 = \lambda$, we can eliminate the last two terms so that the Galilean invariance is partially recovered.

Inamuro *et al*. [2000] built another D2Q9 free-energy model with improved Galilean invariant properties. The equilibrium distribution function of this model is

$$f_i^{(eq)} = 3\omega_i \left[p_0 - \kappa\rho\nabla^2\rho + 2\omega \boldsymbol{u}\cdot\nabla\rho \right] + \omega_i \boldsymbol{G} : \boldsymbol{c}_i\boldsymbol{c}_i + \omega_i\rho\left[\frac{\boldsymbol{c}_i\cdot\boldsymbol{u}}{c_s^2} + \frac{(\boldsymbol{c}_i\cdot\boldsymbol{u})^2}{2c_s^4} - \frac{u^2}{2c_s^2} \right], \quad i \neq 0, \tag{7.88}$$

$$f_0^{(eq)} = \rho - \frac{5}{3}\left[p_0 - \kappa\rho\nabla^2\rho + 2\omega\boldsymbol{u}\cdot\nabla\rho \right] - \omega_0\rho\frac{u^2}{2c_s^2}, \tag{7.89}$$

where $c_s^2 = 1/3$, ω_i is the weight coefficient which is the same as that in the standard D2Q9 model, ω is an adjustable coefficient aiming at eliminating the Galilean variance. The second-order tensor $\boldsymbol{G}$ in Eq. (7.88) is defined by

$$G_{\alpha\beta} = \frac{9}{2}\left[\kappa\frac{\partial\rho}{\partial x_\alpha}\frac{\partial\rho}{\partial x_\beta} + \omega\left(u_\alpha\frac{\partial\rho}{\partial x_\beta} + u_\beta\frac{\partial\rho}{\partial x_\alpha} \right) \right] - \frac{9}{4}\left[\kappa\frac{\partial\rho}{\partial x_\gamma}\frac{\partial\rho}{\partial x_\gamma} + 2\omega u_\gamma\frac{\partial\rho}{\partial x_\gamma} \right]\delta_{\alpha\beta}. \tag{7.90}$$

Asymptotic analysis shows that the parameter ω should be chosen as $\omega = \nu = c_s^2(\tau - 0.5)\delta_t$ in order to recover the Galilean invariance.

Based on the FHP model developed by Swift *et al*., Kalarakis *et al.* [2002] developed another free-energy model satisfying the Galilean invariance by modifying the equilibrium distribution function. The basic idea is to absorb the non-Galilean terms into the pressure tensor. The correction method is similar to that by Swift *et al.*, i.e. introducing two adjustable terms into the thermodynamical pressure tensor $\boldsymbol{P}'$ as given by Eq. (7.86). The two free parameters are chosen as

$$\omega_1 = \omega_2 = \nu\left(1 - 4\frac{\partial p}{\partial\rho} \right). \tag{7.91}$$

Obviously, this correction method is identical to that of Inamuro if $\partial p/\partial\rho$ is neglected.

Recently, Zheng *et al*. [2005, 2006] presented an improved free-energy LBM, in which the D2Q5 lattice velocity model is used to capture the interface for the 2D case. It can recover the macroscopic Cahn-Hilliard equation with the second order of accuracy. All of the above improved free-energy models are shown to be able to reduce the non-Galilean invariant effects. Numerical results demonstrated that the shape of a single droplet or bubble in a uniform flow could be maintained. On the other hand, it seems that the free-energy models for multiphase and multi-component flows have some intrinsic limitations which require further investigations.

Remark: *The main difference between the free-energy models and the pseudo-potential models lies in the force treatments: in the pseudo-potential models, the effects of the interaction force are reflected in the first-order moment of the equilibrium distribution function, while in the free-energy models the effects are reflected in the second-order moment of the equilibrium distribution function. From the microscopic point of view, the inter-particle interactions should influence the momentums of the flow (i.e., the first-order velocity moment). But at mesoscopic scale, the overall effects from the microscopic interactions can be reflected in the thermodynamic pressure tensor. Therefore, as a mesoscopic method, the free-energy LBE model is also an effective approach.*

7.4 LBE Models Based on Kinetic Theories

As shown in Chapter 1, the LBE for simple fluids can be derived from the Boltzmann equation. Similarly, it is also possible to construct LBE models for multiphase/multi-component flows based on corresponding kinetic theories. An advantage of the LBE models obtained in this way is that they will have a solid physical foundation. Recently, some of such models have been developed successfully following this approach.

7.4.1 *Models for single-component multiphase flows*

Kinetic model for dense gases

The evolution of the single-particle distribution function of a dilute gas can be well described by the Boltzmann equation. In a dilute gas, the

mean free path is fairly larger than the molecular diameter. As a result, the singlet distribution function can be treated to be independent from others, and the molecular volume can be ignored during the collision process. However, for a dense gas these assumptions do not hold anymore, and the Boltzmann equation will fail to work. In such cases, the Enskog equation [Chapman and Cowling, 1990] should be used instead, which can be expressed as

$$\frac{\partial f}{\partial t} + \boldsymbol{\xi} \cdot \nabla f + \boldsymbol{a} \cdot \nabla_{\xi} f = \Omega_E \,, \tag{7.92}$$

where $\boldsymbol{a}$ is the acceleration due to an external force, Ω_E is the Enskog collision operator,

$$\begin{aligned} \Omega_E(f) = \int \big[& \chi(\boldsymbol{x} + \tfrac{\sigma}{2}\boldsymbol{k}) f(\boldsymbol{x}, \boldsymbol{\xi}') f(\boldsymbol{x} + \sigma\boldsymbol{k}, \boldsymbol{\xi}_1') \\ & - \chi(\boldsymbol{x} - \tfrac{\sigma}{2}\boldsymbol{k}) f(\boldsymbol{x}, \boldsymbol{\xi}) f(\boldsymbol{x} - \sigma\boldsymbol{k}, \boldsymbol{\xi}_1) \big] B(\theta, |\boldsymbol{V}|) d\theta d\epsilon d\boldsymbol{\xi}_1 \,. \end{aligned} \tag{7.93}$$

Here σ is the diameter of the molecule, $\boldsymbol{k}$ is the unit vector directed from the molecule with velocity $\boldsymbol{\xi}_1$ to that with velocity $\boldsymbol{\xi}$ along the line of centers of the two colliding molecules. $\boldsymbol{\xi}$ and $\boldsymbol{\xi}'$ are the molecular velocities before and after the collision, χ is the radial distribution function (RDF) of two molecules at contact, which is evaluated at location $\boldsymbol{x} + \sigma\boldsymbol{k}/2$. It depends only on the distance between the molecules and is independent of its velocity. Actually, the function χ reflects the increase in the collision probability in a dense gas. Usually, it is a monotonic increasing function of the number density n or the parameter $b\rho \equiv 2n\pi\sigma^3/3 = (2\pi\sigma^3/3m)\rho$. It is clear that $b\rho$ is just one half of the total volume of the gas molecules in a unit volume, $V_\sigma = 4n\pi\sigma^3/3$. As such, $0 \le b\rho \le 0.5$. Generally χ is inversely proportional to $(1 - 2b\rho)^l$ for hard sphere gases (here l is a positive integer). For instance, the Carnahan-Starling model [Carnahan and Starling, 1969] gives

$$\chi = \frac{1 - b\rho}{(1 - 2b\rho)^3} \,. \tag{7.94}$$

For a dilute gas $\chi = 1$ as $b\rho \to 0$, and χ increases gradually as the gas becomes denser. Particularly, when the gas is so dense that the molecules cannot move, we have $b\rho \to 0.5$ and $\chi = \infty$.

The Enskog collision operator Ω_E reflects the finite volume effect in dense gases, and it is a nonlocal operator. The collisions between the finite-size molecules will induce momentum and energy transfer (*collisional transfer*), which is not considered in the Boltzmann equation.

The Chapman-Enskog analysis of the Enskog equation leads to the following hydrodynamic equations

$$\frac{\partial \rho}{\partial t} + \nabla \cdot (\rho \boldsymbol{u}) = 0\,, \tag{7.95}$$

$$\frac{\partial (\rho \boldsymbol{u})}{\partial t} + \nabla \cdot (\rho \boldsymbol{u}\boldsymbol{u} + \boldsymbol{P}) = \rho \boldsymbol{a}\,, \tag{7.96}$$

$$\frac{\partial (\rho e)}{\partial t} + \nabla \cdot (\rho \boldsymbol{u} e + \boldsymbol{q}) = \boldsymbol{P} : \nabla \boldsymbol{u}\,, \tag{7.97}$$

where $\boldsymbol{P}$ and $\boldsymbol{q}$ are the pressure tensor and heat flux including the collision transport,

$$\boldsymbol{P} = p\boldsymbol{I} - \boldsymbol{\tau} = p\boldsymbol{I} - 2\mu_E \overset{\circ}{\boldsymbol{S}} - \varpi(\nabla \cdot \boldsymbol{u})\boldsymbol{I}\,,\ \boldsymbol{q} = -\kappa_E \nabla T\,, \tag{7.98}$$

where ϖ is a parameter from the collision transport,

$$\varpi = \frac{\chi (b\rho)^2 m (RT)^{1/2}}{\pi^{3/2}\sigma^2}\,. \tag{7.99}$$

The pressure is related to the density and temperature through the equation of state,

$$p = \rho RT[1 + b\rho\chi(\rho)]\,. \tag{7.100}$$

The transport coefficients are given by

$$\mu_E = \mu_B b\rho \left[\frac{1}{b\rho\chi} + 0.8 + 0.7614 b\rho\chi\right], \tag{7.101}$$

$$\kappa_E = \kappa_B b\rho \left[\frac{1}{b\rho\chi} + 1.2 + 0.7574 b\rho\chi\right], \tag{7.102}$$

where μ_B and κ_B are the dynamic viscosity and thermal conductivity for dilute gases corresponding to the Boltzmann equation. Equations (7.101)

and (7.102) show that the term $b\rho\chi$ plays an important role in the Enskog theory. For a real non-ideal gas, Enskog suggested specifying $b\rho\chi$ according to the measured equation of state [Chapman and Cowling, 1990],

$$b\rho\chi = \frac{T}{p_{id}}\frac{\partial p}{\partial T} - 1, \tag{7.103}$$

where $p_{id} = \rho RT$ is the equation of state for ideal gases.

Luo's model based on the Enskog equation

The first non-ideal gas LBE model based on the Enskog equation was attributed to Luo [1998, 2000]. In this model, both the distribution function f and the RDF χ in Ω_E were expanded into their Taylor series around $\boldsymbol{x}$ and truncated at the first order, which gives that $\Omega_E = J^{(0)} + J_1^{(1)} + J_2^{(1)} + O(\sigma^2)$, where

$$J^{(0)} = \chi\int\left[f'f_1' - ff_1\right]B(\theta,|\boldsymbol{V}|)d\theta d\epsilon d\boldsymbol{\xi}_1, \tag{7.104}$$

$$J_1^{(1)} = \frac{\sigma}{2}\int\left[f'f_1' + ff_1\right]\boldsymbol{k}\cdot\nabla\chi B(\theta,|\boldsymbol{V}|)d\theta d\epsilon d\boldsymbol{\xi}_1, \tag{7.105}$$

$$J_2^{(1)} = \sigma\chi\int\left[f'\nabla f_1' + f\nabla f_1\right]\cdot\boldsymbol{k}B(\theta,|\boldsymbol{V}|)d\theta d\epsilon d\boldsymbol{\xi}_1, \tag{7.106}$$

where $f' \equiv f(\boldsymbol{\xi}')$, $f_1' \equiv f(\boldsymbol{\xi}_1')$. Obviously, the zeroth-order collision operator $J^{(0)}$ is similar to the Boltzmann one, and can be modeled by the BGK collision model,

$$J^{(0)} = -\frac{\chi}{\tau_c}\left[f_i - f_i^{(eq)}\right], \tag{7.107}$$

where $f_i^{(eq)}$ is the usual Maxwellian distribution function. The two first-order terms, $J_1^{(1)}$ and $J_2^{(1)}$, can be simplified by assuming $f \approx f^{(eq)}$ and noticing that $f^{(eq)}(\boldsymbol{\xi}')f^{(eq)}(\boldsymbol{\xi}_1') = f^{(eq)}(\boldsymbol{\xi})f^{(eq)}(\boldsymbol{\xi}_1)$, i.e.,

$$J_1^{(1)} \approx -f^{(eq)}b\rho\ \boldsymbol{C}\cdot\nabla\chi,\ J_2^{(1)} \approx -2f^{(eq)}b\rho\chi\boldsymbol{C}\cdot\nabla\ln\rho - r, \tag{7.108}$$

where

$$r = f^{(eq)} b\rho\chi \left\{ \frac{D}{(D+2)\theta} \boldsymbol{CC} : \nabla \boldsymbol{u} + \left[\frac{C^2}{(D+2)\theta} - 1 \right] \nabla \cdot \boldsymbol{u} + \frac{1}{2} \left[\frac{DC^2}{(D+2)\theta} - 1 \right] \boldsymbol{C} \cdot \nabla \ln \theta \right\}. \tag{7.109}$$

Here $\theta = RT, \boldsymbol{C} = \boldsymbol{\xi} - \boldsymbol{u}$. For isothermal flows, the last term of r is zero and it can be shown that,

$$\int r d\boldsymbol{\xi} = 0, \quad \int \boldsymbol{\xi}\, r d\boldsymbol{\xi} = 0\,. \tag{7.110}$$

This means that r does not affect the mass and momentum conservations. As such, neglecting it in $J_2^{(1)}$ does not change the final formulation of the hydrodynamic equations, but the transport coefficients may change. As a result, the first-order collision term can be simplified as

$$J^{(1)} \equiv J_1^{(1)} + J_2^{(1)} = -f^{(eq)} b\rho\chi \boldsymbol{C} \cdot \nabla \ln(\chi\rho^2)\,. \tag{7.111}$$

This approximation leads to the following kinetic equation for isothermal dense gases,

$$\frac{\partial f}{\partial t} + \boldsymbol{\xi} \cdot \nabla f + \boldsymbol{a} \cdot \nabla_{\boldsymbol{\xi}} f = -\frac{\chi}{\tau_c} \left[f_i - f_i^{(eq)} \right] - f^{(eq)} b\rho\chi \boldsymbol{C} \cdot \nabla \ln(\chi\rho^2)\,. \tag{7.112}$$

It is clear that the term $J^{(1)}$ acts like a body force in this simplified Enskog model. Actually, this term originates from the volume-exclusion effect, and it can be easily verified that

$$\int \boldsymbol{\xi} J^{(1)}\, d\boldsymbol{\xi} = -\nabla(b\rho^2\chi\theta) \neq 0\,. \tag{7.113}$$

Following the procedure of constructing a standard LBE model from the Boltzmann equation, Luo developed a non-ideal LBE model from the modeled Enskog equation (7.112),

$$f_i(\boldsymbol{x} + \boldsymbol{c}_i\delta_t, t + \delta_t) - f_i(\boldsymbol{x}, t) = -\frac{\chi}{\tau} \left[f_i - f_i^{(eq)} \right] + \delta_t J_i^{(1)} + \delta_t F_i\,, \tag{7.114}$$

where the equilibrium distribution function $f_i^{(eq)}$ is the same as that of standard LBGK model, the discrete first-order collision term and forcing term are defined by

$$J_i^{(1)} = -b\rho\chi f_i^{(eq)} (\boldsymbol{c}_i - \boldsymbol{u}) \cdot \nabla \ln(\chi\rho^2),\ F_i = \omega_i \rho \left[\frac{\boldsymbol{c}_i - \boldsymbol{u}}{c_s^2} + \frac{(\boldsymbol{c}_i \cdot \boldsymbol{u})}{c_s^4} \boldsymbol{c}_i \right] \cdot \boldsymbol{a}\,. \tag{7.115}$$

The fluid density and velocity in Luo's model are defined by

$$\rho = \sum_i f_i \,, \quad \rho \boldsymbol{u} = \sum_i \boldsymbol{c}_i f_i \,. \tag{7.116}$$

It is noted that the definition of the velocity $\boldsymbol{u}$ is not modified according to the external force $\boldsymbol{a}$. If neglecting the errors from the total force due to discrete lattice effects, the derived hydrodynamic equations from the LBE (7.114) will have the same formulation as given by Eqs. (7.95), (7.96), and (7.97), except that the viscous stress tensor becomes $\boldsymbol{\tau} = 2\mu_E \boldsymbol{S}$, with

$$\mu_E = \rho c_s^2 \left(\frac{\tau}{\chi} - \frac{1}{2} \right) \delta_t \,, \tag{7.117}$$

which is different from that from the continuous Enskog equation. However, by adjusting the relaxation time τ the viscosity can be made to be fully consistent with that of the Enskog theory. The pressure in the derived momentum equation is

$$p = c_s^2 \rho (1 + b\rho\chi) \,, \tag{7.118}$$

with $c_s^2 = RT$.

He-Shan-Doolen model based on modified Boltzmann equation

He *et al.* [1998] presented another kinetic-theory-based LBE model for non-ideal gases (referred to as HSD model). But unlike Luo's model, the starting point of the HSD model is a modified Boltzmann-BGK equation,

$$\frac{\partial f}{\partial t} + \boldsymbol{\xi} \cdot \nabla f + \boldsymbol{a}_t \cdot \nabla_{\boldsymbol{\xi}} f = -\frac{1}{\tau_c} \left[f - f^{(eq)} \right], \tag{7.119}$$

where $\boldsymbol{a}_t$ is the acceleration due to the total force including both the external force and internal force,

$$\boldsymbol{a}_t = -\nabla V - b\rho\theta\chi \nabla \ln(\chi\rho^2) + \boldsymbol{g} \,, \tag{7.120}$$

where $\boldsymbol{g}$ is the acceleration due to external body force, and V is a potential related to the attractive force among fluid molecules,

$$V = -2a\rho - \kappa \nabla^2 \rho \,. \tag{7.121}$$

Here the two parameters a and κ depend on the attractive potential ϕ_a,

$$a = -\frac{1}{2}\int_{r>\sigma} \phi_a(r)\,d\mathrm{r}, \quad \kappa = -\frac{1}{6}\int_{r>\sigma} r^2\phi_a(r)\,d\mathrm{r}\,. \tag{7.122}$$

The second term of the total force stems from the repulsive force due to volume-exclusion effects, which is similar to $J^{(1)}$ in Luo's model.

It should be noted that Eq. (7.119) is physically different from the Enskog equation in several aspects. First, in the Enskog theory, the inter-particle interactions (including both attractive and repulsive forces) are included in the collision operator, which means that it takes effects during the collision process. But in the modified Boltzmann equation (7.119), both the internal and external force act on the particles in the streaming process.

Based on Eq. (7.119), He *et al.* proposed the following LBE model,

$$f_i(\boldsymbol{x} + \boldsymbol{c}_i\delta_t, t + \delta_t) - f_i(\boldsymbol{x}, t) = -\frac{1}{\tau}\left[f_i - f_i^{(eq)}\right] + \delta_t F_i\,, \tag{7.123}$$

where $f_i^{(eq)}$ is identical to that in the standard LBE model, and the forcing term is

$$F_i = \frac{(\boldsymbol{c}_i - \boldsymbol{u})\cdot \boldsymbol{a}_t}{RT} f_i^{(eq)}\,. \tag{7.124}$$

The fluid density is defined the same as in Luo's model, but the velocity is defined by

$$\rho\boldsymbol{u} = \sum_i \boldsymbol{c}_i f_i + \frac{\delta_t}{2}\rho\boldsymbol{a}_t\,. \tag{7.125}$$

As mentioned in Chapter 3, this definition of the velocity $\boldsymbol{u}$ can result in the valid hydrodynamics equations, in which the momentum equation is

$$\frac{\partial(\rho\boldsymbol{u})}{\partial t} + \nabla\cdot(\rho\boldsymbol{u}\boldsymbol{u}) = -\nabla\cdot\boldsymbol{P}' + \nabla\cdot\boldsymbol{\tau} + \rho\boldsymbol{a}\,, \tag{7.126}$$

where the viscous stress is the same as that in Luo's model, while the thermodynamic pressure tensor $\boldsymbol{P}'$ is

$$P'_{\alpha\beta} = p\delta_{\alpha\beta} + \kappa\frac{\partial\rho}{\partial x_\alpha}\frac{\partial\rho}{\partial x_\beta}\,, \tag{7.127}$$

where

$$p = \rho RT(1 + b\rho\chi) - a\rho^2 - \kappa\rho\nabla^2\rho - \frac{\kappa}{2} \mid \nabla\rho \mid^2 . \tag{7.128}$$

In the momentum equation (7.126), the term $\nabla \cdot \boldsymbol{P}'$ can be rewritten in a more compact formulation,

$$-\nabla \cdot \boldsymbol{P}' = -\nabla p_0 + \kappa\rho\nabla\nabla^2\rho , \tag{7.129}$$

where $p_0 = \rho RT(1 + b\rho\chi) - a\rho^2$ is the equation of state, while the second term is the surface tension force. In this way the momentum equation can be rewritten as

$$\frac{\partial(\rho\boldsymbol{u})}{\partial t} + \nabla \cdot (\rho\boldsymbol{u}\boldsymbol{u}) = -\nabla p_{id} + \nabla \cdot \boldsymbol{\tau} + \boldsymbol{F}_t , \tag{7.130}$$

where the total effective force is

$$\boldsymbol{F}_t = \rho\boldsymbol{a}_t = -\nabla\psi + \boldsymbol{F}_s + \rho\boldsymbol{a} \quad , \tag{7.131}$$

with $\boldsymbol{F}_s = \kappa\rho\nabla\nabla^2\rho$, and ψ is a function related to equation of state,

$$\psi = p_0 - p_{id} = b\rho^2 RT\chi - a\rho^2 . \tag{7.132}$$

It should be noted that the force formulation and numerical discretization schemes of the gradient can affect the numerical stability and the spurious currents in the vicinity of interfaces, although they are identical mathematically.

The pressure tensor given by Eq. (7.127) is similar to that used in the free-energy model. As a result, $\boldsymbol{P}'$ is consistent with thermodynamic theories, and the viscous stress in the hydrodynamic equations, meaning that the model is Galilean invariant. These properties of the HSD model also demonstrate the advantages of constructing LBE models from kinetic theories.

He-Chen-Zhang model for incompressible multiphase flow

In Luo's model and the HSD model, the large density gradient in the vicinity of interfaces may lead to numerical instability in computations. To overcome this difficulty, He *et al.* developed a LBE model for incompressible multiphase flows (denoted by HCZ model). This model

introduced the following new distribution function based on the original distribution function f,

$$g = fRT + \psi(\rho)\omega(\boldsymbol{\xi}, 0)\,, \tag{7.133}$$

where

$$\omega(\boldsymbol{\xi}, \boldsymbol{u}) = \rho^{-1} f^{(eq)} = \frac{1}{(2\pi RT)^{D/2}} \exp\left[\frac{(\xi - u)^2}{2RT}\right]. \tag{7.134}$$

Then the evolution equation of g can be obtained from the Boltzmann equation,

$$D_t g = RTD_t f + \omega(\boldsymbol{\xi}, 0) D_t \psi(\rho)\,, \tag{7.135}$$

where $D_t \equiv \partial_t + \boldsymbol{\xi} \cdot \nabla + \boldsymbol{a} \cdot \nabla_{\boldsymbol{\xi}}$. For incompressible flows where $\partial_t \rho + \boldsymbol{u} \cdot \nabla\rho = 0$, it can be shown that,

$$D_t \psi(\rho) = D_t \rho \frac{d\psi}{d\rho} = (\boldsymbol{\xi} - \boldsymbol{u}) \cdot \nabla\rho \frac{d\psi}{d\rho} = (\boldsymbol{\xi} - \boldsymbol{u}) \cdot \nabla\psi(\rho)\,. \tag{7.136}$$

Therefore, Eq. (7.135) can be re-expressed as

$$\frac{\partial g}{\partial t} + \boldsymbol{\xi} \cdot \nabla g = -\frac{1}{\tau_c}\left[g - g^{(eq)}\right] + (\boldsymbol{\xi} - \boldsymbol{u}) \cdot \boldsymbol{K}\,, \tag{7.137}$$

where

$$g^{(eq)} = RTf^{(eq)} + \psi(\rho)\omega(\boldsymbol{\xi}, 0)\,, \tag{7.138}$$

$$\boldsymbol{K} = \omega(\boldsymbol{\xi}, \boldsymbol{u})[\boldsymbol{F}_s + \rho\boldsymbol{a}] - [\omega(\boldsymbol{\xi}\,, \boldsymbol{u}) - \omega(\boldsymbol{\xi}\,, 0)]\nabla\psi(\rho)\,. \tag{7.139}$$

Here the forcing term is approximated as

$$\boldsymbol{a}_t \cdot \nabla_{\boldsymbol{\xi}} f \approx \boldsymbol{a}_t \cdot \nabla_{\boldsymbol{\xi}} f^{(eq)} = -\frac{(\boldsymbol{\xi} - \boldsymbol{u}) \cdot \boldsymbol{a}_t}{RT} f^{(eq)}\,. \tag{7.140}$$

Based on Eq. (7.133), the pressure and velocity can be defined from the new distribution function g,

$$p_0 = \int g\, d\boldsymbol{\xi}, \quad \rho RT\boldsymbol{u} = \int \boldsymbol{\xi} g\, d\boldsymbol{\xi}\,. \tag{7.141}$$

The Chapman-Enskog analysis shows that the hydrodynamic equations corresponding to Eq. (7.137) are

$$\frac{1}{\rho RT}\frac{\partial p_0}{\partial t} + \nabla \cdot \boldsymbol{u} = 0\,, \tag{7.142}$$

$$\rho\left[\frac{\partial \boldsymbol{u}}{\partial t}+\boldsymbol{u}\cdot\nabla\boldsymbol{u}\right]=-\nabla p_0+\ \nabla\cdot\boldsymbol{\tau}+\kappa\rho\nabla\nabla^2\rho+\rho\boldsymbol{a}\,. \quad (7.143)$$

In order to obtain the density ρ, an index function ϕ is introduced to track the interface and its evolution is described by the kinetic equation of f. Because the external force and surface tension do not have effects on mass conservation, they can be neglected and the simplified equation for f is

$$\frac{\partial f}{\partial t}+\boldsymbol{\xi}\cdot\nabla f=-\frac{1}{\tau_c}\left[f-f^{(eq)}\right]-\omega(\boldsymbol{\xi},\boldsymbol{u})\frac{(\boldsymbol{\xi}-\boldsymbol{u})\cdot\nabla\psi(\phi)}{RT}, \quad (7.144)$$

where $f^{(eq)}=\phi\omega(\boldsymbol{\xi},\boldsymbol{u})$ and the index function is defined by $\phi=\int f\,d\boldsymbol{\xi}$.

Discretizing Eqs. (7.144) and (7.137) leads to the HCZ LBE model for incompressible multiphase flows,

$$\begin{aligned} &f_i(\boldsymbol{x}+\boldsymbol{c}_i\delta_t,t+\delta_t)-f_i(\boldsymbol{x},t)\\ &\qquad=-\frac{1}{\tau}\left[f_i-f_i^{(eq)}\right]-\left(1-\frac{1}{2\tau}\right)\frac{(\boldsymbol{c}_i-\boldsymbol{u})\cdot\nabla\psi(\phi)}{RT}\omega_i(\boldsymbol{u})\delta_t, \end{aligned} \quad (7.145)$$

$$\begin{aligned} g_i(\boldsymbol{x}+\boldsymbol{c}_i\delta_t,t+\delta_t)-g_i(\boldsymbol{x},t)=&-\frac{1}{\tau}\left[g_i-g_i^{(eq)}\right]+\left(1-\frac{1}{2\tau}\right)\times\\ &(\boldsymbol{c}_i-\boldsymbol{u})\cdot\left\{\omega_i(\boldsymbol{u})(\boldsymbol{F}_s+\rho\boldsymbol{a})-[\omega_i(\boldsymbol{u})-\omega_i(0)]\nabla\psi(\rho)\right\}, \end{aligned} \quad (7.146)$$

where

$$f_i^{(eq)}=\boldsymbol{\phi}\omega_i(\boldsymbol{u})\equiv\omega_i\boldsymbol{\phi}\left[1+\frac{\boldsymbol{c}_i\cdot\boldsymbol{u}}{c_s^2}+\frac{(\boldsymbol{c}_i\cdot\boldsymbol{u})^2}{2c_s^4}-\frac{u^2}{2c_s^2}\right], \quad (7.147)$$

$$g_i^{(eq)}=\omega_i\left[p_0+\rho RT\left(\frac{\boldsymbol{c}_i\cdot\boldsymbol{u}}{c_s^2}+\frac{(\boldsymbol{c}_i\cdot\boldsymbol{u})^2}{2c_s^4}-\frac{u^2}{2c_s^2}\right)\right]. \quad (7.148)$$

The flow variables are computed as

$$\phi=\sum_i f_i,\ p_0=\sum_i g_i-\frac{\delta_t}{2}\boldsymbol{u}\cdot\nabla\psi(\rho),\ \rho\boldsymbol{u}=\frac{1}{RT}\sum_i\boldsymbol{c}_i g_i+\frac{\delta_t}{2}(\boldsymbol{F}_s+\rho\boldsymbol{a})\,. \quad (7.149)$$

The density and viscosity of the mixture are determined from the index function,

$$\rho(\phi)=\rho_l+\frac{\phi-\phi_l}{\phi_h-\phi_l}(\rho_h-\rho_l),\quad \nu(\phi)=\nu_l+\frac{\phi-\phi_l}{\phi_h-\phi_l}(\nu_h-\nu_l)\,, \quad (7.150)$$

where ρ_l and ρ_h are the densities of the light and heavy fluids, respectively, ν_l and ν_h are the corresponding viscosities, while ϕ_l and ϕ_h are the minimum and maximum values of the index function. The relaxation time τ is connected with the index function through the viscosity,

$$\nu(\phi) = c_s^2 \left(\tau(\phi) - \frac{1}{2} \right) \delta_t \,. \tag{7.151}$$

An advantage of the HCZ model is that it has improved numerical stability in comparison with the HSD model. This is because the coefficient before $\nabla\psi$ (which may be rather large near the interface due to the density gradients) in the term $\boldsymbol{K}$ defined by Eq. (7.139), $\omega(\boldsymbol{\xi}, \boldsymbol{u}) - \omega(\boldsymbol{\xi}, 0) \approx M$, is small for low speed flows so that the stiffness of Eq. (7.146) is effectively reduced. The model has been applied to $2D$ [He, Chen and Zhang, 1999] and $3D$ Rayleigh-Taylor instability [He and Zhang *et al.*, 1999] and the interfacial dynamics has been successfully captured.

7.4.2 *Models for multi-component flows*

Kinetic model for gas mixtures

The Boltzmann equation for a dilute gas mixture is [Chapman and Cowling, 1990],

$$\frac{\partial f_s}{\partial t} + \boldsymbol{\xi} \cdot \nabla f_s + \boldsymbol{a}_s \cdot \nabla_{\boldsymbol{\xi}} f_s = \Omega_s \left(f_s \right) \equiv \sum_{\bar{s}} \Omega_{s\bar{s}} (f_s) \,, \tag{7.152}$$

where $\Omega_{s\bar{s}}$ denotes the collision effect between species s and $\bar{s}$,

$$\Omega_{s\bar{s}} (f_s) = \int \left[f_s' f_{\bar{s}}' - f_s f_{\bar{s}} \right] B_{s\bar{s}} (\theta, |\boldsymbol{V}|) d\theta d\epsilon d\boldsymbol{\xi}_{\bar{s}} \,. \tag{7.153}$$

Here $f_s' = f_s(\boldsymbol{\xi}_s')$, $f_{\bar{s}}' = f_{\bar{s}}(\boldsymbol{\xi}_{\bar{s}}')$, and $\boldsymbol{\xi}_s'$ and $\boldsymbol{\xi}_{\bar{s}}'$ are the corresponding velocities before and after collision,

$$\begin{aligned} \boldsymbol{\xi}' &= \boldsymbol{\xi} + \frac{2m_{\bar{s}}}{m_s + m_{\bar{s}}} [(\boldsymbol{\xi} - \boldsymbol{\xi}_{\bar{s}}) \cdot \boldsymbol{k}] \boldsymbol{k} \,, \\ \boldsymbol{\xi}_{\bar{s}}' &= \boldsymbol{\xi}_{\bar{s}} - \frac{2m_s}{m_s + m_{\bar{s}}} [(\boldsymbol{\xi} - \boldsymbol{\xi}_{\bar{s}}) \cdot \boldsymbol{k}] \boldsymbol{k} \,, \end{aligned} \tag{7.154}$$

where $\boldsymbol{k}$ is defined as before, while m_s and $m_{\bar{s}}$ are the molecular mass of species s and $\bar{s}$, respectively. The collision operators satisfy mass, momentum, and energy conservations,

$$\sum_{s,\bar{s}} \int \Omega_{s\bar{s}}\, d\boldsymbol{\xi} = 0, \quad \sum_{s,\bar{s}} \int \boldsymbol{\xi} \Omega_{s\bar{s}}\, d\boldsymbol{\xi} = 0, \quad \sum_{s,\bar{s}} \int (\xi - u)^2 \Omega_{s\bar{s}}\, d\boldsymbol{\xi} = 0\,. \quad (7.155)$$

The number density, mass density, fluid velocity, and internal energy of each component are defined respectively as

$$n_s = \frac{\rho_s}{m_s}, \quad \rho_s = \int f_s\, d\boldsymbol{\xi}, \quad \rho_s \boldsymbol{u}_s = \int \boldsymbol{\xi} f_s\, d\boldsymbol{\xi}, \quad \rho_s e_s = \int \tfrac{1}{2}(\xi - u)^2 f_s\, d\boldsymbol{\xi}\,. \quad (7.156)$$

In addition to these conservative variables, the following conceptions are also important for a mixture, i.e., the partial pressure of each species, $p_s = \rho_s R_s T = n_s k_B T$, the partial pressure tensor, $\boldsymbol{P}_s = \int \boldsymbol{C}\boldsymbol{C} f_s\, d\boldsymbol{\xi}$, species heat flux $\boldsymbol{q}_s = \int \frac{1}{2} \boldsymbol{C} C^2 f_s\, d\boldsymbol{\xi}$, and the total pressure $p = \sum_s p_s = n k_B T$, total pressure tensor $\boldsymbol{P} = \sum_s \boldsymbol{P}_s$, and total heat flux $\boldsymbol{q} = \sum_s \boldsymbol{q}_s$. Another conception in gas mixture is the so called *diffusion velocity*, which is defined as $\boldsymbol{u}_{ds} \equiv \boldsymbol{u}_s - \boldsymbol{u}$, and $\boldsymbol{j}_s \equiv \int \boldsymbol{C} f_s = \rho_s \boldsymbol{u}_{ds}$ is known as diffusion flux of species s.

The Chapman-Enskog analysis shows that the hydrodynamic equations from the Boltzmann equation (7.152) are

$$\frac{\partial \rho_s}{\partial t} + \nabla \cdot (\rho_s \boldsymbol{u}) = -\nabla \cdot \boldsymbol{j}_s\,, \quad (7.157)$$

$$\frac{\partial \rho}{\partial t} + \nabla \cdot (\rho \boldsymbol{u}) = 0\,, \quad (7.158)$$

$$\frac{\partial (\rho \boldsymbol{u})}{\partial t} + \nabla \cdot (\rho \boldsymbol{u}\boldsymbol{u}) = -\nabla p + \nabla \cdot \boldsymbol{\tau} + \sum_s \rho_s \boldsymbol{a}_s\,, \quad (7.159)$$

$$\frac{\partial (\rho e)}{\partial t} + \nabla \cdot (\rho e \boldsymbol{u}) = -\nabla \cdot \boldsymbol{q} + p \nabla \cdot \boldsymbol{u} + \boldsymbol{\tau} : \boldsymbol{S} + \nabla \cdot \sum_s \rho_s e_s \boldsymbol{u}_{ds}\,, \quad (7.160)$$

where the viscous stress is given by $\boldsymbol{\tau} = 2\mu \overset{\circ}{\boldsymbol{S}}$, the same as that for a single-component gas. However, the heat flux is quite different from the single-component counterpart,

$$\boldsymbol{q} = -\lambda \nabla T + \frac{D+2}{2} k_B T \sum_s n_s \boldsymbol{u}_{ds} + \cdots, \quad (7.161)$$

where λ is a function of temperature and concentration. In this book we concentrate mainly on isothermal gas mixtures, and will not discuss about thermal flows any further here. Interested readers can refer to Refs. [Chapman and Cowling, 1990; Harris, 1971].

Similar to the kinetic theory for a single-component gas, an H-function can also be defined for a mixture,

$$H = \sum_s H_s = \sum_s \int f_s \ln f_s \, d\boldsymbol{\xi} d\boldsymbol{x} \,. \tag{7.162}$$

It can be shown that $dH/dt \le 0$, and when the system reaches to its equilibrium state the distribution function $f_s^{(eq)}$ is a Maxwellian one [Chapman and Cowling, 1990],

$$f_s^{(eq)} = E(\boldsymbol{\rho}_s, \boldsymbol{u}, T) \equiv \frac{\boldsymbol{\rho}_s}{(2\pi R_s T)^{D/2}} \exp\left[-\frac{(\boldsymbol{\xi} - \boldsymbol{u})^2}{2R_s T}\right]. \tag{7.163}$$

It is seen that the collision operator in the Boltzmann equation (7.152) is quite complex. Some simplified collision models, such as the BGK one, have been developed [Harris, 1971],

$$\Omega_s(f_s) = -\sum_{\bar{s}} \frac{1}{\tau_{s\bar{s}}}\left[f_s - f_{s\bar{s}}^{(eq)}\right], \tag{7.164}$$

where

$$f_{s\bar{s}}^{(eq)} \equiv E(\boldsymbol{\rho}_s,\ \boldsymbol{u}_{s\bar{s}}, T_{s\bar{s}}) = \frac{\boldsymbol{\rho}_s}{(2\boldsymbol{\pi} R_s T_{s\bar{s}})^{D/2}} \exp\left[-\frac{(\boldsymbol{\xi} - \boldsymbol{u}_{s\bar{s}})^2}{2R_s T_{s\bar{s}}}\right], \tag{7.165}$$

with $T_{s\bar{s}}$ and $u_{s\bar{s}}$ being two adjustable parameters which are not necessarily identical to the temperature and velocity of the mixture. The choices of these two parameters will result in different kinetic models [Andries *et al*., 2002; Gross and Krook, 1956; Hamel, 1966; Morse, 1964; Sirovich, 1962; Sirovich, 1966].

LBE model based on Sirovich's theory

Luo and Girimaji [2002, 2003] proposed an isothermal LBE model for binary mixtures based on Sirovich's BGK model, in which the self-collision operator between molecules of the same species is

$$\Omega_{ss} = -\frac{1}{\tau_s}\left(f_s - f_{ss}^{(eq)}\right), \quad f_{ss}^{(eq)} = E(\rho_s, \boldsymbol{u}_s, T_s)\,, \tag{7.166}$$

where T_s is a temperature parameter, and for isothermal flows we can assume $T_s = T$. For the cross-collision operator for different species, $\Omega_{s\bar{s}}$ is not modelled by the BGK operator directly, but is expanded around the equilibrium distribution function $f_s^{(eq)}$ to obtain

$$\Omega_{s\bar{s}} = \frac{f_s^{(eq)}}{\rho_s R_s T}\left[\mu_D \boldsymbol{C}\cdot(\boldsymbol{u}_s - \boldsymbol{u}_{\bar{s}}) + A_1(T_s - T_{\bar{s}}) + A_2(u_s - u_{\bar{s}})^2\right], \quad (7.167)$$

where μ_D, A_1, and A_2 are three parameters to be determined. For isothermal flows we can assume that $T_s = T_{\bar{s}}$ and $A_2 = 0$, then $\Omega_{s\bar{s}}$ can be expressed as

$$\Omega_{s\bar{s}} = -\frac{1}{\tau_D}\frac{\rho_{\bar{s}}}{\rho}\frac{f_s^{(eq)}}{R_s T}(\boldsymbol{\xi} - \boldsymbol{u})\cdot(\boldsymbol{u}_s - \boldsymbol{u}_{\bar{s}}), \quad (7.168)$$

where τ_D is an adjustable parameter.

Based on the above simplified Sirovich model, an isothermal LBE model was developed following the standard discretization procedure by Luo and Girimaji [2002, 2003]. First the equilibrium distribution function $f_s^{(eq)}$ is expanded in terms of $\boldsymbol{u}$ up to second order,

$$f_s^{(eq)} = \frac{\rho_s}{(2\pi R_s T)^{D/2}} e^{-\xi^2/2R_s T}\left[1 + \frac{\boldsymbol{\xi}\cdot\boldsymbol{u}}{R_s T} + \frac{(\boldsymbol{\xi}\cdot\boldsymbol{u})^2}{2(R_s T)^2} - \frac{u^2}{2R_s T}\right]. \quad (7.169)$$

Now we turn to $f_{ss}^{(eq)}$ given by Eq. (7.166). Note that

$$\exp\left[-\frac{(\boldsymbol{\xi} - \boldsymbol{u}_s)^2}{2R_s T}\right] = \exp\left[-\frac{(\boldsymbol{\xi} - \boldsymbol{u})^2}{2R_s T}\right]\times\exp\left[-\frac{(\boldsymbol{\xi} - \boldsymbol{u})\cdot\delta\boldsymbol{u}_s}{R_s T}\right] \times\exp\left[-\frac{\delta\boldsymbol{u}_s^2}{2R_s T}\right], \quad (7.170)$$

where $\delta\boldsymbol{u}_s = (\boldsymbol{u} - \boldsymbol{u}_s)$. As $|\,\delta\boldsymbol{u}_s\,| \ll 1$,

$$\begin{aligned}\exp\left[-\frac{(\boldsymbol{\xi} - \boldsymbol{u})\cdot\delta\boldsymbol{u}_s}{R_s T}\right] &\approx 1 - \frac{(\boldsymbol{\xi} - \boldsymbol{u})\cdot\delta\boldsymbol{u}_s}{R_s T} + O(\delta u_s^2),\\ \exp\left[-\frac{\delta\boldsymbol{u}_s^2}{2R_s T}\right] &\approx 1 + O(\delta u_s^2),\end{aligned} \quad (7.171)$$

therefore $f_{ss}^{(eq)}$ can be approximated as

$$f_{ss}^{(eq)} = \left[1 + \frac{(\boldsymbol{\xi} - \boldsymbol{u}) \cdot (\boldsymbol{u}_s - \boldsymbol{u})}{R_s T}\right] f_s^{(eq)} . \tag{7.172}$$

Based on this formulation, the velocity space can be discretized by choosing certain proper quadrature rules. It is noteworthy that, however, the discrete velocity $\boldsymbol{c}_{si}$ is related to molecular mass, and can be expressed as $\boldsymbol{c}_{si} = \sqrt{R_s T}\boldsymbol{e}_i$, where $\boldsymbol{e}_i$ is the dimensionless lattice vector.

With these discrete velocities, a LBE model for binary mixture can then be obtained,

$$f_{si}\left(\boldsymbol{x} + \boldsymbol{c}_i \delta_t, t + \delta_t\right) - f_{si}\left(\boldsymbol{x}, t\right) = \Omega_{si} + F_{si}\delta_t , \tag{7.173}$$

where F_{si} is a forcing term related to $\boldsymbol{a}_s$, and the discrete collision operator is

$$\Omega_{si} = -\frac{\delta_t}{\tau_s}\left[f_{si} - f_{ssi}^{(eq)}\right] - \frac{\delta_t}{\tau_D}\frac{\rho_{\bar{s}}}{\rho}\frac{f_{si}^{(eq)}}{R_s T}(\boldsymbol{c}_{si} - \boldsymbol{u}) \cdot (\boldsymbol{u}_s - \boldsymbol{u}_{\bar{s}}) , \tag{7.174}$$

where

$$f_{si}^{(eq)} = E_i(\rho_s, \boldsymbol{u}) \equiv \omega_i \rho_s \left[1 + \frac{\boldsymbol{c}_{si} \cdot \boldsymbol{u}}{2R_s T} + \frac{(\boldsymbol{c}_{si} \cdot \boldsymbol{u})^2}{2(R_s T)^2} - \frac{\boldsymbol{u}^2}{2R_s T}\right], \tag{7.175}$$

$$f_{ssi}^{(eq)} = \left[1 + \frac{(\boldsymbol{c}_{si} - \boldsymbol{u}) \cdot (\boldsymbol{u}_s - \boldsymbol{u})}{R_s T}\right] f_{si}^{(eq)} . \tag{7.176}$$

Note that

$$\boldsymbol{u}_s - \boldsymbol{u} = \frac{\rho_{\bar{s}}}{\rho}(\boldsymbol{u}_s - \boldsymbol{u}_{\bar{s}}) , \tag{7.177}$$

which can be used to rewrite the collision operator,

$$\begin{aligned}\Omega_{si} &= -\frac{\delta_t}{\tau_s}\left[f_{si} - f_{si}^{(eq)}\right] + \delta_t \frac{\tau_D - \tau_s}{\tau_s \tau_D}\frac{\rho_{\bar{s}}}{\rho}\frac{f_{si}^{(eq)}}{R_s T}(\boldsymbol{c}_{si} - \boldsymbol{u}) \cdot (\boldsymbol{u}_s - \boldsymbol{u}_{\bar{s}}) \\ &= -\frac{\delta_t}{\tau_s}\left[f_{si} - f_{si}^{(eq)}\right] + \delta_t \frac{\tau_D - \tau_s}{\tau_s \tau_D}\frac{f_{si}^{(eq)}}{R_s T}(\boldsymbol{c}_{si} - \boldsymbol{u}) \cdot (\boldsymbol{u}_s - \boldsymbol{u}).\end{aligned} \tag{7.178}$$

It can be shown that the hydrodynamic equations of the above LBE model are

$$\frac{\partial \rho_s}{\partial t} + \nabla \cdot (\rho_s \boldsymbol{u}) = -\nabla \cdot \boldsymbol{j}_s, \quad \frac{\partial \rho}{\partial t} + \nabla \cdot (\rho \boldsymbol{u}) = 0 , \tag{7.179}$$

$$\rho_s \frac{\partial \boldsymbol{u}_s}{\partial t} + \rho_s \boldsymbol{u}_s \cdot \nabla \boldsymbol{u}_s = -\nabla p_s + \nabla \cdot \boldsymbol{\tau}_s + \rho_s \boldsymbol{a}_s - \frac{1}{\tau_D} \frac{\rho_s \rho_{\bar{s}}}{\rho} (\boldsymbol{u}_s - \boldsymbol{u}_{\bar{s}}), \quad (7.180)$$

where $p_s = \rho_s R_s T$, and the mass flux and viscous stress are

$$\boldsymbol{j}_s = -\frac{\delta_t}{2} \frac{\rho_s \rho_{\bar{s}}}{\tau_D \rho} (\boldsymbol{u}_s - \boldsymbol{u}_{\bar{s}}), \quad \boldsymbol{\tau}_{\alpha\beta} = R_s T \left(\tau_s - \frac{\delta_t}{2} \right) (\partial_\alpha u_{s\beta} + \partial_\beta u_{s\alpha}) . \quad (7.181)$$

From the expression of $\boldsymbol{j}_s$ and the momentum equation (7.180), we can obtain the diffusion coefficient,

$$D_{s\bar{s}} = \frac{\rho k_B T}{n m_s m_{\bar{s}}} \tau_D . \quad (7.182)$$

It is noteworthy that the discrete velocity $\boldsymbol{c}_{si}$ of the two species are different if they have different molecular masses, which means that special treatments must be adopted during the computation. Therefore, the original model developed by Luo and Girimaji [2002, 2003] is limited to binary mixtures with identical molecular masses. Recently, McCracken and Abraham [2005] proposed two methods to implement the above LBE model for general mixtures. The first one employs one lattice and interpolations are required to obtain the distribution function on the lattice nodes. The second approach employs modified equilibrium distribution functions for the species. For example, in the D2Q9 model, the modified equilibrium distribution functions are

$$f_{si}^{(eq)} = \begin{cases} \rho_s (A_0^s + D_0^s \boldsymbol{u}^2), & i = 0 \\ \rho_s (A_1^s + B_1^s (\boldsymbol{c}_i \cdot \boldsymbol{u}) + C_1^s (\boldsymbol{c}_i \cdot \boldsymbol{u})^2 + D_1^s \boldsymbol{u}^2), & i = 1,2,3,4 \\ \rho_s (A_1^s + B_1^s (\boldsymbol{c}_i \cdot \boldsymbol{u}) + C_1^s (\boldsymbol{c}_i \cdot \boldsymbol{u})^2 + D_1^s \boldsymbol{u}^2), & i = 5,6,7,8 \end{cases} \quad (7.183)$$

where $\boldsymbol{c}_i$ is the discrete velocity independent of species. The parameters in the equilibrium distribution functions satisfy the following relation,

$$\frac{A_0^s}{A_1^s} = \frac{D_0^s}{D_1^s} = \frac{A_1^s}{A_2^s} = \frac{B_1^s}{B_2^s} = r_s , \quad (7.184)$$

and

$$4C_2^s + 2D_1^s + 4D_2^s = 0, \quad C_1^s = \frac{1}{2}, \quad C_2^s = \frac{1}{8}. \quad (7.185)$$

A set of parameters satisfying these conditions is

$$A_2^s=\frac{1}{(r_s+2)^2},\ B_2^s=\frac{r_s}{2(r_s+2)},\ D_1^s=-\frac{1}{r_s+2},\ D_2^s=-\frac{r_s-2}{8(r_s+2)},$$
$$A_1^s=r_sA_0^s,\ A_2^s=r_sA_1^s,\ B_1^s=r_sB_2^s,\ D_0^s=r_sD_1^s\ . \tag{7.186}$$

With these parameters, it can be verified that,

$$\sum_i f_{si}^{(eq)}=\rho_s,\quad \sum_i \boldsymbol{c}_i f_{si}^{(eq)}=\rho_s\boldsymbol{u},\quad \sum_i \boldsymbol{c}_i\boldsymbol{c}_i f_{si}^{(eq)}=\rho_s\boldsymbol{u}\boldsymbol{u}+\rho_sR_sT\boldsymbol{I}\ , \tag{7.187}$$

where $\sqrt{R_sT}$ is the sound speed of species s, and $R_sT=2/(2+r_s)$. It is obvious that these moments are identical to those of the original equilibrium distribution function given by Eq. (7.175), but the third-order moments are different since

$$\sum_i c_{i\alpha}c_{i\beta}c_{i\gamma}f_{si}^{(eq)}=\frac{r_s-4}{r_s+2}\delta_{\alpha\beta\gamma\theta}u_\theta+R_sT(u_\alpha\delta_{\beta\gamma}+u_\beta\delta_{\alpha\gamma}+u_\gamma\delta_{\alpha\beta})\,, \tag{7.188}$$

where $\delta_{\alpha\beta\gamma\theta}$ is a 4-th order tensor, which equals to 1 when $\alpha=\beta=\gamma=\theta$, and 0 otherwise. Obviously, this term vanishes only when $r_s=4$, and the third-order moment is identical to that of the original one.

LBE model based on Hamel's theory

Based on another BGK model (Hamel's model), Asinari [2005, 2006] developed a new LBE model for isothermal binary mixtures. In Hamel's model, the self-collision term is identical to that in Sirovisch's model, i.e. Eq. (7.166). However, the cross-collision term is modeled by a BGK model which employs the mixture velocity in the equilibrium distribution function, and the model can be expressed as

$$\begin{aligned}&\frac{\partial f_s}{\partial t}+\boldsymbol{\xi}\cdot\nabla f_s+\boldsymbol{a}_s\cdot\nabla_{\boldsymbol{\xi}}f_s\\&=-\frac{1}{\tau_s}\left[f_s-f_{ss}^{(eq)}\right]-\frac{1}{\tau_m}\left[f_s-f_{sm}^{(eq)}\right]=-\frac{1}{\tau}\left[f_s-f_s^{(0)}\right],\end{aligned} \tag{7.189}$$

where

$$f_{ss}^{(eq)}=E(\rho_s,\boldsymbol{u}_s,T)\,,\ f_{sm}^{(eq)}=E(\rho_s,\boldsymbol{u},T)\,,\ f_s^{(0)}=(1-\alpha_s)f_s^{(eq)}+\alpha_sf_{sm}^{(eq)}\,, \tag{7.190}$$

with $\alpha_s = \tau_s/(\tau_s+\tau_m)$, and $\tau_s = \tau_s\tau_m/(\tau_s+\tau_m)$. Note that τ_m is species-independent, and so the cross-collision term conserves mass and momentum,

$$\sum_s \int \frac{1}{\tau_m}\left[f_s - f_{sm}^{(eq)}\right] d\boldsymbol{\xi} = 0, \quad \sum_s \int \frac{1}{\tau_m}\boldsymbol{\xi}\left[f_s - f_{sm}^{(eq)}\right] d\boldsymbol{\xi} = 0\,. \quad (7.191)$$

For the forcing term, Asinari used the following approximation:

$$\begin{aligned} \boldsymbol{F}_{si} &\equiv -\boldsymbol{a}_s \cdot \nabla_{\boldsymbol{\xi}} f_s \approx -\boldsymbol{a}_s \cdot \nabla_{\boldsymbol{\xi}} f_s^{(0)} \\ &= (1-\alpha_s)\frac{(\boldsymbol{c}_i - \boldsymbol{u}_s)\cdot \boldsymbol{a}_s}{R_s T} f_{ss}^{(eq)} + \alpha_s \frac{(\boldsymbol{c}_i - \boldsymbol{u})\cdot \boldsymbol{a}_s}{R_s T} f_{sm}^{(eq)}. \end{aligned} \quad (7.192)$$

Based on the above BGK model Asinari [2005] constructed the following LBE model for binary mixtures,

$$f_{si}(\mathrm{x} + \boldsymbol{c}_{si}\delta_t, t+\delta_t) - f_{si}(\mathrm{x}, t) = -\frac{1}{\tau}\left[f_{si} - f_{si}^{(eq)}\right] - F_{si}\delta_t\,, \quad (7.193)$$

where $f_{si}^{(0)} = (1-\alpha_s)f_{ssi}^{(eq)} + \alpha_s f_{smi}^{(eq)}$, $f_{ssi}^{(eq)} = E_i(\rho_s, \boldsymbol{u}_s)$, and $f_{sm}^{(eq)} = E_i(\rho_s, \boldsymbol{u})$, with E_i given by Eq. (7.175). The fluid velocity of each species is defined as

$$\rho_s \boldsymbol{u}_s = \sum_{s'}\left[\left(\frac{2}{2+\omega_m}\delta_{ss'} + \frac{\omega_m}{2+\omega_m}x_{s'}\right)\left(\sum_i \boldsymbol{c}_{si} f_{si} + \frac{\delta_t}{2}\rho_s \boldsymbol{a}_{s'}\right)\right], \quad (7.194)$$

where $\omega_m = \delta_t/\tau_m$. It is noted that in this model the discrete velocities are also related to the species masses, and so special treatment is required in the streaming process.

Asinari [2006] and Asinari and Luo [2008] also developed several MRT-LBE schemes based on Hamel's BGK model,

$$f_{si}(\boldsymbol{x} + \boldsymbol{c}_i\delta_t, t+\delta_t) - f_{si}(\boldsymbol{x}, t) = \Omega_{ij}^s + F_{si}\delta_t\,, \quad (7.195)$$

where two formulations have been adopted for the collision terms. The first one treats the self-collision and cross-collision separately [Asinari, 2006],

$$\Omega_{ij}^s = \Lambda_{ij}^{ss}\left[f_{sj} - f_{ssj}^{(eq)}\right] + \Lambda_{ij}^{sm}\left[f_{sj} - f_{smj}^{(eq)}\right]. \quad (7.196)$$

Another formulation uses only one BGK operator which contains the self-collision and cross-collision effects [Asinari and Luo, 2008],

$$\Omega_{ij}^{s} = \Lambda_{ij}^{s}\left[f_{sj} - f_{sj}^{(0)}\right]. \tag{7.197}$$

Here, Λ^{ss}, Λ^{sm}, and Λ^{s} are the corresponding collision matrices. The self- and cross-collision matrices can be expressed as

$$\Lambda^{ss} = -M_s^{-1}D_sM_s, \quad \Lambda^{sm} = -M_s^{-1}D_mM_s, \tag{7.198}$$

where M_s is the transformation matrix from velocity space to moment space that defines the corresponding moments $m_s = M_s f$; D_s and D_m are the relaxation matrices. Similarly, the effective collision matrix Λ^{s} can be written as

$$\Lambda^{s} = -M^{-1}DM, \tag{7.199}$$

which means that both the collision matrix and the relaxation matrix are species-independent. Due to this property, this MRT-LBE model is only applicable to mixtures of two gases with an identical viscosity [Asinari and Luo, 2008].

LBE model based on quasi-equilibrium state theory

In a quasi-equilibrium system, when the distribution function $f(\boldsymbol{x},\boldsymbol{\xi},t)$ approaches to the equilibrium distribution function $f^{(eq)}$, it can be assumed that it relaxes to a quasi-equilibrium state f^{*} quickly, and then relaxes to $f^{(eq)}$ slowly. This means that the collision operator can be modeled as

$$\Omega(f) = -\frac{1}{\tau_1}\left[f - f^{*}\right] - \frac{1}{\tau_2}\left[f^{*} - f^{(eq)}\right]. \tag{7.200}$$

The relaxation times characterizing the two stages satisfy $\tau_2 \geq \tau_1$, and the model reduces to the standard BGK model as $\tau_2 = \tau_1$. Arcidiacono and coworkers [2006, 2007] applied this idea to mixtures of multi-component gases, and developed a quasi-equilibrium LBE model,

$$f_{si}\left(\boldsymbol{x} + \boldsymbol{c}_i\delta_t, t + \delta_t\right) - f_{si}\left(\mathrm{x}, t\right) = -\frac{1}{\tau_1'}\left[f_{si} - f_{si}^{*}\right] - \frac{1}{\tau_2'}\left[f_{si}^{*} - f_{si}^{(eq)}\right], \tag{7.201}$$

where $\tau_1' = \tau_1/\delta_t - 0.5$ and $\tau_2' = \tau_2\tau_1'/\tau_1$.

Unlike the standard LBGK model, the equilibrium distribution function in the quasi-equilibrium model is constructed by minimizing the following discrete H function

$$H \equiv \sum_s \sum_i f_{si} \ln(f_{si}/\omega_i)\,, \tag{7.202}$$

where ω_i is the weight coefficient related to the lattice and is similar to that in the standard LBGK model. Under the constraints,

$$\rho_s = \sum_i f_{si}, \quad \rho \boldsymbol{u} = \sum_s \sum_i \boldsymbol{c}_{si} f_{si}\,, \tag{7.203}$$

the equilibrium distribution function obtained in this way is

$$f_{si}^{(eq)} = E_i(\rho_s, \boldsymbol{u}) \equiv \rho_s \omega_i \prod_{\alpha=1}^{D} \left(2 - \sqrt{1+3\tilde{u}_\alpha^2}\right) \left(\frac{2\tilde{u}_\alpha + \sqrt{1+3\tilde{u}_\alpha^2}}{1-\tilde{u}_\alpha}\right)^{e_{i\alpha}}, \tag{7.204}$$

where $\tilde{\boldsymbol{u}} = \boldsymbol{u}(R_s T)^{-1/2}$ and $\boldsymbol{e}_i = \boldsymbol{c}_{si}(R_s T)^{-1/2}$ are lattice vectors which are species-independent. Because $f_{si}^{(eq)}$ is obtained from the discrete entropy, this model is also called Entropic LBE (ELBE) model. The formulation of the quasi-equilibrium distribution function in the model is identical to $f_{si}^{(eq)}$ except that the velocity is taken as that of the species, i.e., $f_{si}^{*} = E_i(\rho_s, \boldsymbol{u}_s)$.

The Chapman-Enskog analysis of Eq. (7.201) shows that hydrodynamic equations for each species and the mixture are

$$\frac{\partial \rho_s}{\partial t} + \nabla \cdot (\rho_s \boldsymbol{u}) = -\nabla \cdot \boldsymbol{j}_s\,, \tag{7.205}$$

$$\frac{\partial \rho}{\partial t} + \nabla \cdot (\rho \boldsymbol{u}) = 0\,, \tag{7.206}$$

$$\frac{\partial (\rho \boldsymbol{u})}{\partial t} + \nabla \cdot (\rho \boldsymbol{u}\boldsymbol{u}) = -\nabla p + \nabla \cdot (\mu \boldsymbol{S})\,, \tag{7.207}$$

where $p = nk_B T$, $\boldsymbol{j}_s = \rho_s(\boldsymbol{u}_s - \boldsymbol{u})$, and the viscosity is $\mu = (\tau_1 - 0.5\delta_t) nk_B T$. Furthermore, from the Chapman-Enskog analysis one can derive the expression for $\boldsymbol{j}_s$,

$$\boldsymbol{j}_s = \tau_2 p \big[(y_s - x_s)\nabla \ln p - \nabla x_s\big], \tag{7.208}$$

where $y_s = \rho_s/\rho$ and $x_s = n_s/n$. On the other hand, the Maxwell-Stefan diffusion law gives that

$$\nabla x_s = -\frac{x_s x_{\bar{s}}}{D_{s\bar{s}}}\left(\boldsymbol{u}_s - \boldsymbol{u}_{\bar{s}}\right) + (y_s - x_s)\nabla \ln p\,, \tag{7.209}$$

from which we can identify the diffusion coefficient as

$$D_{s\bar{s}} = \frac{\tau_2 \rho k_B T}{n m_s m_{\bar{s}}}. \tag{7.210}$$

For spatial discretization, Arcidiacono *et al.* [2006, 2007] suggested using two lattices with spacing ratio $\delta_{xs}/\delta_{x\bar{s}} = \sqrt{m_{\bar{s}}/m_s}$. It is obvious that this discretization requires that $\sqrt{m_{\bar{s}}/m_s}$ is a rational number, and for more general cases interpolations should be used.

7.4.3 *Models for non-ideal gas mixtures*

Enskog theory for dense gas mixtures

The Enskog theory for a simple gas can also be generalized to mixtures [Chapman and Cowling, 1990; van Beijeren and Ernst, 1973a; van Beijeren and Ernst, 1973b; Piña *et al.*, 1995]. Specifically, the Enskog equation for a binary mixture of dense gases can be expressed as

$$\frac{\partial f_s}{\partial t} + \boldsymbol{\xi}\cdot\nabla f_s + \boldsymbol{a}_s\cdot\nabla_{\boldsymbol{\xi}} f_s = \Omega_{ss}^E + \Omega_{s\bar{s}}^E\,, \tag{7.211}$$

where

$$\begin{aligned}\Omega_{ss'}^E(f) = \int\big[&\boldsymbol{\chi}_{ss'}(\boldsymbol{x}, \boldsymbol{x}^+ \mid \{n_k\}) f_{s'}(\boldsymbol{x}^+, \boldsymbol{\xi}_1') f_s(\boldsymbol{x}, \boldsymbol{\xi}') \\ &-\boldsymbol{\chi}_{ss'}(\boldsymbol{x}, \boldsymbol{x}^- \mid \{n_k\}) f_{s'}(\boldsymbol{x}^-, \boldsymbol{\xi}_1) f_s(\boldsymbol{x}, \boldsymbol{\xi})\big] d\boldsymbol{\mu}_{ss'}, \quad s' = s, \bar{s},\end{aligned} \tag{7.212}$$

with $\boldsymbol{x}^{\pm} = \boldsymbol{x} \pm \sigma_{ss'}\boldsymbol{k}$ and $\sigma_{ss'} = (\sigma_s + \sigma_{s'})/2$, while $\chi_{ss'}$ is the radical distribution function between species s and s', $d\boldsymbol{\mu}_{ss'}$ is the collision space

$$d\boldsymbol{\mu}_{ss'} = B_{ss'}(\boldsymbol{\theta}, |\boldsymbol{V}|) d\boldsymbol{\theta} d\epsilon d\boldsymbol{\xi}_1 = \boldsymbol{\sigma}_{ss'}^2 \Theta(\boldsymbol{g}\cdot\boldsymbol{k})(\boldsymbol{g}\cdot\boldsymbol{k})\boldsymbol{k}\, d\boldsymbol{k}\, d\boldsymbol{\xi}_1, \tag{7.213}$$

where $\boldsymbol{g} = \boldsymbol{\xi}_1 - \boldsymbol{\xi}$ is the relative velocity between two collision molecules of species s and s' (with velocities $\boldsymbol{\xi}$ and $\boldsymbol{\xi}_1$, respectively), θ is Heaviside step function, i.e. $H(\boldsymbol{x}) = 1$ as $\boldsymbol{x} > 0$ and 0 otherwise. $\boldsymbol{k}$ is the unit vector

directing from the center of molecule s to that of s'. $\boldsymbol{\xi}'$ and $\boldsymbol{\xi}_1'$ are the corresponding post-collision velocities. In the early Enskog theory, the RDF $\chi_{ss'}$ is a function of the homogeneous number density n_k of each species. In the later extended Enskog theory, on the other hand, $\chi_{ss'}$ is a functional of n_k, which depends not only on n_k but also on the gradients.

The density, velocity, and internal energy of each species and the mixture in the Enskog theory are defined similarly to those in the Boltzmann equation for ideal gases. The hydrodynamic equations are also similar to Eqs. (7.157)~(7.160), except that the equation of state is $p = \sum_s p_s$ where

$$p_s = n_s k_B T \left(1 + \sum_{s'} b_{ss'} \rho_{ss'} \chi_{ss'} \right). \tag{7.214}$$

The viscosity and thermal diffusivity also depend on $\chi_{ss'}$.

Similar to the Enskog equation for simple dense gases, the collision operator $\Omega_{ss'}^E$, can also be simplified for isothermal systems and approximated by the BGK model as proposed by Guo and Zhao [2003b]. In this simplified model, the RDFs are set to be $\chi_{ss'}(\boldsymbol{x}, \boldsymbol{x}^{\pm} \mid \{n_k\}) = \chi_{ss'}(\boldsymbol{x} \pm \sigma_{ss'}\boldsymbol{k}/2)$. With the first-order Taylor expansions of f and $\chi_{ss'}$ in the collision term $\Omega_{ss'}^E$, i.e.

$$\begin{aligned} f_{s'}(\boldsymbol{x} \pm \sigma_{ss'}\boldsymbol{k}) &= f_{s'}(\boldsymbol{x}) \pm \sigma_{ss'} \cdot \nabla f_s, \\ \chi_{ss'}(\boldsymbol{x} \pm \sigma_{ss'}\boldsymbol{k}/2) &= \chi_{ss'}(\boldsymbol{x}) \pm \sigma_{ss'} \cdot \nabla \chi_{ss'}, \end{aligned} \tag{7.215}$$

the collision operator can be approximated as

$$\Omega_{ss'}^E = J_{ss'}^{(0)} + J_{ss',1}^{(1)} + J_{ss',2}^{(1)}, \tag{7.216}$$

where

$$J_{ss'}^{(0)} = \chi_{ss'} \int \left[f_s(\boldsymbol{\xi}') f_{s'}(\boldsymbol{\xi}_1') - f_s(\boldsymbol{\xi}) f_{s'}(\boldsymbol{\xi}_1) \right] d\boldsymbol{\mu}_{ss'}, \tag{7.217}$$

$$J_{ss',1}^{(1)} = \frac{\sigma_{ss'}}{2} \int \left[f_s(\boldsymbol{\xi}') f_{s'}(\boldsymbol{\xi}_1') + f_s(\boldsymbol{\xi}) f_{s'}(\boldsymbol{\xi}_1) \right] \boldsymbol{k} \cdot \nabla \chi_{ss'} d\mu_{ss'}, \tag{7.218}$$

$$J_{ss',2}^{(1)} = \sigma_{ss'} \chi_{ss'} \int \left[f_s(\boldsymbol{\xi}') \nabla f_{s'}(\boldsymbol{\xi}_1') + f_s(\boldsymbol{\xi}) \nabla f_{s'}(\boldsymbol{\xi}_1) \right] \cdot \boldsymbol{k} d\mu_{ss'}. \tag{7.219}$$

The Boltzmann part $J_{ss'}^{(0)}$ can be modeled by the BGK model,

$$J_{ss'}^{(0)} = -\frac{\chi_{ss'}}{\tau_{ss'}} \left[f_s - f_{ss'}^{(eq)} \right], \tag{7.220}$$

where $f_{ss'}^{(eq)} = E(\rho_{ss'}, \boldsymbol{u}_{ss'}, T_{ss'})$. In the model by Guo *et al.*, the parameters in the equilibrium distribution functions are set to be $\boldsymbol{u}_{ss'} = \boldsymbol{u}$ and $T_{ss'} = T$, where T and $\boldsymbol{u}$ are the velocity and density of the mixture. With these parameters, $f_{ss'}^{(eq)}$ is independent of species s' explicitly, and the interactions between species are reflected by the mixture velocity $\boldsymbol{u}$. So $f_{ss'}^{(eq)} = f_s^{(eq)} \equiv E(\rho_s, \boldsymbol{u}, T)$ and

$$J_s^{(0)} \equiv \sum_{s'} J_{ss'}^{(0)} = -\frac{1}{\tau_s}\left[f_s - f_s^{(eq)}\right], \tag{7.221}$$

where

$$\frac{1}{\tau_s} \equiv \sum_{s'} \frac{\chi_{ss'}}{\tau_{ss'}}. \tag{7.222}$$

For the two first-order terms $J_{ss',1}^{(1)}$ and $J_{ss',2}^{(1)}$, if we approximate $f_{ss'}$ with $f_{ss'}^{(eq)}$, they can be expressed as

$$J_{ss',1}^{(1)} = -b_{ss'}\rho_{s'} f_s^{(eq)}(\boldsymbol{\xi} - \boldsymbol{u}) \cdot \nabla \chi_{ss'}, \tag{7.223}$$

$$J_{ss',2}^{(1)} = -2b_{ss'}\rho_{s'}\chi_{ss'} f_s^{(eq)}(\boldsymbol{\xi} - \boldsymbol{u}) \cdot \nabla \ln \rho_{s'} + R_{ss'}, \tag{7.224}$$

where

$$R_{ss'} = 2b_{ss'}\rho_{s'}\chi_{ss'} f_s^{(eq)} \left[\left(M_{s's} - \frac{2M_{ss'}}{D+2}\frac{(\boldsymbol{\xi} - \boldsymbol{u})^2}{\theta_{s'}} \right) \nabla \cdot \boldsymbol{u} - \frac{2M_{ss'}}{D+2}\frac{(\boldsymbol{\xi} - \boldsymbol{u})(\boldsymbol{\xi} - \boldsymbol{u})}{\theta_{s'}} : \nabla \boldsymbol{u} \right]. \tag{7.225}$$

Here $M_{ss'}{=}m_s/(m_s + m_{s'})$, $\theta_s{=}n_s k_B T{=}\rho_s R_s T$. $b_{ss'}{=}V_{ss'}/m_{s'}$ is the second virial coefficient, where $V_{ss'}{=}2^{D-1}V_D\sigma_{ss'}^D$ with $V_D{=}(\pi/4)^{D/2}/\Gamma(1 + D/2)$ being the volume of the D-dimensional unit sphere. It can be shown that

$$\int R_{ss'} d\boldsymbol{\xi} = 0, \ \int \boldsymbol{\xi} R_{ss'} d\boldsymbol{\xi} = 0. \tag{7.226}$$

Thus $R_{ss'}$ can be neglected to obtain

$$J_{ss'}^{(1)} \equiv J_{ss',1}^{(1)} + J_{ss',2}^{(1)} = b_{ss'}\rho_{s'}\chi_{ss'} f_s^{(eq)}(\boldsymbol{\xi} - \boldsymbol{u}) \cdot \nabla \ln(\rho_{s'}^2 \chi_{ss'}). \tag{7.227}$$

Based on the above approximations, Guo and Zhao [2003b] obtained a simplified Enskog model for isothermal binary dense gases,

$$\frac{\partial f_s}{\partial t} + \boldsymbol{\xi} \cdot \nabla f_s = -\frac{1}{\tau_s}\left[f_s - f_s^{(eq)}\right] + J_s' + G_s, \tag{7.228}$$

where

$$G_s = f_s^{(eq)}(\boldsymbol{\xi}-\boldsymbol{u})\cdot\boldsymbol{a}_s \,/\, \theta_s\,, \quad J_s' = \sum_{s'} J_{ss'}^{(1)} = -f_s^{(eq)}(\boldsymbol{\xi}-\boldsymbol{u})\cdot\boldsymbol{K}_s\,, \tag{7.229}$$

with $\boldsymbol{K}_s = \sum_{s'} b_{ss'}\rho_{s'}\chi_{ss'}\nabla\ln(\rho_{s'}^2\chi_{ss'})$. Therefore, we can define an effective total force that contains both internal interactions and external force,

$$\boldsymbol{F}_s \equiv -\boldsymbol{K}_s\theta_s + \boldsymbol{a}_s\,. \tag{7.230}$$

In order to enforce mass and momentum conservations, the relaxation time τ_s should take the same form, i.e. $\tau_s = \tau$. It is noted that this choice does not mean that τ is independent of the species. Actually, it can be a function of the species concentrations.

Discrete velocity model for the Enskog equation

Based on the simplified Enskog model (7.228), one can obtain a discrete velocity model,

$$\frac{\partial f_{si}}{\partial t} + \boldsymbol{c}_{si}\cdot\nabla f_{si} = -\frac{1}{\tau}\Big[f_{si} - f_{si}^{(eq)}\Big] + F_{si}\,, \tag{7.231}$$

where

$$f_{si}^{(eq)} = \omega_i\rho_s\left[1 + \frac{\boldsymbol{c}_{si}\cdot\boldsymbol{u}}{\theta_s} + \frac{(\boldsymbol{c}_{si}\cdot\boldsymbol{u})^2}{2\theta_s^2} - \frac{u^2}{2\theta_s}\right],\; F_{si} = \frac{(\boldsymbol{c}_{si}-\boldsymbol{u})\cdot\boldsymbol{F}_s}{\theta_s} f_{si}^{(eq)}. \tag{7.232}$$

The Chapman-Enskog analysis shows that the hydrodynamic equations of the above discrete velocity model are

$$\frac{\partial\rho_s}{\partial t} + \nabla\cdot(\rho_s\boldsymbol{u}) = -\nabla\cdot\boldsymbol{j}_s\,, \tag{7.233}$$

$$\frac{\partial\rho}{\partial t} + \nabla\cdot(\rho\boldsymbol{u}) = 0\,, \tag{7.234}$$

$$\frac{\partial(\rho\boldsymbol{u})}{\partial t} + \nabla\cdot(\rho\boldsymbol{u}\boldsymbol{u}) = -\nabla p + \nabla\cdot\Big[\mu\big(\nabla\boldsymbol{u} + (\nabla u)^T\big)\Big] + \sum_s \rho_s\boldsymbol{a}_s\,, \tag{7.235}$$

where the total pressure is $p = \sum_s p_s$ with $p_s = \theta_s\rho_s(1 + \sum_{s'} b_{ss'}\rho_{s'}\chi_{ss'})$, and the viscosity is $\mu = nk_B\tau$.

From Eq. (7.233) one can derive the following convection-diffusion equation for each species,

$$\rho\left(\partial_t X_s + \boldsymbol{u}\cdot\nabla X_s\right) = -\nabla\cdot\boldsymbol{j}_s, \tag{7.236}$$

where $X_s = \rho_s/\rho$ is the mass concentration. The flux $\boldsymbol{j}_s$ can be obtained from the Chapman-Enskog method, $\boldsymbol{j}_s = -\tau n k_B T \boldsymbol{d}_s$, where $\boldsymbol{d}_s$ is the diffusion force

$$\boldsymbol{d}_s = \frac{\rho_s}{n\rho k_B T}\left[\rho_{\bar{s}}(\boldsymbol{a}_{\bar{s}} - \boldsymbol{a}_s) - \nabla p + \frac{\rho}{m_s}\sum_{s'}\frac{\partial \mu_s}{\partial n_{s'}}\nabla n_{s'}\right], \tag{7.237}$$

with μ_s being the chemical potential of species s that satisfies the following relationship,

$$\frac{\partial \mu_s}{\partial n_{s'}} = \frac{k_B T}{n_s}E_{ss'}, \quad E_{ss'} = \delta_{ss'} + 2b_{ss'}\rho_s\chi_{ss'} + n_s\sum_t b_{st}\rho_t\frac{\partial \chi_{st}}{\partial n_{s'}}. \tag{7.238}$$

The diffusion force derived above is consistent with the result in phenomenological theories. In the absence of external force and pressure gradient, i.e. as $\boldsymbol{a}_s = \nabla p = 0$, it can be shown that

$$\boldsymbol{d}_s = \frac{\rho^2}{m_s m_{\bar{s}} n^2}\frac{L_{\bar{s}}E_{ss} - L_s E_{s\bar{s}}}{L_{\bar{s}}x_{\bar{s}} + L_s x_s}\nabla X_s,\ L_s = E_{\bar{s}s} + E_{ss}. \tag{7.239}$$

Therefore, in this case $\boldsymbol{j}_s = -\rho D_{s\bar{s}}\nabla X_s$, where the binary diffusion coefficient is

$$D_{s\bar{s}} = \frac{\tau\rho k_B T}{m_s m_{\bar{s}} n}\frac{L_{\bar{s}}E_{ss} - L_s E_{s\bar{s}}}{L_{\bar{s}}x_{\bar{s}} + L_s x_s}. \tag{7.240}$$

Obviously, $D_{s\bar{s}}$ is a complex function of the fluid density, molecular diameters, species concentrations, and the RDFs.

LBE model for binary dense gases based on the Enskog theory

Guo and Zhao [2005] proposed a LBE model based on the discrete velocity Enskog equation (7.218). In order to deal with species with different molecular masses, the model was developed following a time

splitting approach, which solves the following collision and propagation equations,

$$\frac{\partial f_{si}}{\partial t} = -\frac{1}{\tau}\left[f_{si} - f_{si}^{(eq)} \right] + F_{si}\,, \tag{7.241}$$

$$\frac{\partial f_{si}}{\partial t} + \boldsymbol{c}_{si} \cdot \nabla f_{si} = 0\,. \tag{7.242}$$

Applying the explicit Euler scheme to the first equation leads to the collision step,

$$f'_{si}(\boldsymbol{x},t) = f_{si}(\boldsymbol{x},t) - \frac{\delta_t}{\tau}\left[f_{si} - f_{si}^{(eq)} \right] + \delta_t \hat{F}_{si}\,, \tag{7.243}$$

where the forcing term $\hat{F}_{si}$ is related to F_{si} that will be given later. For Eq. (7.242) the second-order Lax-Wendroff scheme is adopted, which gives the following streaming method,

$$\begin{aligned} f_{si}(\boldsymbol{x}, t+\delta_t) = {} & f'_{si}(\boldsymbol{x},t) - \frac{A_s}{2}[f'_{si}(\boldsymbol{x}+\boldsymbol{c}_i\delta_t, t) - f'_{si}(\boldsymbol{x}-\boldsymbol{c}_i\delta_t, t)] \\ & + \frac{A_s^2}{2}[f'_{si}(\boldsymbol{x}+\boldsymbol{c}_i\delta_t, t) - 2f'_{si}(\boldsymbol{x},t) + f'_{si}(\boldsymbol{x}-\boldsymbol{c}_i\delta_t)]\,. \end{aligned} \tag{7.244}$$

Here $\boldsymbol{c}_i = c\boldsymbol{e}_i$ is the discrete velocity independent of species, and $c = \delta_x/\delta_t$ is the lattice speed. The parameter A_s is chosen such that $\boldsymbol{c}_{si} = A_s \boldsymbol{c}_i$. In order to remove the discrete lattice effects, the forcing term $\hat{F}_{si}$ and the fluid velocity are defined respectively as

$$\hat{F}_{si} = \left(1 - \frac{\delta_t}{2\tau}\right) F_{si}\,, \quad \rho\boldsymbol{u} = \sum_s \left[\sum_i \boldsymbol{c}_{si} f_{si} + \frac{\delta_t}{2}\boldsymbol{F}_s \right]. \tag{7.245}$$

The Chapman-Enskog analysis of Eqs. (7.243) and (7.244) shows that the corresponding hydrodynamic equations are the same as Eqs. (7.234) and (7.235).

The above time-splitting LBE model adopts only one grid and needs no interpolations in the computation, regardless of the difference between molecular masses. However, the streaming process requires slightly larger computational resources than the standard one. Guo and

Zhao [2003b] presented another model which also uses one lattice but adopts a modified equilibrium distribution function,

$$f_{si}^{(eq)} = \begin{cases} \omega_0 \rho_s \left(\dfrac{1 - r_s}{\omega_0} + r_s - \dfrac{\boldsymbol{u}^2}{2\theta} \right), & i = 0, \\ \omega_i \rho_s \left(r_s + \dfrac{\boldsymbol{c}_i \cdot \boldsymbol{u}}{\theta} + \dfrac{(\boldsymbol{c}_i \cdot \boldsymbol{u})^2}{2\theta^2} - \dfrac{\boldsymbol{u}^2}{2\theta} \right), & i \neq 0, \end{cases} \tag{7.246}$$

where $\theta = RT$ is the reference temperature related to the lattice speed, and $r_s = \theta_s / \theta$.

7.5 Summary

Multiphase and multi-component flows involve complicated interactions among the fluids, and the key point for modeling and simulating such flows is to describe the basic physics of the interactions appropriately. The particle nature of LBE enables it to serve as an efficient method to model the effects of the micro-interactions. The color-gradient in the color models, the pseudo-potential in the potential models, the pressure-tensor used in the equilibrium distribution function in the free-energy models, and the effective force in the models based on kinetic theory, all serve as effective models for the inter-particle interactions among the fluids. The capability of modeling the interactions at mesoscopic scale has been recognized as one of the main advantages of LBE over the traditional CFD methods, and a variety of applications of LBE in studying fundamental phenomena and mechanisms of multiphase as well as multi-components flows have been reported in the literature, which are not included in this book.

Although the LBE method has gained much success in modeling and simulating multiphase/multi-component systems, there are still some common fundamental problems to be revealed. For instance, most of the available LBE models suffer from the spurious velocities, which appear in the vicinity of phase interfaces. Some efforts have been attempted to reduce or eliminate such unphysical artifacts from different viewpoints [Cristea and Sofonea, 2003; Lee and Fischer, 2006; Shan, 2006; Wagner, 2003], and recently it was shown that the spurious currents are due to the

force imbalance between the pressure and intermolecular force [Guo, Zheng and Shi, 2011]. It was also found that checkerboard effects exist in two-phase LBE models and may have significant influence on the velocity field [Guo, Shi and Zheng, 2011]. Another difficulty in multiphase LBE is the numerical instability when dealing with systems with large density and/or viscosity ratios, and studies on this issue are in progress [e.g., Inamuro, 2004; Lee and Lin, 2005a; Mukherjee and Abraham, 2007; Zheng *et al*., 2006]. In a word, developing and applications of efficient LBE models for flows with multiple phases and/or comments are still an active topic in the field.

This page intentionally left blank

Chapter 8

LBE for Microscale Gas Flows

8.1 Introduction

The LBE methods described in the preceding chapters are mainly developed for flows at macroscopic scales where the fluid is treated as a continuum. Now we turn to flows with at least one dimension being in the micro/nanometer scale. With the rapid development of micro/nano technology in recent years, the study of such microscopic flows has become one of the current research hotspots in fluid mechanics [Darhuber and Troian, 2005; Ho and Tai, 1998; Karniadakis and Beskok, 2002]. The hydrodynamics of such flows can differ significantly from that of macro-scale flows in that some factors such as surface force, roughness, and electrostatic force, which are generally ignored in continuum flows, become important and start to dominate the flow behaviors. Consequently, some nontrivial phenomena, which are difficult to explain by conventional hydrodynamic theories, will arise in micro-scale fluid systems.

At macroscopic scale, there will be no difference in the hydrodynamic behaviors between a liquid and a gas provided they have the same characteristic dimensionless numbers such as the Reynolds number and Rayleigh number. At microscopic scale, however, a liquid flow may be quite different from a gas flow due to the size effects. Usually, a liquid can still be treated as a continuum, and the Navier-Stokes equations, with inclusion of some additional forces, such as electrostatic force, still works at microscale scales. Subsequently, the LBE methods described in previous chapters can still be applied to such micro flows. On the other hand, gaseous flows at microscopic scale are mainly affected by the rarefaction effect due to the finite Knudsen

number, and the continuum assumption may break down such that the Navier-Stokes equations fail to work. Consequently, the LBE models designed for solving the Navier-Stokes equations cannot be applied to such flows any longer, and modifications or new models are required in order to simulate micro gaseous flows. In this chapter we will focus on this topic.

The rarefaction of a gas in a confined geometry can be characterized by the Knudsen number, $\mathrm{Kn} = \lambda/L$, where λ is the mean free path of the gas molecules, and L is the characteristic length of the flow domain. According to the magnitude of Kn, four flow regimes can be identified, i.e., continuum flow ($\mathrm{Kn} \leq 0.001$), slip flow ($0.001 < \mathrm{Kn} \leq 0.1$), transition flow ($0.1 < \mathrm{Kn} \leq 10$), and free molecular flow ($\mathrm{Kn} > 10$). Continuum flows can be well described by the Navier-Stokes equations together with the no-slip boundary condition. In the slip regime, some weak rarefaction effects will appear, but are confined in the vicinity of wall surfaces, and the Navier-Stokes equations with certain slip boundary conditions can be employed to describe the bulk flow. In the transition regime, rarefaction effects become more important and take effect in the whole flow field, and continuum models are not applicable any more. For free molecular flows, rarefaction effects dominate the overall flow behaviors, and microscopic models, such as molecular dynamics, or kinetic methods such as direct simulation Monte Carlo (DSMC) [Bird, 1994], discrete velocity model [Wagner, 1995], and discrete ordinate method [Yang and Huang, 1995], should be adopted.

As a mesoscopic method originated from kinetic theory of gases, the LBE has been employed to study microscale gaseous flows recently (Agrawal *et al.*, 2005; Guo *et al.*, 2006; Guo *et al.*, 2007; Guo *et al.*, 2008; Kim *et al.*, 2005; Lee and Lin, 2005b; Lim *et al.*, 2002; Nie *et al.*, 2002; Niu *et al.*, 2004; Sofonea and Sekerka, 2005;Toschi and Succi, 2005; Zhang *et al.*, 2005; Zhang *et al.*, 2006, to name a few). Some results show that LBE is successful in modeling slip flows, but there also exist some works indicating that the results of LBE are not satisfactory for flows even with small Kn [Luo, 2004; Shen *et al.*, 2004]. These studies imply that more careful investigations on LBE for micro gas flows are necessary despite of its superiority over the methods based on continuum models.

8.2 Fundamental Issues in LBE for Micro Gaseous Flows

Two fundamental issues should be considered in the applications of LBE for micro gas flows. The first one is to build up the relationship between the relaxation time(s) in the collision operator of LBE and the Knudsen number of the gas, and the other is to treat the wall velocity slip that is a common feature of micro gaseous flows.

8.2.1 *Relation between relaxation time and Knudsen number*

As shown in Chapter 1, the shear viscosity ν depends on the relaxation time τ in LBGK models or the relaxation times τ_s associated with the moments of shear stress in MRT-LBE models. Therefore, if the relation between the viscosity and the mean-free-path is known, the relationship between the relaxation time(s) and Kn can be established. The initial attempt to apply LBE for simulation of micro channel flows was made by Lim *et al*. [2002], in which a relationship between τ and Kn is established by assuming that the streaming and collision processes happen simultaneously. Later, it was found that the relationship between τ and Kn can also be derived from the kinetic theory [Niu *et al*., 2004; Guo *et al.*, 2006]. The kinetic theory gives that for a hard sphere gas, the mean-free-path is [Chapman and Cowling, 1970],

$$\lambda = \frac{1}{\sqrt{2}n\pi\sigma^2}, \tag{8.1}$$

where n is the number density of the gas and σ is the diameter of the molecule. On the other hand, the Chapman-Enskog analysis shows that the viscosity of the hard sphere gas is [Chapman and Cowling, 1970],

$$\mu \approx 1.016 \times \frac{5}{16}\frac{m}{\sigma^2}\sqrt{\frac{RT}{\pi}}, \tag{8.2}$$

where m is the molecular mass. Approximately, λ and μ satisfy the following relationship,

$$\lambda = \frac{\mu}{p}\sqrt{\frac{\pi RT}{2}}, \tag{8.3}$$

where $p = \rho RT$ is the pressure with $R = k_B / m$ the gas constant and T the temperature. This relation was generalized by Cercignani for general gases [Cercignani, 1988]. An advantage of this definition of the mean-free-path is that the physical quantities on the right hand side of Eq. (8.3) can all be measured experimentally so that λ can also be determined from experimental data.

On the other hand, it is known that the relaxation time τ in the LBGK model is related to the dynamic viscosity μ as follows,

$$\mu = c_s^2 \rho \left(\tau - \frac{1}{2} \right) \delta_t = p \left(\tau - \frac{1}{2} \right) \delta_t . \tag{8.4}$$

Therefore the following equation can be obtained,

$$\lambda = \sqrt{\frac{\pi RT}{2}} \left(\tau - \frac{1}{2} \right) \delta_t . \tag{8.5}$$

Meanwhile, it is known that in LBE the lattice velocity c is also related to the temperature T,

$$c = \frac{\delta_x}{\delta_t} = \sqrt{\chi RT} , \tag{8.6}$$

where χ is a constant associated with the model. For instance, $\chi = 3$ in the D1Q3, D2Q9, D3Q15, and D3Q19 models. Therefore, the τ-Kn relationship in LBGK models can be expressed as

$$\tau = \frac{1}{2} + \frac{\lambda}{\delta_x} \sqrt{\frac{2\chi}{\pi}} = \frac{1}{2} + \sqrt{\frac{2\chi}{\pi}} N\mathrm{Kn} , \tag{8.7}$$

where $N = L/\delta_x$ is the grid number along the characteristic length. This relationship is also valid for the relaxation times τ_s in MRT-LBE models.

It is noted that some other τ-Kn relationships have also been proposed in the literature, which can be expressed generally as,

$$\tau = \frac{\alpha}{2} + \frac{\lambda}{\overline{c} \delta_t} = \frac{\alpha}{2} + \frac{c}{\overline{c}} N\mathrm{Kn} , \tag{8.8}$$

where $\overline{c}$ is a certain microscopic velocity relating to the mean molecular velocity. For the parameter α, two values are usually set, i.e. α = 0

or $\alpha = 1$. Apparently, the latter should be used in LBE due to the discrete effects. Regarding the microscopic velocity $\overline{c}$, equation (8.7) indicates that it should be $\overline{c} = (\pi RT / 2)^{1/2}$. However, the choice of $\overline{c}$ is rather diverse in the literature. For instance, the lattice speed $c = \delta_x / \delta_t$, the mean molecular velocity $(8RT/\pi)^{1/2}$, and the root-mean-square velocity $(3RT)^{1/2}$, have all been adopted in existing studies. Some other formulations of $\overline{c}$ as a function of Kn were also proposed [Guo *et al.*, 2006; Zhang *et al.*, 2006]. Anyway, the τ-Kn relationship should satisfy a consistency requirement [Guo *et al.*, 2006], namely, in the continuum limit ($\mathrm{Kn} \to 0$), the relationship should give $\tau = \mu / p$. Apparently the lattice speed does not satisfy this requirement.

8.2.2 *Slip boundary conditions*

A common knowledge about micro gas flows is that the velocity is discontinuous at a solid surface, or velocity slip occurs. To resolve this discontinuity, slip boundary conditions should be used. For example, we can use a first-order slip boundary condition,

$$u_s \equiv u(\boldsymbol{x}_w) - u_w = l_s \left. \frac{\partial u}{\partial y} \right|_{wall}, \tag{8.9}$$

or

$$U_s = L_s \left. \frac{\partial U}{\partial Y} \right|_{wall}, \tag{8.10}$$

where $u(\boldsymbol{x}_w)$ is the tangential velocity at the wall extrapolated from the bulk region, and u_w is the tangential velocity of the wall, l_s is termed as the slip length, and y is the distance normal to the wall; $Y = y/L$ is the dimensionless distance to the wall, while $U_s = u_s / u_0$ and $L_s = l_s / L$ are the dimensionless slip velocity and slip length, respectively, with u_0 being a characteristic velocity. Generally $l_s \sim \lambda$ and thus $L_s \sim \mathrm{Kn}$. Therefore, for continuous flows ($\mathrm{Kn} \to 0$) the slip velocity at the boundary can be neglected. As Kn is finite, however, the slip velocity must be considered. Under such circumstances, the bounce-back scheme for no-slip boundary conditions is not applicable any more, and a proper scheme which is able to reflect the velocity slip should be devised.

In kinetic theory, the boundary condition for the particle distribution function at a solid wall can be expressed as [Cercignani, 1988],

$$| \boldsymbol{\xi} \cdot \boldsymbol{n} | f(\boldsymbol{\xi}) = \int_{\boldsymbol{\xi}' \cdot \boldsymbol{n} < 0} | \boldsymbol{\xi}' \cdot \boldsymbol{n} | R(\boldsymbol{\xi}' \to \boldsymbol{\xi}) f(\boldsymbol{\xi}') d\boldsymbol{\xi}', \quad \boldsymbol{\xi} \cdot \boldsymbol{n} \geq 0, \quad (8.11)$$

where $\boldsymbol{n}$ is the normal unit vector pointing from the wall to the fluid, $R(\boldsymbol{\xi}' \to \boldsymbol{\xi})$ is the probability distribution function (scattering kernel function) for gas molecules which collides on the wall with the relative velocity $\boldsymbol{\xi}'$ first and then re-enters the gas with a relative velocity $\boldsymbol{\xi}$. If the wall is not penetrable and does not adsorb the gas molecules, R satisfies the normalization condition,

$$\int_{\boldsymbol{\xi} \cdot \boldsymbol{n} > 0} R(\boldsymbol{\xi}' \to \boldsymbol{\xi}) d\boldsymbol{\xi} = 1. \quad (8.12)$$

In this case, the relative velocity normal to the wall is zero

$$\boldsymbol{u} \cdot \boldsymbol{n} = \int \boldsymbol{\xi} \cdot \boldsymbol{n} f(\boldsymbol{\xi}) d\boldsymbol{\xi} = 0. \quad (8.13)$$

Maxwell introduced two simple types of gas-wall interactions, i.e., the specular reflection and full diffuse reflection early in 1879 [Chapman and Cowling, 1970]. The former supposes that

$$f(\boldsymbol{\xi}) = f(\boldsymbol{\xi}'), \quad \boldsymbol{\xi}' = \boldsymbol{\xi} - 2\boldsymbol{n}(\boldsymbol{\xi} \cdot \boldsymbol{n}) \quad (\boldsymbol{\xi} \cdot \boldsymbol{n} > 0), \quad (8.14)$$

which means that a gas molecule is specularly reflected after colliding the wall with a relative velocity $\boldsymbol{\xi}'$, and so the scattering kernel function of the specular reflection is

$$R_s(\boldsymbol{\xi}' \to \boldsymbol{\xi}) = \delta(\boldsymbol{\xi} - \boldsymbol{\xi}' + 2\boldsymbol{n}[\boldsymbol{\xi} \cdot \boldsymbol{n}]) \quad (\boldsymbol{\xi} \cdot \boldsymbol{n} > 0,\ \boldsymbol{\xi}' \cdot \boldsymbol{n} < 0), \quad (8.15)$$

where δ is a generalized delta function. It is easy to prove that there is no energy exchange between gas and the wall with this boundary condition, and the shear stress is zero at the wall. On the other hand, the full diffuse reflection assumes that the gas molecule will be redistributed into the gas with a random velocity after striking the wall, satisfying the following equilibrium distribution,

$$f(\boldsymbol{\xi}) = \frac{\rho_w}{(2\pi R T_w)^{D/2}} \exp\left[-\frac{\boldsymbol{\xi}^2}{2RT_w} \right], \quad \boldsymbol{\xi} \cdot \boldsymbol{n} > 0, \quad (8.16)$$

where ρ_w is the density of gas at the wall, T_w is the wall temperature, and $\boldsymbol{\xi}$ is the relative velocity of gas molecules. The mass conservation requirement, Eq. (8.13), indicates that

$$N^- = N^+ = \rho_w \sqrt{\frac{RT_w}{2\pi}}\,, \tag{8.17}$$

where N^- and N^+ are the flow rates of the incident molecules towards the wall and those departing from the wall,

$$N^\pm = \int_{\boldsymbol{\xi}\cdot\boldsymbol{n}\gtrless 0} \boldsymbol{\xi}\cdot\boldsymbol{n} f(\boldsymbol{\xi})\, d\boldsymbol{\xi}\,. \tag{8.18}$$

The scattering kernel function of the full diffuse reflection can thus be expressed as

$$R_d(\xi' \to \xi) = \frac{\rho_w(\xi\cdot\boldsymbol{n})}{(2\pi RT)^{D/2}} \exp\left[-\frac{\xi^2}{2RT_w}\right], \quad (\xi\cdot\boldsymbol{n} > 0,\ \xi\cdot\boldsymbol{n} < 0)\,. \tag{8.19}$$

A more general gas-wall interaction model is to assume that part of the molecules are reflected specularly while the others are reflected diffusely, i.e.,

$$R(\boldsymbol{\xi}' \to \boldsymbol{\xi}) = (1-\sigma)R_s(\boldsymbol{\xi}' \to \boldsymbol{\xi}) + \sigma R_d(\boldsymbol{\xi}' \to \boldsymbol{\xi})\ , \tag{8.20}$$

where $\boldsymbol{\xi}\cdot\boldsymbol{n} > 0$ and $\boldsymbol{\xi}'\cdot\boldsymbol{n} < 0$, and $0 \le \sigma \le 1$ is termed as tangential momentum accommodation coefficient.

Theoretical analysis of the molecular dynamics reveals that the diffuse reflection produces a velocity slip at the wall [Chapman and Cowling, 1970],

$$u_s \sim \frac{2-\sigma}{\sigma}\lambda\frac{\partial u}{\partial y}\,, \tag{8.21}$$

which means that the full specular reflection will lead to an infinite slip velocity while the full diffuse reflection produces a finite one.

In 2002 Ansumali and Karlin [2002] developed a discrete version of the full diffuse reflection as a boundary condition for LBE,

$$f_i = K f_i^{(eq)}(\rho_w, \boldsymbol{u}_w), \quad (\boldsymbol{c}_i - \boldsymbol{u}_w)\cdot\boldsymbol{n} > 0\,, \tag{8.22}$$

where

$$K = \frac{\sum_{\boldsymbol{\xi}_i' \cdot \boldsymbol{n} < 0} |\boldsymbol{\xi}_i' \cdot \boldsymbol{n}| f_i}{\sum_{\boldsymbol{\xi}_i' \cdot \boldsymbol{n} < 0} |\boldsymbol{\xi}_i' \cdot \boldsymbol{n}| f_i^{(eq)}(\rho_w, \boldsymbol{u}_w)}, \qquad \boldsymbol{\xi}_i' = \boldsymbol{c}_i - \boldsymbol{u}_w . \tag{8.23}$$

The scheme was also generalized for partially diffuse walls (diffuse reflection, DR) [Tang *et al.*, 2005], which can be written as

$$f_i = (1 - \sigma_v) f_{i'} + \sigma_v K f_i^{(eq)}(\rho_w, u_w), \quad (\boldsymbol{c}_i - \boldsymbol{u}_w) \cdot \boldsymbol{n} > 0 , \tag{8.24}$$

where σ_ν is the discrete accommodation coefficient, $f_{i'}$ is the distribution function with velocity $\boldsymbol{c}_{i'} = \boldsymbol{c}_i - 2(\boldsymbol{c}_i \cdot \boldsymbol{n})\boldsymbol{n}$, and the parameter K is defined as

$$K = \frac{\sum_{\boldsymbol{\xi}_i' \cdot \boldsymbol{n} < 0} |\boldsymbol{\xi}_i' \cdot \boldsymbol{n}| \, f_i}{\sum_{\boldsymbol{\xi}_i' \cdot \boldsymbol{n} > 0} |\boldsymbol{\xi}_i' \cdot \boldsymbol{n}| \, f_i^{(eq)}(\rho_w, \boldsymbol{u}_w)}, \qquad \boldsymbol{\xi}_i' = \boldsymbol{c}_i - \boldsymbol{u}_w , \tag{8.25}$$

which is slightly different from that defined by Eq. (8.23).

Succi [2002] presented another type of discrete kinetic boundary condition (BSR) for LBE. This scheme is a combination of the bounce-back scheme for no slip and the specular reflection scheme for free slip,

$$f_i = r f_{\bar{i}} + (1 - r) f_{i'} , \tag{8.26}$$

where $f_{\bar{i}}$ is the distribution function with $\boldsymbol{c}_{\bar{i}} = -\boldsymbol{c}_i$, and the parameter $0 \le r \le 1$ is the combination coefficient representing the bounce-back portion. Obviously as $r = 0$, the BSR scheme defined by Eq. (8.26) reduces to the specular reflection scheme, which is also the case of the DR scheme with $\sigma_\nu = 0$. However, as $r = 1$ the BSR scheme reduces to the bounce-back scheme and the slip velocity is zero, while as $\sigma_\nu = 1$ the DR scheme still produces a finite slip velocity. These facts indicate that the two popular discrete kinetic boundary conditions are closely related but not identical. Further discussions will be given in more detail later.

Finally, it is noteworthy that both the DR and BSR schemes are implemented for the post-streaming distribution functions, and thus the collision step should be carried out on the boundary nodes. In this regard, these two schemes are similar to the modified bounce-back scheme

described in Chapter 2. In addition, several half-way versions of the DR and BSR schemes were also employed in some studies, which are similar to the half-way bounce-back scheme. Owing to the clear picture of the half-way approach, our discussions will be based on this approach in the subsequent sections of this chapter.

8.3 LBE for Slip Flows

In the slip region, the Navier-Stokes equations still hold in the bulk region far away from the walls provided that suitable slip boundary conditions are imposed. Therefore, the standard LBE models for the Navier-Stokes equations can still be used to simulate slip flows, but the relaxation time(s) should be related to the Knudsen number as given by Eq. (8.7), and some kinetic boundary schemes for slip velocity should be employed.

8.3.1 *Kinetic boundary scheme and slip velocity*

For slip flows, the boundary conditions reflect the effective interactions between gas molecules and the solid wall. As such, the kinetic boundary scheme plays an important role for simulating such flows with LBE. Recently Guo *et al*. [2007] made a detailed theoretical analysis on the popular DR and BSR schemes, which will be presented below briefly.

Without loss of generality, we take the isothermal D2Q9 LBGK model as an example,

$$f_i(\boldsymbol{x}+\boldsymbol{c}_i\delta_t, t+\delta_t) - f_i(\boldsymbol{x},t) = -\frac{1}{\tau}\left[f_i - f_i^{(eq)}\right] + \delta_t F_i, \quad i = 0 \sim 8\,. \tag{8.27}$$

The expression of the EDF $f_i^{(eq)}$ can be found in Chapter 1, and the forcing term is given by,

$$F_i = \omega_i \rho \left(1 - \frac{1}{2\tau}\right)\left[\frac{\boldsymbol{c}_i - \boldsymbol{u}}{c_s^2} + \frac{(\boldsymbol{c}_i \cdot \boldsymbol{u})\boldsymbol{c}_i}{c_s^4}\right] \cdot \boldsymbol{a}\,, \tag{8.28}$$

where $\boldsymbol{a}$ is the acceleration. The density and velocities are defined by

$$\rho = \sum_i f_i, \quad \rho\boldsymbol{u} = \sum_i \boldsymbol{c}_i f_i + \frac{\delta_t}{2}\rho\boldsymbol{a}\,. \tag{8.29}$$

In the D2Q9 model $c = (3RT)^{1/2}$, and so the relaxation time can be related to the Knudsen number as (see Eq. (8.7)),

$$\tau = \frac{1}{2} + \sqrt{\frac{6}{\pi}} \frac{\mathrm{Kn}}{\Delta} \tag{8.30}$$

where $\Delta = 1/N = \delta_x / L$.

For a flat wall, the half-way versions of the DR and BSR schemes are sketched in Fig. 8.1. The boundary is located at $j = 1/2$, where j is the subscript of the lattice nodes located at $y_j = (j - 0.5)\,\delta_x$. For simplicity the flow is assumed to be unidirectional, i.e., the density ρ is a constant, the velocity component in y direction is zero, and $\partial_x \phi = 0$ for any flow variable ϕ. In the implementation of the LBE, the collision step is first carried out for all nodes,

$$f_i' = f_i + \frac{1}{\tau}[f_i - f_i^{(eq)}] + \delta_t F_i \,. \tag{8.31}$$

Then the streaming step is performed

$$f_i(\boldsymbol{x} + \boldsymbol{c}_i \delta_t, t + \delta_t) = f_i'(\boldsymbol{x}, t) \tag{8.32}$$

for all lattice points of $j > 1$. At a node at the first layer ($j = 1$), $f_0^{(1)}$, $f_1^{(1)}$, $f_3^{(1)}$, $f_7^{(1)}$ and $f_8^{(1)}$ are known after the streaming step, while $f_2^{(1)}$, $f_5^{(1)}$ and

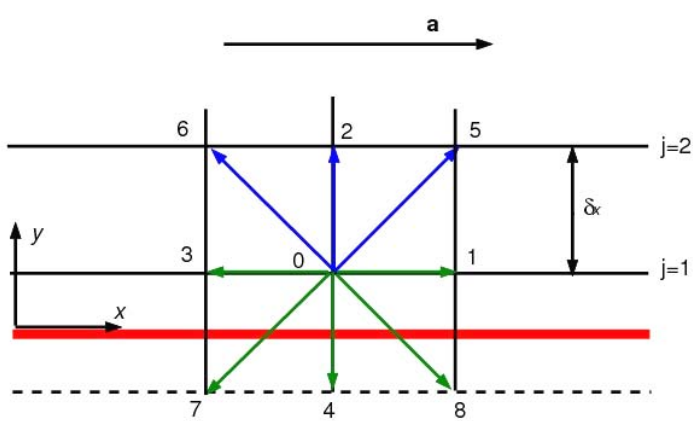

Fig. 8.1. Lattice and boundary arrangement in D2Q9 model.

$f_6^{(1)}$ should be provided by the kinetic boundary condition. For this flat wall the BSR and DR schemes can be written as,

$$\text{BSR:} \quad \begin{cases} f_2 = f_4', \\ f_5 = rf_7' + (1-r)f_8' + 2r\rho\omega_5 \boldsymbol{c}_5 \cdot \boldsymbol{u}_w / c_s^2, \\ f_6 = rf_8' + (1-r)f_7' + 2r\rho\omega_6 \boldsymbol{c}_6 \cdot \boldsymbol{u}_w / c_s^2, \end{cases} \tag{8.33}$$

$$\text{DM:} \quad \begin{cases} f_2 = f_4', \\ f_5 = \sigma_v K f_5^{(eq)}(\boldsymbol{u}_w) + (1-\sigma_v) f_8', \\ f_6 = \sigma_v K f_6^{(eq)}(\boldsymbol{u}_w) + (1-\sigma_v) f_7', \end{cases} \tag{8.34}$$

where $\boldsymbol{u}_w$ is the wall velocity and K is the normalization factor to ensure the mass conservation,

$$K = \frac{f_4' + f_7' + f_8'}{f_2^{(eq)}(\boldsymbol{u}_w) + f_5^{(eq)}(\boldsymbol{u}_w) + f_6^{(eq)}(\boldsymbol{u}_w)}. \tag{8.35}$$

It is noted that the BSR scheme given by Eq. (8.33) is an extension of the original one proposed by Succi which is designed for static walls. As $r = 1$, i.e. the full bounce-back scheme, equation (8.33) is just the half-way bounce-back scheme proposed by Ladd for moving boundaries.

From the definition of the flow velocity and the streaming step, we have

$$\rho u^{(1)} = c\left[f_1^{(1)} - f_3^{(1)} + f_5^{(1)} - f_6^{(1)} + f_8^{(1)} - f_7^{(1)} \right] + \frac{\delta_t}{2} \rho a \,, \tag{8.36}$$

$$\rho u^{(2)} = c\left[f_1^{(2)} - f_3^{(2)} + f_5^{(2)} - f_6^{(2)} + f_8^{(2)} - f_7^{(2)} \right] + \frac{\delta_t}{2} \rho a \,, \tag{8.37}$$

$$f_5^{(2)} - f_6^{(2)} = f_5'^{(1)} - f_6'^{(1)}, \quad f_8^{(2)} - f_7^{(2)} = f_8'^{(2)} - f_7'^{(2)}, \tag{8.38}$$

where a variable with superscript j denotes its value on nodes j. From Eqs. (8.36)~(8.38) and the boundary conditions (8.33) and (8.34), the following relations between $u^{(1)}$ and $u^{(2)}$ can be found:

$$\text{BSR:} \quad u^{(2)} = \frac{1 - 2\tau + 2r(\tau - 2)}{1 - 2\tau + 2r(\tau - 1)} u^{(1)} + \frac{6(2\tau - 1) + r(8\tau^2 - 20\tau + 11)}{(2\tau - 1)[1 - 2\tau + 2r(\tau - 1)]} \delta_t a, \tag{8.39}$$

$$\text{DR:}\quad u^{(2)}=\frac{1-2\tau+\sigma_v(\tau-2)}{1-2\tau+\sigma_v(\tau-1)}u^{(1)}+\frac{6(2\tau-1)+\sigma_v(4\tau^2-10\tau+11/2)}{(2\tau-1)[1-2\tau+\sigma_v(\tau-1)]}\delta_t a. \quad (8.40)$$

It is apparent that as $r=\sigma_v/2$, Eqs. (8.39) and (8.40) are totally identical, indicating that the BSR and DR schemes are equivalent under this condition. However, it is noted that both r and σ_ν are required to take values in [0, 1], so the applicable range of BSR scheme is larger than that of the DR scheme. An example is that the BSR scheme can realize the no-slip boundary condition while the DR scheme cannot.

Now we discuss the slip velocity at the solid wall. At an inner nodes ($j>1$), the neighboring distribution functions are related as follows,

$$\begin{aligned}
&f_1^{(j)}-f_3^{(j)}=f_1'^{(j)}-f_3'^{(j)},\ f_5^{(j)}-f_6^{(j)}=f_5'^{(j-1)}-f_6'^{(j-1)},\\
&f_8^{(j)}-f_7^{(j)}=f_8'^{(j+1)}-f_6'^{(j+1)},\ f_5^{(j+1)}-f_6^{(j+1)}=f_5'^{(j)}-f_6'^{(j)},\\
&f_8^{(j-1)}-f_7^{(j-1)}=f_8'^{(j)}-f_6'^{(j)}.
\end{aligned} \quad (8.41)$$

Based on these relationships and the definition of the fluid velocity, we can obtain

$$\nu\frac{u_{j+1}-2u_j+u_{j-1}}{\delta_x^2}=-a\,, \quad (8.42)$$

which is a second-order finite-difference scheme for the following equation,

$$\nu\frac{\partial^2 u}{\partial y^2}+a=0\,. \quad (8.43)$$

This means that the LBE is just a second-order finite-difference scheme for the Navier-Stokes equations.

Another boundary condition should be supplied in order to solve Eq. (8.42). When considering the force-driven Poiseuille flow between two parallel plates, the boundary condition at the wall located at $y=L$ takes the same formulation as Eq. (8.33) or (8.34). The solution of the difference equation (8.42) can be expressed as,

$$u_j=4u_c\frac{y_j}{H}\left(1-\frac{y_j}{L}\right)+u_s\,, \quad (8.44)$$

where $u_c = aL^2/8\nu$ and u_s is the slip velocity dependent on the boundary condition. Substituting Eq. (8.44) into Eqs. (8.39) and (8.40) leads to

$$U_s \equiv \frac{u_s}{u_c} = \begin{cases} \dfrac{2(1-r)(2\tau-1)}{r}\Delta + \dfrac{4(2\tau-1)^2-3}{3}\Delta^2, & \text{(BSR)} \\ \dfrac{2(2-\sigma_v)(2\tau-1)}{\sigma_v}\Delta + \dfrac{4(2\tau-1)^2-3}{3}\Delta^2. & \text{(DR)} \end{cases} \tag{8.45}$$

With the τ-Kn relationship (8.30), the above results can also be expressed in terms of Kn,

$$U_s = \begin{cases} \dfrac{4(1-r)}{r}\sqrt{\dfrac{6}{\pi}}\mathrm{Kn} + \dfrac{32}{\pi}\mathrm{Kn}^2 - \Delta^2, & \text{(BSR)} \\ \dfrac{4(2-\sigma_v)}{\sigma_v}\sqrt{\dfrac{6}{\pi}}\mathrm{Kn} + \dfrac{32}{\pi}\mathrm{Kn}^2 - \Delta^2. & \text{(DR)} \end{cases} \tag{8.46}$$

The above results indicate that the slip velocity from the BSR and DR schemes includes three parts, i.e., the first-order part (in terms of Kn), second-order part, and grid-dependent part (Δ). For flows in slip regime, the linear part dominates the slip velocity since the second-order part is much smaller for small Kn, while the numerical part depends on the mesh size and can be neglected as the resolution is fine enough. Equation (8.45) or (8.46) also indicates that the BSR scheme with $0 < r \leq 0.5$ is completely equivalent to the DR scheme with $0 < \sigma_v \leq 1$. A special case is that the BSR scheme reduces to the standard half-way bounce-back scheme as $r = 1$. In this case Eq. (8.45) shows that there is a slip velocity $U_s \sim \Delta^2$ on the boundary, which is consistent with the result found in Ref. [He *et al*., 1997]. It should be emphasized that this slip velocity is due to discretization errors and is unphysical.

8.3.2 *Discrete effects in the kinetic boundary conditions*

Equation (8.46) shows that in the Poiseuille flow the DR scheme with a discrete full diffuse condition ($\sigma_v = 1$) yields a slip velocity,

$$U_s = 4\sqrt{\frac{6}{\pi}}\mathrm{Kn} + \frac{32}{\pi}\mathrm{Kn}^2 \approx 5.528\mathrm{Kn} + 10.186\mathrm{Kn}^2. \tag{8.47}$$

On the other hand, the solution of the linearized BGK model with full diffuse walls ($\sigma = 1$) gives a slip velocity [Cercignani, 1988],

$$U_s^{ph}=4\zeta\sqrt{\frac{4}{\pi}}\mathrm{Kn}+\left(\frac{1}{2}+\zeta^2\right)\frac{16}{\pi}\mathrm{Kn}^2 \approx 4.586\mathrm{Kn}+7.804\mathrm{Kn}^2, \qquad (8.48)$$

where ζ=1.01615, Apparently $U_s \neq U_s^{ph}$, which means that using the physical accommodation coefficient σ as the numerical one (i.e., σ_v) in the DR scheme will lead to some errors. It is noted that in some available studies σ_v was set to be σ intuitively.

This difference between U_s and U_s^{ph} is due to the discrete effects in the kinetic boundary condition, which is similar to that in the forcing term discussed in Chapter 3. The key problem now is how to eliminate such unphysical effects. For gaseous flows in slip regime, a widely used slip boundary condition is the following second-order scheme,

$$u_s = A_1\lambda\left.\frac{\partial u}{\partial y}\right|_{wall} - A_2\lambda^2\left.\frac{\partial^2 u}{\partial y^2}\right|_{wall}, \qquad (8.49)$$

where A_1 and A_2 are two parameters dependent on the gas-wall interactions. For instance, $A_1 = 2\zeta\pi^{-1/2} \approx 1.1466$, and $A_2 = (1+2\zeta^2)/\pi \approx 0.9757$ for a full diffuse wall. With the boundary condition (8.49), the slip

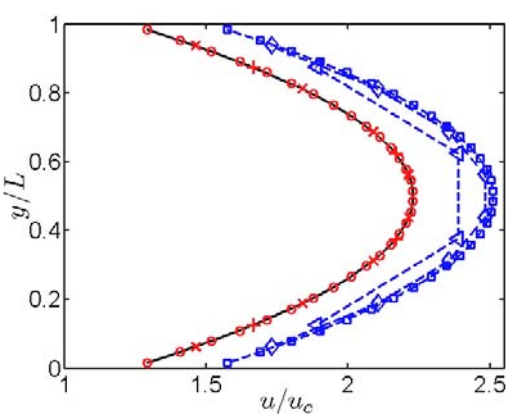

Fig. 8.2. Velocity profiles of the force-driven Poiseuille flow between two full diffuse walls ($\mathrm{Kn} = 0.2$). Solid line: analytical solution from Ref. [Cercignani, 1988]; Symbols with dashed line: $r = 0.5$, and Δ =1/4 (--◁--), 1/8 (--◊--), 1/32 (--□--); Symbols: r is determined by Eq. (8.51) and Δ=1/4 (+), 1/8 (×), 1/32 (○) (Guo *et al.*, Phys. Rev. E 76, 056704, 2007).

velocity of the Poiseuille flow can be obtained by solving the Navier-Stokes equations,

$$U_s = 4A_1\mathrm{Kn} + 8A_2\mathrm{Kn}^2 . \tag{8.50}$$

Therefore, from Eq. (8.46) and (8.50) one can conclude that r and σ_v should be chosen as follows in order to realize the second-order slip boundary condition (8.49):

$$r = \frac{\sigma_v}{2} = \left\{1 + \sqrt{\frac{\pi}{6}}\left[\frac{\Delta^2}{4\mathrm{Kn}} + A_1 + \left(2A_2 - \frac{8}{\pi}\right)\mathrm{Kn}\right]\right\}^{-1} . \tag{8.51}$$

Obviously, the parameters r (σ_v) in the BSR (DR) scheme depends not only on A_1 and A_2, which characterize the gas-wall interactions, but also on the Knudsen number and the grid size.

The force driven Poiseuille flow between two full diffuse walls was simulated by the D2Q9 LBGK model together with the BSR scheme with $r = \sigma/2$ and $r = \sigma_v/2$, where σ_v is calculated from Eq. (8.51). The velocity profiles are shown in Fig. 8.2. It is clear that the LBGK results with $r = \sigma/2$ are grid-dependent and deviate from the analytical solution of the Navier-Stokes equations with the slip boundary condition (8.49), while those with r defined by Eq. (8.51) are in excellent agreement with the theoretical one.

8.3.3 *MRT-LBE for slip flows*

The analysis for the LBGK model shows that the control parameter in the BSR or DR scheme depends not only on the gas-wall interactions, but also on the Knudsen number and the grid size, which is somewhat unphysical. Such defects can be solved in MRT-LBE models due to the additional freedoms in the parameter selection. Such attempts have been made recently in Ref. [Guo, Zheng & Shi., 2008].

Again we take the D2Q9 model as an example. Following an analysis similar to that for the LBGK model described in the above section, we can obtain the slip velocities in the BSR and DR schemes,

$$U_s = \begin{cases} 2(1-r)(2\tau_s - 1)\Delta/r + \boldsymbol{\varpi}\Delta^2/3, & (\mathrm{BSR}) \\ 2(2-\sigma_v)(2\tau_s - 1)\Delta/\sigma_v + \boldsymbol{\varpi}\Delta^2/3, & (\mathrm{DR}) \end{cases} \tag{8.52}$$

or

$$U_s = \begin{cases} \dfrac{4(1-r)}{r}\sqrt{\dfrac{6}{\pi}}\mathrm{Kn} + \dfrac{2\varpi}{\pi(\tau_s-0.5)^2}\mathrm{Kn}^2, & \text{(BSR)} \\ \dfrac{4(2-\sigma_v)}{\sigma_v}\sqrt{\dfrac{6}{\pi}}\mathrm{Kn} + \dfrac{2\varpi}{\pi(\tau_s-0.5)^2}\mathrm{Kn}^2, & \text{(DR)} \end{cases} \tag{8.53}$$

where τ_s is the relaxation time for the shear stress moments p_{xx} and p_{xy}, and τ_q is for the moment associated with the heat flux q, while $\varpi = [16(\tau_s - 0.5)(\tau_q - 0.5) - 3]$.

In Eq. (8.52), the terms relating to Δ^2 depend on τ_s and τ_q, where τ_s is related to the Knudsen number Kn and cannot be adjusted freely. Another relaxation time τ_q is, however, an adjustable parameter, which provides the possibility to realize a prescribed boundary condition. In fact, Ginzburg and d'Humieres [2003] have pointed out that the pure bounce-back scheme can achieve the complete no-slip boundary condition by adjusting τ_q. This strategy can also be used to realize the second-order slip boundary condition (8.49).

Comparing Eqs. (8.53) and (8.50), one can identify that

$$r = \frac{\sigma_v}{2} = \left(1 + \sqrt{\frac{\pi}{6}}A_1\right)^{-1}, \quad \tau_q = \frac{1}{2} + \frac{\pi A_2(2\tau_s - 1)^2 + 3}{8(2\tau_s - 1)}. \tag{8.54}$$

Clearly r and σ_v depend only on the gas-wall interaction parameter A_1, which is more reasonable than that in the LBGK model. However, it is noteworthy that even in the MRT-LBE model, the BSR and DR schemes still contain some discrete effects. An example is as $r = \sigma_v/2 = 0.5$ the slip velocity given by Eq. (8.53) is not that for a full diffuse wall as shown by Eq. (8.48).

8.4 LBE for Transition Flows

8.4.1 *Knudsen layer*

As a gas flows over a solid surface, a kinetic boundary layer, also known as Knudsen layer, will appear (see Fig. 8.3). The thickness of the Knudsen layer is of the order of the mean-free-path of the gas, within

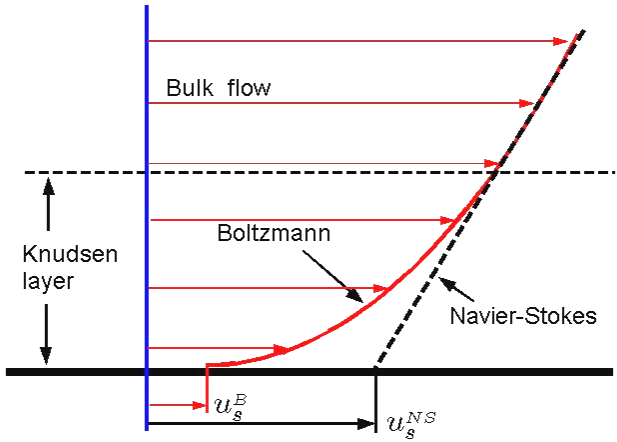

Fig. 8.3. Schematic of the Knudsen layer.

which the inter-molecular collisions are very rare and the quasi-thermodynamic-equilibrium assumption, on which the Navier-Stokes constitution is based, will break down. In the usual macro-scale systems the thickness of the Knudsen layer can be ignored and thus the Navier-Stokes equations can be applied to the entire flow field. On the other hand, for flows in the transition regime, the Knudsen layer takes a large portion and has significant effects on the flow behavior. For instance, Lockerby *et al.* [2005] pointed out that in the plane Poiseuille flow, the contribution of the Knudsen layer with $\mathrm{Kn} = 0.05$ to the overall mass flow rate is over 30%.

Combined with appropriate kinetic boundary conditions, the Boltzmann equation can be used to describe the flow within Knudsen layer. A variety of studies have been made to investigate the velocity structure within the Knudsen layer by solving the Boltzmann equation or simplified model equations, which show that the velocity profile is highly nonlinear in this region. As sketched in Fig. 8.3, the solution of the Boltzmann equation also gives a slip velocity u_s^B, which is different from the usual macroscopic slip velocity u_s^{NS} obtained by extrapolating the solution of the Navier-Stokes equations in the bulk region.

For flows in slip regime, the Knudsen layer takes a relatively small portion of the whole flow domain, and its effects on the bulk flow can be

well modeled by a suitable slip boundary condition for u_s^{NS}, such as the first order one (Eq. (8.9)) and the second-order one (Eq. (8.49)). For transition flows, however, the portion of the Knudsen layer is much larger and simple slip boundary conditions are not adequate to reflect its effects. If one still wants to describe such flows within the framework of continuum fluid dynamics, non-equilibrium hydrodynamic models beyond the Navier-Stokes equations, such as the Burnett equations, super-Burnett equations, and Grad moment equations, should be employed.

8.4.2 *LBE models with Knudsen layer effect*

Most available LBE models are designed for the Navier-Stokes equations, and so they are not suitable for transition flows in principle. Several attempts to extend LBE to transition flows have also been made, which can be classified into two types. The first type is *high-order models*, which is an extension of the standard LBE models for the Navier-Stokes equations. By employing a large set of discrete velocities, high-order LBE models can match the continuous Boltzmann equation at higher levels beyond the Navier-Stokes in terms of the Chapman-Enskog expansion. The second type is *effective-relaxation-time models,* which still employ the framework of standard LBE but the effects of gas-wall collisions are incorporated. In what follows we will present a brief introduction of both types of LBE models.

High-order models

As discussed in Chapter. 1, LBE is a discrete scheme of the continuous Boltzmann equation, and the accuracy depends on the discretizations in velocity space $\boldsymbol{\xi}$, physical space $\boldsymbol{x}$, and time space t. With a finite set of discrete velocities $\{\boldsymbol{c}_i: i = 1, 2, \ldots, b\}$, one can obtain a discrete velocity model (DVM) from the Boltzmann equation,

$$\frac{\partial f_i}{\partial t} + \boldsymbol{c}_i \cdot \nabla f_i = \Omega_i \ , \tag{8.55}$$

where $f_i = w_i f(\boldsymbol{x}, \boldsymbol{c}_i, t)$ is the discrete velocity distribution function and w_i is the weight coefficient. The approximation accuracy between the DVM

(8.55) and the continuous Boltzmann equation can be estimated by comparing the moment equations at each time scale in the Chapman-Enskog analysis. Generally, the discrete velocities $\boldsymbol{c}_i$'s are chosen as the quadrature nodes so that certain velocity moments at some time scales can be evaluated accurately,

$$\int \boldsymbol{\xi}^k f^{(m)}(\boldsymbol{x},\boldsymbol{\xi},t)d\boldsymbol{\xi} = \sum_i W_i \boldsymbol{c}_i^k f^{(m)}(\boldsymbol{x},\boldsymbol{c}_i,t),\ \ k=0\sim K,\ \ \ m=0\sim M\,, \quad (8.56)$$

where $f^{(m)}$ is the distribution function at scale m in the Chapman-Enskog expansion, i.e., $f = f^{(0)} + \varepsilon f^{(1)} + \varepsilon^2 f^{(2)} + \cdots$, K and M are two non-negative integers which determine the accuracy or *physical symmetry* in the velocity discretization [Cao *et al*., 1997; Guo *et al.*, 2006; Shan *et al*., 2006]. In general, if the equation for the k-th order discrete velocity moment of the DVM is required to match that of the continuous velocity moment, the $(k+1)$-th order moment should be accurately evaluated. For instance, for isothermal flows the conservative variables are the density (zeroth-order moment) and momentum (first-order moment), in order to obtain the correct equations for these variables, K should be chosen to be not less than 2; If the energy (second-order moment) is also considered, K should be 3 at least. The parameter M determines the level at which the moment equations of the DVM (8.55) are the same as those of the continuous Boltzmann equation in the Chapman-Enskog analysis. For example, if $M=0$, only the velocity moments of the equilibrium distribution function are accurately evaluated, and the DVM is then consistent with the continuous Boltzmann equation at the ε^0 (Euler) level; if $M=1$ then both are consistent with each other at the ε^1 (Navier-Stokes) level. If M takes further larger values, the DVM can match the Boltzmann equation at higher-order levels (e.g., Burnett, Super-Burnett, *etc.*). A systematic discussion about high-order DVM through Hermite expansion of the distributions has been made in Ref. [Shan *et al*., 2006].

After determining the discrete velocity set and the DVM, standard numerical schemes can be used to discretize the temporal and spatial terms in Eq. (8.55), which lead to different high-order LBE models. If the time and space steps in the discretizations are small enough, the corresponding LBE model will be a good approximation to the DVM (8.55) and can be readily employed to simulate transition flows.

Essentially, high-order LBE models share much with the discrete velocity or discrete ordinate methods for solving the Boltzmann equation. A difficulty in such LBE models is that the required accuracy in the velocity discretization is usually not known *a priori*, and the number of discrete velocities required in high-order LBE models is generally very large, which means expensive computational costs.

Effective-relaxation-time models

Unlike the high order LBE models, the effective-relaxation-time LBE models for transition flows employ the same discrete velocity sets as used in the models for the Navier-Stokes equations, but the Knudsen layer effects are incorporated through effective relaxation time(s).

First, it is known from kinetic theory that the mean free path of a gas molecule follows an exponential distribution [Woods, 1993],

$$p(r) = \frac{r}{\lambda}\exp\left(-\frac{r}{\lambda}\right), \tag{8.57}$$

where λ is the mean free path of gas molecules without boundaries. Actually, the overall mean free path of gas molecules is

$$\int_0^\infty rp(r)\,dr = \lambda\,. \tag{8.58}$$

As the gas is bounded by a solid wall, the free flight paths of some molecules will be cut off by the wall, and consequently the overall mean-free-path of the gas will decrease. In such cases the overall effective mean free path of the gas, λ_e, can be expressed as,

$$\lambda_e = \lambda\psi(\mathrm{Kn})\,, \tag{8.59}$$

where ψ (termed as *correction function*) is a decreasing function of Kn and satisfies

$$\lim_{x\to 0}\psi(x) = 1\,. \tag{8.60}$$

Stops [1970] derived a complicated expression for ψ for a gas between two parallel plates, which can be approximated as [Guo *et al.*, 2006],

$$\psi(x) = \frac{2}{\pi}\mathrm{atan}(\sqrt{2}x^{-3/4})\,. \tag{8.61}$$

The numerical profile of this new expression is very close to that obtained by Stops in a large range of Kn [Guo *et al.*, 2006].

The function defined above reflected the overall effects of the gas-wall interaction on the total mean-free-path of the gas, and the effective mean-free-path λ_e is independent of the distance to the wall. Alternatively, a local effective mean-free-path for the molecules located at position $\boldsymbol{x}$ can also be derived following the approach of Stops,

$$\lambda_e(\boldsymbol{x}) = \lambda\psi(\lambda, \boldsymbol{x}), \tag{8.62}$$

where the correction function $\psi(\lambda, \boldsymbol{x})$ has the following properties,

$$\lim_{|\boldsymbol{x}\cdot\boldsymbol{n}|\to\infty} \psi(\lambda, \boldsymbol{x}) = 1, \quad \lim_{\lambda/L\to 0} \psi(\lambda, \boldsymbol{x}) = 1, \tag{8.63}$$

which imply that $\lambda_e = \lambda$ for molecules far away from the wall or as the gas can be considered as a continuum. Some formulations for the correction functions have been proposed from different view points. For instance, Zhang *et al.* [2006] proposed a formulation based on the idea of wall function,

$$\psi(\lambda, y) = \frac{1}{1 + 0.7e^{-Cy/\lambda}}, \tag{8.64}$$

where y is the distance to the wall and $C > 0$ is an empirical parameter. Alternatively, Guo *et al.* derived another formulation following Stops' theory [Guo, Shi & Zheng, 2007],

$$\psi(\lambda, y) = 1 + (\alpha - 1)e^{-\alpha} - \alpha^2, \tag{8.65}$$

where $\alpha = y/l$, and $E_i(x)$ is the exponential integral function defined by $E_i(x) = \int_1^\infty t^{-1}e^{-xt}dt$.

Based on the relationship between the relaxation time and mean free path, an effective relaxation time for the shear mode with gas-wall collision effects can be obtained,

$$\tau = \left(\frac{\pi RT}{2}\right)^{-1/2} \lambda_e. \tag{8.66}$$

With the relaxation time determined in such way, some LBGK models for transition flows have been developed [Guo *et al.*, 2006; Zhang *et al.*, 2006].

MRT-LBE models with effective relaxation times were also proposed [Guo *et al.*, 2008]. An example is the D2Q9 model,

$$f_i(\boldsymbol{x}+\boldsymbol{c}_i\delta_t, t+\delta_t) - f_i(\boldsymbol{x},t) = -\sum_j (M^{-1}SM)_{ij}[f_j - f_j^{(eq)}] + \delta_t F_i, \qquad (8.67)$$

in which the moments corresponding to the distribution function are given by

$$\boldsymbol{m} = M\cdot\boldsymbol{f} = (\rho, e, \varepsilon, j_x, q_x, j_y, q_y, p_{xx}, p_{xy})^T, \qquad (8.68)$$

and the corresponding diagonal matrix consisting of relaxation times is

$$S = \mathrm{diag}(\tau_\rho, \tau_e, \tau_\varepsilon, \tau_j, \tau_q, \tau_j, \tau_q, \tau_s, \tau_s)^{-1}, \qquad (8.69)$$

where the two relaxation times τ_s are determined from the mean free path, which can be expressed in terms of the Knudsen number as

$$\tau_s = \frac{1}{2} + \sqrt{\frac{6}{\pi}} N\mathrm{Kn}\psi(\lambda, \boldsymbol{x}). \qquad (8.70)$$

Like the MRT-LBE for slip flows, the relaxation time τ_q also depends on the prescribed boundary conditions. A generalized second-order slip boundary condition with the effective mean free path was proposed for transition flows [Guo *et al.*, 2008], which can be expressed as,

$$u_s = A_1\lambda_e\frac{du}{dn} - A_2\frac{\lambda_e}{2}\frac{d}{dn}\left(\lambda_e\frac{du}{dn}\right), \qquad (8.71)$$

where the gas-wall interaction parameters A_1 and A_2 are defined by

$$A_1 = \frac{2-\sigma}{\sigma}(1-0.1817\sigma), \quad A_2 = \frac{1}{\pi} + \frac{1}{2}A_1^2, \qquad (8.72)$$

in which σ is the momentum accommodation coefficient. The BSR scheme can be used in order to achieve this boundary condition, in which the combination parameter r and the relaxation time τ_q are given by

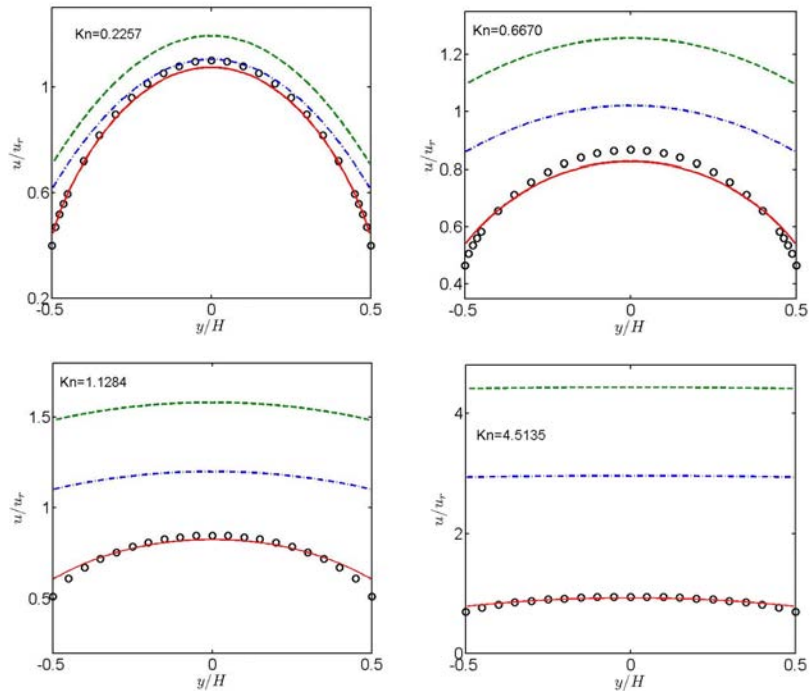

Fig. 8.4. Velocity profiles of the force-driven Poiseuille flow between two diffuse walls. Solid line: MRT-LBE with effective relaxation times; Open circle: Solution of the Boltzmann equation [Ohwada *et al*., 1989]; Dashed line: MRT-LBE with the slip coefficients given in [Cercignanni, 1988]; Dash-dotted line: MRT-LBE with slip coefficients in [Hadjiconstantinou, 2003] (Guo *et al.*, Phys. Rev. E 77, 036707, 2008).

[Guo *et al*., 2008],

$$r = \left[1 + \varsigma A_1 + \frac{\tau_s'(0)\delta_x}{8\tilde{\tau}_s^2(0)}\right]^{-1},$$

$$\tau_q = 0.5 + \frac{3 + 24\varsigma^2\tilde{\tau}_s^2(0)A_2}{16\tilde{\tau}_s(0)} + \frac{\tau_s'(0)\delta_x[12 + 30\tilde{\tau}_s(0)\varsigma A_1]}{16\tilde{\tau}_s^2(0)}, \qquad (8.73)$$

where $\varsigma = (\pi/6)^{1/2}$, $\tilde{\tau}_s = \tau_s - 0.5$ and $\tau_s' = d\tau_s/dy$. It is easy to check that as τ_s is a constant, both r and τ_q defined above reduce to those of the MRT model for slip flows (Eq. (8.54)).

The predicted velocity profiles, normalized by $u_r = aH(2/RT)^{1/2}$ with a the acceleration of the driven force, are shown in Fig. 8.4 at several Kn

in the transition regime. For comparison, the solution of the Boltzmann equation [Ohwada *et al.*, 1989] was also presented. Also shown in the figure were the results of the MRT-LBE for slip flows described in the above section, where the classical second-order slip boundary conditions with the coefficients given in Ref. [Cercignani, 1988] and in Ref. [Hadjiconstantinou, 2003] were employed, respectively. As demonstrated, the MRT-LBE model with effective relaxation times gives better predictions than the standard MRT-LBE. The dimensionless mass flow rate Q, normalized by $\rho a H^2/(2RT)^{1/2}$, was also measured (see Fig. 8.5), which clearly demonstrates good agreement with both theoretical results and experimental data [Dong, 1956]. Particularly, the Knudsen minimum appearing at $\mathrm{Kn} \approx 1$ is successfully captured by the effective MRT-LBE.

8.5 LBE for Microscale Binary Mixture Flows

8.5.1 *General formulation*

Most of available LBE methods for micro-flows focus on single component gases, and much less attention has been paid to gas-mixture

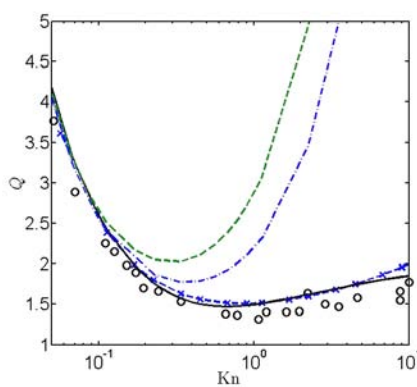

Fig. 8.5. Dimensionless mass rate of the Poiseuille flow against the Knudsen number. Solid line: MRT-LBE with effective relaxation times; Open circle: experimental data [Dong, 1956]; Dashed line with ×: solution of the Boltzmann equation [Ohwada *et al.*, 1989]; Dashed line: MRT-LBE with the slip coefficients given in [Cercignani, 1988]; Dash-dotted line: MRT-LBE with slip coefficients given in [Hadjiconstantinou, 2003] (Guo *et al.*, Phys. Rev. E 77, 036707, 2008).

flows with a finite Knudsen number except for a few attempts. Arcidiacono *et al*. [2007] applied a LBE model based on the Hamel to the micro Couette flow, while Szalmás [2008] made a theoretical analysis of a similar LBE model and proposed a slip boundary condition. These studies were based on certain kinetic models of BGK formulation, which have some limitations for gas mixtures [Andries *et al*., 2002]. On the other hand, Guo *et al*. [2009] developed a LBE with a MRT collision operator for binary gas mixtures. The evolution equation of this model is

$$f_{\sigma i}(\boldsymbol{x}+\boldsymbol{c}_i\delta_t,t+\delta_t)-f_{\sigma i}(\boldsymbol{x},t)=-\sum_j(M^{-1}SM)_{ij}[f_{\sigma j}-f_{\sigma j}^{(eq)}], \quad (8.74)$$

where $f_{\sigma i}$ is the discrete distribution function for species σ (a or b) and $f_{si}^{(eq)}$ is the corresponding EDF, M is the transformation matrix and S is the diagonal matrix of the relaxation rates. It is noted that both M and S are assumed to be independent of the species in the model. Furthermore, the EDF for each species only depends on the individual density,

$$f_{\sigma i}^{(eq)}=w_i\rho_\sigma\left[\alpha_i^\sigma+\frac{\boldsymbol{c}_i\cdot\boldsymbol{u}}{c_s^2}+\frac{(\boldsymbol{c}_i\cdot\boldsymbol{u})^2}{2c_s^4}-\frac{\boldsymbol{u}^2}{2c_s^2}\right], \quad (8.75)$$

where ρ_σ is the species mass density, $\boldsymbol{u}$ is the mixture velocity, and the model parameter $c_s^2=RT$ with $R=k_B/m_r$ is the gas constant with k_B the Boltzmann constant, while $m_r=\min(m_a, m_b)$ is the reference mass (m_σ is the molecular mass), and T is the temperature. Additionally, α_i^σ is a parameter dependent on the molecular mass m_σ and the particle velocity $\boldsymbol{c}_i$. For example, $\alpha_i^\sigma=s_\sigma=m_r/m_\sigma$ for $i\neq 0$ and $\alpha_0^\sigma=(9-5s_\sigma)/4$ in the D2Q9 model,. The mass density ρ and velocity $\boldsymbol{u}$ of the mixture and those of the species (ρ_σ and u_σ) are defined respectively as

$$\rho=\sum_\sigma\sum_i f_{\sigma i},\ \rho\boldsymbol{u}=\sum_\sigma\sum_i\boldsymbol{c}_i f_{\sigma i},\ \rho_\sigma=\sum_i f_{\sigma i},\ \rho_\sigma\boldsymbol{u}_\sigma=\frac{2\tau_d-1}{2\tau_d}\sum_i\boldsymbol{c}_i f_{\sigma i}+\frac{\rho_\sigma\boldsymbol{u}}{2\tau_d}, \quad (8.76)$$

where τ_d is the relaxation time relating to the diffusion flux. The number densities of each species and the mixture are defined as $n_\sigma=\rho_\sigma/m$ and the $n=n_a+n_b$.

For the D2Q9 model with the collision matrix given in Chapter 1, the relaxation matrix for the velocity moments $m_\sigma=(\rho_\sigma, e_\sigma, \varepsilon_\sigma, j_{\sigma x}, q_{\sigma x}, j_{\sigma y},$

$q_{\sigma y},\ p_{\sigma xx}, p_{\sigma xy})^T$ is

$$S = \mathrm{diag}(\tau_\rho, \tau_e, \tau_\varepsilon, \tau_d, \tau_q, \tau_d, \tau_q, \tau_s, \tau_s)^{-1}. \tag{8.77}$$

Because ρ_σ is a conserved variable, τ_ρ can take any value while the other relaxation times should be chosen according to the transport coefficients or boundary conditions, as will be shown later. In the incompressible limit, the hydrodynamic equations corresponding to the above MRT-LBE include

$$\partial_t \rho_\sigma + \nabla \cdot (\rho_\sigma \boldsymbol{u}_\sigma) = 0\,, \tag{8.78}$$

$$\partial_t \rho + \nabla \cdot (\rho \boldsymbol{u}) = 0\,, \tag{8.79}$$

$$\partial_t (\rho \boldsymbol{u}) + \nabla \cdot (\rho \boldsymbol{u}\boldsymbol{u}) = -\nabla p + \nabla \cdot \boldsymbol{S}\,, \tag{8.80}$$

where the first equation is the mass conservation equation for each species, and the other two are the Navier-Stokes equations for the mixture. The total pressure p is the sum of the partial pressures, $p = p_a + p_b = nk_BT$, and the stress tensor $\boldsymbol{S}$ is

$$S_{\alpha\beta} = \mu\left[\partial_\alpha u_\beta + \partial_\beta u_\alpha\right], \tag{8.81}$$

where the dynamic viscosity of the mixture is

$$\mu = \rho\nu = c_s^2 \rho \left(\tau_s - \frac{1}{2}\right)\delta_t\,, \tag{8.82}$$

and the bulk viscosity of each species is given by

$$\zeta_\sigma = c_s^2 (2 - s_\sigma)\left(\tau_e - \frac{1}{2}\right)\delta_t\,. \tag{8.83}$$

On the other hand, the diffusion coefficient is related to the relaxation time τ_d,

$$D_{\sigma\varsigma} = \frac{m_r \rho}{m_\sigma m_\varsigma n} c_s^2 \left(\tau_d - \frac{1}{2}\right)\delta_t\,. \tag{8.84}$$

Therefore, the Schmidt number of the mixture is

$$\mathrm{Sc} \equiv \frac{\nu}{D_{\sigma\varsigma}} = \frac{m_a m_b n}{m_r \rho} \frac{\tau_s - 0.5}{\tau_d - 0.5}\,, \tag{8.85}$$

which can be tuned by changing τ_s and τ_d.

8.5.2 *Extension to micro flows*

In order to simulate microscale flows of binary mixtures using the above MRT-LBE, two fundamental problems similar to those in the LBE for simple gas flows should be addressed first, i.e., (i) incorporating the Knudsen effect into the LBE, and (ii) prescribing a suitable kinetic boundary condition. These two topics will be discussed in order next.

First we discuss the relationship between the relaxation times and the mean-free-paths of the individual species and the mixture. From the Chapman-Enskog analysis of the Boltzmann equation, it is known that the dynamic viscosity and mutual diffusivity of a binary mixture can be expressed as [Cercignani, 1988],

$$\mu = \frac{x_a^2 R_a + x_b^2 R_b + x_a x_b R'_{ab}}{x_a^2 R_a/\mu_a + x_b^2 R_b/\mu_b + x_a x_b R_{ab}}, \quad D_{ab} = \frac{3E}{2nm_0}, \tag{8.86}$$

where $m_0 = m_a + m_b$, $x_\sigma = n_\sigma / n$ is the concentration, and

$$R_\sigma = \frac{2}{3} + \frac{m_\sigma}{m_\varsigma} A, \quad R'_{ab} = T_a + T_b, \quad R_{ab} = \frac{E}{2\mu_a \mu_b} + \frac{4A}{3EM_a M_b}, \tag{8.87}$$

with

$$T_\sigma = \frac{E}{2\mu_\sigma} + \frac{2}{3} - A, \quad M_\sigma = \frac{m_\sigma}{m_0}. \tag{8.88}$$

The parameter A and E depend on the inter-molecular potential. For instances, for a binary mixture of hard-sphere molecules, they are given by [Cercignani, 1988],

$$A = \frac{2}{5}, \quad E = \sqrt{\frac{2k_B T m_0}{\pi M_a M_b}} \frac{1}{8d_{ab}^2}, \tag{8.89}$$

where $d_{ab} = (d_a + d_b)/2$ with d_σ being the molecule diameter of species σ. It is clear that the viscosity and diffusivity of the mixture are both complicated functions of the individual viscosities and concentrations.

On the other hand, the mean-free-path of each species and the mixture, λ_σ and λ, are related to the individual and mixture viscosities,

$$\lambda_\sigma = \frac{\mu_\sigma}{p_\sigma} \sqrt{\frac{\pi k_B T}{2m_\sigma}}, \quad \lambda = \frac{\mu}{p} \sqrt{\frac{\pi k_B T}{2m_x}}, \tag{8.90}$$

where $m_x = \rho / n = x_a m_a + x_b m_b$. Therefore, the relaxation time τ_s can be determined from the mixture viscosity. For the D2Q9 model, the expression is

$$\lambda = \sqrt{\frac{\pi m_x}{2k_B T}} c_s^2 \left(\tau - \frac{1}{2}\right)\delta_t = \sqrt{\frac{\pi m_x}{3m_r}} \left(\tau_s - \frac{1}{2}\right)\delta_t . \tag{8.91}$$

The relaxation time τ_d can be related to the mean-free-path through the diffusivity. For instance, for a binary mixture of hard sphere gases, the mean-free-path of each species is

$$\lambda_\sigma = \frac{1}{\sqrt{2} n_i \pi \sigma_i^2}, \tag{8.92}$$

and the mutual diffusivity is

$$D_{ab} = \frac{3E}{2nm_0} = \frac{3}{2}\sqrt{\frac{m_0 k_B T}{m_a m_b}} \left[\frac{1}{\sqrt{x_a \lambda_a}} + \frac{1}{\sqrt{x_b \lambda_b}}\right]^{-2}. \tag{8.93}$$

Therefore, from Eq. (8.84) we can obtain that

$$\left(\tau_d - \frac{1}{2}\right)\delta_t = \frac{3}{2}\sqrt{\frac{3m_0 m_a m_b}{m_r m_x^2}} \left[\frac{1}{\sqrt{x_a \lambda_a}} + \frac{1}{\sqrt{x_b \lambda_b}}\right]^{-2}. \tag{8.94}$$

Based on the definition of the Knudsen number, τ_s and τ_d can also be recast in terms of the Knudsen numbers of the mixture and/or species.

Now we come to the kinetic boundary conditions for the binary MRT-LBE. A BSR scheme was designed to specify the slip boundary condition by Guo *et al*. [2009]. The formulation is similar to that for the single component LBE models. Again consider the flat surface case as sketched in Fig. 8.1, the BSR scheme is expressed as

$$\begin{cases} f_{\sigma 2} = f'_{\sigma 4}, \\ f_{\sigma 5} = r_\sigma f'_{\sigma 7} + (1 - r_\sigma) f'_{\sigma 8} + 2 r_\sigma \rho_\sigma \omega_i \boldsymbol{c}_5 \cdot \boldsymbol{u}_w / 2c_s^2, \\ f_{\sigma 6} = r_\sigma f'_{\sigma 8} + (1 - r_\sigma) f'_{\sigma 7} + 2 r_\sigma \rho_\sigma \omega_i \boldsymbol{c}_6 \cdot \boldsymbol{u}_w / 2c_s^2, \end{cases} \tag{8.95}$$

where $f'_{\sigma i}$ is the post-collision distribution function, and r_σ represents the bounce-back portion, which can vary for different species. For the half

space shear flow over a stationary wall (i.e., the Kramers problem) where the wall is located at $y=0$ and the gas is sheared by imposing a constant velocity gradient at $y=\infty$, the velocity profiles of each species and the mixture can be obtained from the MRT-LBE:

$$u_\sigma = u_s + \gamma y + k_\sigma e^{-By}\,,\; u = u_s + \gamma y\,,\; B=\left[\nu\left(2\tau_d + \tau_q - \frac{3}{2}\right)\delta_t\right]^{-1/2}\,, \quad (8.96)$$

where $\gamma = du/dy\ (y\to\infty)$ is the applied constant velocity gradient, u_s is the slip velocity at the wall, and k_σ is a constant that satisfies $\rho_a k_a + \rho_b k_b = 0$.

Both u_s and k_σ are complex functions of the relaxation times (τ_s, τ_q and τ_d), the mass concentrations, the parameters r_a and r_b, and the lattice spacing [Guo *et al*., 2009]. However, under the assumption that $r_a = r_b = r$, the expression can be simplified as:

$$u_s = \frac{(1-r)}{r}\frac{\nu\gamma}{c_s^2}\,,\quad k_\sigma = 0\,. \quad (8.97)$$

On the other hand, the slip velocity for the Kramers problem can be obtained from the solution of the linearized Boltzmann equation for binary mixtures [Ivchenko *et al*., 1997],

$$u_s = c_m\lambda\gamma\,, \quad (8.98)$$

where the parameter c_m depends on the molecular properties and gas-wall interactions,

$$c_m = \frac{pM^{1/2}}{\mu}\frac{5\pi}{8}\sum_\sigma\left[(2-\alpha_\sigma)x_\sigma b_\sigma\left(K_1 + \frac{4b_\sigma}{\pi M_\sigma^{1/2}}K_2\right)\right]\,, \quad (8.99)$$

where $0<\alpha_\sigma\le 1$ is the accommodation coefficient of the gas-wall interaction for σ species, and $M = m_x/m_0$; b_σ is related to the intermolecular potential of the gases [Chapman and Cowling, 1970],

$$b_\sigma = \frac{x_\sigma R_\sigma + x_\varsigma T_\varsigma}{p[x_a^2 R_a/\mu_a + x_b^2 R_b/\mu_b + x_a x_b R_{ab}]}\,. \quad (8.100)$$

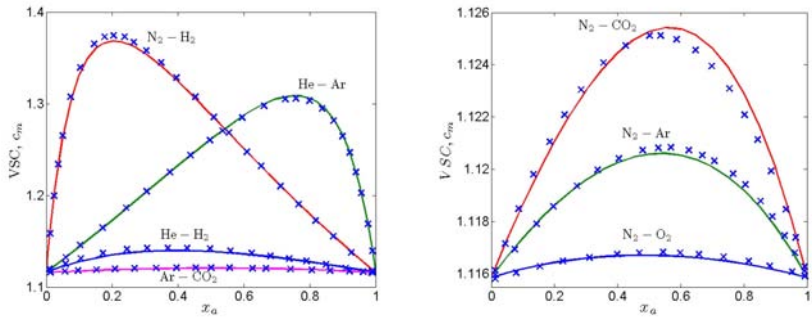

Fig. 8.6. Velocity slip coefficient as a function of concentration of the first species (α_a=α_b). Solid line: LBE results; Symbol: results of linearized Boltzmann equation [Ivchenko *et al*., 1997] (Guo *et al.*, Phys. Rev. E 79, 026702, 2009).

The two parameters K_1 and K_2 in Eq. (8.99) are given by

$$K_1 = \frac{\sum_\sigma (2-\alpha_\sigma) x_\sigma b_\sigma}{\sum_\sigma \alpha_\sigma x_\sigma M_\sigma^{1/2}} K_2 \ , \ K_2 = \frac{1}{4(x_a b_a + x_b b_b)} = \frac{p}{4\mu} \ . \quad (8.101)$$

Comparing Eqs. (8.97) and (8.98), we can see that if the control parameter r in the BSR scheme is chosen as

$$r = \left[1 + \frac{c_m}{3}\sqrt{\frac{\pi m_x}{2k_B T}}\right]^{-1} = \left[1 + c_m \sqrt{\frac{\pi m_x}{6m_r}}\right]^{-1} \ , \quad (8.102)$$

the slip velocity of the MRT-LBE with the BSR scheme matches that of the Boltzmann equation for the Kramers' flow. In the limiting case of $m_a = m_b$, the above result is consistent with that for a simple gas, i.e., Eq. (8.54).

The above LBE model together with the BSR boundary condition was used to simulate the Kramers flow of some binary mixtures, where the gases were modeled as hard-sphere molecules [Guo *et al*., 2009]. The accommodation coefficients of the wall are assumed to be 1 for both species. In Fig. 8.6 the simulated velocity slip coefficients (VSC) are shown as a function of the mole fraction of species *a*, and the results are compared with those of the linearized Boltzmann equation [Ivchenko *et al*., 1997] for Lennard-Jones gases. It is clearly observed that in each

case the simulated VSC is in good agreement with the results of the Boltzmann equation, and its nonlinear dependence on the mole concentration is also clearly shown. The discrepancies can be attributed to the different treatments of the intermolecular interactions in the two methods.

8.6 Summary

The study of fluid flows at micro-scales is a demanding research topic in modern fluid mechanics. The traditional continuum methods suffer from many limitations for such flows, while the LBE method exhibits some appealing features in modeling and simulating such kind of flows due to its kinetic nature. In this chapter, the recent advances of LBE for micro gas flows have been presented. Contrary to the intuition about LBE, the analysis shows that attention should be paid before applying this method to such flows even in the slip regime. Particularly, the τ-Kn relationship and the discrete effects in the boundary conditions should be taken into account carefully. It was also shown that the Knudsen layer takes an important role in gaseous micro-flows. For flows in the slip regime, the effects of the Knudsen layer can be well modeled by a suitable slip boundary condition, while in the transition regime, the effects of the Knudsen layer should be captured by high-order LBE models which employ a large set of discrete velocities, or by effective LBE models in which the Knudsen layer effects are incorporated. LBE for micro flows of binary mixtures was also discussed, but it is still a challenging topic to devise LBE model for mixtures with more species.

LBE methods for micro flows with heat transfer, micro liquid flows, and micro two-phase flows are not discussed in this chapter. But a variety of studies on these topics have been reported, and interested readers can refer to relevant literatures.

This page intentionally left blank

Chapter 9

Other Applications of LBE

In the last chapter of this book, we will talk about some applications of LBE in several other complex fluid systems, particularly particulate flows, flows in porous media, and turbulent flows. In addition, a hybrid method that combines LBE with the immersed boundary technique will be presented for flows with solid objects.

9.1 Applications of LBE for Particulate Flows

Particulate flows arise in many engineering applications. In such flows the fluid and solid particles interact with each other complicatedly. In numerical simulations, the particles can be treated in two different manners. One approach that is widely adopted in engineering applications is to treat a particle as one "mass point" without considering its size and shape. The fluid-particle interactions are usually described by some empirical relationships, and the motion of each particle can be tracked following the Lagrangian method. Usually, in this approach the coupling between the fluid phase and the particulate phase can be described in a "one-way" fashion or a "two-way" fashion. In the former case, only the effects of fluid on the particles are considered while the influences of particulate phase on the flow are neglected; in the latter case, on the other hand, the interactions between the fluid and particulate phase are considered from both sides.

The other approach is the finite-size particle method, where the shape and size of each particle are considered, and the particle surface is just treated as a boundary immersed in the fluid on which a suitable boundary condition is imposed. In this approach the translation motion and rotation of each particle are both tracked, where the hydrodynamic force and

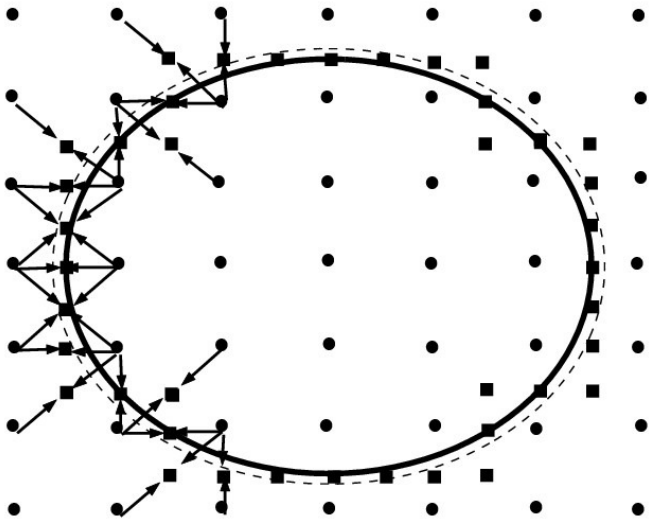

Fig. 9.1. Representation of a solid particle. ● Fluid node; ■ boundary node; thick solid line: real boundary; thin dashed line: kinematic boundary.

torques exerted on the particle by the fluid are obtained from the particle-fluid boundary conditions. The advantage of the finite-size method is that the details of the flow around the particles can be captured, which is important in the study of the fundamental mechanisms in particulate flows.

As an efficient numerical model, the LBE method has been used to simulate particulate flows following both point-source and finite-size approaches, which will be discussed in the next sections.

9.1.1 *LBE method with finite-size particles*

The first application of LBE to particulate flows with finite-size particles was attributed to Ladd [1994a, 1994b]. In this method the fluid flow is governed by the LBE, while each particle is treated as a moving object in the fluid. The particle shape and size are described based on the lattice employed by the LBE (see Fig. 9.1), where the boundary of the particle is represented by the mid-points of the lattice links. This approximation

introduces an error of order $O(\delta_x/r_p)$, where r_p is the radius of the particle and δ_x is the lattice spacing. This error usually makes the estimated radius a little larger than the real one. For instance, for a spherical particle the estimated radius is about $r_p + \Delta$, with $0 \le \Delta < \delta_x$. The magnitude of Δ depends on the relaxation time τ and the particle radius r_p, but is independent of the particle shape and the Reynolds number [Ladd and Verberg, 2001]. Apparently for a fine mesh this error can be ignored. In simulations we can use the corrected radius to improve the numerical accuracy.

It is noteworthy that in Ladd's method, the inner of a particle is also filled with a fluid of which the density is the same as the outer one while the viscosity can be different. Therefore, in this method the solid particle is actually represented by a solid shell, and during the motion of the particle both the inner and outer fluids can pass the shell freely. An advantage of this treatment is that the local mass and momentum are exactly conserved and no special technique is required as the fluid passes through the shell. However, the motion of the inner fluid will lead to some errors that depend on a dimensionless frequency

$$\omega' = \frac{\omega r_p^2}{\nu_i}, \tag{9.1}$$

where ω is the characteristic frequency and ν_i is the viscosity of the inner fluid. Numerical results show that the influence of the inner fluid is weak slightly as $\omega' < 1$. Obviously, this can be achieved by increasing the viscosity of the inner fluid. In this way, the LBE can be written as

$$f_i\left(\boldsymbol{x} + \boldsymbol{c}_i\delta_t, t + \delta_t\right) - f_i\left(\boldsymbol{x}, t\right) = \begin{cases} \Omega_i^{(i)}\left(f\right), & \text{solid nodes} \\ \Omega_i^{(o)}\left(f\right), & \text{fluid nodes} \end{cases}, \tag{9.2}$$

where $\Omega_i^{(i)}$ and $\Omega_i^{(o)}$ are the collision operators for the inner and outer fluids of the particle domains, respectively.

The dynamic equation of each solid particle is

$$M_p \frac{d\boldsymbol{u}_p}{dt} = \boldsymbol{F}_p, \quad \boldsymbol{I}_p \cdot \frac{d\boldsymbol{\omega}_p}{dt} = \boldsymbol{T}_p, \quad \frac{d\boldsymbol{x}_p}{dt} = \boldsymbol{u}_p, \tag{9.3}$$

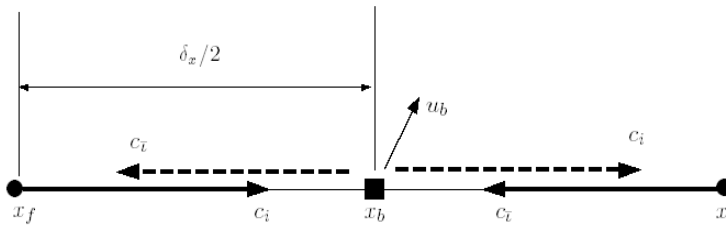

Fig. 9.2. Half-Way bounce back scheme of Ladd's LBE.

where M_p and $\boldsymbol{I}_p$ are the effective mass and moment of inertia of the particle, respectively, $\boldsymbol{u}_p$ and $\boldsymbol{\omega}_p$ are the respective translational velocity and angular velocity, while $\boldsymbol{F}_p$ and $\boldsymbol{T}_p$ are the respective total force and torque on the particle, and $\boldsymbol{x}_p$ is the mass center of the particle. If only hydrodynamic force of the fluid is considered, the total force and torque can be expressed as

$$\boldsymbol{F}_p(t) = \oint_S \boldsymbol{\sigma}(\boldsymbol{x}) \cdot \boldsymbol{n}\, dS\,, \tag{9.4}$$

$$\boldsymbol{T}_p(t) = \oint_S (\boldsymbol{x} - \boldsymbol{x}_p) \times [\boldsymbol{\sigma}(\boldsymbol{x}) \cdot \boldsymbol{n}]\, dS\,, \tag{9.5}$$

where $\boldsymbol{\sigma} = -p\boldsymbol{I} + \boldsymbol{\tau}$ is the stress tensor and S is the particle surface with $\boldsymbol{n}$ being the unit outward normal vector to the surface. The computation of Eqs. (9.4) and (9.5) involves velocity gradients and surface integrations, which may encounter difficulty for irregular particles. In LBE, however, the force and torque can be calculated in a much simpler way, as described below.

In Ladd's method, the solid-fluid interactions are realized by the half-way bounce back rule. As shown in Fig. 9.2, at a boundary point $\boldsymbol{x}_b$ where the discrete velocity $\boldsymbol{c}_i$ intersects with the boundary, the post-collision distribution functions located at $\boldsymbol{x}_s$ and $\boldsymbol{x}_f = \boldsymbol{x}_s - \boldsymbol{c}_i\delta_t$ can be written respectively as

$$f'_{\bar{i}}(\boldsymbol{x}_s, t) = f_{\bar{i}}(\boldsymbol{x}, t) + \Omega_{\bar{i}}^{(i)}(\boldsymbol{x}, t)\,, \quad f'_i(\boldsymbol{x}_f, t) = f_i(\boldsymbol{x}_f, t) + \Omega_i^{(o)}(\boldsymbol{x}, t)\,, \tag{9.6}$$

where $\boldsymbol{c}_{\bar{i}} = -\boldsymbol{c}_i$. After time $\delta_t/2$, these fluid particles move to the boundary node $\boldsymbol{x}_b$ and are bounced back, i.e.,

$$f'_i(\boldsymbol{x}_b, t + \delta_t/2) = f'_{\bar{i}}(\boldsymbol{x}_s, t) + 2\omega_i\rho\frac{\boldsymbol{c}_i \cdot \boldsymbol{u}_b}{c_s^2}\,, \tag{9.7}$$

$$f'_{\bar{i}}(\boldsymbol{x}_b, t+\delta_t/2) = f_i(\boldsymbol{x}_f, t) + 2\omega_{\bar{i}}\rho\frac{\boldsymbol{c}_{\bar{i}}\cdot\boldsymbol{u}_b}{c_s^2}, \tag{9.8}$$

where $\boldsymbol{u}_b = \boldsymbol{u}_p + \omega_p \times (\boldsymbol{x}_b - \boldsymbol{x}_p)$ is the velocity at the particle boundary $\boldsymbol{x}_b$, and ω_i is the weight coefficient of the EDF in the LBE model. After a time duration of $\delta_t/2$, these particles will move to the original locations but with an opposite velocity,

$$f_{\bar{i}}(\boldsymbol{x}_f, t+\delta_t) = f'_{\bar{i}}(\boldsymbol{x}_b, t+\delta_t/2), \quad f_i(\boldsymbol{x}_s, t+\delta_t) = f'_i(\boldsymbol{x}_b, t+\delta_t/2). \tag{9.9}$$

During the fluid-particle collision process, the momenta of the fluid and particle are exchanged. For those fluid particles starting from $\boldsymbol{x}_f$ and $\boldsymbol{x}_s$, represented by $f_i(\boldsymbol{x}_f)$ and $f'_{\bar{i}}(\boldsymbol{x}_s)$ respectively, the momentum changes before and after with the particle at $\boldsymbol{x}_b$ are

$$\begin{aligned}\delta\boldsymbol{m}_i(\boldsymbol{x}_b, t+\tfrac{\delta_t}{2}) &= \delta_x^D\left[\boldsymbol{c}_{\bar{i}} f'_{\bar{i}}(\boldsymbol{x}_b, t+\tfrac{\delta_t}{2}) - \boldsymbol{c}_i f_i(\boldsymbol{x}_f, t)\right] \\ &= -2\delta_x^D\left[f_i(\boldsymbol{x}_f, t) - \omega_i\rho\frac{\boldsymbol{c}_i\cdot\boldsymbol{u}_b}{c_s^2}\right]\boldsymbol{c}_i, \end{aligned}\tag{9.10}$$

$$\begin{aligned}\delta\boldsymbol{m}_{\bar{i}}(\boldsymbol{x}_b, t+\tfrac{\delta_t}{2}) &= \delta_x^D\left[\boldsymbol{c}_i f_i(\boldsymbol{x}_b, t+\tfrac{\delta_t}{2}) - \boldsymbol{c}_{\bar{i}} f'_{\bar{i}}(\boldsymbol{x}_s, t)\right] \\ &= 2\delta_x^D\left[f'_{\bar{i}}(\boldsymbol{x}_s, t) + \omega_i\rho\frac{\boldsymbol{c}_i\cdot\boldsymbol{u}_b}{c_s^2}\right]\boldsymbol{c}_i. \end{aligned}\tag{9.11}$$

Therefore, the force exerted by these fluid particles on the solid particle is

$$\begin{aligned}\boldsymbol{F}_i(\boldsymbol{x}_b, t+\tfrac{\delta_t}{2}) &= -\frac{\delta\boldsymbol{m}_i(\boldsymbol{x}_b, t+\frac{\delta_t}{2}) + \delta\boldsymbol{m}_{\bar{i}}(\boldsymbol{x}_b, t+\frac{\delta_t}{2})}{\delta_t} \\ &= \frac{2\delta_x^D}{\delta_t}\left[f_i(\boldsymbol{x}_f, t) - f'_{\bar{i}}(\boldsymbol{x}_s, t) - 2\omega_i\rho\frac{\boldsymbol{c}_i\cdot\boldsymbol{u}_b}{c_s^2}\right]\boldsymbol{c}_i. \end{aligned}\tag{9.12}$$

The corresponding torque at the location is

$$\boldsymbol{T}_i(\boldsymbol{x}_b, t+\tfrac{\delta_t}{2}) = (\boldsymbol{x}_b - \boldsymbol{x}_p)\times\boldsymbol{F}_i(\boldsymbol{x}_b, t+\tfrac{\delta_t}{2}). \tag{9.13}$$

As a result, the total force and torque experienced by the solid particle are respectively

$$\boldsymbol{F}_p(t+\tfrac{\delta_t}{2}) = \sum_{\boldsymbol{x}_b\in S}\sum_i \boldsymbol{F}_i(\boldsymbol{x}_b), \ \boldsymbol{T}_p\left(t+\tfrac{\delta_t}{2}\right) = \sum_{\boldsymbol{x}_b\in S}\sum_i \boldsymbol{T}_i(\boldsymbol{x}_b). \tag{9.14}$$

The above method for calculating the hydrodynamic force and torques on particles is the so-called "momentum-exchange" method, which avoids the differentiation and integration calculations in the integral method given by Eqs. (9.4) and (9.5). This method can be easily realized in the bounce back rule simultaneously, and thus results in only a slight increase in computation costs. Furthermore, the influences of the particle on the flow also appear naturally during this process, and other types of fluid-particle interaction forces, such as Brownian force caused by random perturbation, fluid lubrication force among particles, and the van der Waals force, can also be incorporated easily into LBE in this way.

After obtaining the force and torque, the dynamic equations of the particle can be solved numerically. Ladd suggested a leapfrog-scheme,

$$\boldsymbol{x}_p(t+\delta_t) = \boldsymbol{x}_p(t-\delta_t)\boldsymbol{u}_p(t)\,,\ \boldsymbol{u}_p(t+\delta_t) = \boldsymbol{u}_p(t-\delta_t) + 2\delta_t \boldsymbol{M}_p^{-1}\boldsymbol{F}_p(t)\,, \tag{9.15}$$

$$\omega_p(t+\delta_t) = \omega_p(t-\delta_t) + 2\delta_t \boldsymbol{I}_p^{-1}\cdot\boldsymbol{T}_p(t)\,, \tag{9.16}$$

where the force, torque and particle velocity at time t are obtained by averaging,

$$\phi(t) = \frac{1}{2}\big[\phi(t-\delta_t) + \phi(t+\delta_t)\big], \quad \phi = \boldsymbol{u}_p\,,\ \boldsymbol{F}_p\,,\ \omega_p\,. \tag{9.17}$$

The numerical stability of the above scheme depends on the density ratio of the fluid and particle [Ladd, 1994b; Ladd and Verberg, 2001]. It was pointed out that the leapfrog scheme is stable as

$$\frac{\rho_s}{\rho} > 1 + \frac{10\delta_x}{r_p}, \tag{9.18}$$

where $\rho_s = M_p/V_p + \rho$ is the real density of the particle and V_p is the volume of the particle. Obviously, a fine mesh should be used to approximate the solid particle as $\rho_s \approx \rho$.

The aforementioned approach is the basic LBE for particulate flows. Because of the requirement of $\rho_s/\rho > 1$ in this method, some improvements have been made later. For instance, Aidun *et al.* developed

a method without fluid inside the particle [Aidun and Lu, 1995; Aidun *et al.*,1998], which can be used for arbitrary density ratios in principle. However, when the particle moves some solid nodes covered by the particle originally can become fluid nodes at the new time step, and the associated distribution functions must be reconstructed. On the contrary, some fluid nodes can also become solid nodes during the particle motion, which means that some mass and momentum will be lost. Consequently, mass and momentum are not conserved in Aidun's LBE. Alternatively, a mass conservation LBE method was developed by Qi [1999] based on Ladd's method, where the inner of the solid particle is also filled with the fluid.

In the both improved LBE methods [Aidun and Lu, 1995; Qi, 1999], the force and torque are calculated from the outside fluid,

$$\boldsymbol{F}_i(\boldsymbol{x}_b, t+\tfrac{\delta_t}{2}) = -\frac{\delta \boldsymbol{m}_i(\boldsymbol{x}_b, t+\frac{\delta_t}{2})}{\delta_t} = \frac{2\delta_x^D}{\delta_t}\left[f_i'(\boldsymbol{x}_f, t) - \omega_i \rho \frac{\boldsymbol{c}_i \cdot \boldsymbol{u}_b}{c_s^2} \right] \boldsymbol{c}_i , \quad (9.19)$$

$$\boldsymbol{T}_i(\boldsymbol{x}_b, t+\tfrac{\delta_t}{2}) = (\boldsymbol{x}_b - \boldsymbol{x}_c) \times \boldsymbol{F}_i(\boldsymbol{x}_b, t+\tfrac{\delta_t}{2}) . \quad (9.20)$$

Furthermore, the both improved methods consider the effects of the nodes coming from or entering the solid particle. For a new solid node $\boldsymbol{x}_I$, it exerts a force and torque on the particle as

$$\boldsymbol{F}_I = \rho(\boldsymbol{x}_I)\boldsymbol{u}(\boldsymbol{x}_I), \quad \boldsymbol{T}_I = (\boldsymbol{x}_I - \boldsymbol{x}_p) \times \boldsymbol{F}_I . \quad (9.21)$$

Similarly, a newly generated fluid node coming from the particle will also exert a force and torque on the particle,

$$\boldsymbol{F}_o = -\rho(\boldsymbol{x}_o)\boldsymbol{u}(\boldsymbol{x}_o), \quad \boldsymbol{T}_o = (\boldsymbol{x}_o - \boldsymbol{x}_p) \times \boldsymbol{F}_o . \quad (9.22)$$

The total force and torque are then obtained by summing up the above three parts.

Some improvements on solving the particle dynamic equations have also been developed. For instance, Lowe *et al.* [1995] presented an implicit scheme with improved numerical stability, in which the hydrodynamic force on the particle is divided into three parts,

$$\boldsymbol{F}_p = \boldsymbol{F}_0 - \boldsymbol{\zeta}_u \cdot \boldsymbol{u}_p - \boldsymbol{\zeta}_\omega \cdot \boldsymbol{\omega} , \quad (9.23)$$

where $\boldsymbol{F}_0$ depends merely on the distribution function after collision,

$$\boldsymbol{F}_0(t+\tfrac{\delta_t}{2}) = \frac{\delta_x^D}{\delta_t}\sum_{\boldsymbol{x}_b\in S} 2f_i'(\boldsymbol{x}_f,t)\boldsymbol{c}_i\,, \tag{9.24}$$

while $\boldsymbol{\varsigma}_u$ and $\boldsymbol{\varsigma}_\omega$ are two matrixes defined by

$$\boldsymbol{\varsigma}_u = \frac{2\rho\delta_x^D}{c_s^2\delta_t}\sum_{\boldsymbol{x}_b\in S}\omega_i\boldsymbol{c}_i\boldsymbol{c}_i\,,\quad \boldsymbol{\varsigma}_\omega = \frac{2\rho\delta_x^D}{c_s^2\delta_t}\sum_{\boldsymbol{x}_b\in S}\omega_i\boldsymbol{c}_i(\boldsymbol{r}_b\times\boldsymbol{c}_i)\,. \tag{9.25}$$

The torque on the particle can be obtained similarly,

$$\boldsymbol{T} = \boldsymbol{T}_0 - \boldsymbol{\zeta}_u\cdot\boldsymbol{u}_p - \boldsymbol{\zeta}_\omega\cdot\boldsymbol{\omega}\,, \tag{9.26}$$

where $\boldsymbol{\zeta}_u$ and $\boldsymbol{\zeta}_\omega$ are two matrixes similar to ς_u and ς_ω. Then the translational velocity and angular velocity can be obtained by solving the following equation,

$$\frac{d\boldsymbol{X}}{dt} = \boldsymbol{A}\cdot\boldsymbol{X} + \boldsymbol{S}_p\,, \tag{9.27}$$

where $\boldsymbol{X} = (\boldsymbol{u}_p,\boldsymbol{\omega}_p)^T$, and $\boldsymbol{A}$ and $\boldsymbol{S}_p$ are the matrix and vector depending on $\boldsymbol{M}_p$ and $\boldsymbol{I}_p$. These algebra equations can be solved implicitly or explicitly with good numerical stability.

In the above LBE methods, the surface of a solid particle is represented by some zigzag points defined by the underlying lattice, which will introduce certain numerical errors inevitably. Later, some methods for curved boundary-conditions were introduced to represent the particle surface more accurately. For instance, Inamuro *et al*. [1995] used the boundary nodes $\boldsymbol{x}_b$ surrounding a particle to represent the surface, on which the distribution functions were determined by the counter-slip boundary condition. A smooth curve surface S was then used to match the discrete nodes, from which the force on the particle is calculated by Eqs. (9.4) and (9.5) where the stress tensor $\boldsymbol{\sigma}$ is obtained by interpolation based on the stress at the boundary node $\boldsymbol{x}_b$ [Inamuro *et al.*, 2000],

$$\boldsymbol{\sigma}(\boldsymbol{x}_b) = -\frac{1}{2\boldsymbol{\tau}}p\boldsymbol{I} - \left(1-\frac{1}{2\boldsymbol{\tau}}\right)\sum_i(\boldsymbol{c}_i-\boldsymbol{u})(\boldsymbol{c}_i-\boldsymbol{u})f_i\,. \tag{9.28}$$

Some boundary conditions for curved walls, as presented in Chapter 2, were also employed to represent a particle surface. For example, Li *et al*.

[2004] analyzed the difference between the momentum-exchange method and the integration method based on the FH scheme, Mei *et al.* [1999, 2002] investigated the force on the particle based on the MLS scheme, and found that for a fixed particle the momentum-exchange method yielded similar results as the integration method, while Lallemand and Luo [2003] applied the interpolation scheme to flows with moving particles. However, it should be noted that these methods are more or less more complicated than Ladd's method, although they can represent a particle more accurately.

9.1.2 *LBE method with point particles*

LBE method with finite-size particles is a true direct numerical simulation method for particulate flows, and is advantageous in exploring intrinsic mechanism of such flows. However, for flows with a large number of particles or when the flow domain is much larger than the particle size, the finite-size particle method is inappropriate due to the expensive computation costs. In such cases a more efficient approach is to treat a particle as a mass point and to describe the fluid-particle interactions with some semi-empirical models. Actually, some methods based on this idea have been developed, and two typical approaches will be presented below.

LBE-Lagrange method

In LBE-Lagrange method, the fluid motion is still governed by the LBE, but the motion of the particles is tracked by solving Eq. (9.3) in a Lagrangian manner without considering the rotation. The total force on the particle includes two parts, $\boldsymbol{F}_p = \boldsymbol{F}_h + \boldsymbol{F}_e$, where $\boldsymbol{F}_h$ and $\boldsymbol{F}_e$ are the hydrodynamic force and external force, respectively. Usually, $\boldsymbol{F}_h$ includes the drag force, Saffman force, added mass force, Basset force, and Magnus force, *etc.*, while $\boldsymbol{F}_e$ usually includes the gravity, electrostatic force, and van der Waals force.

In most applications, only the drag force is considered in $\boldsymbol{F}_h$. For example, the drag force of a single spherical particle can be expressed as

$$\boldsymbol{F}_d = \frac{\pi r_p^2}{2} C_d \rho \mid \boldsymbol{u} - \boldsymbol{u}_p \mid (\boldsymbol{u} - \boldsymbol{u}_p), \tag{9.29}$$

where C_d is the drag coefficient, which is the function of the particle Reynolds number $\mathrm{Re}_p = 2r_p|\boldsymbol{u} - \boldsymbol{u}_p|/\nu$. It is noteworthy that as a large number of particles exist in a region, the particle-particle collisions and hydrodynamic interactions will affect the drag force significantly, and the drag coefficient for a particle should be modified. After determining the forces on the particles, the dynamic equations can be solved numerically to obtain their velocities and positions. The influences of the particles on the flow can be treated following the "one-way" or "two-way" coupling approach, depending on flow conditions.

Filippova and Hänel [1997] were the first who made use of the LBE-Lagrangian method when they simulated the particle deposition process in a filter. In their simulation, only drag force was considered and the effects of the particles on the fluid were neglected. Later, with this method Lantermann and Hänel [2007] further considered the influences of the van der Waals force, electrostatic force, and Brownian force on the particles during the deposition and transportation processes in the filter.

LBE-LGA method

In the LBE-Lagrangian method, the trace of each particle is continuous and the particle location at each time step is not on the lattice usually. Masselot and Chopard [1998] presented an alternative LBE-LGA method in which solid particles also reside on the same lattice occupied by the LBE fluid. The evolution of solid particles can include a number of dynamic processes such as transportation, sinking, and erosion processes. A typical example of the LBE-LGA algorithm where the solid particles undergo the above dynamics can be implemented as follows:

(1) Transportation: Assume N solid particles exist on a lattice node $\boldsymbol{x}$, with the same speed $\boldsymbol{u}_p = \boldsymbol{u}(\boldsymbol{x},t) + \boldsymbol{u}_g$, where $\boldsymbol{u}$ is the fluid velocity and $\boldsymbol{u}_g$ is the velocity induced by the gravity. The time step of the solid particles δ_{pt} may be different from the LBE time step δ_t. In next time step, one of such solid particles will move to $\boldsymbol{x}_p = \boldsymbol{x} + \boldsymbol{u}_p\delta_{pt}$, which is generally not located on the lattice. The particle is then put on a lattice node with certain probability. For the D2Q9 model, the particle is set on the lattice node $\boldsymbol{x}' = \boldsymbol{x} + (r_1\boldsymbol{c}_1 + r_2\boldsymbol{c}_2 + r_3\boldsymbol{c}_3 + r_4\boldsymbol{c}_4)\delta_t$, where r_i is a random Boole variable which takes value 1 with

probability

$$p_i = \max\left\{0, \frac{\boldsymbol{c}_i \cdot \boldsymbol{u}_p \delta_{pt}}{\boldsymbol{c}_i^2 \delta_t}\right\}. \tag{9.30}$$

The computational efficiency can be improved by adjusting the particle time step δ_{pt}. Dupuis and Chopard [2002] also proposed a rule for the FHP model.

(2) Deposition: As a solid particle moves to a lattice node $\boldsymbol{x}_f$ close to the solid wall, the particle will stop moving to sink. If the particle number N on the site exceeds a critical number N_c, $\boldsymbol{x}_f$ will become a solid node, on which the bounce-back rule is implemented for other fluid particles.

(3) Erosion: In some cases, the deposited particles can be picked up by the fluid and reenter the flow domain. This erosion process depends on a number of factors such as the local flow velocities and particle concentration. The process can be implemented as follows: For each of the N_c solid particles deposited on a solid node with some neighboring fluid nodes, it is first thrown up with a probability p_e, then it will stream as usual if the local flow velocity is larger than a critical value, or just go back to original solid node otherwise. The erosion probability p_e usually depends on the particle properties such as the size, density, and shape, as well as particle interactions like friction and electrostatic force.

The above LBE-LGA method has been applied to a number of particulate flows. For example, Masselot and Chopard [1998] studied the effects of wind on snow patterns during transportation, while Dupuis and Chapord [2002] explored the scour formation under submarine pipelines. These studies show that the LBE-LGA method can reproduce many interesting phenomena that are in qualitatively agreement with the real world, although it is still difficult to obtain quantitative results due to the empirical parameters in the method.

9.2 Applications of LBE for Flows in Porous Media

Fluid flows in porous media (porous flows) are special fluid-solid systems where the solid matrix is usually fixed. Such flows are involved

in many areas such as oil and gas engineering, chemical engineering, and environmental science. Generally the velocity of the fluid in porous media is very low, and so such flow is also termed as "seepage flow" sometimes. Porous flow is a typical multiscale system, which usually involves three length scales, namely pore scale, representative elementary volume (REV) scale, and domain scale.

At pore scale, the fluid motion in micro pores are tracked by solving the Navier-Stokes equations, together with suitable boundary conditions imposed on the solid matrix. Therefore, the pore scale simulations can provide detailed flow information within the pores, which is important for understanding the fundamental mechanism of porous flows.

The REV scale is much larger than the pore scale. An REV is a control volume in a porous medium that contains many pores, and its size is much larger than the dimensions of pore but far less than the domain size of interest. At REV scale the porous medium can be viewed as a continuum medium, and some medium and fluid properties can be defined on REV such that they are constant throughout its volume. For example, the porosity at point $\boldsymbol{x}$ is defined as

$$\epsilon(\boldsymbol{x}) = \lim_{V(\boldsymbol{x})\to V_0(P)} \frac{V_f(\boldsymbol{x})}{V(\boldsymbol{x})}$$

where $V(\boldsymbol{x})$, $V_f(\boldsymbol{x})$, and $V_0(\boldsymbol{x})$ are the volumes of the control cell, the pores in the cell, and the basic REV centered around $\boldsymbol{x}$, respectively. Similarly, we can also define some apparent fluid quantities at the REV scale,

$$\phi(\boldsymbol{x},t) = \frac{1}{V(\boldsymbol{x})}\int_{V(\boldsymbol{x})} \phi_f(\boldsymbol{x}',t)d\boldsymbol{x}' \,, \tag{9.31}$$

where $\phi_f(\boldsymbol{x}',t)$ is a specific fluid quantity (e.g., density and velocity) within the pores of the REV. For flows in porous media, the fluid variables can be related through some empirical or semi-empirical models, and the most widely used model is the Darcy law,

$$\boldsymbol{u} = -\frac{K}{\mu}\nabla p \,, \tag{9.32}$$

where K is the permeability depending on the structure of the medium. An example is the well-known Kozeny-Carman relation [Bear, 1972], $K = \epsilon^3 / CS^2$, where S is the specific surface area of the medium and C is a structure-dependent constant.

As an effective numerical method, the LBE has also been successfully applied to porous flows. The applications of LBE for such flows follow two ways, i.e., pore-scale approach and REV approach. In the former approach the flows in the micro pores are described by the standard LBE straightforwardly, and the solid matrix is just treated as solid boundaries on which the bounce-back rule can be implemented. The pore structure is usually extremely irregular and much difficult to handle in classical CFD methods; The simple bounce-back rule, however, makes LBE an ideal tool for pore-scale simulations. Actually, the LBE has been used to study the fundamental mechanisms of porous flows of simple fluids as well as complex fluids such as multiphase fluids and non-Newtonian fluids. Pore-scale simulations with LBE are helpful for understanding the underlying physics of porous flows, which is key for developing REV-scale mathematical models. On the other hand, the pore-scale LBE approach requires the detailed knowledge of the pore structures, and so is limited to media with small dimensions.

On the other hand, LBE based on REV scale does not solve the flows in micro pores, but solve the averaged flows at REV scale. In this approach, the interaction between the fluid and the medium is described by some empirical models. The main advantage of such LBE is that only a few statistical parameters (e.g., porosity and permeability) are required, and so the computational efficiency is much higher than the pore-scale approach. Consequently, REV-scale LBE can be used for engineering problems. However, the accuracy of such simulations relies on the porous flow models. In what follows we will briefly describe the pore-scale and REV-scale LBE approaches.

9.2.1 *Pore-scale approach*

Pore-scale simulation of porous flows is a direct application of LBE, and the models described in previous chapters can be employed without difficulties. A key question for this approach is how to characterize the

pore structures. Generally, the distribution of a porous medium can be described by a phase function $Z(\boldsymbol{x})$, which takes value 1 if $\boldsymbol{x}$ is in the pore and value 0 otherwise. Usually the distribution of micro-pores in a porous medium is rather disorder, and so $Z(\boldsymbol{x})$ can be viewed as a random variable from which some statistical properties of the porous medium can be defined. For example, the porosity can be defined as $\epsilon = \langle \mathrm{Z}(\boldsymbol{x}) \rangle$, and another useful concept, autocorrelation function, can be defined as [Adler, 1992],

$$R_z(\boldsymbol{r}) = \frac{\big\langle (Z(\boldsymbol{x}) - \epsilon)(Z(\boldsymbol{x} + \boldsymbol{r}) - \epsilon) \big\rangle}{\epsilon(1 - \epsilon)}, \tag{9.33}$$

where the symbol $\langle \cdot \rangle$ represents the ensemble average operator. For an isotropic homogeneous medium, $R_z(\boldsymbol{r})$ is a one-dimensional function dependent on $r = |\boldsymbol{r}|$ only.

In pore-scale simulations the pore structure of the medium should be obtained in advance. For most natural porous media such as rocks, soil, and fibers, the data can be acquired by imaging devices such as X-ray computed tomography. On the other hand, some artificial porous media, which are constructed following some rules so that they can satisfy some required statistical properties, can also be employed in pore-scale simulations. For example, we can randomly select a node on a lattice as a solid one with a certain probability, or randomly place some solid objects in the domain, until a given porosity is reached. Some more sophisticated generating methods that could reflect some other statistical properties of the medium have been developed from different viewpoints, such as sphere sedimentation method [Pilotti, 1998], hard-sphere Monte-Carlo method [Maier *et al.*, 2000], score Brownian motion method [Madadi and Sahimi, 2003], random growth method [Zhang *et al.*, 2006], and quartet structure generation set method [Wang *et al.*, 2007].

After obtaining the structure of the medium, the standard LBE method can be applied to the fluid in the micro pores. A key issue in pore-scale simulations is the data structure arrangement. The most straightforward one is the *full-matrix* structure, which uses a lattice of size $N_x \times N_y \times N_z$ to cover the overall domain containing both the pores and the solid matrix, and defines a $N_x \times N_y \times N_z$ state matrix to identify fluid and solid nodes. The distribution functions f_i's $(i = 1 \sim Q)$ are

defined at both fluid and solid nodes, and are stored in a $Q \times N_x \times N_y \times N_z$ full matrix. In this way, the indices of adjacent nodes are naturally linked by the discrete velocities, which makes the realization of LBE easily. A major disadvantage of the full-lattice structure is the waste of memory and the reduction of computational efficiency due to the large amount of solid nodes. A more efficient data structure for implementation is to make use of the *sparse-matrix* technique [Axner *et al.*, 2008; Pan *et al.*, 2004; Schulz *et al.*, 2001], in which only the data at fluid nodes are stored together with an index list to identify neighboring nodes of each fluid node. In practical simulations, the data at fluid nodes and the list of neighboring nodes can be allocated and sorted before the calculation, which makes this technique very flexible and adaptable for pore-scale simulations.

The applications of pore-scale LBE can be dated back to 1989 when Succi *et al.* [1989] tested the Darcy law of a three-dimensional random porous medium, and a number of studies have been reported on this topic since then. For instances, Heijs and Lowe [1995] studied the Carman-Kozeny constant for two types of porous media, while Koponen *et al.* [1998] measured the permeability of fiber media and found that the permeability is an exponential function of the porosity, which coincides with experimental results. Pan *et al.* [2001] studied the relationship between the permeability and the Reynolds number Re for random porous media constituted by spheres. They found that the LBE results agreed with experimental data well as Re is small, and were consistent with the Ergun relation for large values of Re. Furthermore, it was found that the relaxation time of the LBGK model affected the convergence rates and accuracy due to the artifacts in the bounce-back boundary conditions, and they suggested that the problem could be avoided by making use of the MRT-LBE models [Pan *et al*., 2006]. Manz *et al.* [1999] also performed some pore-scale simulations for flows in real porous media at different Reynolds numbers, and the numerical results were in quantitatively agreement with experimental data. Inamuro *et al.* [1999] studied the relationship between the pressure drop and the Reynolds number in a rectangular three-dimensional porous structure consisting of nine identical spherical bodies, and the numerical results

were consistent with the Blake-Kozeny correlation for low Reynolds numbers and with the Ergun correlation for high Reynolds numbers.

Besides flows of simple fluids, LBE has also been employed to study porous flows of complex fluids at pore scale. As early as 1993, Gunstensen and Rothman [1993] simulated the two phase flows in porous media via the color LBE model, and soon Martys and Chen [1996] simulated the two-phase flows in porous media with different wetting properties using the Shan-Chen model. In their method, the interaction force between component σ and the solid matrix is modeled as

$$\boldsymbol{F}_\sigma(\boldsymbol{x}) = -\rho_\sigma(\boldsymbol{x})\sum_i G_i^\sigma s(\boldsymbol{x}+\boldsymbol{c}_i\delta_t)\boldsymbol{c}_i\,, \tag{9.34}$$

where the Boolean variable s takes 0 or 1 for a fluid or solid node. By adjusting the interaction strength G_i^σ, the wetting property of the solid can be changed. With this method, the relative permeabilities of some fluids in sandstones were measured, which were in quantitative agreement with experimental results. Hatiboglu and Babadagli [2007, 2008] also applied the Shan-Chen models to investigate the miscible and immiscible flows in oil-saturated porous media, while Psihogios *et al.* [2007] performed some pore-scale simulations of non-Newtonian fluid flows. Up to date, pore-scale simulations of flows of simple/complex fluids in porous media are still an active topic.

9.2.2 *REV-scale approach*

Unlike pore-scale approach, an LBE at REV scale solves the average flow of an *effective fluid* in porous media. The input data for a REV-LBE model are statistical properties of the medium such as porosity and permeability rather than detailed pore structures. A variety of such models have been devised from different viewpoints, which will be briefly presented below.

LBE based on Brinkman model

The Brinkman model is an extension of the Darcy model by including an viscous term,

$$\nabla p = -\frac{\mu}{K}\boldsymbol{u} + \mu_e\nabla^2\boldsymbol{u}\,, \tag{9.35}$$

where μ_e is an effective viscosity that can be different from the fluid viscosity. This viscous term is important if a solid wall exists in porous media. Several LBE models based on the Brinkman model have been developed.

The first Brinkman-LBE model was constructed based on the pore-scale LBE by Dardis and McCloskey [1998] who combined the bounce-back rule with the evolution of LBE,

$$f_i(\boldsymbol{x}+\boldsymbol{c}_i\delta_t, t+\delta_t) - f_i(\boldsymbol{x},t) = -\frac{1}{\tau}\left[f_i - f_i^{(eq)}\right] + \Delta_i(\boldsymbol{x},t)\,, \qquad (9.36)$$

where $\Delta_i(\boldsymbol{x},t)$ represents the effect of the collisions between fluid particles and solid matrix,

$$\Delta_i(\boldsymbol{x},t) = n_s(\boldsymbol{x}+\boldsymbol{c}_i\delta_t)\left[f_{\bar{i}}(\boldsymbol{x}+\boldsymbol{c}_i\delta_t,t) - f_i(\boldsymbol{x},t)\right], \qquad (9.37)$$

in which n_s is a continuous variable between 0 and 1 that represents the average scattering density of each solid node. The value of n_s depends on the state variable s of the node ($s=0$ for a solid node and 1 for a fluid node), and satisfies $n_s = 1$ if $s=1$ and $n_s = 0$ as $s=0$. It is obvious that $\Delta_i = 0$ as $s=0$, and in this case Eq. (9.36) describes the fluid flow within pores; as $s=1$, the effect of Δ_i is similar to the bounce-back rule at a solid node. In this LBE model, the average density and velocity are defined as those in the standard LBE,

$$\rho = \sum_i f_i\,, \quad \rho\boldsymbol{u} = \sum_i \boldsymbol{c}_i f_i\,. \qquad (9.38)$$

The additional collision term Δ_i in Eq. (9.36) essentially represents the resistance of the solid medium. Actually, an analysis of the pressure-driven flow between the two flat walls shows that the hydrodynamic equation corresponding to the above Brinkman-LBE is

$$\mu\frac{\partial u^2}{\partial y^2} - \rho\alpha u = \frac{\partial p}{\partial x}\,, \qquad (9.39)$$

where x is the flow direction and u is the corresponding velocity component, while $\alpha = 2n_s$ is the resistance parameters. Comparing Eq. (9.39) with the Brinkman model (9.35), it can be identified that

$$\mu_e = \mu\,,\ K = \frac{\mu}{\rho\alpha} = \frac{\mu}{2\rho n_s}\,. \qquad (9.40)$$

These results indicate that the Dardis-McCloskey model (DM-LBE) actually solves the Brinkman equation (9.35).

Spaid and Phelan [1997] also developed a LBE model (SP-LBE) that solves the Brinkman equation directly. This model includes the fluid-solid interaction by modifying the velocity of the equilibrium distribution, just as the treatment of the body force in the Shan-Chen multiphase model. Thus the SP-LBE can be expressed as

$$f_i(\boldsymbol{x} + \boldsymbol{c}_i\delta_t, t + \delta_t) - f_i(\boldsymbol{x}, t) = -\frac{1}{\tau}\left[f_i - f_i^{(eq)}\right], \tag{9.41}$$

where the velocity in the equilibrium distribution function $f_i^{(eq)}(\rho, \boldsymbol{u}^{(eq)})$ is defined by

$$\boldsymbol{u}^{(eq)} = \boldsymbol{u} + \frac{\tau \boldsymbol{F}}{\rho}, \tag{9.42}$$

where $\boldsymbol{F} = -\mu\boldsymbol{u}/K$ is the medium resistance. The definitions of the apparent density and velocity are still given by Eq. (9.38). As discussed in Chapter 3, the inclusion of the resistance force in this way will introduce some errors into the recovered equations. After neglecting these errors, the macroscopic equation corresponding to the SP-LBE is the Brinkman equation for steady flows. With this LBE, Spaid and Phelan [1997, 1998] studied some porous flows involving fibber media. Martys [2001] developed an improved version of the SP-LBE, in which the resistance force was included in the model following the method by Luo [1998]. Apparently this approach is still insufficient to overcome the artefacts induced by the force.

LBE based on a generalized model

For isothermal flows of incompressible fluids in porous media, some more general models beyond the Darcy and Brinkman models have been developed. For example, Nithiarasu *et al*. [1997] proposed a generalized model that contains the linear resistance (Darcy) term, the viscous (Brinkman) term, and the non-linear resistance (Forchheimer) term. The model can be expressed in a formulation of generalized Navier-Stokes equations,

$$\nabla \cdot \boldsymbol{u} = 0\,, \tag{9.43}$$

$$\frac{\partial \boldsymbol{u}}{\partial t} + (\boldsymbol{u}\cdot\nabla)\left(\frac{\boldsymbol{u}}{\epsilon}\right) = -\frac{1}{\rho}\nabla(\epsilon p) + \nu_e\nabla^2\boldsymbol{u} + \boldsymbol{F}\,, \tag{9.44}$$

where ρ is the fluid density, $\boldsymbol{u}$ and p are the apparent velocity and pressure, ν_e is the effective viscosity, $\boldsymbol{F}$ is the total force including both the medium resistance and external forces,

$$\boldsymbol{F} = -\frac{\epsilon\nu}{K}\boldsymbol{u} - \frac{\epsilon F_\epsilon}{\sqrt{K}}|\boldsymbol{u}|\boldsymbol{u} + \epsilon\boldsymbol{G}\,, \tag{9.45}$$

where ν is the fluid viscosity and $\boldsymbol{G}$ is the external body force. The structure function F_ϵ depends on the permeability K and the porosity ϵ. For example, for a porous medium composed of solid particles, the Ergun correlation gives [Ergun, 1952],

$$F_\epsilon = \frac{1.75}{\sqrt{150\epsilon^3}},\quad K = \frac{\epsilon^3 d_p^2}{150(1-\epsilon)^2}\,, \tag{9.46}$$

where d_p is the solid particle diameter. It can be found that in the absence of porous medium ($\epsilon \to 1$), the generalized Navier-Stokes equation (9.44) reduces to the standard Navier-Stokes equations. The second term on the right side of Eq. (9.44) is the Brinkman viscous term which is important near a wall. In many cases, the boundary layer of porous flows is very thin and this term can be neglected. However, for problems involving heat and/or mass transfer through boundaries, this term must be included. In the total force defined by Eq. (9.45), the first and second terms are the linear (Darcy) and nonlinear (Forchheimer) resistance forces, respectively. For high-speed flows, the nonlinear resistance must be considered, but for low-speed flows it can be ignored and in this case Eq. (9.44) reduces to the Brinkman equation.

Guo and Zhao [2002] constructed a LBE model which can be used to solve the generalized Navier-Stokes equations (9.43) and (9.44). The evolution equation is

$$f_i(\boldsymbol{x}+\boldsymbol{c}_i\delta_t, t+\delta_t) - f_i(\boldsymbol{x},t) = -\frac{1}{\tau}\Big[f_i(\boldsymbol{x},t) - f_i^{(eq)}(\boldsymbol{x},t)\Big] + \delta_t F_i\,, \tag{9.47}$$

where

$$f_i^{(eq)} = \omega_i\rho\left[1 + \frac{\boldsymbol{c}_i\cdot\boldsymbol{u}}{c_s^2} + \frac{\boldsymbol{u}\boldsymbol{u}:\left(\boldsymbol{c}_i\boldsymbol{c}_i - c_s^2\boldsymbol{I}\right)}{2\epsilon c_s^4}\right], \tag{9.48}$$

$$F_i = \omega_i \rho \left(1 - \frac{1}{2\tau}\right)\left[\frac{\boldsymbol{c}_i \cdot \boldsymbol{F}}{c_s^2} + \frac{\boldsymbol{u}\boldsymbol{F} : \left(\boldsymbol{c}_i \boldsymbol{c}_i - c_s^2 \boldsymbol{I}\right)}{\epsilon c_s^4}\right]. \tag{9.49}$$

It noted the porosity is included in both the equilibrium distribution function and the force term in this model. Particularly, as $\epsilon = 1$, both $f_i^{(eq)}$ and F_i reduce to the standard ones. In addition, with these definitions the discrete errors induced by the forcing term are removed.

As in the standard LBE, the density and velocity of flow are defined as

$$\rho = \sum_i f_i \,,\ \rho \boldsymbol{u} = \sum_i \boldsymbol{c}_i f_i + \frac{\delta_t}{2} \rho \boldsymbol{F} \,. \tag{9.50}$$

Because the force $\boldsymbol{F}$ also contains the flow velocity $\boldsymbol{u}$, Equation (9.50) is a non-linear equation of the velocity $\boldsymbol{u}$, which can be solved explicitly to give

$$\boldsymbol{u} = \frac{\boldsymbol{v}}{c_0 + \sqrt{c_0^2 + c_1 |\boldsymbol{v}|}}, \tag{9.51}$$

where $\boldsymbol{v}$ is a temporary velocity defined by

$$\rho \boldsymbol{v} = \sum_i \boldsymbol{c}_i f_i + \frac{\delta_t}{2} \epsilon \rho \boldsymbol{G} \,, \tag{9.52}$$

and the parameters c_0 and c_1 are given by

$$c_0 = \frac{1}{2}\left(1 + \epsilon \frac{\delta_t}{2} \frac{\nu}{K}\right),\ c_1 = \epsilon \frac{\delta_t}{2} \frac{F_\epsilon}{\sqrt{K}} \,. \tag{9.53}$$

The corresponding macroscopic equations can be obtained by the Chapman-Enskog analysis of the LBE (9.47), which can be written as

$$\frac{\partial \rho}{\partial t} + \nabla \cdot (\rho \boldsymbol{u}) = 0 \,, \tag{9.54}$$

$$\frac{\partial (\rho \boldsymbol{u})}{\partial t} + \nabla \cdot \left(\frac{\rho \boldsymbol{u}\boldsymbol{u}}{\epsilon}\right) = -\nabla(\epsilon p) + \nabla \cdot \left[\rho \nu_e (\nabla \boldsymbol{u} + \boldsymbol{u} \nabla)\right] + \rho \boldsymbol{F} \,, \tag{9.55}$$

where $p = c_s^2\rho/\epsilon$ and $\nu_e = c_s^2(\tau - 0.5)\delta_t$. In the incompressible limit, the above equations become the generalized Navier-Stokes equations (9.43) and (9.44).

The LBE for the generalized porous flows (GLBE) is a unified model that can be used for flows in different media by choosing different values of porosity and permeability. Particularly, it can be applied to free flows and porous flows within the same framework: in the porous medium the porosity and permeability are set as those of the medium, and in the free flow area we can set $\epsilon = 1$ and $K \to \infty$. Furthermore, if we set $F_\epsilon = 0$, the GLBE reduces to a simplified LBE model (SLBE) for the Brinkman equation (9.35). However, it should be emphasized that even this SLBE is different from the previous SP-LBE and the improved version of Martys: First, the inclusion of the resistance force in these models are different, and the SLBE model can accurately recover the desired macroscopic equations; And second, the porosity is included in the equilibrium distribution function of the GLBE and SLBE, which reflects the characteristics of the media, while those of the two SP-LBE models are just the same as that of the standard LBE for free flows.

9.3 Applications of LBE for Turbulent Flows

Simulation of turbulent flows is a challenging topic in computational fluid dynamics. Generally, numerical methods for turbulence can be classified into three types according to the resolved scales, i.e., direct numerical simulation (DNS) method, large-eddy simulation (LES) method, and Reynolds-averaged Navier-Stokes (RANS) method. The DNS solves the Navier-Stokes equations without any turbulence models, and the whole range of spatial and temporal scales of the turbulence is resolved. Therefore, the resolution of the computational mesh in DNS must be fine enough to capture the eddies with sizes ranging from the smallest dissipative scale (Kolmogorov scale) up to the integral scale (characteristic length of the domain). Turbulence theory shows that the number of grid points in DNS of three-dimensional turbulences is about $O(\mathrm{Re}^{9/4})$, where Re is the turbulent Reynolds number. Therefore the computational costs of DNS are rather expensive for high Reynolds

number turbulent flows. Unlike DNS, the LES solves only the large scale flows by filtering the Navier-Stokes equations with a spatial filter, and the unresolved small scale dynamics is modeled using certain sub-grid scale (SGS) models. Therefore, the range of resolved scales in LES is much smaller than that in DNS, and so the computational costs are significantly reduced. The RANS are ensemble averaged equations of the Navier-Stokes equations, with certain turbulence models to close the additional stress (Reynolds stress) induced by the fluctuations. The RANS method solves only the mean flow at macro scales, and is so the most economical method for turbulence simulation in engineering applications. As a new CFD method, the LBE has also found its applications in turbulence simulations following the above three frameworks.

9.3.1 *LBE-DNS approach*

As discussed in Chapter 2, the LBE can be viewed as a numerical solver for the incompressible Navier-Stokes equations. Therefore, it is natural to use LBE as a direct numerical simulation method for turbulent flows. The smallest scale that can be captured in LBE-DNS is the lattice unit, and the inherent parallelism of LBE enables the DNS to achieve large scale computations on high-performance computers. Another advantage of LBE as a DNS tool is the better isotropic property than traditional second-order numerical schemes. Theoretical analysis has shown that the LBE exhibits relatively low numerical dissipations and small numerical dispersive effects [Lallemand and Luo, 2000], which are crucial for capturing small scale dynamics in turbulence. Actually, soon after its emergence the capability of LBE in turbulence simulation has been verified by comparing with the results of pseudo-spectral methods for two- and three-dimensional decaying homogeneous isotropic turbulences (DHIT) [Chen *et al*., 1992; Martinez *et al*., 1994]. It was reported that the spatial and time distributions of velocities and vortices of both methods were in good agreement. The temporal profiles of turbulent kinetic energy, mean dissipation rate, and the Taylor microscale of DHIT were studied via LBE by Burattini *et al.* [2006], and the results were in good agreement with other simulation data and experimental measurements.

The DHIT in inertial and rotating reference frames was further studied via LBE [Yu *et al*., 2005a, 2005b], and the decay exponents of kinetic energy, the dissipation rate, and the low wave-number scaling of the spectrum, were all found to be in good agreement with the results from experiments and spectral method.

Other than the DHIT, the LBE was also applied to some forced turbulences. For instance, Benzi and Succi [1990] studied the enstrophy cascade in a two-dimensional forced isotropic turbulence, and Qian *et al*. [1995] also simulated the two dimensional forced turbulence to study the energy inverse cascade range. ten Cate *et al.* [2006] simulated a three-dimensional forced turbulence and studied the statistical quantities (e.g., energy dissipation rate and velocity derivative skewness), and the results confirmed that LBE can serve as an accurate method for DNS of turbulence Simulation of three-dimensional forced turbulences was also performed by Valiño *et al.* [2010], where some small scale properties, such as the energy spectrum, integral length, dissipation rate, velocity field, and vorticity structures, were compared with the results of pseudo-spectral method with excellent agreement. Another prototypical turbulent flow, the Kida vortex flow, was simulated using a high-order LBE model [Chikatamarla *et al.*, 2010] with extensive comparisons of some global and local statistical quantities with a spectral solution.

Direct numerical simulations of turbulent shear flows with LBE were also performed by some researchers. Benzi *et al.* [1996] studied the extended self-similarity of anisotropic turbulence with an applied lateral force. The analysis of the structure functions showed that the extended self-similarity depended on the applied shear, and was invalid as the shear was strong. However, they found that a generalized scaling law could be defined so that it held in a wider range of shear. Yu and Girimaji [2005] performed a LBE-DNS of a steady homogeneous shear turbulence to investigate the dependence of the asymptotic state on the initial Reynolds number and strain rate. They found that the initial shear has a small influence on the asymptotic values the production-to-dissipation ratio and the shear stress anisotropy, but affected the normal stress anisotropy greatly. In addition, it was shown that the initial Taylor microscale Reynolds number had significant effects on the turbulence parameters. These results were also compared with experimental data,

confirming that the LBE is a reliable method for anisotropic turbulence. Yu and Girimaji [2006] further simulated the homogeneous turbulence subject to periodic shear to investigate the effects of force frequency on the turbulence behaviors. It was reported that a critical frequency existed at which bifurcation occurred: the kinetic energy grew at lower frequencies but decays at higher ones. They also discussed the applicability of some turbulent closures to unsteady shear turbulences, and pointed out that the inviscid-rapid-distortion theory could not capture the turbulent features, while the second-moment closure models could predict the growth at low frequencies and the decay at high frequencies, but the critical frequency was underestimated.

Turbulent flows involving solid walls were also simulated using LBE as a DNS tool. Early in 1991, Succi *et al*. [1991] simulated the turbulent channel flow to study the bifurcation of a two-dimensional channel flow. It was found that there existed a critical Reynolds number above which the flow exhibited a stable periodic limit cycle, and a secondary bifurcation with a smaller amplitude and a higher frequency could be induced. Eggels [1996] simulated the fully-developed channel flow with heat transfer via a thermal LBE, and the flow statistics obtained from the direct simulations by spatial/time-averaging were compared with previous DNS results. Amati *et al.* [1997] performed a high resolution DNS of the turbulent channel flow on a parallel computer, focusing on the near wall vorticity structure and its effects on the scaling laws. Later they further simulated a channel flow with a Reynolds number up to 3300 [Amati *et al*., 1999], and the second-order statistics were in reasonable agreement with previous database. Toschi *et al.* [1999] studied the intermittency and structure functions of a turbulent channel flow via a three-dimensional LBE, and it was found the increase of intermittency near the wall was strongly related to the mean shear, while the velocity fluctuations at large scales of the channel flow were more intermittent than those of homogeneous isotropic turbulences. Lammers *et al.* [2006] simulated a pressure-driven channel flow based on a grid with resolution down to the Kolmogorov scale, and the one-point statistics compared well with the results of pseudo-spectral method and high-quality experimental data. However, some differences in pressure fluctuations were observed, which were attributed to the weak

compressibility of the LBE. Spasov *et al*. [2009] simulated a turbulent channel flow with an entropic LBE, where the entropy condition was used to render the numerical stability on coarse grids. It was shown the entropy stabilized LBE was able to achieve accurate results even on low resolution grids. DNS of fully-developed turbulent channel flow was also performed by Bespalko *et al.* [2010], with a comparison with data of a spectral method. A two-dimensional decaying turbulence in a square domain with no-slip walls was simulated by Házi, G. and Tóth [2010], who observed strong small-scale vortices near the no-slip walls, which agreed the earlier pseudo-spectral simulations. It was also observed that the decay of the enstrophy and kinetic energy could be described by some power-laws where the exponents depended on the Reynolds number.

9.3.2 *LBE-LES approach*

Like the classical DNS methods based on the Navier-Stokes equations, the LBE-DNS approach for turbulence is limited to moderate Reynolds number flows due to the need for intensive computational resources. In order to improve the capability of LBE for turbulent flows with high Reynolds numbers, some LBE methods coupling with large-eddy simulation (LES) techniques have been developed. Somers [1993] and Eggels and Somers [1995] proposed a collision model for the four dimensional Face-Centered- Hyper-Cubic FCHC LBE in which a SGS model was incorporated directly. The collision operator drives the distribution functions to the desired equilibrium solution,

$$f_i = \frac{m_i\rho}{24}\Big\{1 + 2\boldsymbol{c}_i\cdot\boldsymbol{u} + 3\Big[(\boldsymbol{c}_i\cdot\boldsymbol{u})^2 - \tfrac{1}{2}tr(\boldsymbol{uu}) + \boldsymbol{c}_i\boldsymbol{c}_i : \boldsymbol{\tau} - \tfrac{1}{2}tr(\boldsymbol{\tau})\Big] - 6\nu\Big[\boldsymbol{c}_i\boldsymbol{c}_i : \nabla\boldsymbol{u} - \tfrac{1}{2}\nabla\cdot\boldsymbol{u}\Big]\Big\}, \tag{9.56}$$

where the weight factors m_i are the multiplicities of the edges caused by the projection to *D* dimensional space and satisfy $\sum_i m_i = 24$; ν is the kinematic viscosity, and $\boldsymbol{\tau}$ is the turbulent shear stress given by certain sub-grid scale (SGS) models that vanishes at resolved scales. Using this model, Somers [1993] simulated the turbulent pipe flow at $\mathrm{Re} = 50{,}000$,

and the simulated friction was in quantitative agreement with the Blasius power law. Eggels [1996] also simulated the turbulent flow in a baffled stirred tank reactor, where the effect of the impeller on the flow was considered as a spatially and/or temporally varying force. The statistical results including the mean flow and turbulence intensities were found to be in close agreement with experimental data, indicating that the method could be applied to practical engineering problems. Lu *et al.* [2002] further simulated the turbulent flow in a stirred tank driven by a standard Rushton turbine via this method with a nonuniform mesh, and the statistical results were in good agreement with previous experimental and simulation data.

The LBE-LES method developed by Eggels *et al.* implements the SGS model directly, which requires the explicit computation of the velocity gradients. Hou *et al.* [1996] proposed an alternative LBE-LES approach in which the standard Smagorinsky sub-grid model was incorporated to include the energy dissipation induced by the interaction between resolved and unresolved scales. In this method the local strain intensity and the stress tensor are calculated locally from the moments of the nonequilibrium distribution function, which enables the computation more efficient. Instead of solving the discrete velocity kinetic equation for the original distribution functions, the method solves the a filtered discrete Boltzmann equation,

$$\overline{f}_i(\boldsymbol{x} + \boldsymbol{c}_i\delta_t, t + \delta_t) - f_i(\boldsymbol{x}, t) = \overline{\Omega}_i = \overline{-\frac{1}{\tau}\left(f_i - f_i^{eq}\right)}, \tag{9.57}$$

where the overline symbol represents a filtered quantity, i.e.,

$$\overline{\phi}(\boldsymbol{x}) = \int \phi(\boldsymbol{x}')G(\boldsymbol{x}, \boldsymbol{x}')d\boldsymbol{x}', \tag{9.58}$$

where $G(\boldsymbol{x}, \boldsymbol{x}')$ is a given spatial filter kernel and the integral is over the entire domain. The key problem in developing a LBE sub-grid model lies in the closing of the averaged nonlinear collision operator. Hou *et al.* assumed that the filtered particle distribution would approach to a local filtered equilibrium distribution,

$$\overline{\Omega_i\left(f(\boldsymbol{x}, t)\right)} = \Omega_i\left(\overline{f}(\boldsymbol{x}, t)\right) = -\frac{1}{\overline{\tau}}\left(\overline{f}_i - f_i^{(eq)}(\overline{\rho}, \overline{\boldsymbol{u}})\right), \tag{9.59}$$

where $f_i^{(eq)}$ has the same formulation as the standard one, $\overline{\rho}$ and $\overline{\boldsymbol{u}}$ are the filtered mean density and velocity, and $\overline{\tau}$ is an effective relaxation time dependent on turbulent eddy viscosity,

$$\nu_{total} = \nu_0 + \nu_{eddy} = c_s^2 \left(\overline{\tau} - \frac{1}{2} \right) \delta t \,, \tag{9.60}$$

where ν_0 is the physical kinematic viscosity, and ν_{eddy} is the turbulent eddy viscosity. For the Smagorinsky SGS model, ν_{eddy} is given by

$$\nu_{eddy} = C\Delta^2 \left| \overline{\boldsymbol{S}} \right| , \tag{9.61}$$

where $C\ (>0)$ is a model constant, Δ is the filter width (which is usually set to be the lattice spacing δ_x in LBE), and $\overline{\boldsymbol{S}}$ is the large eddy strain rate given by

$$\overline{S}_{\alpha\beta} = \frac{1}{2} \left(\frac{\partial \overline{u}_\alpha}{\partial x_\beta} + \frac{\partial \overline{u}_\beta}{\partial x_\alpha} \right), \tag{9.62}$$

while $|\overline{\boldsymbol{S}}| = (2\overline{S}_{\alpha\beta}\overline{S}_{\alpha\beta})^{1/2}$ is the magnitude of the strain rate.

An advantage of the above LBE-LES is that the local strain rate can be calculated from the second-order moments of the nonequilibrium distribution [Hou *et al.*, 1996]. It can be shown from the Chapman-Enskog analysis of LBE that (refer to Eq. (1.58)),

$$\overline{\pi}_{\alpha\beta}^{neq} = \sum_i c_{i\alpha} c_{i\beta} \left(f_i - f_i^{(eq)} \right) \approx -2c_s^2 \rho \overline{\tau} \delta_t S_{\alpha\beta} \,, \tag{9.63}$$

and so,

$$\Pi = \sqrt{\overline{\pi}_{\alpha\beta}^{neq} \overline{\pi}_{\alpha\beta}^{neq}} = 2c_s^2 \rho \overline{\tau} \delta_t \left| \boldsymbol{S} \right| . \tag{9.64}$$

Note from Eq. (9.60) that $\overline{\tau}$ is also a function of $|\boldsymbol{S}|$,

$$\overline{\tau} = \frac{\nu_0 + C\Delta^2 \left| \boldsymbol{S} \right|}{c_s^2 \delta_t} + \frac{1}{2} = \tau_0 + \frac{C\Delta^2 \left| \boldsymbol{S} \right|}{c_s^2 \delta_t} . \tag{9.65}$$

Therefore, from Eqs. (9.64) and (9.65) one can obtain

$$\left| \boldsymbol{S} \right| = \frac{-\tau_0 c_s^2 \delta_t + \sqrt{(\tau_0 c_s^2 \delta_t)^2 + 2C\Delta^2 \Pi / \rho}}{2C\Delta^2} . \tag{9.66}$$

The total relaxation time is then

$$\bar{\tau} = \frac{\tau_0 + \sqrt{\tau_0^2 + 2C\Delta^2(\rho c_s^4 \delta_t^2)^{-1}\Pi}}{2}. \tag{9.67}$$

In practical applications, we can first compute $\bar{\pi}_{\alpha\beta}^{neq}$ from the first equation of Eq. (9.63), then obtain its magnitude $\prod$, and finally compute the total relaxation time by Eq. (9.67).

The above LBE-LES method has been applied to a variety of turbulent flows. Hou *et al.* [1996] studied a two-dimensional driven cavity flow at Reynold numbers up to 10^6 on a 256^2 lattice, Yu *et al.* [2005] simulated the decaying homogeneous isotropic turbulence and compared the LBE-LES results with those of the LBE-DNS and the DNS based on the Navier-Stokes equations. It was pointed out that the LBE-LES could accurately capture the prominent large scale behaviors. Djenidi [2006] studied a grid-generated turbulence, and the results agreed quite well with experimental data. He also investigated the turbulent flow over a crossbar at a Reynolds number about 1600, and the vortex structures at the crossbar and the fingerlike structures induced by the intermittent lateral motions, which were observed experimentally, were successfully reproduced. Thürey and Rüde [2009] coupled the LBE-SGS model with a surface capture technique and simulated several free-surface problems such as droplet falling and dam breaking. Mayer *et al.* [2007] studied the flow in a sub-channel of a VVER-440 type fuel rod bundle, and the results agreed well experimental data. The LBE-SGS model was also extended to turbulent particulate flows by coupling a lattice gas method to simulate particle transport problems [Chopard Masselot, 1999; Feng *et al*., 2007].

The above LBE-LES method was also extended from BGK formulation to MRT formulation [Krafczyk *et al.*, 2003], where the eddy viscosity is incorporated into the LBE through the relaxation times for the shear modes. An advantage of the LBE-LES with MRT collision models is that the small scale oscillations, which may not only lead to numerical instability but also compete with the physical turbulent fluctuations and degrade the simulation accuracy, can be reduced by tuning the corresponding relaxation times. Using this method, Yu and Girimaji [2005] and Yu *et al*. [2006] studied the near field behaviors of a

rectangular jet with different aspect ratios and Reynolds numbers. The results were compared with experimental data and good agreements were observed. They also compared the performances of the MRT- and BGK-based LBE-LES methods, which showed that the MRT version was superior in terms of numerical stability, accuracy, and the reachable Reynolds number.

Recently, Premnath *et al.* [2009] extended the MRT-based LBE-LES for wall-bounded turbulent flows by implementing the van Driest damping function for the filter width,

$$\Delta' = \Delta\left[1 - \exp\left(-\frac{z^+}{A^+}\right)\right], \tag{9.68}$$

where A^+ is a model constant, and z^+ is the dimensionless distance from the wall normalized by the viscous length, i.e., $z^+ = z\nu_0/(\tau_w/\rho)^{1/2}$, where τ_w is the wall shear stress and z is the distance to the wall. With this generalized LBE-LES, Premnath *et al.* [2009a] simulated a fully developed turbulent channel flow at Reynolds number 183.6 and a three-dimensional cavity flow at $\mathrm{Re} = 1{,}2000$. They further extended the method by incorporating the dynamic Smagorinsky SGS model into the MRT-LBE [Premnath *et al.*, 2009b], which was achieved by setting the model constant of the eddy viscosity C in Eq. (9.61) dynamically according to two sets of filtered variables,

$$C = -\frac{1}{2}\frac{\left\langle \boldsymbol{L}{:}\boldsymbol{M} \right\rangle}{\left\langle \boldsymbol{M}{:}\boldsymbol{M} \right\rangle}, \tag{9.69}$$

where the operator "$\langle\cdot\rangle$" denotes spatial/temporal averaging, and the two tensors $\boldsymbol{L}$ and $\boldsymbol{M}$ are defined locally by

$$L_{ij} = \widehat{\overline{u}_i\overline{u}_j} - \hat{\overline{u}}_i\hat{\overline{u}}_j, \quad M_{ij} = \hat{\Delta}^2\left|\hat{\overline{\boldsymbol{S}}}\right|\hat{\overline{S}}_{ij} - \Delta^2\widehat{\left|\overline{\boldsymbol{S}}\right|\overline{S}_{ij}}, \tag{9.70}$$

where $\hat{\Delta}$ is the width of a test filter which is larger that Δ, and the symbol "$\hat{}$" represents the filter operator on the test filter. In this method a test-filtered quantity can be obtained by applying the test-filter to the quantity filtered by the original one [Premnath *et al.*, 2009b]. It should be noted that a similar idea was also employed in BGK-based LBE-LES method earlier [Menon and Soo, 2004].

LBE-LES methods with more advanced SGS models other than the Smagorinsky one were also developed recently. For instance, Jafari and Rahnama [2011] proposed a LBE-LES method with the shear-improved Smagorinsky model, while Dong *et al.* [2008] incorporated the inertial-range consistent Smagorinsky model into the LBE, where the eddy viscosity is given by

$$\nu_{eddy} = \sqrt{(C_\infty \Delta/\gamma)^4 \left\langle 2\overline{S}_{ij}\overline{S}_{ij} \right\rangle + \nu_0^2} - \nu_0 \,, \tag{9.71}$$

where C_∞ is the Smagorinsky constant based on infinite Reynolds number and γ is a parameter dependent on the filter kernel function. With this method Dong *et al.* [2008] simulated a three-dimensional decaying homogeneous isotropic turbulence, and the comparison with the DNS and experimental data showed that this LBE-LES was superior to the original one.

Instead of using the concept of eddy-viscosity, Sagaut [2010] and Malaspinas and Sagaut [2011] introduced the Approximate Deconvolution Model (ADM) into LBE, which was constructed directly based on the nonlinear Boltzmann equation. This LBE-LES model involves no implicit assumption on the sub-grid scale dynamics and is therefore more general. The starting point of the ADM-LBE is the filtered Boltzmann equation,

$$\frac{\partial \overline{f}}{\partial t} + \boldsymbol{\xi} \cdot \nabla \overline{f} = \Omega(\overline{f}) + \mathcal{R} \,, \tag{9.72}$$

where $\mathcal{R} = \overline{\Omega(f)} - \Omega(\overline{f})$, and the filtered quantity is defined by $\overline{\phi} = \mathcal{G} * \phi$, where $\mathcal{G}$ is a convolution filter kernel. An approximated inverse filter, $\mathcal{Q}$, is then defined to reconstruct the unfiltered quantity,

$$\mathcal{Q} * \mathcal{G} = I + O(h^m) \,, \tag{9.73}$$

where I is the identity and h the grid resolution, and $m > 0$ is the order of the reconstruction. The reconstructed distribution function is then defined by $f^* = \mathcal{Q} * \overline{f}$, which is an approximation to the unfiltered distribution function f and it can be assumed that $|f - f^*| \ll 1$. Then, the ADM-BGK equation is obtained from Eq. (9.72),

$$\mathcal{G} * \left[\frac{\partial f^*}{\partial t} + \boldsymbol{\xi} \cdot \nabla f^* - \Omega(f^*) \right] = 0 \,, \tag{9.74}$$

from which an ADM-LBE-LES can be constructed. Obviously, the implementation of this method follows two steps, i.e., (1) Standard collision and streaming steps,

$$f_i^{*out}(\boldsymbol{x}+\boldsymbol{c}_i\delta_t,t+\delta_t)-f_i^*(\boldsymbol{x},t)=-\frac{1}{\tau}\Big(f_i^*-f_i^{(eq)}(\rho^*,\boldsymbol{u}^*)\Big), \quad (9.75)$$

where the formulation of $f_i^{(eq)}$ is the same as the standard one, and (2) Filtering the post-streaming distributions,

$$\begin{aligned} f_i^*(\boldsymbol{x},t+\delta_t)&=\mathcal{Q}*\mathcal{G}*f_i^{*out}(\boldsymbol{x},t+\delta_t)\\ &=f_i^{*out}(\boldsymbol{x},t+\delta_t)-\sigma\sum_{j=1}^{D}\sum_{n=-N}^{N}d_n f_i^{*out}(\boldsymbol{x}+n\boldsymbol{e}_j,t+\delta_t), \end{aligned} \quad (9.76)$$

where the $\boldsymbol{e}_j$'s are the *D*-dimensional Cartesian basis vectors, $2N+1$ is the number of points of the filter stencil, σ and d_n are the strength and coefficients of the filter. The ADM-LBE was validated by comparing the simulation results of the three-dimensional time dependent mixing layer with the DNS measurements [Malaspinas and Sagaut, 2011].

Also starting from the filtered Boltzmann-BGK equation, Girimaji derived another LBE-LES method [2007]. Instead of using the particle velocity $\boldsymbol{\xi}$ and the distribution function $f(\boldsymbol{x}, \boldsymbol{\xi}, t)$, a new microscopic velocity space $\boldsymbol{\eta}=\boldsymbol{\xi}-\boldsymbol{u}'$ and a new distribution function $g(\boldsymbol{x}, \boldsymbol{\eta}, t)$ were introduced, where $\boldsymbol{u}'=\boldsymbol{u}-\overline{\boldsymbol{u}}$ is the unresolved turbulent velocity. From the original Boltzmann equation, a kinetic model for the filtered distribution function $\overline{g}$ was derived,

$$\frac{\partial\overline{g}}{\partial t}+\boldsymbol{\eta}\cdot\nabla\overline{g}-\nabla\cdot(\overline{\boldsymbol{u}'\boldsymbol{u}'})\cdot\nabla_{\boldsymbol{\eta}}\overline{g}=-\frac{1}{\tau}\big[\overline{g}-\overline{g}^{eq}(\rho,\overline{\boldsymbol{u}})\big], \quad (9.77)$$

where the sub-grid stress $\overline{\boldsymbol{u}'\boldsymbol{u}'}$ can be modeled with certain SGS models. Then suitable discretizations of this kinetic equation can lead to some LBE-LES schemes. With the Smagorinsky model, Girimaji [2007] simulated the three-dimensional decaying isotropic turbulence and compared the results with the DNS data, and it was claimed that this new method could produce more accurate results than the one developed by Hou *et al.* [1996].

It is noted that LBE-LES methods listed above are designed for isothermal turbulences, and extensions to thermal turbulences were also

reported in the literature [e.g., Eggels and Somers, 1995; Liu *et al*., 2006; van Treeck *et al*., 2006].

9.3.3 *LBE-RANS approach*

The RANS describes the mean motion of turbulent flows, in which each flow variable is decomposed into a mean and a fluctuating parts, e.g., $\boldsymbol{u} = \boldsymbol{U} + \boldsymbol{u}'$ and $p = P + p'$, where $\boldsymbol{U} = \langle \boldsymbol{u} \rangle$ and $P = \langle p \rangle$ are the mean velocity and pressure, respectively, with $\langle \cdot \rangle$ being the ensemble averaging operator. The RANS has the same formulation as the Navier-Stokes equations but with an extra Reynolds stress $\sigma = -\langle \boldsymbol{u}'\boldsymbol{u}' \rangle$ that should be modeled by a turbulence model.

Some LBE methods based on the RANS have been developed. Succi *et al.* [1995] proposed the first such LBE based on the popular k-ε turbulence model. Similar to the LBE-SGS model, in this method the mean flow was solved by a standard LBE with an effective relaxation time,

$$F_i(\boldsymbol{x} + \boldsymbol{c}_i\delta_t, t + \delta_t) - F_i(\boldsymbol{x}, t) = -\frac{1}{\tau_{total}}\left(F_i - f_i^{(eq)}\left(\rho, \boldsymbol{U}\right)\right), \quad (9.78)$$

where $F_i = \langle f_i \rangle$ is the mean distribution function, and the corresponding equilibrium distribution function has the same formulation as that of the standard LBE, while the effective relaxation time τ_{total} is determined from the total viscosity,

$$\tau_{total} = \frac{\nu_0 + \nu_{eddy}}{c_s^2\delta_t} + \frac{1}{2}, \quad (9.79)$$

in which the eddy viscosity is determined by the turbulent kinetic energy k and dissipation rate ε:

$$\nu_{eddy} = C_\mu \frac{k^2}{\varepsilon}, \quad (9.80)$$

with

$$k = \frac{1}{2}\left\langle \left|\boldsymbol{u}'\right|^2 \right\rangle, \; \varepsilon = \frac{\nu_0}{2}\left\langle \left|\partial_\alpha u'_\beta + \partial_\beta u'_\alpha\right|^2 \right\rangle. \quad (9.81)$$

The transports of the turbulent kinetic energy k and dissipation rate ε are governed by the following two equations:

$$\frac{\partial k}{\partial t} + \boldsymbol{U} \cdot \nabla k = \nabla \cdot \left(\frac{\nu_{total}}{\sigma_k} \nabla k \right) + \boldsymbol{\tau} : \boldsymbol{S} - \varepsilon \,, \tag{9.82}$$

$$\frac{\partial \varepsilon}{\partial t} + \boldsymbol{U} \cdot \nabla \varepsilon = \nabla \cdot \left(\frac{\nu_{total}}{\sigma_\varepsilon} \nabla \varepsilon \right) + \frac{\varepsilon}{k} \left(C_{\varepsilon 1} \boldsymbol{\tau} : \boldsymbol{S} - C_{\varepsilon 2} \varepsilon \right), \tag{9.83}$$

where the stress tensor and strain rate are defined from the mean velocity,

$$\tau_{\alpha\beta} = 2\nu_{eddy} S_{\alpha\beta} - \frac{2}{3} k \delta_{\alpha\beta} \,, \; S_{\alpha\beta} = \frac{1}{2} \left(\frac{\partial U_\alpha}{\partial x_\beta} + \frac{\partial U_\beta}{\partial x_\alpha} \right). \tag{9.84}$$

The parameters σ_k, σ_ε, $C_{\varepsilon 1}$, and $C_{\varepsilon 2}$ in Eqs. (9.82) and (9.83) are model constants. The strain rate $\boldsymbol{S}$ can still be computed from the second-order moments of the nonequilibrium distribution functions as in the LBE-LES method [Filippova *et al.*, 2001; Premnath and Abraham, 2004].

The k–ε equations (9.82) and (9.83) are two typical diffusion-advection equations with source terms, and can be solved in the LBE framework as proposed by Succi *et al.* [1995]. The LBE schemes can be expressed as

$$\chi_i(\boldsymbol{x} + \boldsymbol{c}_i \delta_t, t + \delta_t) - \chi_i(\boldsymbol{x}, t) = -\frac{1}{\tau_\chi} \left(\chi_i - \chi_i^{eq} \left(k, \boldsymbol{U} \right) \right) + S_{ki} \,, \tag{9.85}$$

$$\eta_i(\boldsymbol{x} + \boldsymbol{c}_i \delta_t, t + \delta_t) - \eta_i(\boldsymbol{x}, t) = -\frac{1}{\tau_\eta} \left(\eta_i - \eta_i^{eq} \left(\varepsilon, \boldsymbol{U} \right) \right) + S_{\varepsilon i} \,, \tag{9.86}$$

where τ_k and τ_ε are the corresponding relaxation times for the two types of distribution functions, respectively, and S_{ki} and $S_{\varepsilon i}$ are used to recover the source terms in the k–ε equations. In the method of Succi *et al.* [1995], a D-dimensional nearest neighbor lattice was used, and the equilibrium distribution functions were constructed to satisfy

$$k = \sum_{i=1}^{2D} \chi_i = \sum_{i=1}^{2D} \chi_i^{eq} \,, \; \varepsilon = \sum_{i=1}^{2D} \eta_i = \sum_{i=1}^{2D} \eta_i^{eq} \,. \tag{9.87}$$

One such choice is

$$\chi_i^{eq} = \frac{k}{2D} \left[1 + \frac{\boldsymbol{c}_i \cdot \boldsymbol{U}}{c^2 \;/\; D} \right], \;\; \eta_i^{eq} = \frac{\varepsilon}{2D} \left[1 + \frac{\boldsymbol{c}_i \cdot \boldsymbol{U}}{c^2 \;/\; D} \right]. \tag{9.88}$$

The two terms S_{ki} and $S_{\varepsilon i}$ could also be carefully chosen to recover the source terms in Eqs. (9.82) and (9.83).

An alternative approach that combines the LBE with a finite-difference scheme for the k–ε equations was proposed by Teixeira [1998], which was further extended by incorporating a grid-refinement technique as well as a turbulent wall-function model. With this approach, Filippova *et al.* [2001] simulated the flow around a NACA 4412 with small angles of attack at two Reynolds numbers (10^6 and 3×10^6), and the results agreed well with experimental data. The method was also employed to simulate the developed turbulent flow across a two-dimensional periodic array of compressor blades, with satisfactory results in comparison with the inviscid solutions.

Besides the applications of LBE as a numerical tool for turbulent flows, there are also increasing interests in developing turbulence models based on kinetic theory and LBE. For instance, after noticing the analogy between the turbulent fluctuations and molecular thermal fluctuations, Chen *et al.* [2003; 2004] suggested a turbulent BGK equation,

$$\frac{\partial f}{\partial t} + \boldsymbol{u}\cdot\nabla f = -\frac{1}{\tau_{turb}}\left[f - f^{eq}\right], \tag{9.89}$$

where $f(\boldsymbol{x},\boldsymbol{u},t)$ is the distribution function of the fluid parcels (instead of fluid molecules) moving with velocity $\boldsymbol{u}$ at position $\boldsymbol{x}$ and time t, τ_{turb} is the turbulent relaxation time associated with the turbulent eddy interactions, and f^{eq} is the Maxwellian distribution function centered around the turbulent mean velocity $\boldsymbol{U}$ with a half-width of $2k/3$ (k is the turbulent kinetic energy). Similar to the original Boltzmann equation, the averaged turbulent variables can be defined as the moments of $f(\boldsymbol{x},\boldsymbol{u},t)$, i.e.,

$$\rho = \int f \,\mathrm{d}\boldsymbol{u}, \qquad \rho\boldsymbol{U} = \int \boldsymbol{v} f \,\mathrm{d}\boldsymbol{u}, \quad \rho k = \frac{1}{2}\int (\boldsymbol{u}-\boldsymbol{U})^2 f \,\mathrm{d}\boldsymbol{u}\,. \tag{9.90}$$

Furthermore, the Reynolds stress can be defined as

$$\sigma_{\alpha\beta} = \int (c_\alpha - U_\alpha)(c_\beta - U_\beta) f \,\mathrm{d}\boldsymbol{u}\,. \tag{9.91}$$

The turbulent relaxation time in the extended BGK equation could be obtained by the renormalization group method [Chen *et al.*, 2003,

Chen *et al*., 2004],

$$\tau_{turb} = \tau_0 + \Psi(k / \varepsilon, S^{-1}, \cdots), \tag{9.92}$$

where τ_0 is the molecular relaxation time, and S is a measure of the local velocity gradient which is related to turbulent time scales. The functional form of Ψ was suggested to be a harmonic mean of the turbulent time scales [Chen *et al*., 2003], which could be chosen by matching certain turbulence models. Some turbulent LBE models can be derived by discretizing Eq. (9.89) with certain numerical schemes. In addition to developing turbulence models based on kinetic theory, there are also some efforts to construct such models based on LBE directly. For example, Succi *et al.* [2000, 2002] discussed the potential role of re-summation techniques in LBE for developing sub-grid turbulence models, and examined a coarse-grained LBE by incorporating the effects of unresolved scales into a renormalized relaxation time.

9.4 Immersed Boundary-Lattice Boltzmann Method and Its Applications

For simulation of fluid flows by conventional methods, the solution of governing equations is strongly coupled with the implementation of boundary conditions. Due to this feature, when the flow around a complex geometry or a moving object is considered, the computation often involves tedious grid generation and complicated solution process. To ease the computational process, it is desired to develop an approach which can decouple the solution of governing equations and the implementation of boundary conditions. The immersed boundary method (IBM) is such an approach. IBM was initially proposed by Peskin [1977] for simulation of blood flows in the heart. As shown in Fig. 9.3, it uses a fixed Eulerian mesh for the flow field, and a set of Lagrangian points to represent the solid boundary immersed in the fluid. The basic idea of IBM is to treat the physical boundary as deformable with high stiffness. A small distortion of the boundary will yield a force which tends to restore the boundary into its original shape. The balance of such force is distributed into the Eulerian mesh points and the governing equations

with a body force are solved in the whole domain including exterior and interior of the object. Since the governing equations are solved without considering the presence of immersed objects, the computational domain is often chosen as a regular shape and the Cartesian mesh is usually used for Eulerian mesh points. After the work of Peskin [1977], various improvements [Goldstein *et al*., 1993; Lai and Peskin, 2000; Silva *et al*., 2003; Ye *et al.*, 1999] have been made.

In most applications of IBM, the solution of flow field is obtained by solving the incompressible Navier-Stokes equations. As shown in this book, the lattice Boltzmann method (LBM) has been proven to be an efficient approach for simulation of incompressible flows. Like the IBM, the standard LBM is usually applied on Cartesian meshes. Due to this common feature, it is desirable to combine these two methods together. The first attempt for this combination was made by Feng and Michaelides [2004, 2005]. They successfully applied immersed boundary-lattice Boltzmann method (IB-LBM) to simulate the rigid particle motion. Later, Niu *et al.* [2006] proposed a momentum exchange–based IB-LBM for calculation of restoring force at the boundary point. Peng *et al.* [2006] developed a multi-block IB-LBM for simulation of flows around a circular cylinder and an airfoil. Both works adopt the MRT-LBE to get the flow field.

In this section, the basic procedure of IB-LBM and its improvement for satisfying no-slip boundary conditions will be described.

9.4.1 *Conventional immersed boundary-lattice Boltzmann method*

Basic equations

For viscous incompressible flows in a two-dimensional domain Ω containing an immersed boundary in the form of closed curve Γ, as shown in Fig. 9.3, the governing equations of immersed boundary method can be written as

$$\nabla \cdot \boldsymbol{u} = 0\,, \tag{9.93}$$

$$\rho\left(\frac{\partial \boldsymbol{u}}{\partial t} + \boldsymbol{u}\cdot\nabla\boldsymbol{u}\right) + \nabla p = \mu\Delta\boldsymbol{u} + \boldsymbol{f}\,, \tag{9.94}$$

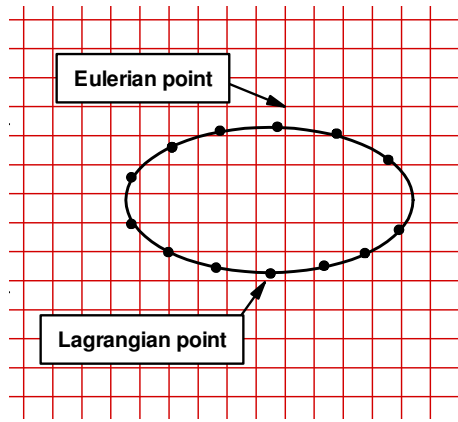

Fig. 9.3. Immersed boundary illustration.

$$\boldsymbol{f}(\boldsymbol{x},t) = \int_{\Gamma} \boldsymbol{F}(s,t)\delta\big(\boldsymbol{x} - \boldsymbol{X}(s,t)\big)ds\,, \tag{9.95}$$

$$\frac{\partial \boldsymbol{X}(s,t)}{\partial t} = \boldsymbol{u}\big(\boldsymbol{X}(s,t),t\big) = \int_{\Omega} \boldsymbol{u}(\boldsymbol{x},t)\delta\big(\boldsymbol{x} - \boldsymbol{X}(s,t)\big)d\boldsymbol{x}\,, \tag{9.96}$$

$$\boldsymbol{F}(s,t) = \boldsymbol{S}\big(\boldsymbol{X}(s,t),t\big). \tag{9.97}$$

Here $\boldsymbol{x}$, $\boldsymbol{u}$, p and $\boldsymbol{f}$ are the Eulerian coordinates, fluid velocity, fluid pressure and force density acting on the Eulerian mesh point, respectively. $\boldsymbol{X}$ and $\boldsymbol{F}$ stand for the Lagrangian coordinates and boundary force density. $\delta(\boldsymbol{x}-\boldsymbol{X}(s,\,t))$ is the Dirac delta function. Equations (9.93) and (9.94) are the continuity and momentum equations for flow field. Equations (9.95) and (9.96) describe the interaction between the immersed boundary and the fluid flow, by distributing the boundary force at the Lagrangian points to Eulerian points and interpolating the velocity at the Eulerian points to Lagrangian points. Equation (9.97) states that the boundary force density on the segment is determined by the boundary configuration at time t.

Under the framework of lattice Boltzmann method, equations (9.93)-(9.94) can be written as [Feng and Michaelides, 2004, 2005]

$$f_i(\boldsymbol{x} + \boldsymbol{c}_i\delta_t, t+\delta_t) - f_i(\boldsymbol{x},t) = -\frac{1}{\tau}\Big[f_i(\boldsymbol{x},t) - f_i^{(eq)}(\boldsymbol{x},t)\Big] + \frac{3}{2}\omega_i \boldsymbol{f}\cdot\boldsymbol{c}_i\delta_t, \tag{9.98}$$

where $\boldsymbol{f}$ is the external force density at an Eulerian point, and ω_i are coefficients which depend on the selected lattice velocity model.

Calculation of restoring force

As $\boldsymbol{f}$ is computed from the force density at the boundary point, $\boldsymbol{F}$, by using Eq. (9.95), the calculation of $\boldsymbol{F}$ is critical in the application of IBM. In the following, we will show three ways to compute $\boldsymbol{F}$.

The first way is the original method of Peskin [1977]. At time t, it is assumed that the center of mass of the rigid body is at $\boldsymbol{X}(t)$, and the instantaneous body rotational matrix is $\boldsymbol{R}(t)$. So the position of a reference point $\boldsymbol{X}_j^r$ can be determined by

$$\boldsymbol{X}_j^r(t) = \boldsymbol{X}(t) + \boldsymbol{R}(t)\left[\boldsymbol{X}_j^r(0) - \boldsymbol{X}(0)\right]. \tag{9.99}$$

For the boundary point $\boldsymbol{X}_j^t$ which is correspondent to the reference point $\boldsymbol{X}_j^r$, it is allowed to be slightly deformed by the fluid. When the reference point and the boundary point are not at the same position, there will be a displacement $\boldsymbol{\xi}_j = \boldsymbol{X}_j^t - \boldsymbol{X}_j^r$, and a restoring force $\boldsymbol{F}_i$ is generated that tends to restore the boundary point back to the reference point. It can be modeled by a linear spring relation

$$\boldsymbol{F}_j = -k\boldsymbol{\xi}_j, \tag{9.100}$$

where k is the spring constant.

Equation (9.100) is very simple. However, there is a user-defined parameter k, which may affect the accuracy of numerical solution. To overcome this drawback, Fadlun *et al.* [2000] proposed the direct forcing method. The idea of this way is very simple. Since the boundary point is also the fluid point, application of Eq. (9.94) at the boundary point directly gives

$$\boldsymbol{f} = \rho\left(\frac{\partial \boldsymbol{u}}{\partial t} + \boldsymbol{u}\cdot\nabla\boldsymbol{u}\right) + \nabla p - \mu\Delta\boldsymbol{u}. \tag{9.101}$$

Suppose that at the time level $t = t_n$, the velocity and pressure fields are known. At the time level $t = t_{n+1}$, the force density at the boundary point can be calculated by

$$\boldsymbol{f}_i^{n+1} = \rho\left(\frac{\boldsymbol{U}_i^{n+1} - \boldsymbol{u}_i^n}{\delta t} + \boldsymbol{u}_i^n\cdot\nabla\boldsymbol{u}_i^n\right) + \nabla p_i^n - \mu\Delta\boldsymbol{u}_i^n, \tag{9.102}$$

where $\boldsymbol{U}^{n+1}$ is the wall velocity. Note that for the application of Eq. (9.102), we need to compute the velocity and pressure gradients at the Eulerian points first, and then interpolate them and the fluid velocity to the boundary points through Delta function interpolation. The calculation of derivatives brings inconvenience to the application of IB-LBM.

The third way to compute the restoring force was proposed by Niu *et al.* [2006]. It is based on Newton's second law (the momentum exchange equals to the impulse). This way is only applicable for the lattice Boltzmann method. By using Lagrangian interpolated polynomials, the density distribution functions on the boundary point at all lattice velocity directions can be calculated by

$$f_i(\boldsymbol{X}_B,t)=\sum_{i,\,j}\left(\prod_{k=1,k\neq i}^{imax}\frac{X_B-x_{kj}}{x_{ij}-x_{kj}}\right)\left(\prod_{m=1,m\neq j}^{jmax}\frac{Y_B-y_{im}}{y_{ij}-y_{im}}\right)f_i(\boldsymbol{x}_{ij},t)\,, \quad (9.103)$$

where $imax$ and $jmax$ are the maximum numbers of the mesh points in the x and y directions, respectively. Note that Eq. (9.103) is applied to all lattice velocity directions. If we view the boundary point from the flow domain, the lattice velocity directions can be classified as outgoing directions (from the flow domain to the boundary point) and incoming directions (from the boundary point to the flow domain). On the other hand, if we view the boundary point from outside of the flow domain (inside the object), the lattice velocity directions can also be classified as outgoing directions (from the boundary point to the flow domain) and incoming directions (from the flow domain to the boundary point). Obviously, incoming directions of one view are outgoing directions of another view. Similarly, outgoing directions of one view are incoming directions of another view. Therefore, the application of bounce back rule at the boundary point is equivalent to exchanging the density distribution functions between a pair of opposite lattice velocity directions. By using the bounce back rules for the density distribution functions of all directions, the no-slip boundary condition is satisfied and we have a new set of distribution functions on the boundary points as shown below,

$$f_{\bar{i}}(\boldsymbol{X}_B,t)=f_i(\boldsymbol{X}_B,t)-2\omega_i\rho\frac{\boldsymbol{c}_i\cdot\boldsymbol{U}_B}{c_s^2}\,, \quad (9.104)$$

where $\bar{i}$ denotes the opposite direction of i; $\boldsymbol{U}_B(=\boldsymbol{U}+\boldsymbol{\Omega}\times(\boldsymbol{X}_B-\boldsymbol{X}))$ is the velocity of the boundary with $\boldsymbol{U}$ and $\boldsymbol{\Omega}$ representing the translational

and angular velocity of the rigid body, and $\boldsymbol{X}$ is the mass center of the body, $\boldsymbol{X}_B$ is its boundary position. Consequently, the boundary force density can be calculated via the momentum- exchange method, that is,

$$\boldsymbol{F}(\boldsymbol{X}_B,t) = -\sum_{\bar{i}} \boldsymbol{c}_{\bar{i}} \left[f_{\bar{i}}(\boldsymbol{X}_B,t) - f_i(\boldsymbol{X}_B,t) \right]. \tag{9.105}$$

Note that according to Newton's third law, the hydrodynamic force exerted on the boundary by the fluids and the force exerted on the fluids by the boundary have the same magnitude and opposite direction.

δ-function interpolation

The application of Eqs. (9.95) and (9.96) involves the surface and volume integrals, and continuous δ-function interpolation. In practice, the integral forms are often replaced by the discrete forms. The two-dimensional discrete forms can be given by

$$\boldsymbol{f}(\boldsymbol{x}_{ij},t) = \sum_l \boldsymbol{F}(\boldsymbol{X}_B^l,t) D_{ij}(\boldsymbol{x}_{ij} - \boldsymbol{X}_B^l) \Delta s_l \,, \tag{9.106}$$

$$\boldsymbol{u}(\boldsymbol{X}_B^l,t) = \sum_{i,j} \boldsymbol{u}(\boldsymbol{x}_{ij},t) D_{ij}(\boldsymbol{x}_{ij} - \boldsymbol{X}_B^l) \Delta x \Delta y \,, \tag{9.107}$$

where Δs_l is the arc length of the boundary element, Δx and Δy are respectively the mesh spacing in the x and y directions. D_{ij} is a kernel distribution, which can be written as

$$D_{ij}(\boldsymbol{x}_{ij} - \boldsymbol{X}_B^l) = \frac{1}{\Delta x \Delta y} \delta\left(\frac{x_{ij} - X_B^l}{\Delta x} \right) \delta\left(\frac{y_{ij} - Y_B^l}{\Delta y} \right). \tag{9.108}$$

There are many ways to define the δ-function, and two popular formulations are given as follows,

$$\delta\big(r\big) = \begin{cases} \dfrac{1}{4}\big[1 + \cos(\pi |r|/2)\big], & |r| \le 2, \\ 0, & |r| > 2, \end{cases} \tag{9.109}$$

$$\delta(r) = \begin{cases} \dfrac{1}{8}\Big(3 - 2\,|r| + \sqrt{1 + 4\,|r| - 4\,|r|^2}\,\Big), & |r| \le 1, \\ \dfrac{1}{8}\Big(5 - 2\,|r| - \sqrt{-7 + 12\,|r| - 4\,|r|^2}\,\Big), & 1 \le |r| \le 2, \\ 0, & |r| > 2. \end{cases} \tag{9.110}$$

For the application of IB-LBM, at first, we need to compute the force density at the boundary points and then distribute it onto the Eulerian points. After that, we solve the LBE with the force term $\boldsymbol{f}$ to update the velocity field. Then we interpolate the new (corrected) velocity field from the lattice (Eulerian points) to the boundary points and re-calculate the force density at the boundary point. The process continues until the convergence criterion is satisfied.

It should be noted that in the conventional IB-LBM, the force density is pre-calculated. With the known force density $\boldsymbol{f}$, the new (corrected) velocity field is explicitly determined. In the process, there is no guarantee that the velocity at the boundary point obtained from interpolation of corrected velocity field at Eulerian points equals to the wall velocity. This means that the no-slip boundary condition may not be satisfied. This drawback may cause flow penetration to the solid body, which can be clearly observed in Fig. 9.4.

In the following, we will present a boundary condition-enforced IB-LBM, in which the force density is considered as an unknown, and is determined from the no-slip boundary condition.

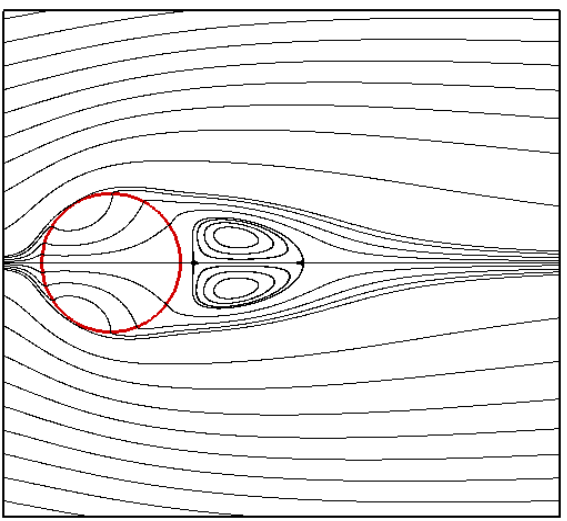

Fig. 9.4. Flow penetration in the results of conventional IB-LBM for flow around a circular cylinder (Re = 20).

9.4.2 *Boundary condition-enforced immersed boundary-lattice Boltzmann method*

We start with the LBE. As shown by Guo *et al*. [2002a], the LBE with external force (Eq. (9.98)) cannot properly consider the discrete lattice effects to the density and momentum. In order to correctly recover the viscous and incompressible Navier-Stokes equations involving the external force, the contribution of the force to both momentum $\rho \boldsymbol{u}$ and momentum flux $\rho \boldsymbol{u}\boldsymbol{u}$ should be considered. To have a better representation of the forcing term in LBE, Guo *et al.* [2002a] proposed a formulation with higher-order terms in $\boldsymbol{u}$. With this scheme, the LBE can be written as

$$f_i(\boldsymbol{x} + \boldsymbol{e}_\alpha \delta_t, t + \delta_t) - f_i(\boldsymbol{x}, t) = -\frac{1}{\tau}\left[f_i(\boldsymbol{x}, t) - f_i^{(eq)}(\boldsymbol{x}, t) \right] + F_i \delta_t \,, \tag{9.111}$$

$$F_i = \left(1 - \frac{1}{2\tau}\right) w_i \left(\frac{\boldsymbol{e}_i - \boldsymbol{u}}{c_s^2} + \frac{\boldsymbol{e}_i \cdot \boldsymbol{u}}{c_s^4} \cdot \boldsymbol{e}_i \right) \cdot \boldsymbol{f} \,, \tag{9.112}$$

$$\rho \boldsymbol{u} = \sum_i \boldsymbol{e}_i f_i + \frac{1}{2} \boldsymbol{f} \delta_t \,. \tag{9.113}$$

It can be seen clearly from Eq. (9.113) that the fluid velocity consists of two parts. One is contributed from the density distribution function (solution of Eq. (9.111)), and the other is contributed from the force density $\boldsymbol{f}$. If we define the intermediate velocity $\boldsymbol{u}^*$ as

$$\rho \boldsymbol{u}^* = \sum_i \boldsymbol{e}_i f_i \,, \tag{9.114}$$

and the velocity correction $\delta \boldsymbol{u}$ as

$$\rho \delta \boldsymbol{u} = \frac{1}{2} \boldsymbol{f} \delta_t \,, \tag{9.115}$$

then Eq. (9.113) can be written as

$$\boldsymbol{u} = \boldsymbol{u}^* + \delta \boldsymbol{u} \,. \tag{9.116}$$

In the conventional IBM, $\boldsymbol{f}$ is computed in advance. From Eqs. (9.115) and (9.116), we can see clearly that the velocity correction $\delta \boldsymbol{u}$ and corrected velocity $\boldsymbol{u}$ are explicitly calculated. Thus, there is no guarantee that the velocity at the boundary point interpolated from $\boldsymbol{u}$ satisfies the

no-slip boundary condition. To overcome this drawback, we have to consider the force density $\boldsymbol{f}$ as an unknown, which is determined in such a way that the velocity at the boundary point interpolated from $\boldsymbol{u}$ satisfies the no-slip boundary condition. Similar to Eq. (9.95), the velocity correction $\delta\boldsymbol{u}$ at Eulerian points is distributed from the velocity correction at the boundary (Lagrangian) points. Here, we can set an unknown velocity correction vector $\delta\boldsymbol{u}_B^l$ at all boundary points. The velocity correction $\delta\boldsymbol{u}$ at the Eulerian point can be obtained by the following Dirac delta function interpolation

$$\delta\boldsymbol{u}(\boldsymbol{x},t) = \int_\Gamma \delta\boldsymbol{u}_B(\boldsymbol{X}_B,t)\delta(\boldsymbol{x}-\boldsymbol{X}_B(s,t))ds\,, \tag{9.117}$$

The discrete form of Eq. (9.117) can be written as

$$\delta\boldsymbol{u}(\boldsymbol{x},t) = \sum_l \delta\boldsymbol{u}_B^l(\boldsymbol{X}_B^l,t)D_{ij}(\boldsymbol{x}_{ij}-\boldsymbol{X}_B^l)\Delta s_l\,. \tag{9.118}$$

According to Eq. (9.116), the fluid velocity at Eulerian points can be corrected as

$$\boldsymbol{u}(\boldsymbol{x}_{ij},t) = \boldsymbol{u}^*(\boldsymbol{x}_{ij},t) + \delta\boldsymbol{u}(\boldsymbol{x}_{ij},t)\,, \tag{9.119}$$

where $\boldsymbol{u}^*(\boldsymbol{x}_{ij},t)$ is the intermediate fluid velocity obtained from Eq. (9.114). Note that the unknowns in Eqs. (9.118) and (9.119) are the velocity corrections at the boundary points, $\delta\boldsymbol{u}_B^l$. To satisfy the no-slip boundary condition, the fluid velocity at the boundary points obtained by interpolation using the smooth delta function must be equal to the wall velocity $\boldsymbol{U}_B^l(\boldsymbol{X}_B^l,t)$ at the same position. Its mathematical expression is

$$\boldsymbol{U}_B^l(\boldsymbol{X}_B^l,t) = \sum_{i,j}\boldsymbol{u}(\boldsymbol{x}_{ij},t)D_{ij}(\boldsymbol{x}_{ij}-\boldsymbol{X}_B^l)\Delta x\Delta y\,. \tag{9.120}$$

Substituting Eq. (9.119) into Eq. (9.120), we can get the following equation system

$$\begin{aligned}\boldsymbol{U}_B^l(\boldsymbol{X}_B^l,t) = &\sum \boldsymbol{u}^*(\boldsymbol{x}_{ij},t)D_{ij}(\boldsymbol{x}_{ij}-\boldsymbol{X}_B^l)\Delta x\Delta y\\ &+\sum_{i,j}\sum_l \delta\boldsymbol{u}_B^l(\boldsymbol{X}_B^l,t)D_{ij}(\boldsymbol{x}_{ij}-\boldsymbol{X}_B^l)\Delta s_l D_{ij}(\boldsymbol{x}_{ij}-\boldsymbol{X}_B^l)\Delta x\Delta y,\end{aligned} \tag{9.121}$$

which can be further put as the following matrix form

$$\boldsymbol{A}\boldsymbol{X} = \boldsymbol{B}\,, \tag{9.122}$$

where

$$\boldsymbol{X} = \begin{pmatrix} \delta \boldsymbol{u}_B^1 \\ \delta \boldsymbol{u}_B^2 \\ \vdots \\ \delta \boldsymbol{u}_B^M \end{pmatrix}, \ \boldsymbol{B} = \begin{pmatrix} \boldsymbol{U}_B^1 \\ \boldsymbol{U}_B^2 \\ \vdots \\ \boldsymbol{U}_B^M \end{pmatrix} - \Delta x \Delta y \begin{pmatrix} D_{11} & D_{12} & \cdots & D_{1N} \\ D_{21} & D_{22} & \cdots & D_{2N} \\ \vdots & \vdots & \ddots & \vdots \\ D_{M1} & D_{M2} & \cdots & D_{MN} \end{pmatrix} \begin{pmatrix} \boldsymbol{u}_1^* \\ \boldsymbol{u}_2^* \\ \vdots \\ \boldsymbol{u}_N^* \end{pmatrix}, \quad (9.123)$$

$$\boldsymbol{A} = \Delta x \Delta y \begin{pmatrix} D_{11} & D_{12} & \cdots & D_{1N} \\ D_{21} & D_{22} & \cdots & D_{2N} \\ \vdots & \vdots & \ddots & \vdots \\ D_{M1} & D_{M2} & \cdots & D_{MN} \end{pmatrix} \begin{pmatrix} D_{11}^T \Delta s_1 & D_{12}^T \Delta s_2 & \cdots & D_{1M}^T \Delta s_M \\ D_{21}^T \Delta s_1 & D_{22}^T \Delta s_2 & \cdots & D_{2M}^T \Delta s_M \\ \vdots & \vdots & \ddots & \vdots \\ D_{N1}^T \Delta s_1 & D_{N2}^T \Delta s_2 & \cdots & D_{NM}^T \Delta s_M \end{pmatrix}. \quad (9.124)$$

Here D_{ij}^T is the element of the transpose matrix of $[D_{ij}]$, M is the number of Lagrangian (boundary) points and N is the number of the adjacent Eulerian points around the boundary. Note that the elements of matrix $\boldsymbol{A}$ are only related to the boundary points and their adjacent Eulerian points. By solving the above equation system (9.122), we can obtain the unknown velocity correction at all boundary points. The number of unknowns in (9.122) is the same as the number of boundary points and the velocity corrections at all the boundary points can be computed simultaneously by using a direct method or iterative method to solve (9.122). After obtaining the velocity correction at the boundary point, the velocity correction and the corrected velocity at the Eulerian points can then be calculated by Eqs. (9.118) and (9.119).

Since the no-slip boundary condition is satisfied in the boundary condition-enforced IB-LBM, the problem of flow penetration is avoided in its results. This can be seen clearly in Fig. 9.5, which compares the streamlines for the flow around a circular cylinder at $\mathrm{Re} = 40$ obtained respectively by the conventional IB-LBM and boundary condition-enforced IB-LBM.

Another advantage of IB-LBM is the simple calculation of force on the boundary point. From Eq. (9.115), we can easily compute the force density (force per area) at the boundary point by

$$\boldsymbol{f}_B^l = 2\,\rho \delta \boldsymbol{u}_B^l \Big/ \delta t\,. \quad (9.125)$$

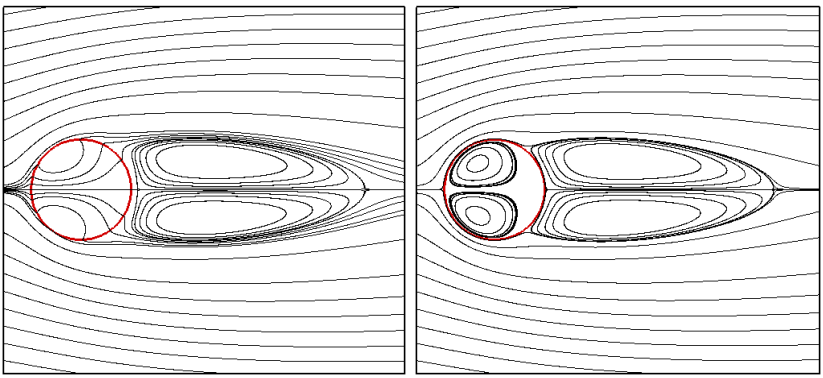

Fig. 9.5. Streamlines for the flow over a cylinder at $\mathrm{Re} = 40$. Left: Conventional IB-LBM; Right: Boundary condition-enforced IB-LBM.

The integration of $\boldsymbol{f}_B^l$ over the whole surface of the immersed object will give the total force on the object.

9.5 Summary

As an efficient new numerical method for fluid flows, the LBE has found wide applications in a variety of complex flows that classical CFD methods may encounter difficulties. In this chapter we have presented a brief introduction of the applications in particulate flows, flows in porous media, turbulent flows, which reveals the potential of LBE in these fields. We also presented the development of hybrid LBE with the immersed boundary method for flows with complex geometries or moving objects. Besides these applications, LBE has also been being employed in many other areas with successes, such as electronic kinetic flows [e.g., Guo *et al*., 2005; He and Li, 2000; Wang and Kang, 2010], magnetohydrodynamics [e.g., Breyiannis and Valougeorgis, 2004; Chatterjee and Amiroudine, 2010; Dellar, 2002], non-Newtonian flows [e.g., Aharonov and Rothman, 1993; Boek *et al.*, 2003; Yoshino *et al*., 2007], soft matter systems [e.g., Dünweg and Ladd, 2009], shallow water flows [e.g., Zhou, 2004], reaction and combustion [Ayodele *et al*., 2011; Kang *et al.*, 2010; Machado, 2012; Succi *et al.*, 1997; Filippova and Hänel, 2000], radiation

heat transfer [Asinari *et al*., 2010; Ma *et al*., 2011; Mishra and Roy, 2007], relativistic hydrodynamics and quantum mechanics [Dellar *et al*., 2011; Mendoza *et al*., 2010], and so on. Actually, after about two decades of rapid development, the LBM has achieved much progress in a wide variety of fields, and the applications are spreading rapidly from the classical fluid mechanics to other more complex fields. However, there are still many challenging problems, and it is now still an active research area.

Appendix A

Source Code for 2D Cavity Flow

This appendix provides the source code (based on the D2Q9 model) for the 2D cavity flow described in Chapter 4. The code combines the subroutines into one single file, which can be compiled using C or C++ compiler. The BGK and MRT collisions can be switched in the code.

```
//============================================================
//------------------------------------------------------------
//          ----- Header file of the D2Q9 model -----
//------------------------------------------------------------
//File name: D2Q9.h
#include <stdio.h>
#include <stdlib.h>
#include <math.h>
#define  Nx 256      // number of cells in the x-direction
#define  Ny 256      // number of cells in the y-direction
#define Nx1 (Nx+1)
#define Ny1 (Ny+1)
#define L (Ny+1)     // width of the cavity
#define  Q 9         // number of discrete velocities
#define rho0 1.0     // initial density
#define ux0  0.0     // initial velocity component in x direction
#define uy0  0.0     // initial velocity component in y direction
#define uw  0.1
#define Re 400.0

int cx[Q]={0, 1, 0, -1, 0, 1, -1, -1, 1};
int cy[Q]={0, 0, 1, 0, -1, 1, 1, -1, -1};

double f[Ny1][Nx1][Q]; //array of the distribution functions (DFs)
double f_post[Ny1][Nx1][Q]; // array of the post-collision DFs
double rho[Ny1][Nx1], ux[Ny1][Nx1], uy[Ny1][Nx1];
                        // arrays of fluid density and velocity
double tau;  // relaxation time for BGK model
double s[Q]; // relaxation rates for MRT model
double D[Q]={9, 36, 36, 6, 12, 6, 12, 4, 4};   // D = M*MT
```

```
double    w[Q]={4.0/9,1.0/9,1.0/9,1.0/9,1.0/9,1.0/36,1.0/36,
1.0/36,1.0/36}; // the weights in the EDF
int rc[Q]={0,3,4,1,2,7,8,5,6}; // index of reversed velocity

void Init_Eq(void);        //Initialization
double feq(double RHO, double U, double V, int k);
                           // Equilibrium distribution function
void Coll_BGK(void);       // BGK collision
void Coll_MRT(void);       // MRT collision
double meq(double RHO, double U, double V, int k);
                           // Equilibrium  momenta
void Streaming(void);      // Streaming
void Den_Vel(void);        // Fluid variables
void Bounce_back(void);    // Bounce-back boundary condition
double Err(void);          // Difference in velocity field
double u0[Ny1][Nx1],v0[Ny1][Nx1];
void Data_Output(void);    // Output simulation data
//===========================================================

//===========================================================
void main()
{
  int k,M2,N2;
  double err;
  M2=Ny/2; N2=Nx/2;

  k=0;
  err=1.0;
  tau=3*L*uw/Re+0.5; // relaxation time for BGK
  s[7]=s[8]=1.0/tau;    s[0]=s[3]=s[5]=0.0;   s[4]=s[6]=8*(2-
 s[7])/(8-s[7]);  s[1]=1.6;  s[2]=1.8; // relaxation rates for MRT

  Init_Eq();

  while(err>1.0e-6)
  {
    k++;
    Coll_BGK();     //BGK collision
//    Coll_MRT();    //MRT collision
    Streaming();    // Streaming
    Bounce_back(); // No-Slip boundary condition
    Den_Vel();      // Fluid variables

    if(k%1000==0)
    {
      err=Err();    // Velocity differences between two successive 1000 steps
      printf("err=%e ux_center=%e  uy_center=%e k=%d\n",err,
```

```
        ux[M2][N2],uy[M2][N2], k);  // Display some results
     }
   }
   Data_Output();    // Output simulation data
}


//============================================================
//------------------------------------------------------------
// Subroutine: initialization with the equilibrium method
//------------------------------------------------------------
//
void Init_Eq()
{
   int j, i, k;
   for (j=0;j<=Ny;j++) for(i=0;i<=Nx;i++)
   {
     rho[j][i]=rho0;
     ux[j][i]=ux0;
     uy[j][i]=uy0;
     for(k=0;k<Q;k++)
     f[j][i][k]=feq(rho[j][i],ux[j][i],uy[j][i],k);
    }
}
//============================================================

//============================================================
//------------------------------------------------------------
// Subroutine: calculation the equilibrium distribution
//------------------------------------------------------------
//
double feq(double RHO, double U, double V, int k)
{
  double cu, U2;
  cu=cx[k]*U+cy[k]*V; // c k*u
  U2=U*U+V*V;         // u*u;
  return w[k]*RHO*(1.0+3.0*cu+4.5*cu*cu-1.5*U2);
}
//============================================================

//============================================================
//------------------------------------------------------
// Subroutine: BGK collision
//------------------------------------------------------
void Coll_BGK()
{
int j, i, k;
  double FEQ;
  for (j=0;j<=Ny;j++) for(i=0;i<=Nx;i++) for(k=0;k<Q;k++)
```

```
  {
    FEQ=feq(rho[j][i],ux[j][i],uy[j][i],k); // EDF
    f_post[j][i][k] = f[j][i][k]-(f[j][i][k]-FEQ)/tau;
                                                    // Post-collision DFs
}
}
//============================================================

//============================================================
//------------------------------------------------------
// Subroutine: MRT collision
//------------------------------------------------------
void Coll_MRT()
{
  int j, i, k;
  double MEQ;
  double m[Q];
  for (j=0;j<=Ny;j++) for(i=0;i<=Nx;i++)
  {
 // Transformation from velocity space to moment space:
    m[0]=f[j][i][0]+f[j][i][1]+f[j][i][2]+f[j][i][3]+f[j][i]
          [4]+f[j][i][5]+f[j][i][6]+f[j][i][7]+f[j][i][8];
    m[1]=-4*f[j][i][0]-f[j][i][1]-f[j][i][2]-f[j][i][3]-f[j]
          [i][4]+2*(f[j][i][5]+f[j][i][6]+f[j][i][7]+f[j][i
          ][8]);
    m[2]=4*f[j][i][0]-2*(f[j][i][1]+f[j][i][2]+f[j][i][3]+
          f[j][i][4])+f[j][i][5]+f[j][i][6]+f[j][i][7]+f[j]
          [i][8];
    m[3]=f[j][i][1]-f[j][i][3]+f[j][i][5]-f[j][i][6]-
          f[j][i][7]+f[j][i][8];
    m[4]=-2*(f[j][i][1]-f[j][i][3])+f[j][i][5]-f[j][i][6]-
          f[j][i][7]+f[j][i][8];
    m[5]=f[j][i][2]-f[j][i][4]+f[j][i][5]+f[j][i][6]-
         f[j][i][7]-f[j][i][8];
    m[6]=-2*(f[j][i][2]-f[j][i][4])+f[j][i][5]+f[j][i][6]-
          f[j][i][7]-f[j][i][8];
    m[7]=f[j][i][1]-f[j][i][2]+f[j][i][3]-f[j][i][4];
    m[8]=f[j][i][5]-f[j][i][6]+f[j][i][7]-f[j][i][8];

// Relaxation in moment space:
   for(k=0;k<Q;k++)
   {
      MEQ = meq(rho[j][i],ux[j][i],uy[j][i],k);
      m[k]= m[k]-s[k]*(m[k]-MEQ);  // relaxation
      m[k]/=D[k];                  // rescaling
   }
 // Transforming back to the velocity space:
    f_post[j][i][0]= m[0]-4*(m[1]-m[2]);
    f_post[j][i][1]=m[0]-m[1]-2*(m[2]+m[4])+m[3]+m[7];
```

```
    f_post[j][i][2]=m[0]-m[1]-2*(m[2]+m[6])+m[5]-m[7];
    f_post[j][i][3]=m[0]-m[1]-2*(m[2]-m[4])-m[3]+m[7];
    f_post[j][i][4]=m[0]-m[1]-2*(m[2]-m[6])-m[5]-m[7];
    f_post[j][i][5]=m[0]+m[1]+m[1]+m[2]+m[3]+m[4]+m[5]+m[6]
                    +m[8];
    f_post[j][i][6]=m[0]+m[1]+m[1]+m[2]-m[3]-m[4]+m[5]+m[6]
                    -m[8];
    f_post[j][i][7]=m[0]+m[1]+m[1]+m[2]-m[3]-m[4]-m[5]-m[6]
                    +m[8];
    f_post[j][i][8]=m[0]+m[1]+m[1]+m[2]+m[3]+m[4]-m[5]-m[6]
                    -m[8];
  }
}
//===========================================================

//===========================================================
//-----------------------------------------------------------
// Subroutine: calculation the equilibrium moment
//-----------------------------------------------------------
double meq(double RHO, double U, double V, int k)
{
  double x;
  switch(k)
  {
   case 0: {x=RHO; break;}
   case 1: {x=RHO*(-2+3*(U*U+V*V));break;}
   case 2: {x=RHO*(1-3*(U*U+V*V));break;}
   case 3: {x=RHO*U;break;}
   case 4: {x=-RHO*U;break;}
   case 5: {x=RHO*V;break;}
   case 6: {x=-RHO*V;break;}
   case 7: {x=RHO*(U*U-V*V);break;}
   case 8: {x=RHO*U*V;break;}
   default: x=0;
  }
  return x;
}
//===========================================================

//===========================================================
//-----------------------------------------------------------
// Subroutine: Streaming
//-----------------------------------------------------------
void Streaming()
{
  int j, i, jd, id, k;
  for (j=0;j<=Ny;j++) for(i=0;i<=Nx;i++) for(k=0;k<Q;k++)
   {
        jd=j-cy[k]; id=i-cx[k]; // upwind node
```

```
          if(jd>=0 && jd<=Ny && id>=0 && id<=Nx) // fluid node
          f[j][i][k]=f_post[jd][id][k]; // streaming
    }
}
//============================================================

//============================================================
//------------------------------------------------------------
// Subroutine: Bounce-back scheme
//------------------------------------------------------------
void Bounce_back()
{
  int i,j;
 // j=Ny: top plate
  for(i=0;i<=Nx;i++)
  {
    f[Ny][i][4]=f_post[Ny][i][2];
    f[Ny][i][7]=f_post[Ny][i][5]+6*rho[Ny][i]*w[7]*cx[7]*uw;
    f[Ny][i][8]=f_post[Ny][i][6]+6*rho[Ny][i]*w[8]*cx[8]*uw;
  }

 // j=0: bottom plate
  for(i=0;i<=Nx;i++)
  {
     f[0][i][2]=f_post[0][i][4];
     f[0][i][5]=f_post[0][i][7];
     f[0][i][6]=f_post[0][i][8];
  }

 // i=0: left wall
  for(j=0;j<=Ny;j++)
  {
     f[j][0][1]=f_post[j][0][3];
     f[j][0][5]=f_post[j][0][7];
     f[j][0][8]=f_post[j][0][6];
  }

 // i=Nx: right wall
  for(j=0;j<=Ny;j++)
  {
     f[j][Nx][3]=f_post[j][Nx][1];
     f[j][Nx][7]=f_post[j][Nx][5];
     f[j][Nx][6]=f_post[j][Nx][8];
  }

}
//============================================================
```

```
//============================================================
//------------------------------------------------------------
// Subroutine: Fluid variables (density and velocity)
//------------------------------------------------------------
void Den_Vel()
{
  int j, i;
  for(j=0;j<=Ny;j++) for(i=0;i<=Nx;i++)
  {
    rho[j][i]=f[j][i][0]+f[j][i][1]+f[j][i][2]+f[j][i][3]
              +f[j][i][4]+f[j][i][5]+f[j][i][6]+f[j][i][7]+
              f[j][i][8];
    ux[j][i]=(f[j][i][1]+f[j][i][5]+f[j][i][8]-f[j][i][3]-
              f[j][i][6]-f[j][i][7])/rho[j][i];
    uy[j][i]=(f[j][i][5]+f[j][i][6]+f[j][i][2]-f[j][i][7]-
              f[j][i][8]-f[j][i][4])/rho[j][i];
  }
}

//============================================================

double Err()   // Calculating the relative difference in velocity between two steps
{
  int j, i;
  double e1,e2;
    e1=e2=0.0;
  for(j=1;j<Ny;j++) for(i=0;i<Nx;i++)
  {
    e1+=sqrt((ux[j][i]-u0[j][i])*(ux[j][i]-u0[j][i])
             +(uy[j][i]-v0[j][i])*(uy[j][i]-v0[j][i]));
    e2+=sqrt(ux[j][i]*ux[j][i]+uy[j][i]*uy[j][i]);
    u0[j][i]=ux[j][i];v0[j][i]=uy[j][i];
  }
  return e1/e2;
}


void  Data_Output() // Output data
{
  int i,j;
  FILE *fp;

  fp=fopen("x.dat","w+");
  for(i=0;i<=Nx;i++) fprintf(fp,"%e \n", (i+0.5)/L);
  fclose(fp);

  fp=fopen("y.dat","w+");
  for(j=0;j<=Ny;j++) fprintf(fp,"%e \n", (j+0.5)/L);
  fclose(fp);
```

```
  fp=fopen("ux.dat","w");
  for(j=0;j<=Ny;j++) {
    for (i=0; i<=Nx; i++) fprintf(fp,"%e ",ux[j][i]);
    fprintf(fp,"\n");
  }
  fclose(fp);

  fp=fopen("uy.dat","w");
  for(j=0;j<=Ny;j++){
    for (i=0; i<=Nx; i++) fprintf(fp,"%e ",uy[j][i]);
    fprintf(fp,"\n");
  }
  fclose(fp);

  fp=fopen("rho.dat","w");
  for(j=0;j<=Ny;j++){
    for (i=0; i<=Nx; i++) fprintf(fp,"%e ",rho[j][i]);
    fprintf(fp,"\n");
  }
  fclose(fp);
}
```

Bibliography

Adler, P. M. (1992). *Porous Media: Geometry and Transports* (Butterworth, London).

Agrawal, A., Djenidi, L. and Antonia, R. A. (2005). Simulation of gas flow in microchannels with a sudden expansion or contraction, *J. Fluid. Mech*., 530, pp. 135−144.

Aharonov, E. and Rothman, D. (1993). Non-Newtonian flow through porous media: A lattice-Boltzmann method, *Geophys. Res. Lett.*, 20, pp. 679–682.

Aidun, C. K. and Clausen, J. R. (2010). Lattice-Boltzmann method for complex flows, *Annu. Rev. Fluid Mech.*, 42, pp. 439–72.

Aidun, C. K. and Lu, Y. (1995). Lattice Boltzmann simulation of solid particles suspended in fluid, *J. Stat. Phys*., 81, pp. 49–61.

Aidun, C. K., Lu, Y. and Ding, E. (1998). Direct analysis of particulate suspensions with inertia using the discrete Boltzmann equation, *J. Fluid. Mech*., 373, pp. 287–311.

Alexander, F. J., Chen, S. and Grunau, D. W. (1993). Hydrodynamic spinodal decomposition: Growth kinetics and scaling, *Phys. Rev. B*, 48, pp. 634–637.

Alexander, F. J., Chen, S. and Sterling, J. D. (1993). Lattice Boltzmann thermo-hydrodynamics, *Phys. Rev. E*, 47, pp. R2249–2252.

Amati, G., Succi, S. and Piva, R. (1997). Massively parallel lattice-Boltzmann simulation of turbulent channel flow, *Int. J. Mod. Phys. C*, 8, pp. 869–878.

Amati, G., Succi, S. and Piva, R. (1999). Preliminary analysis of the scaling exponents in channel flow turbulence, *Fluid Dyn. Res*., 24, pp. 201–209.

Anderson, J. D. (1995). *Computational Fluid Dynamics: The Basics with Applications* (McGraw-Hill, New York).

Andries, P., Aoki, K. and Perthame, B. (2002). A consistent BGK-type model for gas mixtures, *J. Stat. Phys.*, 106, pp. 993–1018.

Arcidiacono, S., Ansumali, S., Karlin, I. V., Mantzaras, J. and Boulouchos, K. B. (2006). Entropic lattice Boltzmann method for simulation of binary mixtures, *Math. Comput. Simul.*, 72, pp. 79–83.

Arcidiacono, S., Mantzaras, J., Ansumali, S., Karlin, I. V., Frouzakis, C. E. and Boulouchos, K. B. (2006). Simulation of binary mixtures with the lattice Boltzman method, *Phys. Rev. E*, 74, p. 056707.

Arcidiacono, S., Karlin, I. V., Mantzaras, J. and Frouzakis, C. E. (2007). Lattice Boltzmann model for the simulation of multicomponent mixtures, *Phys. Rev. E*, 76, p. 046703.

Aristov, V. V. (2001). *Direct Methods for Solving the Boltzmann Equation and Study of Nonequilibrium Flows* (Kluwer Academic, Dordrecht).

Asinari, P. (2005). Viscous coupling based lattice Boltzmann model for binary mixtures, *Phys. Fluids*, 17, p. 067102.

Asinari, P. (2006). Semi-implicit-linearized multiple-relaxation-time formulation of lattice Boltzmann schemes for mixture modeling, *Phys. Rev. E*, 73, p. 056705.

Asinari, P. and L. S. Luo (2008). A consistent lattice Boltzmann equation with baroclinic coupling for mixtures, *J. Comput. Phys.*, 227, pp. 3878–3895.

Asinari, P., Mishra, S. C. and Borchiellini, R. (2010). A lattice Boltzmann formulation for the analysis of radiative heat transfer problems in a participating medium, *Num. Heat Trans. B*, 57, pp. 126–146.

Axner, L., Bernsdorf, J., Zeiser, T. *et al.* (2008). Performance evaluation of a parallel sparse lattice Boltzmann solver, *J. Comput. Phys*., 227, pp. 4895–4911.

Ayodele, S. G., Varnik, F. and Raabe, D. (2011). Lattice Boltzmann study of pattern formation in reaction-diffusion systems, *Phys. Rev. E*., 83, p. 016702.

Bartoloni, A., Battista, C., Cabasino, S. *et al.* (1993). LBE simulations of Rayleigh-Benard convection on the APE100 parallel processor, *Int. J. Mod. Phys. C*, 4, pp. 993–1006.

Batchelor, G. K. (1967). *An Introduction to Fluid Dynamics* (Cambridge University Press, Cambridge).

Bear, J. (1972). *Dynamics of Fluids in Porous Media* (Dover, New York).

Benzi, R., Struglia, M. V. and Tripiccione R. (1996). Extended self-similarity in numerical simulations of three-dimensional anisotropic turbulence, *Phys. Rev. E*, 53, pp. 5565–5568.

Benzi, R. and Succi, S. (1990). Two-dimensional turbulence with the lattice Boltzmann equation, *J. Phys. A*, 23, pp. 1–5.

Benzi, R., Succi, S. and Vergassola, M. (1992). The lattice Boltzmann equation: theory and applications, *Phys. Rep.* 222, pp. 145–197.

Bernaschi, M., Rossi, L., Benzi, R. *et al.* (2009). Graphics processing unit implementation of lattice Boltzmann models for flowing soft systems, *Phys. Rev. E*, 80, p. 066707.

Bernaschi, M. and Succi, S. (2003). Accelerated lattice Boltzmann scheme for steady-state flows, *Int. J. Mod. Phys. B*, 17, pp. 1–7.

Bernaschi, M., Succi, S., Chen, H. and Zhang, R. (2002). Computing steady state flows with an accelerated lattice Boltzmann technique, *Int. J. Mod. Phys. C*, 13, pp. 675–687.

Bespalko, D., Pollard, A. and Uddin, M. (2010). Direct numerical simulation of fully-developed turbulent channel flow using the lattice Boltzmann method and analysis of openmp scalability, *Lect. Notes Comput. Sci*., 5976, pp. 1–19.

Bhatnagar, P. L., Gross, E. P. and Krook, M. (1954). A model for collision processes in gases I: small amplitude processes in charged and neutral one-component systems, *Phys. Rev*., 94, pp. 511–525.

Bird, G. A. (1994). *Molecular Gas Dynamics and the Direct Simulation of Gas Flows* (Clarendon, Oxford).

Boek, E. S., Chin, J. and Coveney, P. V. (2003). Lattice Boltzmann simulation of the flow of non-Newtonian fluids in porous media, *Int. J. Mod. Phys. B*, 1, pp. 99–102.

Botella, O. and Peyret, R. (1998). Benchmark spectral results on the lid-driven cavity flow, *Comput. Fluids*, 27, pp. 421–433.

Bouzidi, M., Firdaouss, M. and Lallemand, P. (2001). Momentum transfer of a lattice Boltzmann fluid with boundaries, *Phys. Fluids*, 13, pp. 3452–3459.

Bouzidi, M., d'Humières, D., Lallemand, P. and Luo, L.-S. (2001). Lattice Boltzmann equation on a two-dimensional rectangular grid, *J. Computat. Phys*., 172, pp. 704–717.

Breyiannis, G. and Valougeorgis, D. (2004). Lattice kinetic simulations in three-dimensional magnetohydrodynamics, *Phys. Rev. E*, 69, pp. 65–72

Buick, J. M. and Greated, C. A. (2000). Gravity in a lattice Boltzmann model, *Phys. Rev. E*, 61, pp. 5307–5320.

Burattini, P., Lavoie, P., Agrawal, A., Djenidi, L. and Antonia, R. A. (2006). Power law of decaying homogeneous isotropic turbulence at low Reynolds number, *Phys. Rev. E*, 73, p. 066304.

Cao, N., Chen, S. Y., Jin, S. and Martinez, D. (1997). Physical symmetry and lattice symmetry in the lattice Boltzmann method, *Phys. Rev. E*, 55, 21–24.

Caiazzo, A. (2005). Analysis of lattice Boltzmann initialization routines, *J. Stat. Phys.*, 121, pp. 37–48.

Carnahan, N. F. and Starling, K. E. (1969). Equation of state for non-attracting rigid spheres, *J. Chem. Phys.*, 51, pp. 635–636.

Cercignani, C. (1988). *The Boltzmann Equation and Its Applications* (Springer-Verlag, New York).

Chapman, S. and Cowling, T. G. (1970). *The Mathematical Theory of Non-Uniform Gases* 3rd Ed. (Cambridge Univ Press, Cambridge, England).

Chatterjee, D. and Amiroudine, S. (2010). Lattice kinetic simulation of nonisothermal magnetohydrodynamics, *Phys. Rev. E*, 81, p. 066703.

Chen, F., Xu, A. G., Zhang, G. C., Li, Y. J. and Succi, S. (2010). Multiple-relaxation-time lattice Boltzmann approach to compressible flows with flexible specific-heat ratio and Prandtl number, *Europhys. Lett.*, 90, p. 54003.

Chen, F., Xu, A. G., Zhang, G. C. and Li, Y. J. (2011). Multiple-relaxation-time lattice Boltzmann model for compressible fluids, *Phys. Lett. A*, 375, pp. 2129–2139.

Chen, H., Kandasamy, S., Orszag, S. A. *et al.* (2003). Extended Boltzmann kinetic equation for turbulent flows, *Science*, 301, pp. 633–636.

Chen, H., Orszag, S. A., Staroselsky, I. and Succi, S. (2004). Expanded analogy between Boltzmann kinetic theory of fluids and turbulence, *J. Fluid Mech*., 519, pp. 301–314.

Chen, H., Teixeira, C. and Molvig, K. (1997). Digital physics approach to computational fluid dynamics: Some basic theoretical features, *Int. J. Mod. Phys. C*, 8, pp. 675–684.

Chen, S., Chen, H., Martinez, D. O. and Matthaeus, W. H. (1991). Lattice Boltzmann model for simulation of magnetohydrodynamics, *Phys. Rev. Let.*, 67, pp. 3776–3779.

Chen S. and Doolen G. D. (1998). Lattice Boltzmann method for fluid flows, *Annu. Rev. Fluid Mech.*, 30, pp. 329–64.

Chen, S., Martinez, D. and Mei, R. (1996). On boundary conditions in lattice Boltzmann methods, *Phys. Fluids*, 8, pp. 2527–2531.

Chen, S., Wang, Z., Shan, X. W. and Doolen, G. D. (1992). Lattice Boltzmann computational fluid dynamics in three dimensions, *J. Stat. Phys*., 68, pp. 379–400.

Chen, Y. and Ohashi, H. (1997). Lattice-BGK methods for simulating incompressible fluid flows, *Int. J. Mod. Phys. C*, 8, pp. 793–803.

Chen, Y., Ohashi, H. and Akiyama, M. (1994). Thermal lattice Bhatnagar-Gross-Krook model without nonlinear deviations in macrodynamic equations, *Phys. Rev. E*, 50, pp. 2776–2783.

Chen, Y., Ohashi, H. and Akiyama, M. (1995). Heat transfer in lattice BGK modeled fluid, *J. Stat. Phys.*, 81, pp. 71–85.

Chen, Y., Ohashi, H. and Akiyama, M. (1997). Two-parameter thermal lattice BGK model with a controllable Prandtl number, *J. Sci. Comput.*, 12, pp. 169–185.

Cheremisin, F. G. (1991). Fast solutions of the Boltzmann equation, in *Rarefied Gas Dynamics* (ed. A. Beylich, VCH, pp. 273).

Chew, Y. T., Shu, C. and Niu, X. D. (2002). A new differential lattice Boltzmann equation and its application to simulate incompressible flows on non-uniform grids, *J. Stat. Phys.*, 107, pp. 329–342.

Chew, Y. T., Shu, C. and Peng Y. (2002) On implementation of boundary conditions in the application of finite volume lattice Boltzmann method, *J. Stat. Phys.*, 107, pp. 539–556.

Chikatamarla, S. S., Frouzakis, C. E., Karlin, I. V. *et al.* (2010). Lattice Boltzmann method for direct numerical simulation of turbulent flows, *J. Fluid Mech*., 656, pp. 298–308.

Choi, Y.-H. and Merkle, C. L. (1993). The application of preconditioning to viscous flows, *J. Comput. Phys*., 105, pp. 207–233.

Chopard, B. and Masselot, A. (1999). Cellular automata and lattice Boltzmann methods: a new approach to computational fluid dynamics and particle transport, *Future Generation Comput. Syst.*, 16, pp. 249–257.

Chun, B. and Ladd, A. J. C. (2007). Interpolated boundary condition for lattice Boltzmann simulations of flows in narrow gaps, *Phys. Rev. E*, 75, p. 066705.

Cristea, A. and Sofonea, V. (2003). Reduction of spurious velocity in finite difference lattice Boltzmann models for liquid–vapor systems, *Int. J. Mod. Phys. C*, 14, pp. 1251–1266.

Coutanceau, M. and Bouard, R. (1977). Experimental determination of the main features of the viscous flow in the wake of a circular cylinder in uniform translation. Part 1. Steady flow, *J. Fluid Mech.*, 79, pp. 231–256.

Crouse, B., Rank, E., Krafczyk, M. and Tölke, J. (2003). A LB-based approach for adaptive flow simulations, *Int. J. Mod. Phys. B*, 17, pp. 109–112.

Dardis, O. and McCloskey, J. (1998). Lattice Boltzmann scheme with real numbered solid density for the simulation of flow in porous media, *Phys. Rev. E*, 57, pp. 4834–4837.

Darhuber, A. A. and Troian, S. M. (2005). Principles of microfluidic actuation by modulation of surface stresses, *Annu. Rev. Fluid Mech.*, 37, pp. 425–455.

Dellar, P. J. (2002), Lattice kinetic schemes for magnetohydrodynamics, *J. Comput. Phys.*, 179, pp. 95–126.

Dellar, P. J. (2008). Two routes from the Boltzmann equation to compressible flow of polyatomic gases, *Prog. Comput. Fluid Dyn.*, 8, pp. 84–96.

Dellar, P. J., Lapitski, D., Palpacelli, S. and Succi, S. (2011). Isotropy of three-dimensional quantum lattice Boltzmann schemes, *Phys. Rev. E*, 83, p. 046706.

Desplat, J.-C., Pagonabarraga, I. and Bladon, P. (2001). LUDWIG: A parallel lattice-Boltzmann code for complex fluids, *Comput. Phys. Commun.*, 134, pp. 273–290.

d'Humières, D., Lallemand, P. and Frisch, U. (1986). Lattice gas model for 3D hydrodynamics, *Europhys. Lett*., 2, p. 291.

d'Humières, D. (1992). Generalized lattice Boltzmann equations, *Prog. Aeronaut Astronaut.*, 159, pp. 450–458.

d'Humières, D., Ginzburg, I., Krafczyk, M. *et al.* (2002). Multiple-relaxation-time lattice Boltzmann models in three dimensions, *Phil. Trans. R. Soc. Lond. A*, 360, pp. 437–451.

Ding, H. and Shu, C. (2006). A stencil adaptive algorithm for finite difference solution of incompressible viscous flows, *J. Comput. Phys.*, 214, pp. 397–420.

Djenidi, L. (2006). Lattice-Boltzmann simulation of grid-generated turbulence, *J. Fluid Mech*., 552, pp. 13–35.

Dong, W. (1956). Vacuum flow of gases through channels with circular, annular and rectangular cross sections. *University of California Report*, No. UCRL-3353.

Dong, Y.-H., Sagaut, P. and Marie, S. (2008). Inertial consistent sub-grid model for large-eddy simulation based on the lattice Boltzmann method, *Phys. Fluids*, 20, p. 035104.

d'Ortona, U., Salin, D., Cieplak, M., Rybka, R. and Banavar, J. (1995). Two-color nonlinear Boltzmann cellular automata: Surface tension and wetting, *Phys. Rev. E*, 51, pp. 3718–3728.

Du, R., Shi, B. C. and Chen, X. W. (2006). Multi-relaxation-time lattice Boltzmann model for incompressible flow, *Phys. Lett.s A*, 359, pp. 564–572.

Dünweg, B. and Ladd, A. J. C. (2009). Lattice Boltzmann simulations of soft matter systems, *Adv. Polym. Sci*., 221, pp. 89–166.

Dupuis, A. and Chopard, B. (2002). Lattice gas modeling of scour formation under submarine pipelines, *J. Comput. Phys*., 178, pp. 161–174.

Dupuis, A. and Chopard, B. (2003). Theory and applications of an alternative lattice Boltzmann grid refinement algorithm, *Phys. Rev. E*, 67, p. 066707.

Düster, A., Demkowicz, L. and Rank, E. (2006). High-order finite elements applied to the discrete Boltzmann equation, *Int. J. Numer. Meth. Eng*. 67, pp. 1094−1121.

Eggels, J. G. M. (1996), Direct and large-eddy simulation of turbulent fluid flow using the lattice-Boltzmann scheme, *Int. J. Heat Fluid Flow*, 17, pp. 307–323.

Eggels, J. G. M. and Somers, J. A. (1995). Numerical simulation of the free convective flow using the lattice-Boltzmann scheme, *Int. J. Heat Fluid Flow*, 16, pp. 357–364.

Ergun, S. (1952). Flow through packed columns, *Chem. Eng. Prog*., 48, pp. 89–94.

Fadlun, E., Verzicco, R., Orlandi, P., Mohd-Yusof, J. (2000). Combined immersed-boundary finite-difference methods for three dimensional complex flow simulations, *J. Comput. Phys.*, 161, pp. 35–60.

Feng, Y. T., Han, K. and Owen, D. R. J. (2007). Coupled lattice Boltzmann method and discrete element modelling of particle transport in turbulent fluid flows: Computational issues, *Int. J. Numer. Meth. Engng*., 72, pp. 1111–1134.

Feng, Z. and Michaelides, E. (2004). The immersed boundary-lattice Boltzmann method for solving fluid-particles interaction problems, *J. Comput. Phys.*, 195, pp. 602–628.

Feng, Z. and Michaelides, E. (2005). Proteus: a direct forcing method in the simulations of particulate flows, *J. Comput. Phys.*, 202, pp. 20–51.

Ferzige, J. H. and Peric, M. (2002). *Computational Methods for Fluid Dynamics* 3rd Ed. (Springer-Verlag, Berlin).

Filippova, O. and Hänel, D. (1997). Lattice-Boltzmann simulation of gas-particle flow in filters, *Comput. Fluids*, 26, pp. 697−712.

Filippova, O. and Hänel, D. (1998). Grid refinement for lattice-BGK models, *J. Comput. Phys.*, 147, pp. 219–228.

Filippova, O. and Hänel, D. (2000). A novel lattice BGK approach for low Mach number combustion, *J. Comput. Phys.*, 158, pp. 139–160.

Filippova, O., Succi, S., Mazzocco, F. *et al.* (2001). Multiscale Lattice Boltzmann Schemes with Turbulence Modeling, *J. Comput. Phys*., 170, pp. 812–829.

Flekkøy, E. G. (1993). Lattice Bhatnagar-Gross-Krook models for miscible fluids, *Phys. Rev. E*, 47, pp. 4247–4257.

Frisch, U., Hasslacher, B. and Pomeau, Y. (1986). Lattice-gas automata for the Navier-Stokes equations, *Phys. Rev. Lett.*, 56, pp. 1505–1508.

Frisch, U., d'Humiéres, D., Hasslacher, B. *et al.* (1987). Lattice gas hydrodynamics in two and three dimensions, *Complex Syst.*, 1, pp. 649–707.

Gan, Y. B., Xu, A. G., Zhang, G. C. *et al*. (2008). Two-dimensional lattice Boltzmann model for compressible flows with high Mach number, *Physica. A*, 387, pp. 1721−1732.

Ghia, U., Ghia, K. N. and Shin, C. T. (1982). High resolution of Navier-Stokes equations in primitive variables, *J. Comput. Phys*., 48, pp. 387–411.

Ginzbourg, I. and Adler, P. M. (1994). Boundary flow condition analysis for the three-dimensional lattice Boltzmann model, *J. Phys. II. France*, 4, pp. 191–214.

Ginzbourg, I. and d'Humières, D. (2003). Multireflection boundary conditions for lattice Boltzmann models, *Phys. Rev. E*, p. 066614.

Girimaji, S. S. (2007). Boltzmann kinetic equation for filtered fluid turbulence, *Phys. Rev. Lett*., 99, p. 034501.

Goldstein, D., Hadler, R. and Sirovich, L. (1993). Modeling a no-slip flow boundary with an external force field, *J. Comput. Phys*., 105, pp. 354–366.

Gross E. P. and Krook, M. (1956). Models for collision process: Small-amplitude oscillations of charged two-component systems, *Phys. Rev*., 102, pp. 593–604.

Grunau, D., Chen, S. and Eggert, K. (1993). A lattice Boltzmann model for multiphase fluid flows, *Phys. Fluids A*, 5, pp. 2557–2562.

Gunstensen, A. K. and Rothman, D. H. (1993). Lattice Boltzmann studies of immiscible two phase flow through porous media, *J. Geophys. Res*., 98, pp. 6431–6341.

Gunstensen, A. K., Rothman, D. H., Zaleski, S. and Zanetti, G. (1991). Lattice Boltzmann model of immiscible fluids, *Phys. Rev. A*, 43, pp. 4320–4327.

Guo, Z. L., Asinari, P. and Zheng, C. G. (2009). Lattice Boltzmann equation for microscale gas flows of binary mixtures, *Phys. Rev. E*, 79, p. 026702.

Guo, Z. L., Shi, B. C. and Wang, N. C. (2000). Lattice BGK model for incompressible Navier-Stokes equation, *J. Comput. Phys.*, 165, pp. 288–306.

Guo, Z. L., Shi, B. C., Zhao, T. S. and Zheng, C. G. (2007). Discrete effects on boundary conditions for the lattice Boltzmann equation in simulating microscopic gas flows, *Phys. Rev. E*, 76, p. 056704.

Guo, Z. L., Shi, B. C. and Zheng C. G. (2002). A coupled lattice BGK model for the Boussinesq equations, *Int. J. Numer. Meth. Fluids*, 39, pp. 325–342.

Guo, Z. L., Shi, B. C. and Zheng, C. G. (2007). An extended Navier-Stokes formulation for gas flows in Knudsen layer near a wall, *Europhys. Lett.*, 80, p. 24001.

Guo, Z. L., Shi, B. C. and Zheng, C. G. (2011). Chequerboard effects on spurious currents in the lattice Boltzmann equation for two-phase flows, *Phil. Trans. R. Soc. A*, 369(1944), pp. 2283–2291.

Guo, Z. L. and Zhao, T. S. (2002). Lattice Boltzmann method for flow through porous media, *Phys. Rev. E*, 66, p. 036304.

Guo, Z. L. and Zhao, T. S. (2003a). Explicit finite-difference lattioce Boltzmann method for curvilinear coordinates, *Phys. Rev. E*, 67, p. 066709.

Guo, Z. L. and Zhao, T. S. (2003b). Discrete velocity and lattice Boltzmann models for binary mixtures of nonideal fluids, *Phys. Rev. E*, 68, p. 035302.

Guo, Z. L. and Zhao, T. S. (2005). Finite-difference-based lattice Boltzmann model for dense binary mixtures, *Phys. Rev. E*, 71, p. 026701.

Guo, Z. L., Zhao, T. S. and Shi, Y. (2004). Preconditioned lattice-Boltzmann method for steady flows, *Phys. Rev. E*, 70, p. 066706.

Guo, Z. L., Zhao, T. S. and Shi, Y. (2005). A lattice Boltzmann algorithm for electro-osmotic flows in microfluidic devices, *J. Chem. Phys*., 122, p. 144907.

Guo, Z. L., Zhao, T. S. and Shi, Y. (2006). Physical symmetry, spatial accuracy, and relaxation time of the lattice Boltzmann equation for micro gas flows, *J. Appl. Phys.*, 99, p. 074903.

Guo, Z. L. and Zheng, C. G. (2007). Analysis of lattice Boltzmann equation for microscale gas flows: Relaxation times, boundary conditions and the Knudsen layer, *Int. J. Comput. Fluid Dynamics*, 22, pp. 465–43.

Guo, Z. L., Zheng, C. G. and Shi, B. C. (2002a). Non-equilibrium extrapolation method for velocity and pressure boundary conditions in the lattice Boltzmann method, *Chinese Phys*., 11, pp. 366–374.

Guo, Z. L., Zheng, C. G. and Shi, B. C. (2002b). An extrapolation method for boundary conditions in lattice Boltzmann method, *Phys. Fluids*, pp. 2007–2010.

Guo, Z. L., Zheng, C. G. and Shi, B. C. (2002c). Discrete lattice effects on the forcing term in the lattice Boltzmann method, *Phys. Rev. E*, 65, p. 046308.

Guo, Z. L., Zheng, C. G. and Shi, B. C. (2003). Domain decomposition technique in lattice Boltzmann method, *Int. J. Mod. Phys. B*, 17, pp. 129–133.

Guo, Z. L., Zheng, C. G. and Shi, B. C. (2007). Thermal lattice Boltzmann equation for low Mach number flows: Decoupling mode, *Phys. Rev. E*, 75, p. 36704.

Guo, Z. L., Zheng, C. G. and Shi, B. C. (2008). Lattice Boltzmann equation with multiple effective relaxation times for gaseous microscopic flow, *Phys. Rev. E*, 77, p. 036707.

Guo, Z. L., Zheng, C. G. and Shi, B. C. (2011). Force imbalance in lattice Boltzmann equation for two-phase flows, *Phys. Rev. E*, 83, p. 036707.

Guo, Z. L. and Zhou, Y. (2004). Numerical simulation of oscillating-cylinder effects on a downstream cylinder wake using lattice Boltzmann method, *Fluid Mech. its Appl.*, 75, pp. 415–424.

Hadjiconstantinou, N. G. (2003). Comment on Cercignani's second-order slip coefficient, *Phys. Fluids*, 15, pp. 2352–2354.

Hamel, B. B. (1966). Two fluid hydrodynamic equations for a neutral, disparate, mass, binary mixture, *Phys. Fluids*, 9, pp. 12–22.

Hardy, J., Pomeau, Y. and de Pazzis O. (1973a). Time evolution of a two-dimensional classical lattice system, *Phys. Rev. Lett.*, 31, pp. 276–279.

Hardy, J., Pomeau, Y. and de Pazzis O. (1973b). Time evolution of two-dimensional model system I: Invarient states and time correlation functions, *J. Math. Phys.*, 14, 1746–1759.

Harris, S. (1971). *An Introduction to the Theory of the Boltzmann Equation* (Holt, Rinehart and Winston, New York).

Hatiboglu, C. U. and Babadagli, T. (2007). Lattice-Boltzmann simulation of solvent diffusion into oil-saturated porous media, *Phys. Rev. E*, 76, p. 066309.

Hatiboglu, C. U. and Babadagli, T. (2008). Pore-scale studies of spontaneous imbibition into oil-saturated porous media, *Phys. Rev. E*, 77, p. 066311.

Házi, G. and Tóth, G. (2010). Lattice Boltzmann simulation of two-dimensional wall bounded turbulent flow, *Int. J. Mod. Phys. C*, 21, pp. 669–680.

He, X., Chen, S. and Doolen, G. D. (1998). A novel thermal model for the lattice Boltzmann method in incompressible limit, *J. Comput. Phys.*, 146, pp. 282–300.

He, X., Chen, S. and Zhang, R. (1999). A lattice Boltzmann scheme for incompressible multiphase flow and its application in simulation of Rayleigh-Taylor instability, *J. Comput. Phys.*, 152, pp. 642–663.

He, X. and Doolen, G. (1997). Lattice Boltzmann method on curvilinear coordinates system: Flow around a circular cylinder, *J. Comput. Phys.*, 134, pp. 306–315.

He, X., Doolen, G. D. and Clark, T. (2002). Comparison of the lattice Boltzmann method and the artificial compressibility method for Navier-Stokes equations, *J. Comput. Phys.*, 179, 439–451.

He, X. and Li, N. (2000). Lattice Boltzmann simulation of electrochemical systems, *Comput. Phys. Comm*., 129, pp. 158–166.

He, X. and Luo, I.-S. (1997). Lattice Boltzmann model for the incompressible Navier-Stokes equation, *J. Stat. Phys.*, 88, pp. 927–944.

He, X., Luo, L.-S. and Dembo, M. (1996). Some progress in lattice Boltzmann method 1: Nonuniform mesh grids, *J. Comput. Phys*., 29, pp. 357–363.

He, X., Zou, Q., Luo, L.-S. and Dembo, M. (1997). Analytic solutions of simple flow and analysis of non-slip boundary conditions for the lattice Boltzmann BGK model, *J. Stat. Phys.*, 87, pp. 115–123.

He, X., Luo, L.-S. and Dembo, M. (1997). Some progress in the lattice Boltzmann method: Reynolds number enhancement in simulations, *Phys. A*, 239, pp. 276–285.

He, X., Shan, X. and Doolen, G. D. (1998). Discrete Boltzmann equation model for nonideal gases, *Phys. Rev. E*, 57, pp. 13–16.

He, X., Zhang, R., Chen, S. and Doolen, G. D. (1999). On the three-dimensional Rayleigh-Taylor instability, *Phys. Fluids*, 11, pp. 1143–1152.

He, X., Zou, Q., Luo, L. S. and Dembo, M. (1997). Analytic solutions of simple flow and analysis of non-slip boundary conditions for the lattice Boltzmann BGK model, *J. Stat. Phys*., 87, pp. 115–123.

Heijs, A. and Lowe, C. P. (1995). Numerical evaluation of the permeability and the Kozeny constant for two types of porous media, *Phys. Rev. E*, 51, pp. 4346–4352.

Higuera, F. and Jimenez, J. (1989). Boltzmann approach to lattice gas simulations, *Europhys. Lett.*, 9, pp. 663–668.

Higuera, F. J. and Succi, S. (1989). Simulating the flow around a circular cylinder with a lattice Boltzmann equation, *Europhys. Lett*., 8, pp. 517–521.

Higuera, F., Succi, S. and Benzi, R. (1989). Lattice gas dynamics with enhanced collisions, *Europhys. Lett.*, 9, pp. 345–349.

Ho, C.-M. and Tai, Y.-C. (1998). Micro-electro-mechanicalsystems (MEMS) and fluid flows, *Annu. Rev. Fluid Mech*., 30, pp. 579–612.

Holway, L. H. (1966). New statistical models for kinetic theory: methods of construction, *Phys. Fluids*, 9, pp. 1658–1673.

Hoogerbrugge, P. J. and Koelman, J. (1992). Simulating microscopic hydrodynamic phenomena with dissipative particle dynamics, *Europhys. Lett.*, 19, pp. 155–160.

Hou, S., Shan, X., Zou, Q., Doolen, G. D. and Soll, W. E. (1997). Evaluation of two lattice Boltzmann models for multiphase flows, *J. Comput. Phys.*, 138, pp. 695–713.

Hou, S., Sterling, J., Chen, S. and Doolen, G. D. (1996). A lattice Boltzmann sub-grid model for high Reynolds number flows, *Fields Inst. Comm.*, 6, pp. 151–166.

Hou, S. and Zou, Q. (1995). Simulation of cavity flow by the lattice Boltzmann method, *J. Comput. Phys.*, 118, pp. 329–347.

Hu, S. X., Yan, G. W. and Shi, W. P. (1997). A lattice Boltzmann model for compressible perfect gas, *Acta Mech. Sinica*, 13, pp. 218–226.

Inamuro, T., Konishi, N. and Ogino, F. (2000). A Galilean invariant model of the lattice Boltzmann method for multiphase fluid flows using free-energy approach, *Comput. Phys. Commun*, 129, pp. 32–45.

Inamuro, T., Maeba, K. and Ogino, F. (2000). Flow between parallel walls containing the lines of neutrally buoyant circular cylinders, *Int. J. Multiphase Flow*, 26, pp. 1981–2004.

Inamuro, T., Ogata, T., Tajima, S. and Konishi, N. (2004). A lattice Boltzmann method for incompressible two-phase flows with large density differences, *J. Comput. Phys.*, 198, pp. 628–644.

Inamuro, T., Yoshino, M. and Ogino, F. (1995). A non-slip boundary condition for lattice Boltzmann simulations, *Phys. Fluids*, 7, pp. 2928–2930.

Inamuro, T., Yoshino, M. and Ogino, F. (1999). Lattice Boltzmann simulation of flows in a three-dimensional porous structure, *Int. J. Numer. Meth. Fluids*, 29, pp. 737–748.

Ivchenko, I. N., Loyalka, S. K. and Tompson, R. V. (1997). Slip coefficients for binary gas mixtures, *J. Vac. Sci. Tech. A*, 15, pp. 2375–2371.

Izquierdo, S. and Fueyo, N. (2008). Preconditioned Navier-Stokes schemes from the generalised lattice Boltzmann equation, *Prog. Comput. Fluid Dyn.*, 8, pp. 189–196.

Izquierdo, S. and Fueyo, N. (2009). Optimal preconditioning of lattice Boltzmann method, *J. Comput. Phys.*, 228, pp. 6479–6495.

Jafari, S. and Rahnama, M. (2011). Shear-improved Smagorinsky modeling of turbulent channel flow using generalized lattice Boltzmann equation, *Int. J. Numer. Meth. Fluids*, 67, pp. 700–712.

Jameson, A., Schmidt, W. and Turkel, E. (1981). Numerical solution of the Euler equations by finite volume methods using Runge-Kutta time-stepping scheme, *AIAA* paper 81−1259.

Ji, C. Z., Shu, C. and Zhao, N. (2009). A lattice Boltzmann method-based flux solver and its application to solve shock tube problem, *Mod. Phys. Lett. B*, 23, pp. 313–316.

Joshi, H., Agarwal, A., Puranik, B., Shu, C. and Agrawal, A. (2010). A hybrid FVM-LBM method for single and multi-fluid compressible flow problems, *Int J. Numer. Meth. Fluid*, 62, pp. 403–427.

Junk, M. and Yang, Z. X. (2005a). Asymtotic analysis of lattice Boltzmann boundary conditions, *J. Stat. Phys.*, 121, pp. 3–35.

Junk, M. and Yang, Z. X. (2005b). One-point boundary condition for the lattice Boltzmann method, *Phys. Rev. E*, 72, p. 066701.

Kalarakis, A., Burganos, V. and Payatakes, A. C. (2002). Galilean-invariant lattice-Boltzmann simulation of liquid-vapor interface dynamics, *Phys. Rev. E*, 65, p. 056702.

Kang, Q., Lichtner, P. C. and Janecky, D. R. (2010). Lattice Boltzmann method for reacting flows in porous media, *Adv. Appl. Math. Mech.*, 2, pp. 545–563.

Kandhai, D., Koponen, A., Hoekstra, A. *et al.* (1998). Lattice-Boltzmann hydrodynamics on parallel systems, *Comp. Phys. Comm.*, 111, pp. 14–26.

Kandhai, D., Koponen, A., Hoekstra, A. *et al.* (1999). Implementation aspects of 3D lattice-BGK: boundaries, accuracy, and a new fast relaxation method, *J. Comput. Phys.*, 150, pp. 482–501.

Kanki, T. and Iuchi, S. (1973). Poiseuille flow and thermal creep of a rarefied gas between parallel plates, *Phys. Fluids*, 16, pp. 594–599.

Kao, P.-H. and Yang, R.-J. (2008). An investigation into curved and moving boundary treatments in the lattice Boltzmann method, *J. Comput. Phys.*, 227, pp. 5671–5690.

Karniadakis, G. E. and Beskok, A. (2002) *Micro Flows* (Springer-Verlag, New York).

Kataoka, T. and Tsutahara, M. (2004a). Lattice Boltzmann method for the compressible Navier-Stokes equations with flexible specific-heat ratio, *Phys. Rev. E*, 69, p. R035701.

Kataoka, T. and Tsutahara, M. (2004b). Lattice Boltzmann method for the compressible Euler equations, *Phys. Rev. E*, 69, p. 056702.

Kim, W. T., Jhon, M. S., Zhou, Y. *et al*. (2005). Nanoscale air bearing modeling via lattice Boltzmann method, *J. Appl. Phys*., 97, p. 10P304.

Koelman, J. (1991). A simple lattice Boltzmann scheme for Navier-Stokes fluid flow, *Europhys. Lett.*, 15, pp. 603–607.

Koponen, A., Kandhai, D., Hellén, E. *et al.* (1998). Permeability of three-dimensional random fiber webs, *Phys. Rev. Lett*., 80, pp. 716–719.

Krafczyk, M., Tölke, J. and Luo, L.-S. (2003). Large-eddy simulations with a multiple-relaxation- time LBE model, *Int. J. Mod. Phys. B*, 7, pp. 33–39.

Ladd, A. J. C. (1994a). Numerical simulations of particulate suspensions via a discretized Boltzmann equation. Part I. Theoretical foundation, *J. Fluid Mech.*, 271, pp. 285–310.

Ladd, A. J. C. (1994b). Numerical simulations of particulate suspensions via a discretized Boltzmann equation. Part II. Numerical results, *J. Fluid Mech*., 271, pp. 311–339.

Ladd, A. J. C. and Verberg, R. (2001). Lattice-Boltzmann simulations of particle-fluid suspensions, *J. Stat. Phys.*, 104, pp. 1191–1251.

Lai, Y. G., Lin, C. L. and Huang, J. C. (2001). Accuracy and efficiency study of lattice Boltzmann method for steady-state flow simulations, *Num. Heat Transf. Part B*, 39, pp. 21–43.

Lai, M. C. and Peskin, C. S. (2000). An immersed boundary method with formal second-order accuracy and Reduced numerical viscosity, *J. Comput. Phys*., 160, pp. 705–719.

Lallemand, P. and Luo, L.-S. (2000). Theory of the lattice Boltzmann method: Dispersion, dissipation, isotropy, Galilean invariance, and stability, *Phys. Rev. E*, 61, pp. 6546–6562.

Lallemand, P. and Luo, L.-S. (2003). Theory of the lattice Boltzmann method: Acoustic and thermal properties in two and three dimensions, *Phys. Rev. E*, 68, pp. 036706.

Lammers, P., Beronov, K. N., Volkert, R. *et al.* (2006). Lattice BGK direct numerical simulation of fully developed turbulence in incompressible plane channel flow, *Comput. Fluids*, 35, pp. 1137–1153.

Lantermann, U. and Hänel, D. (2007). Particle Monte Carlo and lattice-Boltzmann methods for simulations of gas-particle flows, *Comput. Fluids*, 36, pp. 407–422.

Lee, D. (1996). Local Preconditioning of the Euler and the Navier-Stokes Equations. Ph.D. thesis, University of Michigan.

Lee, T. and Fischer, P. F. (2006). Eliminating parasitic currents in the lattice Boltzmann equation method for nonideal gases, *Phys. Rev. E*, 74, p. 046709.

Lee, T. and Lin, C.-L. (2001). A characteristic Galerkin method for discrete Boltzmann equation, *J. Comput. Phys.*, 171, pp. 336–356.

Lee, T. and Lin, C. L. (2003). An Eulerian description of the streaming process in the lattice Boltzmann equation, *J. Comput. Phys.*, 185, pp. 445–471.

Lee, T. and Lin, C.-L. (2005a). A stable discretization of the lattice Boltzmann equation for simulation of incompressible two-phase flows at high density ratio, *J. Comput. Phys*., 2106, pp. 16–47.

Lee, T. and Lin, C. L. (2005b). Rarefaction and compressibility effects of the lattice Boltzmann equation method in a gas microchannel, *Phys. Rev. E*, 71, p. 046706.

Li, H. B., Lu, X., Fang, H. P. and Qian, Y. H. (2004). Force evaluations in lattice Boltzmann simulations with moving boundaries in two dimensions, *Phys. Rev. E*, 70, p. 026701.

Li, Q., He, Y. L., Wang, Y. and Tao, W. Q. (2007). Coupled double-distribution-function lattice Boltzmann method for the compressible Navier-Stokes equations, *Phys. Rev. E*, 76, p. 056705.

Li, Q., He, Y. L., Wang, Y. and Tang, G. H. (2009). Three-dimensional non-free-parameter lattice-Boltzmann model and its application to inviscid compressible flows, *Phys. Lett. A*, 373, pp. 2101–2108.

Li, W., Wei, X. M. and Kaufman, A. (2004). Implementing lattice Boltzmann computation on graphics hardware, *Visual Comput.*, 19, pp. 444–445.

Li, Y., LeBoeuf, E. J. and Basu, P. K. (2004). Least-squares finite-element lattice Boltzmann method, *Phys. Rev. E*, 69, p. 065701.

Lim, C. Y., Shu, C., Niu, X. D. and Chew, Y. T. (2002). Application of lattice Boltzmann method to simulate microchannel flows, *Phys. Fluids*, 14, pp. 2299–2308.

Lin, Z., Fang, H. P. and Tao, R. B. (1996). Improved lattice Boltzmann model for incompressible two-dimensional steady flows, *Phys. Rev. E*, 54, pp. 6323–6330.

Liu, H. J., Zou, C., Shi, B. C. *et al.* (2006). Thermal lattice-BGK model based on large-eddy simulation of turbulent natural convection due to internal heat generation, *Int. J. Heat Mass Transf.*, 49, pp. 4672–4680.

Lockerby, D. A., Reese, J. M. and Gallis, M. A. (2005). The usefulness of higher-order constitutive relations for describing the Knudsen layer, *Phys. Fluids*, 17, p. 100609.

Lowe, C., Frenkel, D. and Masters, A. J. (1995). Long-time tails in angular momentum correlations, *J. Chem. Phys.*, 103, pp. 1582–1587.

Lu, X.-Y. and Dalton, C. (1996). Calculation of the timing of vortex formation from an oscillating cylinder, *J. Fluids Struct.*, 10, pp. 527–541.

Lu, Z., Liao, Y., Qian, D. *et al.* (2002). Large eddy simulations of a stirred tank using the lattice Boltzmann method on a nonuniform grid, *J. Comput. Phys.*, 181, pp. 675–704.

Luis, V., Jesus, M. and Gabor, H. (2010). Dynamics of isotropic homogeneous turbulence with linear forcing using a lattice Boltzmann method, *Flow Turb. Combust.*, 84, pp. 219–237.

Luo, L.-S. (1997). Analytic solutions of linearized lattice Boltzmann equation, *J. Stat. Phys.*, 88, pp. 913–926.

Luo, L.-S. (1998). Unified theory of the lattice Boltzmann models for nonideal gases, *Phys. Rev. Lett.*, 81, pp. 1618–1621.

Luo, L. (2000). Theory of the lattice Boltzmann method: Lattice Boltzmann models for nonideal gases, *Phys. Rev. E*, 62, pp. 4982–4996.

Luo, L. S. (2004). Comment on "Discrete Boltzmann equation for microfluidics", *Phys. Rev. Lett.*, 92, p. 139401.

Luo, L.-S., Liao, W., Chen, X. W. *et al.* (2011). Numerics of the lattice Boltzmann method: Effects of collision models on the lattice Boltzmann simulations, *Phys. Rev. E*, 83, p. 056710.

Luo, L. S. and Girimaji, S. S. (2002). Lattice Boltzmann model for binary mixtures, *Phys. Rev. E*, 66, p. 035301.

Luo, L. S. and Girimaji, S. S. (2003). Theory of the lattice Boltzmann method: Two-fluid model for binary mixtures, *Phys. Rev. E*, 67, p. 036302.

Ma, Y., Dong, S. and Tan, H. P. (2011). Lattice Boltzmann method for one-dimensional radiation transfer, *Phys. Rev. E*, 84, p. 016704.

Machado, R. (2012). Numerical simulations of surface reaction in porous media with lattice Boltzmann, *Chem. Eng. Sci.*, 69, pp. 628–643.

Madadi, M. and Sahimi, M. (2003). Lattice Boltzmann simulation of fluid flow in fracture networks with rough, self-affine surfaces, *Phys. Rev. E*, 67, p. 026309.

Maier, R. S., Bernard, R. S. and Grunau, D. W. (1996). Boundary conditions for the lattice Boltzmann method, *Phys. Fluids*, 8, pp. 1788–1793.

Maier, R. S., Kroll, D. M., Benard, R. S. *et al.* (2000). Pore-scale simulation of dispersion, *Phys. Fluids*, 12, pp. 2065–2079.

Malaspinas, O. and Sagaut, P. (2011). Advanced large-eddy simulation for lattice Boltzmann methods: The approximate deconvolution model, *Phys. Fluids*, 23, p. 105103.

Manz, B., Gladden, L. F. and Warren, P. B. (1999). Flow and dispersion in porous media: Lattice-Boltzmann and NMR studies, *AIChE J*., 45, pp. 1845–1854.

Martinez, D. O., Matthaeus, W. H., Chen, S. and Montgomery, D. C. (1994). Comparison of spectral method and lattice Boltzmann simulations of two-dimensional hydrodynamics, *Phys. Fluids*, 6, pp. 1285–1298.

Martys, N. S. (2001). Improved approximation of the Brinkman equation using a lattice Boltzmann method, *Phys. Fluids*, 6, pp. 1807–1810.

Martys, N. S. and Chen, H. (1996). Simulation of multicomponent fluids in complex three-dimensional geometries by the lattice Boltzmann method, *Phys. Rev. E*, 53, pp. 743–750.

Martys, N. S., Shan, X. and Chen, H. (1998). Evaluation of the external force term in the discrete Boltzmann equation, *Phys. Rev. E*, 58, pp. 6855–6857.

Masselot, A. and Chopard, B. (1998). A lattice Boltzmann model for particle transport and deposition, *Europhys. Lett*., 42, pp. 259–264.

Mattila, K., Hyvaluoma, J., Rossi, T. *et al*. (2007). An efficient swap algorithm for the lattice Boltzmann method, *Comput. Phys. Commun*., 176, pp. 200–210.

Mavriplis, D. (2006). Multigrid solution of the steady-state lattice Boltzmann equation, *Comp. Fluids*, 35, pp. 793804.

Mayer, G., Páles, J. and Házi, G. (2007). Large eddy simulation of subchannels using the lattice Boltzmann method, *Ann. Nucl. Energy*, 34, pp. 140–149.

McCracken, M. E. and Abraham, J. (2005). Lattice Boltzmann methods for binary mixtures with different molecular weights, *Phys. Rev. E*, 71, p. 046704.

McNamara, G. R., Garcia, A. L. and Alder, B. J. (1995). Stabilization of thermal lattice Boltzmann models, *J. Stat. Phys.*, 81, pp. 395–408.

McNamara, G. R., Garcia, A. L. and Alder, B. J. (1997). A hydrodynamically correct thermal lattice Boltzmann model, *J. Stat. Phys.*, 87, pp. 1111–1121.

McNamara, G. R. and Zanetti, G. (1988). Use of the Boltzmann equation to simulate lattice gas automata, *Phys. Rev. Lett*., 61, pp. 2332–2335.

Mei, R., Luo, L.-S., Lallemand, P. and d'Humières, D. (2006). Consistent initial conditions for lattice Boltzmann simulations, *Comput. Fluids*, 35, 855–862.

Mei, R., Luo, L.-S. and Shyy, W. (1999). An accurate curved boundary treatment in the lattice Boltzmann method, *J. Comput. Phys.*, 155, pp. 307–330.

Mei, R. and Shyy, W. (1998). On the finite difference-based lattice Boltzmann method in curvilinear coordinates, *J. Comput. Phys.*, 143, pp. 426–448.

Mei, R., Yu, D. and Shyy, W. (2002). Force evaluation in lattice Boltzmann method involving curved geometry, *Phys. Rev. E*, 65, p. 041203.

Mendoza, M., Boghosian, B. M., Herrmann1, H. J. and Succi, S. (2010). Fast lattice Boltzmann solver for relativistic hydrodynamics, *Phys. Rev. Lett*., 105, p. 014502.

Menon, S. and Soo, J.-H. (2004). Simulation of vortex dynamics in three-dimensional synthetic and free jets using the large-eddy lattice Boltzmann method, *J. Turb.*, 5, pp. 1–26.

Mezrhab, A., Bouzidi, M. and Lallermand, P. (2004). Hybrid lattice-Boltzmann finite-difference simulation of convective flows, *Comput. Fluids*, 33, pp. 623–641.

Min, M. and Lee, T. (2011). A spectral-element discontinuous Galerkin lattice-Boltzmann method for incompressible flows, *J. Comput. Phys.*, 230, pp. 245–259.

Mishra, S. C. and Roy, H. K. (2007). Solving transient conduction and radiation heat transfer problems using the latticeBoltzmann method and the finite volume method, *J. Comput. Phys*., 223, pp. 89–107.

Morse, T. (1964). Kinetic model equations for a gas mixture, *Phys. Fluids*, 7, pp. 2012–2013.

Mukherjee, S. and Abraham, J. (2007). A pressure-evolution-based multi-relaxation-time high-density-ratio two-phase lattice-Boltzmann model, *Comput. Fluids*, 36, pp. 1149–1158.

Nannelli, F. and Succi, S. (1992). The lattice Boltzmann-equation on irregular lattices, *J. Stat. Phys.*, 68, pp. 401–407.

Nie, X. B., Doolen, G. D. and Chen, S. (2002). Lattice-Boltzmann simulations of fluid flows in MEMS, *J. Stat. Phys*., 107, pp. 279–289.

Nithiarasu, P., Seetharamu, K.N. and Sundararajan, T. (1997). Natural convective heat transfer in a fluid saturated variable porosity medium, *Int. J. Heat Mass Tran*., 40, pp. 3955–3967.

Nieuwstadt, F. and Keller, H. B. (1973). Viscous flow past circular cylinders, *J. Fluid Mech.*, 1, 59–71.

Niu, X. D., Chew Y. T. and Shu, C. (2003). Simulation of flows around an impulsively started circular cylinder by Taylor series expansion and least squares-based lattice Boltzmann method, *J. Comput. Phys.*, 188, pp. 176–193.

Niu, X. D., Shu, C. and Chew, Y. T. (2004). A lattice Boltzmann BGK model for simulation of micro flows, *Europhys. Lett*., 67, pp. 600–606.

Niu, X. D., Shu, C., Chew, Y. T. and Peng, Y. (2006). A momentum exchange-based immersed boundary-lattice Boltzmann method for simulating incompressible viscous flows, *Phys. Lett. A*, 354, pp.173–182.

Noble, D. R., Chen, S., Georgiadis, J. G. and Buckius, R. O. (1995). A consistent hydrodynamic boundary condition for the lattice Boltzmann method, *Phys. Fluids*, 7, pp. 203–209.

Noble, D. R., Georgiadis, J. G. and Buckius, R. O. (1995). Direct assessment of lattice Boltzmann hydrodynamics and boundary conditions for recirculating flows, *J. Stat. Phys.*, 84, pp. 17–33.

Noble, D. R. and Holdych, D. J. (2007). Full Newton lattice Boltzmann method for time-steady flows using a direct linear solver, *Int. J. Mod. Phys. C*, 4, pp. 652–660.

Ohwada, T., Sone, Y. and Aoki, K. (1989). Numerical analysis of the Poiseuille and thermal transpiration flows between two parallel plates on the basis of the Boltzmann equation for hard-sphere molecules, *Phys. Fluids A*, 1, pp. 2042–2049.

Ohwada, T., Asinari, P. and Yabusaki, D. (2011). Artificial compressibility method and lattice Boltzmann method: similarities and differences, *Comput. Math. Appl.*, 61, pp. 3461–3474.

Palmer, B. J. and Rector, D. R. (2000a). Lattice Boltzmann algorithm for simulating thermal flow in compressible fluids, *J. Comput. Phys.*, 161, pp. 1–20.

Palmer, B. J. and Rector, D. R. (2000b). Lattice-Boltzmann algorithm for simulating thermal two-phase flow, *Phys. Rev. E*, 61, pp. 5295–5306.

Pan, C., Hilpert, M. and Miller, C. T. (2001). Pore-scale modeling of saturated permeabilities in random sphere packings, *Phys. Rev. E*, 64, p. 066702.

Pan, C., Luo, L.-S. and Miller, C. T. (2006). An evaluation of lattice Boltzmann schemes for porous medium flow simulation, *Comput. Fluids*, 35, pp. 898–909.

Pan, C., Prins, J. and Miller, C. T. (2004). A high-performance lattice Boltzmann implementation to model flow in porous media, *Comput. Phys. Commu.*, 158, pp. 89–105.

Patankar, S. (1980). *Numerical Heat Transfer and Fluid Flow* (Hemisphere Publishing Company, New York).

Patila, D. V. and Lakshmish, K. N. (2009). Finite volume TVD formulation of lattice Boltzmann simulation on unstructured mesh, *J. Comput. Phys.*, 228, pp. 5262–5279.

Pavlo, P., Vahala, G. and Vahala, L. (1998). Higher-order isotropic velocity grids in lattice methods, *Phys. Rev. Lett.*, 80, pp. 3960–3963.

Pavlo, P., Vahala, G. and Vahala, L. (2002). Preliminary results in the use of energy-dependent octagonal lattices for thermal lattice Boltzmann simulations, *J. Stat. Phys.*, 107, pp. 499–519.

Peng, G. W., Xi, H. W. and Duncan, C. (1998). Lattice Boltzmann method on irregular meshes, *Phys. Rev. E*, 58, 4124–4127.

Peng, G. W., Xi, H. W. and Duncan, C. (1999). Finite volume scheme for the lattice Boltzmann method on unstructured meshes, *Phys. Rev. E*, 59, pp. 4675–4682.

Peng, Y., Shu, C. and Chew, Y. T. (2003). Simplified thermal lattice Boltzmann model for incompressible thermal flows, *Phys. Rev. E*, 68, p. 026701.

Peng, Y., Shu, C., Chew, Y. T. *et al.* (2006). Application of multi-block approach in the immersed boundary-Lattice Boltzmann method for viscous fluid flows, *J. Comput. Phys.*, 218, pp.460–478.

Peskin, C. S. (1977). Numerical analysis of blood flow in the heart, *J. Comput. Phys.*, 25, pp. 220–252.

Philippi, P. C., Hegele Jr, L. A., dos Santos, L. O. E. and Surmas, R. (2006). From the continuous to the lattice Boltzmann equation: The discretization problem and thermal models, *Phys. Rev. E*, 73, p. 056702.

Pilotti, M. (1998). Generation of realistic porous media by grains sedimentation, *Trans. Porous Media*, 33, pp. 257–278.

Piña, E., García-Colín, L. S. and Goldstein, P. (1995). A new generalization of Enskog's equation for mixtures of dense gases, *Physica A*, 217, pp. 87–106.

Pohl, T., Kowarschik, M., Wilke, J. *et al.* (2003). Optimization and profiling of the cache performance of parallel lattice Boltzmann codess, *Parallel Process. Lett.*, 13, pp. 549–560.

Prasianakis, N. and Boulouchos, K. (2007). Lattice Boltzmann method for simulation of weakly compressible flows at arbitrary Prandtl number, *Int. J. Mod. Phys. C*, 18, pp. 602–609.

Premnath, K. and Abraham, J. (2004). Discrete lattice BGK Boltzmann equation computations of transient incompressible turbulent jets, *Int. J. Modern Physics C*, 15, pp. 699–719.

Premnath, K. N. and Pattison, M. J. (2009). Steady state convergence acceleration of the generalized lattice Boltzmann equation with forcing term through preconditioning, *J. Comput. Phys.*, 228, pp. 746–769.

Premnath, K. N., Pattison, M. J. and Banerjee, S. (2009a). Generalized lattice Boltzmann equation with forcing termfor computation of wall bounded turbulent flows, *Phys. Rev. E*, 79, p. 026703.

Premnath, K. N., Pattison, M. J. and Banerjee, S. (2009b). Dynamic sub-grid scale modeling of turbulent flows using lattice-Boltzmann method, *Physica A*, 388, pp. 2640–2658.

Psihogios, J., Kainourgiakis, M. E., Yiotis, A. G. *et al.* (2007). A Lattice Boltzmann study of non-newtonian flow in digitally reconstructed porous domains, *Transp. Porous Media*, 70, pp. 279–292.

Qi, D. (1999). Lattice-Boltzmann simulations of particles in non-zero-Reynolds-number flows, *J. Fluid. Mech.*, 385, pp. 41–62.

Qian, Y. (1993). Simulating thermohydrodynamics with lattice BGK models, *J. Sci. Comput.*, 8, pp. 231–242.

Qian, Y. H., d'Humières, D. and Lallemand, P. (1992). Lattice BGK models for Navier-Stokes equation, *Europhys. Lett.*, 17, pp. 479–484.

Qian, Y., Succi, S. and Orszag, S. A. (1995). Recent advances in lattice Boltzmann computing, *Ann. Rev. of Comp. Phys.*, 3, pp. 195–242.

Qu, K. (2009). Development of lattice Boltzmann method for compressible flows, PhD Thesis, National University of Singapore.

Qu, K., Shu, C. and Chew, Y. T. (2007a). Alternative method to construct equilibrium distribution functions in lattice-Boltzmann method simulation of inviscid compressible flows at high Mach number, *Phys. Rev. E*, 75, p. 036706.

Qu, K., Shu, C. and Chew, Y. T. (2007b). Simulation of shock-wave propagation with finite volume lattice Boltzmann method, *Int. J. Mod. Phys. C*, 18, pp. 447–454.

Rapaport, D. C. (2004). *The Art of Molecular Dynamics Simulation*, 2nd Ed. (Cambridge University Press, Cambridge).

Roe P. L. (1981). Approximate Riemann solvers, parameter vectors, and difference schemes, *J. Comput. Phys.*, 43, pp. 357–372.

Rossi, N., Ubertini, S., Bella, G. and Succi, S. (2005). Unstructured lattice Boltzmann method in three dimensions, *Int. J. Numer. Meth. Fluids*, 49, pp. 619–633.

Rothman, D. H. and Keller, J. M. (1988). Immiscible cellular-automaton fluids, *J. Stat. Phys.*, 52, 1119–1127.

Rothman, D. H. and Zaleski, S. (1997). *Lattice-Gas Cellular Automata: Simple Models of Complex Hydrodynamics* (Cambridge University Press, Cambridge).

Sagaut, P. (2010). Toward advanced sub-grid models for lattice-Boltzmann-based large-eddy simulation: Theoretical formulations, *Comput. Math. Appl.*, 59, pp. 2194–2199.

Schulz, M., Krafczyk, M., Toelke, J. and Rank, E. (2001). Parallelization strategies and efficiency of CFD computations in complex geometries using lattice-Blotzmann methods on high-performance computers, *Proc. 3rd Int. FORTWIHR Conf. HPSEC*, pp. 115–122

Seta, T. and Takahashi, R. (2002). Numerical stability analysis of FDLBM, *J. Stat. Phys.*, 107, pp. 557–572.

Shan, X. (1997). Simulation of Rayleigh-Bénard convection using a lattice Boltzmann method, *Phys. Rev. E*, 55, pp. 2780–2788.

Shan, X. (2006). Analysis and reduction of the spurious current in a class of multiphase lattice Boltzmann models, *Phys. Rev. E*, 73, p. 047701.

Shan, X. and Chen, H. (1993). Lattice Boltzmann model for simulating flows with multiple phases and components, *Phys. Rev. E*, 47, pp. 1815–1819.

Shan, X. and Chen, H. (1994). Simulation of nonideal gases and liquid-gas phase transitions by the lattice Boltzmann equation, *Phys. Rev. E*, 49, pp. 2941–2948.

Shan, X. and Doolen, G. D. (1995). Multicomponent lattice-Boltzmann model with interparticle interaction, *J. Stat. Phys*., 81, 379–393.

Shan, X., Yuan, X.-F. and Chen, H. (2006). Kinetic theory representation of hydrodynamics: a way beyond the Navier-Stokes equation, *J. Fluid Mech*., 550, pp. 413–441.

Shen, C., Tian, D. B., Xie, C. and Fan, J. (2004). Examination of the LBM in simulation of microchannel flow in transitional regime, *Microscopic Thermophys. Eng*., 8, pp. 423–432.

Shi, W. P., Shyy, W. and Mei, R. W. (2001). Finite-difference-based lattice Boltzmann method for inviscid compressible flows, *Numer. Heat Trans. B*, 40, pp. 1–21.

Shi, X., Lin, J. and Yu, Z. (2003). Discontinuous Galerkin spectral element lattice Boltzmann method on triangular element, *Int. J. Numer. Meth. Fluids*, 42, pp. 1249–1261.

Shi, Y., Zhao, T. S. and Guo, Z. L. (2004). Thermal lattice Bhatnagar-Gross-Krook model for flows with viscous heat dissipation in the incompressible limit, *Phys. Rev. E*, 70, p. 066310.

Shu, C., Chew, Y. T. and Niu, X. D. (2001). Least square-based LBM: A meshless approach for simulation of flows with complex geometry, *Phys. Rev. E.*, 64, p. 045701.

Shu, C., Niu, X. D. and Chew, Y. T. (2002). Taylor series expansion- and least square-based lattice Boltzmann method: two-dimensional formulation and its applications, *Phys. Rev. E*, 65, p. 036708.

Shakhov, E. M. (1968). Generalization of the Krook kinetic Equation, *Fluid Dyn*. 3, pp. 95–96.

Siebert, D. N., Hegele Jr., L. A., dos Santos, L. O. E. and Philippi, P. (2007), Thermal lattice Boltzmann in two dimensions, *Int. J. Mod. Phys. C*, 18, pp. 546–555.

Silva, L. F. Lima E, Silveira-Neto A. and Damasceno, J. J. R. (2003). Numerical simulation of two-dimensional flows over a circular cylinder using the immersed boundary method, *J. Comput. Phys.*, 189, pp. 351–370.

Sirovich, L. (1962). Kinetic modelling of gas mixtures, *Phys. Fluids*, 5, pp. 908–918.

Sirovich, L. (1966). mixtures of maxwell molecules, *Phys. Fluids*, 9, pp. 2323–2326.

Skordos, P. A. (1993). Initial and boundary conditions for the lattice Boltzmann method, *Phys. Rev. E*, 48, pp. 4823–4842.

Sofonea, V. and Sekerka, R. F. (2005). Boundary conditions for the upwind finite difference lattice Boltzmann model: evidence of slip velocity in micro-channel flow, *J. Comput. Phys.*, 207, pp. 639–659.

Somers, J. A. (1993). Direct simulation of fluid flow with cellular automata and the lattice-Boltzmann equation, *Appl. Sci. Res*., 51, pp. 127–133.

Sone, Y., Ohwada, T. and Aoki, K. (1989). Temperature jump and Knudsen layer in a rarefied gas over a plane wall, *Phys. Fluids A*, 1, pp. 363–370.

Spaid, M. A. A. and Phelan, F. R. (1997). Lattice Boltzmann methods for modeling microscale flow in fibrous porous media, *Phys. Fluids*, 9, pp. 2468–2474.

Spaid, M. A. A. and Phelan, F. R. (1998). Modeling void formation dynamics in fibrous porous media with the lattice Boltzmann method, *Composit. Part A*, 29A, pp. 749–755.

Spasov, M., Rempfer, D. and Mokhasi, P. (2009). Simulation of a turbulent channel flow with an entropic Lattice Boltzmann method, *Int. J. Num. Meth. Fluids*, 60, pp. 1241–1258.

Stiebler, M., Tölke, J. and Krafczyk, M. (2006). An upwind discretization scheme for the finite volume lattice Boltzmann method, *Comput. Fluids*, 35, pp. 814–819.

Stops, D. W. (1970). The mean free path of gas molecules in the transition regime, *J. Phys. D*, 3, pp. 685–696.

Succi, S. (2001). *The Lattice Boltzmann Equation for Fluid Dynamics and Beyond* (Clarendon, Oxford).

Succi, S., Amati, G. and Benzi, R. (1995). Challenges in lattice Boltzmann computing, *J. Stat. Phys*., 81, pp. 5–16.

Succi, S., Bella, G. and Papetti, F. (1997). Lattice kinetic theory for numerical combustion, *J. Sci. Comput.*, 12, pp. 395–408.

Succi, S., Chen, H., Karlin, I. and Orszag, S. (2000). Resummation techniques in the kinetic-theoretical approach to subgrid turbulence modeling, *Physica A*, 280, pp. 92–98.

Succi, S., Filippova, O., Chen, H. and Orszag, S. (2002). Towards a renormalized lattice Boltzmann equation for fluid turbulence, *J. Stat. Phys*., 107, pp. 261–278.

Succi, S. (2002). Mesoscopic modeling of slip motion at fluid-solid interfaces with heterogeneous catalysis, *Phys. Rev. Lett*., 89, p. 064502.

Succi, S., Benzi, R. and Higuera, F. (1991). The lattice Boltzmann equation: a new tool for computational fluid dynamics, *Physica D*, 47, pp. 219–230.

Succi, S., Foti, E. and Higuera, F. (1989). Three-dimensional flows in complex geometries with the lattice Boltzmann method, *Europhys. Lett*., 10, pp. 433–438.

Suh, Y. K., Kang, J. and Kang, S. (2008). Assessment of algorithms for the no-slip boundary condition in the lattice Boltzmann equation of BGK model, *Int. J. Numer. Meth. Fluids*, 58, pp.1353–1378.

Sukop, M. C. and Thorne, D. T. Jr. (2006). *Lattice Boltzmann Modeling: An Introduction for Geoscientists and Engineers* (Springer, New York).

Sun, C. H. (1998). Lattice-Boltzmann models for high speed flows, *Phys. Rev. E*, 58, pp. 7283–7287.

Sun, C. H. (2000a). Adaptive lattice Boltzmann model for compressible flows: viscous and conductive properties, *Phys. Rev. E*, 61, pp. 2645–2653.

Sun, C. H. (2000b). Simulations of compressible flows with strong shocks by an adaptive lattice Boltzmann model, *J. Comput. Phys.*, 161, pp. 70–84.

Sun, C. H. and Hsu, A. T. (2003). Three-dimensional lattice Boltzmann model for compressible flows, *Phys. Rev. E*, 68, p. 016303.

Sun, C. H. and Hsu, A. T. (2004). Multi-level lattice Boltzmann model on square lattice for compressible flows, *Comput. Fluids*, 33, pp. 1363–1385.

Swift, M. R., Orlandini, E., Osborn, W. and Yoemans, J. M. (1996). Lattice Boltzmann simulations of liquid-gas and binary fluid systems, *Phys. Rev. E*, 54, pp. 5041–5052.

Swift, M. R., Osborn, W. and Yoemans, J. M. (1995). Lattice Boltzmann simulation of nonideal fluids, *Phys. Rev. Lett.*, 75, pp. 830–833.

Szalmás, L. (2008). Variable slip coefficient in binary lattice Boltzmann models, *Cent. Eur. J. Phys*., 6, pp. 786–791.

Tang, G. H., Tao, W. Q. and He, Y. L. (2005). Lattice Boltzmann method for gaseous microflows using kinetic theory boundary conditions, *Phys. Fluids*, 17, p. 058101.

Teixeira, C. (1998). Incorporating turbulence models into the lattice-Boltzmann method, *Int. J. Mod. Phys. C*, 9, pp. 1159–1175.

Teixeira, C., Chen, H. and Freed, D. M. (2000). Multi-speed thermal lattice Boltzmann method stabilization via equilibrium under-relaxation, *Comput. Phys. Commun*., 129, pp. 207–226.

ten Cate, A., van Vliet, E., Derksen, J. J. and den Akker, H. (2006). Application of spectral forcing in lattice-boltzmann simulations of homogeneous turbulence, *Comput. Fluids*, 35, pp. 1239–1251.

Thürey, N. and Rüde, U. (2009). Stable free surface flows with the lattice Boltzmann method on adaptively coarsened grids, *Comput. Visual. Sci*., 12, pp. 247–263.

Tölke, J. (2009). Implementation of a lattice Boltzmann kernel using the compute unified device architecture developed by nVIDIA, *Comput. Visual Sci.*, 13, pp. 29–39.

Tölke, J., Freudiger, S. and Krafczyk, M. (2006). An adaptive scheme using hierarchical grids for lattice Boltzmann multi-phase flow simulations, *Comput. Fluids*, 35, pp. 820–830.

Tölke, J., Krafczyk, M. and Rank, E. (2002). A mutligrid-solver for the discrete Boltzmann-equation, *J. Stat. Phys.*, 107, pp. 573–591.

Tölke, J., Krafczyk, Schulz, M. and Rank, E. (1998). Implicit discretization and nonuniform mesh refinement approaches for FD discretization of LBGK models, *Int. J. Mod. Phys. C*, 9, pp. 1143–1157.

Tölke, J., Krafczyk, M., Schultz, M. and Rank, E. (2002). Lattice Boltzmann simulations of binary fluid flow through porous media, *Philos Trans. Royal Soc London. A*, 360, pp. 535–545.

Toschi, F. and Succi, S. (2005). Lattice Boltzmann method at finite Knudsen numbers, *Europhys. Lett.*, 69, pp. 549–555.

Toschi, F., Amati, G., Succi, S. *et al.* (1999). Intermittency and structure functions in channel flow turbulence, *Phys. Rev. Lett*., 82, pp. 5044–5047.

Turkel, E. (1999). Preconditioning techniques in computational fluid dynamics, *Annu. Rev. Fluid Mech.* 31, pp. 385–416.

Ubertini, S. and Succi, S. (2005). Recent advances of lattice Boltzmann techniques on unstructured grids, *Prog. Comput. Fluid Dyna.*, 5, pp. 85–96.

van Albada, G. D., van Leer, B. and Roberts, W. W. (1982). A comparative study of computational methods in cosmic gas dynamics, *Astron. Astrophys.*, 108, pp. 76–84.

Van Beijeren, H. and Ernst, M. (1973a). The modified Enskog equation, *Physica*, 68, pp. 437–456.

Van Beijeren, H. and Ernst, M. (1973b). The modified Enskog equation for mixtures, *Physica*, 70, pp. 225–242.

van Leer, B. (1982). Flux-vector splitting for the Euler equations, *Lecture Notes in Physics*, 170, pp. 507–512.

van Treeck, C., Rank, E., Krafczyk, M. *et al.* (2006). Extension of a hybrid thermal LBE scheme for large-eddy simulation of turbulent convective flows, *Comput. Fluids*, 35, pp. 863–871.

Verberg, R. and Ladd. A. J. C. (1999). Simulation of low-Reynolds-number flow via a time-independent lattice-Boltzmann method, *Phys. Rev. E*, 60, pp. 3366–3373.

Verhaeghe, F., Blanpain, B. and Wollants, P. (2007). Lattice Boltzmann method for double-diffusive natural convection, *Phys. Rev. E*, 75, p. 046705.

Wagner, A. J. (2003). The origin of spurious velocities in lattice Boltzmann, *Int. J. Mod. Phys. B*, 17, pp. 193–196.

Wagner, L. (1994). Pressure in lattice Boltzmann simulations of flow around a cylinder, *Phys. Fluids*, 6, pp. 3516–3518.

Wagner, L. and Hayot, F. (1995). Lattice Boltzmann simulations of flow past a cylindrical obstacle, *J. Stat. Phys.*, 81, pp. 63–70.

Wager, W. (1995). Approximation of the Boltzmann equation by discrete velocity models, *J. Stat. Phys*., 78, pp. 1555−1570.

Wang, M. R. and Kang, Q. J. (2010). Modeling electrokinetic flows in microchannels using coupled lattice Boltzmann method, *J. Comput. Phys*., 229, pp. 728–744.

Wang, M., Wang, J., Pan, N. and Chen, S. (2007). Mesoscopic predictions of the effective thermal conductivity for microscale random porous media. *Phys. Rev. E*, 75, p. 036702.

Watari, M. and Tsutahara, M. (2003). Two-dimensional thermal model of the finite-difference lattice Boltzmann method with high spatial isotropy, *Phys. Rev. E*, 67, p. 036306.

Wellein, G., Lammers, P., Hager, G. *et al.* (2006). Towards optimal performance for lattice Boltzmann applications on terascale computers, *Proc. 2005 Int. Conf. Parallel Comput. Fluid Dyn*., pp. 31–40.

Williamson, C. H. K. and Roshko, A. (1988). Vortex formation in the wake of an oscillating cylinder, *J. Fluids Struct*., 2, pp. 355–381.

Williamson, C. H. K. (1996). Vortex dynamics in the cylinder wake, *Ann. Rev. Fluid Mech*., 28, pp. 477–539.

Wolfram, S. (1986). Cellular Automaton Fluids 1: Basic Theory, *J. Stat. Phys*., 45, pp. 471–529.

Wolf-Gladrow, D. A. (2000). *Lattice-Gas Cellular Automata and Lattice Boltzmann Models: An Introduction* (Springer, New York).

Woods, L. C. (1993). *An Introduction to the Kinetic Theory of Gases and Magneto-plasmas* (Oxford University Press, USA).

Wu, J. and Shu, C. (2011). A solution-adaptive lattice Boltzmann method for two-dimensional incompressible viscous flows, *J. Comput. Phys.*, 230, pp. 2246–2269.

Xi, H. W., Peng, G. W. and Chou, S. H. (1999a). Finite-volume lattice Boltzmann method, *Phys. Rev. E*, 59, pp. 6202–6205.

Xi, H. W., Peng, G. W. and Chou, S. H. (1999b). Finite-volume lattice Boltzmann schemes in two and three dimensions, *Phys. Rev. E*, 60, pp. 3380–3388.

Xu, K. (1993). *Numerical hydrodynamics from gas-kinetic theory*, Ph.D. Thesis, Columbia University.

Xu, S. J. and Zhou, Y. (2002). Effect of a streamwise oscillating cylinder on a downstream cylinder wake, *Proc. 11th Int. Symp. Appl. Laser Techn. Fluid Mech*., Lisbon, 8-11 July, 2002. Paper 34.4.

Yan, G. W., Chen, Y. S. and Hu, S. X. (1999). Simple lattice Boltzmann model for simulating flows with shock wave, *Phys. Rev. E*, 59, pp. 454–459.

Yang, J. Y. and Huang, J. C. (1995). Rarefied flow computations using nonlinear model Boltzmann equation, *J. Comput. Phys*., 120, pp. 323−329.

Yang, L. M., Shu, C. and Wu, J. (2012). Development and comparative studies of three non-free parameter lattice Boltzmann models for simulation of compressible flows, *Adv. Appl. Math. Mech.*, 4, pp. 454–472.

Ye, T., Mittal, R., Udaykumar, H. S. and Shyy, W. (1999). An accurate Cartesian grid method for viscous incompressible flows with complex boundaries, *J. Comput. Phys*., 156, pp. 209–240.

Yoshino, M., Hotta, Y., Hirozane, T. and Endo, M. (2007). A numerical method for incompressible non-Newtonian fluid flows based on the lattice Boltzman method, *J. NonNewtonian Fluid Mech.*, 147, pp. 69–78.

Yu, Z. and Fan, L.-S. (2009). An interaction potential based lattice Boltzmann method with adaptive mesh refinement (AMR) for two-phase flow simulation. *J. Comput. Phys.*, 228, pp. 6456–6478.

Yu, D. and Girimaji, S. S. (2005). DNS of homogeneous shear turbulence revisited with the lattice Boltzmann method, *J. Turbul.*, 6, pp. 1–17.

Yu, D. and Girimaji, S. S. (2006). Direct numerical simulations of homogeneous turbulence subject to periodic shear, *J. Fluid Mech*., 566, pp. 117–151.

Yu, D., Mei, R., Luo, L.-S. and Shyy, W. (2003). Viscous flow computations with the method of lattice Boltzmann equation, *Prog. Aero. Sci.*, 39, 329–367.

Yu, D., Mei, R. and Shyy, W. (2002). A multi-block lattice Boltzmann method for viscous fluid flows, *Int. J. Numer. Meth. Fluids*, 39, pp. 99–120.

Yu, D., Mei, R. and Shyy, W. (2003). A unified boundary treatment in lattice Boltzmann method, *Proc. 41st Aero. Sci. Meeting Exhibit.*, AIAA, p. 2003–0953.

Yu, H. D. and Girimaji, S. S. (2005). Near-field turbulent simulations of rectangular jets using lattice Boltzmann method, *Phys. Fluids*, 17, p. 125106.

Yu, H. D., Girimaji, S. and Luo, L.-S. (2005a) Lattice Boltzmann simulations of decaying homogeneous isotropic turbulence, *Phys. Rev. E*, 71, p. 016708.

Yu, H. D., Girimaji, S. and Luo, L.-S. (2005b). DNS and LES of decaying isotropic turbulence with and without frame rotation using lattice Boltzmann method, *J. Comput. Phys.*, 209, pp. 599–616.

Yu, H. D., Luo, L.-S. and Girimaji, S. S. (2006). LES of turbulent square jet flow using anMRT lattice Boltzmann model, *Comput. Fluids*, 35, pp. 957–965.

Yu, H. D. and Zhao, K. H. (2000). Lattice Boltzmann method for compressible flows with high Mach numbers, *Phys. Rev. E*, 61, pp. 3867–3870.

Zdravkovich, M. M. (1987). The effects of interference between circular cylinders in cross flow, *ASME J. Fluids Eng*., 1, pp. 239–261.

Zhang, H. F., Ge, X. S. and Ye, H. (2006). Randomly mixed model for predicting the effective thermal conductivity of moist porous media, *J. Phys. D*, 39, pp. 220–226.

Zhang, J. F. and Kwok, D. Y. (2006). Pressure boundary condition of the lattice Boltzmann method for fully developed periodic flows, *Phys. Rev. E*, 73, p. 047702.

Zhang, Y. H., Gu, X. J., Barber, R. W. and Emerson, D. R. (2006). Capturing Knudsen layer phenomena using a lattice Boltzmann model, *Phys. Rev. E*, 74, p. 046704.

Zhang, Y. H., Qin, R. and Emerson, D. R. (2005). Lattice Boltzmann simulation of rarefied gas flows in microchannels, *Phys. Rev. E*, 71, p. 047702.

Zhao, Y. (2008). Lattice Boltzmann based PDE solver on the GPU, *Visual Comput*., 24, pp. 323–333.

Zheng, H. W., Shu, C. and Chew, Y. T. (2005). Lattice Boltzmann interface capturing method for incompressible Flows, *Phys. Rev. E*, 72, p. 056705.

Zheng, H. W., Shu, C. and Chew, Y. T. (2006). A lattice Boltzmann model for multiphase flows with large density ratio, *J. Comput. Phys*., 218, pp. 353–371.

Zheng, Z. C. and Zhang, N. (2008). Frequency effects on lift and drag for flow past an oscillating cylinder, *J. Fluids Struct*., 24, pp. 527–541. pp. 382–399.

Zhou, J. G. (2004). *Lattice Boltzmann Methods for Shallow Water Flows* (Springer, New York).

Zou, Q. and He, X. (1997). On pressure and velocity boundary conditions for the lattice Boltzmann BGK model, *Phys. Fluids*, 9, pp. 1591–1597.

Zou, Q., Hou, S., Chen, S. and Doolen, G. D. (1995). An improved incompressible lattice Boltzmann model for time-independent flows, *J. Stat. Phys.*, 81, pp. 35–48.

Index